An experimental investigation of the crossflow over tube bundles.

Balabani, Stavroula

AN EXPERIMENTAL INVESTIGATION OF THE CROSSFLOW OVER TUBE BUNDLES

Stavroula BALABANI

Thesis submitted for the degree of Doctor of Philosophy in the University of London

King's College London
Department of Mechanical Engineering

July 1996

To my parents

ABSTRACT

The thesis describes an experimental investigation of the crossflow over heat exchanger tube bundles. The velocity characteristics of three tube bundle configurations, one in-line and two staggered arrays with a transverse pitch ratio S_T/d of 3.6 and longitudinal pitch ratios S_L/d of 2.1, 1.6 and 2.1 respectively, were investigated in a water tunnel under subcritical flow conditions. The mean velocities and turbulence level distributions in the first five rows of the tube bundles were determined from ensemble-averaged LDA measurements in the axial and transverse directions. Spectra, time- and length-scales and dissipation rates were determined from time-resolved LDA measurements taken in the staggered array with S_L/d=1.6. The effect of Reynolds number on the recirculation characteristics and the pressure drop was studied. A series of experiments was carried out with rough and tapered tubes, in order to determine the extent that the flow characteristics in the tube bundles are affected by surface roughness and tube shape in relation to fouling. The crossflow of a dilute suspension of particles over the in-line tube array was also investigated using an amplitude discrimination technique. Liquid crystal thermographic techniques were employed to measure tube surface temperatures in the in-line tube array.

The geometry of the bundle was found to affect significantly the mean velocities and the turbulence structure. The staggered arrays were found to generate higher levels of turbulence and higher pressure drop than the in-line array. The turbulence in the wake regions in all three geometries is anisotropic with transverse r.m.s. velocities being higher than the axial ones. This finding suggests that CFD modelling of the flow based on the assumption of isotropic eddy viscocity may not be appropriate. A discrete flow periodicity associated with vortex shedding with a Strouhal number of 0.26 was identified in the staggered array with S_L/d=1.6. Vortex shedding was pronounced between the third and fourth rows. This flow periodicity broadened the

random turbulence levels by almost 50 % in some locations. Increasing the longitudinal spacing in the staggered array resulted in lower r.m.s. levels in the wakes and affected the recirculating parameters of the bundle but had a negligible effect on the pressure drop. Surface roughness did not affect the flow but there was a pronounced influence of the forebody shape of the cylinders. The application of the liquid crystal thermographic technique yielded the first such temperature data on tube bundle flows. The implications of the results for CFD predictions of flows over tube bundles are discussed.

ACKNOWLEDGEMENTS

It gives me great pleasure to acknowledge the assistance of a number of people during the course of the research and the preparation of this thesis. I acknowledge with gratitude the constant supervision, encouragement, guidance and valuable advice and criticism of Prof. M. Yianneskis. I am obliged, for the time and knowledge generously given by Dr. K. C. Lee, who introduced me to experimental techniques and helped me with the graphics software and other computing related issues.

I am grateful to Messrs D. Elgar, P. LeForte, R. Moslin, J. Greenberg and especially A. Heaney for their help in the design and construction of the experimental equipment, and to J. Laker, M. Distelhoff and L. Y. Ong of Imperial College for modifying one of the frequency counters and the data acquisition software used in this work.

I would like to thank D. Bouris and Prof. Bergeles of the National Technical University of Athens for providing me with numerical data and for fruitful discussions on CFD, and all my colleagues for their help and assistance.

I am indebted to the Commission of the European Union for the financial support provided for this work.

Finally, I wish to thank my parents, who have always supported me in all my endeavours throughout the years, my brother George who motivated me and was instrumental in my undertaking these postgraduate studies and Petros for his support and understanding.

TABLE OF CONTENTS

Abstract i
Acknowledgements iii
Table of Contents iv
Nomenclature vii
List of Captions xi
List of Tables xvii
1 INTRODUCTION 1
1.1 Preamble 1
1.2 Literature Review 5
1.2.1 Single Cylinder in Cross-Flow 6
1.2.2 Small Groups of Cylinders 8
1.2.3 Tube Bundles in Cross-Flow 10
1.3 Objectives of the Present Investigation 32
1.4 Outline of the Thesis 33
2 FLOW CONFIGURATIONS AND MEASUREMENT TECHNIQUES 36
2.1 Introduction 36
2.2 Flow Configurations 37
2.2.1 Tube Bundle Models 37
2.2.2 Rough - Surfaced Tubes 39
2.2.3 Simulation of Fouled Tubes 41
2.3 Experimental Rig 42
2.4 Flow Measurement Techniques 43
2.4.1 Laser Doppler Anemometry 43
2.4.2 Optical Configuration 45
2.4.3 Signal Processing and Data Acquisition 49
2.5 Measurement Errors and Uncertainty 62
2.5.1 Positional Errors 62
2.5.2 Frequency Shifting 63
2.5.3 Bias Effects 63
2.5.4 Broadening Effects 65
2.5.5 Count Ambiquity 66
2.5.6 Statistical Errors 67
2.6 Closure 67

3 VELOCITY CHARACTERISTICS OF A TYPICAL STAGGERED ARRAY 80

3.1 Introduction 80

3.2 Mean Velocity Distributions 82

3.3 Turbulence Level Distributions 84

3.4 Flow Periodicity, Turbulence Spectra and Scales 86

3.4.1 Spectral Characteristics 88

3.4.2 Filtered r.m.s. levels and Turbulent Scales 93

3.4.3 Rate of Dissipation 98

3.5 Wake Characteristics 100

3.5.1. Centreline mean and r.m.s. Velocities 100

3.5.2 Recirculating Parameters 102

3.6 Effect of Reynolds Number 106

3.6.1 Centreline mean and r.m.s. Velocities 107

3.6.2 Pressure Drop 108

3.7 Closure 109

4 THE EFFECTS OF TUBE SPACING AND TUBE ARRANGEMENT 136

4.1 Introduction 136

4.2 The Effect of Tube Spacing - 3.6 x 2.1 Staggered Array 137

4.2.1 Mean Velocity Distributions 137

4.2.2 Turbulence Level Distributions 142

4.2.3 Wake Characteristics 143

4.2.4 Effect of Reynolds Number 150

4.3 Effect of Tube Arrangement - 3.6 x 2.1 In-Line Array 153

4.3.1 Mean Velocity Distributions 153

4.3.2 Turbulence Level Distributions 153

4.3.3 Wake Characteristics 154

4.3.4 Pressure Drop 158

4.4 Closure 158

5 THE EFFECTS OF SURFACE ROUGHNESS, TUBE SHAPE AND PARTICLE LADEN FLOWS 191

5.1 Introduction 191

5.2 The Effect of Surface Roughness 193

5.2.1 Mean Velocity Distributions 193

5.2.2 Turbulence Level Distributions 195

5.2.3 Wake Characteristics 196

5.2.4 Pressure Drop 199

5.3 The Effect of Tube Shape 199
5.3.1 Mean Velocity Characteristics 199
5.3.2 Turbulence Characteristics 201
5.3.3 Recirculating Parameters 202
5.4 Particle Velocities of a Solid/Liquid Flow over the In-Line Array .205
5.5 Closure 211
6 APPLICATION OF LIQUID CRYSTAL THERMOGRAPHIC TECHNIQUES IN TUBE BUNDLES 239
6.1 Introduction 239
6.2 Liquid Crystals 241
6.3 Thermographic Applications of Liquid Crystals 244
6.4. Colour Specification 249
6.5 Data Acquisition and Image Processing System 254
6.6 Experimental Procedures 255
6.6.1 Flow Configuration 255
6.6.2 Calibration 258
6.7 Temperature Distribution Measurements 259
6.8 Closure 262
7 CONCLUSIONS AND RECOMMENDATIONS FOR FUTURE WORK 272
7.1 The Present Contribution and Main Findings 272
7.2 Recommendations for Future Work 278
References 281
Appendix I 301
Appendix II 303
Appendix III 306

NOMENCLATURE

Roman symbols		*Units*
b	Laser beam diameter	m
b_o	Laser beam waist at $1/e^2$ intensity	m
b_x	Diameter of measurement volume	m
b_y	Length of measurement volume	m
C_D	Drag coefficient of particles	
c_k, c_o, c_1, c_2	Constants in notch filtering function	
d	Cylinder diameter	m
d_k, d_1, d_2	Constants in notch filtering function	
ΔP	Pressure drop across bundle	Pa
d_p	Mean diameter of particles	m
E(f)	One-dimesional energy spectrum	m^2/s
f	Frequency	Hz
f_1, f_2, f_3	Focal lengths of lenses of the anemometer	m
f_c	Nyquist frequency	Hz
f_D	Doppler frequency	Hz
f_S	Frequency shift	Hz
$\overline{G}_k$	Power spectral density as defined by Bendat and Piersol (1971)	m^2/s
h	CIE 1976 *u'*, *v'* hue angle	°
h	Sampling time interval	s
H(f)	Filter frequency response function	
H_k	Discrete Fourier Transform	
h_k	Discrete values of a continuous function h(t); also discrete inverse Fourier Transform	
k	Height of surface roughness elements	m
k	Turbulence kinetic energy	m^2/s^2
K	Kurtosis or flatness factor of velocity p.d.f.	
L	Characteristic length scale; cylinder length	m
l/d	Dimensionless distance from tube surface	
l_r	Recirculation length	m
m	Order of diffracted beams	
$\dot{m}_r$	Recirculating mass flowrate per unit length of cylinder, normalised with $\frac{1}{2}\rho U_\infty d$,	kg/m s

N	Number of transverse rows in a tube bundle	
n	Number of lines in grating	
$\vec{n}$	Preferred direction of molecular axes in liquid crystals	
$\bar{n}$	Mean refractive index	
N_G	Rotational speed of the grating	rev/min
p	Pitch of the cholesteric helical structure	m
P(f)	Power spectral density as defined by Press et al (1986)	m^2/s^2
R	Correlation coefficient of curve fitting	
$R(\tau)$	Autocorrelation function coefficient	
R_f	Fouling resistance	$W^{-1}m^2K$
R, G, B	CIE 1931 standard colorimetric observer red, green and blue tristimulus values	
s	CIE 1976 *u'*, *v'* saturation	
S_L	Longitudinal spacing (centre-to-centre distance)	m
S_T	Transverse spacing (centre-to-centre distance)	m
S	Skewness of velocity p.d.f.; also spacing in standard tube bundle and two-cylinder configurations	m
T	Temperature	°C
T_E	Integral timescale	s
u	Instantaneous fluctuating velocity component in x-direction	m/s
u'	Axial r.m.s velocity	m/s
u'	Characteristic velocity scale	m/s
u', v'	CIE 1976 uniform chromaticity scale co-ordinates	
u'_n , v'_n	CIE 1976 uniform chromaticity scale co-ordinates for a reference white	
u'_f	Single-phase fluid axial r.m.s. velocity	m/s
u'_p	Particle axial r.m.s. velocity	m/s
U	Mean velocity in x - direction	m/s
U_f	Single-phase axial mean fluid velocity	m/s
U_g	Mean velocity in minimum cross-sectional area	m/s
U_{max}	Maximum axial velocity at the shear layer	m/s
U_{min}	Axial mean velocity at the interface between the shear layer and the recirculation bubble	m/s
U_p	Particle axial mean velocity in two-phase flow	m/s
$U_{particle}$	Velocity of particles crossing the measurement volume	m/s
U_T	Particle terminal velocity	m/s
U_∞	Upstream bulk velocity	m/s

v	Instantaneous fluctuating velocity component in y-direction	m/s
v'	R.m.s. velocity in y-direction	m/s
V	Mean velocity in y - direction	m/s
w	Instantaneous fluctuating velocity component in z-direction	m/s
w'	R.m.s. velocity in z-direction	m/s
w_r	Recirculation half-width	m
W	Mean velocity in z-direction	m/s
x, y, z	Co-ordinates in three orthogonal directions	m
x, y, z	Chromaticity co-ordinates	
X, Y, Z	CIE 1931 tristimulus values	

Greek Symbols

α	Width of frequency notch as a fraction of ω_o	
δ	Dimensionless vorticity thickness, expressed in tube diameters	
δ'	Dimensionless spreading rate of δ	
ΔP	Pressure drop	Pa
ΔT	Temperature variation	°C
ε	Rate of dissipation of k,	m^2/s^3
ζ	Pressure drop coefficient, $\Delta P / (N(\rho / 2)U_g^2$.	
$(\partial U / \partial y)_{max}$	Maximum gradient within the shear layer	s^{-1}
θ	Angle of intersection of laser beams	°
θ_I	Angle of illumination	°
θ_S	Angle of observation	°
κ	Wavenumber	m^{-1}
λ	Wavelength	m
λ^*	Fringe spacing	m
Λ_f	Integral length scale	m
λ_f	Micro length scale	m
μ	Dynamic viscocity of fluid	kg/m/s
ν	Kinematic viscosity of fluid	m^2/s
ρ	Fluid density	kg/m^3
ρ_p	Particle density	kg/m^3
τ	Correlation time	s
τ_E	Micro timescale	s
τ_f	Fluid response time	s

τ_p	Particle relaxation time	s
ϕ	Angular distance from the front stagnation point of a cylinder	°
ω	Parametric frequency variable, tan(πfh) (bilinear transformation)	
ω_o	Centre frequency of the notch	

Dimensionless numbers

Re_d	Reynolds number, $U_g d/\nu$
Re_p	Particle Reynolds number, $U_T d_p/\nu$
Re_∞	Reynolds number, $U_\infty d/\nu$
St	Strouhal number, f d/U_g.

Abbreviations

CFD	Computational Fluid Dynamics
CIE	Commision Internationale de l' Eclairage
DC	Direct current
FFT	Fast Fourier Transform
HSI (or HSV)	Hue, saturation and intesity (or value) decomposition of colour images
LDA	Laser Doppler Anemometry
NTUA	National Technical University of Athens
p.d.f.	Probability density function
PPC	Public Power Corporation of Greece
PSD	Power spectral density
r.m.s.	Root mean square
RGB	Red, green, blue decomposition of colour images
VDU	Visual display unit

LIST OF CAPTIONS

1.1. In-line and staggered tube bundle geometries 35

1.2. Standard tube bundle geometries 35

2.1. Cross-section of the three tube bundle configurations investigated 76

2.2. Roughness patterns applied to the tube surface of the 3.6 x 1.6 staggered tube bundle 77

2.3. Tube shapes of the fouled cylinders in the first (a) and second row (b) of a staggered tube bank as predicted by NTUA fouling model after 8 hours of fouling by Al_2O_3 particles 77

2.4. Schematic layout of the experimental facility 78

2.5. Optical configuration of the LDA system used 78

2.6. Signal processing system for ensemble-averaged LDA measurements 79

2.7. Characteristic Doppler signals from: (a) solid particles and (b) micron size particles following the fluid motions (impurities in the water in the present study) 79

3.1. Velocity vectors in the 3.6 x 1.6 staggered array (Re_d = 12,858) 112

3.2. Distribution of axial mean velocities, U/U_∞, in the 3.6 x 1.6 staggered array (Re_d = 12,858) 113

3.3. Distribution of transverse mean velocities, V/U_∞, in the 3.6 x 1.6 staggered array (Re_d = 12,858) 114

3.4. Distribution of axial r.m.s. velocities, u'/U_∞, in the 3.6 x1.6 staggered array (Re_d = 12,858) 115

3.5. Distribution of transverse r.m.s. velocities, v'/U_∞, in the 3.6 x1.6 staggered array (Re_d = 12,858) 116

3.6. Distribution of v'/u' in the 3.6 x1.6 staggered array (Re_d = 12,858) 117

3.7. Distribution of $|v'-u'| / U_\infty$ in the 3.6 x1.6 staggered array (Re_d = 12,858) 118

3.8. Profiles of w'/U_∞ in the 3.6 x1.6 staggered array (Re_d = 12,858) 119

3.9. Distribution of the turbulence kinetic energy, k/U_∞^2, in the 3.6 x 1.6 staggered tube bank (Re_d = 12,858) 120

3.10. Typical velocity recordings obtained in the 3.6 x 1.6 staggered array (Re_d = 12,858) 121

3.11. Typical autocorrelation function obtained in the second row of the 3.6 x 1.6 staggered array (x/d = 1.6, y/d = 0.6; Re_d = 12,858) 122

3.12(a). Amplitude spectra of the axial velocity component in the 3.6 x 1.6 staggered array (Re_d = 12,858); half rows indicate a location

midway between successive rows 123

3.12(b). Amplitude spectra of the transverse velocity component in the 3.6 x 1.6 staggered array (Red = 12,858) 124

3.13. Row-to-row variation of the normalised amplitude of the dominant frequency (34 Hz) observed in the 3.6 x 1.6 staggered array (Re_d = 12,858) 125

3.14. Typical power spectrum obtained at x/d=1.6 and y/d=0.6 in the 3.6 x 1.6 staggered array (Re_d = 12,858) 125

3.15. Axial r.m.s. velocities for unfiltered and filtered data compared with numerical predictions in the 3.6 x 1.6 staggered array (Re_d = 12,858) 126

3.16. Experimental and numerical estimates of integral timescales T_E in the 3.6 x 1.6 staggered bank (Re_d = 12,858) 126

3.17. Micro timescales τ_E estimated from filtered data in the 3.6 x 1.6 staggered bank (Re_d = 12,858) 127

3.18. Macro length scales Λ_f estimated from filtered data in the 3.6 x 1.6 staggered bank (Re_d = 12,858) 127

3.19. Micro length scales λ_f estimated from the filtered data in the 3.6 x 1.6 staggered bank (Re_d = 12,858) 128

3. 20. Estimates of the rate of dissipation ε computed from $\varepsilon = u'^3/d$ and comparisons with numerical values in the 3.6 x 1.6 staggered bank (Re_d = 12,858) 128

3. 21. Estimates of the rate of dissipation ε computed from ε (= u'^3/Λ_f) and comparisons with numerical values in the 3.6 x 1.6 staggered bank (Re_d = 12,858) 129

3. 22. Estimates of the rate of dissipation ε computed from $\varepsilon = 30\nu u'^2/\lambda_f^2$ and comparisons with numerical values in the 3.6 x 1.6 staggered bank (Re_d = 12,858) 129

3.23. Development of the axial mean velocities, U/U_∞, downstream of the first four rows in the 3.6 x 1.6 staggered array (Re_d = 12,858) 130

3.24. Development of the axial r.m.s. velocities, u'/U_∞, downstream of the first four rows in the 3.6 x 1.6 staggered array (Re_d = 12,858) 130

3.25. Streamline patterns in the 3.6 x 1.6 staggered array (Re_d = 12,858) 131

3.26. Effect of Re_d on the centreline development of U downstream of the first (a) and third (b) rows of the 3.6 x 1.6 staggered array 132

3.27. Variation of recirculation length with Re_d in the 3.6 x 1.6 staggered array 133

3.28. Effect of Re_d on the centreline development of u' downstream of the first (a) and third (b) rows of the 3.6 x 1.6 staggered array 134

3.29. Variation of pressure drop coefficient ζ with Re_d in the 3.6 x 1.6 staggered array 135
4.1. Velocity vectors in the 3.6 x 2.1 staggered array (Re_d = 12,858) 160
4.2. Distribution of axial mean velocities, U/U_∞, in the 3.6 x 2.1 staggered array (Re_d = 12,858) 161
4.3. Distribution of transverse mean velocities, V/U_∞, in the 3.6 x 2.1 staggered array (Re_d = 12,858) 162
4.4. Distribution of axial velocity skewness in the 3.6 x 2.1 staggered array (Re_d = 12,858) 163
4.5. Distribution of transverse velocity skewness in the 3.6 x 2.1 staggered array (Re_d = 12,858) 164
4.6. Distribution of axial velocity kurtosis (or flatness) in the 3.6 x 2.1 staggered array (Re_d = 12,858) 165
4.7. Distribution of transverse velocity kurtosis (or flatness) in the 3.6 x 2.1 staggered array (Re_d = 12,858) 166
4.8. Distribution of axial r.m.s. velocities, u'/U_∞, in the 3.6 x 2.1 staggered array (Re_d = 12,858) 167
4.9. Distribution of transverse r.m.s. velocities, v'/U_∞, in the 3.6 x 2.1 staggered array (Re_d = 12,858) 168
4.10. Distribution of v'/u' in the 3.6 x 2.1 staggered array (Re_d = 12,858) 169
4.11. Distribution of $|v'-u'| / U_\infty$ in the 3.6 x 2.1 staggered array (Re_d = 12,858) 170
4.12. Development of the axial mean velocities, U/U_∞, downstream of the first four rows in the 3.6 x 2.1 staggered array (Re_d = 12,858) 171
4.13. Comparison of the centreline U/U_∞ profiles between the 3.6 x 1.6 and 3.6 x 2.1 staggered arrays and the 3.6 x 2.1 in-line array (Re_d = 12,858) 172
4.14. Development of the axial r.m.s. velocities, u'/U_∞, downstream of the first four rows in the 3.6 x 2.1 staggered array (Re_d = 12,858) 173
4.15. Comparison of the centreline u'/U_∞ profiles between the 3.6 x 1.6 and 3.6 x 2.1 staggered arrays and the 3.6 x 2.1 in-line array (Re_d = 12,858) 174
4.16. Development of the transverse r.m.s. velocities, v'/U_∞, downstream of the first and third rows of the 3.6 x 2.1 staggered array (Re_d = 12,858) 175
4.17. Centreline profiles of v'/u' (a) and $|v'-u'| / U_\infty$ (b) in the 3.6 x 2.1 staggered array (Re_d = 12,858) 176
4.18. Streamline patterns in the 3.6 x 2.1 staggered array (Re_d = 12,858) 177

4.19. Effect of Re_d on the centreline development of U downstream of the first (a) and third (b) rows of the 3.6 x 2.1 staggered array 178

4.20. Effect of Re_d on the centreline development of u' downstream of the first (a) and third (b) rows of the 3.6 x 2.1 staggered array 179

4.21. Variation of the pressure drop coefficient ζ with Re_d in the 3.6 x 2.1 staggered array compared with the 3.6 x 1.6 staggered and the 3.6 x 2.1 in-line array 180

4.22. Velocity vectors in the 3.6 x 2.1 in-line array (Re_d = 12,858) 181

4.23. Distribution of axial mean velocities, U/U_∞, in the 3.6 x 2.1 in-line array (Re_d = 12,858) 182

4.24. Distribution of transverse mean velocities, V/U_∞, in the 3.6 x 2.1 in-line array (Re_d = 12,858) 183

4.25. Distribution of axial r.m.s. velocities, u'/U_∞, in the 3.6 x 2.1 in-line array (Re_d = 12,858) 184

4.26. Distribution of transverse r.m.s. velocities, v'/U_∞, in the 3.6 x 2.1 in-line array (Re_d = 12,858) 185

4.27. Distribution of v'/u' in the 3.6 x 2.1 in-line array (Re_d = 12,858) 186

4.28. Distribution of $|v'-u'| / U_\infty$ in the 3.6 x 2.1 in-line array (Re_d = 12,858) 187

4.29. Development of the axial mean velocities, U/U_∞, downstream of the first four rows in the 3.6 x 2.1 in-line array (Re_d = 12,858) 188

4.30. Development of the axial r.m.s. velocities, u'/U_∞, downstream of the first four rows in the 3.6 x 2.1 in-line array (Re_d = 12,858) 189

4.31. Streamline patterns in the 3.6 x 2.1 in-line array (Re_d = 12,858) 190

5.1. U/U_∞ profiles in the 3.6 x 1.6 rough staggered array with evenly distributed roughness and comparison with the smooth tube array (Re_d = 12,858) 213

5.2. V/U_∞ profiles in the 3.6 x 1.6 rough staggered array with evenly distributed roughness and comparison with the smooth tube array (Re_d = 12,858) 214

5.3. Velocity vectors in the 3.6 x 1.6 rough staggered array with randomly distributed roughness (Re_d = 12,858) 215

5.4. Distribution of axial mean velocities, U/U_∞, in the 3.6 x 1.6 rough staggered array with randomly distributed roughness (Re_d = 12,858) 216

5.5. Distribution of transverse mean velocities, V/U_∞, in the 3.6 x 1.6 rough staggered array with randomly distributed roughness (Re_d = 12,858) 217

5.6. u'/U_∞ profiles in the 3.6 x 1.6 rough staggered array with evenly distributed roughness and comparison with the smooth array

(Re_d = 12,858) 218

5.7. v'/U_∞ profiles in the 3.6 x 1.6 rough staggered array with evenly distributed roughness and comparison with the smooth tube array (Re_d = 12,858) 219

5.8. Distribution of axial r.m.s. velocities, u'/U_∞, in the 3.6 x 1.6 rough staggered array with randomly distributed roughness (Re_d = 12,858) 220

5.9. Distribution of transverse r.m.s. velocities, v/U_∞, in the 3.6 x 1.6 rough staggered array with randomly distributed roughness (Re_d = 12,858) 221

5.10. Distribution of v'/u' in the 3.6 x 1.6 rough staggered array with randomly distributed roughness (Re_d = 12,858) 222

5.11. Distribution of $|v'-u'| / U_\infty$ in the 3.6 x 1.6 rough staggered array with randomly distributed roughness (Re_d = 12,858) 223

5.12. Comparison of the centreline U/U_∞ profiles between the smooth and rough staggered arrays (Re_d = 12,858) 224

5.13. Streamline patterns in the 3.6 x 1.6 rough staggered array with randomly distributed roughness (Re_d = 12,858) 225

5.14. Comparison of the centreline u'/U_∞ profiles between the smooth and rough staggered arrays (Re_d = 12,858) 226

5.15. The effect of tube surface roughness on the pressure drop across the 3.6 x 1.6 staggered array 227

5.16. Distribution of axial mean velocities, U/U_∞, in the 3.6 x 1.6 staggered array with tapered cylinders in the first two rows (Re_d = 12,858) 228

5.17. Centreline development of U/U_∞ in the 3.6 x 1.6 staggered array with tapered cylinders in the first two rows and comparison with circular cylinders (Re_d = 12,858) 229

5.18. Distribution of axial r.m.s. velocities, u'/U_∞, in the 3.6 x 1.6 staggered array with tapered cylinders in the first two rows (Re_d = 12,858) 230

5.19. Centreline development of u'/U_∞ in the 3.6 x 1.6 staggered array with tapered cylinders in the first two rows and comparison with circular cylinders (Re_d = 12,858) 231

5.20. Streamline patterns in the 3.6 x 1.6 staggered array with tapered cylinders in the first two rows (Re_d = 12,858) 232

5.21. Single-phase and particle axial mean velocity profiles, U/U_∞, in the 3.6 x 2.1 in-line array (Re_d = 12,858) 233

5.22. Single-phase and particle axial r.m.s. velocity profiles, u'/U_∞, in the 3.6 x 2.1 in-line array (Re_d = 12,858) 236

6.1. Molecular arrangement in smectic liquid crystals 263

6.2. Molecular arrangement in nematic liquid crystals 263

6.3. Molecular arrangement in cholesteric liquid crystals 264
6.4. The CIE *x*, *y* chromaticity diagram 265
6.5. The CIE *u'*, *v'* chromaticity diagram showing the definitions of hue and saturation 265
6.6. European colour television primaries shown in (a) the x, y chromaticity diagram and (b) the *u'*, *v'* chromaticity diagram 266
6.7. Data acquisition and image processing system 267
6.8. Schematic diagram of a copper tube covered with liquid crystal film 268
6.9. Video image of the modified in-line tube bundle model for temperature measurements using liquid crystals 268
6.10. Calibration curves for the first and second row tubes 269
6.11. Wall temperatures measured in first (a) and second (b) row tubes (in-line tube bundle with $S_T/d = 3.6$, $S_L/d = 2.1$; $Re_d = 12{,}858$) 271
III.1. Amplitude spectrum of velocity recording at x/d=1.6 and y/d=0.6 before(a) and after (a) applying notch filtering to the vortex shedding frequency; dc component is also removed 310
III.2. Low and high frequency variations obtained at x/d=1.6 and y/d=0.6 when notch filtering is applied; only part of the record is shown 311
III.3. Low and high frequency variations obtained at x/d=1.6 and y/d=0.6 when moving window averaging is applied (window size = 41); only part of the record is shown 311
III.4. Amplitude spectra of the high (a) and low (b) frequency oscillations at x/d=1.6 and y/d=0.6 obtained with moving window averaging (window size=41) 312
III.5. Low and high frequency variations obtained at x/d=1.6 and y/d=0.6 when low pass filtering is applied (cut-off frequency = 49 Hz); only part of the record is shown 313

LIST OF TABLES

2.1. Dimensions and geometrical parameters of the tube bundle models 39

2.2. Characteristics of the LDA system used 48

2.3. Studies of spectral analysis techniques and estimation of turbulence quantities 69

3.1. Recirculating parameters in 3.6 x 1.6 staggered configuration 103

3.2. Maximum centreline r.m.s. velocity fluctuations, u'_{max}/U_{∞}, in 3.6 x 1.6 staggered tube bank 108

4.1. Recirculating parameters in 3.6 x 2.1 staggered array compared with those of the 3.6 x 1.6 staggered array 148

4.2. Maximum normalised centreline r.m.s. velocity fluctuations, u'_{max}/U_{∞}, in 3.6 x 2.1 staggered tube bank compared with 3.6 x 1.6 staggered bank 152

4.3. Recirculation characteristics of the 3.6 x 2.1 in-line configuration 158

5.1. Length and width of the recirculation bubbles in 3.6 x 1.6 staggered array with randomly rough cylinders 198

5.2. Recirculating parameters for the 3.6 x 1.6 staggered bank with tapered cylinders 204

5.3. Particle properties and characteristic parameters 208

6.1. Chromaticities of the three primaries used in television 254

CHAPTER 1

INTRODUCTION

1.1 PREAMBLE

This thesis is concerned with experimental investigations of tube bundles in cross-flow. The main part of the work is concerned with the velocity characteristics of tube bundle flows which were quantified by laser Doppler anemometry. A liquid crystal thermographic technique was also developed in order to determine tube surface temperature distributions.

Tube bundles in cross-flow are of substantial practical interest due to their wide applications in shell-and-tube heat exchangers found in the process and power generation industries. In the power generation industry, for example, tube bundles are used as superheaters or economisers in lignite utility boilers to recover heat from the flue gases. The efficiency and performance of such heat exchangers is determined by the flow and heat transfer characteristics of the tube bundles which in turn depend to a large extent on the tube bundle geometry and flow conditions.

During normal operation of heat exchangers both the inner and outer surfaces of the tubes are subjected to fouling by fluid impurities. For example, in lignite utility boilers ash particles from the combustion of coal deposit on the outer tube surface of heat exchangers resulting in the so-called gas-side fouling. Fouling of the tube surface imposes a serious constraint in the design and operation of heat exchanger equipment: it increases the resistance to heat transfer and therefore inhibits efficient utilisation and management of both the energy output and the pumping requirements. It has been

estimated that heat exchanger fouling alone may result to a cost to the European Community in excess of 10 billion ECU per annum, with 2-3 billion of this representing energy losses (Pilavachi and Isdale, 1992). Higher capital expenditure through oversized plants, maintenance (including cleaning and use of anti-foulants) and loss of production during shutdown also contribute to this high penalty incurred by fouling.

Current practice in the design of heat exchanger equipment is to determine the overall heat transfer coefficient allowing for an extra thermal resistance due to fouling, the fouling factor. Knowledge of the convection coefficients, geometrical parameters and the fouling factors is therefore required. Convection coefficients are usually estimated from empirical correlations which are available in many heat exchanger design handbooks. These correlations are valuable tools in the design process but have their limitations. They are often applicable to specific geometries and flow situations and may vary from each other. Their accuracy is limited since it is difficult to take all the relevant parameters into account. Values of the fouling factor are usually obtained from published data, such as the Standards of the Tubular Exchanger Manufacturers Association (TEMA, 1988) or other 'experience-based' sources of questionable accuracy. These values are usually constants and in general fail to take into account the time-dependent nature of fouling.

Flow periodic phenomena are also present in tube bundles which may incite tube vibrations in liquid and intense noise in gas flows. Four excitation mechanisms have been identified: turbulent buffeting, vorticity shedding, fluid-elastic instability and acoustic resonance. The nature of these mechanisms has been the subject of considerable controversy for many years. The vorticity shedding excitation has been attributed either to vortices shed from the tubes or to instabilities of the flows between tubes. An empirical approach is normally used in order to design against tube and acoustic resonance which involves mismatching of the potential vortex shedding

frequencies and the tube natural frequencies or the acoustic natural frequencies of the heat exchanger shell. Knowledge of the Strouhal number (i.e. the non-dimensional frequency of vortex shedding) is required for a given tube bundle geometry. However, there is considerable scatter in the published Strouhal number data due to the variety of configurations, measuring locations, experimental conditions and techniques employed, as well as due to the existence of multiple Strouhal numbers.

Computer-aided analysis techniques have advanced the engineering design in many areas of practical interest. Recently, Computational Fluid Dynamics (CFD) techniques have emerged as a powerful engineering tool in the design and simulation of industrial processes due to rapid developments in computational power and speed and in numerical methodologies. The lower cost of a computational investigation compared to the expenses involved in experimentation has attracted many researchers and designers. By simulating the fluid flow and heat transfer phenomena in tube bundles, reliable design guidelines and performance criteria for heat exchangers may be established. CFD analysis involves the numerical solution of the governing differential equations for fluid and heat transfer. The effect of turbulence is taken into account using appropriate turbulence models such as the k-ε or Reynolds stress models. With the recent developments in two-phase flow models, particle trajectories can also be predicted and particle deposition models can be developed for the prediction of fouling in heat exchangers. The accuracy of the CFD modelling, however, depends on the initial and boundary conditions specified or the turbulence models employed. The latter are usually based on various assumptions and simplifications about the structure of turbulence which are not always fulfilled in complex flows such as those in tube bundles. The existence of flow periodicities complicates the problem further and extensive validation against experiments is often required. Thus, despite the current CFD capabilities some experimentation is still necessary. Detailed and accurate experimental velocity data are needed in order to gain a better understanding of the flow structures in tube bundles and improve the numerical modelling of such flows.

Such data can only be obtained with non-interfering techniques such as laser Doppler anemometry (LDA). The validity of numerical predictions of heat transfer coefficients can also be ascertained with surface temperature data obtained using non-obtrusive techniques such as liquid crystal thermography.

Although the flow over a single cylinder has been extensively investigated, tube bundles have received less attention due to the complexity of the flows and the associated measurement difficulties. The problem is further complicated by the vast number of configurations encountered in practice, resulting in different flow patterns, and by the effects of parameters such as Reynolds number, surface roughness and free stream turbulence. Most of the early experimental studies were concerned with the overall pressure drop and heat transfer coefficients since these parameters are of prime interest in the design of heat exchangers. Only a few LDA studies, concerned with specific tube arrangements, have been reported. Characterisation of the flow field around the first rows of a tube bundle in terms of flow instabilities, turbulence structure and wake properties is of great interest. This region is known to experience discrete flow periodicities (Ziada and Oengöeren,1991; Polak and Weaver, 1991; Weaver et al, 1991, 1993; Oengöeren and Ziada, 1995) and severe fouling (Bergeles et al, 1996; Bemrose and Bott, 1984) and its prediction by CFD techniques is often very difficult.

In view of the complexity of tube bundle flows it is not surprising that the volume of experimental studies on particle-laden cross-flows is considerably small. Moreover, the gas-side fouling characteristics of tube bundles have not been widely investigated: a different degree of fouling from row to row and different shapes of the deposited layer have been observed but the effect of parameters such as tube arrangement and spacing has not been the subject of a systematic investigation. Fouling alters the shape of the tubes and the surface roughness which affect the flow field around the tubes

and subsequent particle deposition. These effects, however, are not well documented in the literature.

Previous experimental investigations of flows in tube bundles are reviewed in the following section in order to outline the current state of knowledge, identify the relevant parameters and variables of interest and formulate the objectives of the present work. The present work comprises part of a research programme investigating the effects of fouling on the efficiency of heat exchangers in lignite utility boilers (Bergeles et al., 1996). The main objectives of the programme were to study the flow and heat transfer characteristics of typical tube bundle arrangements in order to improve the understanding of the processes involved in gas-side fouling and develop a numerical computer code extensively validated against experimental data for the prediction of fouling in tube bundle heat exchangers. In conjunction with the present experimental work, CFD predictions of the flow and the fouling process were carried out in the National Technical University of Athens and observations of ash fouling in lignite utility boilers were performed by the Public Power Corporation of Greece.

1.2 LITERATURE REVIEW

Since to date entire books have been written on the subject of fluid flow and heat transfer in tube bundles an exhaustive review of all previous work cannot be given in this thesis. Therefore, this section presents a review of the most pertinent literature on the flow and heat transfer phenomena in tube bundles. Emphasis is placed upon the experimental investigations on fluid flow over tube bundles but heat transfer is also briefly considered. Both single-phase and two-phase flows are considered. The flows over a single cylinder and groups of two or three cylinders were chosen as a starting point in this review since they represent simpler cross-flow situations and will aid the understanding of the more complicated nature of tube bundle flows. A more extensive review can be found in Balabani and Yianneskis (1993a).

1.2.1 SINGLE CYLINDER IN CROSS-FLOW

The simplest form of cross-flow to consider is that over a single circular cylinder. The literature on the flow past a single cylinder is voluminous due to its relative simplicity. It is beyond the scope of the present investigation to review this literature in detail. However, a brief account of the main features of the flow over a single cylinder is essential in understanding more complicated flows such as these over tube bundles.

The flow past a single circular cylinder is primarily determined by the Reynolds number, Re_d, where d is the cylinder diameter. Various flow regimes have been identified for different Re_d ranges, each characterised by the corresponding boundary layer behaviour. At very low Re_d (< 1.0) the inertia forces are negligible and the flow pattern is potential in nature. If Re_d is increased in the range 2 - 30, two symmetrical vortices are formed behind the cylinder and the flow is laminar and steady. With increasing Re_d the vortices elongate and at about Re_d = 40 - 70 a periodic oscillation of the wake is observed. At a Re_d range of 90 - 300 the vortices break off from each side alternately, forming two rows of vortices in the wakes known as vortex street (similar to the von Karman vortex street). The *subcritical regime* is established for Re_d > 300, characterised by laminar boundary layer separation at about 80° to 85° from the front stagnation point. The wake formed behind the cylinder is wider than the cylinder diameter (Roshko, 1961). This regime persists up to the *critical* Re_d of 2 x 10^5 at which *transition* of the boundary layer from laminar to turbulent occurs. Laminar separation bubbles followed by turbulent reattachment and delayed final separation at about 140° are the main features of this regime. A narrower wake, with a width smaller than the cylinder diameter, is also formed. For higher Re_d the *supercritical* regime is established; transition occurs closer to the front stagnation point and separation moves upstream while for even higher Re_d (>3.5 x 10^6) the *transcritical regime* is established. Transition to turbulence in the boundary layer occurs sufficiently close to the front stagnation point so that the flow becomes

independent of Re_d. A broader wake - but narrower than the cylinder diameter (Roshko, 1961) - is formed. Both the drag coefficient and the Strouhal number are different in each flow regime.

Transition from one flow regime to another may occur at slightly different Re_d's than the ones mentioned earlier depending on a number of parameters such as the turbulence of the oncoming flow, nearness of other solid objects, surface roughness and aspect ratio (length / diameter) of the cylinder. For example, surface roughness or increased turbulence can promote transition to turbulence in the boundary layer and result in a reduction of the critical Re_d.

Experimental investigations of flows over circular cylinders often concentrate on certain regions of the flow, specific ranges of Re_d or examine a particular physical phenomenon. The flow around the separation point and the wake (near, intermediate or far wake) of a cylinder in subcritical flow has been the subject of many investigations (Bloor,1964; Gerrard, 1966, 1967; Bloor and Gerrard, 1966; Maekawa and Mizuno, 1967; Cantwell and Coles, 1983; Varty and Currie, 1984a; McKillop and Durst, 1984; Absil, 1988; Massons et al, 1989; Telionis et al, 1992; Antonia et al, 1993). A table with relevant early contributions has been compiled by Cantwell and Coles (1983). Four characteristic lengths have been found to be significant in characterising the near wake flow of a cylinder in the subcritical regime: these are the *length of the separated laminar shear layer*, the *length of the vortex formation region*, *the length of the recirculation bubble* and the *diffusion length*. The end of the formation region is where fluid from outside the wake first crosses the axis by the action of the growing vortex on the other side. The diffusion length is the thickness of the shear layer at the end of the formation region where the layer is drawn across the wake. Usually the length of the formation region is greater than the length of the recirculation bubble (Gerrard, 1966). All the aforementioned lengths vary with Re_d. There is some discrepancy in the published values due to the different definitions

employed for the determination of these lengths. McKillop and Durst (1984) presented a comprehensive study of the subcritical flow (Re_d = 15, 000) over a single cylinder in which all the above parameters were estimated and compared with previously reported ones. They found that a separated laminar shear layer occurred for up to 0.4 d behind the cylinder and became turbulent further downstream. The recirculation bubble extended up to 1.65 d and the formation region up to 1.9 d.

The three-dimensional effects of large-scale vorticity in the far wake flow have also been addressed by a number of investigators (Bisset et al, 1990a; Bisset et al, 1990b; Ferre et al, 1990; Wu et al, 1994). A great effort has been directed at understanding the flow features in the critical and supercritical Re_d numbers (Roshko, 1961; Farell and Blessman, 1983). A number of investigators reported on the effects of surface roughness at high Re_d by measuring drag and lift coefficients and Strouhal numbers (Batham, 1973; Achenbach, 1971; Güven et al, 1980; Nakamura and Tomonari, 1982; Ribeiro, 1990a,b; Shih et al, 1993). It has now been well recognised that surface roughness can not only promote the boundary layer transition from laminar to turbulent but also affects significantly the subsequent flow development at Re_d's well above the critical.

1.2.2 SMALL GROUPS OF CYLINDERS

The flow interference between two circular cylinders in various arrangements has been reviewed by Zdravkovich (1977, 1987). All possible arrangements of two cylinders were grouped in in-line (tandem), side-by-side and staggered configurations. Zdravkovich (1987) distinguished between four kinds of flow interference between two cylinders:

- *proximity interference* which takes place when the cylinders are close to each other but the downstream cylinder is not submerged in the wake of the other,

- *wake interference* which takes place when one cylinder is near or submerged into the wake of the other,
- a third interference regime in which a combination of the above effects may occur and
- a regime of negligible interference in which the flow around each cylinder is identical to that around a single cylinder.

The occurrence of different flow regimes depends primarily on the spacing between the two cylinders. Parameters such as those mentioned earlier for the flow past a single cylinder are also influential, i.e. the upstream conditions, Re_d, turbulence intensity and length scale, the aspect ratio of the tubes, surface roughness etc.

Zdravkovich identified three flow patterns in subcritical flow over an in-line arrangement of two cylinders. These depended on the spacing (S/d) and consequently whether the shear layer separating from the upstream tube rolled up in front of the downstream tube, reattached on the front of the downstream tube or formed vortices behind the downstream tube without reattachment. The exact spacings at which transition from one regime to another occurs were found to depend on Re_d. The flow was found to be bistable at these spacings. Ljungkrona et al (1991a) and Ljungkrona and Sundén (1993) identified a *critical spacing* of about S/d = 3.5 by an abrupt increase in the drag coefficient and St number. The critical spacing was found to decrease with increasing Re_d in the range $3{,}300 < Re_d < 12{,}000$.

Wu et al (1994) studied the vortex shedding and spanwise coherence of velocity fluctuations of two cylinders in tandem. They found that for small spacings (S/d < 3) the vortex shedding from the upstream cylinder was suppressed and the spanwise coherence was higher whereas for large spacings (S/d > 4) the flow downstream of the first cylinder was more turbulent and three-dimensional and spanwise coherence was reduced.

Three flow patterns were also identified when two cylinders are placed side-by-side under laminar or subcritical flow conditions (Zdravkovich, 1987). For small spacings a single vortex street is formed behind both cylinders. For intermediate spacings a narrow and a wide wake is formed behind the first and second cylinder respectively and the gap flow forms a jet biased towards the narrow wake. The flow is bistable, i.e. the jet switches to the opposite direction at irregular time intervals and the narrow and wide wakes interchange behind the cylinders. For large spacings both near wakes are equal in size, the two vortex streets are coupled and shedding is synchronised.

Staggered arrangements produce very complicated flow patterns compared to the in-line and side-by-side arrangements due to the variety of interference effects that may occur and classification is difficult. Zdravkovich attempted to classify the various arrangements according to the sign of the lift force or whether the drag force is greater or less than that of a single cylinder.

LDA velocity measurements of the flows over a single cylinder, two cylinders side by side and three cylinders side by side and in staggered arrangements at very low Re_d (laminar flow) have been reported by Bates (1982). He showed that the size of the eddies varies appreciably with each configuration.

1.2.3 TUBE BUNDLES IN CROSS-FLOW

Numerous experimental studies have been carried out on the fluid flow and heat transfer in tube bundles due to their wide applications in heat exchangers. Until recently the majority of the investigations were concerned primarily with the overall pressure drop and heat transfer. Pierson (1937), Huge (1937) and Grimison (1937) were among the first to study systematically the heat transfer and pressure drop of staggered and in-line tube bundles of various arrangements in cross-flow of gases. A substantial amount of data on heat transfer and pressure drop were gathered at the

University of Delaware. Some of these data were presented by Bergelin et al (1949) while Mueller (1983) reviewed and discussed this work.

Extensive studies have been performed at the Academy of Sciences, Lithuania. This work has been summarised in two publications by Zukauskas (1972, 1989) which provide a very large set of data and a comprehensive discussion of the fluid dynamics, heat transfer and flow-induced vibrations in tube bundles. A wide range of configurations and Re_d numbers are considered and correlations for the total pressure drop and heat transfer coefficients are presented. The flow patterns, surface pressure and shear stress profiles around a tube in a bundle and the velocity and turbulence in tube bundles have been reviewed by Nishimura (1986).

A number of studies have been also performed on rough and finned surfaces since surface roughness has attracted considerable attention as a means of augmenting heat transfer. Work at higher Reynolds numbers exceeding the critical one has been reported by Achenbach (1983, 1989, 1991) for both smooth and rough bundles.

In recent years a great deal of research has been conducted on the flow induced vibration phenomena in tube bundles. Although this thesis is not concerned with these phenomena per se, the underlying mechanisms such as vortex shedding are of great influence in the flow patterns and the velocity characteristics of tube bundles in cross-flow. A review of the flow-induced phenomena in cross-flow heat exchangers is given by Weaver and Fitzpatrick (1988), Pettigrew and Taylor (1991) and Zukauskas (1989).

Two-phase flows occur in many industrial applications employing shell-and-tube heat exchangers such as condensers, boilers and economisers used in coal-fired boilers, to name but a few. In view of the complexity of multiphase flows in tube banks, it is not

surprising that the volume of experimental studies is considerably smaller than for single-phase flow.

Two are the most common tube bundle arrangements: in-line and staggered, in which the tubes are either aligned or staggered with respect to the direction of the fluid velocity upstream of the bundle, U_∞, as shown in Figure 1.1. Each configuration is characterised by the following geometrical parameters: the tube diameter d, the transverse S_T and the longitudinal S_L spacings between the tubes, the so-called transverse and longitudinal pitches (centre-to-centre distances). The non-dimensional spacings, S_T/d and S_L/d respectively, are sufficient to describe a particular geometry. For simplicity, a specific geometry is henceforth referred to as "S_T/d x S_L/d". Investigations of standard geometries such as normal square, rotated square, normal triangular and parallel triangular are often reported in the literature. These geometries, shown in Figure 1.2, are described by a single spacing parameter, S/d.

It is interesting to note that various definitions of Reynolds numbers have been employed by investigators. The Reynolds number used here, Re_d, is based on the tube diameter d, and the maximun velocity, U_g, at the minimum flow area and it is the most commonly used. U_g occurs at the transverse plane in in-line arrangement whereas in staggered ones it may occur at either the transverse or the diagonal plane, depending on the spacing. Another Reynolds number definition, based on the upstream velocity and tube diameter, Re_∞, has also been employed.

Flow regimes

The basic interference flow regimes identified in small groups of cylinders in cross-flow (Zdravkovich, 1987) are not sufficient to describe the additional interactions in larger groups of cylinders since the flows may become more complex as the number of cylinders in cross-flow increases. However, various flow regimes can be identified

in tube bundles in cross-flow depending on the arrangement and geometrical parameters of the tube bank, Reynolds number, freestream turbulence intensity and surface roughness, in a manner similar to that in the flow past a single cylinder. The occurrence of different flow patterns may depend on the aspect ratio of the tubes as well. However, this effect has not been well documented and relatively few studies (for example, Hill et al, 1986) have been concerned with this parameter.

The following flow regimes have been distinguished by Zukauskas (1989):

1. predominantly laminar flow ($Re_d < 10^3$) ,
2. mixed or subcritical flow ($Re_d < 2x10^5$),
3. predominantly turbulent or critical flow ($Re_d > 2x10^5$), and
4. supercritical flow ($Re_d > 4x10^5$).

A transcritical regime also exists at very high Re_d numbers as reported by Achenbach (1983, 1989, 1991). However, transition from one regime to another may start at different values of Re_d depending on the tube bundle arrangement, tube location or surface roughness. For example, Nishimura et al (1993) studied the transitional flow at Re_∞ ranging from 50 to 1,000 in in-line and staggered tube bundles with the same spacings ($S_L/d = S_T/d = 2.0$). The transition from steady to unsteady (periodic) flow occurred at a critical Re_∞ around 100 in inner rows and moved to upstream rows with increasing Re_∞. The upstream development of flow transition due to vortex shedding was much faster in the staggered array than the in-line one, probably due to the higher frequency of vortex shedding occurring in the staggered array. Achenbach studied experimentally the flow and heat transfer characteristics of both smooth and rough, in-line and staggered tube bundles at Re_d's up to 7×10^6. His results revealed the existence of a critical Reynolds number, similar to that in a single cylinder in cross-flow, indicating the transition of the laminar boundary layer to a turbulent one. The critical Reynolds number depended on the surface roughness. With increasing surface roughness the critical Reynolds number decreased, causing thus a premature transition

from a laminar to a turbulent boundary layer. Correlations reflecting that dependence were proposed for both in-line and staggered arrangements.

A number of flow visualisation studies have been performed in tube bundles, mainly in order to gain insight into the flow periodicities encountered in tube bundles. Wallis (1939) was among the first to visualise the free surface flow through various in-line and staggered tube bundles at Re_∞ from 135 to 2,700. His photographs showed that attached eddies were formed alternatively on one side and the other at the back of each tube and the eddies were occasionally dragged into the main stream. The eddy motion was found to be quite distinct from the high speed main stream in the flow lanes between the tube columns and differed from row to row. The longitudinal pitch determined the number of eddies in the wake regions of in-line arrays and the degree of interaction between the flow in the main stream and the wakes. Increasing the transverse spacing reduced the velocity both in the main stream and the wake flows. In the staggered arrays the flow lanes were clearly defined up to the fourth row. Further downstream the flow became irregular and it was difficult to distinguish between the flow lanes and the recirculation regions. When the diagonal gaps were made half the transverse ones the recirculation regions were eliminated and the main stream flowed without noticeable eddying.

Clear alternate vortex shedding in the first rows of normal triangular arrays was observed by Oengöeren and Ziada (1995) at Re_d higher than those investigated above. Flow visualisation in arrays with intermediate spacings (S/d = 2.08) for $1{,}000 < Re_\infty < 10{,}000$ showed that alternating vortex shedding occurred behind the first row. The vortices were convected downstream and promoted vortex shedding from the second row. The latter occurred in a symmetric mode which switched intermittedly to an anti-symmetric mode as well. Downstream of the third row no organised motion was observed. For large spacings (S/d = 3.41) symmetric shedding occurred at the lower

end of Re_d whereas anti-symmetric at the higher range. Conversely, only symmetric vortices were shed in the second row in arrays with small spacings (S/d = 1.61).

The occurrence of clear alternate vortex shedding in normal triangular arrays has been confirmed by a number of investigators (e.g. Polak and Weaver, 1991; Hill et al, 1986; Weaver et al, 1991, 1993) for subcritical Reynolds numbers. Alternate vortex shedding occurs in the first two rows and it is indistinguishable from the turbulence further downstream in the absence of tube motion or acoustic resonance. In an attempt to reveal the nature of the vorticity shedding excitation occurring in in-line arrays Ziada and Oengöeren (1991) carried out visualisation studies. It was found that in arrays with intermediate spacings large scale vortices were formed symmetrically at both sides of each flow lane and anti-symmetrically in the tube wakes (Re_d = 15,000). It should be mentioned, however, that for lower Re_d (Re_d = 7,000) small scale vortex formation not related to the vorticity shedding excitation was observed in the shear layers from the second row tubes. The shear layers did not oscillate up to the fourth row and the thickness of the jet remained uniform. Oscillations started downstream of the fourth row and as the Re_d increased to 15,000 they moved upstream to the third row and the vortex formation occurred behind the first row. Sideway oscillations of the shear layers became more intense when Re_d increased further. The observed anti-symmetric vortex formation was similar but not related to the alternate vortex shedding from isolated cylinders. The same vortex pattern occurred for large spacings, in contrast to the closely packed arrays in which a symmetric vortex pattern was detected in the tube wakes as a result of the smaller size of the vortices and the fact that no mass was transferred across the wakes (Ziada et al, 1989). Flow visualisation in a closely spaced in-line array showed that two stable attached vortices occurred for Re_d up to 1,000. At this Re_d the shear layers started oscillating symmetrically with respect to the flow lanes up to the fifth row. As the Re_d was increased further, the flow at downstream rows became less organised and biased to one side, allowing vortices to be shed sporadically to the main stream. For example, at Re_d = 2,450 symmetric

vortex formation was still visible behind the third row but moved upstream with increasing Re_d. By Re_d = 12,000 well defined vortices could be seen only behind the first row.

Price et al (1995) visualised the interstitial flow in a rotated square array with S/d =1.5 and a parallel triangular one with S/d = 1.375, for 80 < Re_∞ < 1,300. In the rotated array stable symmetric attached vortices were observed at low Re_∞. Periodic extension and contraction of the vortices and consequently a periodic motion of the recirculating flow within the vortices occurred. As the Re_∞ was increased the vortical motion started to oscillate and alternate periodicity of the wake set on. The Re_∞ at which this oscillation started differed between the inner and first rows. The vortex formation process was also found to be different. For example, the vortices behind the first row were formed in the near wake region whereas in inner rows and at lower Re_∞ in the region behind the maximum width of the cylinder. However, little vortical motion was observed in the parallel triangular array. The vortical motion was confined to the wake regions and the vortices remained attached to the cylinders. The vortical motion became more pronounced when the tube vibrated. Vortex shedding in the presence of tube vibrations has also been observed by Weaver and Abd-Rabbo (1985) and Abd-Rabbo and Weaver (1986) in square in-line and rotated square arrays. It was not clear, however, whether that vortex shedding was associated with the tube motion or existed independently. The authors stressed that the observed vortex shedding occurred at very low Re_d in the laminar regime only and was not the same as the phenomenon referred to as vorticity shedding or periodic wake shedding in the literature.

It is clear from the flow visualisation studies referred to above that there is still considerable uncertainty over the existence of large scale vortices in various tube bundle configurations and the mechanisms producing vortical motion. A lot of information about the flow structure and especially about the behaviour of the

boundary layer can be extracted from the distributions of the surface pressure, shear stress, local heat transfer or mass transfer around the tubes of in-line and staggered arrangements. For example, pressure distributions have shown (Aiba et al, 1982a, 1982b) that the flow around the first tubes resembles that of a single cylinder in both in-line and staggered arrays. The separation point might shift slightly further downstream as a result of the blockage caused by neighbouring tubes. The distributions in subsequent rows differ substantially between staggered and in-line arrays. This is due to the fact that the distributions measured in inner rows of in-line arrays are determined by the point of impact, namely the point at the front of the tube where the shear layer from the preceding row reattaches. Asymmetric distributions have been reported for in-line arrays with small spacings (Sterritt and Murray, 1992; Aiba, 1982a; Ljungkrona et al, 1991b).

Achenbach (1989, 1991) investigated the pressure, shear stresses and local heat transfer distributions in smooth and rough tube banks with intermediate spacings ($S_T/d = 2.0$ and $S_L = 1.4$) at high Reynolds numbers ($Re_d = 5 \times 10^4 - 6 \times 10^6$). In in-line arrays the impact point occurred near $\phi = 30°$ for subcritical conditions ($Re_d < 4 \times 10^5$) and it shifted to $\phi = 40° - 45°$ at supercritical and transcritical conditions, where ϕ represents angular distance from the front stagnation point of the cylinders. The surface area covered by a boundary layer ranged from about $\phi = 30°$ to 140°, showing a small variation of the locations of impact and separation with Re_d. A laminar boundary layer existed in that area for subcritical conditions ($Re_d = 1.7 \times 10^5$) which became turbulent at about $\phi = 90°$ for $Re_d = 4 \times 10^5$. With increasing Re_d number the transition point shifted upstream (supercritical flow regime). For $Re_d = 6.1 \times 10^6$ the transition occurred immediately near the impact point indicating the establishment of the transcritical flow regime.

Achenbach's results for a rough in-line tube bundle indicated that even at the lower Re_d examined the flow was transcritical, i.e. the boundary layer was turbulent from

the impact point to the separation point. The point of impact was found to be located near the position identified for the smooth bundle at transcritical conditions, namely at $\phi = 45°$. The point of boundary layer separation, however, moved upstream to $\phi = 110°$. Hence, with increasing surface roughness the transcritical flow separation occurs further upstream, provoking a broader wake and leading to a larger angle of impact in the following row.

Similarly, in a staggered tube bundle with the same spacings (Achenbach, 1989) the boundary layer was found to be still laminar at $Re_d = 1.7 \times 10^5$, indicating subcritical flow conditions, and the separation point occurred at $\phi = 90°$. For $Re_d = 3.8 \times 10^5$, transition to a turbulent boundary layer was observed near $\phi = 70°$. With increasing Reynolds number that location shifted upstream approaching the front stagnation point ($\phi = 10°$ for $Re_d = 6.2 \times 10^6$).

Velocity measurements

Aiba et al (1982a, b) measured the axial mean and r.m.s. velocities with a hot-wire anemometer in in-line and staggered tube banks with small spacings for $Re_d = 30{,}000$ - 41,000. Steep velocity gradients, reversed flows and high velocities in the flow lanes were the main flow features reported. Decreasing the spacing from 1.6 to 1.2 in the square in-line tube bundle resulted in the flow being deflected as a whole, resulting in very irregular velocity and turbulence intensity distributions.

In recent years, detailed information about the velocity and turbulence characteristics of the tube banks became available through LDA measurements. Several LDA studies of tube bundle flows have been reported. Some investigators used the refractive-index matching technique to overcome the measuring difficulties associated with the complex geometry of the tube bundles. However, these investigations were taken either at very low Reynolds numbers (e.g. Nowshiravani et al. 1982) or they were

concerned with complex heat exchangers model (Elphick et al, 1982; Varty and Currie, 1984b). The investigations most relevant to the present work are reviewed below.

Halim (1988) measured axial and transverse mean and r.m.s.velocities in staggered and in-line geometries with spacings lying between 1.5 and 1.8 diameters and Re_d ranging from 60,000 to 110,000. Higher transverse mean velocities were found in the staggered array but in general the turbulence levels were similar in magnitude in both geometries. Results for the staggered array (a normal triangular array with S/d = 1.58) obtained by Halim and Turner (1986) showed pronounced recirculation downstream of the first row with reverse velocities of approximately 40 % of the mean velocity within the bank. The recirculation region extended up to 1.0 d downstream of the centre of the first row tube. This length was found to be independent of Re_d in the range investigated. The flow was considered fully developed after the third row. The turbulence intensity reached a maximum downstream of the second row. In general the turbulence was found to be approximately isotropic except near the rear stagnation point.

Simonin and Barcouda (1986, 1988) measured two velocity components and the Reynolds shear stresses in a rotated square array with S/d = 1.47, for Re_d = 20,000. The results were compared with predictions from a numerical code employing the k-ε turbulence model. It was found that the turbulence was highly anisotropic with the maximum value of turbulence kinetic energy occurring downstream of the second row. The k-ε turbulence model was found to underestimate the turbulence levels in the wakes both in the developing region and the fully developed regions. Meyer (1994) also measured two velocity components and Reynolds stresses in a rotated square array with S/d = 2.0 at Re_d = 32,000. Measurements were taken only between two successive rows in the fully developed region with the purpose of validating CFD models using both the k-ε and a Reynolds stress model. The recirculation bubble was

found to extend up to one diameter from the tube centre. The Reynolds stresses in the recirculation regions were found to be three times higher than those in the main stream. The k-ε model was found to underestimate k in the recirculation region and overestimate it in the rest of the flow and to underestimate the recirculation length. Conversely, the Reynolds stress model predicted longer and narrower recirculation regions and Reynolds stresses much lower than the measured ones.

Flow periodicity

As already mentioned tube bundle heat exchangers are subject to vibration damage or intense noise; the latter is normally generated by the excitation of acoustic standing waves in the heat exchanger enclosure. Vibration occurs when liquid is used as the shell-side fluid, for example as in pressurised water reactors, whereas acoustic problems are usually encountered with boilers or gas reactors. A great deal of research has been carried out and a substantial number of papers has been published on flow-induced vibration phenomena. A comprehensive review of flow-induced vibrations is provided by Weaver and Fitzpatrick (1988). It is generally accepted that four mechanisms may occur in tube bundles: *vortex shedding, turbulence buffeting, fluidelastic instability* and *acoustic resonance*. Only the first two mechanisms are of relevance in the present work.

The vortex shedding excitation manifests itself by a constant Strouhal number (St) periodicity and its origin has been a subject of debate. Early studies disputed the existence of discrete vortex shedding deep inside tube arrays. For example, Fitzpatrick and Donaldson (1980) found a transitional nature of the turbulence beyond the fourth row in in-line arrays with the discrete vorticity found in the first rows giving way to a broader turbulence spectrum. This transition was attributed to the existence of a buffeting frequency in tube banks, according to the theory of Owen (1965). Many experimental studies have been performed since then: turbulence spectra have been

obtained from hot-wire anemometry measurements in order to estimate Strouhal numbers and flow visualisation studies have been performed to reveal the nature of the flow periodicities; these were discussed earlier in this section. The vorticity shedding excitation has been shown to originate from alternate vortex shedding occurring in the first rows of staggered arrays (Weaver et al, 1991; 1993; Polak and Weaver, 1995) and symmetric or anti-symmetric jet instabilities in in-line arrays (Ziada and Oengöeren, 1991).

Cross-flow Strouhal numbers have been measured by many investigators (for example, Rae and Wharmby, 1987; Collinson and Robinson, 1991 and Weaver et al, 1991). St has been found to depend strongly on the tube arrangement and the spacing between the tubes, Re_d, the location within the array (Collinson and Robinson, 1991) and even on the number of rows and columns in the tube bundle (Oengöeren and Ziada, 1995). There may even be multiple St's at a given Re_d in the first rows of an array. For example, Hill et al (1986) observed two dominant frequencies in a staggered configuration with $S_T/d = 2.67$ and $S_L/d = 2.31$. The first frequency was attributed to von Karman vortex shedding but the origin of the second periodicity remained uncertain. A jet-flipping instability or coupling of frequencies were suggested as possible causal mechanisms. Conversely, an in-line tube bundle with the same spacings, exhibited a single dominant frequency attributed to von Karman vortex streets. Polak and Weaver (1995) studied the same staggered configuration as Hill et al and also found two discrete frequencies. It was shown that the two frequencies were due to alternate vortex shedding from the first and second rows and their existence was closely related to the spacing. Thus, a second St was present in normal triangular arrays with $S/d > 2$ at high Reynolds numbers while a single St occurred for $S/d < 2.0$.

Two dominant frequencies have also been reported for rotated square arrays (Weaver et al, 1993). Their origin was found to be alternate vortex shedding at different

frequencies from the first and second rows. A recent study by Oengöeren and Ziada (1995) reported three frequency components in normal triangular arrays. Two components were attributed to alternate vortex shedding from the front and rear rows, while the third component was due to non-linear interaction of the other two. The multiple-frequency nature of vortex shedding and the relative importance of each component was found to depend strongly on Re_d, pitch ratio, location within the array and, in some cases, the number of rows and columns in the tube bank.

Published Strouhal numbers have been collected and plotted in various forms (Chen, 1977; Weaver et al, 1987, 1993; Oengöeren and Ziada, 1995; Polak and Weaver, 1995). Empirical relations have also been proposed for the prediction of St in standard geometries such as normal triangular, parallel triangular, square and rotated square arrays. There is a lot of scatter in the published data, however, due to the different measuring locations, experimental conditions, techniques employed, and the existence of multiple St's.

Heat transfer and pressure drop

The determination of the mean heat transfer and total pressure drop in tube bundles in cross-flow has attracted considerable attention, in an attempt to improve the performance and efficiency of shell-and-tube heat exchangers. In general, staggered tube bundles exhibit higher heat transfer coefficients but also higher pressure drop compared to in-line ones. However, both the heat transfer and pressure drop depend primarily on the tube bundle geometry, Re_d, the physical properties of the fluid and the number of tube rows. A number of other parameters such as surface roughness and freestream turbulence are also significant. Mean heat transfer coefficients and pressure drop have been determined by many investigators for a wide range of arrangements and Re_d. Pierson (1937) and Huge (1937) were the first to measure these parameters in various tube bundle arrangements. Their data were analysed and

correlated by Grimison (1937) and Jacob (1938). Other relevant studies include those by Bergelin et al (1949), Zukauskas (1972, 1989), Aiba et al (1982a, b) and Achenbach (1989, 1991).

In most of the studies mentioned above, the heat transfer coefficients have been determined from surface temperature measurements obtained with thermocouples embedded on the wall of an electrically heated (or cooled) test tube. Constant heat flux or constant tube wall temperature conditions have been used. Single-point thermocouple measurements usually require a large number of sensors to resolve the temperature distributions around the tube surface and can be laborious and time-consuming. A simple and cost-effective method, that allows fast and accurate determination of the heat transfer coefficients over the whole tube circumference, is clearly needed.

Experimental data on heat transfer from tube bundles have been correlated with geometric and flow parameters. Empirical correlations have been proposed for the calculation of the mean heat transfer coefficient - expressed in terms of a Nusselt number, Nu - for a range of tube bundle configurations and Re_d's. Similar empirical correlations have been developed for the prediction of the pressure drop (ΔP) across a tube bundle. A list of published correlations can be found in Balabani and Yianneskis (1993a). A comparison of published experimental data for staggered and in-line arrangements (Zukauskas, 1972) showed that at low Re_d the heat transfer of an in-line bank is considerably lower than that of staggered banks. With an increase of Re_d, the heat transfer of in-line banks increases more rapidly and at high Re_d's it approaches the heat transfer intensity of staggered banks. In both staggered and in-line tube bundles the pressure drop is a function of the relative transverse pitch and increases with decreasing pitch.

A great effort has been directed towards effective ways of enhancing heat transfer. For example, Zukauskas and Ulinskas (1978) found that the transition from subcritical to critical flow enhanced the heat transfer significantly. Tube vibrations (Michaelides et al, 1986), asymmetric arrangements (Katinas and Tumosa, 1992) and free stream turbulence intensity (Stephan and Traub, 1986; Traub, 1990) have also been found to improve heat transfer. The effect of freestream turbulence was found to be more pronounced in the first rows in which heat transfer coefficients increased with Re_d and turbulence level. The influence of turbulence on heat transfer was higher for smaller longitudinal spacings and the enhancement of heat transfer was greater in in-line than in staggered arrangements (Stephan and Traub, 1986; Traub, 1990).

The effect of surface roughness on heat transfer and pressure drop has been studied experimentally by some investigators (Zukauskas 1983, 1989; Zukauskas and Ulinskas, 1983; Achenbach, 1983, 1989, 1991). While the surface roughness reduces the critical Re_d, with rough tubes enhancement of heat transfer starts at lower Re_d than in smooth ones. Thus, the heat transfer data for smooth and rough bundles were found to coincide at subcritical and transcritical conditions, while an improvement of heat transfer was observed for rough bundles in the critical and supercritical flow range (Achenbach, 1989, 1991). The influence of surface roughness on heat transfer is more important for staggered arrangements than for in-line. The pressure drop coefficients for the smooth and the rough tube banks coincided in subcritical Re_d's for both staggered and in-line arrangements. However, the pressure drop coefficient of staggered banks increased with increasing roughness parameter at transcritical flow conditions, whereas that of the in-line tube bundle decreased.

Particle-laden flows

Particle-laden flows are of particular interest in tube bundles, primarily because of their effect on fouling. Much of the experimental work on the velocity characteristics of two-phase flows has concentrated on pipe, jet or baffled flows. Detailed reviews have been published by Nouri et al (1984) and Hardalupas et al (1989). The velocities of the dispersed and the carrier phase are usually measured by various LDA techniques (see Yianneskis, 1987). The most widely used is the amplitude discrimination technique, which is described in detail in Chapter 2, but phase-Doppler anemometry has also been employed by some investigators (for example, Hardalupas et al, 1989, 1992).

Few two-phase flow studies in tube bundles in cross-flow have been reported and most of them have dealt with the effect of solid particles on the local heat transfer characteristics of tube bundles (for example, Murray and Fitzpatrick, 1991; Sterritt et al, 1992; Sterritt and Murray, 1992). The presence of solid particles was found to enhance the heat transfer in the first row of a triangular array (Murray and Fitzpatrick, 1991). The heat transfer enhancement was attributed to an increased thermal capacity of the suspension. In contrast, the heat transfer coefficients were reduced in subsequent rows due to effects such as turbulence suppression and delayed boundary layer separation. Both trends were also observed in an in-line array at different Re_d's: heat transfer enhancement for a Re_d = 6,000 and decreased heat transfer coefficients for a Re_d = 12,000 in all rows except the first one (Sterritt et al, 1992; Sterritt and Murray, 1992).

A dispersed particulate phase is known to modulate the turbulence intensity of the carrier phase (for example, Owen, 1969; Nouri et al, 1984; Gore and Crowe, 1991). The relation between the particle size and the scales of the carrier phase determine whether the addition of the particles will increase or decrease the turbulence intensity

of the carrier phase. Fitzpatrick et al (1992) studied the effect of particles on the boundary layer characteristics in the near separation region for a single cylinder and a cylinder located in the second row of a staggered array. It was found that the presence of particles (150 μm) in the staggered array resulted in a significant reduction in r.m.s. velocities, boundary layer thinning and delay in the boundary layer separation.

Little information exists on how particles disperse in recirculating flows akin to those in tube bundles in cross-flow. Nouri et al (1984, 1987) found that neutrally boyant particles suspended in a liquid flow around axisymmetric baffles, in general, followed the fluid motion. The mean flow results showed small differences in the solid and liquid velocities only in regions where there was considerable acceleration or deceleration of the flow. Velocity measurements of a gas/solid particle flow over a single cylinder (Lambert et al, 1988) showed that the particles, 100 μm in diameter, did not follow the recirculating flow in the wake and appeared to move towards the centreline. The concentration of the particles was found to be substantially reduced in the wake regions. Hardalupas et al (1992) studied particle dispersion in a vertical round sudden expansion by phase-Doppler anemometry. Their results showed that particles (40 μm and 80 μm in diameter) dispersed in the recirculation region formed in the lee of the expansion step by interaction with eddies, which were characterised by length and velocity scales of the order of the expansion step height and the downstream area-averaged velocity respectively.

Fouling

At the outset of the present work a literature survey on gas-side fouling - deposition from gas streams - was carried out in order to identify the parameters of importance in relation to tube bundle flows. The results of that survey are reported in Balabani and Yianneskis (1993b). This section intends to give no more than an introduction to the

subject and highlight those aspects of fouling that are closely related to the characteristics of tube bundle flows.

Fouling has been described as the major unresolved problem in heat transfer (Taborek et al, 1972). Although the understanding and modelling of the processes involved in fouling has been improved over the last years, fouling continues to be a serious constraint in the design and operation of heat exchanger equipment. As already mentioned earlier in this chapter, a widely used and often criticised technique for incorporating the effects of fouling into the design process is by means of the so-called fouling resistance or fouling factor, R_f. R_f determines the extra surface area that has to be added to a heat exchanger to maintain the required performance until the level of fouling represented by R_f is reached. The main compilation of R_f values for shell-and-tube heat exchangers is that of TEMA (1988). Although in practice R_f varies with time - asymptotically in many fouling situations - TEMA values are single figures and not necessarily asymptotic fouling resistances. They also do not distinguish between the shell-side and the tube-side and they do not take operating variables such as flow velocity or surface temperature into account.

Various types of fouling have been identified depending on the key physical/chemical process essential to a particular fouling phenomenon. Particulate fouling is the type of fouling most likely to be associated with gas-side fouling in lignite utility boilers but chemical reaction, solidification and corrosion fouling are also important. Three major processes are involved in particulate fouling *deposition* (transport of particles to the wall), *adhesion* and *re-entrainment*. Depending on their size, particles can reach the surface by one of the following mechanisms: molecular or Brownian diffusion, eddy diffusion, interception, inertial impaction and gravitation. In the presence of electrical charges, temperature or concentration gradients, phoretic effects such as electrophoresis, thermophoresis and diffusiophoresis respectively, become significant especially for small particles.

The mechanisms and the rates of particle deposition are determined by a number of factors, the most significant of which are the particle size, the fluid velocity and surface temperature (Papavergos and Hedley, 1984; Bott, 1988; Epstein, 1988). A high velocity is believed to minimise fouling but it also increases the risk of erosion wear of the heating surfaces and tube failures. Surface roughness has an increasing effect on the rate of depositing particles in comparison with smooth surfaces (Papavergos and Hedley, 1984).

Industrial observations suggest that the first rows of a tube bundle experience more severe fouling (Bergeles et al, 1996). That was confirmed experimentally by Bemrose and Bott (1984) who introduced a fouling effectiveness factor to account for the different degree of fouling experienced in different rows of a tube bundle. It has also been reported that under the same operating conditions staggered tube bundle arrangements experience one half of the fouling experienced by in-line ones (Zukauskas, 1989) due to the absence of stagnant zones between tubes of the same column which increases deposition on both the rear and front parts of each tube.

Most of the fouling models published in the literature are concerned with the overall performance of the heat exchanger and they do not take the geometry of the bundle into account. Reliable experimental data on particle deposition in tube bundles are scarce and as a consequence very few fouling models are based on data from tube bundle flows (for example, Bemrose and Bott, 1984; Glen et al, 1992). Many published models have been developed on the basis of experimental or industrial data collected by means of a cylindrical accumulation probe (for example, Glen and Howarth, 1988; 1989).

The thickness, shape and characteristics of the deposit layer also vary with time (Tufte and Beckering,1975) and therefore operating parameters such as the local velocity field, surface temperatures and surface roughness will vary accordingly. Depending

on the deposition mechanisms involved, particles can be deposited only on the front or on the rear, on both the front and the rear or around the whole perimeter of the tubes (Skiepko and Lach, 1992). Hence, particle deposition and re-entrainment processes are expected to be modified after an initial deposit is formed. Under favourable conditions, the mass of deposit per unit area of tube eventually reaches a steady value at which the new deposited material is just balanced by the loss due to re-entrainment.

Summary of the findings

The main findings of the preceding literature survey can be summarised as follows:

1. The flows in tube bundles are far more complex than those past a single cylinder (Zdravkovich, 1987). The phenomena associated with interference of the flows around different tubes are highly non-linear and difficult to quantify and classify. The flow pattern in a tube bundle depends on the tube arrangement and geometrical parameters of the bundle, Re_d, free-stream turbulence level and surface roughness and various flow regimes have been identified.

2. The first row in both staggered and in-line arrangements exhibits a behaviour similar to that of a single cylinder in cross-flow, especially with large spacings (see for example, Aiba et al, 1982a, 1982b; Zukauskas, 1989). The flow in subsequent rows differs considerably between staggered and in-line arrangements, as the boundary layer development is different and the interactions between the main stream and the wake flows are different.

3. The velocity characteristics of tube bundles have not been investigated in detail. There are very few LDA studies, which are concerned mainly with staggered arrays with specific spacings (for example, Halim and Turner, 1986; Simonin and Barcouda, 1986, 1988; Meyer, 1994). The flow in the first rows is characterised by pronounced

reversal and steep velocity gradients. The turbulence increases from row to row and reaches a maximum downstream of the second row. It is also highly anisotropic but the degree of anisotropy in various configurations has not been quantified. It is clear that detailed and accurate velocity measurements are needed in a wider range of configurations in order to assess the effect of the tube geometry and also improve the accuracy of CFD calculations of the flows.

4. CFD predictions of the flow fail to predict the correct levels of k especially in the recirculation regions (Simonin and Barcouda, 1986, 1988; Meyer, 1994). Characteristic turbulence quantities, such as scales of turbulence or the rate of dissipation of the turbulent kinetic energy, which may aid turbulence modelling have not been determined experimentally.

5. The pressure drop in a tube bundle decreases with Re_d in subcritical flow but increases beyond the critical Re_d. It is also affected by the transverse pitch and in general is higher in staggered than in in-line tube banks (Jacob, 1938, Zukauskas, 1989).

6. The mean heat transfer coefficients depend on Re_d, tube arrangement and the physical properties of the fluid. Inner rows have higher heat transfer coefficients than the entrance section of the bank (Zukauskas, 1989). Increasing levels of free-stream turbulence or transition from subcritical to critical flow enhances the heat transfer. There is little progress in the techniques employed for the measurement of the heat transfer coefficients. Conventional techniques, based on single-point thermocouple measurements of the surface temperatures are laborious and time-consuming. It is clear that a more cost-effective technique should be developed to measure distributions of local heat transfer coefficients in tube bundles.

7. Surface roughness causes a premature transition from laminar to turbulent boundary layer (Achenbach, 1989, 1991). Thus, the heat transfer improves whereas the pressure drop increases in staggered banks but decreases in in-line banks. The effect of the surface roughness on the local velocities, the wake characteristics and the turbulence structure has not been studied in detail.

8. Turbulence spectra in the first rows in tube bundles show a discrete periodicity at a constant Strouhal number, which is associated with alternate vortex shedding in staggered tube bundles and jet instabilities in in-line ones (Ziada and Oengöeren,1991; Polak and Weaver, 1991; Weaver et al, 1991, 1993; Oengöeren and Ziada, 1995). In downstream rows the discrete vorticity is indistinguishable from the background turbulence. The effect of this periodicity on turbulence quantities such as k or ε has not been quantified. The associated Strouhal numbers depend on arrangement, pitch ratio, Re_d and location in the bank. Multiple Strouhal numbers have also been detected (Weaver et al, 1993; Polak and Weaver, 1995; Oengöeren and Ziada, 1995).

9. The presence of solid particles in suspension may increase or decrease the heat transfer in a tube bundle (for example, Murray and Fitzpatrick, 1991; Sterritt et al, 1992; Sterritt and Murray, 1992). A dispersed phase may increase or decrease the turbulence intensity of the carrier phase (Owen, 1969; Nouri et al, 1984; Gore and Crowe, 1991). Little information exists on how particles disperse in recirculating flows akin to those in tube bundles in cross-flow. Particles may follow (Nouri et al, 1984, 1987) or not the flow in the recirculation region (Lambert et al, 1988). In view of the differing observations concerning the behaviour of particles in recirculating flows, it is evident that further investigation is needed to give insight into the behaviour of a particulate phase in more complicated flows such as those in tube bundles.

10. The mechanisms and the rate of particle deposition in particulate fouling depend primarily on the local fluid velocities (Epstein, 1988). A different degree of fouling in different rows of a tube bundle has been observed (Bergeles et al, 1996; Bemrose and Bott, 1984). The thickness, shape and characteristics of the deposit layer vary with time (Tufte and Beckering,1975). Depending on the deposition mechanisms involved, particles can be deposited only on the front or on the rear, on both the front and the rear or around the whole perimeter of the tubes (Skiepko and Lach, 1992). As a result, the surface roughness characteristics and the shape of the tubes are modified. It is important to know to what extent the flow field around the tubes of a bundle is affected by such changes. Knowledge of the fundamental processes involved in tube bundle flows will also provide a good guide for accurate prediction and minimisation of fouling.

1.3 OBJECTIVES OF THE PRESENT INVESTIGATION

It is clear from the preceding review of the published literature that the information available for the flows over tube bundles is far from complete. The velocity characteristics of the flows produced by various tube bundle configurations have not been fully determined. A number of parameters that affect the flow structure have been identified but have not been studied in detail since individual investigations dealt with specific tube bundle arrangements. The wake properties and the turbulent aspects of the flow have not received considerable attention and therefore detailed appraisal and improvement of CFD models is not possible. Finally the extent to which the flow characteristics of the tube bundles are affected by fouling have been overlooked.

In view of the findings of the literature survey the present investigation is aimed primarily at improving the body of knowledge on cross-flows over tube bundles and secondarily in providing information suitable for the development and validation of CFD models of the flows by:

1. Obtaining accurate velocity data in tube bundle configurations representative of those found in lignite utility boilers.

2. Identifying flow periodicities and quantifying their effect on the measured quantities.

3. Characterising the turbulence structure by quantifying the degree of anisotropy and estimating quantities such as time scales and the rate of dissipation of the kinetic energy of turbulence.

4. Assessing quantitatively the effect of tube arrangement and spacing on the velocity characteristics of tube bundles.

5. Assessing the extent to which the flow features are modified by fouling and/or erosion by studying particle-laden flows, flows over rough and deformed tubes.

6. Developing and applying a liquid crystal thermographic technique for the qualitative and quantitative determination of the tube surface temperature distributions.

1.4 OUTLINE OF THE THESIS

The remainder of this thesis is divided into six chapters. The following chapter describes the tube bundle configurations and the experimental facility and techniques used for the investigation of the velocity and turbulence characteristics. The results obtained in a typical staggered tube bundle configuration are presented and discussed in Chapter 3. Chapter 4 presents velocity measurements made in an in-line and a

staggered tube bundle configurations chosen so that the effect of tube spacing and tube layout can be studied. Chapter 5 examines the extent to which the flow in tube bundles is affected by roughness and deformation resulting from fouling or erosion of the outer surface of the tubes and presents velocity measurements obtained with particle-laden flows. The development and application of a liquid thermographic technique in tube bundles is described and the wall temperature distributions obtained are presented in Chapter 6. The findings of the investigation are summarised in Chapter 7 and recommendations for future work are made.

Three appendices are given at the end of the thesis: Appendix I contains a description of the Fast Fourier Transform definition used in order to transform the velocity data from the time domain to the frequency domain. Appendix II presents the definitions and the techniques used to estimate power spectra. Finally, Appendix III details the techniques considered for the removal of the periodic component from the velocity spectra and their application to velocity data obtained in the present investigation.

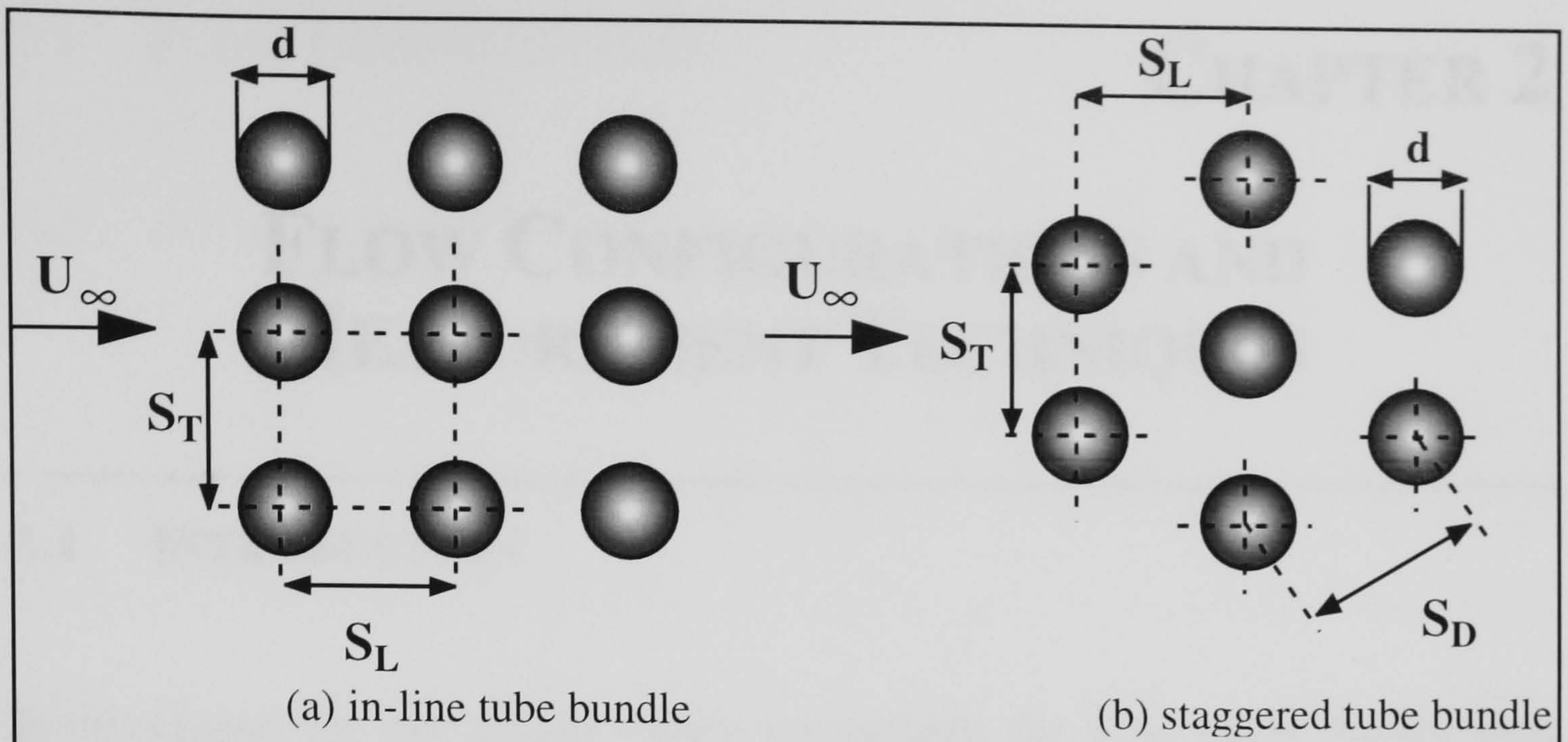

(a) in-line tube bundle (b) staggered tube bundle

Figure 1.1. In-line and staggered tube bundle geometries.

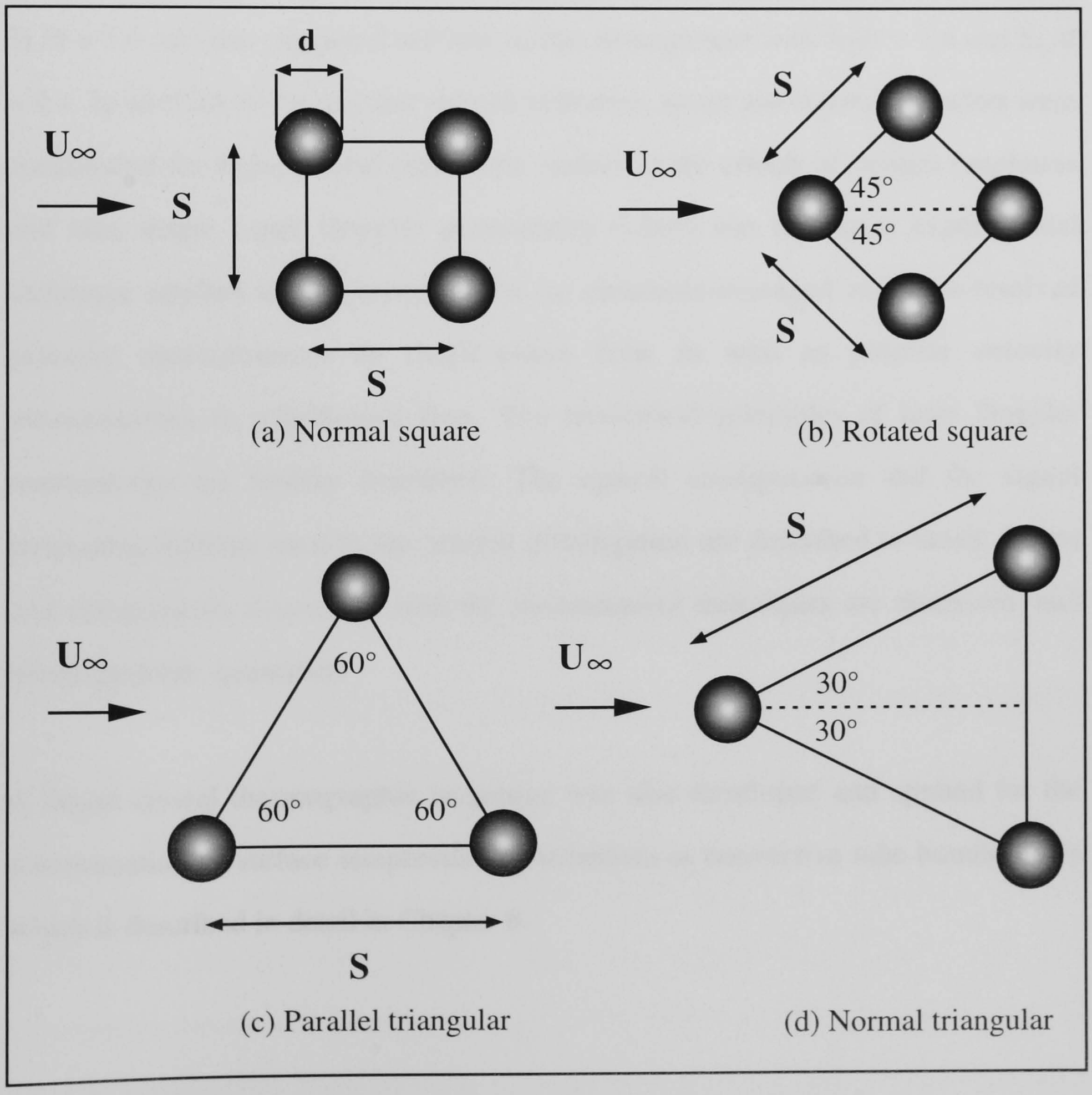

Figure 1.2. Standard tube bundle geometries.

CHAPTER 2

FLOW CONFIGURATIONS AND MEASUREMENT TECHNIQUES

2.1 INTRODUCTION

In this chapter the tube bundle models investigated, the water tunnel facility used and the flow measurement techniques employed are described. Three tube bundle models were constructed and tested: one staggered arrangement with $S_T/d = 3.6$ and $S_L/d = 1.6$ and one staggered and one in-line arrangement with $S_T/d = 3.6$ and $S_L/d = 2.1$. In addition to the circular smooth cylinders, rough and tapered cylinders were constructed for experimental parametric studies of the effects of surface roughness and tube shape. Laser Doppler anemometry (LDA) was the major experimental technique applied in this investigation for ensemble-averaged and time-resolved velocity measurements in single-phase flow as well as particle velocity measurements in solid/liquid flow. The theoretical principles of laser Doppler anemometry are briefly described. The optical configuration and the signal processing systems used in the present investigation are described in detail. Errors and uncertainties associated with the measurement techniques are discussed, and where possible, quantified.

A liquid crystal thermographic technique was also developed and applied for the determination of surface temperature distributions in convective tube bundle flows which is described in detail in Chapter 6.

2.2 FLOW CONFIGURATIONS

2.2.1 TUBE BUNDLE MODELS

As already mentioned in Chapter 1 most of the experiments described in this thesis were carried out as part of a research programme investigating flows in heat exchangers in lignite utility boilers in the power generation industry. The Public Power Corporation (PPC) of Greece was the industrial partner in the programme. Thus, some of the tube bundle models constructed were scale models of the actual heat exchanger tube bundles used in the PPC lignite utility boilers. The latter consisted of tubes, 38 mm in diameter, arranged either in a staggered or an in-line arrangement with transverse spacing, S_T, equal to 138 mm and longitudinal spacings, S_L, equal to 60 mm and 80 mm respectively.

Appropriate considerations of geometric and dynamic similarity, boundary layer growth and optical access were made in order to design suitable tube bundle models. For geometric similarity, the tube spacings of the bundle normalised with the tube diameter, i.e. the transverse and longitudinal pitch ratios (centre-to-centre distances to diameter ratios) were the only parameters that needed to be matched. The tube diameter of the industrial configurations was scaled down by a factor of 3.8. As a result, a staggered and an in-line tube bundle model with square cross-sections (72 mm x 72 mm) was designed and manufactured from transparent cast acrylic material (poly-methyl methacrylate - Perspex) with cast acrylic rods, 10 mm in diameter, used as tubes. The aspect ratio of the rods, L/d, was equal to 7.2, which was considered to be sufficient in ensuring two-dimensional flow conditions over the central part of the span (Fox and West, 1990). The staggered test section consisted of 6 transverse rows and 5 columns of tubes with transverse pitch ratio, S_T/d, equal to 3.6 and longitudinal pitch ratio, S_L/d, equal to 1.6. Conversely, the in-line tube bundle model consisted of 5 rows and 3 columns of tubes with $S_T/d = 3.6$ and $S_L/d =$

2.1. Two of the tube columns mentioned above comprised half rods which were fixed along the side walls - in alternate rows in the staggered arrangement and at each row in the in-line one - to simulate an infinite tube bundle and minimise wall boundary layer effects. The rods were fixed horizontally in the test section and they were rigidly mounted by pressing them tightly into holes drilled on the Perspex plates to eliminate possible resonance effects that might interfere with the flow parameters measured. This versatile design also enabled easy removal and cleaning of the rods in case of fouling by the impurities in the water as well as mounting of rods with alternative shapes and surface patterns for parametric studies.

A third tube bundle model was also constructed to facilitate parametric studies of the effects of tube spacing and arrangement to be carried out simultaneously by comparing with the tube bundles described earlier. That was a staggered tube bundle model that comprised 6 rows and 5 columns of tubes with pitch ratios equal to those in the in-line tube bundle, i.e. $S_T/d = 3.6$ and $S_L/d = 2.1$. That allowed for direct comparisons between the staggered and in-line arrangements to be made as well as comparisons with the other staggered tube bundle to determine the effect of tube spacing.

Pressure tappings were installed in all the staggered and in-line test sections, upstream and downstream of the tube bundle, to measure the pressure drop across the tube bundle. The latter was measured by means of an inverted U-tube manometer. Table 2.1 summarises the dimensions and the geometrical parameters of the three tube bundle models. A schematic of their cross-sections is shown in Figure 2.1 together with the co-ordinate system employed. The origin of the latter is taken at the centre of the first row cylinder.

Table 2.1. Dimensions and geometrical parameters of the tube bundle models.

Dimensions (mm x mm x mm)	72x72x196	72x72x156	72x72x196
Arrangement	staggered	in-line	staggered
Tube diameter, d (mm)	10	10	10
Transverse pitch, S_T/d	3.6	3.6	3.6
Longitudinal pitch, S_L/d	1.6	2.1	2.1
No. rows, N	6	5	6
No. columns	5	3	5
Aspect ratio, L/d	7.2	7.2	7.2

2.2.2 ROUGH - SURFACED TUBES

During normal operation of the utility boilers particles contained in the flue gases may foul or erode the outer surface of the tubes (gas-side fouling). Particle deposition or erosion can modify significantly the surface roughness, nominal diameter and shape of the tubes and consequently the flow structure and subsequent particle deposition in the tube bundle. The surface roughness of a tube bundle subjected to fouling is difficult to predict, therefore both uniformly and randomly distributed roughness were considered. The cast acrylic rods used in the construction of the test sections were roughened using two different techniques in order to generate an evenly- and a randomly-distributed surface roughness. The evenly-roughened tubes described below are more likely to occur in a real gas-side fouling environment when ash particles cause erosion of the tube surface and the randomly-roughened ones when particles deposit on a surface due to a combination of fouling mechanisms.

The evenly distributed roughness pattern comprised a regular arrangement of tightly spaced pyramidal elements and was generated by a knurling process. The height of

the pyramidal elements was 1.4 mm. The length and width of their base was 1.6 mm and 0.9 mm respectively. Due to the knurling process the nominal diameter of the rods was reduced from 10 mm to 8.6 mm. It is noted that the tube diameter of the knurled rods is defined at half-height of the pyramidal elements. Thus, the corresponding relative roughness, *k*/d, was equal to 0.16. The height of the rough elements was greater than the thickness of the boundary layer which according to numerical predictions of the flow carried out by the National Technical University of Athens (NTUA) (Bouris, 1995; Bergeles et al, 1996) was estimated to be equal to 0.17 mm at 90 ° from the front stagnation point of the first row cylinder[1]. A loss of stability of the boundary layer was therefore expected (Zukauskas, 1983).

The random roughness pattern was produced by gluing spherical ballotini (glass) particles, of 0.66 mm average diameter, on the surface of the tubes. The nature of the resulting roughness was examined by image processing techniques. It was found that a first layer of particles was glued over the whole tube surface increasing the nominal diameter of the tubes from 10 mm to 11.6 mm on average, i.e. by approximately 12 %. The average height of protrusions resulting from a second layer of particles randomly distributed over the first one was found to be 0.46 mm approximately. The average relative roughness, *k*/d, was equal to 0.04. However, this is a rough indication of the relative surface roughness since the latter may vary significantly over the perimeter of the cylinder.

The details of the two surface patterns produced can be seen in Figure 2.2. The two sets of rough-surfaced rods were mounted on the staggered test section with S_T/d = 3.6 and S_L/d = 1.6 and detailed velocity measurements of the axial and transverse velocity components were taken in order to investigate the effects of roughness on the velocity characteristics of tube bundles, which are described in Chapter 5.

[1]Numerical predictions refer to the flow over a staggered array with S_T/d = 3.6 and S_L/d = 1.6, d = 10 mm and Re_d = 12,858 in flow of water. These are the flow configuration and conditions in which the rough-surfaced tubes were investigated.

2.2.3 SIMULATION OF FOULED TUBES

Depending on the deposition mechanisms involved in a gas-side fouling situation, ash particles can be deposited only on the front or on the rear, on both the front and the rear or around the whole perimeter of the tubes (Skiepko and Lach, 1992). As a result, a number of different tube shapes may arise in different rows of a heat exchanger tube bundle affecting the flow field around the tubes and subsequent particle deposition. In order to study the effect of the altered tube shape on the velocity characteristics of tube bundles, tube shapes that are likely to occur in a real fouling environment were sought.

According to the ash fouling model developed by the NTUA (Bouris-Burry and Bergeles, 1994; Bergeles et al, 1996) particle deposition under actual operating conditions occurs in a typical lignite utility boiler only on the front of the tubes and mainly in the first two rows of a staggered tube bundle with $S_T/d = 3.6$ and $S_L/d = 1.6$. The predicted fouled tube shapes in the first two row cylinders were approximated by two different tapered cylinders for the first and second rows respectively. That was achieved by fitting various curves to the predicted shapes of the deposited layers on the first and second row cylinders of the above array after 8 hours of fouling. Predictions were based on deposition of Al_2O_3 particles under conditions similar to the actual operating ones of a typical utility boiler used by PPC of Greece: a carrier phase of air at a temperature of 900 ° with velocities of 12 m/s, d = 38 mm and a mean particle diameter of 216 μm were assumed.

The predicted deposited layers on the first and second cylinders could be approximated by the shape of two intersecting cylindrical sections with a radius of 10.59 mm and 20.20 mm respectively. Three cast acrylic attachments were then manufactured, one for the first row tube and two for the second row ones. The attachments were glued on the rod surfaces. Their edges were trimmed off and the

contact points were filled so that there were no gaps between the attached section and the rods. Photographs of the cross-section of the tapered rods can be seen in Figure 2.3. The latter were mounted in the staggered test section with $S_T/d = 3.6$ and $S_L/d = 1.6$ and detailed measurements of the axial velocities were taken which are described in Chapter 5.

2.3 EXPERIMENTAL RIG

A closed-loop flow rig was designed and manufactured to accommodate the test sections described earlier and facilitate single-phase and two-phase LDA experiments in flow of water. The major design criteria of the water tunnel were that the flow entering the test sections had a uniform velocity profile, low turbulence content and a Re_d similar to that of a tube bundle in a typical lignite boiler under real operating conditions so that dynamic similarity could be achieved. A schematic diagram of the flow rig is shown in Figure 2.4.

A centrifugal pump was used to circulate the working fluid from the tank. A by-pass valve was installed to regulate the flowrate which was monitored with two precision-bore flow-meters (KGD 2000). The working fluid flowed downwards through a straightening section to the test section. The flow straightener utilised a piece of an hexagonal cell honeycomb made of aluminium for the effective removal of lateral mean velocity variations. A proportional temperature control system (Eurotherm 818) consisting of a cooling coil, an immersion heater and a thermocouple was built and installed in the tank, in order to maintain the temperature of the working fluid to within ± 0.05 °C. A solenoid valve was used to control the water flowrate through the cooling coil.

The pipework, fluid tank and all components were arranged with their axes vertical and designed so that there are no stagnant regions in the flow; in this way, complete

particle re-entrainment into the flow in two-phase flow studies was ensured every time the experiment was re-started. The experimental rig had a maximum capacity of 290 lit/min corresponding to a maximum upstream velocity, U_∞, equal to 0.93 m/s with tap water at 20 ° C used as working fluid. The corresponding maximum Re_d that could be achieved was 12,858. Re_d is defined by the tube diameter, d, and the maximum velocity at the gap between adjacent tubes in a row, U_g, which is, by simple continuity, equal to 1.38 U_∞ (1.29 m/s) for all the tube bundle arrangements investigated. The equivalent Reynolds number defined by the upstream velocity, U_∞, and the hydraulic diameter of the duct upstream of the bundle was equal to 66,862.

Measurements were carried out upstream of the first row of the tube bundles at x/d = -2.1 in order to ensure that the approaching flow was uniform. The two-dimensionality of the flow was established both upstream and inside the bundle (at x/d = -2.1 and 2.8 respectively) by measuring mean velocity profiles at three different z-planes (z/d = -0.6, 0, 0.6).

2.4 FLOW MEASUREMENT TECHNIQUES

2.4.1 LASER DOPPLER ANEMOMETRY

Laser Doppler anemometry (LDA) is a well established optical technique for fluid flow measurements. Its key advantage is that it does not disturb the flow which makes it very suitable for velocity measurements in highly turbulent and recirculating flow conditions such as those prevailing in tube bundles. The technique is based on the measurement of the Doppler shift of laser light scattered from small particles carried along with the fluid. The laser Doppler anemometer can be set up in many optical configurations. The fringe-type mode is probably the most widely used and was employed in this study. The basic principles of LDA are briefly summarised below. More details concerning the principles and practice of the technique can be

found for example, in Drain (1980), Durst et al (1976), Buchhave et al (1979), George and Lumley (1973).

The fringe-type (or 'dual beam') system makes use of two intersecting laser beams of equal intensity to produce an interference fringe pattern within their volume of intersection (measurement volume). The fringe spacing, λ^*, defined as the spacing between the light and dark bands, is given by the following expression:

$$\lambda^* = \frac{\lambda}{2\sin(\theta/2)} \tag{2.1}$$

where λ and θ are the wavelength of the laser light and the angle of intersection of the laser beams respectively.

When small particles moving with the fluid cross the fringes they scatter laser light, the intensity of which rises and falls at a rate proportional to their velocity. This intensity modulation results in the generation of the Doppler bursts or Doppler signals which can be detected by a photodetector. The frequency of the intensity modulation of the scattered light (Doppler frequency), f_D, is directly related to the velocity component of the particle perpendicular to the fringes by the following expression:

$$f_D = \frac{U_{particle}}{\lambda^*} = \frac{2U_{particle}\sin(\theta/2)}{\lambda} \tag{2.2}$$

If the particles are sufficiently small so that they can be assumed to follow the flow faithfully, then $U_{particle}$ represents the fluid velocity component perpendicular to the fringes and accurate velocity measurements can be obtained by moving the measurement volume throughout the flow field of interest and determining the Doppler frequency using appropriate signal processing techniques.

In turbulent or recirculating flows the fluid velocity can be negative. The Doppler frequency defined earlier is independent of the direction of the particle velocity - and consequently the flow velocity - for stationary fringes. Therefore only the magnitude of the velocity can be determined from equation (2.2) and not the sign. A technique called frequency shifting is used to remove this directional ambiquity: the frequency of the two intersecting beams is shifted causing the interference fringes to move with respect to the optical axis with a velocity proportional to the frequency shift f_S applied. The velocity of the particle crossing the fringes will now depend on whether it is travelling in the same or the opposite direction with the 'moving' fringes. In that way both the sign and the magnitude of the particle velocity can be determined from equation (2.2) rewritten as follows:

$$U_{particle} = (f_D \pm f_s)\frac{\lambda}{2\sin(\theta/2)} \qquad (2.3)$$

The anemometer used in this study is based on the above principles. The exact configuration and the optical elements used are described in detail below.

2.4.2 OPTICAL CONFIGURATION

Figure 2.5 shows a schematic layout of the fringe-type LDA system used in this study. The LDA operated in forward-scatter and made use of a 10 mW He-Ne laser (Spectra Physics model 106) operating at a wavelength of 632.8 nm (red). The major criteria in selecting the most appropriate combination of optical components were the dimensions of the measurement volume and the half-angle between the beams. The turbulent and recirculating flow conditions and the associated steep velocity gradients expected in the tube bundle flows necessitated the choice of a small measurement volume so that errors could be minimised. The measurement volume is usually defined by the $1/e^2$ boundary of the maximum beam intensity and for Gaussian laser beams it is ellipsoidal in shape. Its diameter, b_X, is given by:

$$b_x = \frac{b}{\cos(\theta / 2)} \tag{2.4}$$

and its length, b_y, by:

$$b_y = \frac{b}{\sin(\theta / 2)} \tag{2.5}$$

where b is the beam waist of the focused laser beams in the measurement volume given by:

$$b = \frac{4\lambda f_1 f_3}{\pi b_o f_2} \tag{2.6}$$

where b_o is the diameter of the beam emitted by the laser and f_1, f_2, f_3 the focal lengths of the lenses L_1, L_2 and L_3 employed.

The optics were optimised by calculating the above parameters for a number of available lenses. As a result, the laser beam, 0.83 mm in diameter, was focused by a plano-convex lens with a focal length, f_1, of 200 mm onto a radial diffraction grating with 4,000 lines. The latter was used to split the beams and for frequency shifting. It was mounted on a rotating shaft fitted on a purpose-built unit, which was belt driven by a bi-directional variable speed DC motor. The grating unit could be rotated through 90 ° about the optical axis. In that way the plane of the beams could be altered, allowing other velocity components to be measured. The motor could operate over a speed range up to 6,500 rev/min and the pulley ratio was 3:1. Therefore, the maximum rotational speed that could be reached was 19,500 rev/min. The corresponding maximum frequency shift, f_S, between the first order beams was 2.6 MHz. The latter is determined from the following equation:

$$f_s = \frac{2mnN_G}{60} \tag{2.7}$$

where m is the order of diffraction, n is the number of lines on the grating and N_G is the rotational speed of the grating in rev/min.

The pair of the first order beams were collimated by a second plano-convex lens placed at a distance of one focal length (f_2 = 500 mm) from the grating. The two parallel beams were then focused by a third plano-convex lens with a focal length, f_3, of 125 mm to cross and form the measurement volume inside the test section. Scattered light from particles crossing the measurement volume was collected through a zoom lens with an adjustable aperture and focused on a photomultiplier (EMI 9658B) powered by a Brandenburg 10 - 2,000 Volts DC power supply.

The transmitting and receiving optics were mounted on a three-dimensional traversing mechanism enabling the optical bench to be traversed in three orthogonal directions x, y, z. In this way the measurement volume could be positioned anywhere in the flow field. The accuracy of the traversing mechanism was 0.05 mm in all three directions. Special care was taken to eliminate possible backlash when traversing in the x direction. The optical bench was aligned to the test section in such a way that the optical axis was perpendicular to the front wall and parallel to the rod axes of the tube bundles. The characteristics of the LDA system used are summarised in Table 2.2.

Table 2.2. Characteristics of the LDA system used.

Laser (He-Ne)	
Wavelength, λ (nm)	632.8 (red)
Power (mW)	10
Beam diameter, b_O (mm)	0.83
Lens	
f_1 (mm)	200
f_2 (mm)	500
f_3 (mm)	125
Diffraction grating	
Number of lines, n	4,000
Max. rotational speed, N_G (rev/min)	19,500
Max. frequency shift, f_S (MHz)	2.6
Measurement volume dimensions	
(at $1/e^2$ intensity)	
Diameter, b_X (μm)	48.8
Length, b_Y (μm)	466
Number of fringes (stationary)	16
Angle of intersection, θ in air (°)	5.98
Fringe spacing, λ*(μm)	3.04
Frequency to velocity conversion factor (m/s/MHz)	3.04

The axial velocities (U, u') were measured with the two laser beams lying on the vertical plane. In order to measure the transverse velocities (V, v') the diffraction grating was rotated through 90 ° resulting in the two beams lying on a horizontal plane. All measurements were taken at the plane of symmetry (z/d = 0). In order to

measure the third component, (W, w'), the whole test section was rotated by 90 ° around the vertical axis so that the optical axis was perpendicular to the rod axes and the beams were in a horizontal plane. Measurements of this component were possible only midway between successive rows due to the restricted optical access.

The flow was not seeded with particles for the single-phase flow experiments. The impurities in the tap water used as working fluid provided good quality signals and high data rates for the ensemble-averaged velocity measurements. The data rate was further increased for time-resolved measurements by introducing a few drops of diluted milk in the flow.

2.4.3 SIGNAL PROCESSING AND DATA ACQUISITION

The frequency counting technique was employed for the processing of the Doppler signals. Two different frequency counters were used for the determination of ensemble - averaged and time-resolved measurements respectively.

Ensemble-averaged LDA measurements

An ensemble average of a random process is an average over repeats of an experiment (called an ensemble). Ensemble-averaged LDA measurements determine the mean and r.m.s. velocity at a point in a flow by averaging the velocities measured over a number of individual Doppler bursts. According to the ergodic hypothesis the ensemble average of a process is equivalent to a time average if the process is statistically stationary. A steady turbulent flow can generally be assumed stationary and therefore ensemble-averaged quantities are equivalent to the time-averaged ones.

A frequency counter designed and built in Imperial College London (Model 2) was used for the determination of the ensemble-averaged mean and r.m.s. velocities in tube bundle flows. The signal processing procedure performed by the counter processor has been described in detail by Suen (1992). A schematic layout of the processing system is shown in Figure 2.6: the Doppler signal from the photomultiplier was filtered using a low-pass passive filter and a high-pass variable active filter (Kronhite model 3200) for noise and pedestal removal respectively. The pedestal is a low frequency component present in the Doppler signal, associated with particle transit through light beams. The filtered signal was then amplified and fed to the counter and a two-channel oscilloscope (Tektronix model 5111), which was used to monitor the signal quality (in Channel A) and the amplitude validation rate as described below. The counting procedure as well as the data processing were controlled by a microcomputer interfaced to the counter.

The frequency counter determined the Doppler frequency by measuring the time required for a set number of cycles in a Doppler burst. The counting circuit was activated when the signal exceeded a threshold value specified by the user (amplitude validation). An amplitude validation pulse was then produced by the counter, which was input to Channel B of the oscilloscope. By adding the signal in Channel A with the counter amplitude validation pulses in Channel B, the level of the threshold could be monitored and adjusted accordingly. The threshold setting is a crucial factor: too low a setting will produce a high validated data rate and a high Doppler frequency due to counting on noise, while a high one eliminates the chances of counting on noise but may result in low data rate. A frequency validation procedure followed in which the frequency computed from the first 5 (or 10) cycles within a validated burst was compared with that computed from the first 8 (or 16) cycles. If the two frequencies agreed within a pre-set tolerance (0% - 1.6 %), the measured Doppler frequency was registered as valid and was considered for the determination of the ensemble-averaged values.

2,000 validated data were taken per measurement and the ensemble mean and r.m.s. velocities and the probability density function (p.d.f.) were calculated. The shape of the p.d.f. was used to check the quality of the measurements and whether the filters and the frequency shift were properly selected.

Time-resolved LDA measurements

Time-resolved measurements of the axial and transverse components were taken in the staggered tube bundle with $S_T/d = 3.6$ and $S_L/d = 1.6$ at a $Re_d = 12{,}858$. Detailed measurements of the axial component were taken between the first and second rows to estimate time scales of the flow and dissipation rates. Measurements of the axial and transverse component were also taken in downstream locations, primarily in order to identify dominant frequencies and their amplitudes. All flow and optical characteristics for these experiments were identical to those employed for the ensemble-averaged measurements.

Time-resolved measurements involve recording instantaneous values of the velocity at specific time intervals over a period of time. The time intervals can be evenly or randomly distributed depending on the sampling technique employed. The former is the most common approach since most signal processing tools require equi-spaced data. The reciprocal of the time interval is called the sampling rate (or sampling frequency) and it expresses the number of samples recorded per second. The result is a time series of velocity data points which can be analysed further to yield information about the frequencies that are present in the flow (frequency spectrum) and how adjacent fluctuations in time are related to each other (autocorrelation function).

As already mentioned most of the algorithms for spectral analysis require equi-spaced data. However, individual realisations obtained with an LDA system are

randomly distributed in time. A zero-order interpolation is used to reconstruct the set of data in which the velocity signal is sampled at the arrival of a valid signal burst and the values are held until another valid signal arrives. This procedure, known as a hold-and-sample procedure, is appropriate when on average the data arrival rate is high enough to resolve the velocity fluctuations. High data rates and low burst density (i.e. elimination of burst overlap to avoid 'phase' or 'ambiguity' noise) provide the optimum conditions for such measurements (Adrian and Yao, 1987). If the data rate is too high, the 'step' noise, which arises from the jumps that occur at new random sample times, vanishes and the sample-and-hold signal is statistically unbiased for any turbulence intensity. If data rates are low then the spectrum is distorted. Spectral estimates are underpredicted at high frequencies and overpredicted at low frequencies (Tropea, 1987; McDonnell and Fitzpatrick, 1992). For flows with low data rates random sampling is more appropriate since there is no need to satisfy the Nyquist criterion as described below. Various spectral analysis techniques have been proposed for randomly sampled data, based on correlation or direct Fourier techniques. A review of the relevant literature is given in Table 2.3 at the end of the Chapter. Table 2.3 also includes studies concerned with the estimation of turbulence scales and dissipation rates due to their relevance to the present work.

From the foregoing discussion, it becomes apparent that two are the most important factors in taking accurate time-resolved measurements: the validated data rate and the sampling rate. The section that follows describes the criteria for selecting an appropriate sampling rate for a given validated data rate.

Sampling rate and aliasing. The choice of sampling rate is crucial. Sampling at too high frequencies will yield correlated and highly redundant data. Sampling at too low frequencies will lead to confusion between the low and high frequency components in the original data (aliasing). However, in order to define a frequency component in the original data two samples per cycle are required. Hence, if a

sampling rate of 1/h is used with h being the sampling time interval (in seconds), the highest frequency that can be defined is 1/2h Hz. The cut-off frequency:

$$f_c = \frac{1}{2h} \tag{2.8}$$

is called the Nyquist frequency or folding frequency. Frequencies above f_c are aliased with those in the range $0 \leq f \leq f_c$. Two practical methods exist for handling the aliasing problem. The first is to choose h sufficiently small so that is physically unreasonable for data to exist above the associated f_c. In general f_c is selected to be one-and-a-half or two times greater than the maximum anticipated frequency. The second method is to filter the data prior to sampling so that information above a maximum frequency of interest is no longer contained in the filtered data. Subsequently, choosing f_c equal to the maximum frequency of interest will give accurate results for frequencies below f_c (Bendat and Piersol, 1971).

The Nyquist criterion cannot be always satisfied due to an upper limit imposed by the validated data rate: one cannot sample faster than the data rate. Validated data rates up to 5 kHz could be reached in the experimental facility with naturally occurring particles in the water. For a given optical configuration data rates can be increased further either by seeding the flow or by modifying the gain of the counter. Care has to be exerted, however, as such modifications may introduce phase ambiguity and/or affect signal quality. In the present study the only means used to increase the data rate was by inserting a few drops of diluted milk to the flow. The latter increased slightly the data rate without affecting the signal quality.

The higher frequency of interest in the flow can be estimated from reported turbulent scales. At the time of this investigation no published scales for the cross-flow over tube bundles were available in the literature. Therefore, estimates of the Kolmogorov time scales were used as a guide in the selection of sampling rates. Kolmogorov time

scales can be roughly estimated using dimensional relationships (Tennekes and Lumley, 1972). Values vary from 0.3 to 5 ms in the flow field of interest. According to the Nyquist criterion, sampling frequencies ranging from 400 Hz to 6 kHz are needed to resolve these time scales. However, since the time scales of interest (Taylor time scales) are expected to be higher and given that the validated data rates in the flow vary from 1 to 5 kHz, sampling rates in the range of 1 to 4 kHz were considered appropriate for measurements in the axial direction. The sampling frequency is not critical if only the dominant frequencies are to be identified. As a result measurements of the transverse component were taken at a sampling rate of 1 kHz.

A second limitation in the choice of the sampling frequency is phase ambiguity noise, arising from the fact that at a given time there may be more than one particles in the control volume. The frequency at which phase ambiguity noise becomes a significant factor can be estimated (Kresta, 1991) from the wavenumber, κ, as defined by Hinze (1975) and the diameter of the control volume, b_X, for measurements in the axial direction:

$$\kappa = \frac{2\pi f}{U} = \frac{1}{b_x} \tag{2.9}$$

Above that frequency the frequency spectrum will be composed of white noise.

For the measurement locations in this study, the maximum measurable frequency estimated using the above formula was found to be much higher than the corresponding sampling rates with the exception of very few points with low mean velocity. Thus, phase ambiguity noise was not expected to be significant in the present measurements.

Another criterion considered in relation to the sampling rate was the velocity bias criterion according to which the appropriate sampling frequency should be one tenth of the validated data rate (Kresta, 1991). Varying the sampling frequency at the same measuring location had no observable effect on the mean and r.m.s. values or in the frequency spectrum in the present experiments.

Other criteria suggested for the selection of the sampling frequency can also be found in the literature: the product of the Taylor microscale and the particle arrival rate should be greater than five (Cenedese et al, 1992), or the mean data rate should be about twenty times the largest frequency at which undistorted measurements are desired in order to reduce the white 'step' noise in the sample-and-hold signal (Adrian and Yao, 1987). It is not possible however to satisfy all these criteria since an upper limit is imposed by the data rates that can be achieved in a given experimental facility.

Signal processing system. The signal processing and data acquisition system used was different to that employed for the ensemble-averaged measurements. The frequency counter used was a TSI model 1990B signal processor. The principles of frequency counting and time validation were the same as before but unlike the first counter, this one was equipped with built-in variable band pass filters and a variable gain. In addition, the counter had a fixed threshold level of 50 mV for amplitude validation. Thus, the signal from the PM tube was firstly pre - amplified and fed to the counter where it was first band-pass filtered for noise and pedestal removal and then amplified by the variable gain. The quality of the signal was monitored with a dual channel oscilloscope (Hitachi model V-525). The counter operated in the 'single measurement per burst' mode and 8 Doppler cycles were counted. A valid measurement was made when the time required for 8 cycles in the Doppler burst agreed with that for 5 cycles within a tolerance limit of 3 %. The counter was interfaced to a PC equipped with appropriate data acquisition software. A

comparison of the operating characteristics of the two counters used in this work can be found in Suen (1992).

Blocks of 6000 velocity data points were acquired at each location. Velocity data points lying outside ± 3 standard deviations from the mean value were removed from the records. The number of these data was very small, well below 1%, and therefore they were not expected to affect the spectral estimates (Srikantaiah and Coleman, 1985). Typical velocity recordings are shown in Chapter 3. For the analysis of the data a numerical algorithm was developed using the commercial software called *Mathematica*. This application software is equipped with built-in functions for Fast Fourier Transformations which are the principal tools in analysing time-resolved measurements and random data in general. Analysis of the data included the estimation of amplitude and power spectra, autcorrelation functions, filtering of periodic components and estimation of turbulent scales and dissipation rates.

Fourier Transform. By applying Fast Fourier Tansform (FFT) the velocity data are transformed from the time domain to the frequency domain where they are described by a series of amplitudes as functions of the corresponding frequencies. Typical amplitude spectra obtained are shown in Chapter 3. A brief description of the Fourier and inverse Fourier Transform definitions is given in Appendix I.

Power spectra. Although raw Fourier transformed data convey a lot of information about the frequencies present in a signal it is common practice to display and interpret spectral information by means of power spectra, where the amplitude of the spectrum is defined in terms of the power spectral density (PSD) that is the power per frequency interval. There are two techniques normally employed for the estimation of power spectral density: using FFT procedures (a periodogram) or via correlation estimates (a correlogram). More recent techniques are also available: a comparative study of techniques for the estimation of turbulence energy spectrum is

given by Rajan and Munukutla (1992). The periodogram technique was used in the present study. The definitions of the PSD estimates used are presented in Appendix II. The window functions and smoothing techniques employed to reduce the variance and the effects of leakage are also discussed in Appendix II.

Autocorrelation function. The autocorrelation function of the fluctuating velocity component u is defined as :

$$R(\tau) = \frac{\overline{u(t)u(t+\tau)}}{u'^2} \tag{2.10}$$

where u (t) and u (t+τ) are the instantaneous fluctuating velocities at times t and (t+τ), τ is the separation in time and u' is the r.m.s. velocity (equivalent to the standard deviation of the data, defined as the square root of the variance-also known as second moment). An overbar denotes an average quantity.

Alternatively, the autocorrelation function can be computed from the power spectral density function by applying an inverse Fourier transform since these two functions form a Fourier transform pair. From a computational point of view this technique is more efficient than the direct implementation of equation (2.10) and it has been used successfully by Kresta (1991). However, autocorrelation estimates obtained through FFT computations require an appropriate normalisation in order to be consistent with the ones calculated using (2.10). Normalisation depends of course on the PSD estimator used and it is not immediately apparent. Thus, the direct calculation of the autocorrelation coefficients was preferred in this study, at the expense of computational effort involved, in order to avoid any normalisation uncertainties.

Turbulent scales. Once the autocorrelation function has been estimated, the integral time scale T_E, referred to as the Eulerian integral time scale (Hinze, 1975) and defined as:

$$T_E = \int_0^\infty R(\tau)d\tau \tag{2.11}$$

can be computed. In practice, however, the integral time scale is computed by integrating R(t) from zero to its first zero crossing and not to infinity. The value of the integral time scale is a rough measure of the time interval over which u(t) is correlated with itself (Tennekes and Lumley, 1972) or a rough measure of the largest connection in the turbulent behaviour of u(t) (Hinze, 1975).

The micro time scale τ_E, also referred to as the Eulerian dissipation time scale (Hinze, 1975), is defined by the curvature of the autocorrelation function at the origin:

$$\frac{1}{\tau_E^{\,2}} = -\frac{1}{2}\left[\frac{\partial^2 R(\tau)}{\partial t^2}\right]_{t=0} \tag{2.12a}$$

which can be simplified by a Taylor series expansion to:

$$\frac{1}{\tau_E^{\,2}} = \frac{1}{2u'^2}\overline{\left(\frac{\partial u}{\partial t}\right)^2}_{t=0} \tag{2.12b}$$

The micro time scale is a measure of the most rapid changes that occur in the fluctuations of u(t) and can be approximated by the intercept of the parabola that matches the autocorrelation function at the origin:

$$R(\tau) \cong 1 - \frac{\tau^2}{\tau_E^2} \tag{2.13}$$

If the flow field has a mean value that is large with respect to the turbulence fluctuations ($U >> u'$) so that Taylor's hypothesis (Hinze, 1975) is valid and the

flow can be assumed to be homogeneous, then the length scales can be computed using the following equations:

Integral length scale

$$\Lambda_f = U\,T_E \tag{2.14}$$

Micro length scale (or dissipation scale)

$$\lambda_f = U\,\tau_E \tag{2.15}$$

An alternative convective velocity should be used when Taylor's hypothesis is not valid. The use of alternative convective velocities is examined in Chapter 3.

Dissipation rate. The rate of dissipation of the turbulence kinetic energy, ε, is a parameter of great interest in the characterisation of turbulence. Several methods have been proposed for the determination of ε. One of the most common expressions for ε found in the literature is:

$$\varepsilon = A\,\frac{u'^3}{L} \tag{2.16}$$

where A is a constant of proportionality, usually assumed to be equal to unity, u' is a characteristic velocity scale and L a characteristic length scale representing the average size of the energy containing eddies (Hinze, 1975) or, in approximate terms, the width of the flow (Tennekes and Lumley, 1972). Either the axial r.m.s. velocity (for isotropic turbulence) or the square root of the turbulence kinetic energy k may be chosen as a characteristic velocity scale. The cylinder diameter, d, can be used as a characteristic length for a tube bundle. It is also reasonable to assume that the integral length scale, Λ_f, which is mainly determined by the size of the larger energy containing eddies, is of the same order as the average size of these eddies L used in formula (2.16).

The dissipation rate can also be expressed in terms of the Taylor micro length scale or dissipation scale λ_f (Hinze, 1975):

$$\varepsilon = 30\nu\frac{u'^2}{\lambda_f^2} \tag{2.17}$$

where ν is the kinematic viscocity and λ_f is the micro length scale or dissipation scale as defined in equation (2.15). It must be noted that λ_f in equation (2.15) is estimated by making use of Taylor's hypothesis which might not be valid everywhere in the flow.

In the present study, dissipation rates were estimated using both equations (2.16) and (2.17). The axial r.m.s. velocity is used as a characteristic velocity scale and either the cylinder diameter or the integral length scale are used as characteristic length scales in equation (2.16). The results were compared with the numerical values of ε predicted by NTUA employing the k-ε model (Bouris, 1995).

Filtering techniques for the removal of periodic components. In order to isolate the high frequency fluctuations that represent the real turbulence and subsequently estimate the autocorrelation function and the turbulent scales, the frequency spectrum must be filtered first to remove any frequencies associated with the variation of the mean flow. Three techniques were examined:

a) the notch filtering technique;

b) low-pass filtering in the frequency domain;

c) moving window averaging in the time domain;

The three techniques are described in detail in Appendix III where the reasoning for the selection of the notch-filtering technique, which was found to be the most appropriate for the present work, is also given.

Amplitude discrimination technique

Particle-laden flows are of particular interest not only in relation to fouling but to many other engineering applications. Recent developments in measuring techniques based on laser-Doppler anemometry enable measurements in two-phase systems for a wide range of particle sizes and concentrations. A detailed review on velocity, particle and concentration techniques for multiphase flows can be found in Yianneskis (1987). Also, Hardalupas et al (1989) discuss the advantages and disadvantages of the available techniques and reviews LDA studies of particle - laden jets.

The amplitude discrimination technique was employed to distinguish between the Doppler signals corresponding to the two separate phases, the discrete one (particles) and the carrier one (water). With this technique the Doppler signals of the two phases, shown in Figure 2.7, can be distinguished by virtue of their pedestal amplitudes, by setting an appropriate discrimination level. In order to do that the photomultiplier voltage was reduced after completing the single-phase measurements, so that no signals corresponding to the fluid were detected. Then Diakon particles were introduced to the flow and their velocity components were measured. The LDA and signal processing system were the same as those used for ensemble-averaged LDA measurements in single-phase flows. The technique is simple and straightforward. Its main drawback is that simultaneous measurements of the two phases cannot be achieved. Some other limitations of the technique like trajectory ambiguity, depth of field, etc. are discussed by Hardalupas et al (1989).

Diakon (acrylic) particles were suspended in the flow over the in-line tube bundle and their mean and r.m.s. velocities were measured using the amplitude discrimination technique. The size range of the particles was 250-355 μm with a mean diameter equal to to 282 μm. The volumetric concentration was approximately

equal to 0.024 %. The characteristic properties of the particles are described in detail in Chapter 5. The solid/liquid phase flow experiments were carried out in the experimental facility used for single-phase flow experiments. Special attention had been paid during the design stage of the facility to align most parts of it vertically and minimise horizontal pipe sections so that settling of particles in particle/laden flow experiments would be avoided or minimised.

2.5 MEASUREMENT ERRORS AND UNCERTAINTY

The major errors involved in the present experimental study are briefly discussed in this section.

2.5.1 POSITIONAL ERRORS

The uncertainty in locating the measurement volume depends on the accuracy of the traversing mechanism, the dimensions of the control volume and also on the accuracy in locating a reference point for the measurement volume. As mentioned earlier, the optical axis was set parallel to the z-direction of the compound table. The accuracy of the traversing table was 0.05 mm in all three directions. Positional errors were minimised by re-setting the reference position of the measurement volume in the x-direction at each tube row encountered. The positional error in the z-direction was not important since all measurements were taken at the same plane defined by z = 0 mm. The errors associated with locating a reference position for the measurement volume by visual observation were estimated to be equal to 0.42 mm in the x and y directions and 0.23 mm in the z direction respectively.

2.5.2 FREQUENCY SHIFTING

As mentioned earlier, the frequency shift needed to resolve directional ambiguities was provided by a radial diffraction grating that was rotated by a bi-directional DC motor. The maximum frequency shift that could be applied between the first order beams was equal to 2.6 MHz. A shift of 1.6 MHz was used for measurements taken at the highest Re_d employed in this study, i.e. at Re_d = 12,858. Lower frequency shifts were used at lower Re_d's in order to improve the resolution of the measurements.

Variations in the rotational speed of the grating were minimised by the use of a voltage stabiliser which reduced the effects of surges in the main supply. The maximum r.m.s. variation in speed was about 0.5 % and the maximum speed fluctuation within ± 1 %. The influence of such variations on the measured r.m.s. values has been shown to be small (Melling, 1977); the errors introduced did not exceed 2 % even in regions of low turbulence intensity.

2.5.3 BIAS EFFECTS

The fact that particles cross through the measurement volume at a rate proportional to the instantaneous velocity (given a uniform particle distribution) gives rise to bias errors when statistical quantities are formed by direct ensemble-averaging of the accumulated sample values. However, the bias effect associated with the fluctuating velocity is only one of a number of possible biasing effects occurring in burst-type LDA processing. The sampling rate may also be correlated with velocity direction and with fluctuations in particle concentration resulting from density fluctuations, mixing of different fluids, or chemical reactions (Buchhave et al, 1979).

The velocity bias effect on the formation of ensemble averages from burst-type LDA signal processors was first studied by McLaughlin and Tiederman (1973) who showed the effects of bias on the velocity probability distribution (p.d.f.): skewing towards higher velocities is likely to occur due to the fact that more fast moving than slow moving particles are observed crossing the control volume over the measuring period. Bias effects and correction methods have been the subject of investigations by many researchers. However, it has not been firmly established under which conditions the correction techniques suggested are valid; therefore their reliability is often questionable.

McLaughlin and Tiederman (1973) suggested a bias correction for one component measurements. By weighting each sample by a weighting factor inversely proportional to the velocity component of the sample, a correction of the resulted statistical quantities results which gives the correct values in the case of one-dimensional flow fluctuations or steady flow but overcompensates when the velocity is fluctuating in two or three dimensions (Buchhave et al, 1979).

Residence-time weighting seems more promising in turbulence measurements especially of high intensity (Buchhave et al, 1979; George, 1975), according to which the velocity data from individual particles are weighted with their residence time. In order to implement this technique, measurement of the residence time is required by the signal processor in addition to the velocity output provided. This information was not available with the counter used in this study. An alternative correction technique has been suggested by Durâo et al (1980) in which the particle arrival rate is used instead of the particle residence time since these two are directly related. Durâo and Whitelaw (1976) overcame the bias introduced by the correlation between particle arrival time and velocity by sampling the already discrete samples at random instants in time by a Poisson sampling device. The disadvantage of this approach is the large amount of data that is not processed.

Halim and Turner (1986) applied residence time-and particle arrival time-weighting to the velocity data obtained downstream of the first and fourth rows of a staggered tube bundle in cross-flow. The results were interesting but complex and difficult to interpret. Application of the residence time- and arrival rate-weighting to the first row mean velocity data produced results that differed from the uncorrected ones by 10 % and 5 % respectively. No significant effect of the correction methods was observed in the flow passages where the turbulence intensity was low. However, the fourth row measurements showed that the residence time-weighting led to corrections of up to 10 % in regions of high velocity gradients whereas the arrival time-weighting produced negligible correction. Halim (1988) concluded in his thesis that the arrival time weighting was the most appropriate correction since it corrected only the values that were in error whereas the one dimensional correction and the residence time altered the mean velocities in the wakes by up to 35 %.

In view of the controversy associated with the significance of these errors and the type of bias correction techniques that should be used, the velocity data in the present work were not corrected for bias effects. An opposite bias effect - i.e. towards lower velocities - may occur due to the averaging characteristics of the photomultiplier which acts to mitigate the velocity bias and reduce the overall bias effect (Yianneskis, 1982). Durâo et al (1980) showed that neglecting the velocity and photomultiplier bias effects can result in insignificant error for a range of flow configurations. Therefore, bias is not expected to affect significantly the trends shown by the present data.

2.5.4 BROADENING EFFECTS

Broadening effects cause the p.d.f. of Doppler frequency to be wider than that of velocity. These effects result from the finite transit time of scatterers crossing the measurement volume, small scale turbulent fluctuations within the scattering

volume, gradients in mean velocity, finite instrument bandwidth, Brownian motion and the laser linewidth. Broadening from Brownian motion and the laser linewidth is negligible (Durst et al, 1976). Both the finite transit time broadening and the finite instrument bandwidth errors are significant in measurements made with a spectrum analyser or a frequency tracker but not in frequency counting systems. Therefore, only gradient and small scale fluctuation broadening might affect the velocity data in this work.

Velocity gradient broadening occurs when the measurement volume is located in regions of steep velocity gradients. In that case particles crossing different parts of the measurement volume will have different velocities resulting in broadening and skewing of the Doppler frequency spectrum. An approximate expression for the estimation of the error introduced to the mean velocity can be found in Durst et al (1976). The magnitude of the error depends on the particular velocity distribution and the dimensions of the measurement volume parallel to the gradient. A large error is expected when the velocity gradients are steep and non-linear which is more likely to occur in recirculating flows such as those in tube bundles. However, due to the small measurement volume employed in this study the error is expected to be minimal. Suen (1992) estimated the broadening effect in a flow with similar velocity gradients to be less than 2 % in most regions of the flow and 8 % in regions of highly non-linear gradients. Broadening from small scale velocity fluctuations has been approximated by George and Lumley (1973) but the correction suggested is of little use without the prior estimation of the turbulence dissipation. Melling (1975) estimated this error to be of the same order as the velocity gradient broadening.

2.5.5 COUNT AMBIGUITY

Count ambiguity is an inherent error in all counting systems associated with the $\pm$ 1 count error in counting the number of pulses for a large number of gate openings.

The magnitude of the error depends on the measured frequency, the frequency of the crystal oscillator of the counter and the number of Doppler cycles counted (Durst et al, 1976). Since the measured frequencies in the present study were relatively small, this error was estimated to be of the order of 0.01 % for both counters used (the error is smaller for the TSI counter since its resolution is higher).

2.5.6 STATISTICAL ERRORS

The number of samples over which ensemble averages of the mean and r.m.s. velocities are estimated can also introduce an experimental error, which can be estimated from statistical analysis (Yanta, 1973). The errors introduced by the number of samples used in this work (2000) are estimated to be approximately 1.6 % and 2.85 % for the mean and r.m.s. velocity respectively, assuming a turbulence intensity of 50 % and a confidence level of 95 %.

2.6 CLOSURE

A number of possible sources of error and uncertainty may occur in LDA measurements. An accurate estimation of these errors is a laborious task. The use of a comparatively small measurement volume, an appropriate sample size as well as the use of a dense measurement grid especially in regions of steep velocity gradients were shown to minimise most of the errors involved. No correction techniques were employed in this study due to the uncertainties involved in their implementation. Suen (1992) and Cheung (1989) checked the accuracy of measurements performed using a system similar to that employed in this study by measuring the known velocity of a pin rotated by a DC motor. The errors in determining the mean and r.m.s. velocities were found to be approximately equal to 1 - 2 % and 2 - 3 % respectively. The overall errors in the mean and r.m.s. velocities measured were calculated as 1 - 5% and 5 - 10% respectively, with the higher errors occurring in

regions of steep velocity gradients. Numerical integration of the mean velocity profiles obtained showed that the estimated mass flow rate agreed with the bulk one within 5%. Due to the inherent interpolation errors in the integration, the experimental error in the velocity measurements might be expected to be lower. The techniques described above were employed to measure the mean and r.m.s. velocities in the staggered tube bundle with $S_T/d = 3.6$ and $S_L/d = 1.6$, which are presented in the following chapter.

Table 2.3. Studies of spectral analysis techniques and estimation of turbulence quantities.

Author	Flow configuration / Technique	Remarks
Heskestad (1965)	An approximate relation between the partial time and space derivatives obtained for free shear flows with high turbulence intensity where the Taylor's hypothesis fails.	An approximate relation for the mean-square space and time derivatives was derived from the momentum equation assuming independence of large-scale and small-scale motions: $\overline{(\frac{\partial u}{\partial t})^2} = U^2 \overline{(\frac{\partial u}{\partial x})^2} \left[1 + \frac{\overline{u^2}}{U^2} + 2\frac{\overline{v^2}}{U^2} + 2\frac{\overline{w^2}}{U^2} \right]$ The relation, expected to be valid for high turbulence intensities, was supported by experimental results taken in a plane turbulent air jet where Taylor's hypothesis was not applicable.
George and **Lumley (1973)**	Review of LDA technique.	Spatial and temporal resolution of the LDA examined and criteria for meaningful measurements established. The effect of Doppler ambiguity on measurements of the instantaneous velocity and statistical quantities examined. Criteria for minimising Doppler ambiguity presented.
Gaster and **Roberts (1975)**	Techniques of analysing randomly sampled data (Poisson distributed samples) presented and discussed.	Regular sampling: extremely powerful and very fast but two inherent failings: 1) aliasing, necessary to employ analogue filtering to ensure that there is no significant power in the signal at frequencies greater than one half the sampling frequency. 2) spectral estimates are generated at equal intervals in the transform plane and this can be inconvenient e.g. when analysis is carried out over a wide band of frequencies. Random sampling: preferable no aliasing, spectral estimates can be computed at selected intervals.
Gaster and **Roberts (1977)**	Spectral analysis of randomly sampled data discussed. Power spectra estimates by direct transform compared with those obtained by correlation techniques. The variability of spectral estimates and its relation to sampling rates discussed.	Spectral estimation can be improved when a suitable data window is used. Variability of periodically sampled data can be reduced by: a) averaging PSD estimates over frequency bands; b) dividing record into N blocks each of period T, estimating PSD and averaging over the number of blocks at each frequency.

Norsworthy (1979)	Five techniques for spectral analysis of randomly sampled data are compared: 1. FFT in time domain. 2. Single frequency regression in time domain. 3. Multiple frequency regression in time domain. 4. FFT in correlation coefficients. 5. Multiple frequency regression in correlation coefficients.	All techniques equivalent for continuous or periodic signal observations. For randomly sampled data: -signal and correlation FFT equivalent performance, –single and multiple frequency regression overcame induced spectral folding. -S/N of single frequency regression no better than that of FFT methods. -multiple frequency regression gives excellent spectral measurements if all high amplitude frequencies can be solved for simultaneously; expected to exhibit improved S/N performance.
Habib and **Whitelaw (1979)**	Velocity characteristics of a confined coaxial jet determined by hot-wire anemometry. Coaxial pipe arrangement with d = 16.1 & 21.6 (inner pipe), 44.5 mm (outer pipe). Velocity ratios Ua/Ub = 3.0 & 1.0 and Re_a=85,000 & 55, 200 and Re_b=20,600 & 38,900. Experimental data compared with CFD predictions using k-ε model.	Centreline macro- and micro-length scales estimated by extrapolating/ integrating specta as follows: $L_f = \frac{\pi}{2} \lim_{k\to 0} F(\kappa)$, and $\frac{1}{\lambda_f^2} = \frac{1}{2}\int_0^\infty \kappa^2 F(\kappa) d\kappa$. Distributions found consistent with turbulence energy, maximum macroscales corresponded to the maximum in turbulence energy and velocity gradient. Dissipation estimated using: $\varepsilon = 15\nu\overline{u^2} / \lambda_f^2$. Experimental values were lower than CFD in upstream regions: k-ε model tends to connect the dissipation rate too strongly to the local mean velocity field which is inappropriate since the dissipation occurs in the finest scales of motion and these do not reflect the local mean strain field. This tends to increase ε.
Buchhave et al (1979)	Review of LDA technique.	Correlation and spectral measurements reviewed with reference to random sampling.
Roberts and **Gaster (1980)**	A method for improving estimates of the power spectral density from randomly sampled data presented. It involves filtering out some parts of the spectral energy so that analysis can be performed on data of smaller mean square. The specific case of mean removal was considered first and subsequently the general case of removing any set of spectral components.	The mean value estimated from the data in which a window function had been applied was subtracted from the data. The method can be extended to other spectrum components as follows: - apply a Fourier transform to the data (in which a data window has been applied first) - carry out inverse Fourier transform only to the spectral estimates to be removed - subtract the real values found from the "smoothed" data.

Table 2.3 (cont.)

Roberts et al (1980)	Spectral analysis techniques for randomly sampled signals were applied to data acquired by LDA operating in a burst mode. Measurements were taken in the centreline of seeded air jet. Spectral analysis of data was discussed and compared with results from hot wire signals.	The results confirmed the assumption of Poisson distribution for the sample arrival times for turbulent flows of low intensity. A direct Fourier transform and block mean removal were applied to the data. No data window was used. Block mean removal reduced the variability introduced in the spectral estimates by random sampling for high sampling rates. Removal of other harmonic components as suggested by Roberts and Gaster (1980) believed to be more effective.
Rask (1981)	Cycle-by-cycle data reduction techniques for LDA measurements in engine cylinder flows are compared. Four data sets from measurements in an L-head engine were processed by three techniques: window (ensembled), smoothed-ensemble and cycle-by-cycle.	window analysis: mean velocity evaluated over a crank angle range. Large window size introduced errors into the mean and rms (crank angle broadening). smoothed-ensemble: data split into 1° windows, a velocity is calculated at each window and a mean velocity curve is fitted using cubic spline routines. Smoothing is a type of low-pass filtering where more smoothing means lower cut-off frequency. cycle-by-cycle analysis: similar to the smoothed-ensemble except that only one cycle of data is used for each fit. A 5° window seemed appropriate. Various sizes should be used to see how the results were affected. Differences between window and smoothed-ensemble were quite modest.
Ball et al (1983)	Velocities in the piston bowl of a swirling DI Diesel engine measured by LDA with data rates up to 28 kHz. Moving window averaging applied to separate the cycle-to-cycle variations of the mean from turbulence. Power spectra estimated by FFT of the autocorrelation using a Hanning window. Integral time scales estimated by integrating $R(\tau)$ and micro time scales from the second derivative of the $R(\tau)$ at the origin.	Macro and micro time scales estimated at compression TDC differ by a factor of less than 2. The ratio increased after TDC. Time scales reduced as engine speed increased and the scales in terms of crank degrees remained fairly constant.

Table 2.3 (cont.)

Srikantaiah and **Coleman (1985)**	Basic techniques to analyse randomly sampled data such as slotting correlation (Mayo et al, 1974) and direct transform (Gaster & Roberts, 1977) were discussed. The application of the techniques to simulated data and the effect of removing 'bad points' and adding white noise were examined. Techniques were applied to LDA data obtained in a simulated coal fired magnetohydrodynamic flow field (using short blocks in 102,400 data points).	Direct transform method has advantages: no highest frequency information is lost, filtering out of the ambiguity spectrum due to uncorrelated data. Correlation technique suffers from aliasing. Spectral estimates obtained after removing 'bad' points (validated points as result of noise and points for which the time interval between two successive measured points exceeds the maximum time interval which the LDA counter/interface/computer system can count) did not vary significantly as long as the total number of bad points removed was within about 1 % of the total sampled points.
Press et al (1986)	Algorithms for Fourier Transform spectral methods given.	Extensive documentation of Fourier transforms in general, discrete Fourier transforms, power spectra estimation, filtering and data windowing. Notch filtering described can be used for removing narrow band frequencies. Hanning window can be applied to the data to reduce variability.
Adrian and **Yao (1987)**	Power spectrum and correlation of LDA velocity signals obtained by sampling and holding the velocity at each new Doppler burst studied. Two cases examined: low fluctuation intensity and arbitrary data density and high data density and arbitrary fluctuation intensity.	Spectrum consists of the velocity plus a white 'step' noise spectrum each of which is low-pass filtered by virtue of the holding action between samples. Holding results in missing high frequency information. The step noise arises from the jumps that occur at new random sample times in the sampled and held signal and it obscures the low spectral energy density regions of the velocity spectrum, i.e. the high frequency end of a turbulent power spectrum. In the limit of high data density the step noise vanishes and the sample-and-hold signal is statistically unbiased for any turbulence intensity. As a guideline the mean data rate should be about 20 times the largest frequency at which undistorted measurements are desired.
Tropea (1987)	LDA data with known moments and spectral contents were generated numerically using first and second order autoregressive models, and processed by 1) direct transform (Roberts et al., 1980); 2) using a 'controlled processor' that cannot sample every available data point; 3) resampling at regular intervals the analogue output of the signal processor which uses a 'hold' circuit during drop out periods. A comparison of the various approaches and the influence of particle seed rate and turbulence level were presented.	Direct transform technique found to produce reliable estimates for low turbulence intensities and low particle densities. For modest to high particle densities the analog signal approach can be more efficiently computationally. For high turbulence intensities the spectrum estimated using the direct transform approach was found to be qualitatively correct but quantitatively biased. The controlled processor was found to perform well in specific cases, as for example at very low particle rates. No adequate means of spectral estimation was found for the case of both low particle density and high turbulence levels.

Table 2.3 (cont.)

Absil (1988)	LDA measurements in the wake of a circular cylinder (air, Re=1,300, U_∞ =10 m/s, d=2 mm). 2 colour LDA system for mean turbulence and time correlation measurements. Spatial correlations and autocorrelation obtained by a cross-correlation technique.	R(τ) estimated using the slotting technique. Findings: at x/d = 125 -the turbulence structure became uncorrelated after about 10 ms. -integral time scale was estimated to be 0.7 ms. -difficult to determine micro time scale τ_ε because R(τ) decayed fast. -R(τ) did not completely reach unity and still showed a small spike near the origin.
Wu et al (1989)	Methods of estimating ε experimentally were discussed. Time-resolved LDA measurements in a stirred vessel made at 200 rev/min (impeller Re = 27,000). Velocities were measured in three directions. Length scales were estimated from time scales using as convective velocity: $U_c = \sqrt{U^2 + u'^2}$.	At the disk plane only the fundamental frequency was observed but near the blade edges 2 frequencies were evident. These periodic components were removed from the velocity fluctuations by correcting the autocorrelation function. This was achieved by matching a periodic wave to the long time portions of the autocorrelations. Spectra, corrected rms and ε profiles were presented for the radial velocity component. Only the radial velocity component was taken into account in the estimation of ε. The flow was not strongly anisotropic in the measured locations, so the effect of the other two velocity components on the estimated ε values was expected to be small. A double peak was observed in the ε profiles near the impeller blade. The ε values were found to be effectively zero at the impeller stream edges. The constant A in equation (2.16) was evaluated by comparing the total power dissipated in the vessel with the spatial integration of the measured ε values and was found to be very close to 1.
Le Coz et al (1990)	LDV measurements in a four-valve engine. Low-pass filtering employed to discriminate the cycle-resolved turbulence.	In order to implement the low-pass filtering the irregularly sampled signal was transformed into a temporary regularly sampled one by linear interpolation. FFT and low-pass filtering applied to the latter (the Fourier coefficients above a cut-off frequency were set to zero). An inverse FFT yielded the regularly sampled low frequency signal which was transformed to an irregularly sampled one by interpolation. The high frequency contributions were found to decrease with increasing cut-off frequency. Power spectra exhibited the classical -5/3 slope meaning that turbulence was in equilibrium state around TDC.

Table 2.3 (cont.)

Kresta (1991)	Flow visualisation and time-resolved LDA measurements were carried out in stirred vessels. Time scales and dissipation rates were estimated. CFD predictions based on k-ε model also reported.	A regular sampling approach was used. A Fortran computer code developed for spectral analysis based on algorithms given by Press et al. (1986). $R(\tau)$ estimated from the inverse FFT of the power spectrum. Peaks corresponding to blade passages filtered out using notch filtering as described by Press et al. (1986). Methods of estimating dissipation rates were described and compared.
McDonnell and **Fitzpatrick (1992)**	Time-resolved LDA and hot wire in triangular array with a relative spacing of 2.0 (air, U_∞ = 5 m/s). Two techniques of spectral analysis are examined: correlation based slotting technique and direct FFT. The effect of sampling rate on the latter was examined. Comparisons with spectra obtained with hot wire and LDA were made.	Correlation slotting technique: average sampling rate 5kHz, Lanczos low pass filter implemented to prevent aliasing. Spectra obtained from cosine transform of the computed $R(\tau)$. Spectra & $R(\tau)$ subjected to two passes through a Hanning window. Filtered data were also analysed with FFT. Both techniques yielded a vortex shedding frequency and its first harmonic. Effect of sampling rate on FFT: reducing sampling rate (5, 2.5, 1 and 0.4 kHz used) caused a systematic bias positive in low frequencies and negative in high frequencies. The peaks could be determined even with the poorest data rate. With high sample rates and correctly implemented digital filtering direct FFT has less variability & computational advantage.
Rajan and **Munukutla (1992)**	Comparative study of three spectral analysis techniques: periodogram, correlogram and autoregressive (AR) model., applied to velocity fluctuations of turbulent free air jet. (AR parametric method: a random process is modelled as the output of a causal system with transfer function $H(z)=1/A(z)$ excited by a zero mean white noise process $u[n]$ with variance ρ)	PSD obtained from one block of data and by averaging estimates over blocks of data. Rectangular & Hanning windows were used. In the periodogram method 1024 points FFT of the 1024 rectangular windowed data was used. Spectrum looked smoother if average estimates over 300 blocks obtained. The variance of the spectrum was highest with the periodogram technique which was the fastest. AR technique faster than correlogram and of a reasonably high accuracy.

Table 2.3 (cont.)

Cenedese et al (1992)	LDA measurements of three velocity components in the boundary layer of rectangular duct in water. Re=3,500. Mean data rate 2000 Hz. 60% validation. Zero-order interpolation to reconstruct time histories. Equispaced resampling at a sampling frequency equal to the minimum data rate between the three components.	Spectral density estimated using 4 methods: 1) direct FFT on all samples (nearest power of 2); 2) FFT of the correlation function on the first 16,384 samples; 3) Mean value of 20 FFT s in data blocks of 16,384 samples; 4) same as 3 but cosine tapered window used on each block. Method (1): best resolution but higher noise. Method (4) gave the best results. Correlation function estimated by 4 methods, 3 with FFT and one with direct calculation. No significant differences except for the windowed data. Integral time scale obtained by integration but Taylor microscale by counting the number of zero crossings per unit time of the fluctuating component (Hinze 1959, p.133).
Gould and **Benedict (1994)**	Spatial- and auto-correlation measurements in an axisymmetric sudden expansion using LDA. Step height=25.4 mm, fluid:air Re=114,000; centreline velocity=18 m/s. Autocorrelation function estimated using the slotting technique, with the zero lag autoproducts being omitted to minimise noise effects as suggested by Srikantaiah & Coleman (1985).	Integral length and time scales were estimated by integrating the spatial and auto correlation functions respectively. Dissipation lengths were estimated by fitting a parabola at the origin of the spatial correlation function and the Eulerian micro timescale by applying a Taylor series expansion to the $R(\tau)$ near $\tau=0$. Integral length scales Λ_f, Λ_g varied from 23-35 mm (longitudinal) and 8-15 mm (lateral). $\Lambda_g \sim \Lambda_f / 2$ implying anisotropy of the large scales. Time scales were lower in locations of low turbulence and higher in the shear layer where higher turbulence and large velocity gradients were present. Length scales obtained from the timescales using Taylor's hypothesis were overestimated in low turbulence locations and underestimated in the shear layer. Large microscales resulted from poor resolution of autocorrelation function near zero lag.
Djenidi and **Antonia (1995)**	A sample-and-hold interpolation was applied to LDA signals obtained in the far-wake of a cylinder (Re_d =1700 in water) to calculate power spectra using a direct FFT algorithm.	Spectral estimates were obtained by applying FFT to blocks of data and averaging over the number of blocks. The LDA spectra were in reasonable agreement with hot-wire spectra for a range of wavenumbers. The agreement was found to be improved when a noise correction was applied by subtracting the spectrum obtained by measuring at each location without the cylinder being present.

Table 2.3 (cont.)

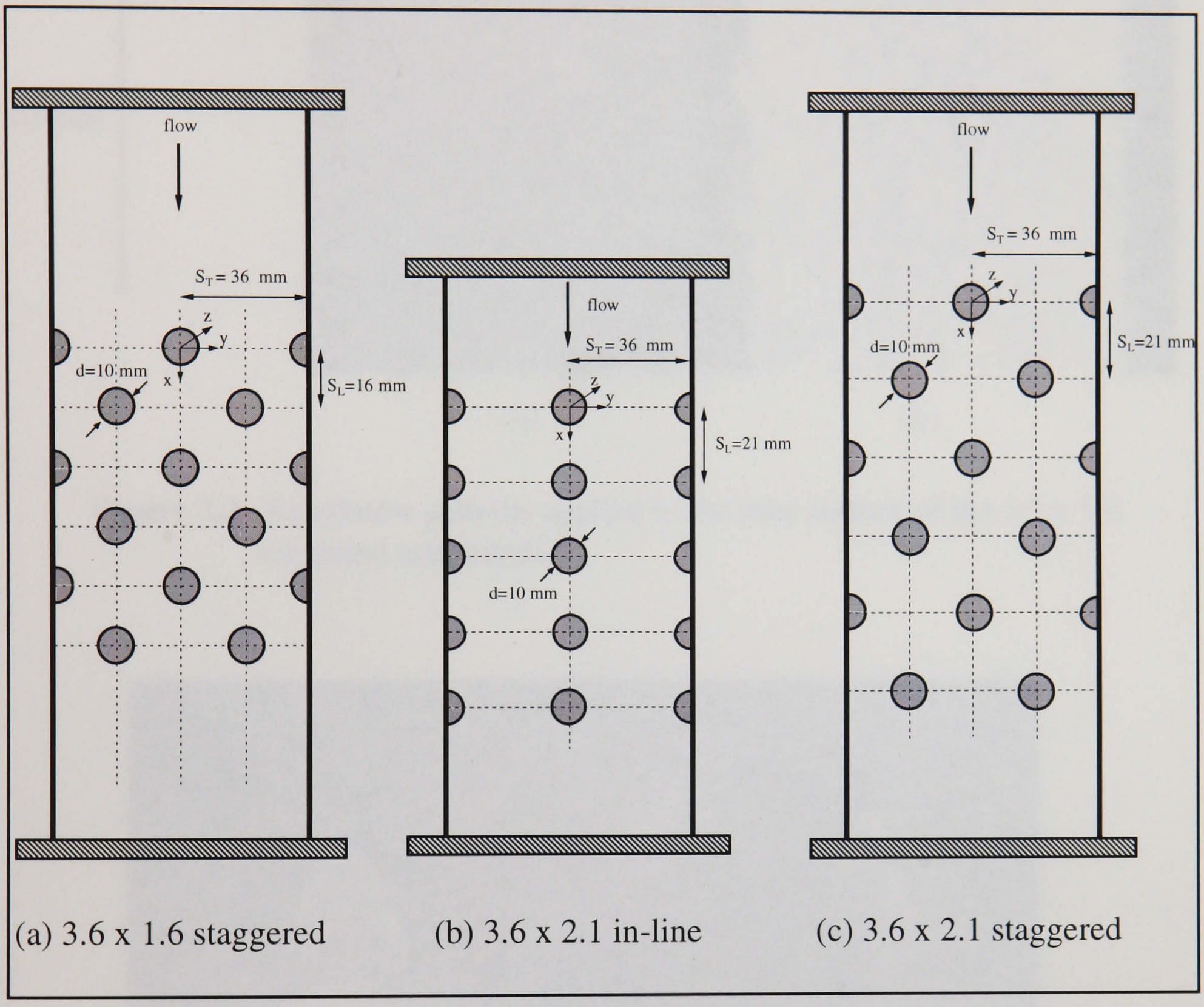

Figure 2.1. Cross-section of the three tube bundle configurations investigated.

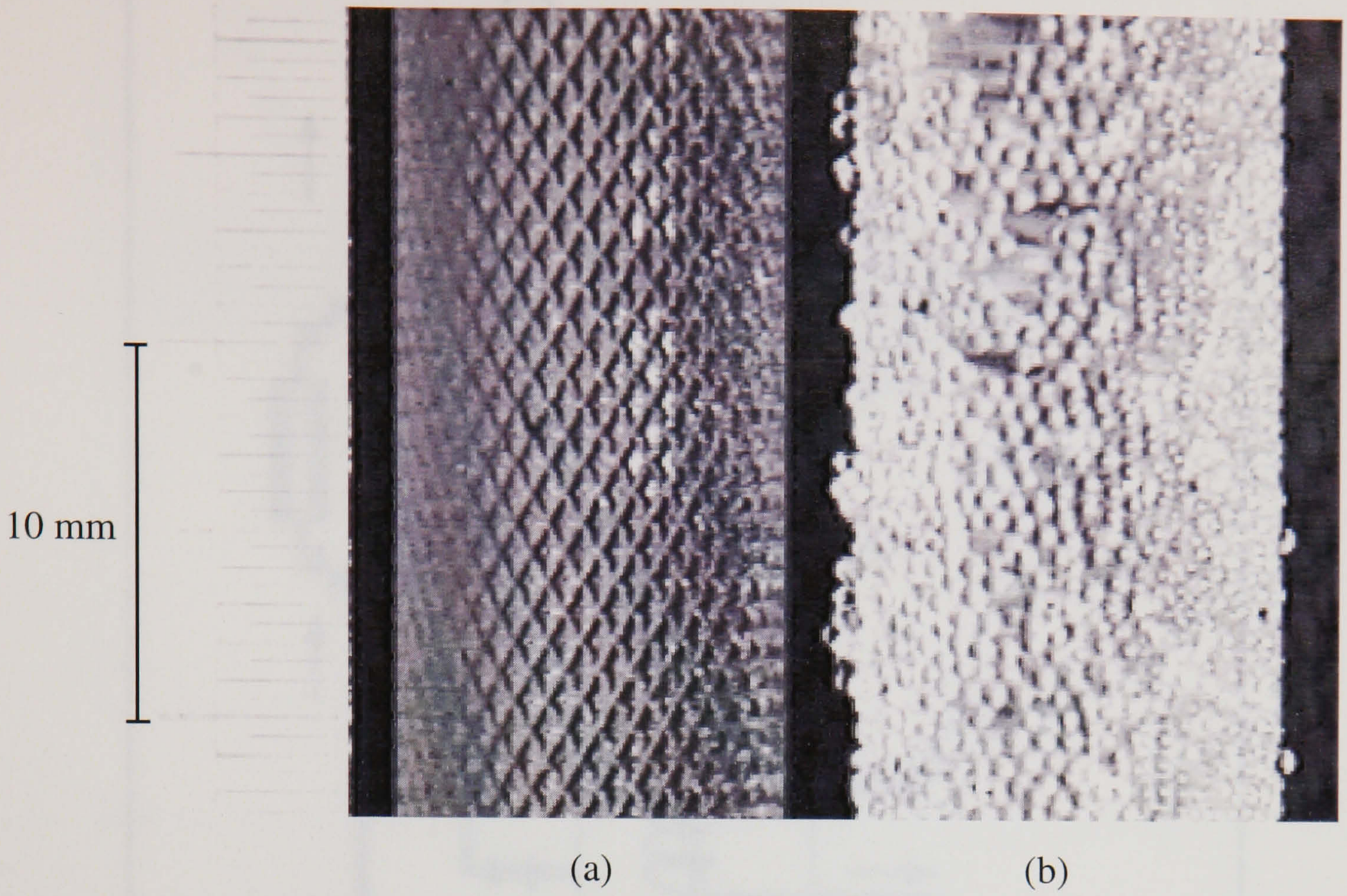

Figure 2.2. Roughness patterns applied to the tube surface of the 3.6 x 1.6 staggered tube bundle.

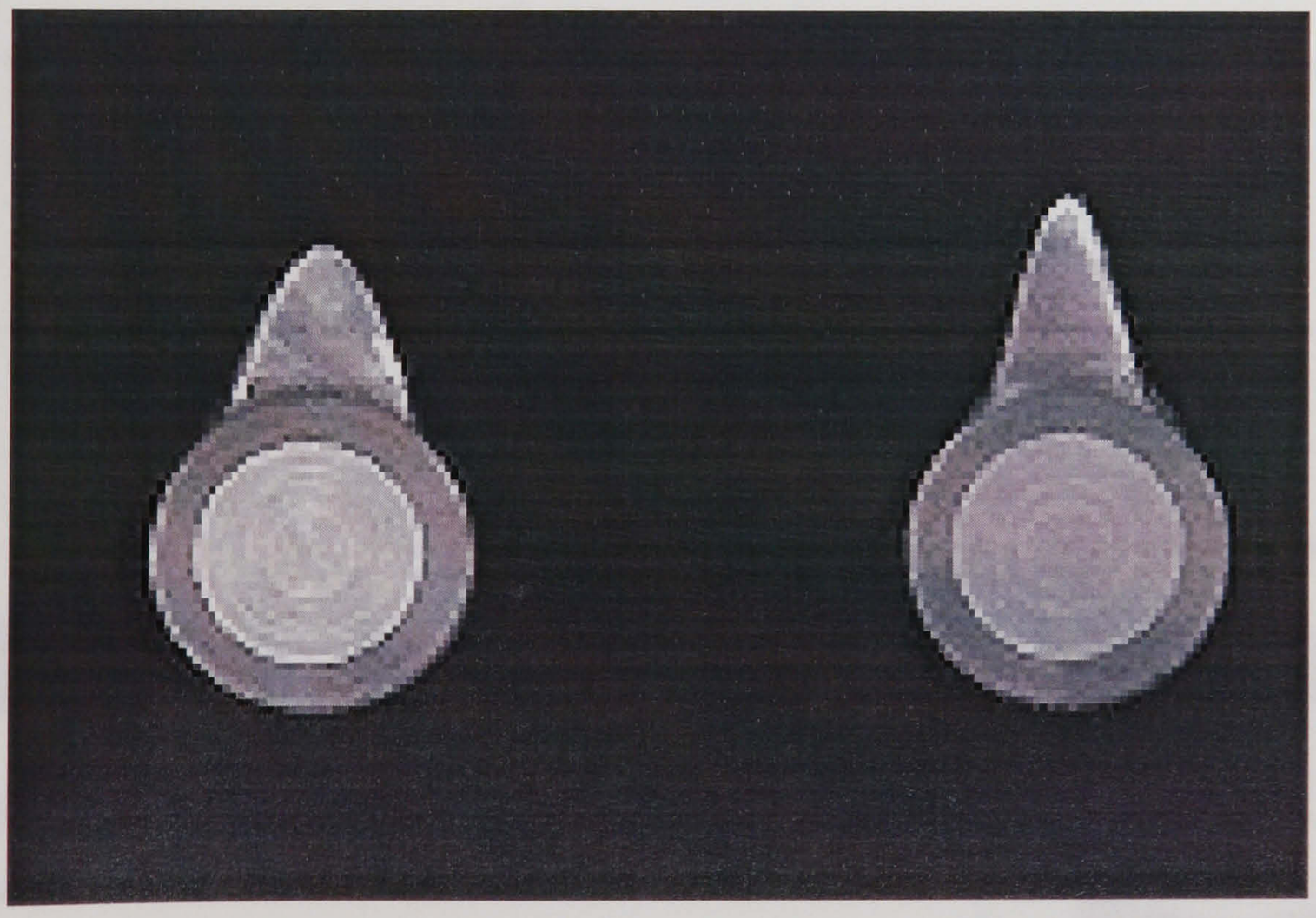

Figure 2.3. Tube shapes of the fouled cylinders in the first (a) and second row (b) of a staggered tube bank as predicted by NTUA fouling model after 8 hours of fouling by Al_2O_3 particles.

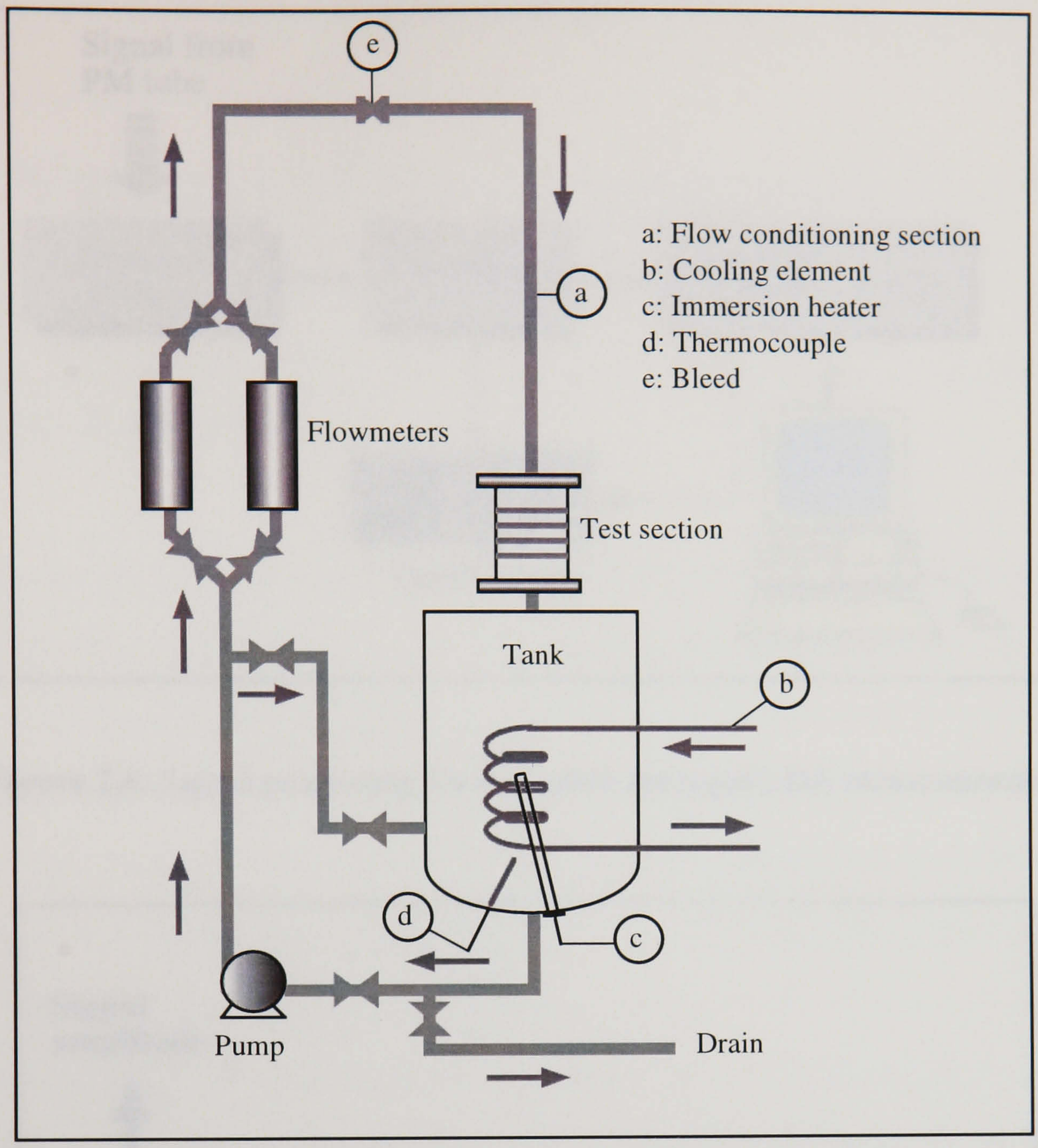

Figure 2.4. Schematic layout of the experimental facility.

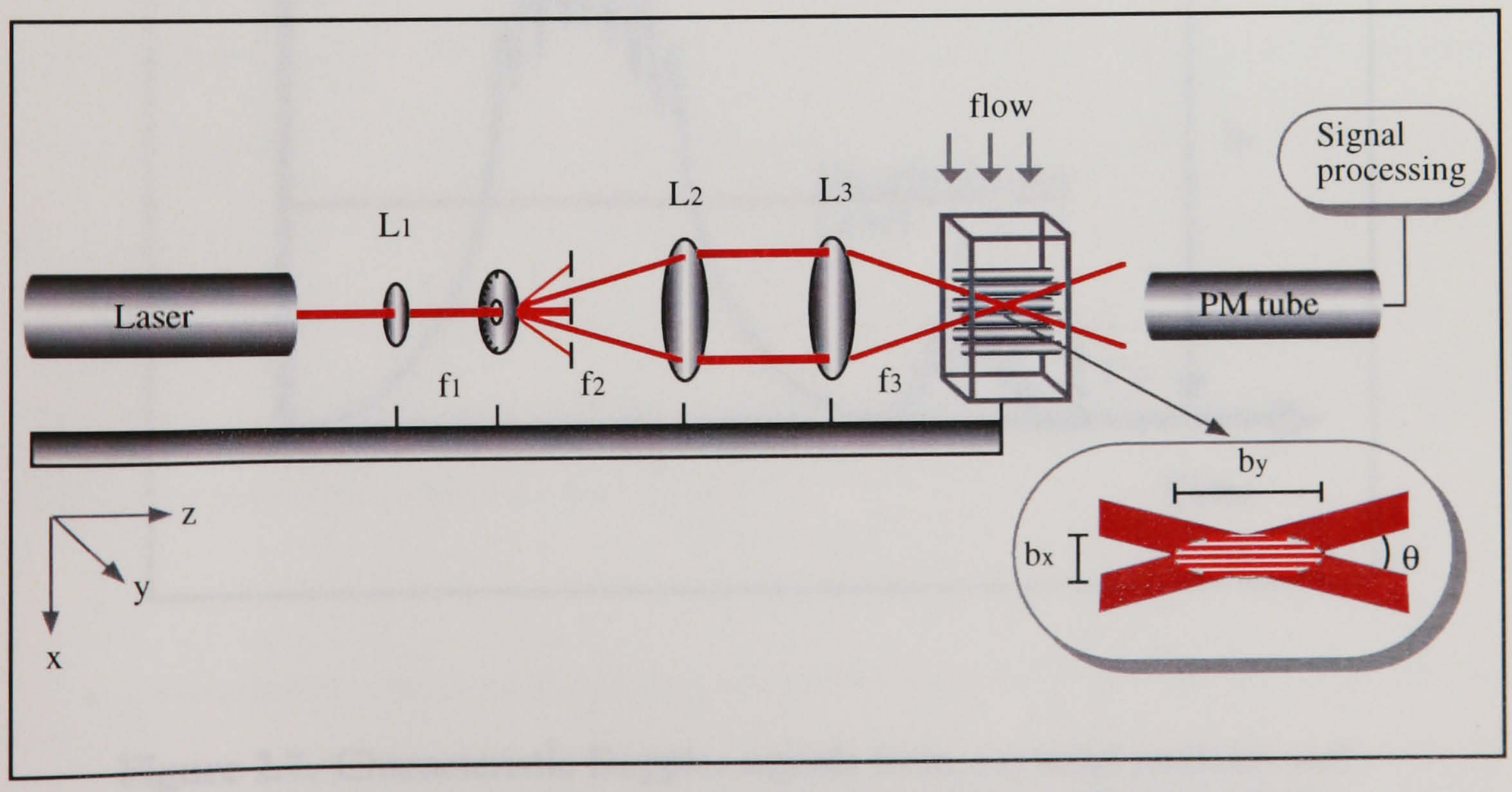

Figure 2.5. Optical configuration of the LDA system used.

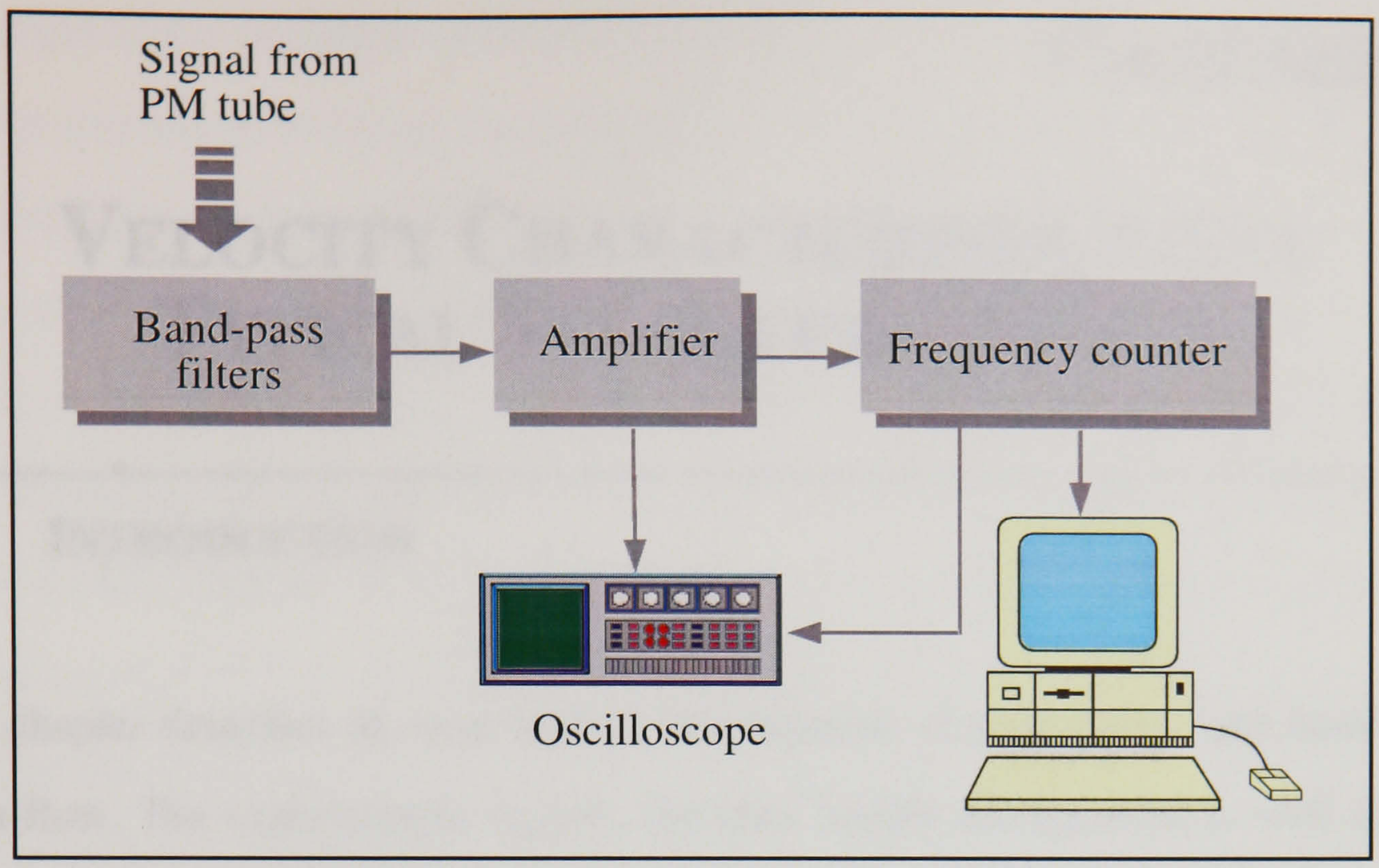

Figure 2.6. Signal processing for ensemble-averaged LDA measurements.

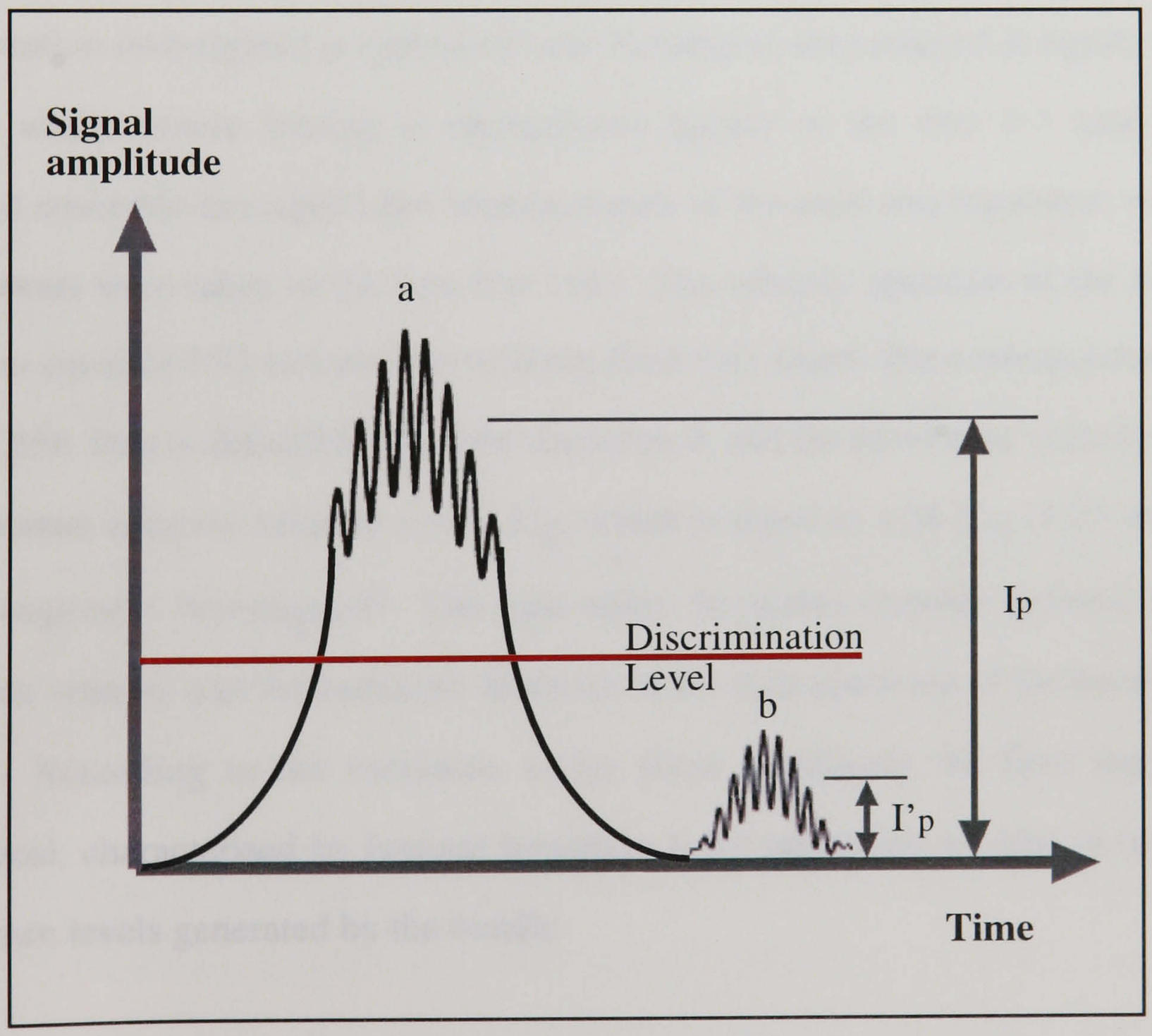

Figure 2.7. Characteristic Doppler signals from: (a) solid particles and (b) from micron size particles following the fluid motions (impurities in the water in the present study).

CHAPTER 3

VELOCITY CHARACTERISTICS OF A TYPICAL STAGGERED ARRAY

3.1 INTRODUCTION

This chapter describes an experimental investigation of a staggered tube bundle in cross-flow. The experimental facility, the tube bundle arrangement as well as the LDA experimental techniques employed in this investigation have been described in Chapter 2. The array was 6 rows deep and 5 columns wide[1] and the transverse and longitudinal spacings were equal to 3.6 and 1.6 tube diameters respectively. This configuration investigated is typical of heat exchangers encountered in lignite utility boilers where severe fouling is encountered mainly in the first 2-3 tube rows. Detailed ensemble-averaged LDA measurements of the axial and transverse velocity components were taken in the first five rows. The velocity upstream of the bundle, U_∞, was equal to 0.93 m/s and the working fluid was water. The corresponding Re_d was 12,858. Re_d is defined by the tube diameter, d, and the maximum velocity at the gap between adjacent tubes in a row, U_g, which is equal to 1.38 U_∞ (1.29 m/s) for the arrangement investigated[2]. The equivalent Reynolds number defined by the upstream velocity and the hydraulic diameter of the duct upstream of the bundle was 66,862. According to the literature, under these conditions the flow regime is subcritical, characterised by laminar boundary layer separation in spite of the high turbulence levels generated by the bundle.

---

[1] Three tube columns consist of full cylinders whereas the other two of half cylinders placed on the side walls.

[2] It is common practice in studies of the crossflow over tube banks to define the Reynolds number in this way. Depending on the spacings of a staggered configuration the maximum velocity U_g used in the definition of Re_d can occur either at the transverse plane between tubes at the same row or the diagonal plane between tubes of successive rows. In the present investigation the maximum velocity calculated from consideration of mass conservation occurs at the transverse plane.

The origin of the co-ordinate system is located at the centre of the middle cylinder in the first row and all locations are described in terms of normalised co-ordinates (x/d, y/d, z/d). Measurements were taken at the plane of symmetry (z/d = 0)[3] in the region $0.0 \leq y/d \leq 1.8$ and $0.0 \leq x/d \leq 6.4$ since the flow approaching the tube bundle was found to be two-dimensional and the interstitial flow was found to be symmetrical with respect to the x-axis. The axial mean and r.m.s. velocities (U, u') were measured first, then the diffraction grating and consequently the control volume was rotated through 90° and the transverse velocities (V v') were measured. In order to measure the third component, (W,w'), the whole test section was rotated by 90 ° around the vertical axis. Measurements of the axial and transverse components were taken at step intervals of 3 mm and 4 mm in the normal and streamwise directions respectively. The third velocity component (W, w') was measured at only 4 transverse planes midway between successive rows (x/d = 0.8, 2.4, 4.0 and 5.6) due to optical access restrictions. Detailed velocity measurements were also made along the wake axes for Re_d's in the range 3,104 - 12,858 in order to estimate recirculating parameters such as the length and width of the recirculation bubble and the recirculating mass-flow rate. The effect of Re_d on the development of the centreline mean and r.m.s. velocities as well as on the pressure drop was also studied.

Time-resolved LDA measurements were taken in selected locations in order to identify flow instabilities and characterise fully the turbulence structure. Instantaneous values of the axial and transverse velocity components were recorded at regular time intervals over a period of time. Sampling rates in the range of 1 to 4 kHz were employed and blocks of 6000 velocity data points were acquired at each location. Amplitude spectra were obtained for both the axial and transverse components through a Fast Fourier Transform of the time-resolved velocity recordings. Periodic oscillations were filtered from the axial velocity spectra obtained in the three first rows and parameters such as scales of turbulence and

[3]The vertical plane located midway along the span of the tubes.

dissipation rates were estimated. The results are compared with numerical predictions obtained for this geometry employing the k-ε turbulence model (Bergeles et al , 1996).

In order to facilitate comparisons with other tube bundle configurations presented later in this thesis all mean and r.m.s velocities are normalised with the upstream velocity, U_∞. The turbulence kinetic energy is also normalised with U_∞^2. The results are presented either as profiles or in contour form and the same reference scale or contour levels are used throughout the thesis for comparison purposes. The interstitial distributions of mean and r.m.s. velocities are presented both as profiles and contours. As it was felt that although the profiles provide accurate quantitative information about the measured values the contour plots offer a better visualisation of the distribution of the latter despite the interpolations involved. A small area adjacent to the cylinders is usually left undefined in the contour plots since interpolation by assuming zero values at the walls of the cylinders led to an unrealistic representation of the distributions in that region.

The accuracy of the mean velocity and turbulence level measurements was calculated as 1-5% and 5-10% respectively, with the higher errors occurring in regions of steep velocity gradients. Numerical integration of the axial velocity profiles showed that mass conservation across the banks is established within 5 %: due to the inherent interpolation errors in the integration, the experimental error in the velocity measurements might be expected to be lower.

3.2 MEAN VELOCITY DISTRIBUTIONS

The mean velocity vectors obtained in the 3.6 x 1.6 staggered array are shown in Figure 3.1. Both the vector length and heads are proportional to the velocity magnitude. The flow field is characterised by areas of high velocity at the flow

passages between tube columns and flow reversals and low velocities in the wake regions. Flow reversal is pronounced downstream of the first and second cylinders and consequently long recirculation bubbles are evident downstream of these rows but these features are less evident further downstream. Vectors are uniform and vertical on entrance to the bank but deflect as the fluid passes through the gaps between successive rows. The flow accelerates as it passes over the shoulder of each cylinder. In the wakes the flow decelerates as it approaches the downstream cylinder.

The distribution of the axial mean velocities, U/U_∞, is shown in Figures 3.2 (a) and (b) as profiles and contours, respectively. Positive axial mean velocities indicate velocities in the downward direction. The axial mean velocity profiles are quite uniform upon entry in the tube bundle. A steep velocity gradient can be seen in the shear layer separating from the first row cylinder. Flow reversal is pronounced downstream of the first cylinder with negative velocities reaching values up to 0.47 U_∞. The same features can be seen downstream of the second row with similarly high negative velocities in the recirculation region but are less pronounced further downstream. Negative velocities do not exceed 0.25 U_∞ downstream of the third and fourth rows. High velocities are observed along the centre of the narrow flow passages between tube columns with an almost constant value of 1.50 to 1.75 U_∞. Flow acceleration takes place close to the shoulder of the cylinders with velocities reaching values up to 2 U_∞.

The distributions of the transverse mean velocities (V/U_∞) at the same locations are shown in Figures 3.3 (a) and (b). The velocity scale in the profiles and the contour levels are the same as those in Figures 3.2 (a) and (b). Positive V values represent velocities away from the x-axis. Transverse mean velocities reach higher values (up to 0.5 U_∞) at the gaps between successive rows and alternate between negative and positive values as the flow passes through successive gaps. An interesting observation was made during measurements of this component. The velocities

exhibited bimodal distributions, probably due to a flapping action of the separated shear layer. Flow instability is a well-known feature of the flow in tube bundles and further investigation is needed to clarify this observation. Measurements of the third mean velocity component (W) confirmed the two-dimensionality of the flow since their values were found to be equal to zero.

3.3 TURBULENCE LEVEL DISTRIBUTIONS

In order to visualise better the generation of turbulence in the rod bundle the axial and transverse components of the r.m.s. velocities, u'/U_∞ and v'/U_∞, have been plotted both as profiles and in contour form in Figures 3.4 (a), (b) and 3.5 (a), (b) respectively. The normalised axial r.m.s. velocities (Figures 3.4 (a) and (b)) are relatively low behind the first row but start rising downstream of the second row. The distributions downstream of the second and subsequent rows are similar; r.m.s. levels of up to 0.6 U_∞ are found in the wakes whereas in the mainstream values are lower (up to 0.5 U_∞) and more uniform.

The distribution of v'/U_∞ (Figures 3.5 (a) and (b)) is different, with higher v' values in the wakes compared to the u' ones, indicating intense lateral mixing. The maximum value of v', 0.8 - 0.9 U_∞, was attained downstream of the second row. Turbulence levels in the mainstream between the third and fifth rows are almost constant with values comparable to u'.

In order to compare the distributions of the two fluctuating components and therefore assess the degree of anisotropy in the turbulence generated by the tube bank the ratio of the r.m.s. velocities, v'/u', was estimated and is plotted in contour form in Figure 3.6. The ratio is approximately equal to 1 everywhere in the flow lanes between tube columns but deviates from 1 in the wake regions where transverse r.m.s. velocities reach higher values than the axial ones. The effect is

more pronounced downstream of the second row where the magnitude of the transverse r.m.s. velocities is exceedingly large compared with the axial ones. The average ratio of v'/u' was found to be equal to 1.02 ± 0.3 throughout the measurement region. However, this is not an indication of isotropy since the aforementioned distributions are different.

Contours of the absolute value of the difference between the two r.m.s. components normalised with U_∞, $|v'-u'|/U_\infty$, are shown in Figure 3.7. These contours were plotted for the following two reasons: firstly the difference in the two components is expressed in terms of a constant, U_∞, and secondly the ratio v'/u' - although it is sometimes used as an anisotropy coefficient - can be misleading if v' and u' have small and similar values. It can be seen that the two r.m.s. components have similar values, within 20 % of U_∞, in most parts of the flow field. A pronounced difference between the two can be observed downstream of the second row (50 % of U_∞) whereas differences up to 30 % of U_∞ occur downstream of other rows. These findings suggest that numerical predictions of the flow using the k-ε turbulence model may fail to reproduce the turbulence levels in the tube bank due to the implicit assumption of isotropic eddy viscosity.

The profiles of w'/U_∞ midway between successive rows (Figure 3.8) exhibit the same trends with the corresponding v'/U_∞ profiles but the w' values are slightly smaller. The average ratio of v'/w' in these positions was found to be equal to 1.24 ± 0.29. This ratio was used to estimate w' values in other locations and consequently to provide estimates of the turbulence kinetic energy, k. The k estimates are normalised with U_∞^2 and presented in contour plot in Figure 3.9. The same trends as those identified in the v'/U_∞ contour plot (Figure 3.5 (b)) can be observed. This might be expected since the distributions of the two components v' and w' are assumed to be similar. k is low behind the first row and starts rising after the second row. Higher values are observed in the wakes whereas low values of k can be seen in the main

stream between the tubes. Surprisingly, the highest values of k (70 - 80 % of U_∞^2) are reached behind the second row. This effect has been observed by other investigators (Halim and Turner, 1986; Simonin and Barcouda, 1988) but it has not been explained. It is likely that this maximum is associated either with intense vorticity shedding or other sort of flow instability occurring there. Indeed, a recent study (Polak and Weaver (1995)) attributed the higher turbulence levels observed behind the second rows of triangular arrays to the vortex shedding at different frequencies from the first and second rows. Since the two discrete frequencies detected had their maximum amplitude in the second and third row respectively the wake of the second row cylinder is subjected to a strong interaction between the coherent structures from the first and second row cylinders. Almost constant values of k equal to 20 - 30 % of U_∞^2 can be observed in the main stream between the third and fifth rows of the staggered array.

3.4 FLOW PERIODICITY, TURBULENCE SPECTRA AND SCALES

Ensemble-averaged measurements showed evidence of flow instabilities as bimodal velocity probability density functions (p.d.f.'s) were recorded. As already shown in Chapter 1 it is well established that a flow periodicity is present in tube bundles which may incite tube vibrations in liquid and acoustic resonance in gas flows. The nature of this flow periodicity has not been resolved. Four basic excitation mechanisms have been identified: turbulent buffeting, vorticity shedding, fluid-elastic instability and acoustic resonance (Weaver and Fitzpatrick, 1987; Ziada and Oengöeren, 1991). The vorticity shedding excitation has been attributed either to vortices shed from the tubes - by analogy to vortex shedding from isolated cylinders in cross-flow - or to instabilities of the jets issuing between the tubes. Recent studies have shown clearly that alternate vortex shedding occurs in staggered tube bundles and jet instability in in-line arrays (Weaver et al., 1993; Ziada and Oengöeren, 1991). Regardless of its nature, the so-called vortex shedding excitation in tube bundles

manifests itself by a narrow band discrete event in the turbulence and pressure spectra whose frequency varies with the flow velocity. The associated Strouhal number (St), however, is constant and depends on the tube arrangement (i.e. in-line or staggered) and the spacing between the tubes, the Re_d, the location within the array (Collinson and Robinson, 1991) and, according to a recent study (Oengöeren and Ziada, 1995), to the number of rows and columns in the tube bundle. There may even be multiple St's at a given Re_d in the first rows of an array (Weaver et al, 1993; Oengöeren and Ziada, 1995).

In view of the foregoing discussion the tested staggered array is expected to exhibit a flow periodicity due to alternate vortex shedding from the first rows with a St number lying between 0.2 - 0.4 (Chen, 1977). The presence of such a flow periodicity introduces a 'pseudo-turbulence' contribution to the measured velocity fluctuations due to the variation of the mean flow, which broadens the random turbulence levels. As a result, the turbulence level and k values presented earlier may overestimate the true amount of turbulence in the flow. This may partly explain the differences observed between the measured r.m.s. velocities and the corresponding numerical predictions of the flow using the k-ε model (Bergeles et al, 1996) since the vortex shedding is not accounted for in the flow modelling. The discrepancies between experiments and predictions can also be attributed to the well known shortcomings of the k-ε model in recirculating flows (Bergeles et al, 1996; Rodi and Scheuerer, 1986; Gosman and Ahmed, 1987).

From these considerations it becomes apparent that time-resolved measurements are required to identify any flow periodicities and to estimate the real levels of turbulence generated and other associated quantities such as turbulence scales and the rate of dissipation of k (ε).

3.4.1 SPECTRAL CHARACTERISTICS

Typical axial and transverse instantaneous velocity recordings are shown in Figures 3.10 (a) and 3.10 (b) respectively. It should be noted that velocities were recorded at different sampling rates and only part of the record is shown in these figures. The velocity variation indicates clearly that a periodicity is present in the flow. The periodicity is more clearly defined in the axial component than the transverse one. It is hardly discernible in the first row (Figure 3.10 (a)) but very well defined in the second and subsequent rows in which the periodicity gains amplitude. This periodicity is also evident in the autocorrelation functions computed from the axial instantaneous velocities using equation (2.10). A typical autocorrelation function obtained in the second row (at x/d = 1.6 and y/d = 0.6) is shown in Figure 3.11. In order to determine the frequency of this periodicity, amplitude spectra were obtained for both the axial and transverse components through a Fast Fourier Transform of the time-resolved velocity recordings (see also Balabani and Yianneskis, 1996a). The spectra obtained from measurements of the axial velocity component (Figure 3.12(a)) revealed a discrete flow periodicity with an average frequency of 34 Hz as soon as the flow enters the tube bank. The amplitude of the dominant frequency is low up to the second row, increases considerably further downstream reaching a maximum value between the third and fourth rows and decreases thereafter. A higher harmonic is also present between the third and fourth rows where the maximum amplitude of the vortex shedding frequency is observed. Measurements carried out by McDonnell and Fitzpatrick (1992) in triangular arrays showed also evidence of subsidiary peaks of sub and multiple harmonics in the near wake regions. A higher harmonic - twice the fundamental frequency - was also detected by Ziada and Oengöeren (1991) in an in-line tube bank. The occurrence of this higher harmonic was believed to be an inherent feature of separated flows. According to the non-linear hydrodynamic instability theory higher harmonics are generated when the fundamental component exceeds about 4 % of the mean flow (Ziada and Oengöeren,

1991). Indeed, in the present investigation the amplitude of the dominant frequency between the third and fourth rows is substantially higher than 4 % of the d.c. component; this confirms the existence of the higher harmonic in that location according to the aforementioned theory.

The same dominant frequency of 34 Hz was observed in the spectra of the transverse velocity component (Figure 3.12(b)). Similar observations to those recorded above for the u spectra can be made. However, the amplitude is significantly lower and no harmonic was detected. The row-to-row variation of the amplitude of the dominant frequency in the velocity spectra is plotted in Figure 3.13. The data are normalised with the largest amplitude measured. Clearly higher amplitudes are attained in the axial component. However, for both the axial and transverse components the amplitude increases considerably after the first row, reaching a maximum between the third and fourth rows and decreasing further downstream. Weaver et al (1991, 1993) studied a normal triangular array with a pitch ratio of 1.71[4]. They found that the discrete periodicity is generated in the first two rows and is rapidly dissipated by turbulence since negligible periodicity was measured in the first and third rows whereas the maximum periodicity strength occurred at the second row. A maximum of vorticity shedding in the second row has also been reported by Polak and Weaver (1995). As it has already been mentioned the latter was attributed to the two different vortex shedding modes observed in the first two rows of triangular arrays. In contrast to those findings, the discrete periodicity observed in the present investigation attains a maximum midway between the third and fourth rows and persists up to the fifth row. The higher transverse r.m.s. observed downstream of the second row of the staggered array (Figure 3.5) might be associated with the location of the maximum vorticity shedding (i.e. between the third and fourth row), since the latter is adjacent to the wake of the second row cylinder.

---

[4]The equivalent transverse and longitudinal spacings as defined in the present investigation were 1.71 and 1.48 diameters respectively.

It should be mentioned that another distinct frequency was observed in the amplitude spectra at 200 Hz. This peak was also observed upstream of the bundle and it may be attributed to a periodicity imposed by the pump. However, there is little energy contained in this peak and through filtering tests it was found that its effect on the estimated time scales was negligible.

The Strouhal number, St, is defined by the cylinder diameter and the gap velocity:

$$St = \frac{f\,d}{U_g} \tag{3.1}$$

The St corresponding to the dominant frequency observed is 0.26. The measured St lies within the range given by published St charts (Chen, 1977) but it is higher than the value of 0.20 reported for a single cylinder under subcritical flow conditions despite of the relatively large spacings employed (Massey, 1983; Roshko, 1961). There are many relevant studies in the published literature. The associated St numbers have been collected and plotted in various forms and empirical relations have been proposed for the prediction of St. The latter are usually valid for 'standard' geometries, such as normal triangular or rotated square arrays, shown schematically in Figure 1.2 in Chapter 1 (e.g. Weaver et al, 1993; Oengöeren and Ziada, 1995; Polak and Weaver, 1995). The present geometry is not included in the 'standard' ones, therefore direct comparisons are not possible. There is also a lot of scatter in the published data which can be attributed to the fact that measurements are taken at different locations within the bundle, at different Re_d's or using different experimental techniques. In addition, the existence of multiple St's complicates the interpretation of the data further. Consequently, a discussion of the St values reported in the literature is given below in an attempt to relate the findings of the present investigation to those of earlier studies.

Hill et al (1986) observed two dominant frequencies in a staggered configuration with relative spacings of 2.67 and 2.31. The associated Strouhal numbers were 0.2 and 0.29. The first one was attributed to von Karman vortex shedding. The origin of the second periodic phenomenon, the St number of which was very similar to the one found in the present configuration, remained uncertain. A jet - flipping instability or coupling of frequencies were suggested as possible causal mechanisms. Polak and Weaver (1995), however, studied the same configuration and found two discrete frequencies with St of 0.22 and 0.31, comparable to those reported by Hill et al. Flow visualisation and coherence measurements showed that the two frequencies were associated with alternate vortex shedding from the first and second rows. Vortex shedding from the second row occurred at a lower St than that from the first row one and it was always weaker, less steady and appeared in normal triangular arrays with pitch ratios larger than 2 and sufficiently high Reynolds numbers. On the contrary, in arrays with pitch ratios smaller than 2.0 a single St was found while for the smallest pitch ratio studied (1.14) no discrete frequency was detected. St was found to increase with decreasing pitch ratio and asymptoted to about 0.2 for large pitch ratios, similar to the results for a single cylinder. A single St number of 0.50 was reported by Weaver et al (1991) for a normal triangular array with a pitch ratio of 1.71 at Re_∞ = 830 - 15,000. A similar St was found by McDonnell and Fitzpatrick (1992) in a triangular array with a pitch ratio of 2.

Two dominant frequencies have been reported for rotated square arrays. Weaver et al (1993) observed alternate vortex shedding at different frequencies from the first and second rows of a rotated square array with a pitch ratio of 1.70. The two distinct St - equal to 0.36 and 0.55 - were evident in a range of pitch ratios from 1.21 to 2.83 and they did not relate to each other. They converged to a single value for the smallest pitch ratio studied (1.21), but two St values were present even for relatively large spacings, indicating that the existence of the neighbouring tubes is sufficient to cause significant differences between the vortex shedding from the first and second row

tubes. The authors concluded that vortices are shed at different frequencies because of the local flow velocities near the point of separation and the minimum wake widths that govern the vortex shedding process. They also found that if the St number was computed using these parameters, a unique St for the array could be found.

A recent study by Oengöeren and Ziada (1995) reported three frequency components in normal triangular arrays with spacings 1.61, 2.08 and 3.41. Two components were attributed to alternate vortex shedding from the front (higher frequency) and rear (lower frequency) rows. The third and lowest component was due to the non-linear interaction between the other two and was mostly present behind the second row where transition from the higher frequency to the lower frequency component occurred. The multiple-frequency nature of vortex shedding and the relative importance of each component was found to depend strongly on Re_d, pitch ratio, location within the array and in some cases the number of rows and columns in the tube bank. In the intermediate spacings both components were found to be strong. Increasing the spacing resulted in a reduction of the higher frequency component. The opposite occurred when the spacing was reduced. As the Re_d was increased the vortex shedding developed into a single frequency event. Empirical relations were proposed to predict St for a range of spacings. The latter are of limited use, however, since they are restricted to normal triangular geometries only.

The aforementioned published data emphasise the significant effect of the bundle geometry on the formation of coherent flow structures in staggered tube bundles. First row alternate vortex shedding appears to occur in every pitch ratio while second row-vortex shedding may occur in some geometries. In general, smaller pitch ratios result in higher St numbers while a trend towards the vortex shedding from an isolated cylinder is expected for large spacings.

The staggered arrangement investigated could be approximated by a 'standard' geometry, a rotated square with a pitch ratio equal to the diagonal pitch in the present array, i.e. equal to 2.41. Published empirical correlations (Weaver and Fitzpatrick, 1987) predict a St of 0.25 for such a rotated square array which is very similar to the St of 0.26 found in the present investigation. According to the St data published by Weaver et al (1993), two St numbers approximately equal to 0.27 and 0.40 might be expected. The lower St number is very similar to the one found in the present study. The second St would correspond to a frequency of 52 Hz. No such frequency peak was observed in the spectra in the present work. A possible explanation for the existence of a single vortex shedding frequency in the present investigation, in accordance with Weaver et al (1993), might be that the velocities near the point of separation from the first and second rows are very similar. The same is true for the wake widths estimated downstream of the first and second rows, which are presented later in this Chapter. However, the estimated wake widths in the present work are the maximum wake widths as opposed to the minimum ones referred to by Weaver et al (1993).

Power spectra were also estimated from the time-resolved velocity data using the periodogram technique: block averaging and a Hanning window function were applied. A typical power spectrum is shown in Figure 3.14. The peak associated with flow periodicity is evident at 34 Hz. At the higher (turbulent) frequencies, the slope of the spectrum is approximately -5/3, which is typical of the inertial subrange region. It should be mentioned that the turbulence at the location concerned is nearly isotropic since the two r.m.s. components differ by only 0.05 U_∞.

3.4.2 FILTERED R.M.S. LEVELS AND TURBULENT SCALES

In order to remove the low frequency variations due to vortex shedding from the spectra all the three filtering techniques mentioned in Chapter 2 were applied,

namely notch filtering, moving window averaging and low-pass filtering. A detailed description of the three techniques is given in Appendix III. The notch filtering technique was found to be the most appropriate since it removed only the narrow frequency band corresponding to vortex shedding. In contrast, the moving window and low-pass filtering techniques removed some of the low-frequency turbulence content of the spectrum as well. Furthermore, the results were found to be sensitive to the selected cut-off frequency or window sizes respectively. Therefore, the data presented below were obtained using the notch filtering technique.

The axial r.m.s. velocities obtained after filtering out the dominant frequency peak are shown in Figure 3.15. The data are compared with the raw (unfiltered) values and corresponding numerical predictions using $u' = (2k/3)^{0.5}$ (Bergeles et al, 1996, Balabani et al, 1994; Bouris, 1995). There are no significant differences between the filtered and unfiltered data in the x/d = 0.0 and 0.8 profiles. This is not surprising since vortex shedding is not pronounced in these locations. On the contrary, most r.m.s. levels at x/d = 1.6 are up to 50 % lower when filtering is applied. The filtered values are closer to the predicted r.m.s. levels than the unfiltered ones. This finding suggests that vortex shedding phenomena should be accounted for in numerical modelling of flows over tube bundles.

In order to characterise the turbulence structure more fully and to be able to estimate the rate of dissipation of k, ε, the turbulence time and length scales were calculated from the filtered time-resolved data. Figure 3.16 shows the integral time scales, T_E, determined by integrating the autocorrelation function up to the first zero crossing using equation (2.11) in Chapter 2. The autocorrelation function was computed from the filtered data - using equation (2.10) - unlike the one shown in Figure 3. 11. The measured T_E values range from 1.5 to 8 ms with an average value of 4 ms. The distribution of T_E shows higher values in areas of low velocities and smaller values in the mainstream flow. These trends seem reasonable since time scales are expected

to be shorter in regions of high velocities. The values are compared with those estimated from the CFD predictions (Bouris, 1995) which were obtained using the following formula:

$$T_E = 0.09\frac{(k^{3/2}/\varepsilon)}{(2k/3)^{1/2}} \tag{3.2}$$

There is quantitative agreement between experimental and numerical values in some locations. However, qualitative differences can be found in some locations: numerical values are lower in areas of low velocities (i.e. in the wake regions) and higher in the flow passages between tube columns, contrary to expectations. It must be noted however, that due to the uncertainties and approximations involved both in the experimental and numerical determinations of T_E, any comparisons should be made with care. The authors are not aware of any similarly extensive comparisons in the literature, mainly due to the difficulties involved in measuring T_E. Therefore, notwithstanding the differences between measurement and prediction in many locations, the agreement obtained in some locations is very encouraging.

The micro timescales, τ_E, were calculated from equation (2.12b) given in Chapter 2. Attempts were made to estimate the micro time scales by fitting a parabola to the autocorrelation function computed from the filtered data as suggested by equation (2.13). However, the autocorrelation function decays very fast and the resolution near the origin is poor. Thus, some points close to the origin must be determined by interpolation. Different parabolas can be fitted depending on the points selected and as a result different values of the micro time scales can be obtained. For this reason, the parabola-fitting method was not employed.

The estimated micro time scale values, τ_E, are shown in Figure 3.17. Values range from 0.4 to 2.2 ms with an average value of 0.7 ms. The x/d = 0.0 and 1.6 profiles are nearly uniform. At x/d = 0.8, τ_E is higher close to the recirculation bubble where

the mean velocity is lower and conversely τ_E is lower in the higher speed flow at $0.6 < y/d < 1.2$. Surprisingly, the estimated τ_E values are of the same order of magnitude with the Kolmogorov time scales of the flow determined from dimensional arguments. The latter, however, are just rough estimates and are not considered to yield reliable values. The values around 2 ms found at $x/d = 0.8$ are higher than in any other point in the flow. On average, T_E values differ from the τ_E ones by a factor of 7 which is reasonable (Tennekes and Lumley, 1972).

Integral (Λ_f) and micro (λ_f) length scales were estimated by multiplying the calculated T_E and τ_E values with the mean velocity U at each location as suggested by equations (2.14) and (2.15) respectively. The results are shown in Figures 3.18 and 3.19 respectively. Estimates obtained using an alternative convective velocity - as described later in this section - are also shown in these figures[5]. Integral length scales (Λ_f) vary from 0.1 to 8 mm with an average value of 4.6 mm, i.e. around half the cylinder diameter, whereas micro ones (λ_f) vary from 0.04 mm to 1.6 mm with an average value of 0.74 mm. Both the integral and micro length scales are found to be lower in the wake regions and higher in the flow lanes between tube columns although the opposite distribution would be expected. This may be partly due to the fact that Taylor's hypothesis that relates the time and space derivatives in the momentum equation is not expected to be valid in areas of high turbulence intensity, i.e. in the wake region of the first cylinder where U is smaller or similar to the r.m.s. velocities. As a result the convective velocity $U_c = U$ used may not be appropriate (Heskestad, 1965). Similarly unexpected length scale distributions were reported for the flow past an axisymmetric poppet valve by Yianneskis et al (1991) and it may therefore be more appropriate to determine length scales from velocity traces obtained simultaneously at 2 locations in the flow. According to the generalised

---

[5] In these and subsequent figures where only one set of data is shown in some locations, the other sets of data are identical and covered by those shown.

Taylor's hypothesis suggested by Heskestad (1965) for highly turbulent shear flows a convective velocity given by:

$$U_c = \sqrt{U^2 + u'^2 + 2v'^2 + 2w'^2} \tag{3.3}$$

would be more appropriate. Since only the axial velocities were measured in detail and at appropriate sampling rates such a convective velocity could not be determined from the time-resolved data without some postulation about the two transverse fluctuating components v' and w'. Therefore, the use of an alternative U_c in that case would yield little constructive information. However, a simplified version of U_c can be used by neglecting the two transverse fluctuating components, i.e. :

$$U_c = \sqrt{U^2 + u'^2} \tag{3.4}$$

as suggested by Wu et al (1989). For comparison purposes, Λ_f and λ_f estimates based on the above convective velocity are shown by the red symbols in Figures 3.18 and 3.19 respectively. It can be seen that the use of the convective velocity suggested by equation (3.4) results in higher length scale estimates in the wake regions (for example, at x/d = 0.8 and y/d = 0.3 and x/d = 1.6 and y/d = 0.0). However, the trends exhibited are similar.

There are no data from similar flows to allow quantitative comparisons to be made. Estimated time scales have been reported for a number of other flow configurations. For example, T_E = 0.7 ms was measured by Absil (1988) in the wake of a 2 mm single cylinder in cross-flow at a distance of 125 d from the cylinder and Re_d = 1,300. Yianneskis et al (1991) reported time and length scales of the flow past a poppet valve. On average, τ_E values were found to be around one order of magnitude lower than T_E, in agreement with the present data. Cenedese et al (1992) estimated time scales in the boundary layer of the flow in duct. T_E values in the axial direction

were found approximately equal to the duct dimension divided by the mean velocity. T_E values were significantly lower in the other two directions. τ_E values estimated by counting the number of zero crossings per unit time of the fluctuating velocity component were found to be around one order of magnitude lower than T_E. Gould and Benedict (1994) carried out spatial- and auto-correlation measurements using LDA in an axisymmetric sudden expansion. Time scales were found to be lower in locations of low turbulence and higher in the shear layer, while length scales obtained from the time scales using Taylor's hypothesis were overestimated in low turbulence locations and underestimated in the shear layer. Their findings therefore are in agreement with those of the present study.

3.4.3 RATE OF DISSIPATION

Figure 3.20 shows estimates of the dissipation rate, ε, determined from equation (2.16) in Chapter 2 with the cylinder diameter d = 10 mm as a characteristic length L, the filtered axial r.m.s velocity u' as a characteristic velocity scale u' and A = 1 (i.e. with $\varepsilon = u'^3/d$). Estimates are compared with CFD predictions (Bouris (1995)). Measured dissipation rates are very low (0.05 m^2/s^3) in the flow passages between tube columns where the turbulence levels are small and high, up to 4 m^2/s^3, in the wake region where high r.m.s. velocities are present. Agreement with the corresponding CFD values is poor in the wake region ($x/d = 0.8$, $y/d \leq 0.4$) and next to the second cylinder ($x/d = 1.6$, $y/d \geq 0.6$). Good qualitative, and in some locations quantitative, agreement is observed at $x/d = 0.0$, $y/d > 0.6$, $x/d = 0.8$, $0.5 < y/d < 0.9$ and at $x/d = 1.6$, $y/d < 0.6$. Predicted dissipation rates are low in the flow lanes, increase sharply in regions with steep velocity gradients (e.g. the interface between the recirculation bubble and the shear layer) and decrease thereafter. Extremely high numerical values are observed at $x/d = 0.0$ and 1.6 close to the cylinders.

Figure 3.21 shows ε values estimated using equation (2.16) with the integral length scale Λ_f as a characteristic length. The numerical predictions of ε are also shown in the same figure. Extremely high values of ε are found in the wake region as a result of the very small integral length scales Λ_f estimated there. Λ_f estimates based on the convective velocity given by equation (3.4) result in smaller ε values in these locations (for example, at x/d = 0.8, y/d = 0.3 and x/d = 1.6 and y/d = 0.0). If these points are excluded the values differ from those estimated using the cylinder diameter (Figure 3.20) as characteristic length by a factor of 2 since the integral length scales are on average equal to the cylinder radius. The agreement between experimental and numerical estimates is good in some locations in the flow passages as discussed in the previous paragraph.

Finally, Figure 3.22 shows the dissipation rates estimated using equation (2.17) compared with numerical predictions. Experimental values range from 0.06 to 1067 m^2/s^3. Again, extremely high values of ε are found in the wake region as a result of the very small Taylor length scales λ_f estimated there. The use of the convective velocity given by equation (3.4) in the estimation of λ_f results in smaller ε values in these locations. If these values are ignored the dissipation rates estimated using this method differ from those in Figure 3.20 by a factor of 7 on average. Again the agreement with the numerical values in different regions is similar to that mentioned earlier.

All three methods used to estimate ε are subject to uncertainties. Clearly, the use of d as a characteristic length scale is only an approximation while those expressions employing λ_f and Λ_f may not be appropriate for the reasons explained earlier for the length scale estimates. Furthermore, the use of the axial fluctuating velocity as a characteristic velocity scale assumes that the turbulence is isotropic which is not true in the wake regions. On the other hand, the well-known shortcomings of the k-ε model in regions of recirculation or with strong streamline curvature are likely to

affect the predicted ε results. These arguments are supported by the similarity of values estimated with all three methods and the predicted ones over most of the x/d = 0.0 profile for 0.6 < y/d < 1.0 at x/d = 0.8 and for 0.3 < y/d < 0.6 at x/d = 1.6. At these locations the assumptions employed in estimating ε are more appropriate and streamline curvature/recirculation effects may have a smaller influence on the ε values predicted with the k-ε model. As in the k-ε turbulence model formulation ε is linked very strongly to the local mean strain field, but relatively weakly to the small scale eddies where dissipation takes place (Habib and Whitelaw, 1979) it might be expected that ε is overpredicted in some regions as indicated by the above comparisons.

In conclusion, although the comparisons of predicted and measured values of ε should be made with great care due to the approximations involved in both experiment and calculation, the present results provide the only published comparison of ε data known to the authors and give not only a useful assessment of the levels of ε in the flow but also show promise for more extensive evaluation of CFD predictions in future than has been possible hereto.

3.5 WAKE CHARACTERISTICS

3.5.1. CENTRELINE MEAN AND R.M.S. VELOCITIES

The velocity characteristics downstream of each row can be compared by examining the centreline development of the axial mean and r.m.s velocities shown in Figures 3.23 and 3.24 respectively. Both mean and r.m.s. velocities are normalised with U_∞ and they are plotted against normalised distance (l/d) from the tube surface and not from the centre of the cylinder. The profiles of U/U_∞ downstream of the first and the second rows are similar and exhibit characteristics typical of the flows over bluff bodies, that is a region of recirculation with negative mean velocities followed by a

region of flow acceleration up to a maximum velocity and then a velocity decay. The magnitude of the negative velocities increases with distance from the tube reaching a maximum equal to 0.47 U_∞ and 0.49 U_∞ at about 0.6 and 0.5 diameters from the surface of the first and second row cylinders respectively. The rear stagnation point, defined as the location of zero mean velocity, is reached at 1.15 and 1.1 diameters downstream of the first and second rows respectively. Downstream of the stagnation point the mean velocity increases reaching a maximum positive velocity approximately equal to 0.44 U_∞ and 0.47 U_∞ in the first and second rows respectively. These maxima occur downstream of the minimum cross-sectional area between adjacent tubes of a row - which is located at 1.6 diameters from the tube surface - since the recirculation region alters the effective cross sectional area between adjacent tubes. A velocity decay region is not immediately apparent since the development of the centreline profiles is restricted by the downstream tubes.

Centreline profiles downstream of the third and fourth rows are also similar. They are mainly characterised by a region of flow acceleration to a maximum positive velocity equal to 0.82 U_∞ and 0.92 U_∞ respectively and a region of velocity decay further downstream since the rear stagnation point is reached earlier than in the first two rows. The maximum positive velocities are observed 1.5 diameters downstream of the tube surface. A few locations with negative velocities can be observed downstream of the third row but no flow reversal is evident downstream of the fourth row within the measurement region. The rear stagnation points are reached at 0.48 diameters downstream of the third row and - by extrapolation - at 0.3 diameters downstream of the fourth row.

The centreline development of u'/U_∞ is shown in Figure 3.24. A large increase of the axial velocity fluctuations up to the rear stagnation point can be seen downstream of the first and second tubes followed by a slight decay. The profiles for the third and fourth rows are nearly identical. Apparently, the maximum u'/U_∞ is reached earlier

since the rear stagnation point is closer to the tube and u'/U_∞ decreases gradually with distance from the tube surface. The maximum centreline u'/U_∞ increases gradually from 0.43 U_∞ downstream of the first row to 0.54 U_∞ downstream of the fourth row. The maximum values downstream of the third and fourth rows are equal, within the experimental error. In general, the centreline r.m.s. velocities reach higher values downstream of the second row in the vicinity of the rear stagnation point.

3.5.2 RECIRCULATING PARAMETERS

The length of the recirculation bubbles, l_r, formed downstream of the cylinders is defined by the point of a zero centreline axial mean velocity (rear stagnation point) and indicates how rapidly the axial mean velocity defect in the wake has recovered. l_r values estimated from the centreline U/U_∞ profiles in Figure 3.23 are shown in Table 3.1. Other parameters such as the width of the separated shear layer, w_r, the vorticity thickness δ and its spreading rate δ' as well as the recirculating mass-flow rate $\dot{m}_r$ were also estimated; these parameters are defined below and their values are listed in Table 3.1 (see also Balabani and Yianneskis, 1994). All these parameters are important since they quantify the transfer of momentum within the recirculation region.

The recirculation bubble length downstream of the first row is equal to 1.15 d and very similar to that of the second row (1.1d). The estimated l_r for the first two rows is almost twice as large the length reported by Halim and Turner (1986) for an equilateral triangle arrangement with a pitch to diameter ratio of 1.6, but very close to the length of the recirculation zone behind a circular cylinder (l_r/d = 1.65) reported by McKillop and Durst (1984) at a similar Re_d, bearing in mind that they measured the length starting from the centre of the cylinder, unlike Halim and Turner (1986) who measured recirculation length from the tube surface. This

observation suggests that the flow downstream of the first row resembles that downstream of a single cylinder in cross-flow.

Table 3.1. Recirculating parameters in 3.6 x 1.6 staggered configuration.

Row	**x/d (l/d)**	$\mathbf{w_r/d}$	$\mathbf{l_r/d}$	$\dot{m}_r/\dot{m}$	δ	δ'
1	0.8 (0.3)	0.46 (0.59)	1.15	0.15	0.14 (0.12)	0.18 (0.15)
	1.2 (0.7)	0.37 (0.52)			0.23 (0.19)	0.19 (0.16)
2	2.4 (0.3)	0.46	1.1	0.10	0.18	0.23
	2.8 (0.7)	0.34			0.32	0.26
3	4.0 (0.3)	0.21	0.475	0.02	0.40	0.50
4			0.3			

- l/d represents distance from the surface and x/d the corresponding axial location at which the width and vorticity thickness are estimated.
- Figures in brackets correspond to the results for a single cylinder in cross-flow as estimated by McKillop and Durst (1984).

The width of the recirculation bubble has been defined in many different ways in the literature. Gerrard (1967) defined the width of the shear layer separated from a cylinder as the width at half-height of $(r/U_\infty)(dU/dy)$ as a function of y/r, where U_∞ is the free-stream velocity, r the cylinder radius and U the local mean velocity. Nebres and Batill (1993) determined the spacing between the shear layers separating from a cylinder using a conditional averaging technique. A hot wire probe was traversed laterally across the wake at a distance d/4 behind the cylinder and samples were conditionally acquired based on information simultaneously obtained from a phasing probe which was located 1.64 diameters away from the cylinder axis in the transverse direction. The spacing between the inner probe positions corresponding to 99% of the maximum mean velocities was defined as the shear layer spacing. McKillop and Durst (1984) estimated the thickness of the separated shear layer and its spreading rate using the definition of the vorticity thickness (or the velocity-

profile maximum-slope thickness) given by Brown and Roshko (1974) for plane turbulent mixing layers:

$$\delta = \frac{U_{max} - U_{min}}{(\partial U / \partial y)_{max}} \tag{3.5}$$

Its derivative is the spreading rate and is given by:

$$\delta' = \frac{d\delta}{dx} = \frac{\delta}{x - x(0)} \tag{3.6}$$

U_{max} was defined as the maximum axial velocity at the shear layer and U_{min} as the axial mean velocity at the interface between the shear layer and the recirculation bubble; this interface was defined as the transverse location at which the stream function is zero. $(\partial U / \partial y)_{max}$ was defined as the maximum gradient within the shear layer. x(0) denoted the axial co-ordinate at the origin of the co-ordinate system, i.e. the centre of the cylinder (x = 0 mm). However, McKillop and Durst found that the separated shear layer from the cylinder did not exhibit the expected pattern of turbulent mixing layers, that is having a steady spreading rate.

In the present study the recirculation width w_r was evaluated from the separation streamlines, a common approach in flows over bluff bodies (Taylor and Whitelaw, 1984). The separation streamlines are equivalent to what McKillop and Durst (1984) defined as interface between the shear layer and the recirculation bubble. The calculated flow streamlines for the 3.6 x 1.6 staggered array are shown in Figure 3.25. These were constructed by evaluating the stream function from the measurements of the axial mean velocity. The stream function is defined as zero at y/d = 0.0 and has a maximum value at y/d = 1.8. The w_r estimated in all possible locations downstream of each cylinder are shown in Table 3.1. The values are expressed in tube diameters and are compared with published data on single

cylinders in cross-flow (McKillop and Durst, 1984). More specifically these values represent the width of the separated boundary layer or the half-width of the recirculation bubble. The wake width of a single cylinder in cross-flow is usually larger than its diameter under subcritical flow conditions and becomes smaller in the supercritical and transcritical regime due to the fact that the separation point moves further downstream (Roshko, 1961). On the contrary, in the present investigation the shear layers separating from the first and second row tubes have maximum half-widths (0.46 d) smaller than the tube radius probably due to the interference from neighbouring tubes. The flow streamlines undergo a mild curvature towards the centreline as the subsequent row is encountered due to an increase in the transverse mean velocities. As a result the pressure field associated with the wake flow is significantly affected and the recirculation bubbles are not formed as freely as in the case of a single cylinder or other single bluff body in cross-flow. The estimated half-width downstream of the third row is less than half of those in the first two rows. The half-width downstream of the fourth row could not be estimated since no flow reversal was evident at the points closest to the surface that could be measured.

Weaver et al (1993) found that the wake width of the second row of a rotated square array with pitch ratio 1.70 was substantially wider than the one in the first row, in contrast to the present findings. Wider second-row widths were also found in normal triangular arrays by Polak and Weaver (1995). Differences between the present results and those of Weaver et al may be attributed to the fact that the velocities they measured near the point of separation of the first and second row cylinders differed by 0.50 U_∞ whereas in our study this difference is only 0.12 U_∞. Also, the wake width they referred to is the minimum wake width which they estimated roughly from flow visualisation studies.

Estimates of the vorticity thickness, δ, expressed in tube diameters, and its spreading rate, δ', are also shown in Table 3.1 and are compared with the results of McKillop

and Durst (1984). Again the results for the first row agree well with those for a single cylinder. Both the vorticity thickness and its spreading rate increase from row to row, probably due to the fact that velocity gradients are less steep, as further downstream rows are encountered.

Another parameter that was estimated from the calculated stream function is the recirculating mass-flow rate, the values of which are also given in Table 3.1, normalised by $\dot{m} = \frac{1}{2}\rho U_\infty d$. The recirculating mass-flow rate depends on the magnitude of the reverse velocities and the width of the recirculation zone and consequently the values downstream of the first and second rows are very similar. A very small amount of mass is found in the recirculation downstream of the third row cylinder.

The similarities observed between the first and second row cylinders may be due to the fact that the flow approaching them is uniform since they are located at the entrance of the tube bundle. On the contrary, the downstream row cylinders are subjected to a shear flow that affects the pressure distribution around them and consequently the location of the separation points and the evolution of the wakes.

3.6 EFFECT OF REYNOLDS NUMBER

In order to study the effect of Re_d on the flow characteristics of the staggered tube bank, measurements of the axial mean and r.m.s. velocities were taken downstream of the first and third rows at Re_d varying from 3,104 to 12,858 as well as measurements of the pressure drop, ΔP, for Re_d in the range from 4,000 to 12,858.

3.6.1 CENTRELINE MEAN AND R.M.S. VELOCITIES

The variation of the centreline U with Re_d downstream of the first and third rows is shown in Figures 3.26 (a) - (b). In general, decreasing the Re_d results in lower negative velocities in the recirculation and also lower positive velocities in the near wake. The rear stagnation point is found further downstream as Re_d is decreased. As a consequence the length of the recirculation region varies with Re_d. The recirculation length at different Re_d was determined from Figures 3.26 (a) and (b) and the values are plotted in Figure 3.27. The data can be correlated by logarithmic expressions similar to that suggested by McKillop and Durst (1984) for a single cylinder. The recirculation lengths for the first and third row vary with Re_d in a similar manner, i.e. the curvature of the two logarithmic expressions is similar, but they are offset from one another by a constant value. There is agreement between the first row data and those for a single cylinder at low Re_d but as the Re_d is increased the corresponding logarithmic curves diverge. It should be noted, however, that the curve fitting for the first row data is not as good as that for the third row although the opposite trends would be expected: in view of the similarities observed between the first row and a single cylinder, it was expected that the variation of l_r with Re_d for the first row would be similar to that for a single cylinder while that for the third data would show dissimilar trends due to the complexity of the flows in downstream rows.

The centreline development of u' downstream of the first and third rows for various Re_d can be seen in Figures 3.28 (a) - (d). The maximum values, u'_{max}, obtained at each Re_d are summarised in Table 3.2. These values are normalised with the corresponding U_∞ for each Re_d. For comparison purposes, the maxima measured downstream of the second and fourth rows for Re_d = 12,858 are also shown in Table 3.2. The u'_{max}/U_∞ values gradually increase from the first to the fourth row for Re_d = 12,858. However, the difference in the values downstream of the second, third and

fourth rows is not significant. The relative magnitudes of the maxima, i.e. normalised values, do not change significantly with Re_d, especially in the third row. The lowest Re_d data is an exception but the experimental uncertainty is higher there.

Table 3.2. Maximum centreline r.m.s. velocity fluctuations, u'_{max}/U_∞, in 3.6 x 1.6 staggered tube bank.

u'_{max}/U_∞					
Re_d	**U_∞** (m/s)	Row **1**	Row **2**	Row **3**	Row **4**
12,858	0.93	0.43	0.50	0.53	0.54
10,198	0.74	0.36		0.53	
7,981	0.58	0.41		0.52	
5,764	0.42	0.43		0.55	
3,104	0.22	0.50		0.59	

3.6.2 PRESSURE DROP

The pressure drop across the tube bundle, ΔP, was measured at various Re_d's. The results are presented in Figure 3.29 in the form of a pressure drop coefficient, ζ, defined as:

$$\zeta = \frac{\Delta P}{\frac{1}{2} N \rho U_g^2} \tag{3.7}$$

where N is the number of rows and U_g is the maximum velocity in the gap between tubes at the same row.

It can be seen that the pressure drop decreases slightly with increasing Re_d. This is a characteristic trend of staggered tube bundles in subcritical flow conditions

(Grimison, 1938; Zukauskas, 1989). The pressure drop data can be correlated using a dimensionless relation of the form $\zeta = a\,Re_d^{-b}$. For the range of Re_d investigated the constants a and b were found to be equal to 0.1692 and 0.192 respectively. This correlation is only valid to the particular staggered geometry. Empirical published correlations usually refer to tube bundles with 10 rows or more (for example, Jacob, 1938; Zukauskas, 1989) or 'standard' geometries such as normal triangular. Therefore, comparisons with the present data should be made with great care. It is interesting to note, however, that the power index of Re_d derived from the present data (-0.192) is in agreement with published values. For example, Jacob (1938) suggested that the pressure drop in staggered arrays varies with $Re_d^{-0.16}$ for Re_d = 4,000-32,000 which agrees well with the present findings. Simpson et al (1984) correlated pressure drop data obtained in a triangular array with $Red^{-0.102}$ for Re_d = 1,000- 100,000. Finally, Zukauskas (1989) suggested a $Re_d^{-0.29}$ dependence of the pressure drop in normal triangular arrays for Re_d = 7,000 - 200,000. A list of published pressure drop correlations can be found in Balabani and Yianneskis (1993a).

3.7 CLOSURE

The interstitial flow in a 3.6 x 1.6 staggered tube bundle was investigated experimentally using ensemble-averaged and time-resolved LDA measurements. Experiments were carried out in flow of water and at Re_d = 3,104 - 12,858 (subcritical flow conditions). The results illustrated the complex nature of the flow over staggered arrays resulting from interference from neighbouring tubes. High turbulence levels are generated by this configuration. Wake regions are highly anisotropic with transverse r.m.s velocities reaching generally higher values than the axial ones. The effect is more pronounced downstream of the second row where the maximum value of the turbulence kinetic energy is observed.

A flow periodicity is present in this configuration due to vortex shedding. The associated St number is approximately equal to 0.26 which is in agreement with published data. Vortex shedding is pronounced between the third and fourth rows where a higher harmonic is also generated. This flow periodicity broadens the random turbulence levels by almost 50 % in some locations. Agreement between experimental and numerical predictions of the flow is improved when this periodicity is removed from the turbulence spectra. The estimated integral time scales range from 1.5 to 8 ms with an average value of 4 ms and micro time scales from 0.4 to 2.2 ms with an average value of 0.7 ms. Length scales estimated using the mean velocity as a convective velocity show trends opposite to what expected due to the fact that the Taylor's hypothesis is not valid in the wake regions . A more appropriate convective velocity was shown to improve the accuracy of the estimates in the wake regions. Estimates of the rate of dissipation making use of the estimated length scales lead to sharply increasing values in the wake regions and only the ε formulation based on a dimensional argument seemed to give reasonable results. Qualitative and/or quantitative agreement with numerical estimates was achieved in some locations in the flow which is encouraging given the uncertainties and the approximations involved in the estimation of ε.

Despite the relatively large spacings employed the wake flows in the tube bundle were shown to be far more complicated than those downstream of a single cylinder or a single bluff body in cross-flow. There are similarities between the first rows and a single cylinder but the wake characteristics in downstream rows are significantly affected by the non-uniform flow field around the cylinders.

In the following chapter an investigation of the effect of tube spacing and tube arrangement on the velocity characteristics of tube bundles will be presented. Ensemble-averaged LDA measurements taken in a staggered and an in-line array

with transverse and longitudinal spacings of 3.6 and 2.1 respectively will be presented and compared.

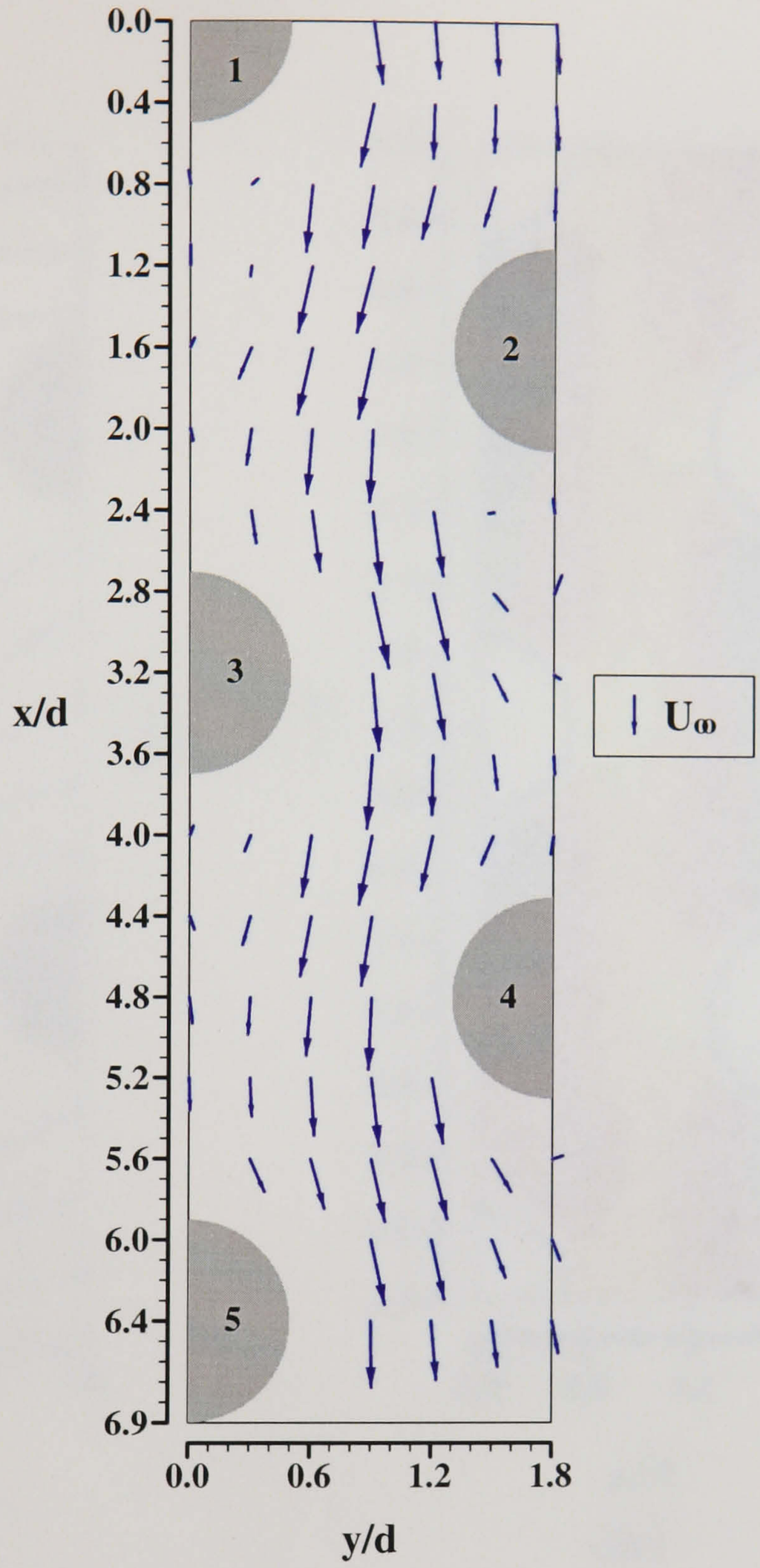

Figure 3.1. Velocity vectors in the 3.6 x 1.6 staggered array (Re_d = 12,858).

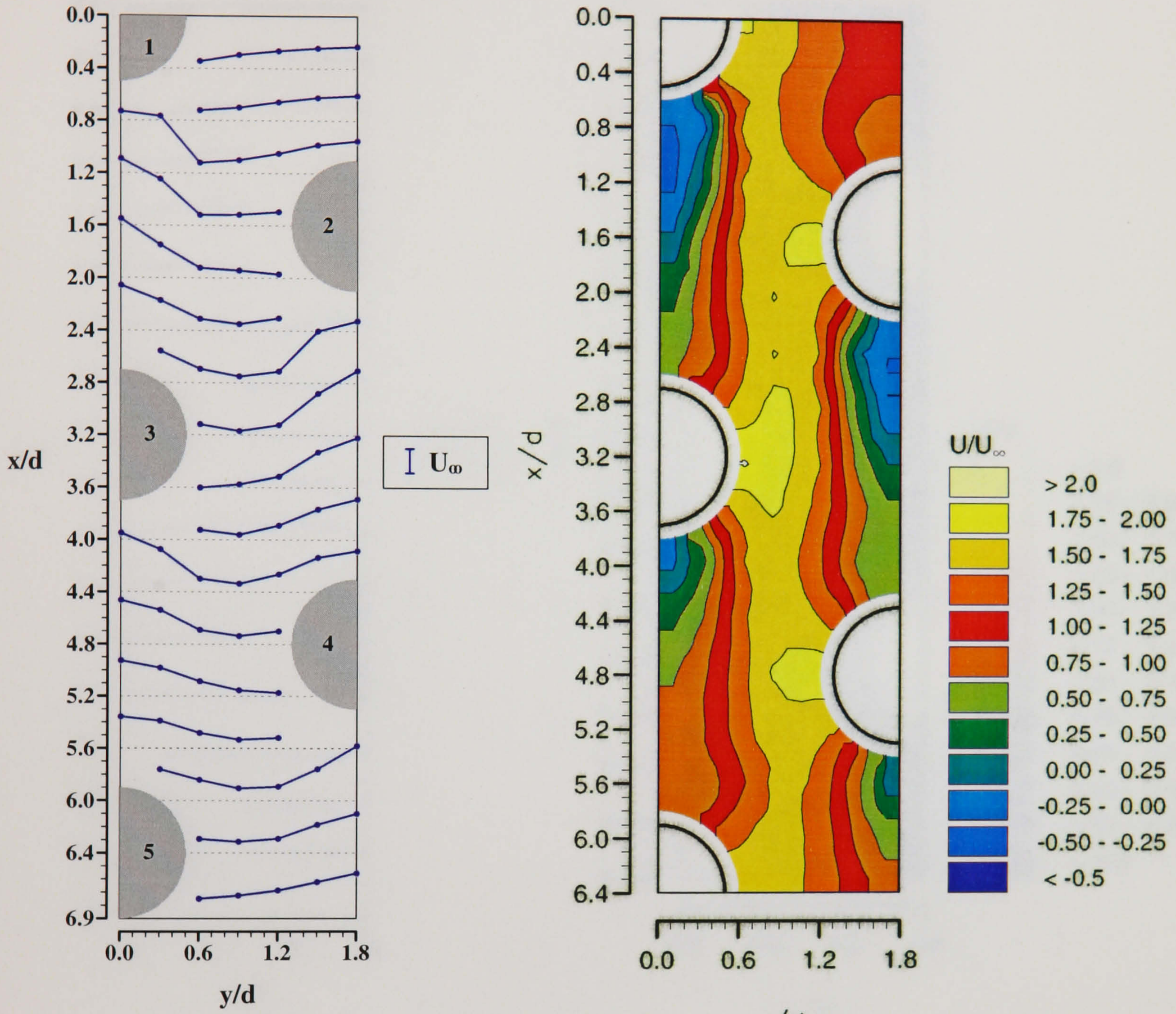

Figure 3.2. Distribution of axial mean velocities, U/U_∞, in the 3.6 x 1.6 staggered array (Re_d = 12,858).

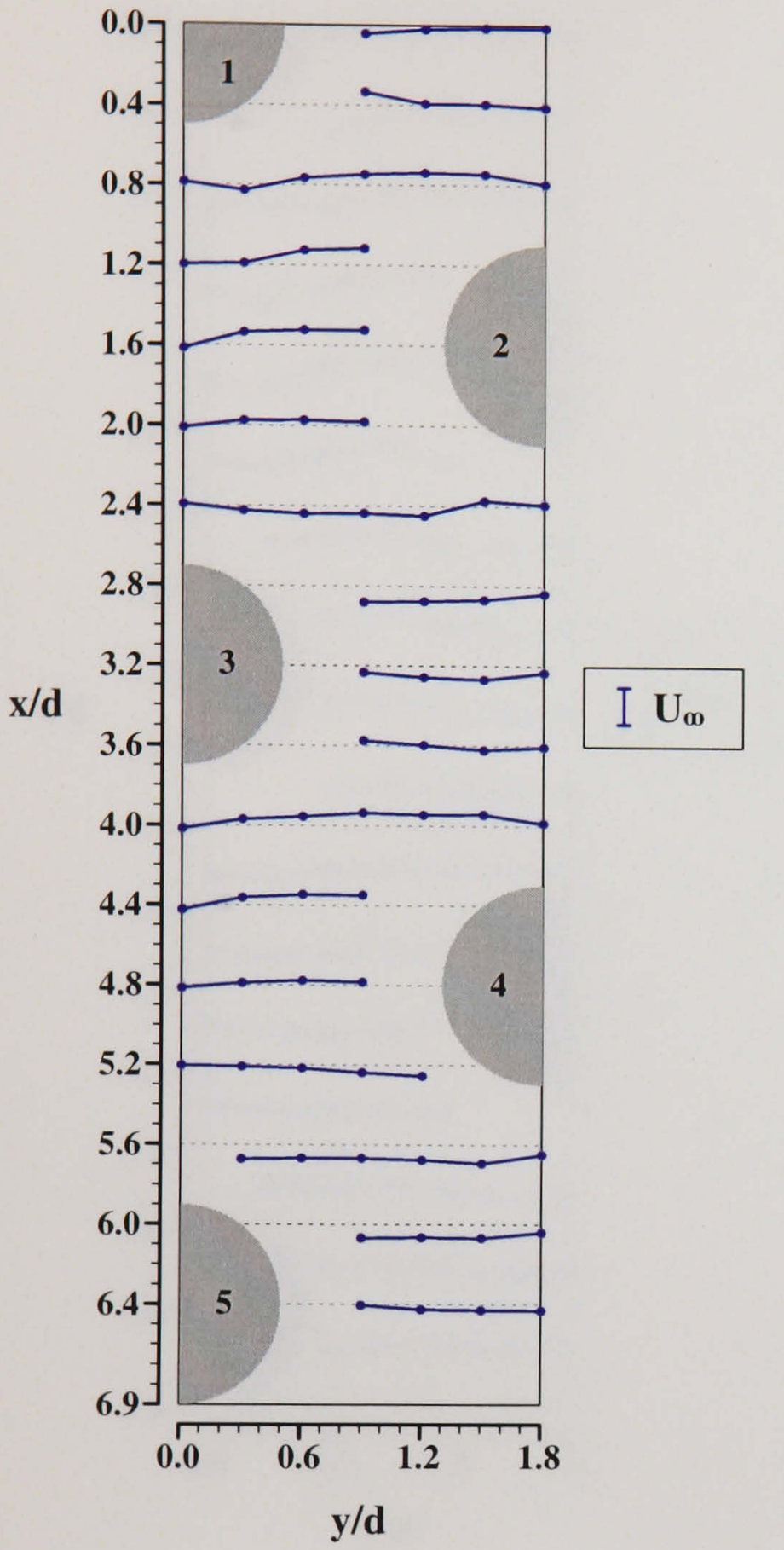

(a)

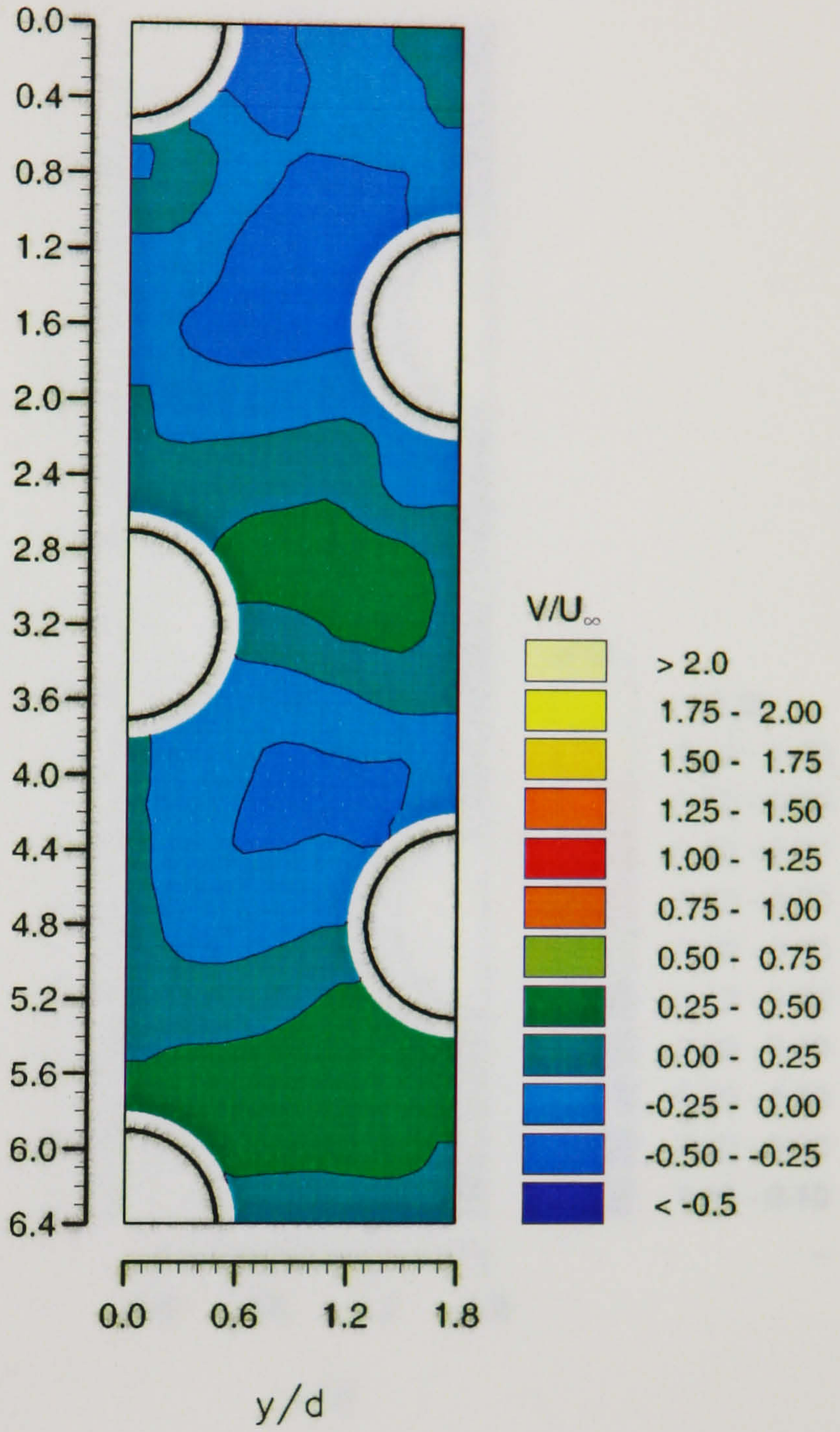

(b)

Figure 3.3. Distribution of transverse mean velocities, V/U_∞, in the 3.6 x 1.6 staggered array (Re_d = 12,858).

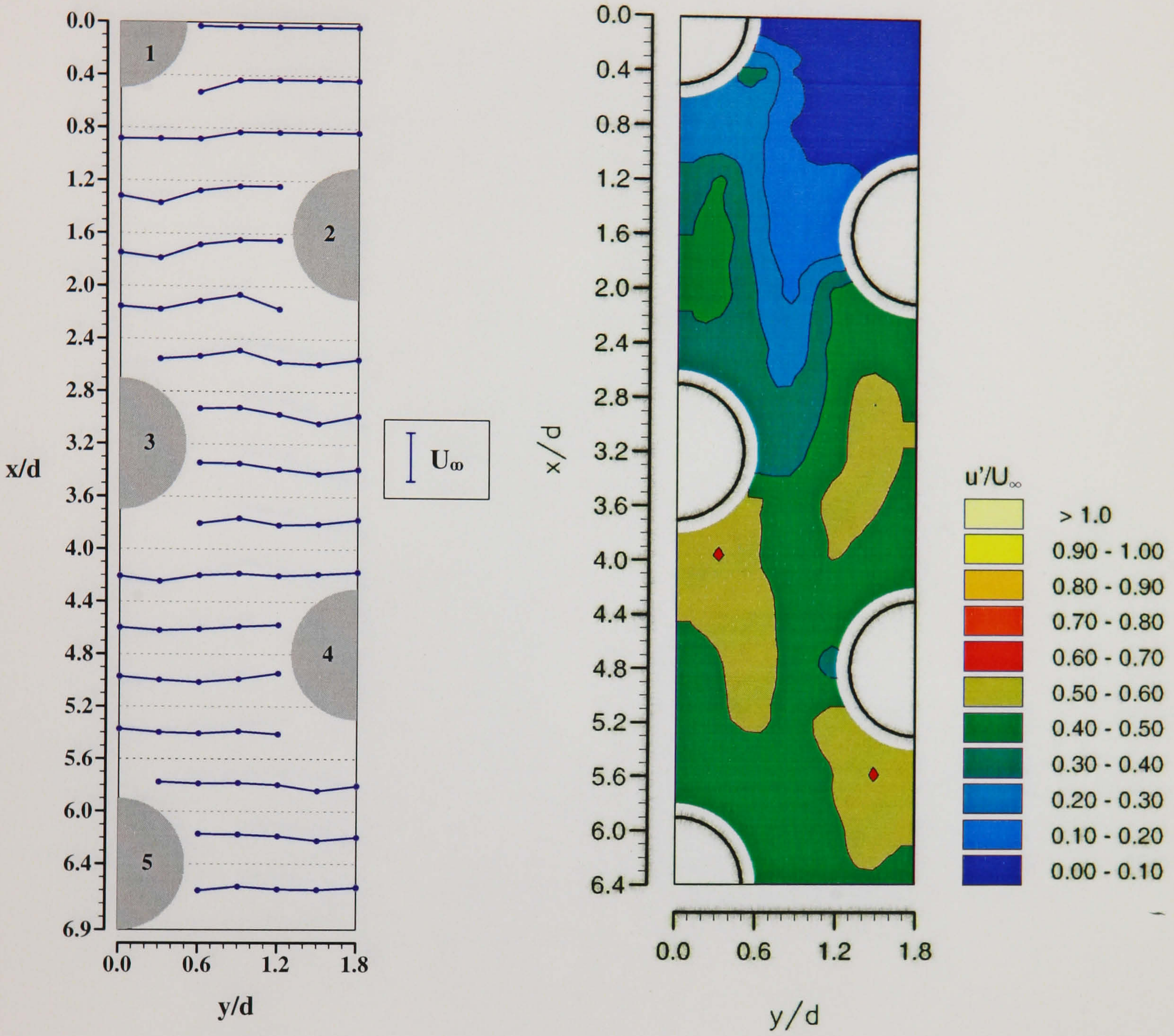

Figure 3.4. Distribution of axial r.m.s. velocities, u'/U_∞, in the 3.6 x 1.6 staggered array (Re_d = 12,858).

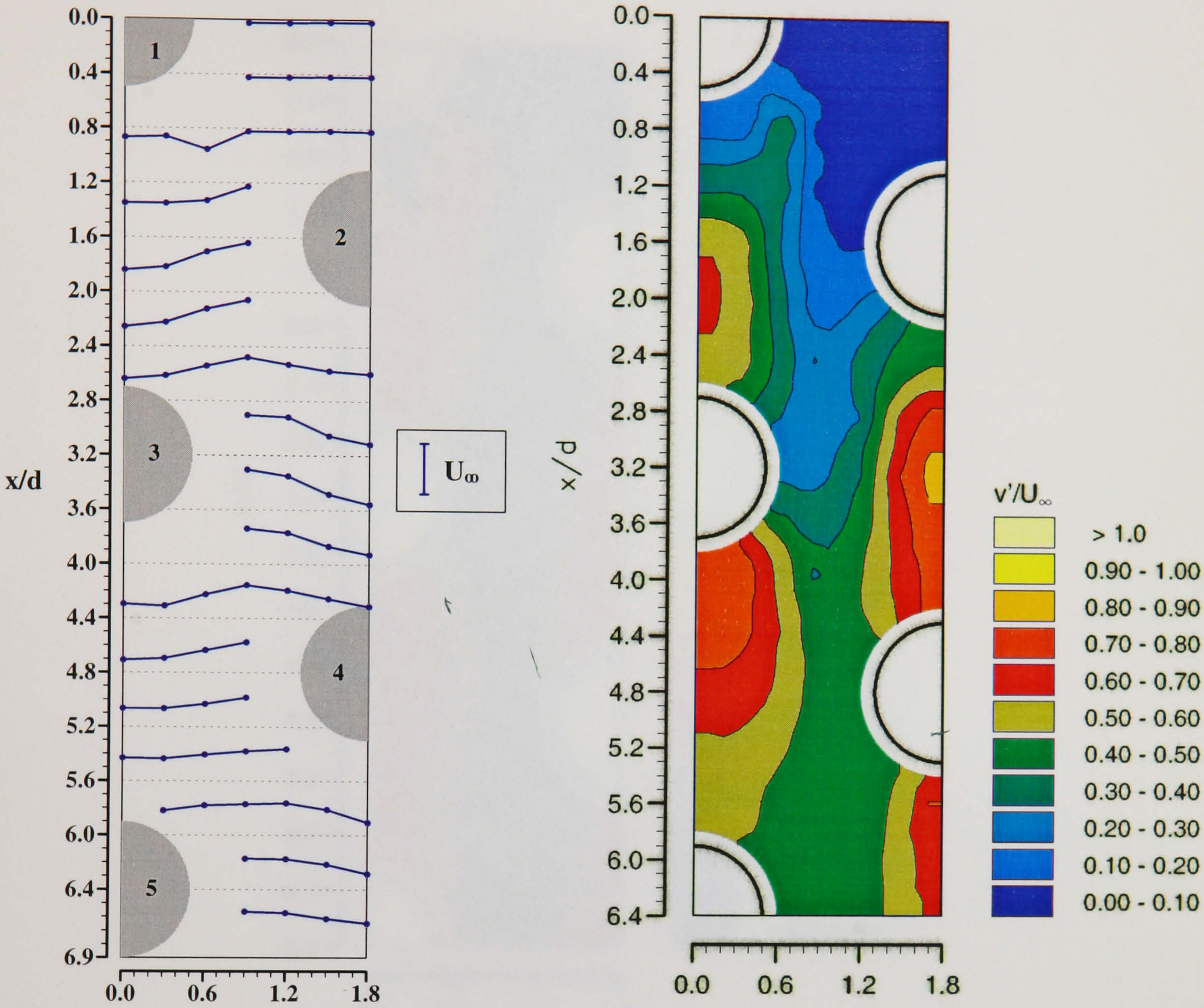

Figure 3.5. Distribution of transverse r.m.s. velocities, v'/U_∞, in the 3.6 x 1.6 staggered array (Re_d = 12,858).

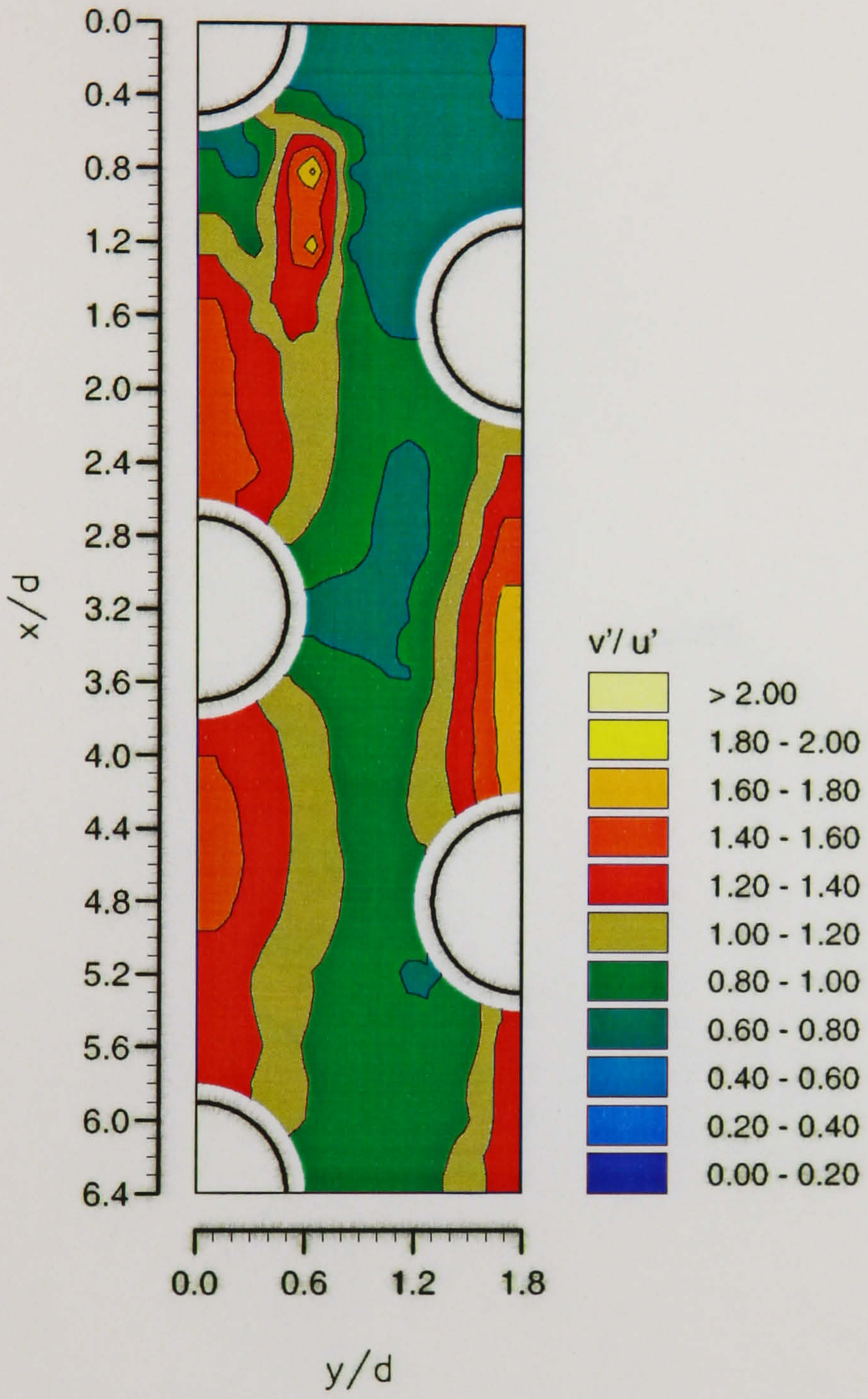

Figure 3.6. Distribution of v'/u' in the 3.6 x 1.6 staggered array (Re_d = 12,858).

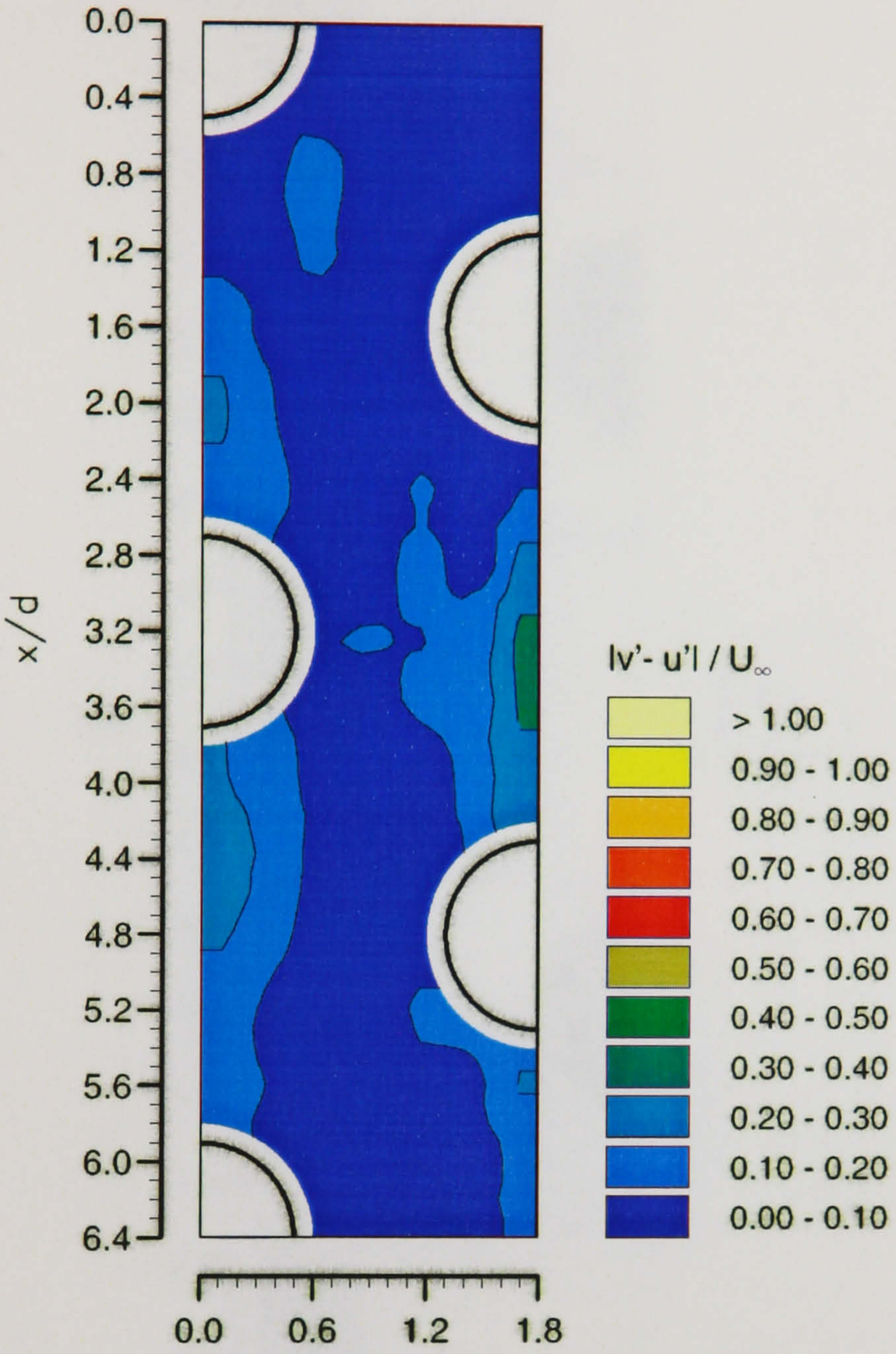

Figure 3.7. Distribution of $|v'-u'| / U_\infty$ in the 3.6 x 1.6 staggered array (Re_d = 12,858).

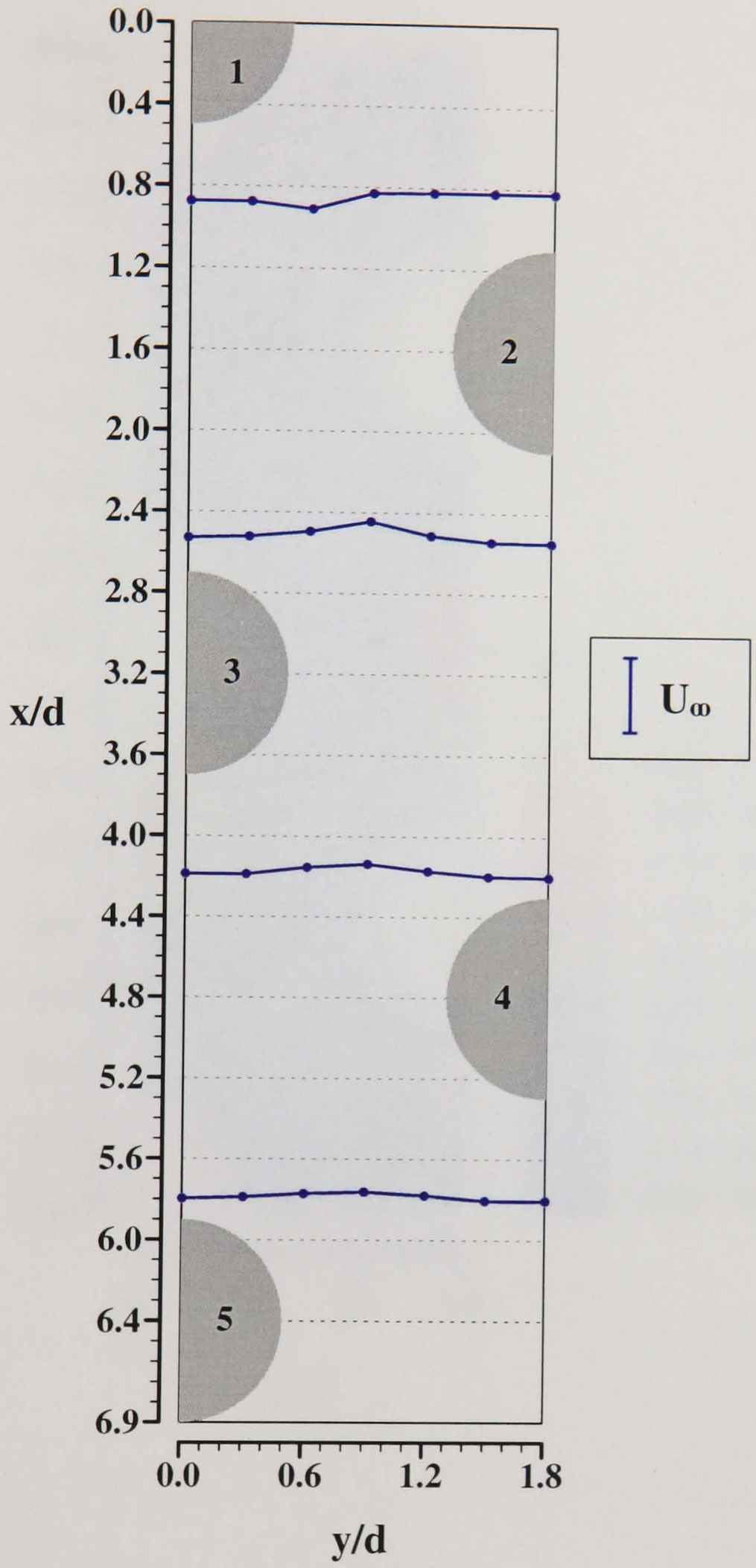

Figure 3.8. Profiles of w'/U_∞ in the 3.6 x 1.6 staggered array (Re_d = 12,858).

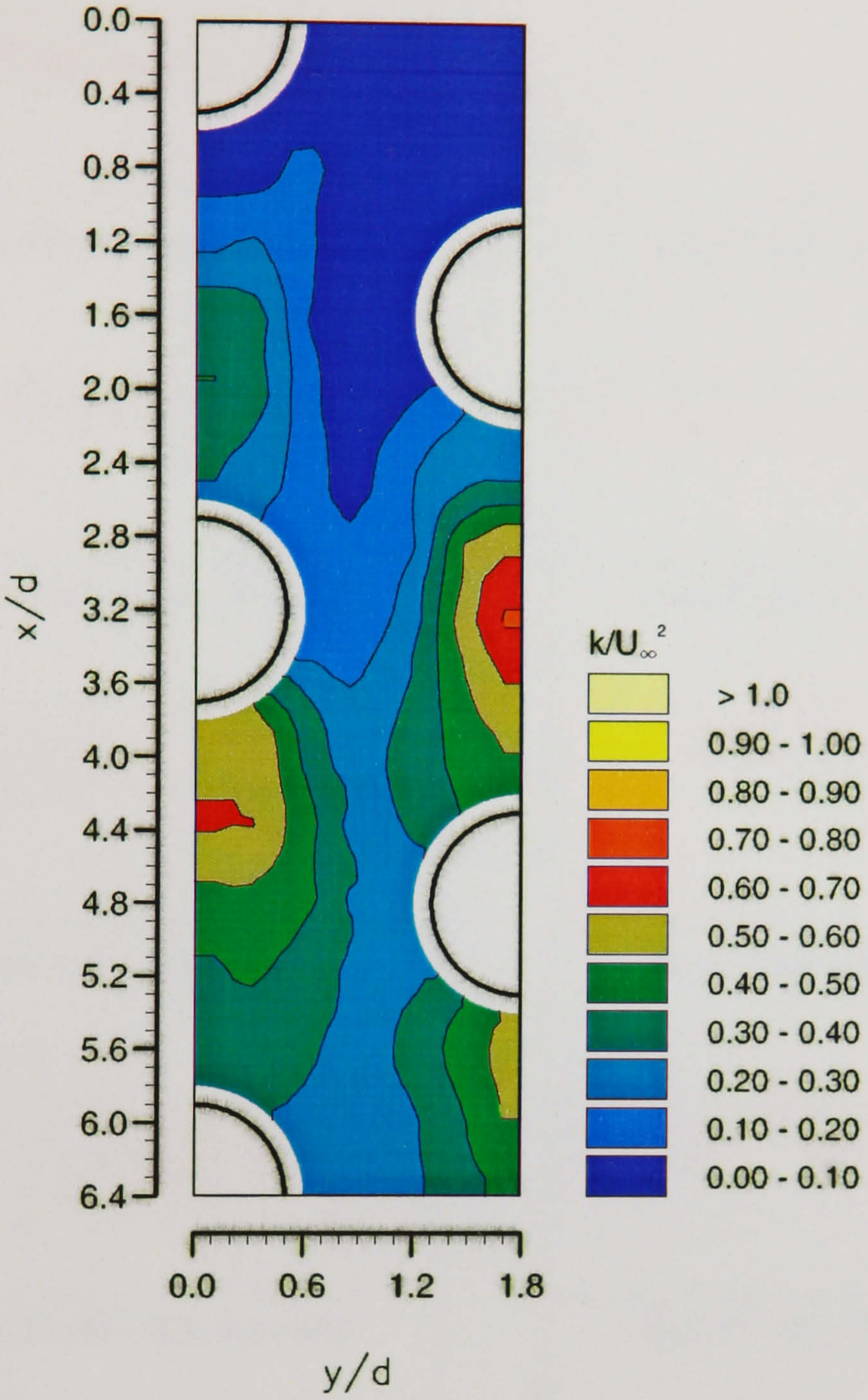

Figure 3.9. Distribution of the turbulence kinetic energy, k/U^2_∞ , in the 3.6 x 1.6 staggered tube bank (Re_d = 12,858).

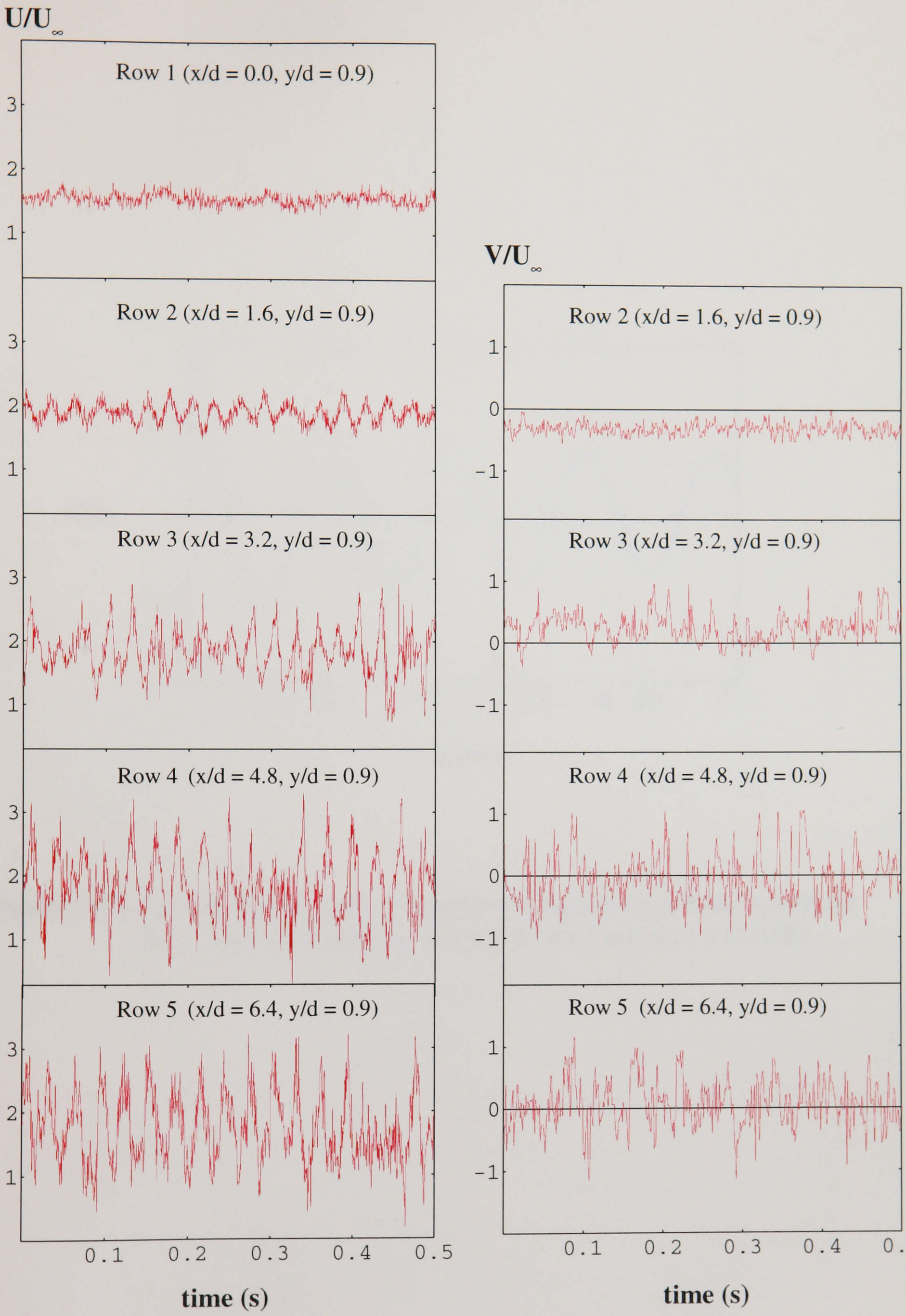

(a) axial (b) transverse

Figure 3.10. Typical velocity recordings obtained in the 3.6 x 1.6 staggered array (Re_d = 12,858).

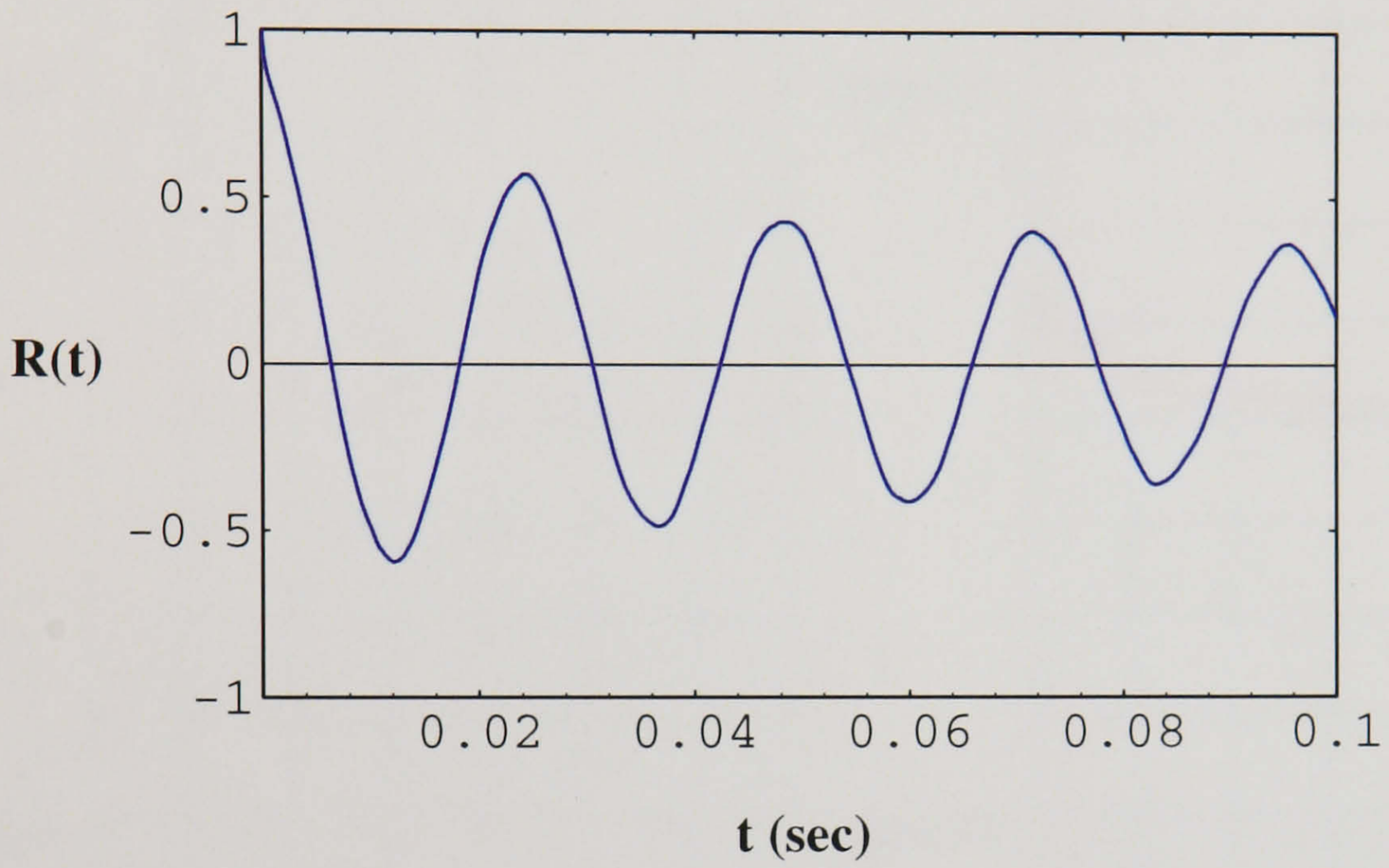

Figure 3.11. Typical autocorrelation function obtained in the second row of the 3.6 x 1.6 staggered array (x/d = 1.6, y/d = 0.6; Red = 12,858).

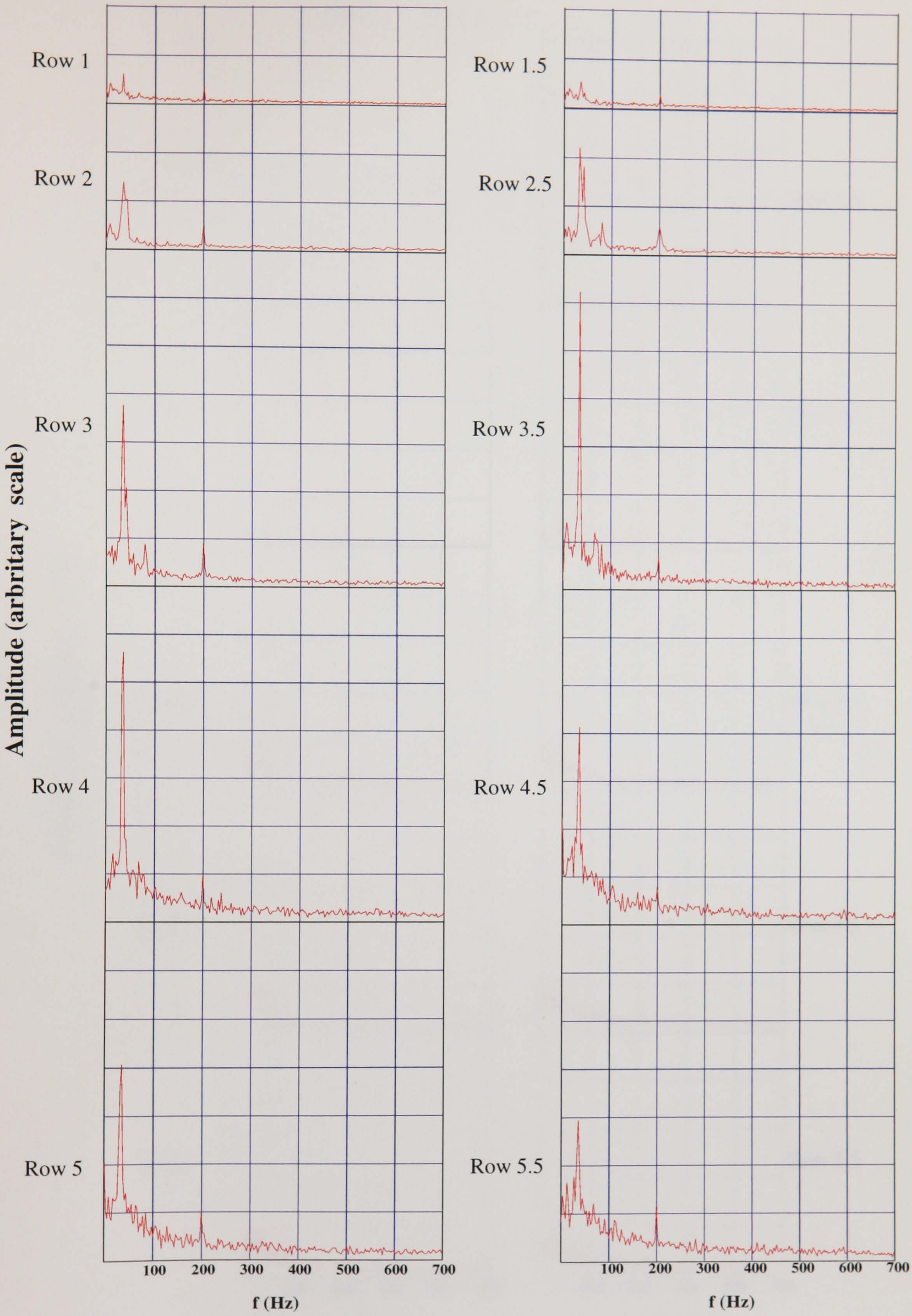

Figure 3.12(a). Amplitude spectra of the axial velocity component in the 3.6 x 1.6 staggered array (Re_d = 12,858); half rows indicate a location midway between successive rows.

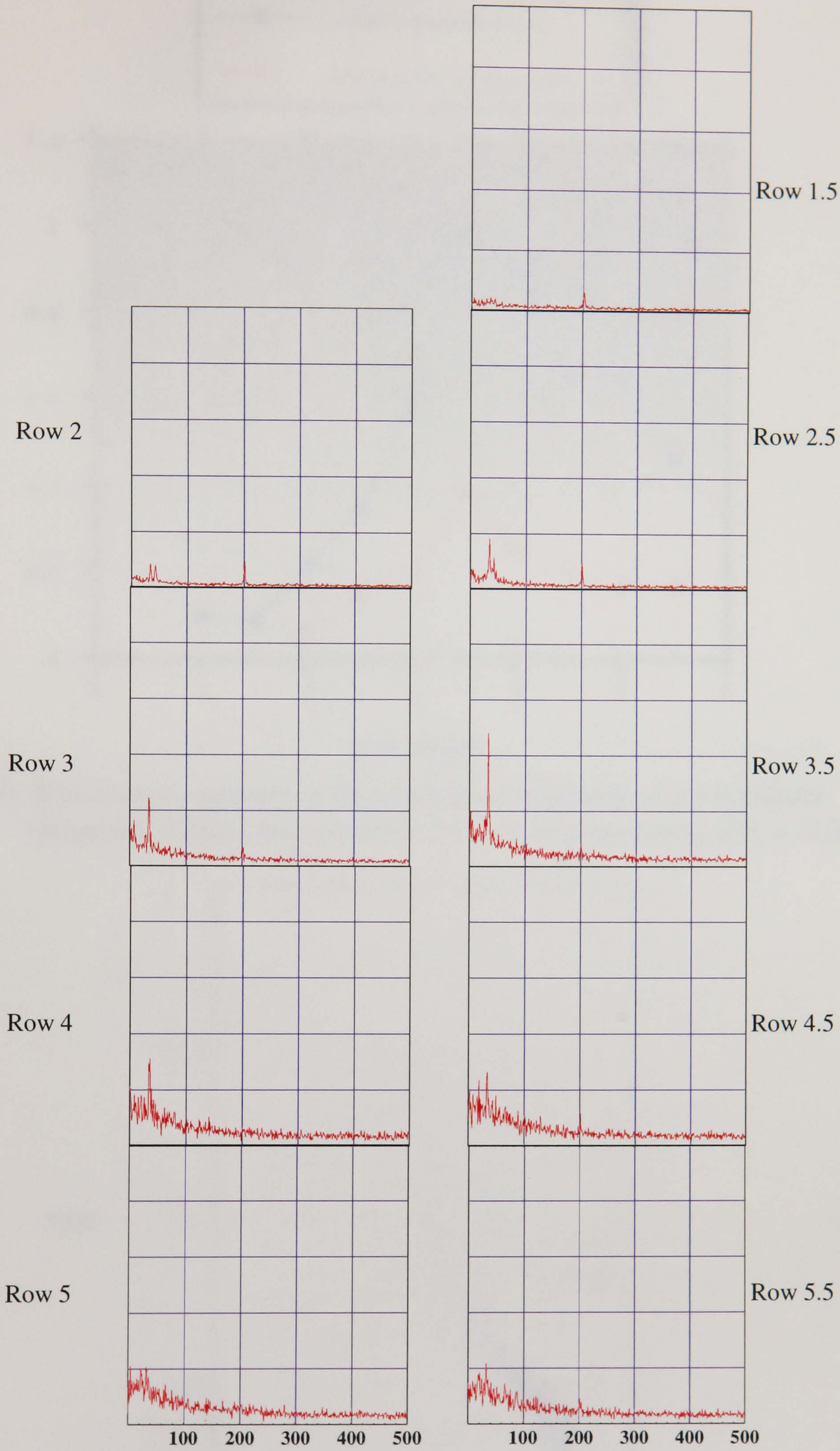

Figure 3.12(b). Amplitude spectra of the transverse velocity component in the 3.6 x 1.6 staggered array (Re_d = 12,858).

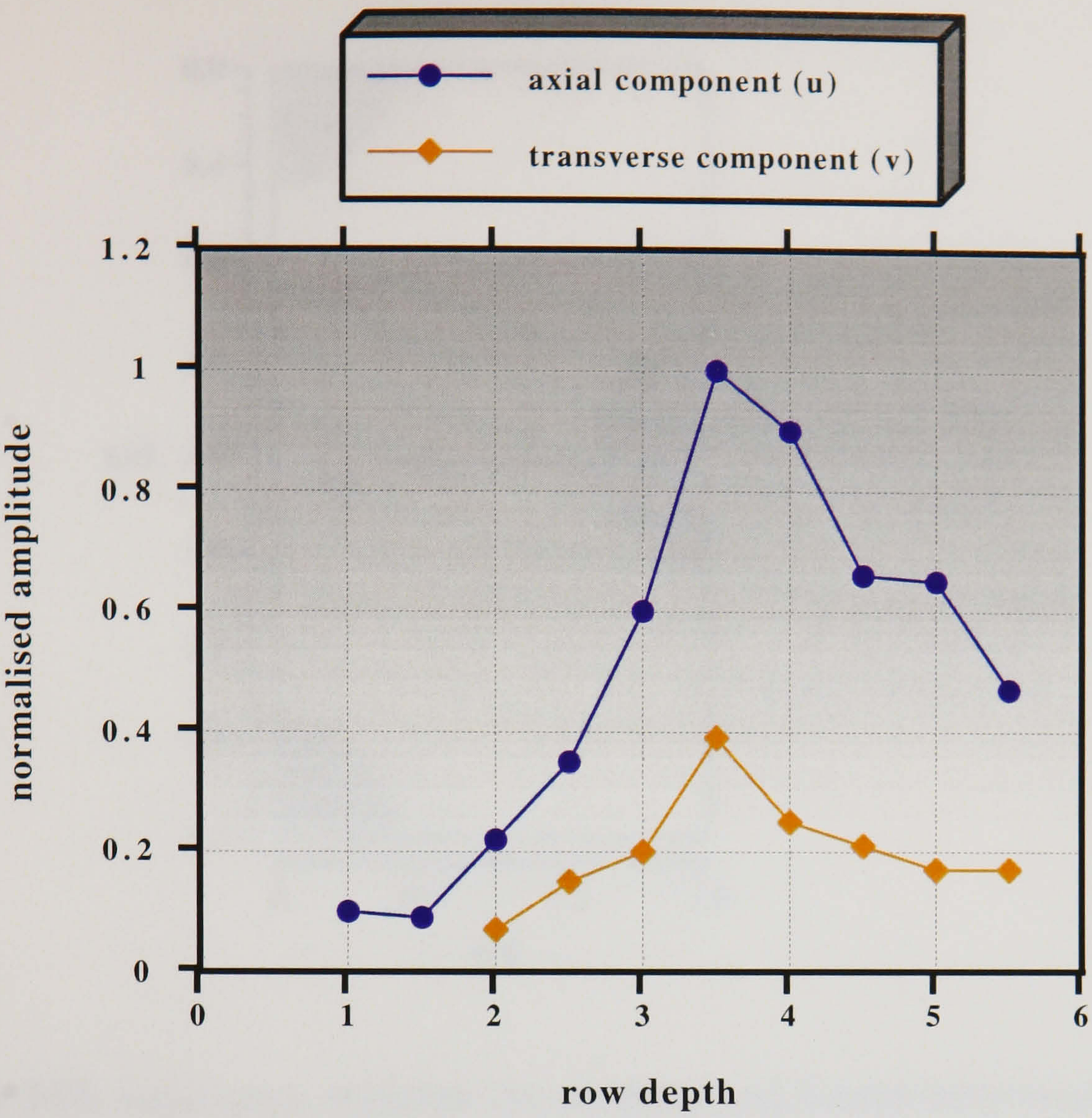

Figure 3.13. Row-to-row variation of the normalised amplitude of the dominant frequency (34 Hz) observed in the 3.6 x 1.6 staggered array (Re_d = 12,858).

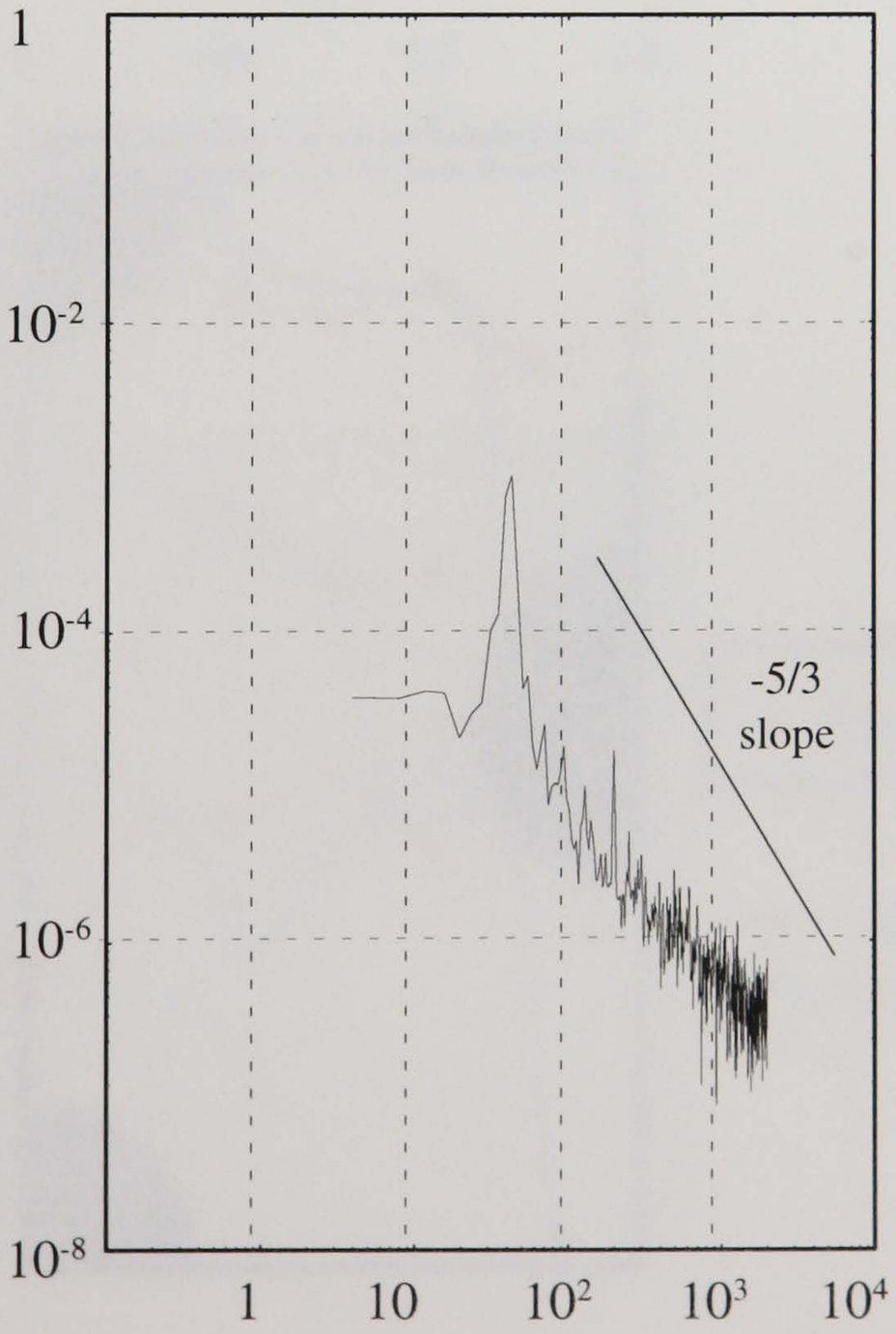

Figure 3.14. Typical power spectrum obtained at x/d=1.6 and y/d=0.6 in the 3.6 x 1.6 staggered array (Re_d = 12,858).

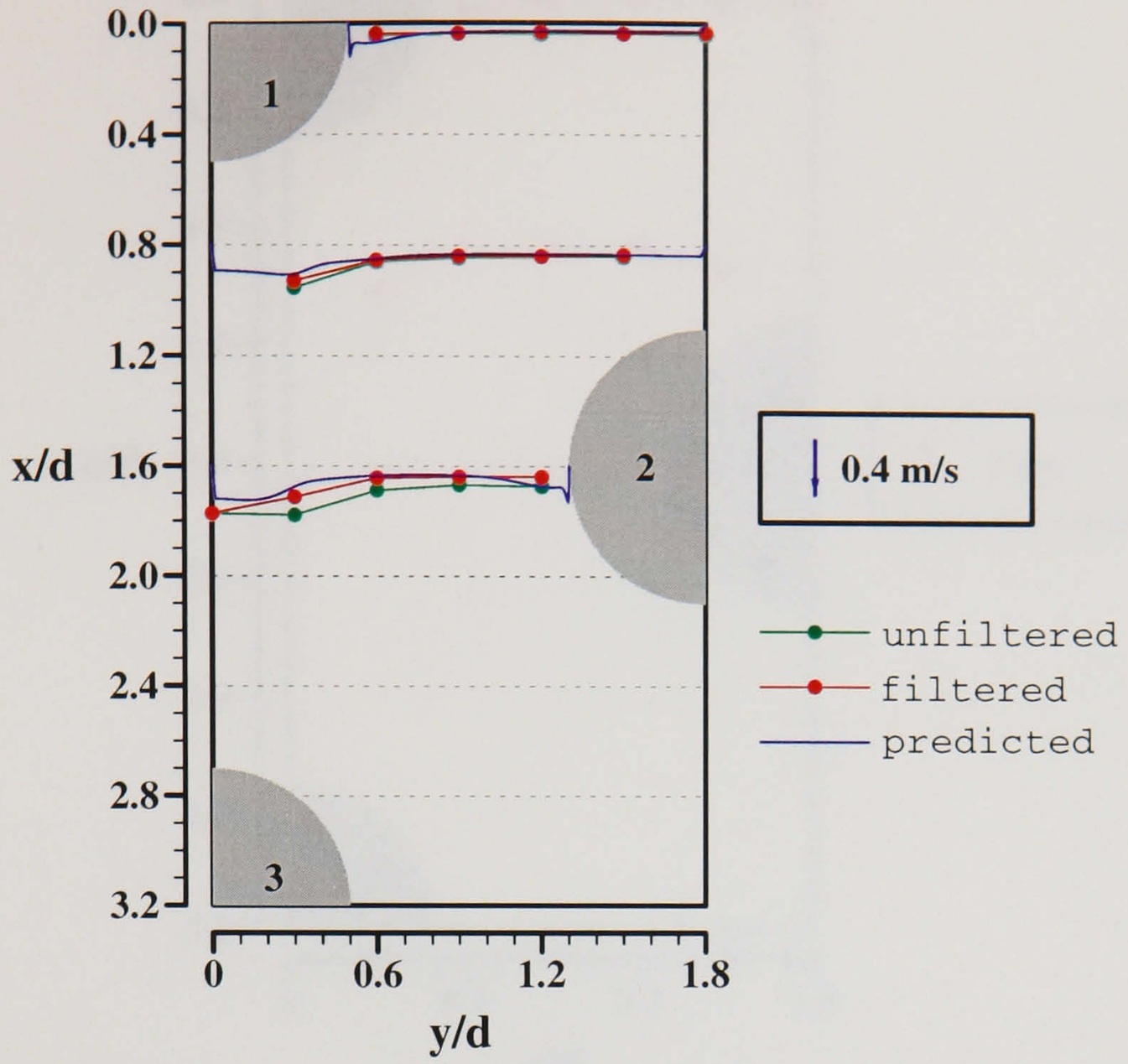

Figure 3.15. Axial r.m.s. velocities for unfiltered and filtered data compared with numerical predictions in the 3.6 x 1.6 staggered array (Re_d = 12,858).

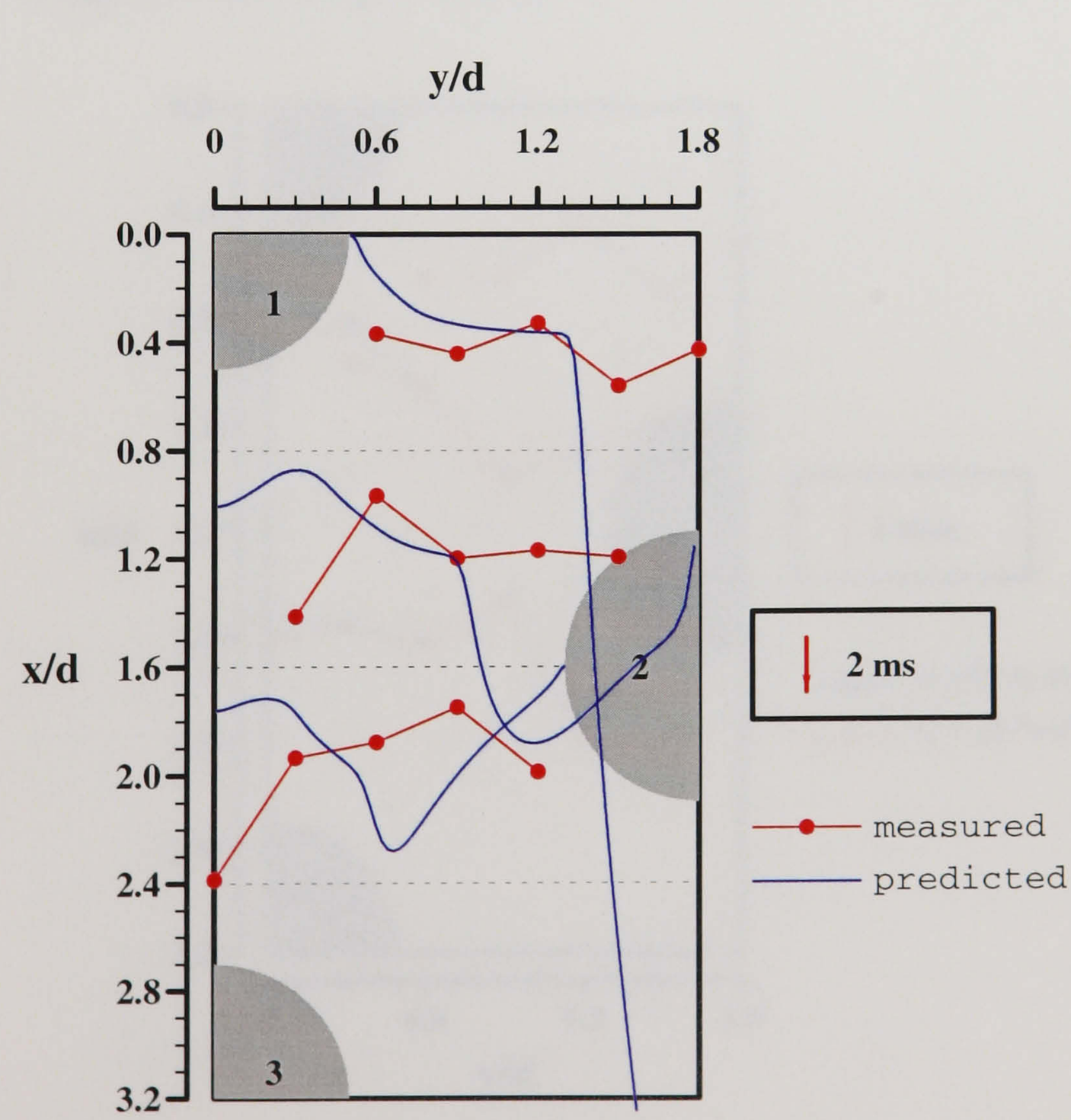

Figure 3.16. Experimental and numerical estimates of integral timescales T_E in the 3.6 x 1.6 staggered bank (Re_d = 12,858).

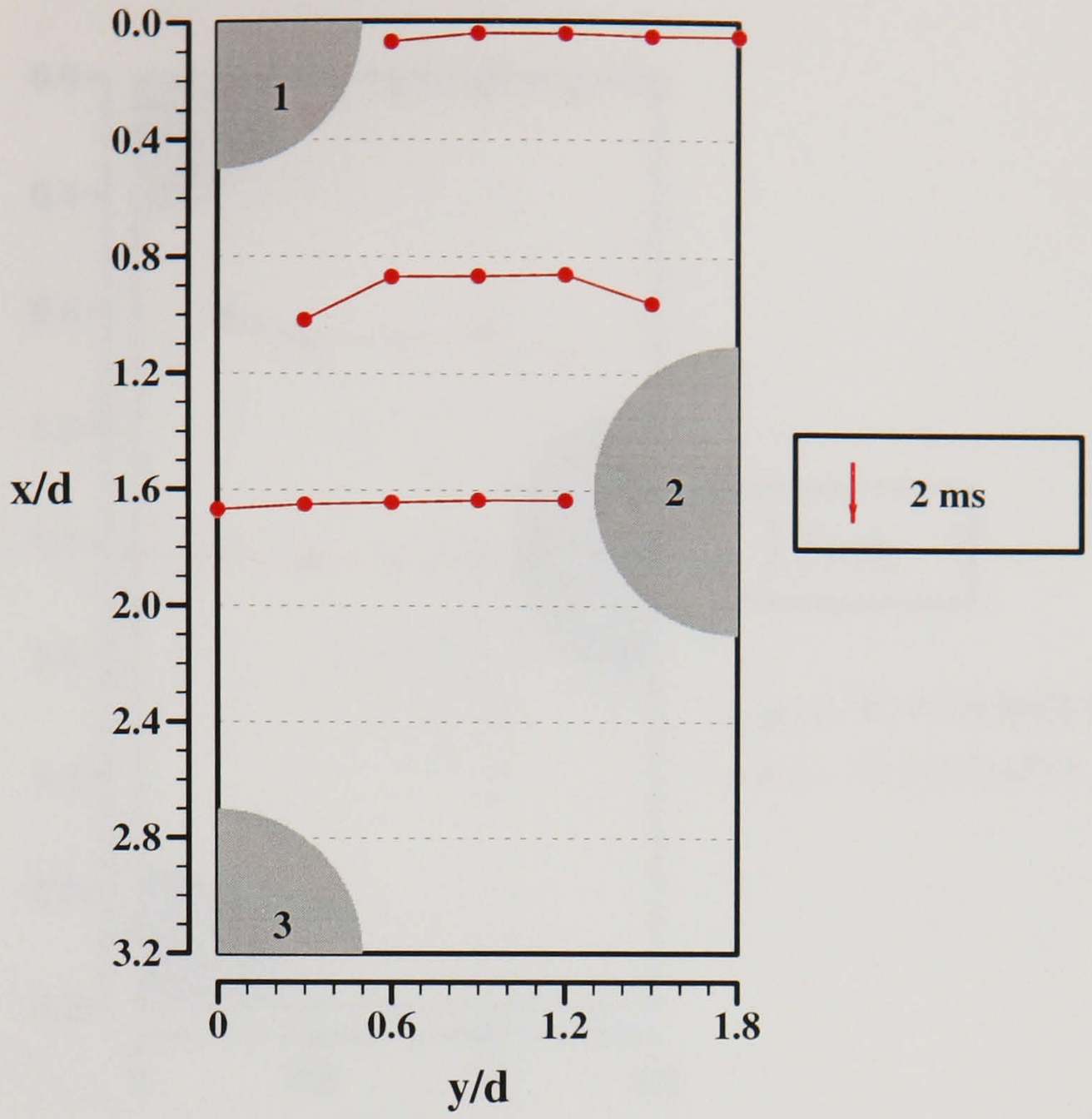

Figure 3.17. Micro timescales τ_E estimated from filtered data in the 3.6 x 1.6 staggered bank (Re_d = 12,858).

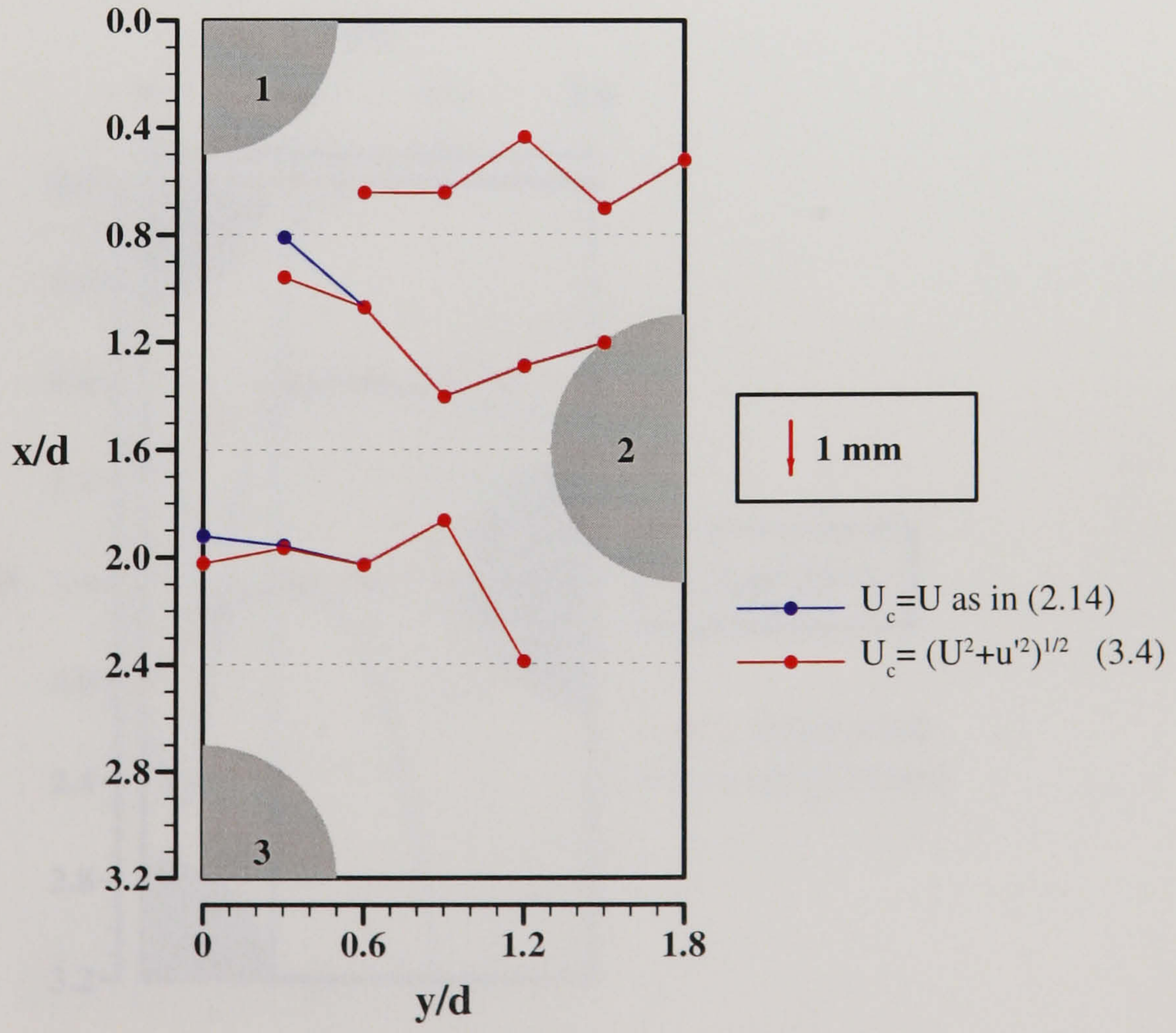

Figure 3.18. Macro length scales Λ_f estimated from filtered data in the 3.6 x 1.6 staggered bank (Re_d = 12,858).

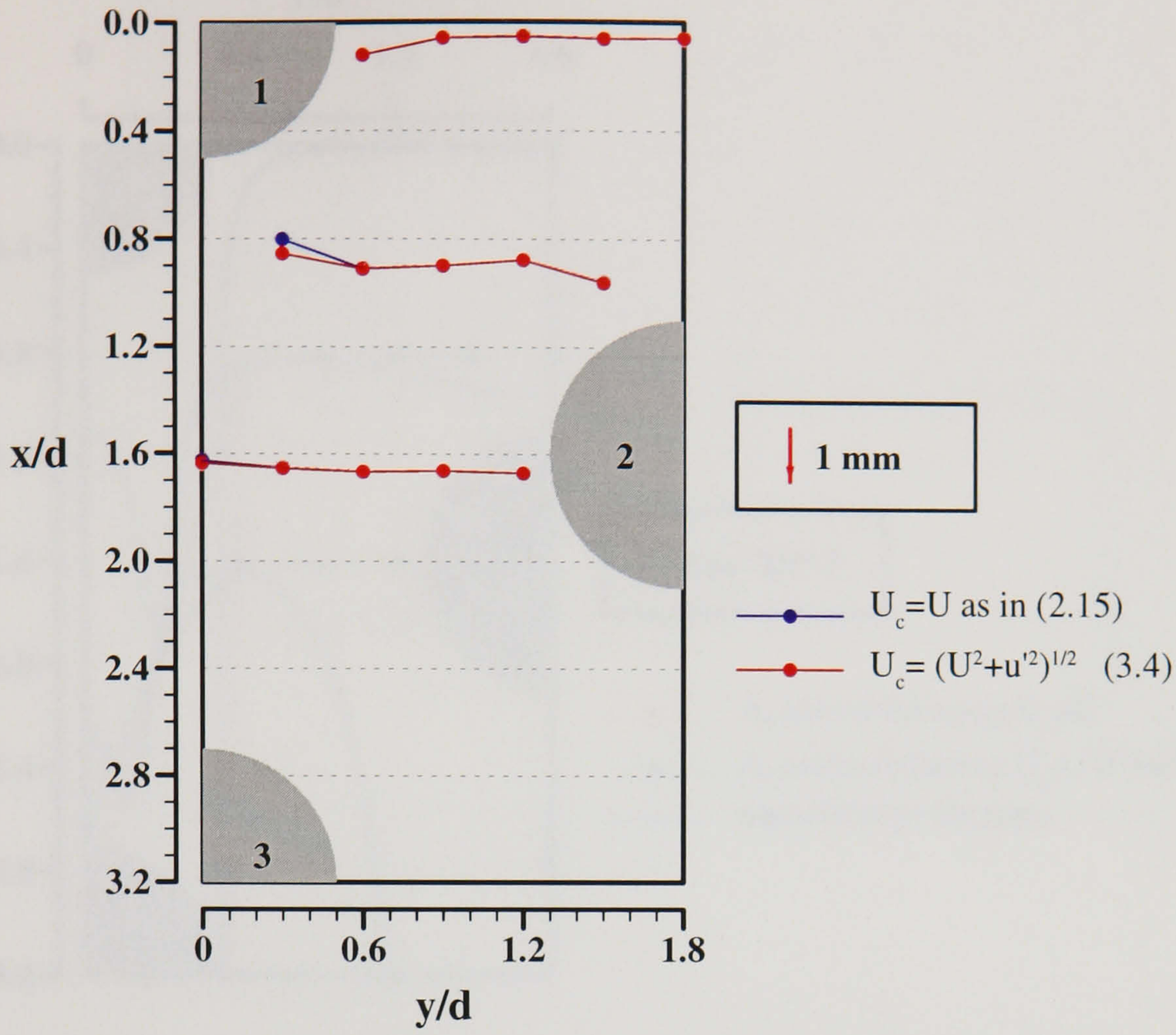

Figure 3.19. Micro length scales λ_f estimated from the filtered data in the 3.6 x 1.6 staggered bank (Re_d = 12,858).

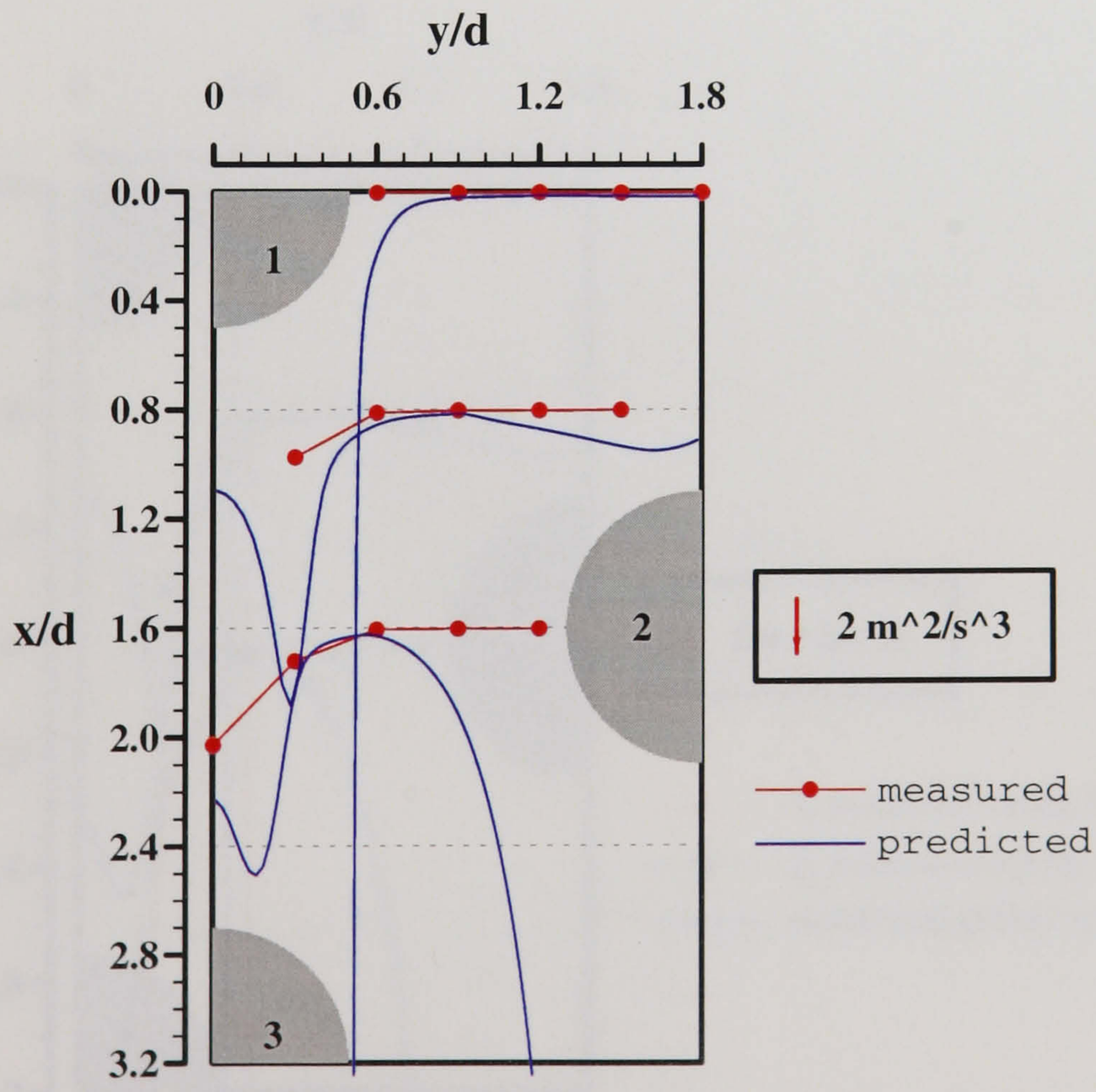

Figure 3. 20. Estimates of the rate of dissipation ε computed from $\varepsilon = u'^3/d$ and comparisons with numerical values in the 3.6 x 1.6 staggered bank (Re_d = 12,858).

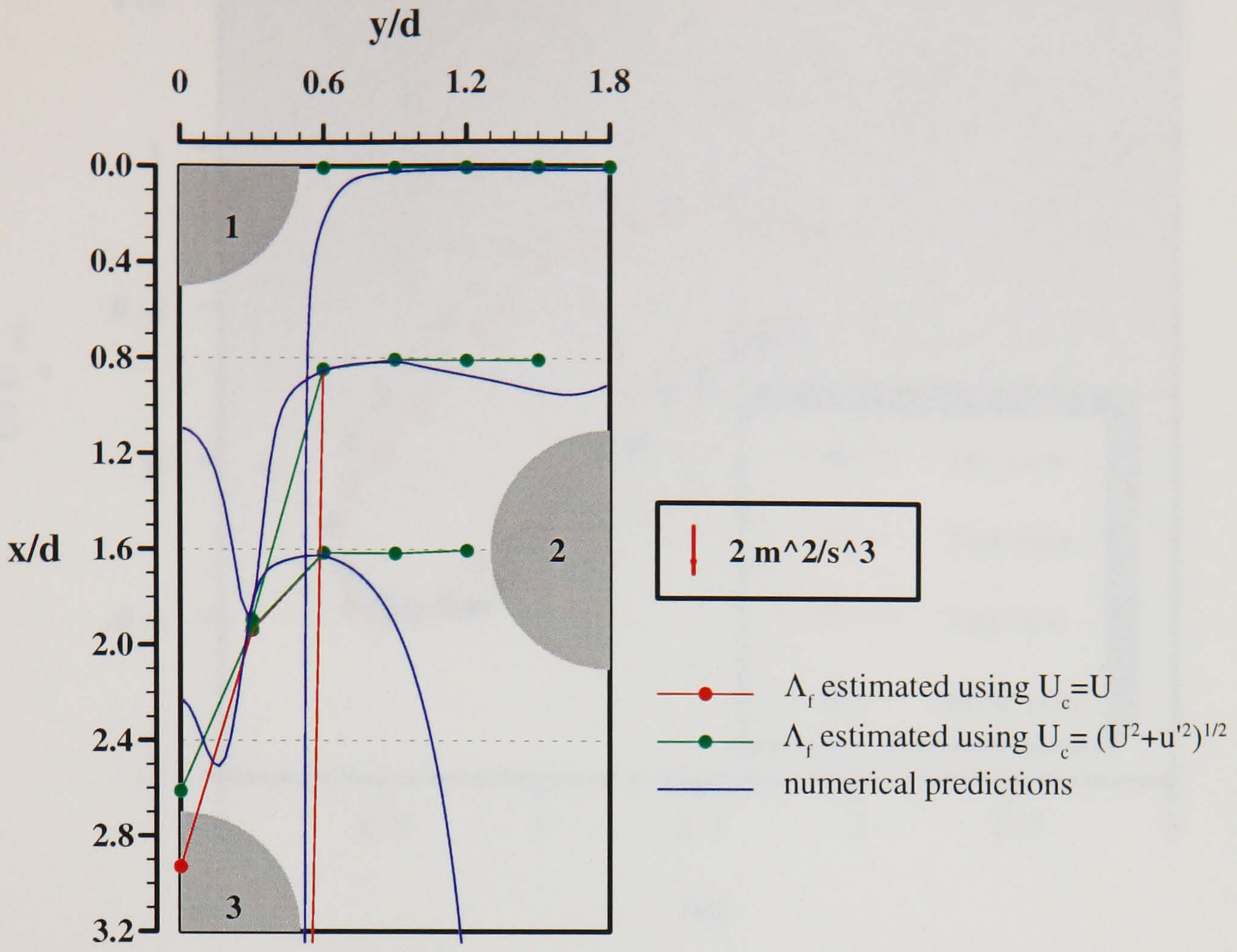

Figure 3.21. Estimates of the rate of dissipation ε (=u'^3/Λ_f) and comparisons with numerical values in the 3.6 x 1.6 staggered tube bank (Re_d = 12,858).

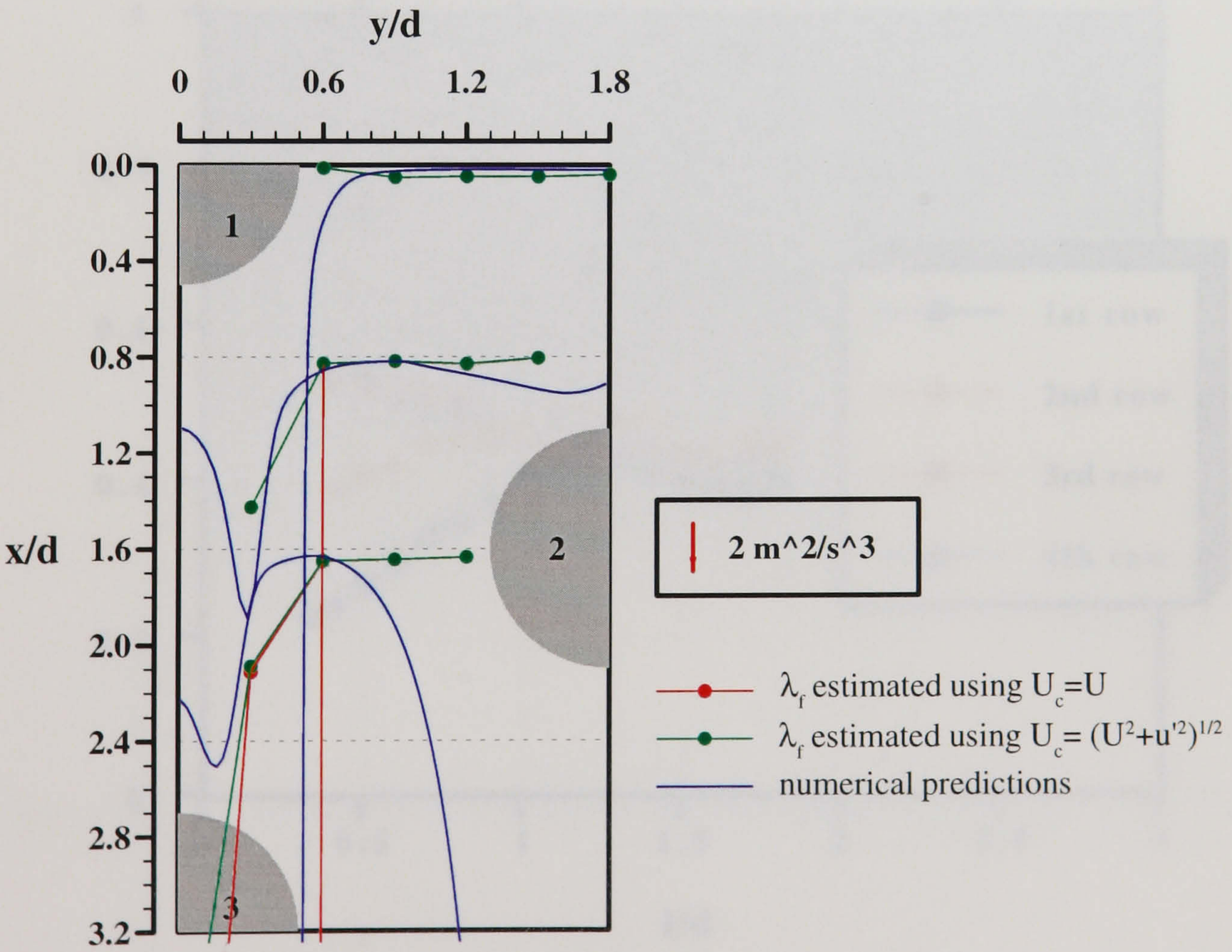

Figure 3. 22. Estimates of the rate of dissipation ε computed from $\varepsilon=30\nu u'^2/\lambda_f^2$ and comparisons with numerical values in the 3.6 x 1.6 staggered bank (Re_d = 12,858).

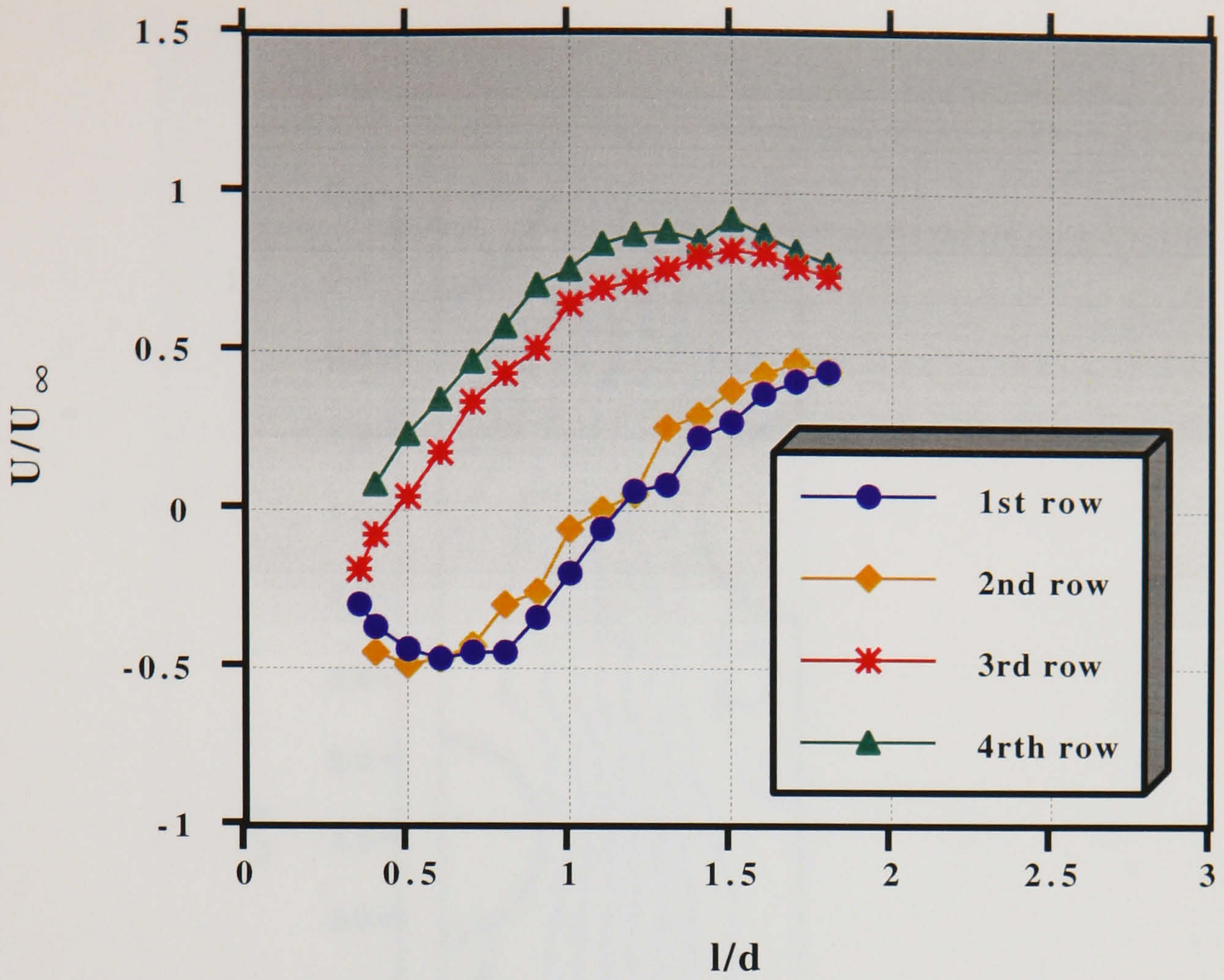

Figure 3.23. Development of the axial mean velocities, U/U_∞, downstream of the first four rows in the 3.6 x 1.6 staggered array (Re_d = 12,858).

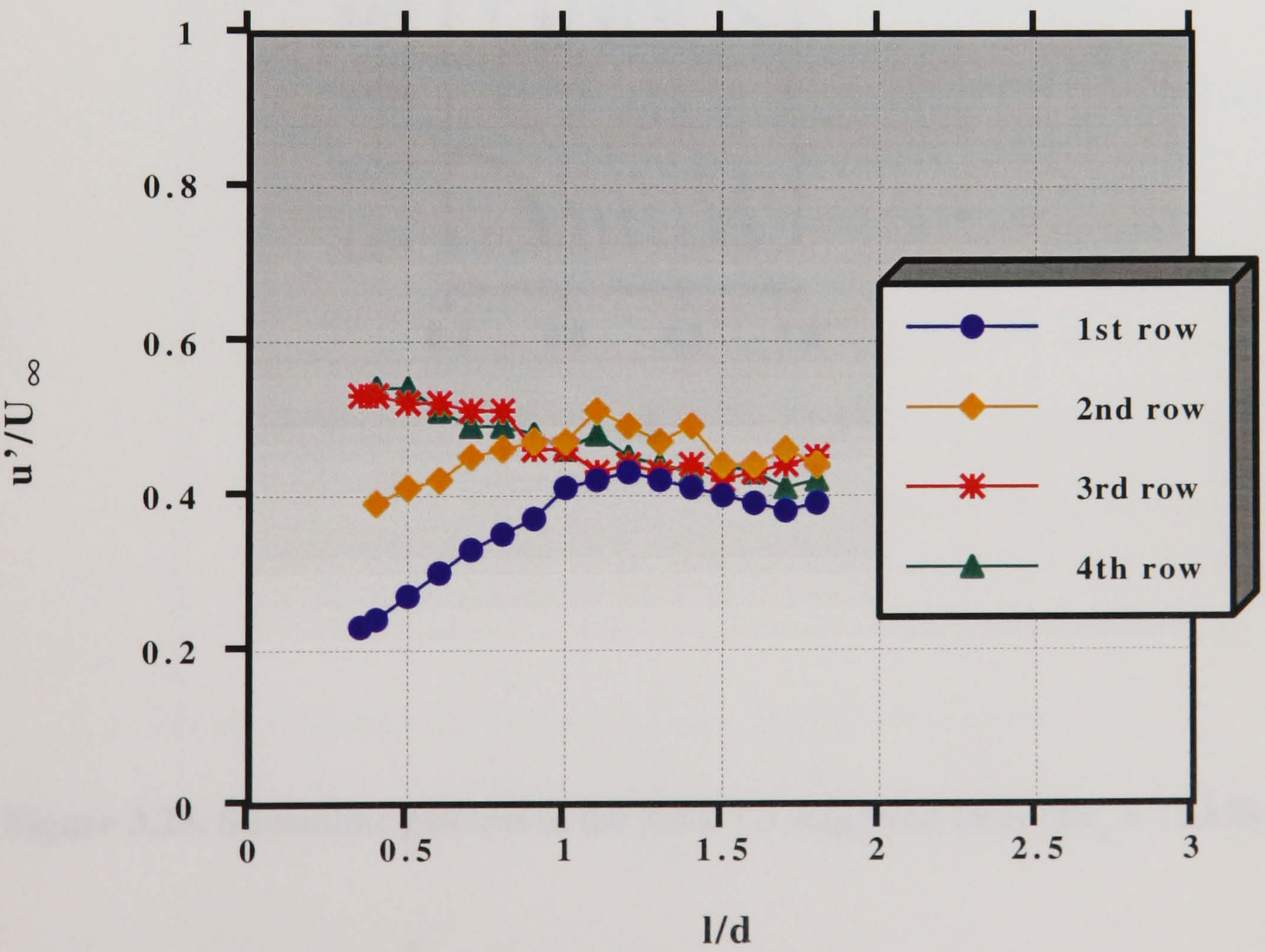

Figure 3.24. Development of the axial r.m.s. velocities, u'/U_∞, downstream of the first four rows in the 3.6 x 1.6 staggered array (Re_d = 12,858).

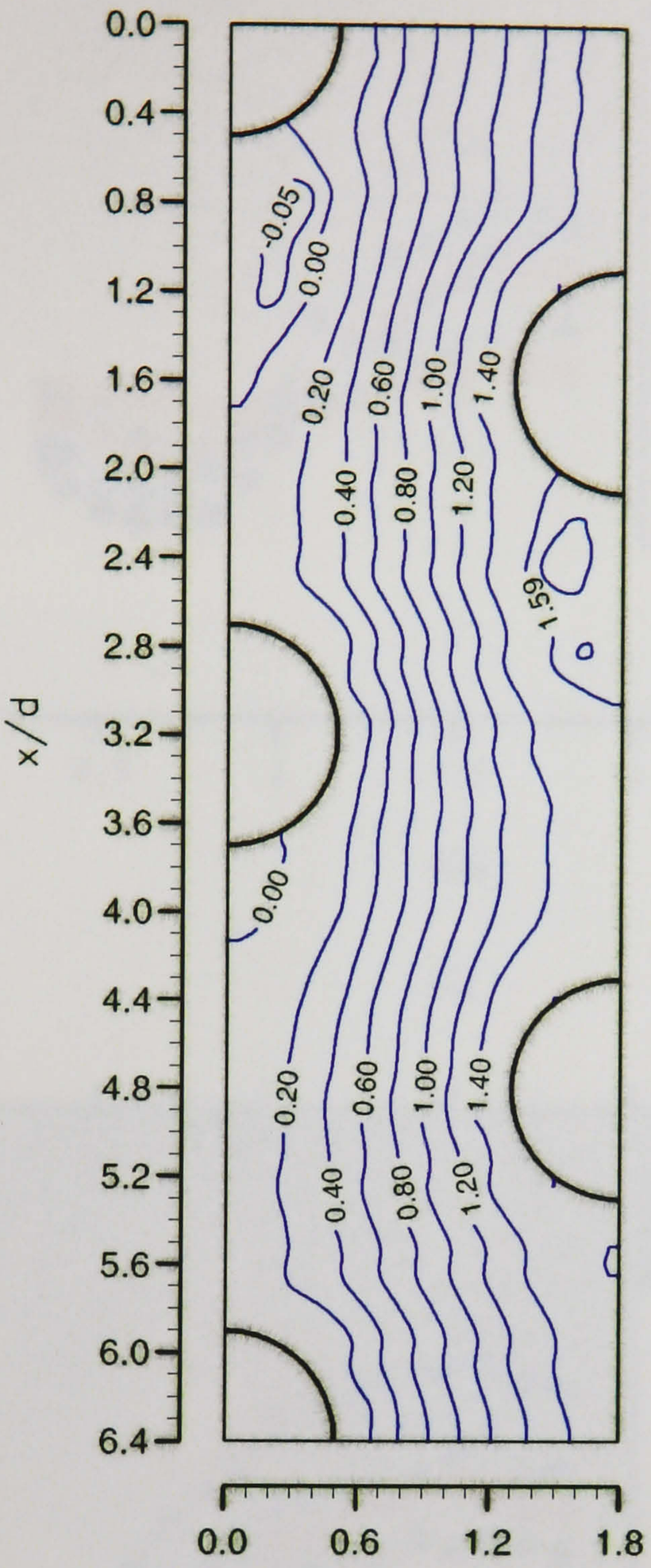

Figure 3.25. Streamline patterns in the 3.6 x 1.6 staggered array (Re_d = 12,858).

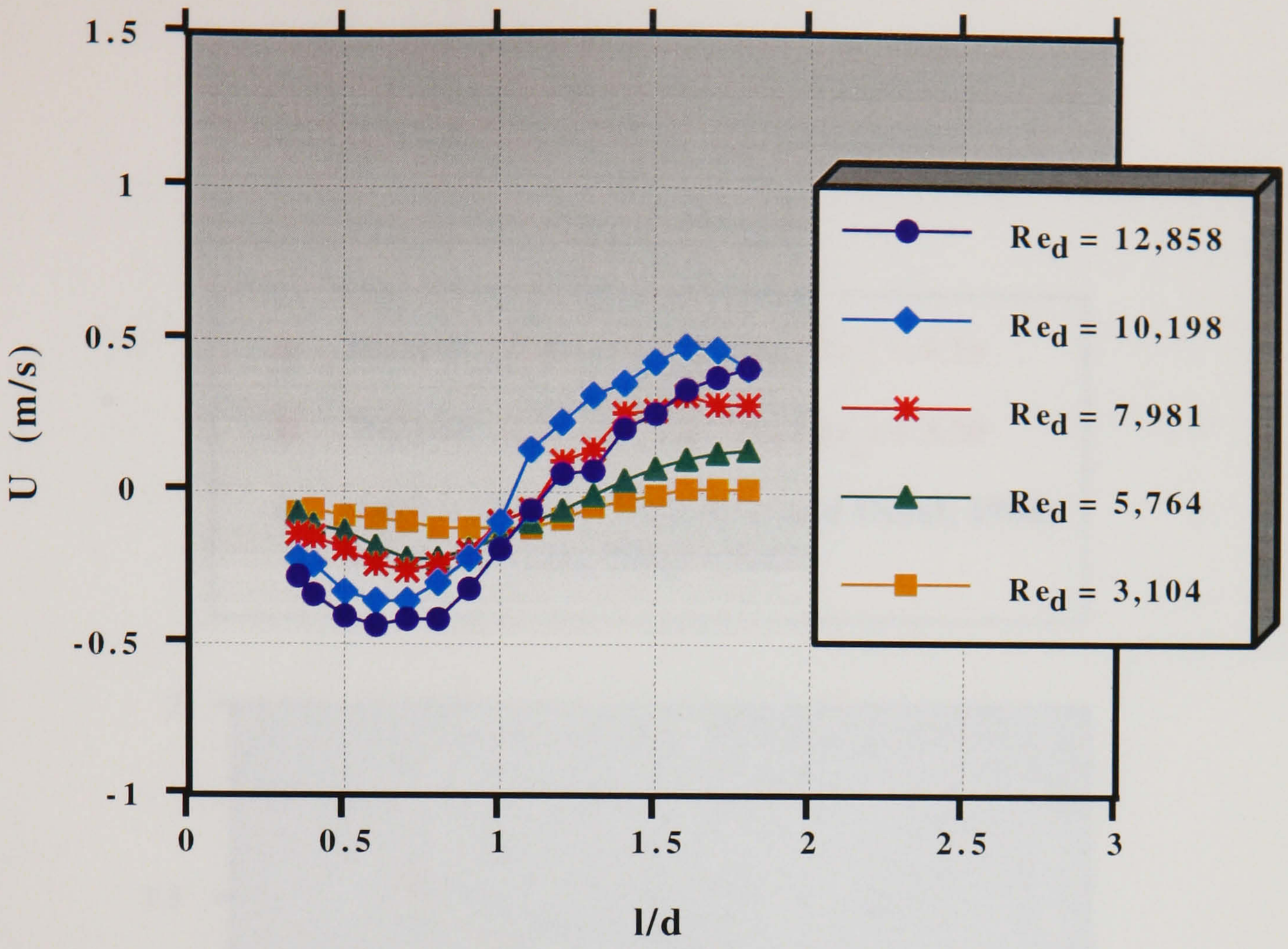

(a)

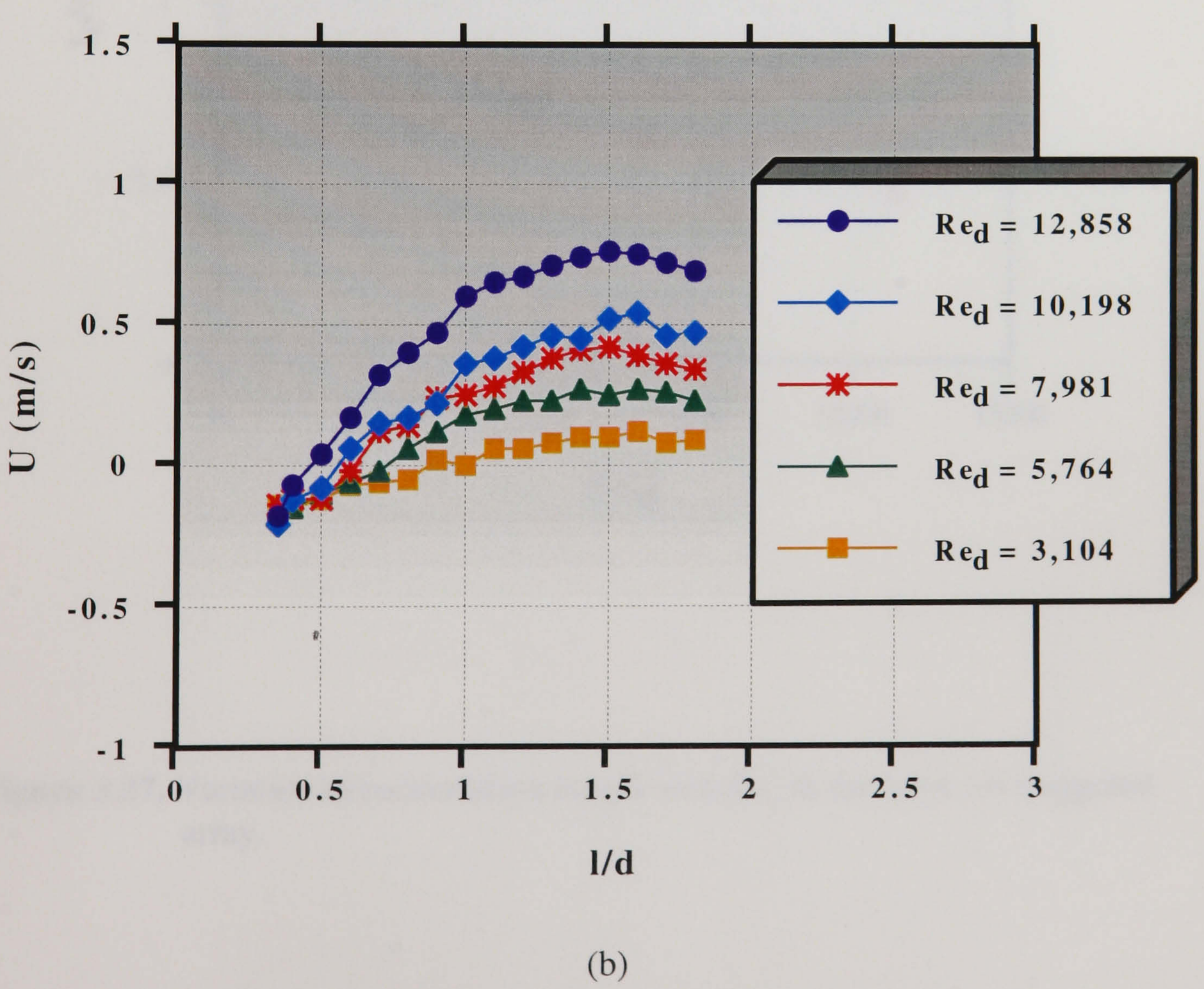

(b)

Figure 3.26. Effect of Re_d on the centreline development of U downstream of the first (a) and third (b) rows of the 3.6 x 1.6 staggered array.

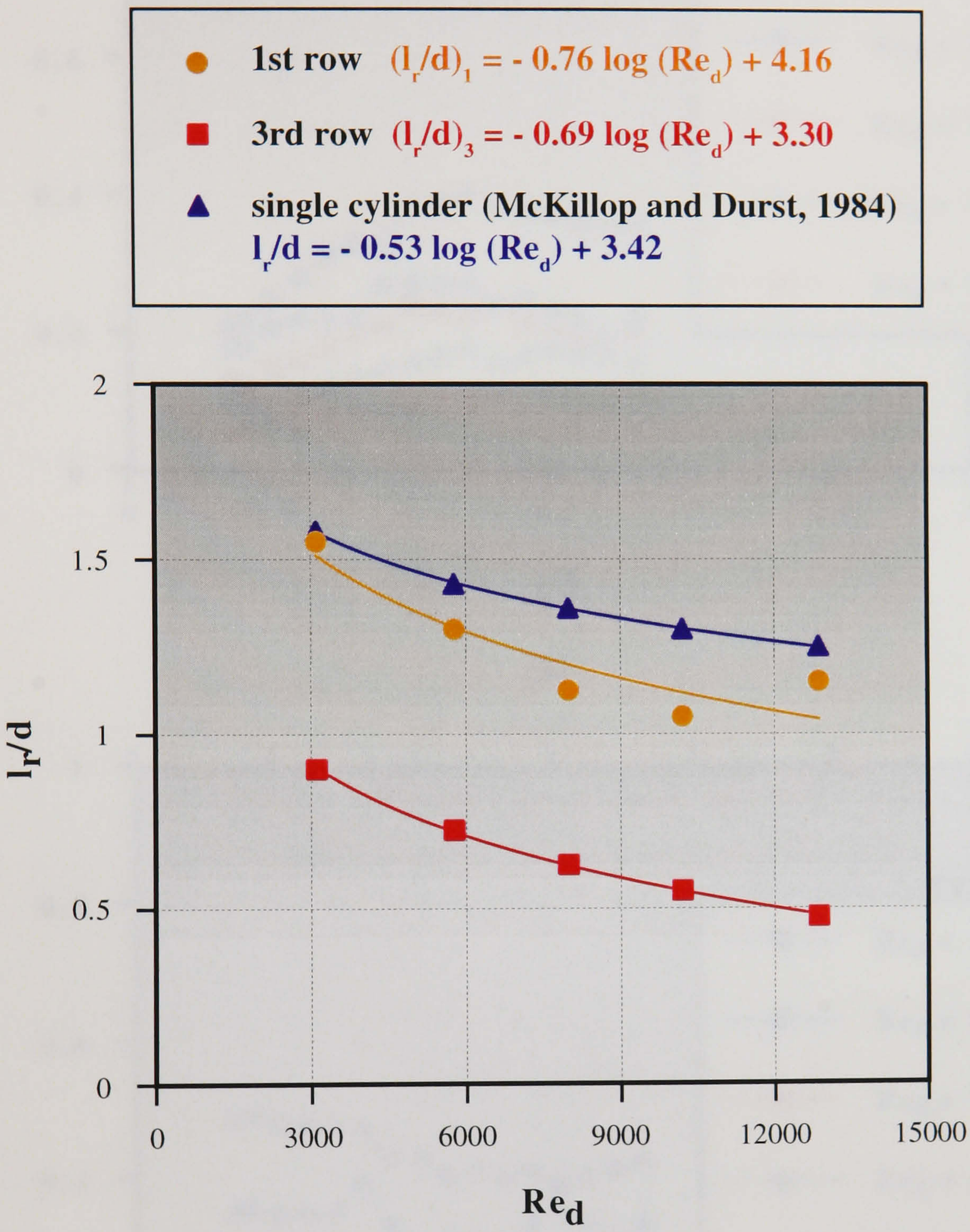

Figure 3.27. Variation of recirculation length with Re_d in the 3.6 x 1.6 staggered array.

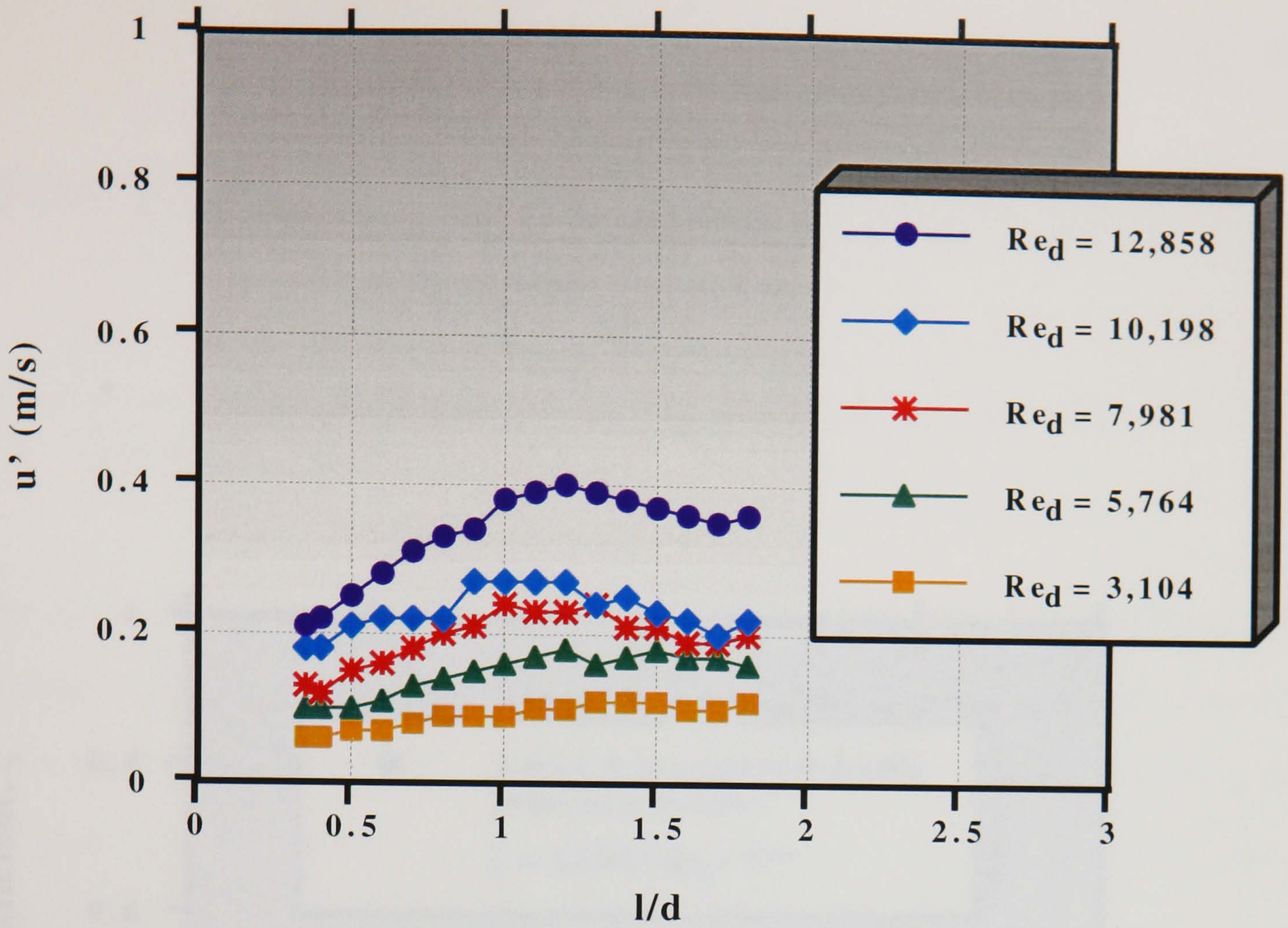

(a)

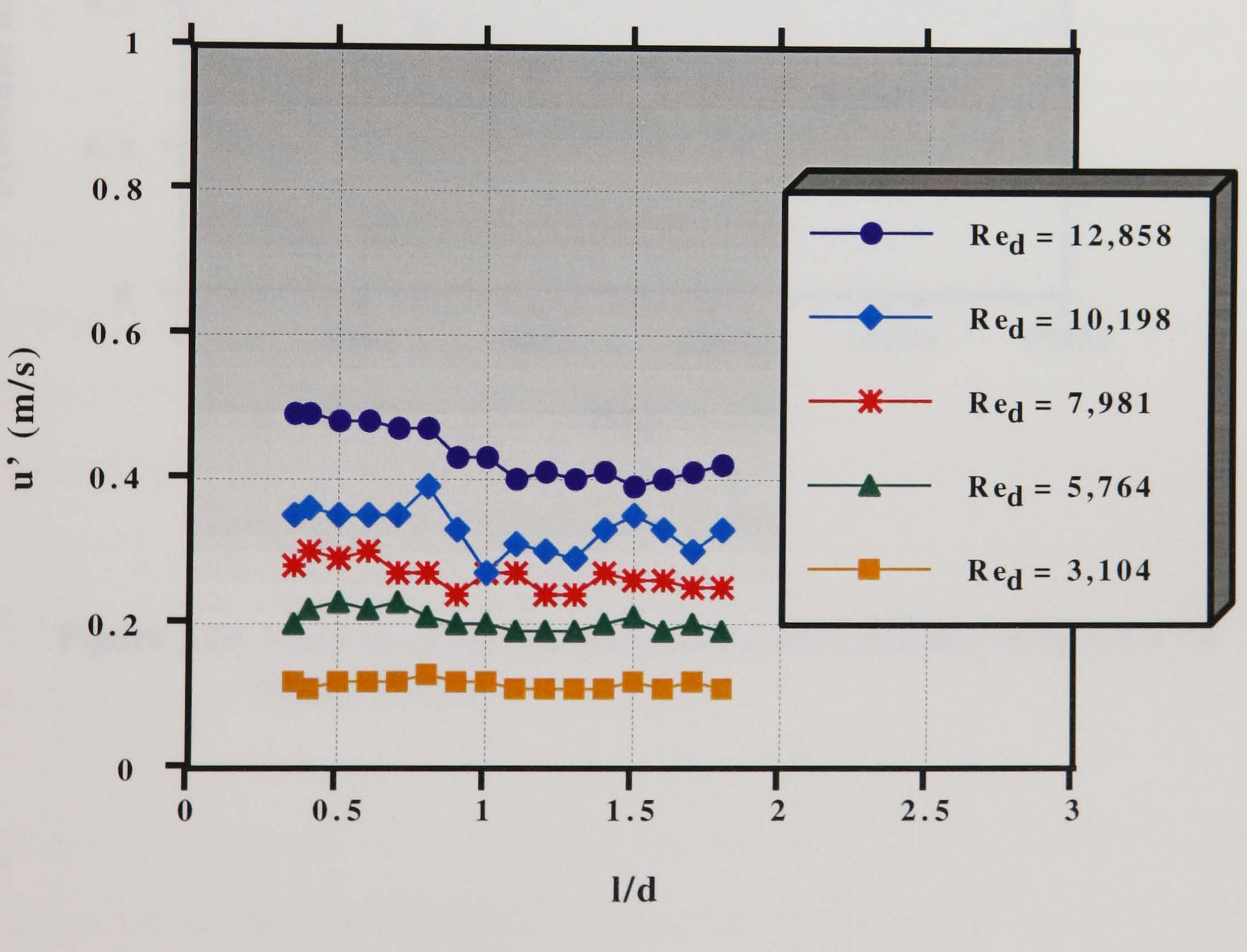

(b)

Figure 3.28. Effect of Re_d on the centreline development of u' downstream of the first (a) and third (b) rows of the 3.6 x 1.6 staggered array.

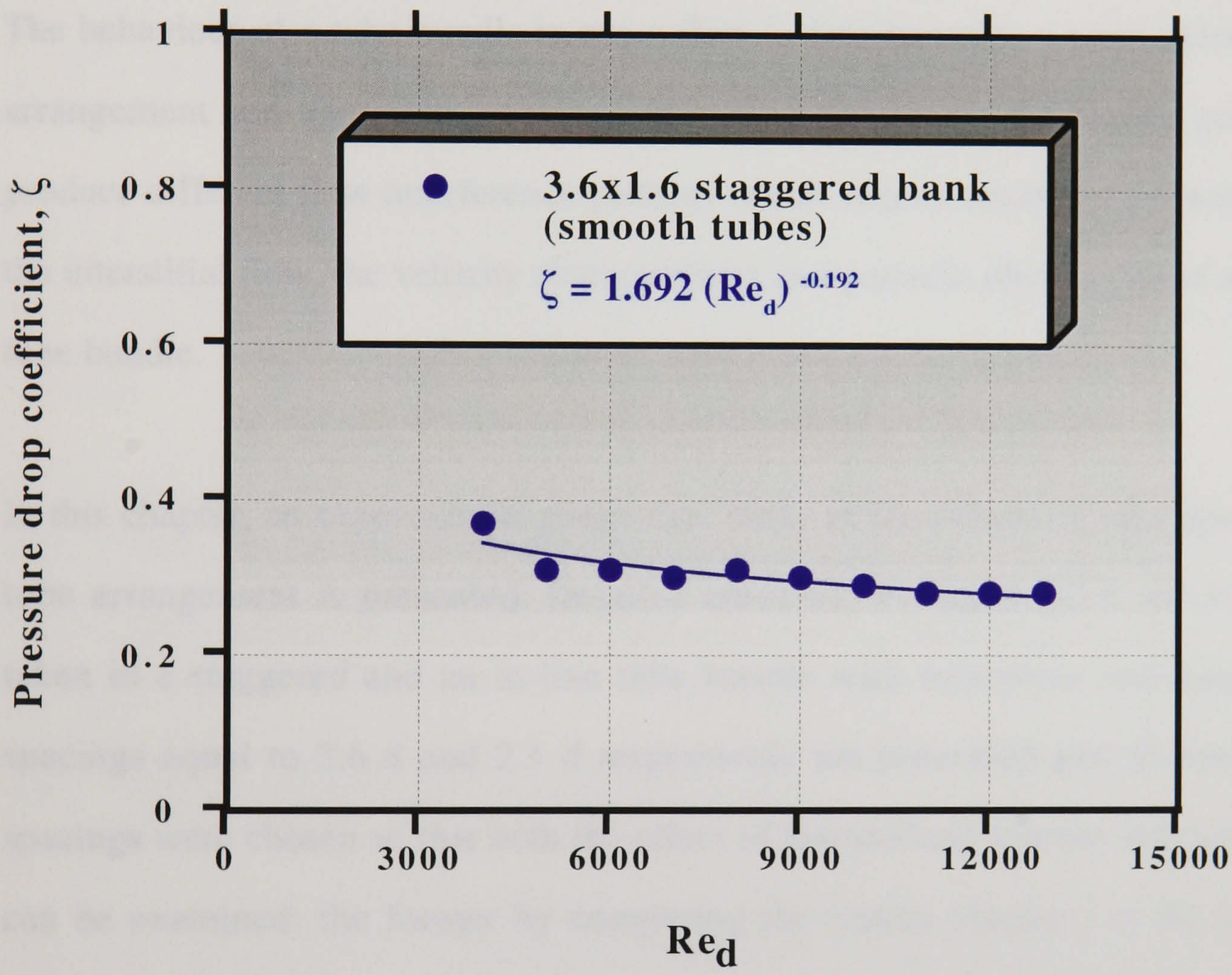

Figure 3.29. Variation of pressure drop coefficient ζ with Re_d in the 3.6 x 1.6 staggered array.

CHAPTER 4

THE EFFECTS OF TUBE SPACING AND TUBE ARRANGEMENT

4.1 INTRODUCTION

The behaviour of a tube bundle in cross-flow is determined to a great extent by the arrangement and the spacing between the tubes. Different tube bundle geometries produce different flow interference patterns which in turn determine the structure of the interstitial flow, the velocity characteristics and periodic phenomena of a specific tube bundle.

In this chapter, an experimental parametric study of the effects of tube spacing and tube arrangement is presented. Detailed ensemble-averaged LDA measurements taken in a staggered and an in-line tube bundle with transverse and longitudinal spacings equal to 3.6 d and 2.1 d respectively are presented and discussed. The spacings were chosen so that both the effect of longitudinal spacing and tube layout can be examined: the former by comparing the results obtained in the 3.6 x 2.1 staggered array with those for the 3.6 x 1.6 staggered array reported in Chapter 3 and the latter by comparing the results for the 3.6 x 2.1 staggered array with those for the 3.6 x 2.1 in-line array. The experimental facility and the details of the two tube bundle geometries have been described in Chapter 2.

The co-ordinate system was the same as that used in the study of the 3.6 x 1.6 staggered array. The larger longitudinal spacing employed in comparison to the 3.6 x 1.6 staggered array allowed more data to be obtained between successive rows of tubes. A denser measurement grid was used in the normal direction: step intervals of 1 mm and 2 mm in the regions of steep velocity gradients and the mainstream flow

respectively were employed. Measurements of the axial and transverse velocity components were taken at the plane of symmetry (z/d = 0) and in the region $0.0 \leq y/d \leq 1.8$ and $0.0 \leq x/d \leq 8.4$ in both the staggered and in-line arrays. In order to determine the extent that the wake characteristics are modified by the bundle geometry, detailed velocity measurements were taken along the wake axes. The working fluid was water and the Re_d was 12,858, the same as that in the study of the 3.6 x 1.6 staggered array. The effect of Re_d on the development of the centreline mean and r.m.s. velocities and on the pressure drop was also studied in the ranges $3{,}104 \leq Re_d \leq 12{,}858$ and $4{,}000 \leq Re_d \leq 12{,}858$ respectively.

Since extensive comparisons with the data for the 3.6 x 1.6 array are made throughout this Chapter, repetition of some results presented earlier could not be avoided.

4.2 THE EFFECT OF TUBE SPACING - 3.6 x 2.1 STAGGERED ARRAY

4.2.1 MEAN VELOCITY DISTRIBUTIONS

The mean velocity vectors measured in the 3.6 x 2.1 staggered array are shown in Figure 4.1. The same features as those observed in the 3.6 x 1.6 staggered array can be seen, i.e. a jet-like flow with high velocities in the gaps between successive rows and recirculating flows downstream of each cylinder. Again flow reversal is pronounced downstream of the first and second rows whereas little flow reversal is evident downstream of subsequent rows. Due to the larger longitudinal spacing the flow path through the array becomes less tortuous than that in the 3.6 x 1.6 arrangement.

Profiles and contours of the normalised axial mean velocities, U/U_∞, are shown in Figures 4.2 (a) and (b) respectively. Positive U/U_∞ values indicate velocities in the downward direction. Profiles (Figure 4.2 (a)) are quite uniform upon entrance to the tube bundle. Steep velocity gradients can be distinguished in the shear layer separating from the first and second cylinders whereas less steep gradients are observed in subsequent rows. Flow reversal is pronounced downstream of the first and second cylinders with negative velocities reaching up to 0.55 U_∞ and 0.42 U_∞ respectively. The flow accelerates as it passes over the shoulder of the cylinders with velocity magnitudes approaching 2.0 U_∞.

The distribution of the transverse mean velocities (V/U_∞) at the same locations is shown in Figures 4.3 (a) and (b). Positive values represent velocities away from the x-axis. Transverse mean velocities reach higher values (up to 0.63 U_∞) at the gaps between successive rows and alternate between negative and positive values as the flow passes through successive gaps. In comparison, transverse mean velocities in the 3.6 x 1.6 configuration did not exceed 0.48 U_∞. Zero transverse velocities are observed along the centreline downstream of each cylinder, as expected.

The frequency counter/data acquisition software was modified for this work to allow the determination of two more parameters of interest: the skewness and the kurtosis (or flatness factor) of the velocity probability density function (p.d.f.). These parameters can be helpful in identifying flow instabilities without the need for time-resolved measurements which are time-consuming. Skewness and kurtosis are defined as follows:

$$\text{Skewness (S)} \qquad S = \frac{\overline{u^3}}{u'^3} = \frac{\frac{1}{N}\sum_{i=1}^{N}(U_i - U)^3}{u'^3} \qquad (4.1)$$

Kurtosis (K) or flatness factor:

$$K = \frac{\overline{u^4}}{u'^4} = \frac{\frac{1}{N}\sum_{i=1}^{N}(U_i - U)^4}{u'^4} \qquad (4.2)$$

For a Gaussian p.d.f. the values of the skewness and kurtosis are 0 and 3 respectively. When instabilities cause a low velocity region to move into a measuring location where high velocities are mostly present, low velocities are recorded intermittently and thus the velocity p.d.f. is skewed towards the higher velocities. The skewness is negative in that case, implying that the flow on average has large fluctuations below the mean more often than above it. Conversely, at low velocity locations the p.d.f. is skewed towards the low velocities if high velocities are recorded intermittently and the skewness is positive. Such intermittent flows might also cause the kurtosis to differ from a value of 3. A kurtosis larger than 3 implies that the p.d.f. is spread more than a Gaussian p.d.f., i.e. very dissimilar velocity scales are recorded and the reverse is true when kurtosis is less than 3 (Nadarajah, 1992). Large kurtosis values are associated with spiky velocity characteristics and probability distributions with long tails (Tennekes and Lunley, 1972).

Figures 4.4 and 4.5 show contours of the axial and transverse velocity skewness respectively measured in the 3.6 x 2.1 staggered array. The axial velocity skewness (Figure 4.4) is approximately zero upon entrance to the bank and in most of the jets issuing from the gaps between successive rows of tubes. It varies from zero to low positive values (up to 0.40) in the recirculation regions and also in the middle of the jet issuing from the gap between the third and fourth rows. High negative skewness values (up to - 0.80) are observed in the vicinity of the shear layers separating from the first and second rows. The p.d.f. is skewed towards higher velocities in these locations which may imply that low velocities are recorded intermittedly from vortices shed by the first and second row cylinders. The low positive skewness observed in some locations within the recirculation regions can be attributed to

intermittent recording of high velocities from the jets. Similarly, the positive skewness observed in the middle of the narrow passage between the third and fourth rows may imply that higher velocities occurring at the shoulders of the third and fourth row cylinders are recorded intermittently due to instabilities of the corresponding shear layers.

The deviations from Gaussian behaviour are greatest in the transverse velocity component. High positive values of the transverse velocity skewness (> 1.0) are observed (Figure 4.5) in the vicinity of the wake region downstream of the first row and the inner edge of the jet issuing from the two first rows. As transverse mean velocities have low values in these locations, the positive skewness values indicate that higher jet velocities are recorded intermittedly, skewing the p.d.f. towards lower velocities. The opposite trend, i.e. high negative skewness values (< -1.0) are observed in the jet issuing from the gap between the second and third rows. Transverse velocities are relatively high at these locations and the negative skewness implies that low velocities from vortices shed by the second cylinder may be recorded intermittently. The same features of the flow can be seen further downstream, but to a lesser extent.

Contours of the axial and transverse kurtosis (flatness factor) are shown in Figures 4.6 and 4.7. The distribution of the axial velocity kurtosis (Figure 4.6) shows that the p.d.f.'s are approximately Gaussian, within 20 %. The highest deviation from the Gaussian probability function is observed downstream of the second row. In contrast, the distribution of the transverse kurtosis (Figure 4.7) exhibits large values (> 4.0) in the area of high transverse skewness observed between the second and third rows (Figure 4.5) and low values (< 2.0) downstream of the stagnation points in the wake regions. The large transverse kurtosis values may also be attributed to turbulent mixing between two sets of eddies (Nadarajah, 1992).

The above findings indicate that intermittent flow instabilities are present in this staggered configuration. The nature of these flow instabilities cannot be revealed by means of skewness and kurtosis distributions. However, in view of the published literature and the predominant frequency observed in the 3.6 x 1.6 staggered array, it is reasonable to attribute the non-Gaussian velocity characteristics shown above to vortex shedding from the cylinders and turbulent mixing. Due to the larger longitudinal spacing employed vortex shedding is expected to occur at a slightly lower frequency than in the 3.6 x 1.6 array. Consequently, the corresponding St number might be expected to be lower than that found in the closely spaced array (St = 0.26).

Several investigators utilised skewness and kurtosis distributions to identify flow instabilities. For example, Durâo and Whitelaw (1978) studied the velocity p.d.f. characteristics in an annular jet configuration comprising an annular jet and a disk. The probability distributions were found to be nearly Gaussian in the recirculation region downstream of the disk. On the contrary, large values of skewness and kurtosis, with rapid changes in the sign of the former, were found in the vicinity of the shear layers. Kurtosis values, significantly larger than 3, were observed in the jet core associated with spiky velocity characteristics. These were attributed to the low turbulence intensity due to the upstream contraction. Skewness values were negative in that region as a result of the turbulent mixing caused by the recirculation behind the disk. Bimodal distributions were found close to the outer edge of the jet - associated with an extremely high kurtosis value (13.53) - which gave way to large positive skewness values at larger radii and eventually to Gaussian distributions. Spectral measurements in the regions where bimodal p.d.f.'s were observed, revealed the existence of predominant frequencies linked to the outer shear layer of the jet. It should be noted that the skewness and kurtosis values reported by Durâo and Whitelaw were significantly larger than those in the present study. Also, deviations

from Gaussian behaviour were found to be greater in the axial direction, in contrast to the findings of the present study.

Nadarajah (1992) illustrated the effect of intermittent flows on the measured skewness and kurtosis of the velocity p.d.f. by simple analysis. Skewness and kurtosis distributions were obtained in the flow in the inlet port and cylinder of an engine in order to identify intermittent flow instabilities. Non-Gaussian values were observed in some locations which were attributed to jet flapping, turbulent mixing and precession of the swirl centre.

4.2.2 TURBULENCE LEVEL DISTRIBUTIONS

The distribution of the axial r.m.s. velocities, u'/U_∞, is presented in profile and contour form in Figures 4.8 (a) and (b). Qualitatively the distributions are similar to those obtained in the 3.6 x 1.6 staggered configuration: axial r.m.s. levels are very low upon entrance to the bank and they increase gradually after the flow encounters the cylinders. Turbulence levels as high as 0.43 U_∞ are found in the flow passages between the cylinders within the first three rows and slightly higher levels (approximately 0.50 U_∞) further downstream. The highest axial r.m.s. levels (up to 0.70 U_∞) are observed at the interfaces between the recirculation bubble downstream of the second row and the shear layer since steep velocity gradients exist there. As a result of the larger longitudinal spacing turbulence levels in the near wake regions are almost 20 % lower than those in the closely spaced staggered arrangement.

The distribution of v'/U_∞ is shown in Figures 4.9 (a) and (b). In the narrow flow passages, v'/U_∞ values are low as the fluid enters the tube bundle and increase downstream of the third row reaching values up to 0.43 U_∞. R.m.s. levels are higher in the wake regions in the vicinity of the rear stagnation point. A maximum is

observed downstream of the second row with values approximately equal to U_∞. The same feature - albeit less pronounced - was also observed in the 3.6 x 1.6 staggered configuration. The larger longitudinal spacing results in the high turbulence generated in the wakes being dissipated more than in the 3.6 x 1.6 array before the next cylinder is encountered and as a result the r.m.s. levels in the near wake regions as well as in the mainstream flow are lower by approximately 0.10 U_∞ than those in the 3.6 x 1.6 configuration.

In order to assess the influence of the tube spacing on the anisotropy of turbulence in the wake regions, the distribution of the ratio of the r.m.s. velocities, v'/u', is plotted in Figure 4.10. Qualitatively the contour plot is similar to that obtained in the 3.6 x 1.6 staggered array: v'/u' is approximately equal to 1 in the flow passages between tube columns but it is substantially higher in the wake regions. v'/u' reaches higher values downstream of the second row as compared to the 3.6 x 1.6 array. It is also lower in the near wake of the first row cylinder, a feature not evident in the closely spaced staggered array. Similarly, the distribution of $|v'-u'|/U_\infty$, shown in Figure 4.11, is qualitatively similar to that in the 3.6 x 1.6 array: the two r.m.s. components have similar values, within 0.20 U_∞ in most parts of the flow field. A pronounced difference between the two fluctuating components can be observed downstream of the second row (0.60 U_∞) whereas differences up to 0.30 U_∞ occur in other rows. Therefore, in spite of the larger longitudinal spacing, the turbulence in the second row wake region is far from isotropic.

4.2.3 WAKE CHARACTERISTICS

Centreline mean and r.m.s. velocities

The centreline development of U/U_∞ downstream of the first four rows of the 3.6 x 2.1 staggered configuration is shown in Figure 4.12. Again characteristics typical of

the flows over bluff bodies can be seen and to a greater extent than in the 3.6 x 1.6 arrangement due to the larger longitudinal spacing between the tubes. Flow reversal is pronounced downstream of the first row. The rear stagnation point is found progressively closer to the tube in downstream rows, while the positive velocities show a rapid acceleration and converge to almost constant levels - equal to U_∞ - in all four rows.

Centreline profiles are compared with those obtained in the 3.6 x 1.6 staggered array in Figures 4.13 (a) through (d). The centreline axial mean velocities measured in the 3.6 x 2.1 in-line array are also shown in these figures in order to minimise repetition of data. These results, however, are discussed later in this chapter. Downstream of the first row (Figure 4.13 (a)) reverse velocities are identical close to the cylinder but the 3.6 x 2.1 array exhibits higher negative velocities downstream of l/d = 0.6 with a maximum equal to 0.55 U_∞. This maximum occurs at 0.7 - 0.8 d from the tube surface, a location similar to that in the 3.6 x 1.6 tube bank. The rear stagnation point is reached at 1.3 d in the 3.6 x 2.1 array, further downstream than in the 3.6 x 1.6 array. Positive velocities reach substantially higher values than those in the 3.6 x 1.6 array. The maximum positive centreline axial velocity is approximately equal to U_∞ as compared to 0.44 U_∞ in the 3.6 x 1.6 array. This maximum is observed at 2.3 - 2.4 d from the tube surface further downstream than the corresponding one in the 3.6 x 1.6 array and it does not coincide with the minimum cross-sectional area between adjacent tubes of the subsequent row.

Downstream of the second row of the 3.6 x 2.1 staggered array (Figure 4.13 (b)) negative velocities are lower than in the first row, a trend opposite to that observed in the 3.6 x 1.6 configuration where the negative velocities downstream of the first two rows were identical. The magnitude of the negative velocities reaches a maximum value of 0.42 U_∞ at 0.4 d from the tube surface. This is slightly lower than the corresponding one in the 3.6 x 1.6 configuration and occurs earlier. U/U_∞

values increase sharply further downstream and the rear stagnation point is reached at 0.8 d, 0.3 d earlier than that in the 3.6 x 1.6 staggered configuration. As a result of the earlier occurrence of the stagnation point, positive velocities attain higher values (exceeding U_∞) than those in the first row. The latter are significantly higher than those in the 3.6 x 1.6 staggered arrangement, due to the larger longitudinal spacing and the earlier stagnation.

Centreline profiles of U/U_∞ downstream of the third and fourth rows of the two staggered arrays are compared in Figures 4.13 (c) and 4.13 (d) respectively. Both staggered arrays are characterised mainly by a region of flow acceleration to a maximum positive velocity which is in general higher in the 3.6 x 2.1 array than in the 3.6 x 1.6: this velocity is equal to U_∞ and 1.1 U_∞ in the third and fourth rows of the 3.6 x 2.1 array respectively as opposed to 0.8 and 0.9 U_∞ in the 3.6 x 1.6 array. The rear stagnation points occur further downstream, at 0.65 d and 0.45 d respectively for the third and fourth rows, than the corresponding ones in the 3.6 x 1.6 staggered configuration.

Figure 4.14 presents the centreline development of u'/U_∞ downstream of the first four rows in the 3.6 x 2.1 staggered configuration. R.m.s velocities increase with distance from the tube surface up to the rear stagnation point where a maximum is observed and decrease thereafter. They are relatively low downstream of the first row with a maximum value of 0.37 U_∞ in the vicinity of the rear stagnation point. Higher centreline r.m.s. velocities are observed in downstream rows with maximum values around 0.50 U_∞. A comparison between the two staggered arrays investigated can be seen in Figures 4.15 (a) through (d). Profiles obtained with the 3.6 x 2.1 in-line array are also shown in these figures for the reasons explained earlier. Downstream of the first row u'/U_∞ values are generally higher in the closely spaced array while downstream of the second row u'/U_∞ are higher in the 3.6 x 2.1 array up to 1 d from the tube surface but the opposite is true further downstream. R.m.s levels

are comparable in downstream rows: u'/U_∞ levels are identical in the vicinity of the rear stagnation points, while further downstream they are slightly higher in the 3.6 x 1.6 array. These results highlight the effect of the longitudinal spacing on the turbulence levels generated by staggered geometries: the larger the spacing the lower the axial r.m.s. levels in the wake regions.

Figure 4.16 shows characteristic centreline profiles of v'/U_∞ downstream of the first and third rows of the 3.6 x 2.1 arrangement. The trends are identical to those identified in the u'/U_∞ profiles: v'/U_∞ levels increase up to the rear stagnation point and decrease further downstream. The maximum values are 0.54 and 0.69 U_∞ for the first and third rows respectively. However, v'/U_∞ values are generally higher than u'/U_∞ ones highlighting the considerable influence of the transverse velocity component on the turbulent mixing process. This can be seen in Figures 4.17 (a) and (b) in which v'/u' and $|v'-u'|/U_\infty$ are plotted respectively. The ratio v'/u' (Figure 4.17 (a)) increases with distance from the tube surface downstream of the first row with values ranging from 0.8 to around 1.8. Values range from 1.2 to 1.6 downstream of the third row; they are identical to those in the first row in the vicinity of the corresponding rear stagnation points but they are generally lower further downstream. In terms of their absolute difference (Figure 4.17 (b)), the two components differ by up to 0.20 U_∞: the difference between the two components is more pronounced in the third row up to 1.5 diameters from the tube surface but the opposite is true further downstream. The finding of larger v' is in agreement with published results on the wake characteristics of bluff bodies. For example, Durâo and Whitelaw (1978) observed that the radial fluctuating velocities in the region around the rear stagnation point downstream of a disk were much larger (more than double in some locations) than the axial fluctuations.

Recirculating parameters

In order to quantify the effect of the tube spacing on the wake characteristics of the tube bundles, parameters such as the recirculation length, the wake width, the vorticity thickness and its spreading rate as well as the recirculating mass-flow rate have been estimated in a manner similar to that described in Chapter 3. The results are listed in Table 4.1 and compared with those estimated for the 3.6 x 1.6 staggered array.

The length of the recirculation bubbles l_r formed downstream of the first four rows in the 3.6 x 2.1 staggered array was determined from the centreline axial mean velocity profiles (Figure 4.12). The length of the recirculation downstream of the first row in the 3.6 x 2.1 staggered tube bundle - measured from the tube surface - is equal to 1.3 d. The latter is 13 % larger than the corresponding length in the 3.6 x 1.6 staggered configuration (1.15 d) and the same trend can be seen downstream of the third and fourth rows. Surprisingly, the opposite trend is observed downstream of the second row with the recirculation length of the 3.6 x 2.1 configuration being equal to 0.8 d as opposed to 1.1 d in the 3.6 x 1.6 tube bundle.

Table 4.1. Recirculating parameters in 3.6 x 2.1 staggered array compared with those of the 3.6 x 1.6 staggered array.

	l_r/d		w_r/d			$\dot{m}_r/\dot{m}$		δ		δ'	
Row	**3.6x2.1**	**3.6x1.6**	**l/d**	**3.6x2.1**	**3.6x1.6**	**3.6x2.1**	**3.6x1.6**	**3.6x2.1**	**3.6x1.6**	**3.6x2.1**	**3.6x1.6**
1	1.3	1.15	0.35	0.55	0.46 (0.59)	0.185	0.15	0.08	0.14 (0.12)	0.09	0.18 (0.15)
			0.75	0.45	0.37 (0.52)			0.17	0.23 (0.19)	0.14	0.19 (0.16)
2	0.8	1.1	0.35	0.53	0.46	0.188	0.1	0.12	0.18	0.14	0.23
			0.75	0.33	0.34			0.29	0.32	0.23	0.26
3	0.65	0.48	0.35	0.48	0.21	0.133	0.02	0.22	0.4	0.25	0.5
4	0.45	0.3	0.35	0.18		0.015		0.31		0.37	

- l/d represents distance from the surface at which the width and vorticity thickness are estimated. Estimates for the 3.6 x 1.6 were calculated at 0.3 d and 0.8 d from the tube surface.
- Figures in brackets correspond to the results for a single cylinder in crossflow as estimated by McKillop and Durst (1984).

The width of the recirculation bubble, w_r, estimated from the separation streamlines is also shown in Table 4.1 compared with those obtained in the 3.6 x 1.6 array as well as with published data on single cylinders in cross-flow (McKillop and Durst, 1984). The estimated flow streamlines for the 3.6 x 2.1 staggered array are shown in Figure 4.18. The recirculation bubbles formed downstream of the first and second rows of the 3.6 x 2.1 arrangement have maximum half-widths larger than the tube radius, with values equal to 0.55 d and 0.53 d respectively. These values are larger by 20 % and 15 % respectively than the corresponding ones in the 3.6 x 1.6 staggered configuration and are in agreement with the expected wake width of a single cylinder in cross-flow under subcritical flow conditions (Roshko, 1961). Due to the larger longitudinal spacing the interference from neighbouring tubes in the 3.6 x 2.1 is not as strong as in the 3.6 x 1.6 bank and consequently the wakes are less confined. Thus a closer resemblance between the wake of the first row and that downstream of a single cylinder is evident with respect to wake width. This is also confirmed by the pattern of the centreline U/U_∞ profile downstream of the first row shown in Figure 4.12. The estimated w_r's downstream of the third and fourth rows of the 3.6 x 2.1 tube bank are 0.48 d and 0.18 d respectively. The w_r/d value downstream of the third row is almost twice that in the 3.6 x 1.6 arrangement, but no comparison can be made for the fourth row since the corresponding width for the 3.6 x 1.6 arrangement could not be estimated from our data - no flow reversal was evident at the points closest to the surface that could be measured.

Both the vorticity thickness, δ, and the spreading rate, δ', estimated from equations (3.5) and (3.6) respectively, are lower than the ones found in the 3.6 x 1.6 arrangement (see Table 4.1). This can be attributed to the different characteristics of the axial mean velocity profiles in the two arrays as suggested by the definition of δ - also referred to as the velocity-profile maximum-slope thickness (Brown and Roshko, 1974). Maximum velocity gradients in the shear layers of the 3.6 x 2.1 bank are higher than those in the 3.6 x 1.6 array. The differences between the maximum

velocity in the shear layers and the velocities at the interface between the recirculation bubble and the shear layer are also smaller in the 3.6 x 2.1 array and therefore from equation (3.5) δ values will be lower.

The normalised recirculating mass-flow rate $\dot{m}_r / \dot{m}$ has similar values downstream of the first and second rows, due to the similarities in the magnitude of the reversed velocities and the width of the recirculation bubbles. The estimated $\dot{m}_r / \dot{m}$ values in these rows are higher than those in the 3.6 x 1.6 arrangement. Downstream of the third row of the 3.6 x 2.1 bank $\dot{m}_r / \dot{m}$ is 72 % of that in the first row and almost 7 times higher than that in the corresponding row of the 3.6 x 1.6 configuration. The value of $\dot{m}_r / \dot{m}$ downstream of the fourth row is only 8 % of that in the first row.

4.2.4 EFFECT OF REYNOLDS NUMBER

Centreline mean and r.m.s. velocities

The variation of the centreline profiles of U with Re_d downstream of the first and third rows of the 3.6 x 2.1 staggered array is shown in Figures 4.19 (a) and 4.19 (b) respectively. The centreline velocities are not normalised with the corresponding U_∞ since their profiles would be practically identical in that case. As expected, decreasing the Re_d results in lower negative velocities in the recirculation and also lower positive velocities in the near wake regions. However, in contrast to the features of the 3.6 x 1.6 staggered array, the position of the rear stagnation point does not change at all in the first row and changes very little in the third row in the 3.6 x 2.1 staggered tube bank. As a consequence there is a negligible effect of Re_d on the length of the recirculation region. This finding is not in agreement with the trends found in the 3.6 x 1.6 staggered array, where the recirculation length was found to vary logarithmically with Re_d in a similar manner to that suggested by McKillop and Durst (1984) for a single cylinder. Apparently, the flow interference

phenomena in the tube bundles are highly non-linear and the wake flows in a staggered array are far more complicated than those in single bluff bodies, since only the first row cylinder is subjected to a uniform flow and subsequent rows are not. This does not allow any generalised conclusions to be drawn on how the recirculating parameters associated with each row are affected by the longitudinal spacing.

The centreline development of u' downstream of the first and third rows for various Re_d numbers can be seen in Figures 4.20 (a) and 4.20 (b) respectively. Again the centreline r.m.s. velocities are presented in a non-normalised form as the normalised values are very similar. R.m.s. levels decrease with decreasing Re_d and they are almost constant for the lowest Re_d studied. The u' maxima, non-dimensionalised by the upstream velocity U_∞, are summarised in Table 4.2 and compared with those obtained with the 3.6 x 1.6 staggered array. Maximum axial r.m.s. velocities gradually increase from the first to the fourth row. However, the difference in the values downstream of the second, third and fourth rows is not significant. Although the maximum u'/U_∞ downstream of the first row is lower in the 3.6 x 2.1 than in the 3.6 x 1.6 tube bank, the differences in subsequent rows are smaller, except for the low Re_d. The magnitude of the maxima does not change significantly with Re_d and this trend is more evident in the 3.6 x 2.1 rather than in the 3.6 x 1.6 tube bank.

Table 4.2. Maximum normalised centreline r.m.s. velocity fluctuations, u'_{max}/U_∞. in 3.6 x 2.1 staggered tube bank compared with 3.6 x 1.6 staggered bank.

u'_{max}/U_∞									
		Row **1**		Row **2**		Row **3**		Row **4**	
Re_d	**U_∞ (m/s)**	**3.6x2.1**	**3.6x1.6**	**3.6x2.1**	**3.6x1.6**	**3.6x2.1**	**3.6x1.6**	**3.6x2.1**	**3.6x1.6**
12,858	0.93	0.37	0.43	0.51	0.50	0.52	0.53	0.54	0.54
10,198	0.74	0.37	0.36			0.51	0.53		
7,981	0.58	0.37	0.41			0.50	0.52		
5,764	0.42	0.38	0.43			0.50	0.55		
3,104	0.22	0.40	0.50			0.51	0.59		

Pressure drop

The pressure drop across the 3.6 x 2.1 staggered tube bank, ΔP, was measured at various Re_d ranging from 4,000 to 12,858. The results are presented in Figure 4.21 and compared with those for the 3.6 x 1.6 staggered array. The pressure drop coefficients measured across the in-line array have been plotted in the same figure but will be discussed later in this chapter. No significant differences can be observed between the two tube banks: the pressure drop decreases slightly with increasing Re_d. The data for the 3.6 x 2.1 bank can be correlated using the relation: $\zeta = 0.956 Re_d^{-0.138}$ which is valid only for the present array and for the range of Re_d investigated. Thus, the effect of longitudinal spacing on the pressure drop is very small since the pressure drop coefficients in the two staggered configurations differ by 7 % on average. It is the transverse spacing that mainly affects the pressure drop and this is reflected in the published pressure drop correlations which include the transverse spacing as a correlating parameter (for example, Jacob, 1938; Zukauskas, 1989).

4.3 EFFECT OF TUBE ARRANGEMENT - 3.6 x 2.1 IN-LINE ARRAY

4.3.1 MEAN VELOCITY DISTRIBUTIONS

The mean velocity vectors for the 3.6 x 2.1 in-line configuration are shown in Figure 4.22. The flow pattern is characterised by a uniform high speed flow in the flow passages between tube columns. Steep velocity gradients are observed in the shear layer separating from the first row cylinder. Reverse velocities are pronounced downstream of the first row but there is increasingly less evidence of recirculation in downstream rows.

The distribution of the axial mean velocities (U/U_∞) is shown in Figures 4.23 (a) and (b). Velocities are uniform along the flow passages, indicating very little interference from neighbouring tubes in the normal direction. Steep velocity gradients can be observed as the shear layer separates from the first row. The flow accelerates as it passes over the relatively wide recirculation region downstream of the first row cylinder. Flow reversal is also pronounced there with negative velocities reaching up to 0.47 U_∞. Some flow reversal is observed downstream of the second row whereas there is no evidence of flow reversal in downstream rows indicating that the rear stagnation points are located very close to the surface of the tubes. Transverse mean velocities (V/U_∞) have near zero values along the flow passages and low negative velocities, discernible in the profiles only, in the vicinity of the tubes after each row is encountered (Figures 4.24 (a) and (b)).

4.3.2 TURBULENCE LEVEL DISTRIBUTIONS

u'/U_∞ profiles and contours are presented in Figures 4.25 (a) and (b) respectively. The distribution of u'/U_∞ is qualitatively and quantitatively different to those obtained with the staggered geometries. In general, u'/U_∞ velocities are much lower

than those in the 3.6 x 1.6 staggered tube bank. u' levels are very low in the flow passages between tube columns with values not exceeding 0.30 U_∞. Higher values are observed at the edges of the recirculation regions, with a maximum of up to 0.50 U_∞ in the shear layers separating from the third and fourth rows. The transverse r.m.s. velocities, v'/U_∞ (Figures 4.26 (a) and (b)) also exhibit different patterns to those observed in the staggered arrays . They are low and equal to the axial levels in the flow passages, but they reach higher values than u' in the wake regions. v' increases progressively from row to row, reaching maximum values equal to 0.80 - 0.90 U_∞ downstream of the third and fourth rows.

The above distributions indicate little turbulent mixing in the in-line configuration in comparison to the staggered ones. Turbulence is generated primarily in the wake regions and spreads slowly to the rest of the flow domain. Despite the fact that the distributions are very similar downstream of the third and fourth rows, the flow up to the fifth row is still developing. This is indicated by the increased levels of mainstream turbulence from row to row, and suggests that the entrance effects in an in-line tube bundle reach more rows than in a staggered one. The turbulence in the wake regions is highly anisotropic, especially downstream of the third and fourth rows (Figures 4.27 and 4.28): the two r.m.s. velocity components differ by up to 0.60 U_∞. The transverse component attains values twice as high as the axial one in the aforementioned locations.

4.3.3 WAKE CHARACTERISTICS

Centreline mean and r.m.s. velocities

The centreline development of U/U_∞ downstream of the first four rows is shown in Figure 4.29. Relatively few measurements have been taken since there is little space between the cylinders in the streamwise direction in comparison with the staggered

arrays. Consequently, the development of the centreline axial mean velocities is blocked by the presence of the downstream cylinder, their recovery is restricted and the profiles are not similar to those obtained in flows over bluff bodies. For these reasons, measurements were not taken at other Re_d's in the wake regions since the information that could be extracted was very limited. The U and u' distributions are presented below and compared with the staggered array values for consistency of presentation.

Downstream of the first row there is a maximum negative velocity, 0.47 U_∞, located at 0.6 d from the tube surface. The rear stagnation point has not been reached even at 0.35 diameters upstream of the surface of the second row, which is the last point that can be measured along the centreline. This may imply that the shear layer separated from the first tube reattaches on the front of the second row tube. Ljungkrona et al (1991) visualised the flow around two cylinders in an in-line configuration for various spacings and Re_d. They observed that, for a spacing greater than 2 diameters and a Re_d similar to that used in the present study, the shear layer from the first cylinder reattached on the front of the second cylinder. The profiles obtained downstream of the second, third and fourth rows suggest that the shear layer separating from the tubes in these rows rolls up in front of the downstream tubes in contrast to the first row. This is not in agreement with the results of Achenbach (1991) who found that for a 2.0 x 1.4 in-line tube bundle the impact point for a tube in the fifth row is located at $\phi = 30°$ from the front stagnation point for subcritical flow conditions. This may be attributed to the closer longitudinal spacings in Achenbach's configuration.

Negative velocities are lower downstream of the second row with a maximum value equal to 0.10 U_∞. The rear stagnation point is located at 0.7 d from the tube surface. The rear stagnation point in subsequent rows must have been reached earlier since only positive centreline mean velocities were detected within the range where

measurements could be taken. By extrapolation it can be assumed that the rear stagnation point in the third and fourth rows is located at around 0.3 d from the tube surface.

A comparison with the centreline U/U_∞ profiles obtained in the two staggered arrangements (Figures 4.13 (a) - (d)) shows that the negative U/U_∞ values measured downstream of the first row of the in-line array are similar to those obtained in the closely spaced staggered array, whereas those downstream of the second row are significantly lower. The positive velocities measured downstream of the third and fourth row attain values similar to those in the 3.6 x 1.6 staggered array in some locations but their recovery is restricted as already mentioned.

The centreline development of u'/U_∞ downstream of the first four rows of the in-line array can be seen in Figure 4.30. R.m.s. velocities are almost constant downstream of the first row with values equal to 0.28 U_∞. Similar r.m.s. levels were measured downstream of the second row up to 0.6 d followed by a slight increase at the rear stagnation point where the maximum centreline r.m.s. value is usually observed. This maximum r.m.s. velocity is equal to 0.32 U_∞. Turbulence levels are similar downstream of the third and fourth rows and decrease with distance from the tube surface. A comparison with the staggered arrays (Figures 4.15 (a) - (d)) confirms once again the low levels of turbulence generated by an in-line tube bank as opposed to a staggered one.

Recirculating parameters

The recirculating parameters that could be estimated for the in-line tube bank, shown in Table 4.3, were few in comparison with the staggered arrays, for the reasons mentioned earlier (no sign change in measured velocities, no separation streamlines in some of the rows studied). A recirculation length of 0.7 d was estimated

downstream of the second row cylinder, very similar to that found in the equivalent staggered arrangement (3.6 x 2.1). It appears from the centreline U/U_∞ profiles (Figure 4.29) that the recirculation length is shorter in downstream rows, approximately equal to 0.3 d (by extrapolation). The wake width downstream of the first and second rows was estimated from the separation streamlines. Streamline patterns obtained in the in-line tube bank are shown in Figure 4.31; they illustrate the uniformity of the flow in the flow passages and the lack of interaction between them. The shear layer separating from the first row appears to reattach in the front of the second row cylinder. A well defined recirculation bubble is evident downstream of the second row while very small bubbles can be seen further downstream. However, caution is needed in interpreting the streamline patterns due to the interpolation involved in their construction.

A maximum half-width of 0.64 diameters was found in the shear layer separating from the first row. This maximum value occurred at an axial position of 1.25 d and not closer to the tube as observed in the staggered configurations. The estimated width is greater than those estimated in the staggered tube banks since there is less interference by neighbouring tubes. On the contrary, the recirculation width downstream of the second row was found to be 0.26 d, significantly narrower than the corresponding one in the staggered banks. Similar trends were observed in the estimates of the recirculating mass-flow rates, since these depend on the magnitude of the reverse velocities and the width of the recirculation region. The vorticity thickness, δ, and the spreading rate, δ', were also estimated and their values, listed in Table 4.3 below, are close to those for the 3.6 x 2.1 staggered array downstream of the first row and close to the tube surface. However, δ and δ' values do not show any significant variation with distance from the surface of the first tube as opposed to those in the staggered array. δ and δ' values downstream of the second row are much higher than the corresponding ones for the 3.6 x 2.1 staggered array.

Table 4.3. Recirculation characteristics of the 3.6 x 2.1 in-line configuration.

Row	x/d (l/d)	w_r/d	l_r/d	$\dot{m}_r / \dot{m}$	δ	δ'
1	0.85 (0.35)	0.61		0.17	0.10	0.12
	1.25 (0.75)	0.64		0.26	0.11	0.09
2	2.95 (0.35)	0.26	0.7	0.02	0.65	0.76

4.3.4 PRESSURE DROP

The variation of the pressure drop coefficient ζ with Re_d in the in-line array has been presented already in Figure 4.21 compared with the coefficients obtained with the two staggered arrays. The pressure drop is significantly lower in the in-line array than in the staggered arrays: the pressure drop coefficient for the 3.6 x 2.1 staggered tube bank is more than twice that for the 3.6 x 2.1 in-line bank. The trends, however, are the same. The data for the in-line tube bank can be correlated using the relation: $\zeta = 0.584\,Re_d^{-0.169}$. This relation is valid only for the present arrangement and range of Re_d. The power index of Re_d is very close to the $Re_d^{-0.15}$ dependence reported by Jacob (1938) for in-line arrays.

4.4 CLOSURE

Ensemble-averaged LDA measurements were taken in a staggered and an in-line tube bundle, with transverse and longitudinal pitch ratios equal to 3.6 and 2.1 respectively, in order to investigate the effects of the tube spacing and tube arrangement on the flow characteristics of the bundles. The results showed that increasing the longitudinal spacing, S_L, from 1.6 d to 2.1 d in a staggered configuration results in lower turbulence levels in the near wake regions. An increase in S_L also affects the recirculating parameters of the tube bank, but has a negligible effect on pressure drop. The tube arrangement has a significant effect on the velocity

and pressure drop characteristics of a tube bank: an in-line tube bank generates less turbulence than a staggered one with the same pitch ratios and produces a significantly lower pressure drop. The wake regions in the in-line configuration are confined by downstream tubes but they are highly anisotropic. In the chapter that follows experimental studies carried out in the 3.6 x 1.6 staggered array with rough and tapered tubes as well as experiments with a particle-laden flow over the 3.6 x 2.1 in-line configuration are presented.

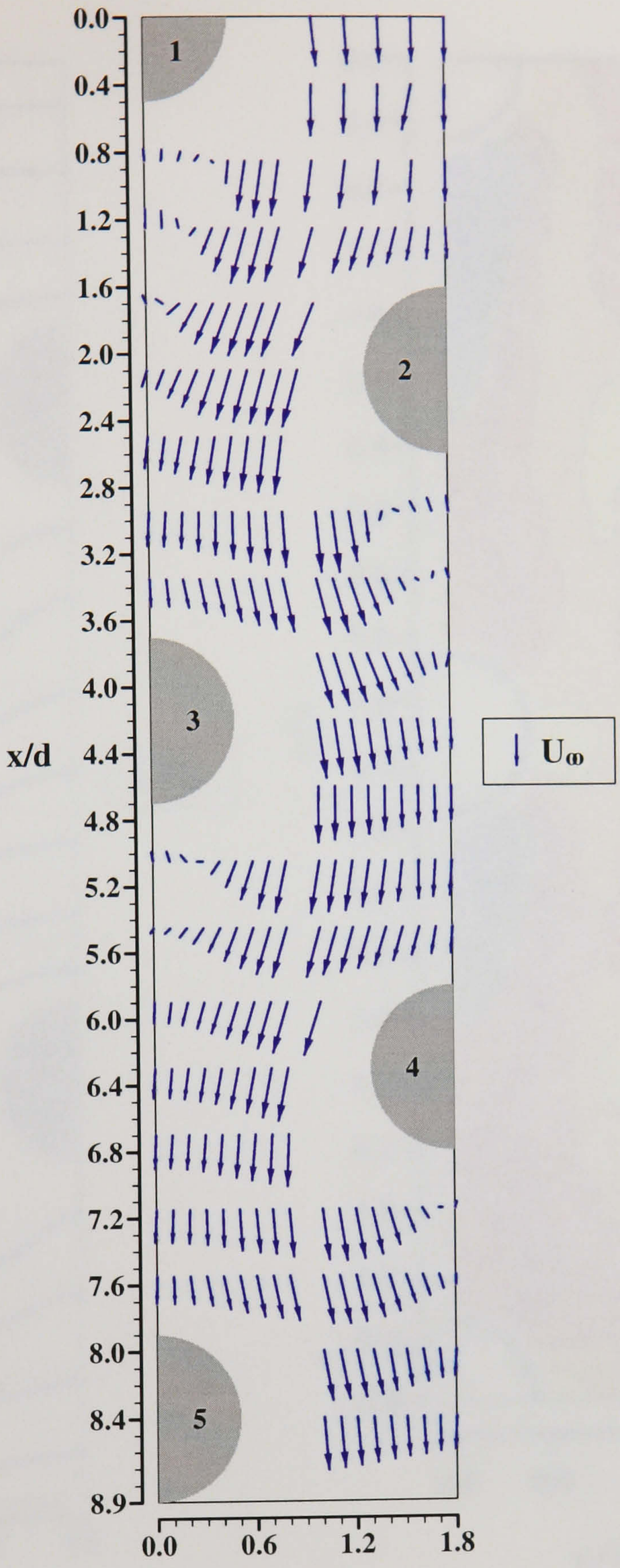

Figure 4.1. Velocity vectors in the 3.6 x 2.1 staggered array (Re_d = 12,858).

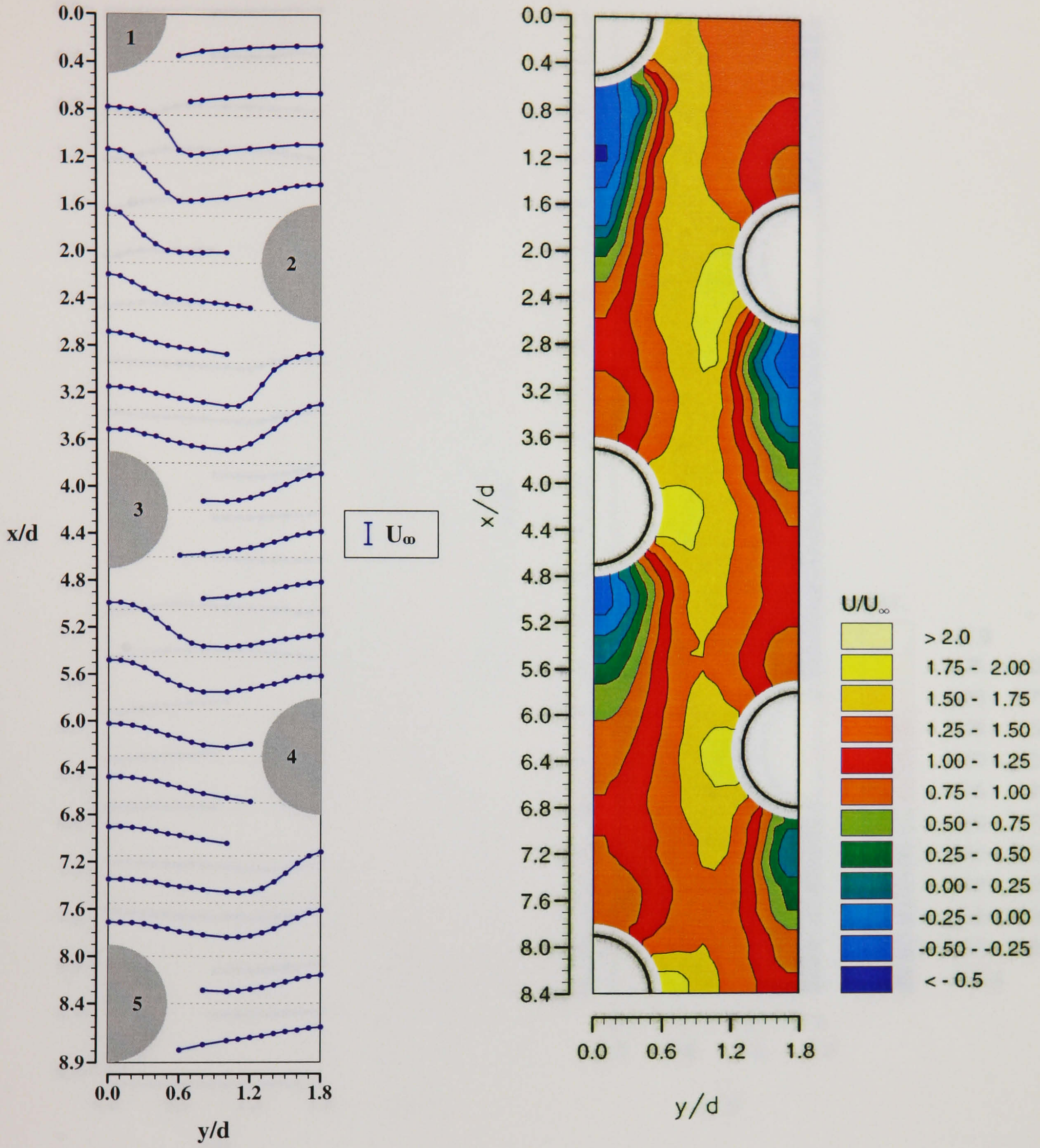

(a) U/U_∞ profiles

(b) U/U_∞ contours

Figure 4.2. Distribution of axial mean velocities, U/U_∞, in the 3.6 x 2.1 staggered array (Re_d = 12,858).

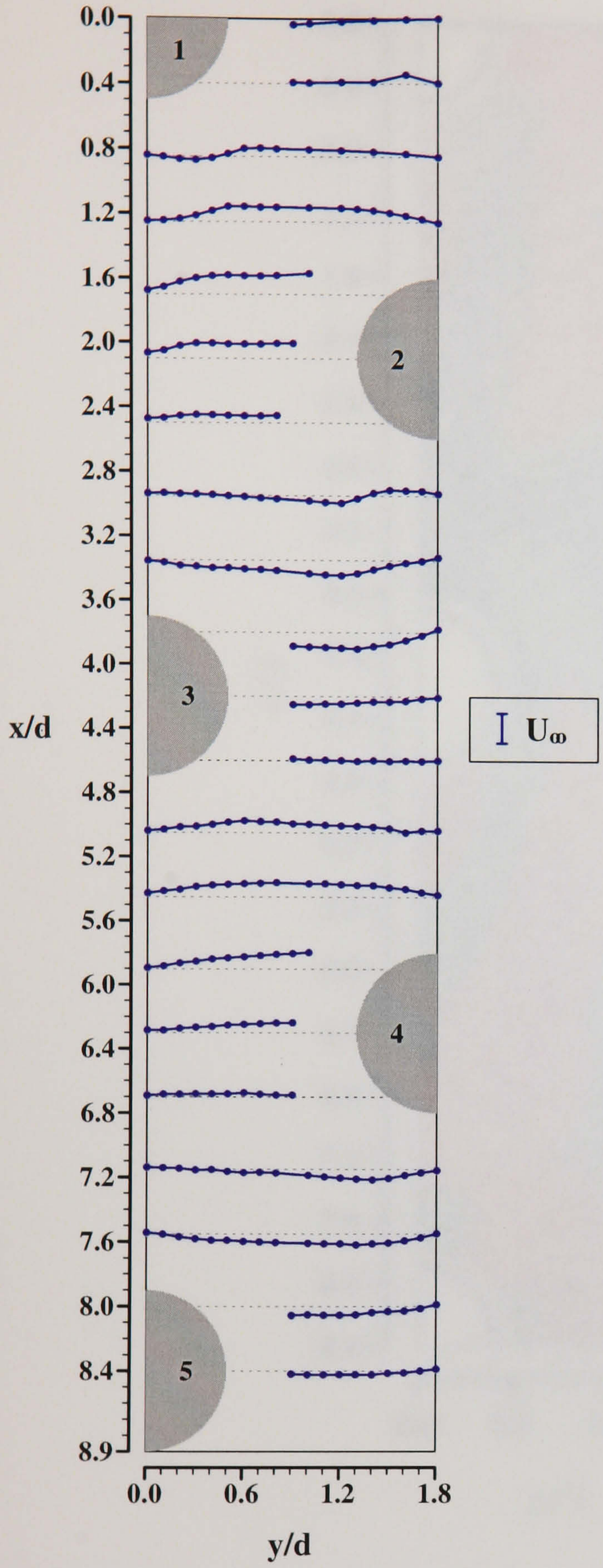

(a) V/U_∞ profiles

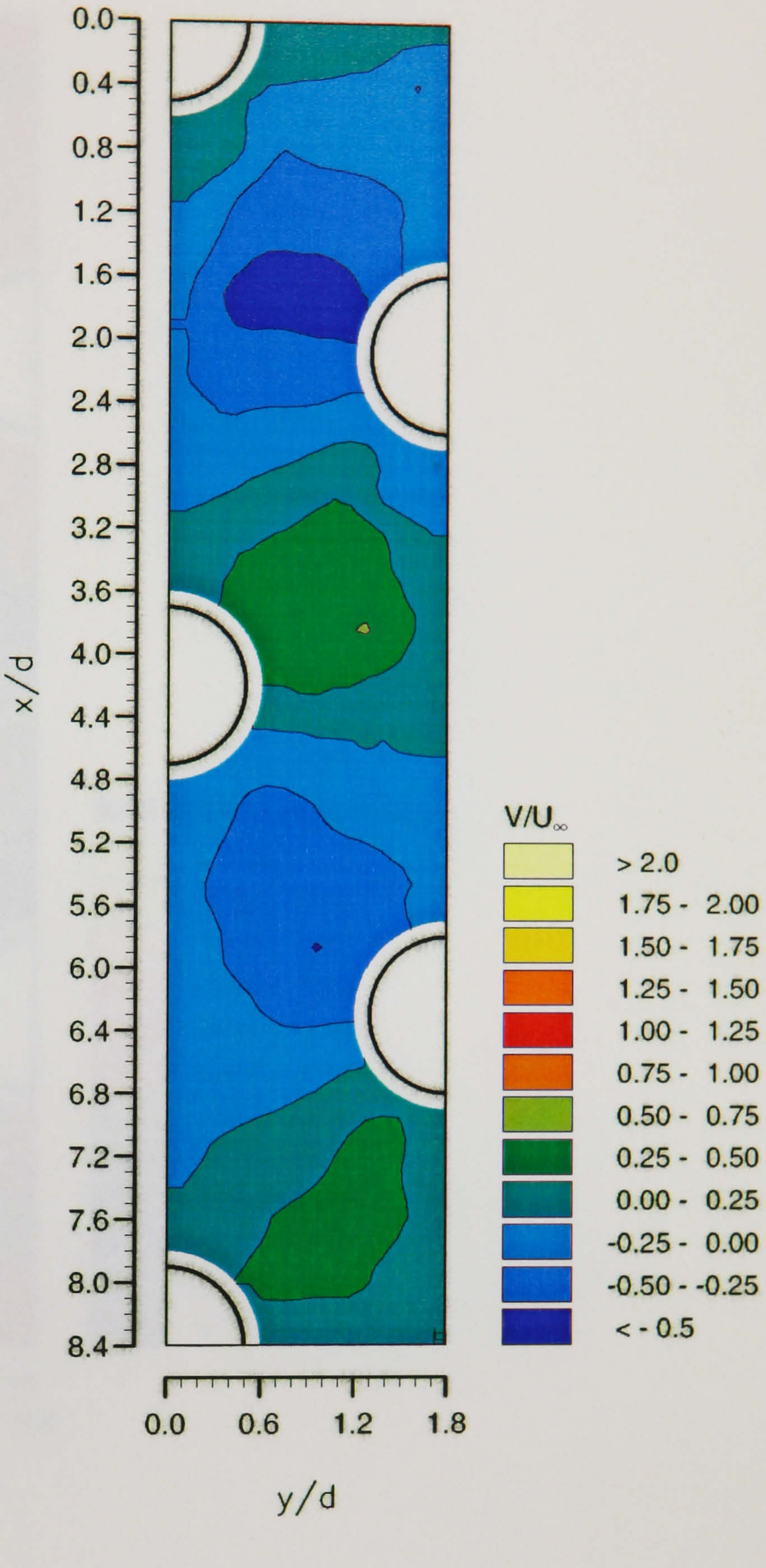

(b) V/U_∞ contours

Figure 4.3. Distribution of transverse mean velocities, V/U_∞, in the 3.6 x 2.1 staggered array (Re_d = 12,858).

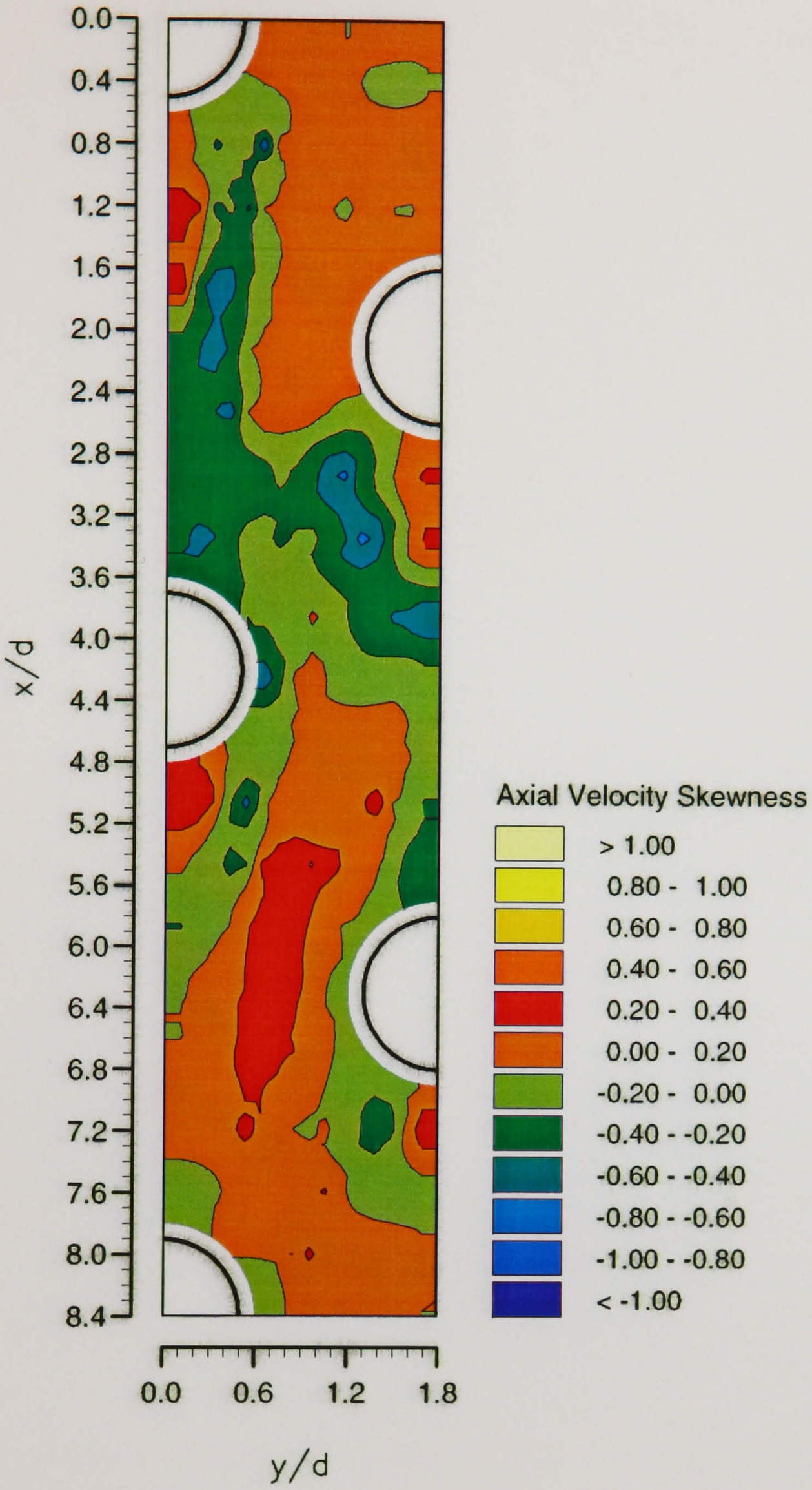

Figure 4.4. Distribution of axial velocity skewness in the 3.6 x 2.1 staggered array (Re_d = 12,858).

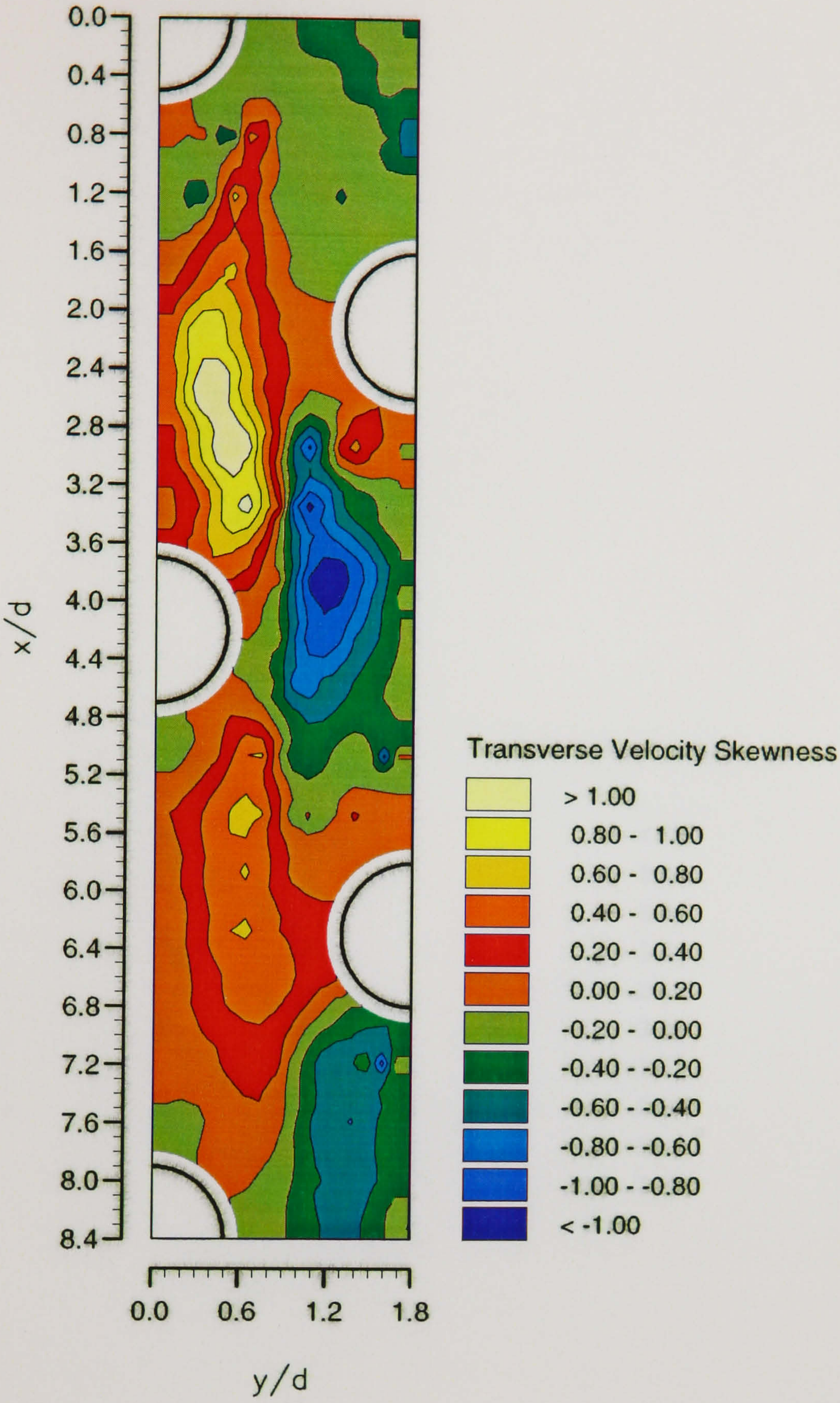

Figure 4.5. Distribution of transverse velocity skewness in the 3.6 x 2.1 staggered array (Re_d = 12,858).

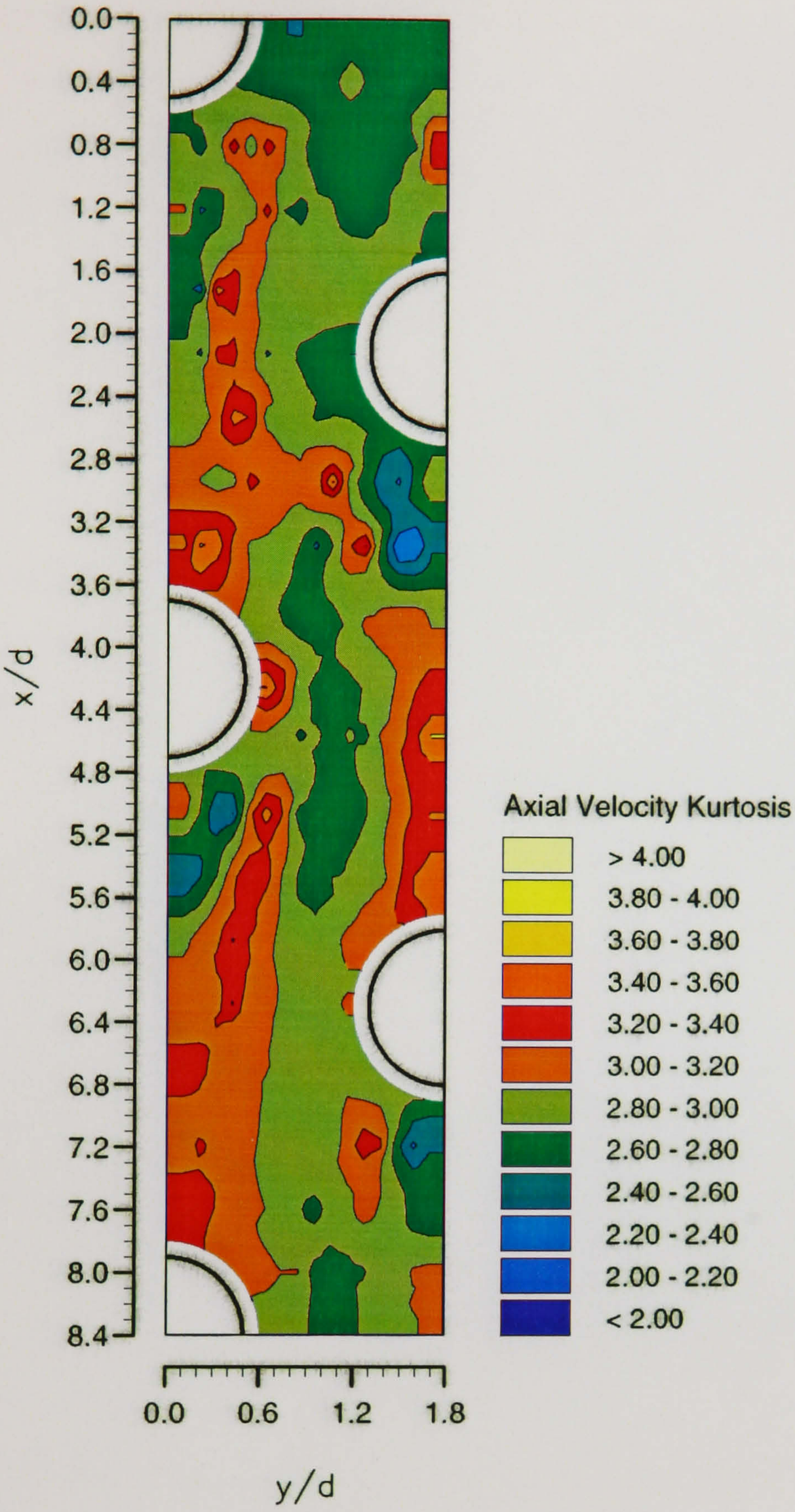

Figure 4.6. Distribution of axial velocity kurtosis (or flatness) in the 3.6 x 2.1 staggered array (Re_d = 12,858).

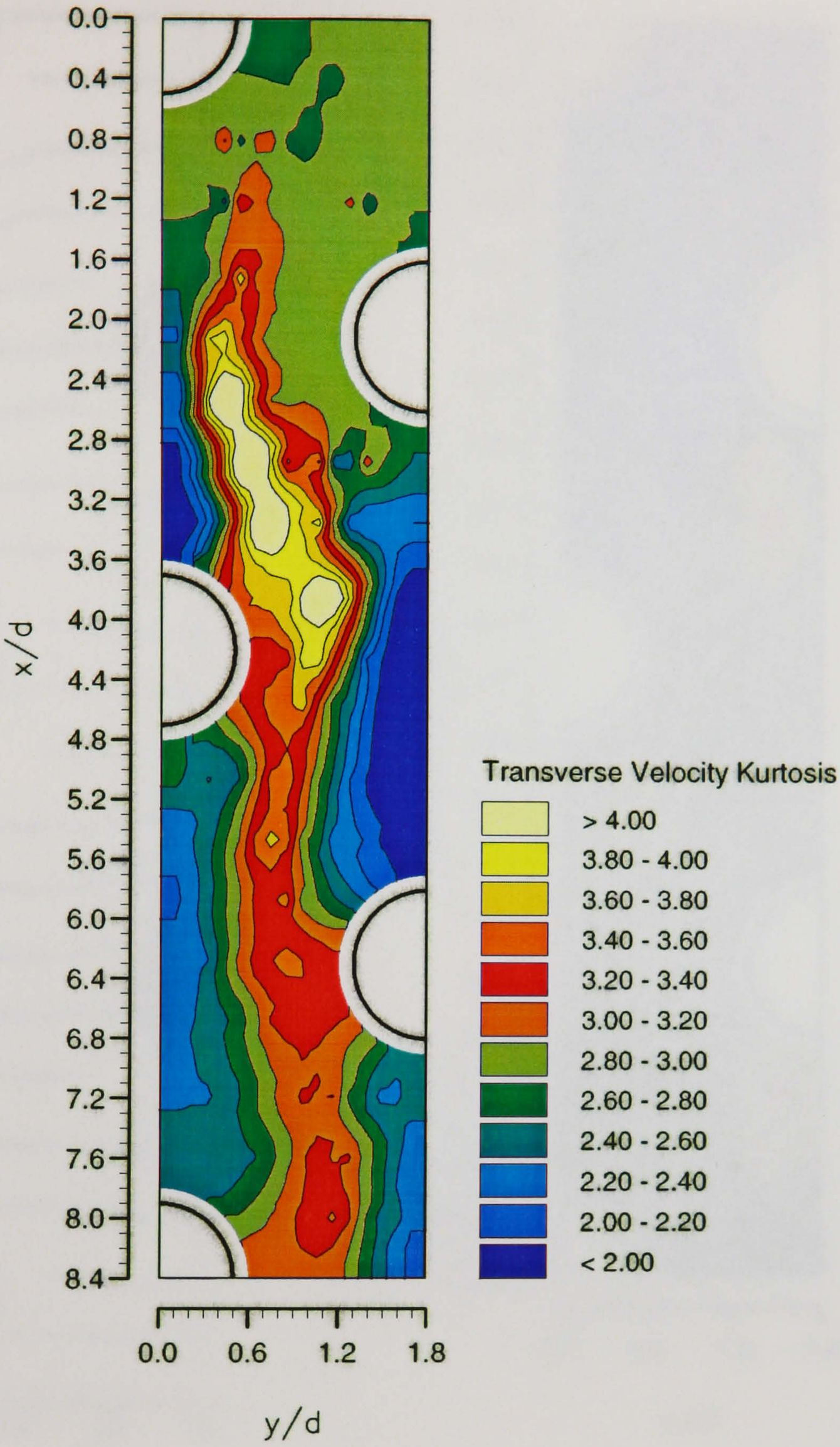

Figure 4.7. Distribution of transverse velocity kurtosis (or flatness) in the 3.6 x 2.1 staggered array (Re_d = 12,858).

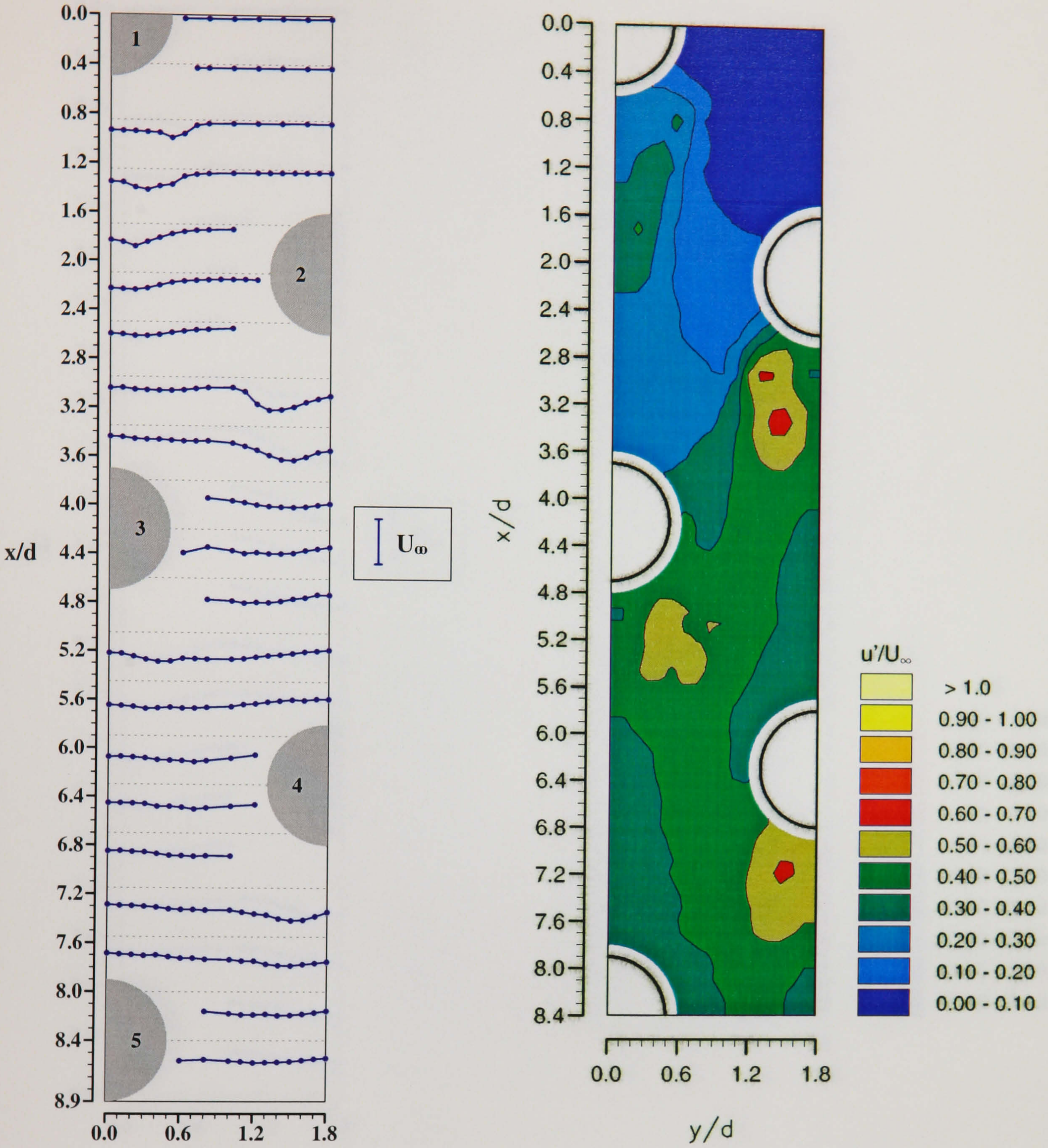

(a) u'/U_∞ profiles (b) u'/U_∞ contours

Figure 4.8. Distribution of axial r.m.s. velocities, u'/U_∞, in the 3.6 x 2.1 staggered array (Re_d = 12,858).

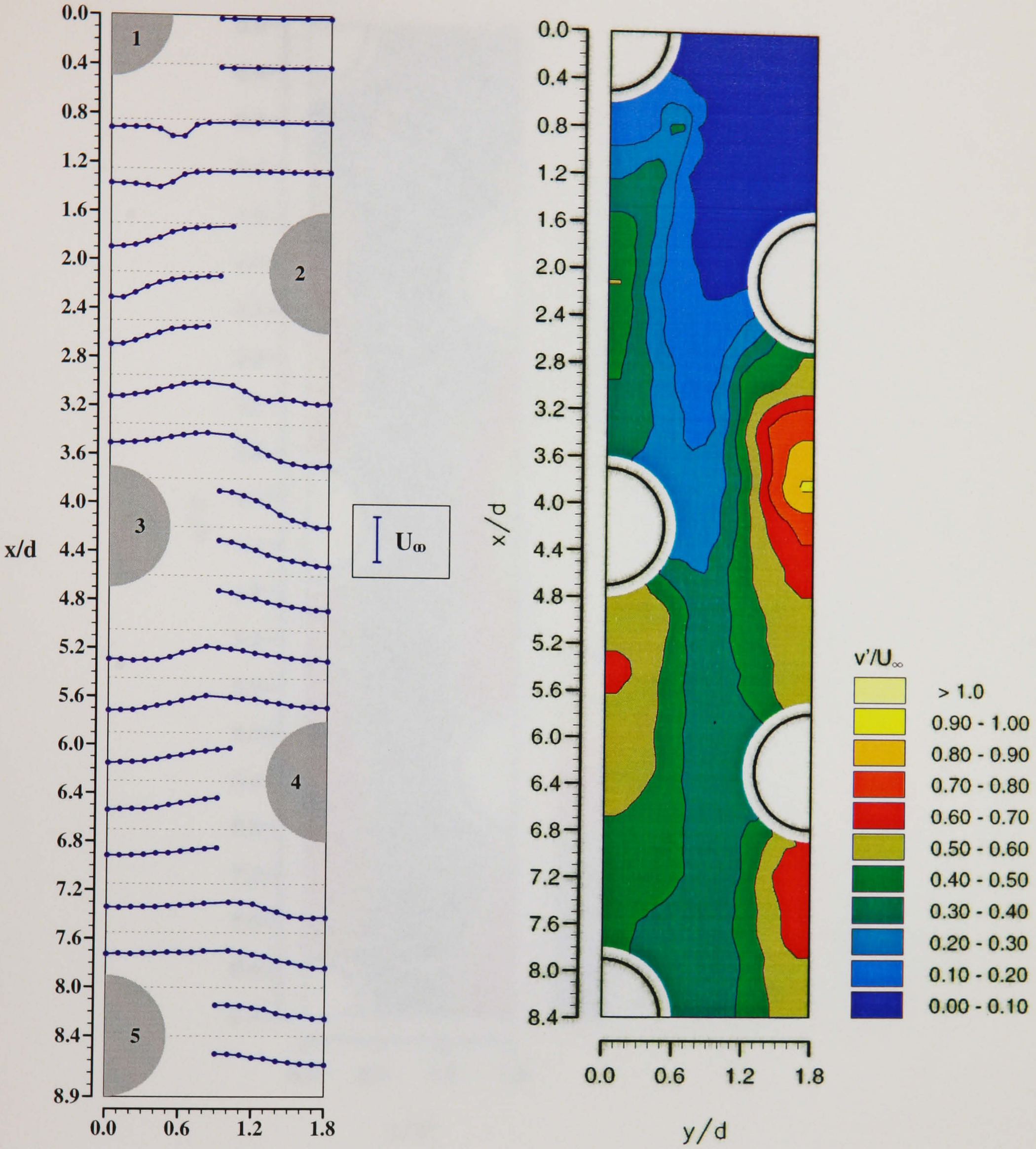

(a) v'/U_∞ profiles (b) v'/U_∞ contours

Figure 4.9. Distribution of transverse r.m.s. velocities, v'/U_∞, in the 3.6 x 2.1 staggered array (Re_d = 12,858).

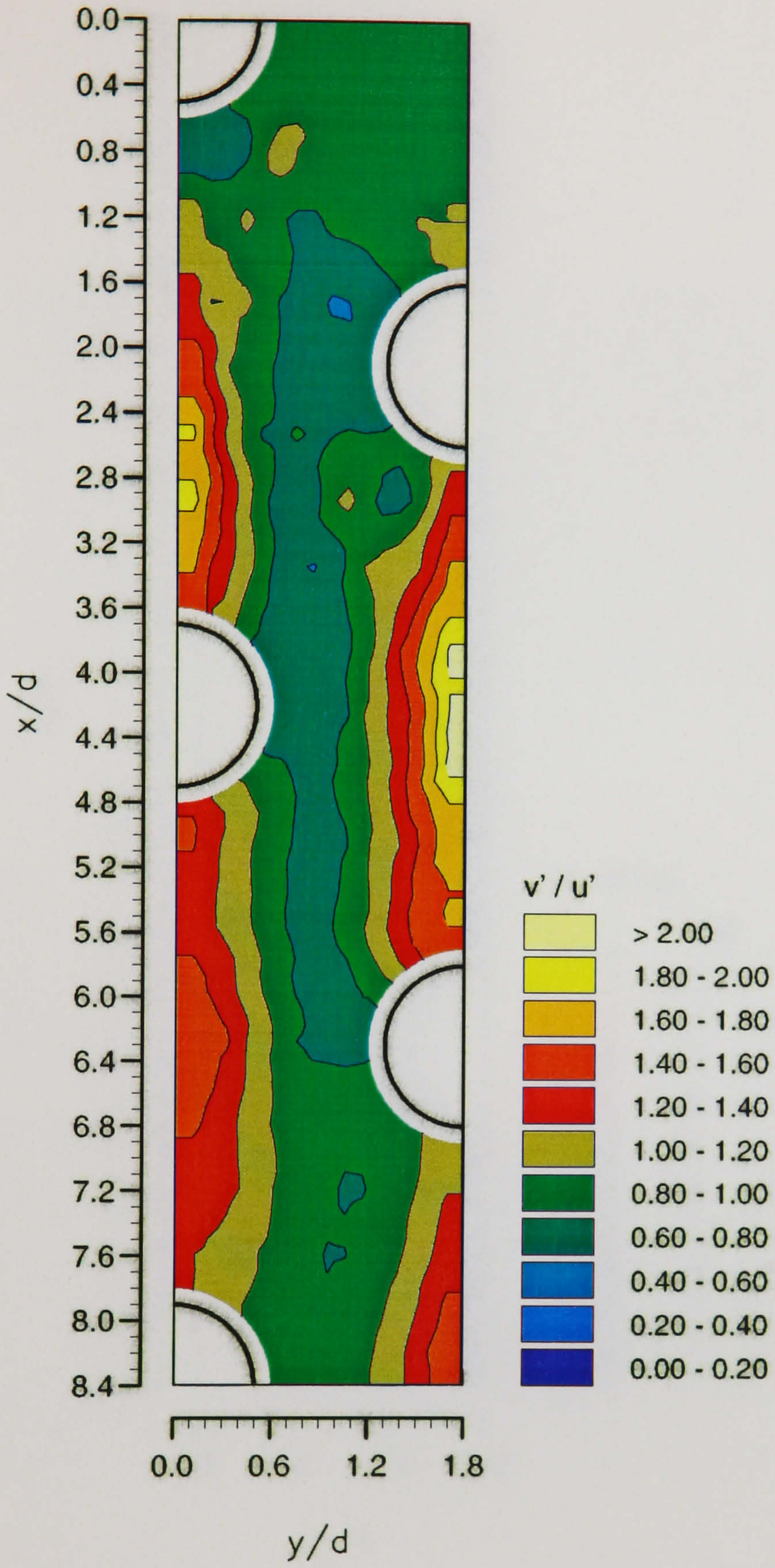

Figure 4.10. Distribution of v'/u' in the 3.6 x 2.1 staggered array (Re_d = 12,858).

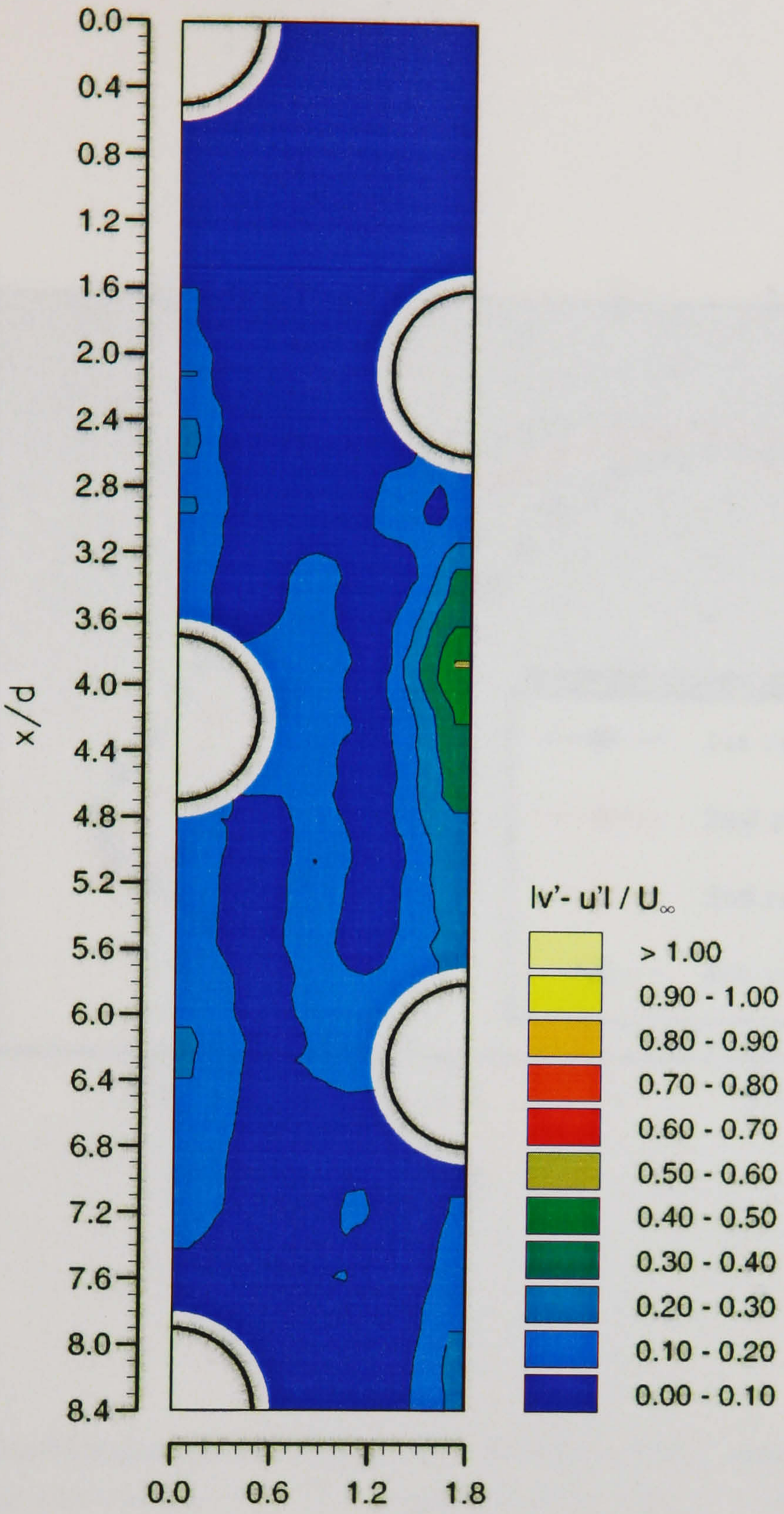

Figure 4.11. Distribution of $|v'-u'| / U_\infty$ in the 3.6 x 2.1 staggered array ($Re_d = 12{,}858$).

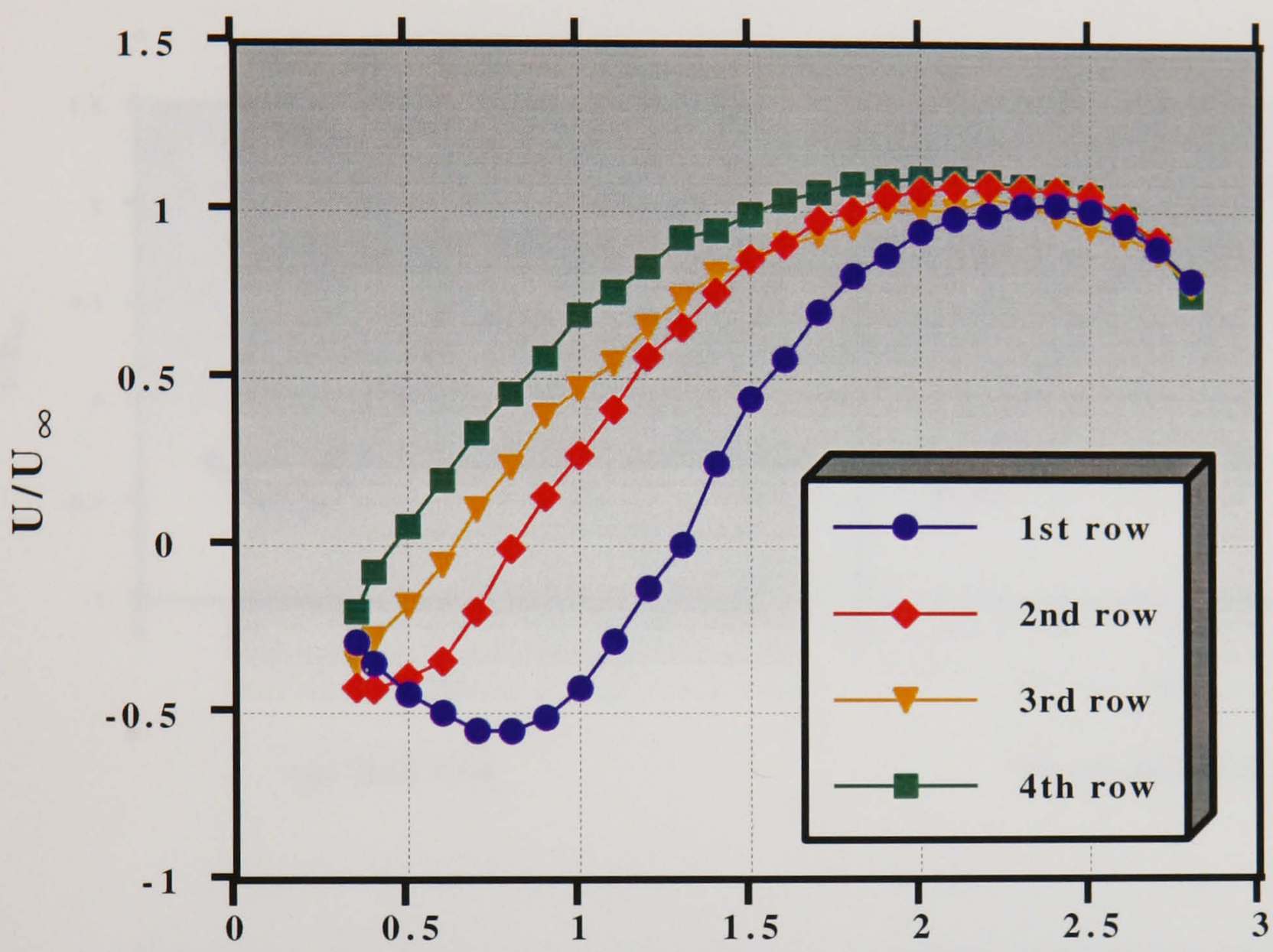

Figure 4.12. Development of the axial mean velocities, U/U_∞, downstream of the first four rows in the 3.6 x 2.1 staggered array (Re_d = 12,858).

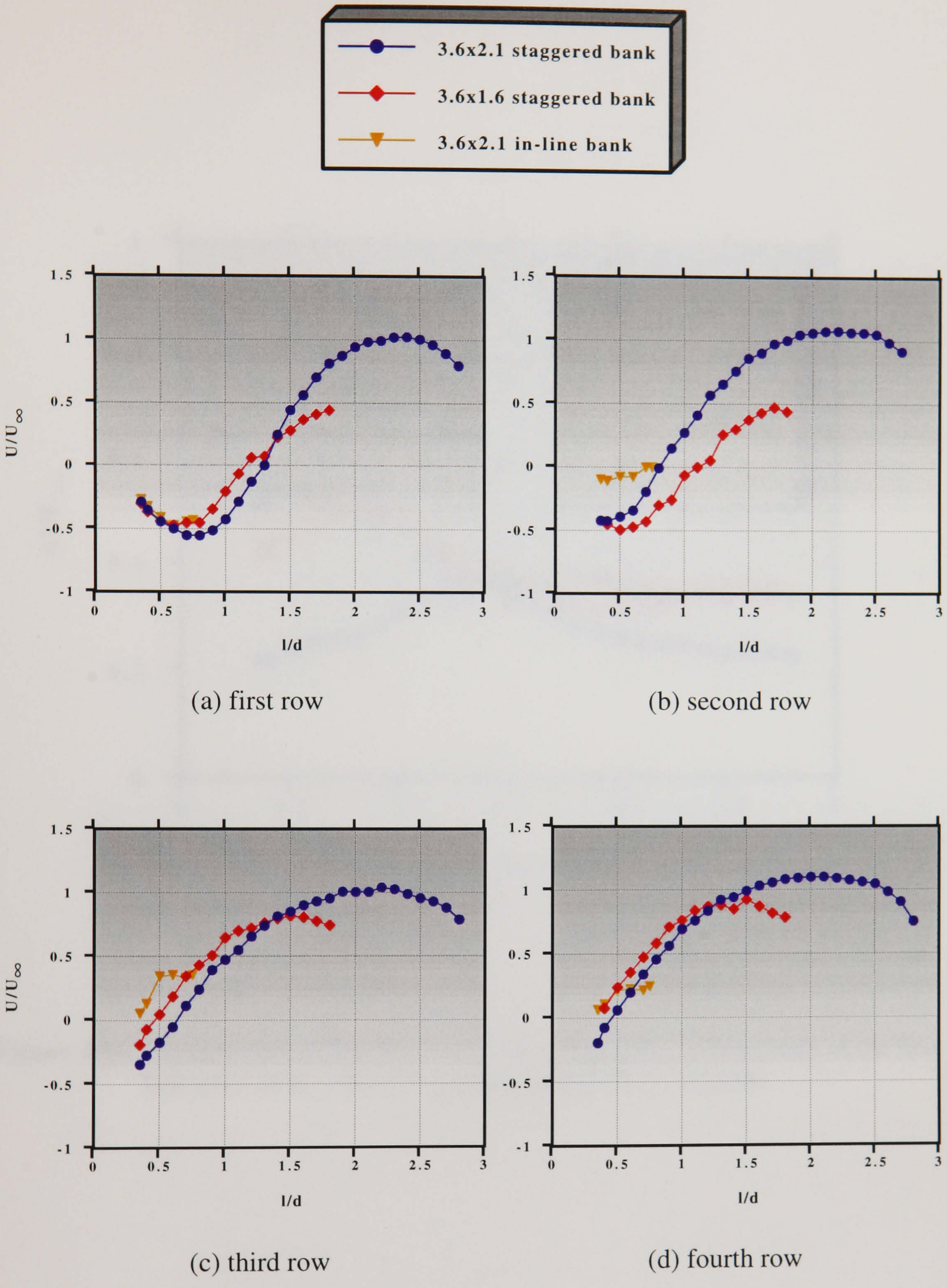

(a) first row

(b) second row

(c) third row

(d) fourth row

Figure 4.13. Comparison of the centreline U/U_∞ profiles between the 3.6 x 1.6 and 3.6 x 2.1 staggered arrays and the 3.6 x 2.1 in-line array (Re_d = 12,858).

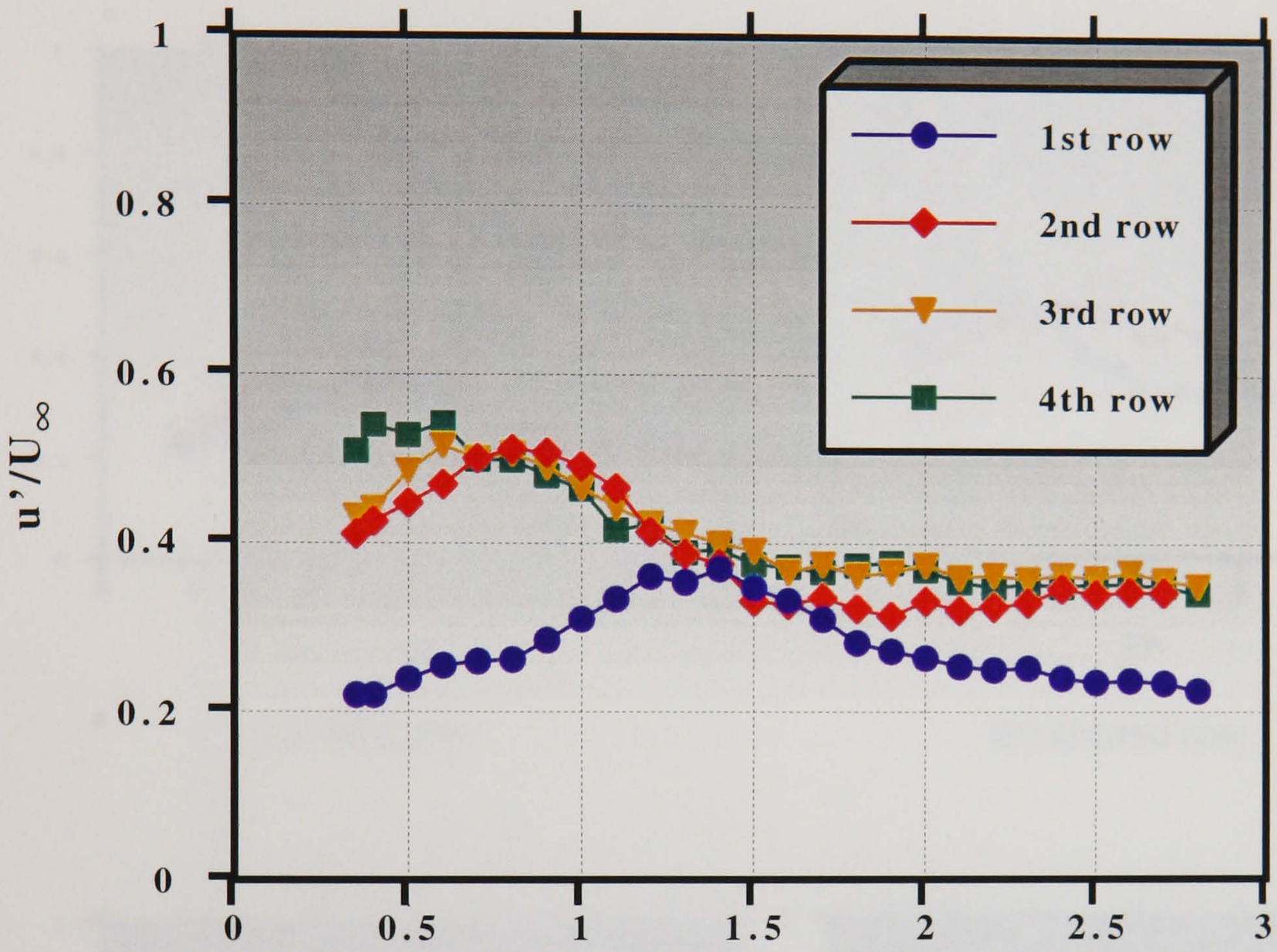

Figure 4.14. Development of the axial r.m.s. velocities, u'/U_∞, downstream of the first four rows in the 3.6 x 2.1 staggered array (Re_d = 12,858).

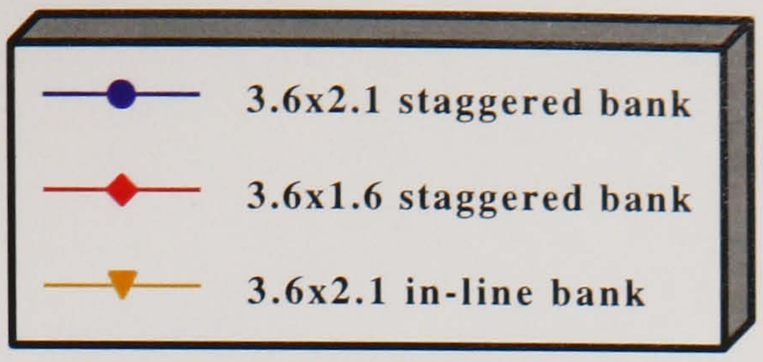

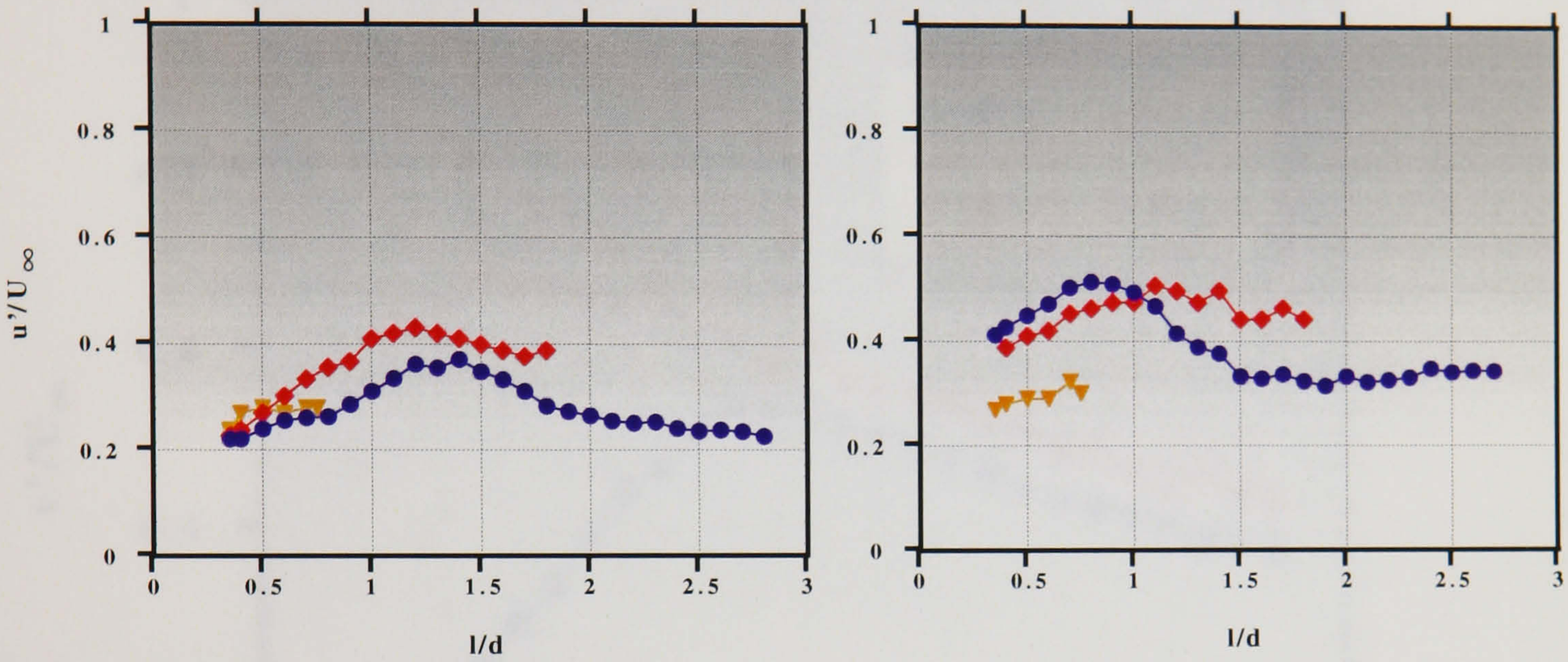

(a) first row (b) second row

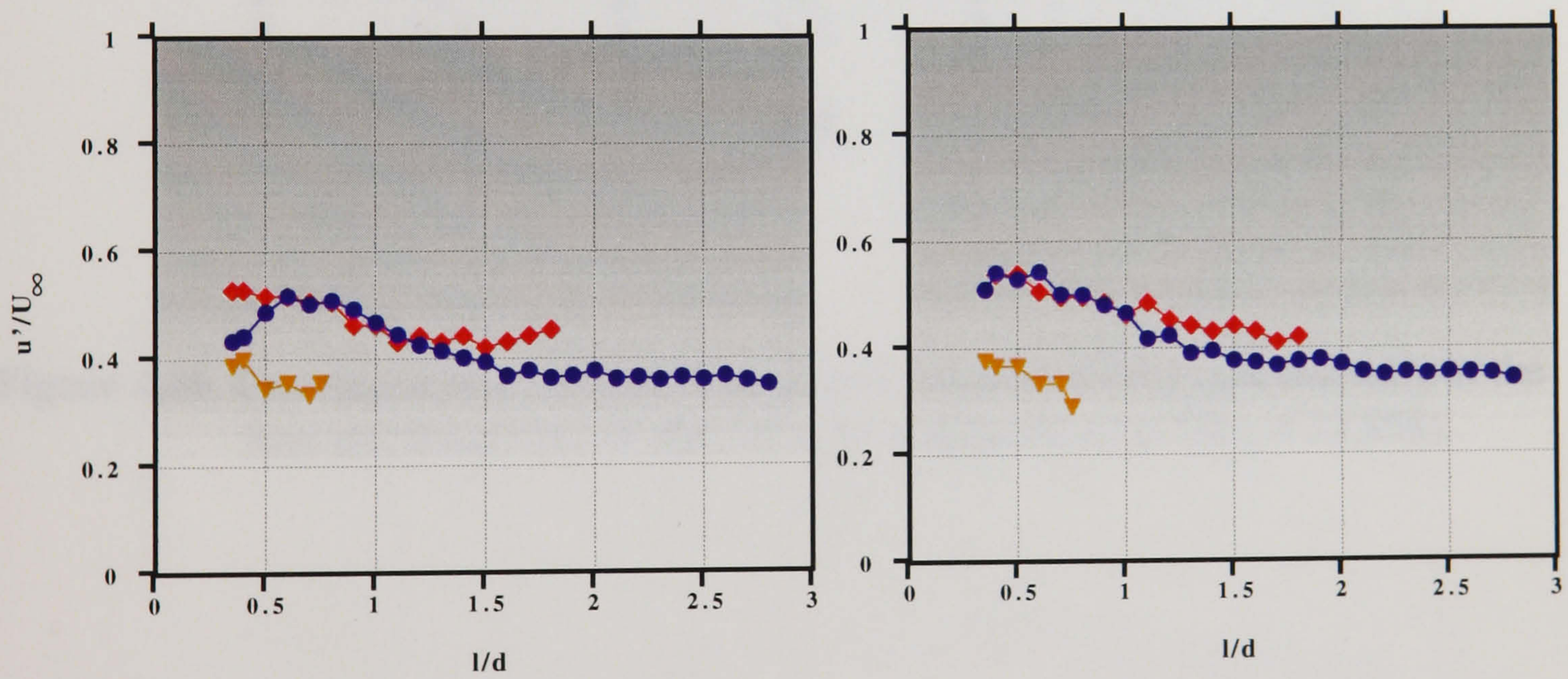

(c) third row (d) fourth row

Figure 4.15. Comparison of the centreline u'/U_∞ profiles between the 3.6 x 1.6 and 3.6 x 2.1 staggered arrays and the 3.6 x 2.1 in-line array (Re_d = 12,858).

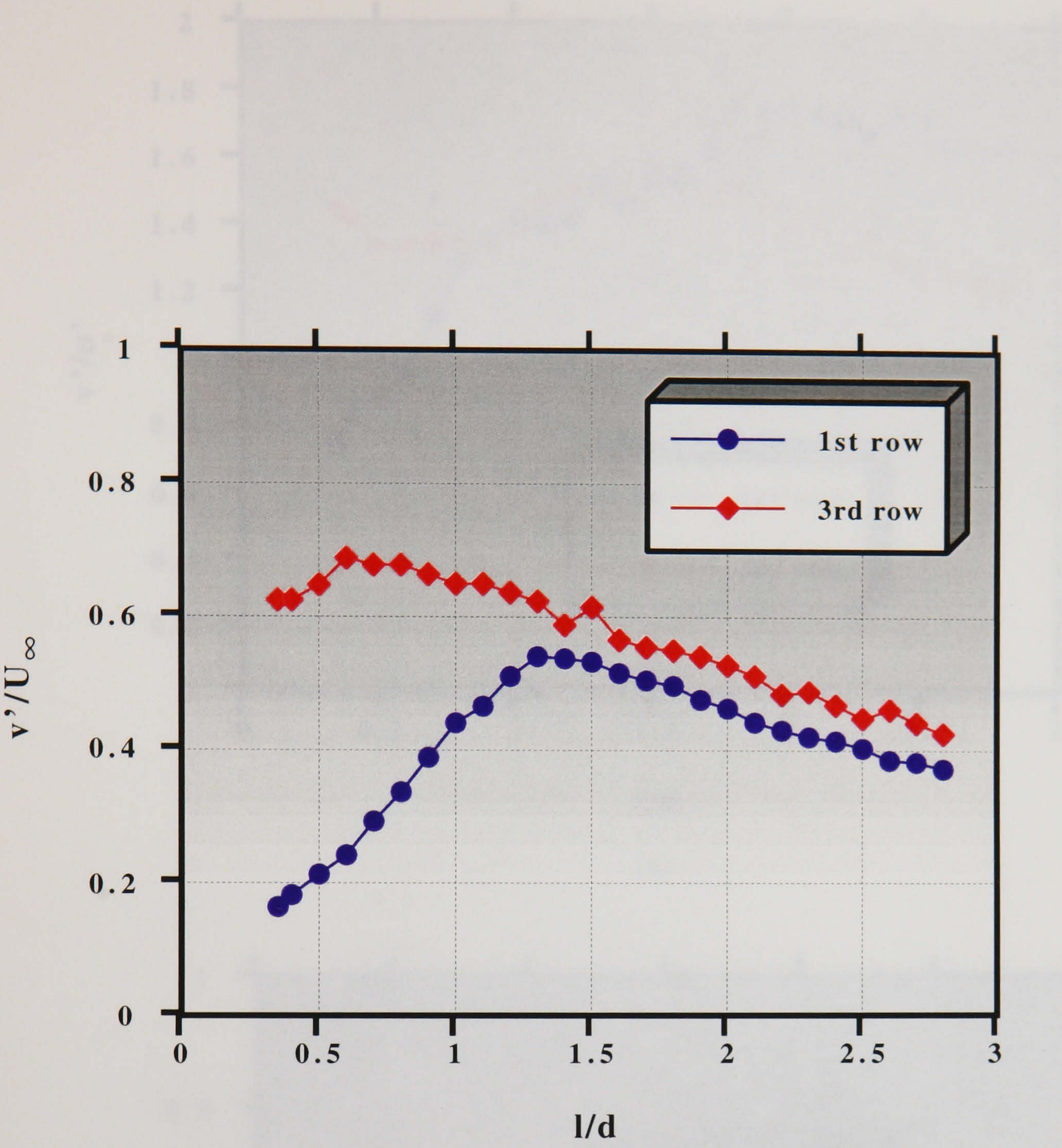

Figure 4.16. Development of the transverse r.m.s. velocities, v'/U_∞, downstream of the first and third rows of the 3.6 x 2.1 staggered array (Re_d = 12,858).

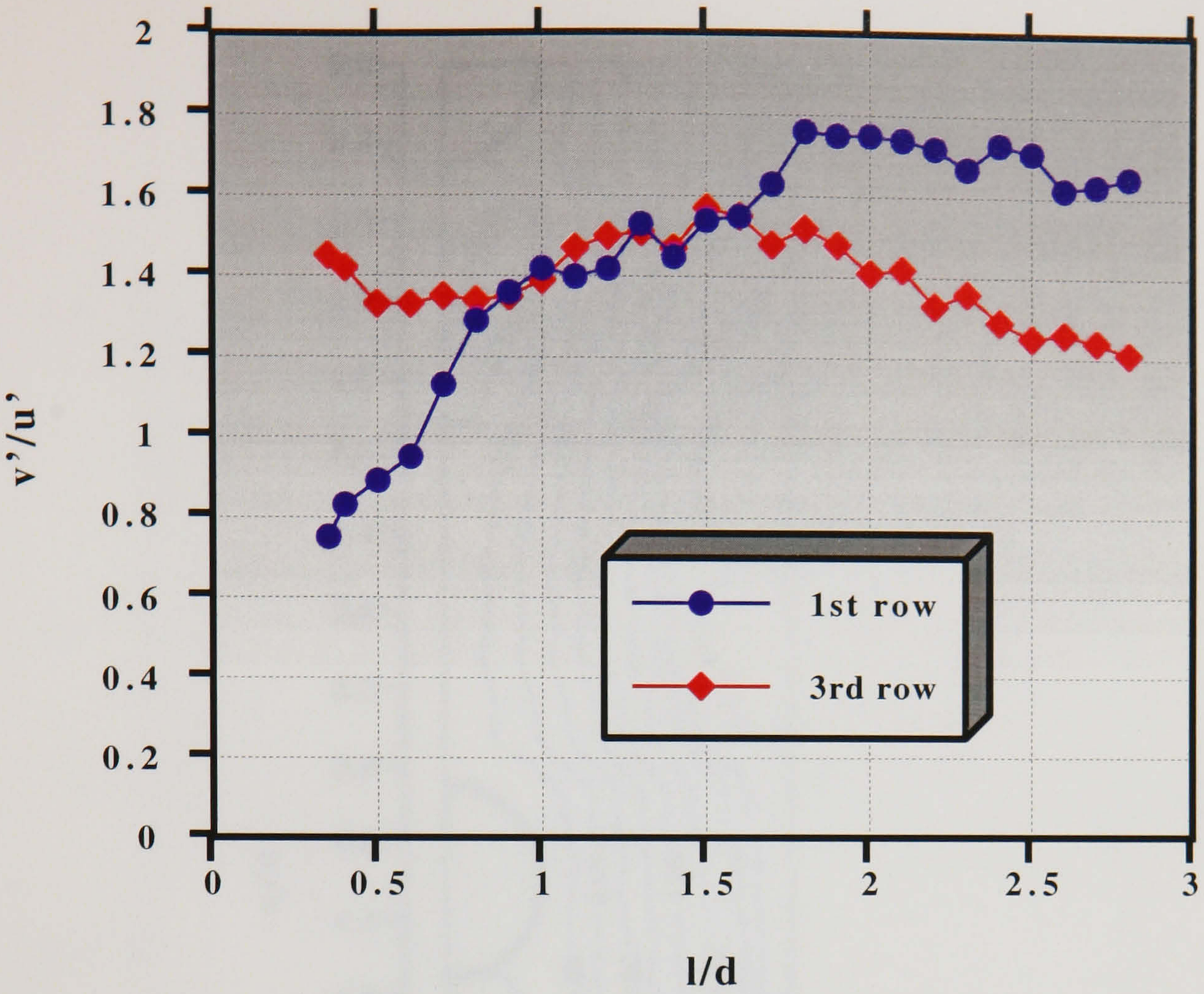

(a)

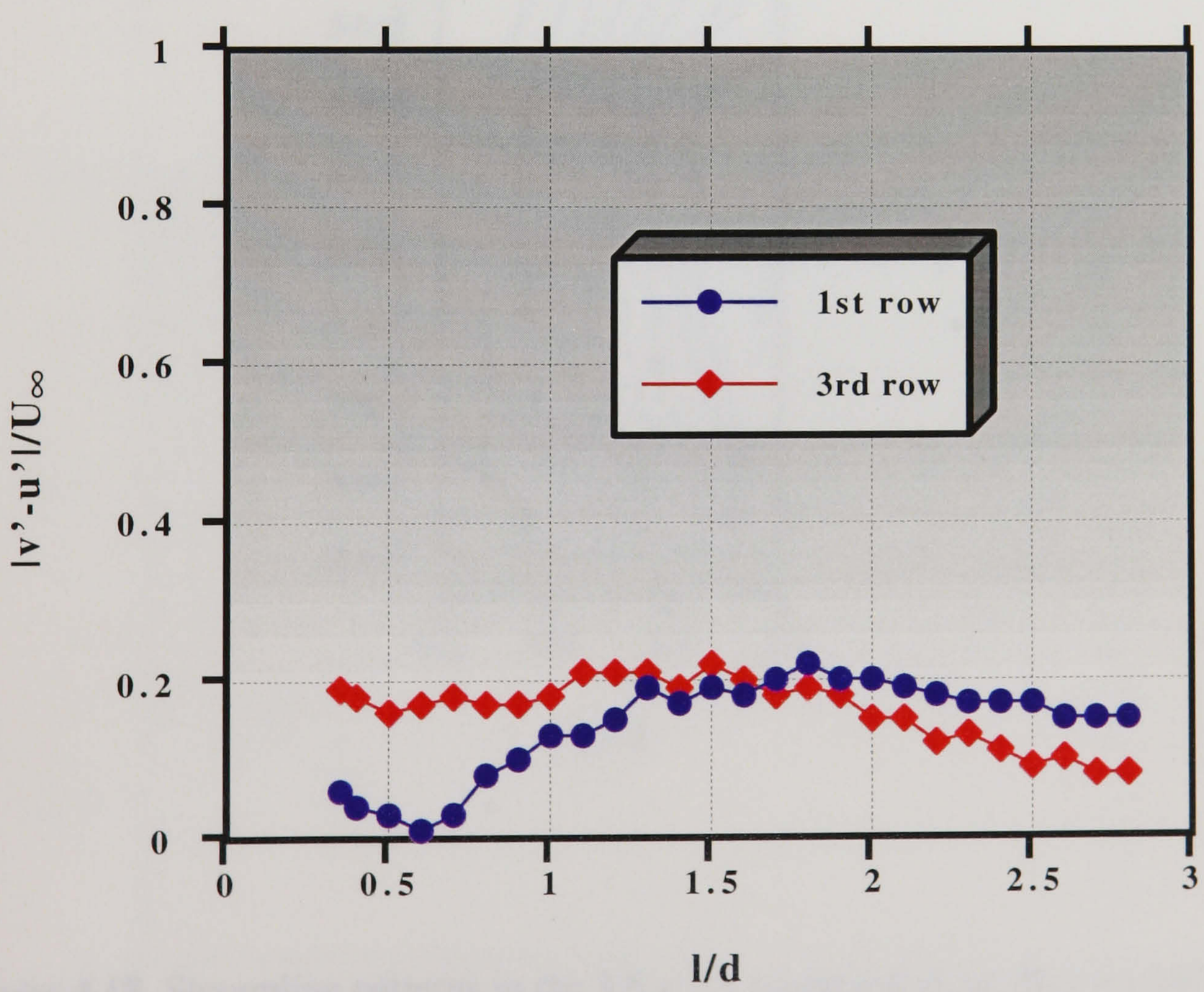

(b)

Figure 4.17. Centreline profiles of v'/u' (a) and |v'-u'| / U_∞ (b) in the 3.6 x 2.1 staggered array (Re_d = 12,858).

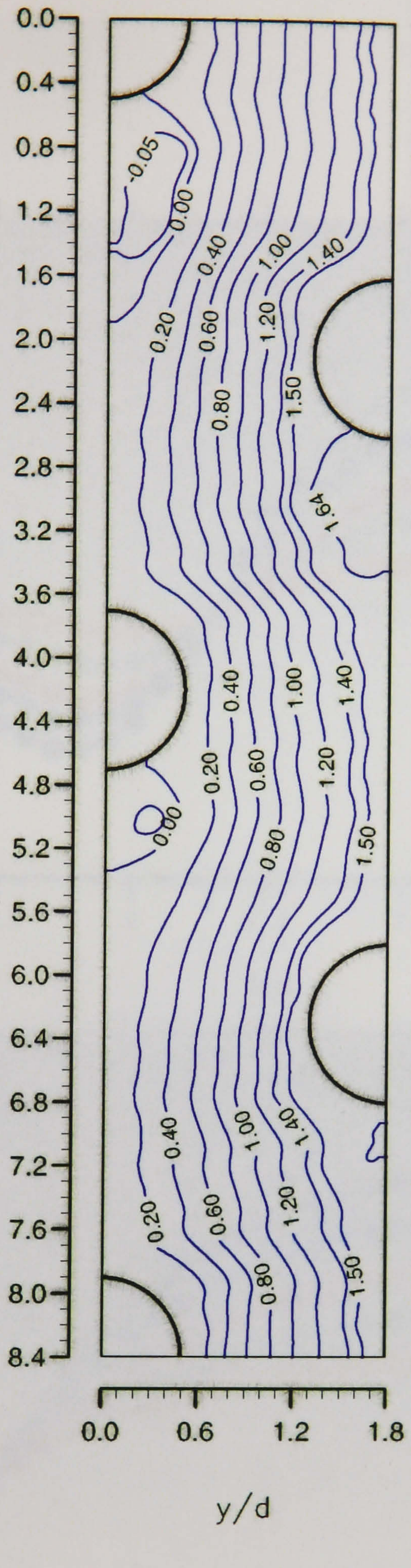

Figure 4.18. Streamline patterns in the 3.6 x 2.1 staggered array (Re_d = 12,858).

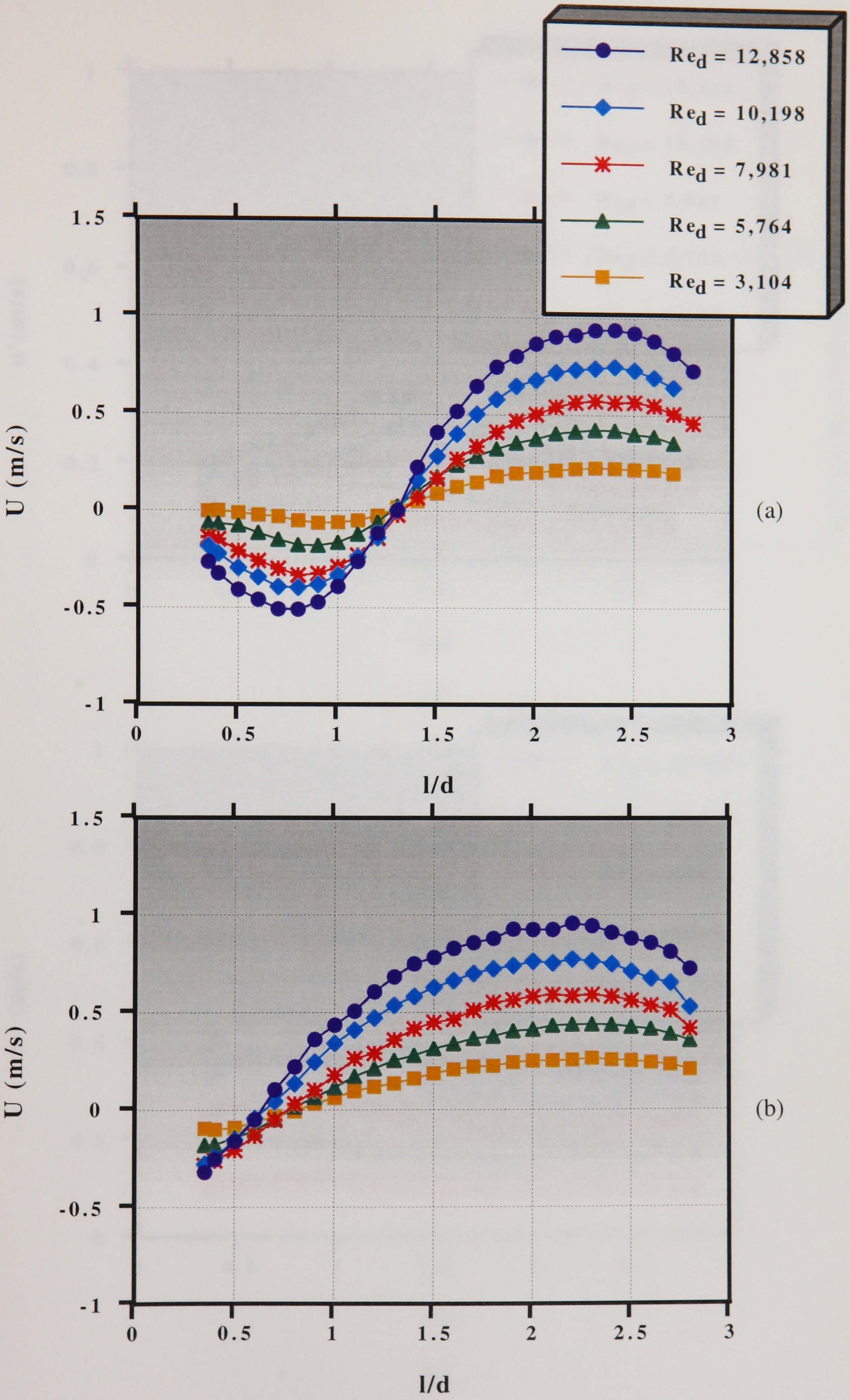

Figure 4.19. Effect of Re_d on the centreline development of U downstream of the first (a) and third (b) rows of the 3.6 x 2.1 staggered array.

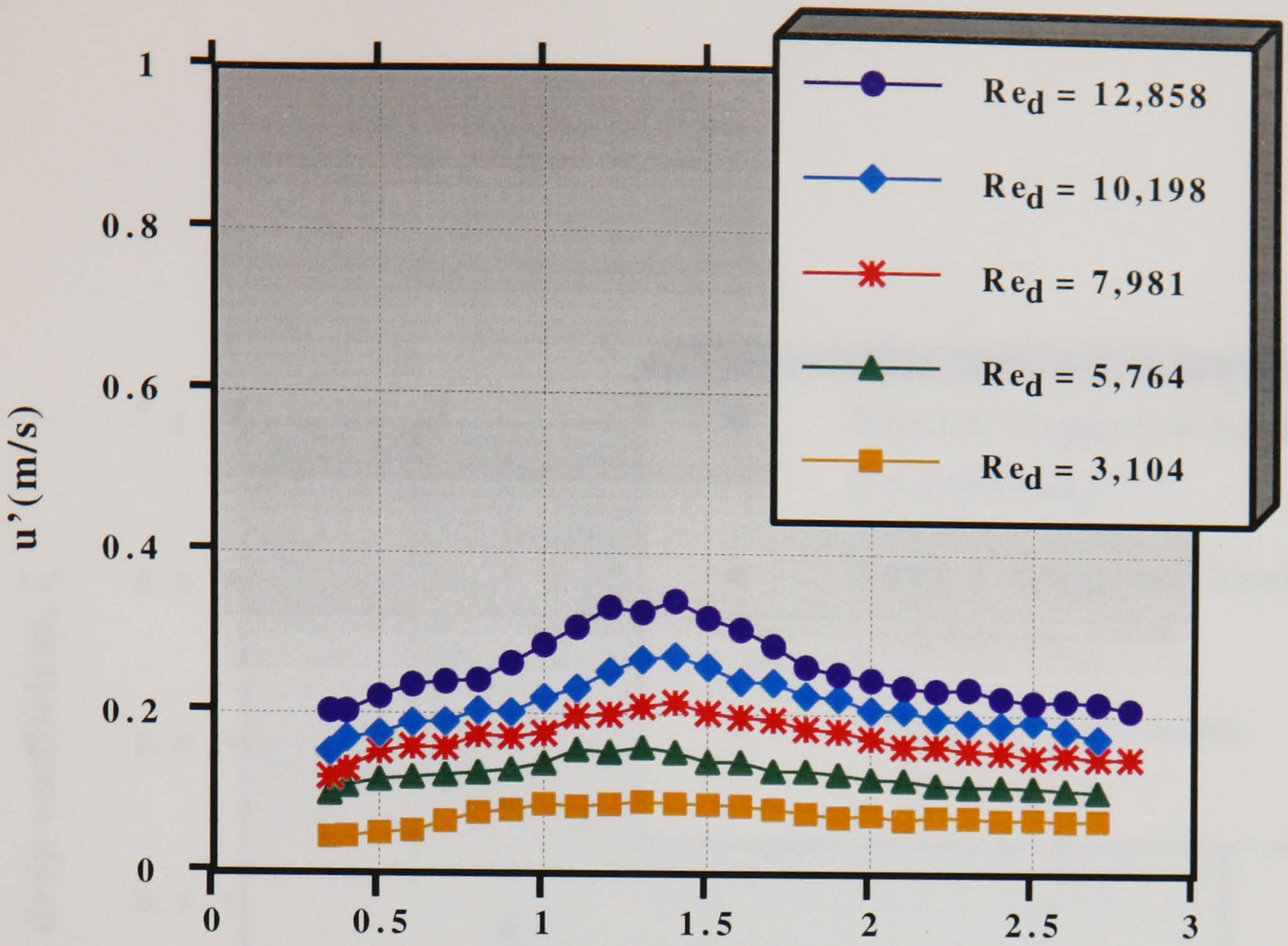

(a)

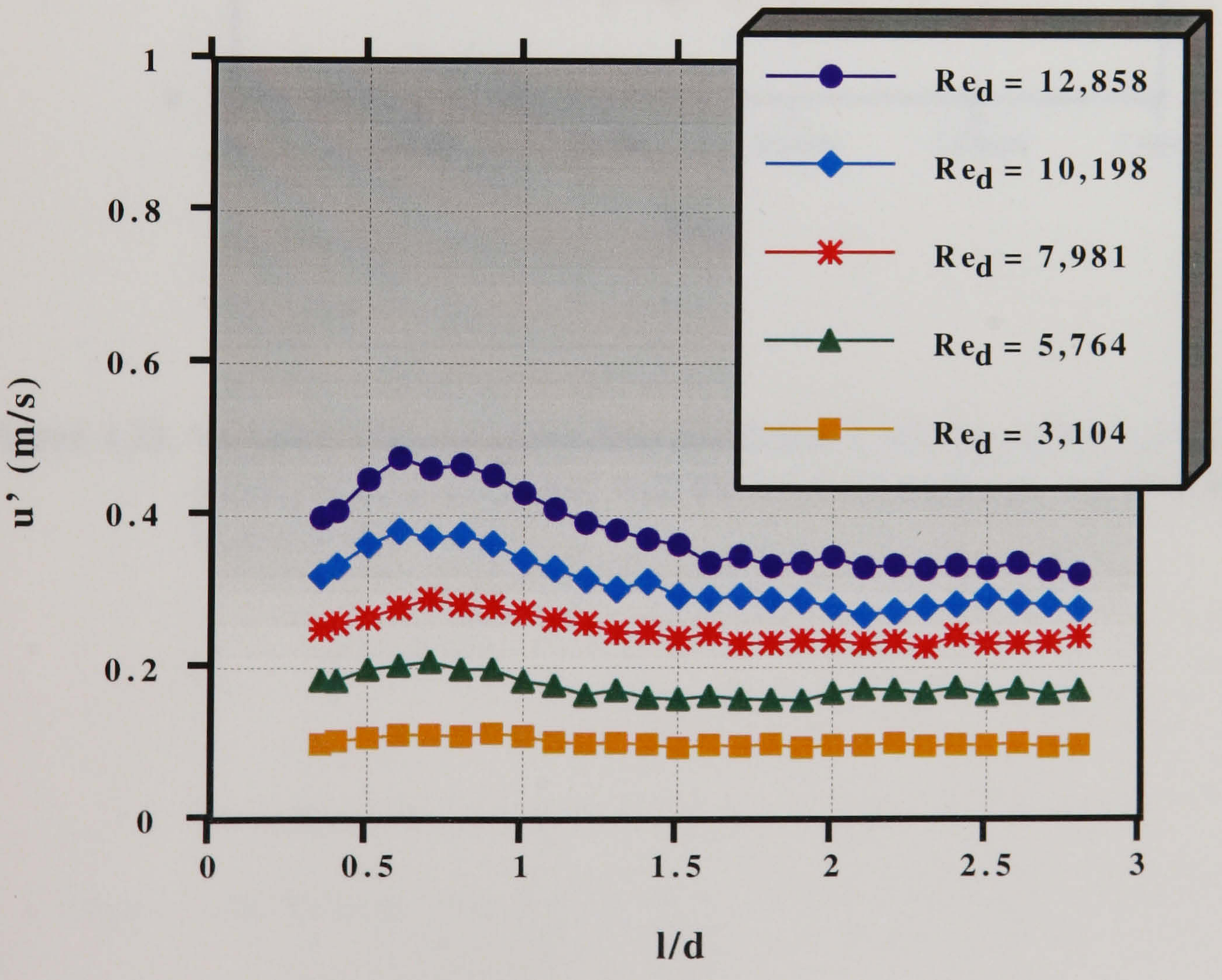

(b)

Figure 4.20. Effect of Re_d on the centreline development of u' downstream of the first (a) and third (b) rows of the 3.6 x 2.1 staggered array.

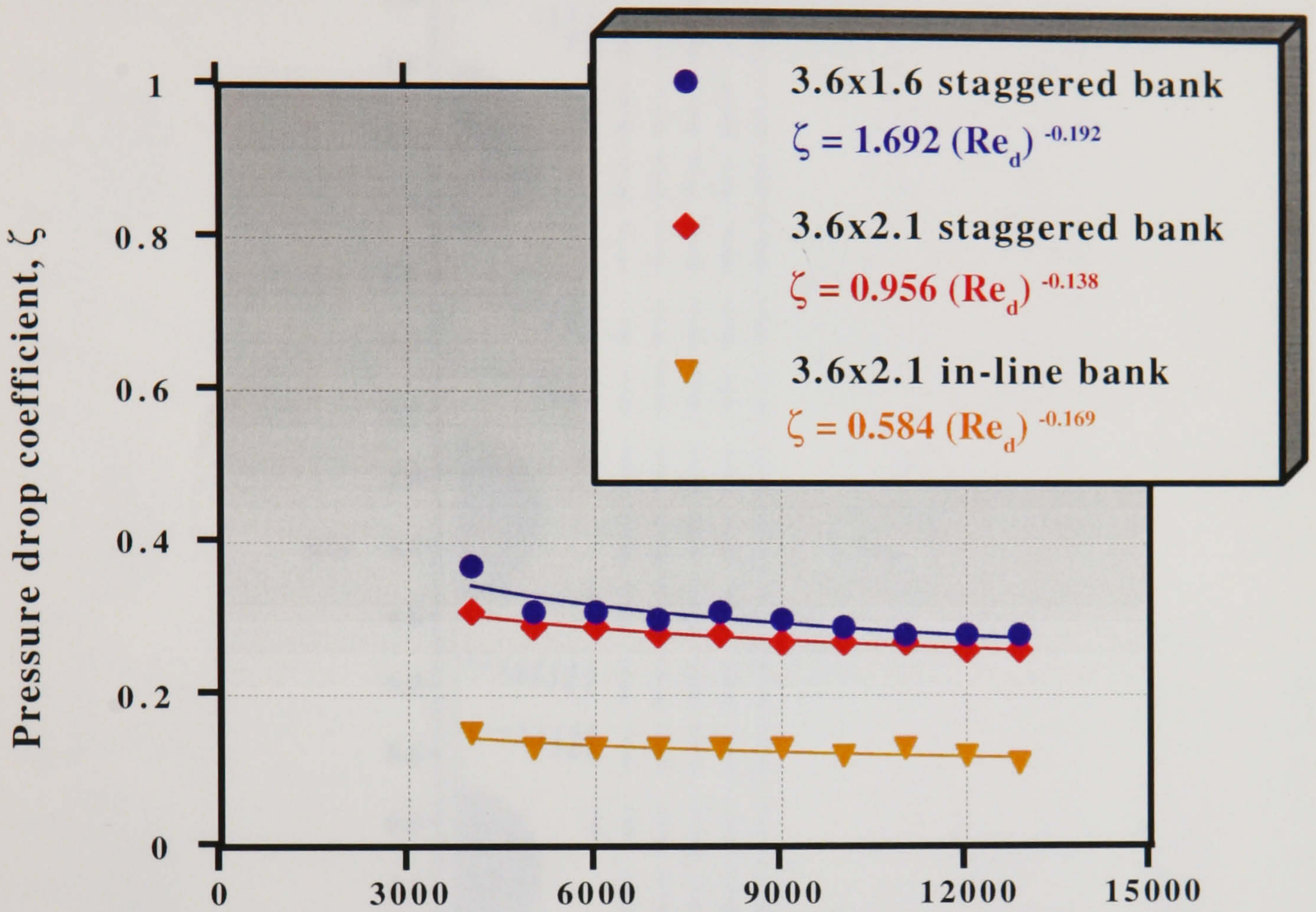

Figure 4.21. Variation of the pressure drop coefficient ζ with Re_d in the 3.6 x 2.1 staggered array compared with the 3.6 x 1.6 staggered and the 3.6 x 2.1 in-line array.

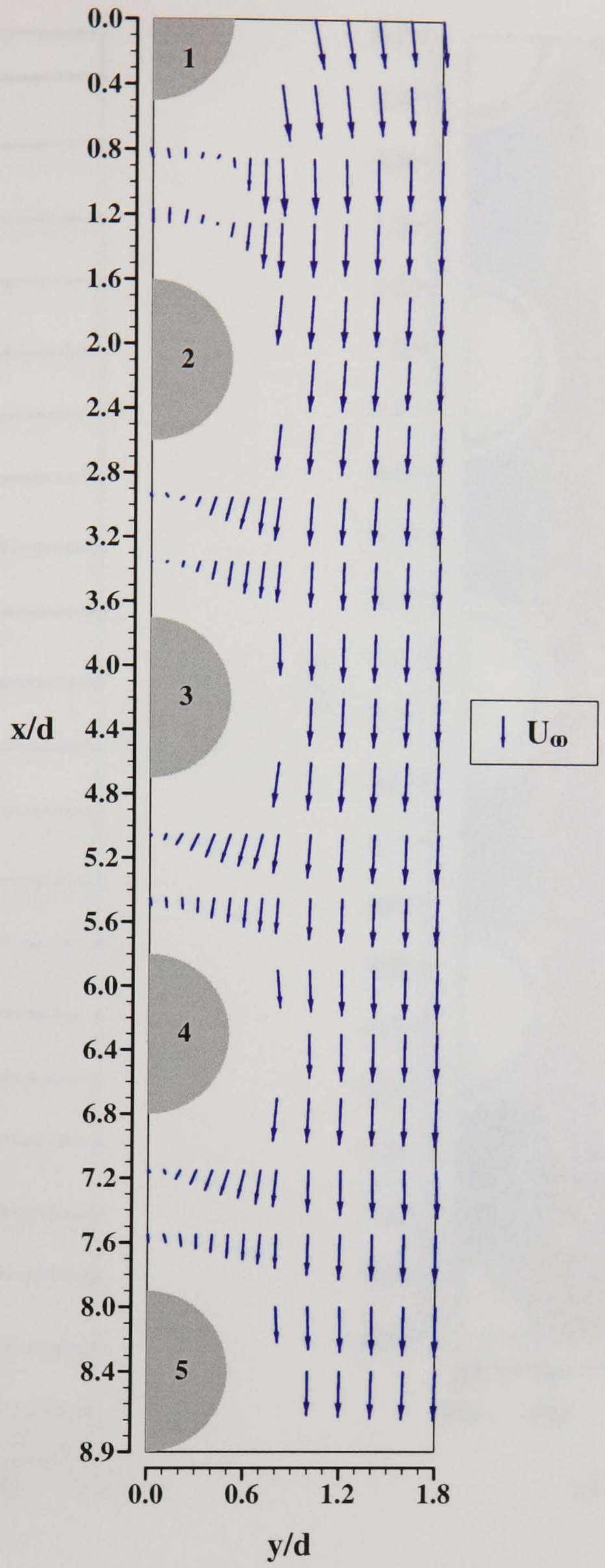

Figure 4.22. Velocity vectors in the 3.6 x 2.1 in-line array (Re_d = 12,858).

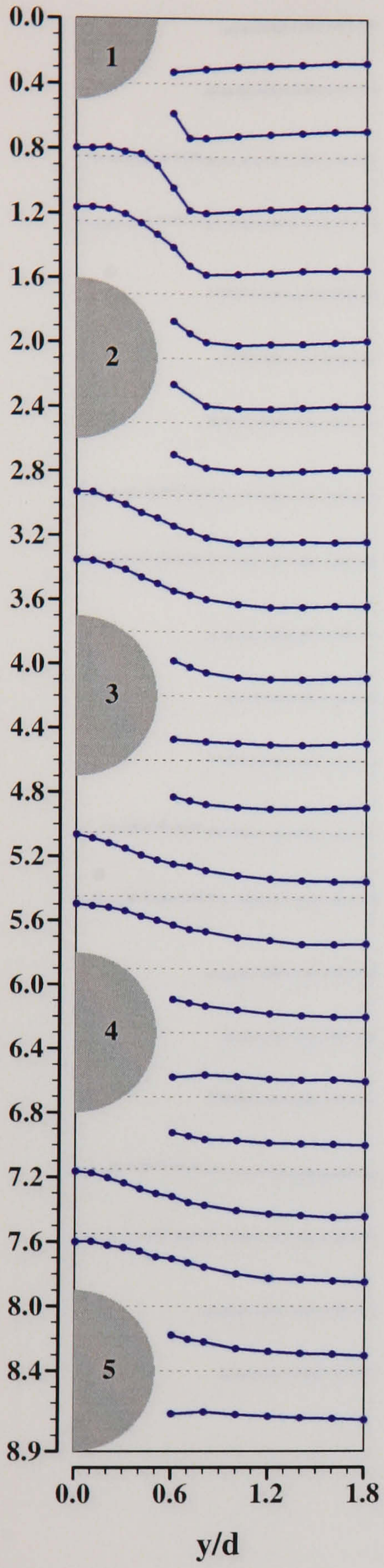

(a) U/U_∞ profiles

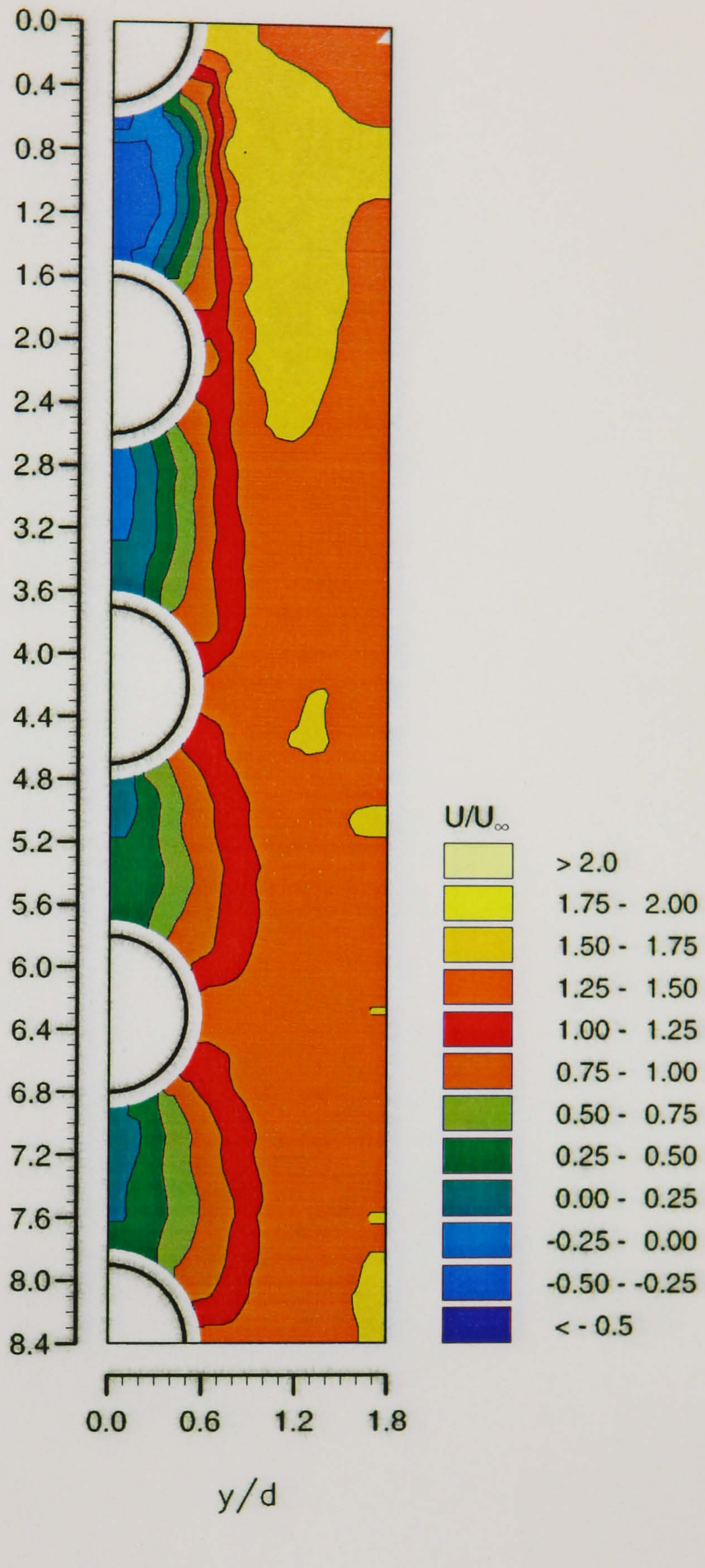

(b) U/U_∞ contours

Figure 4.23. Distribution of axial mean velocities, U/U_∞, in the 3.6 x 2.1 in-line array (Re_d = 12,858).

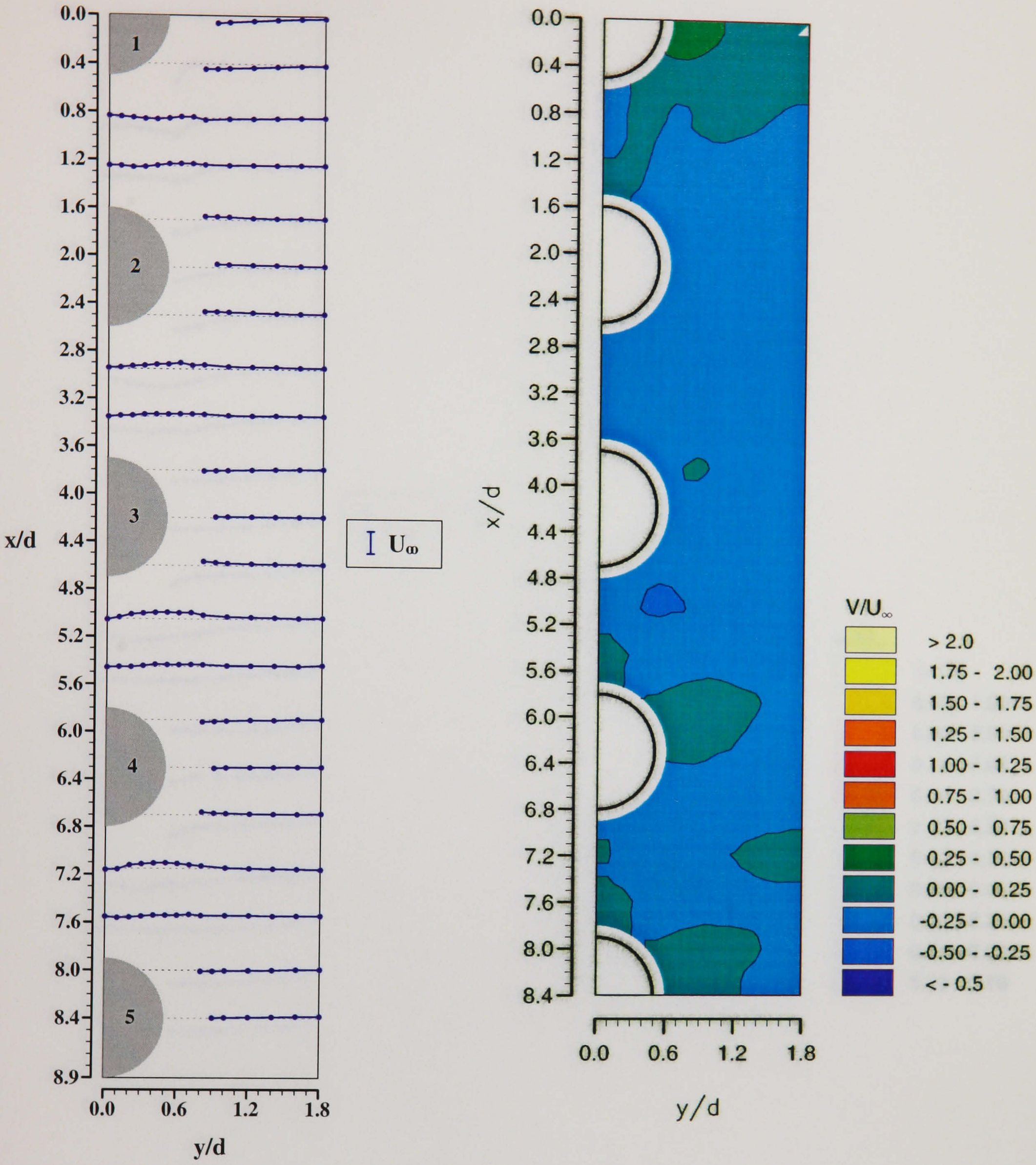

(a) V/U_∞ profiles

(b) V/U_∞ contours

Figure 4.24. Distribution of transverse mean velocities, V/U_∞, in the 3.6 x 2.1 in-line array (Re_d = 12,858).

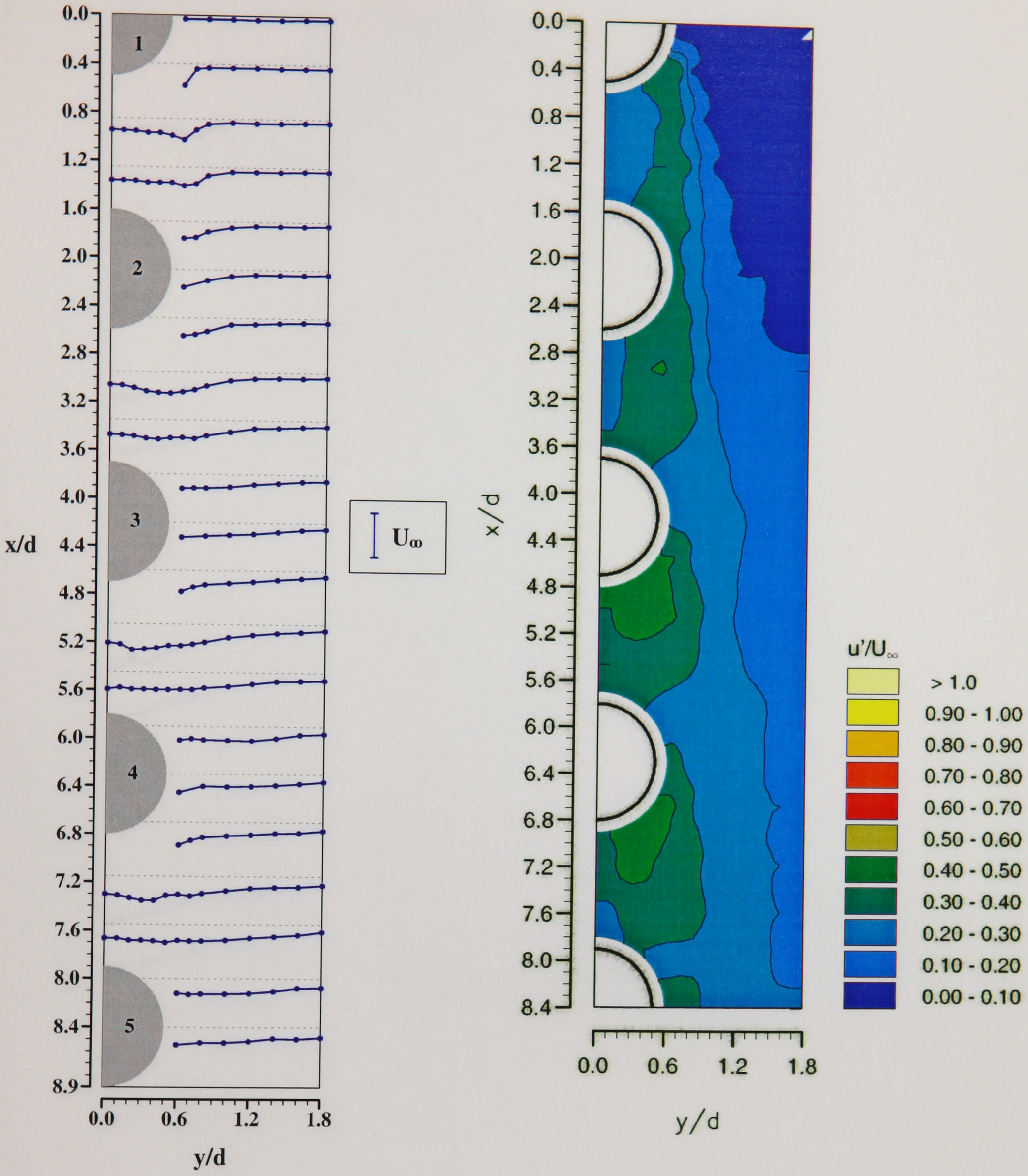

(a) u'/U_∞ profiles

(b) u'/U_∞ contours

Figure 4.25. Distribution of axial r.m.s. velocities, u'/U_∞, in the 3.6 x 2.1 in-line array (Re_d = 12,858).

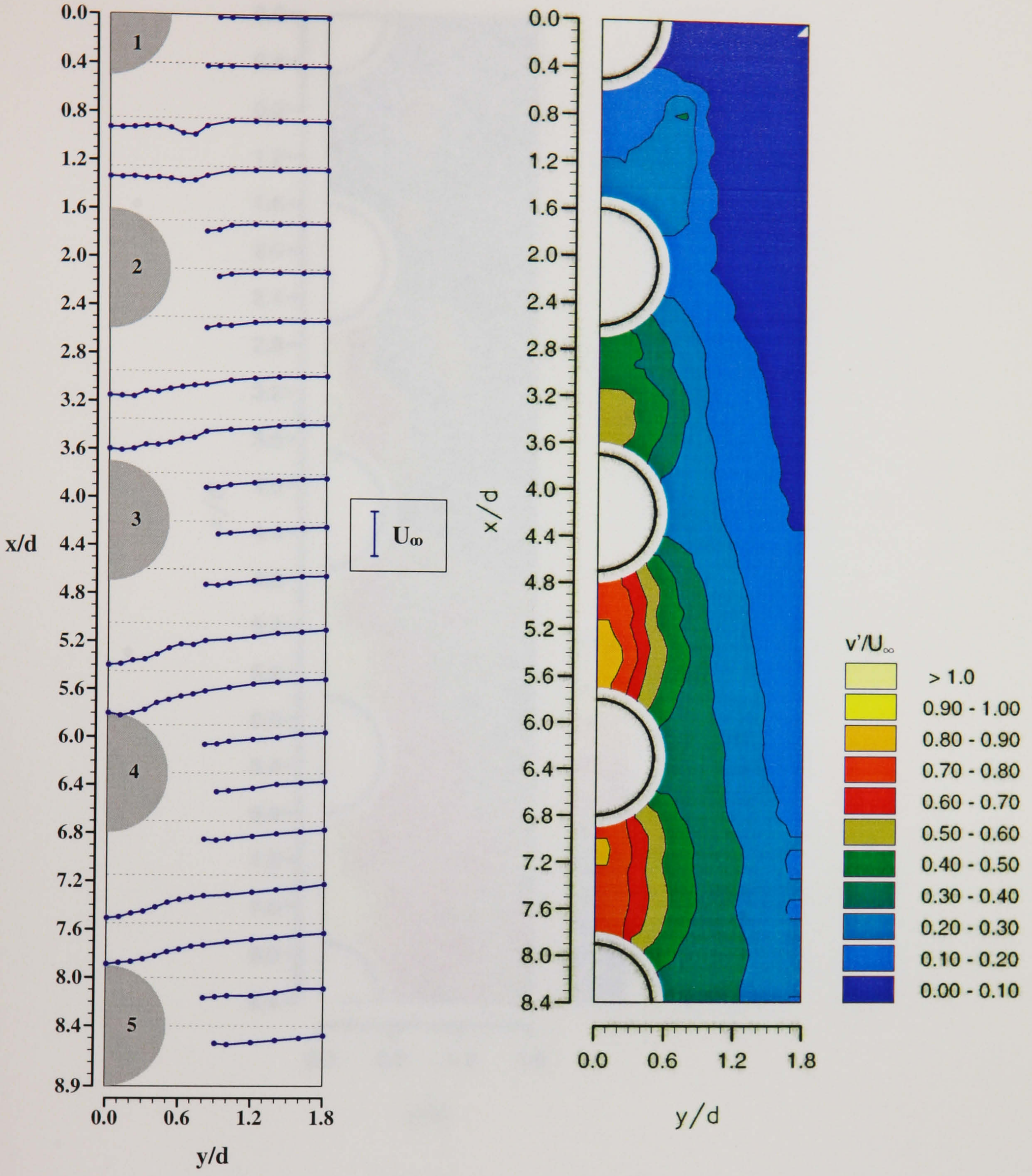

(a) v'/U_∞ profiles (b) v'/U_∞ contours

Figure 4.26. Distribution of transverse r.m.s. velocities, v'/U_∞, in the 3.6 x 2.1 in-line array (Re_d = 12,858).

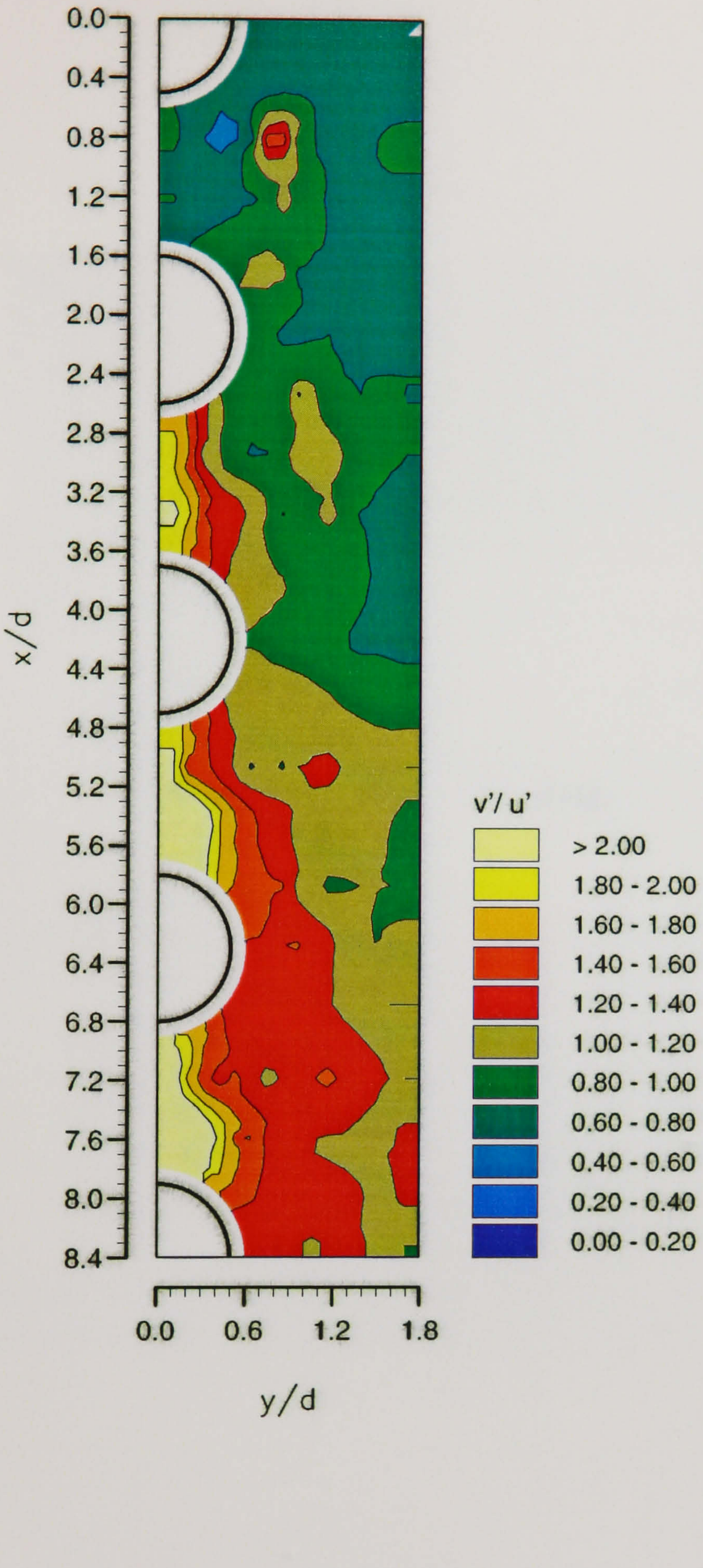

Figure 4.27. Distribution of v'/u' in the 3.6 x 2.1 in-line array (Re_d = 12,858).

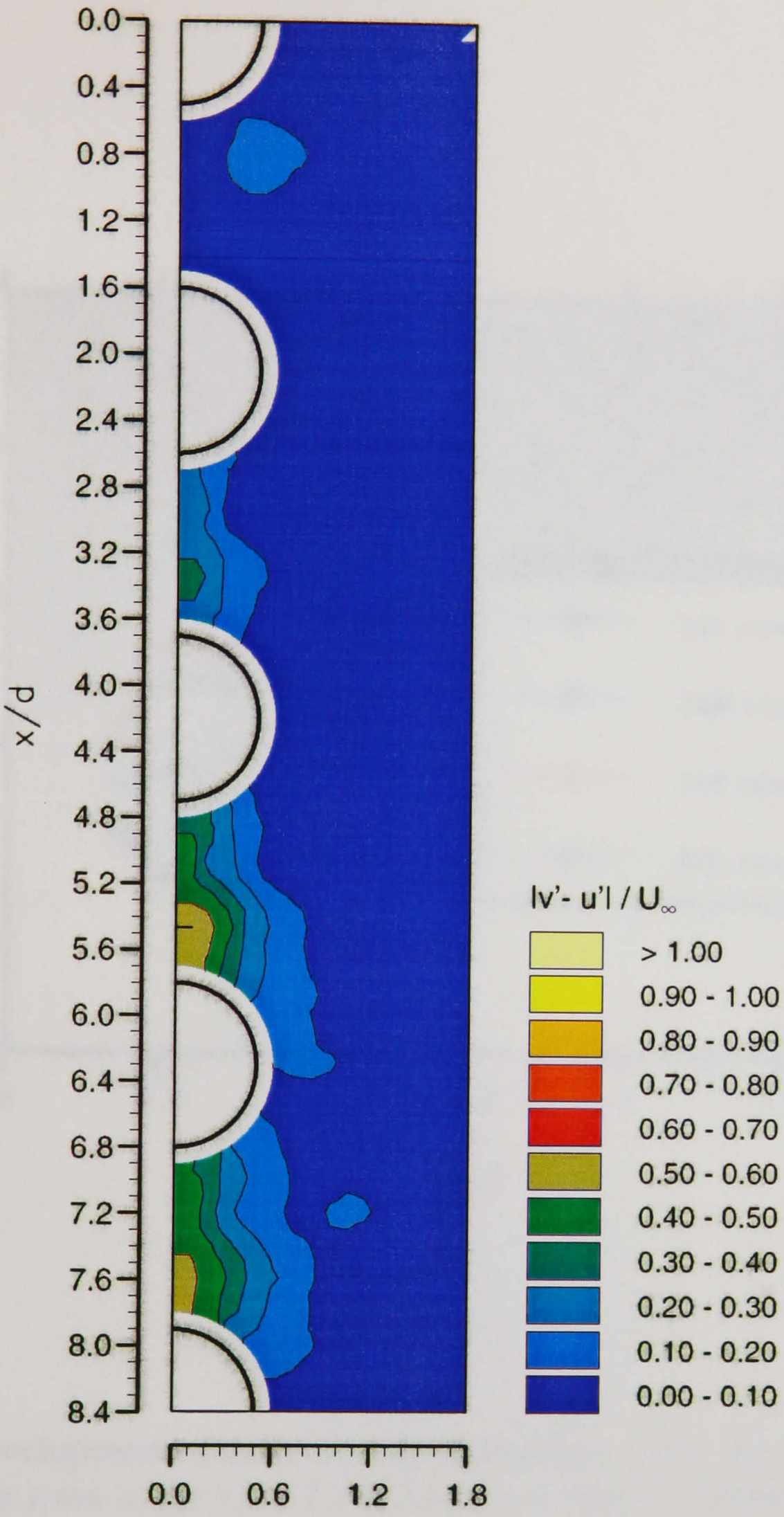

Figure 4.28. Distribution of $|v'-u'| / U_\infty$ in the 3.6 x 2.1 in-line array (Re_d = 12,858).

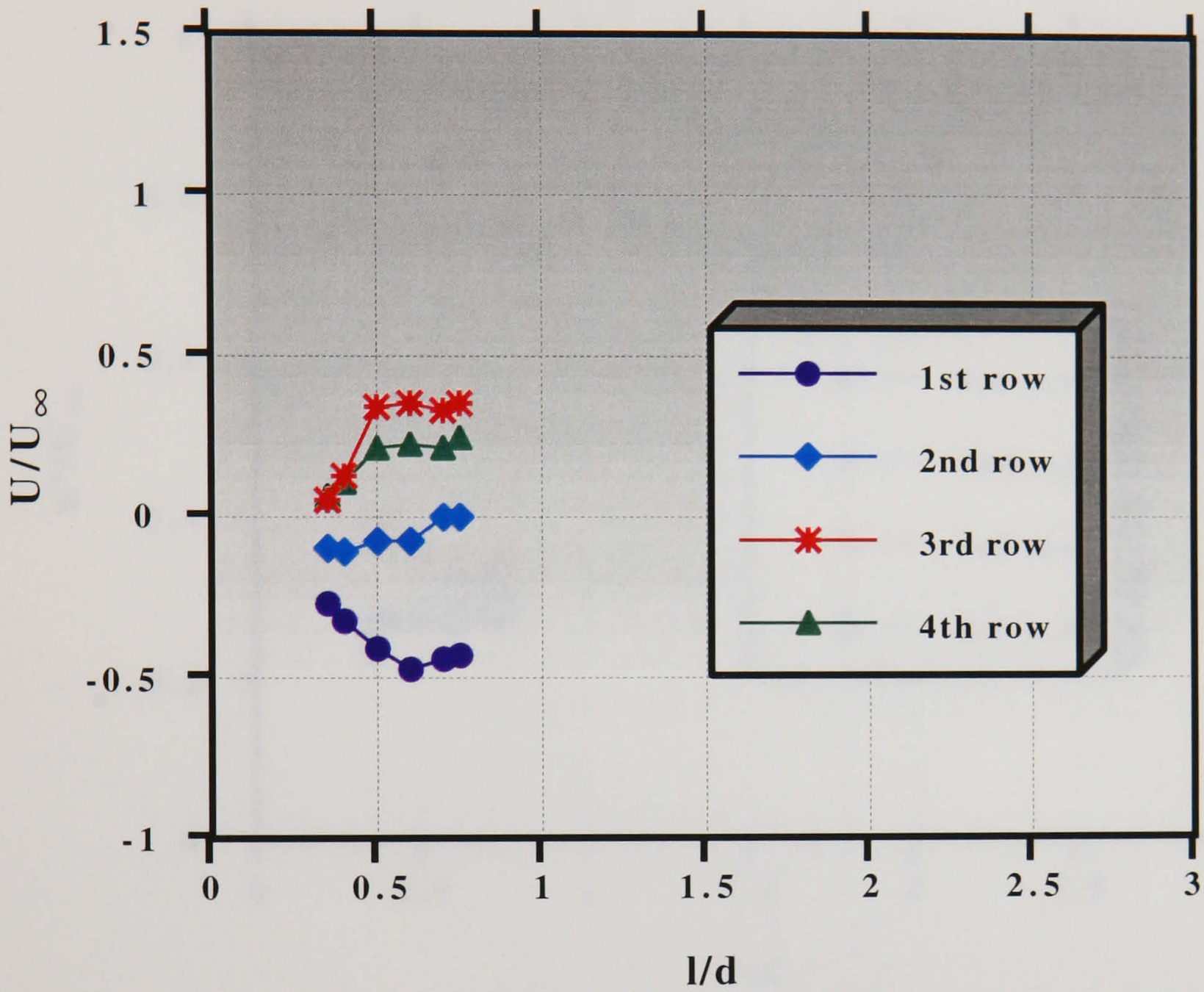

Figure 4.29. Development of the axial mean velocities, U/U_∞, downstream of the first four rows in the 3.6 x 2.1 in-line array (Re_d = 12,858).

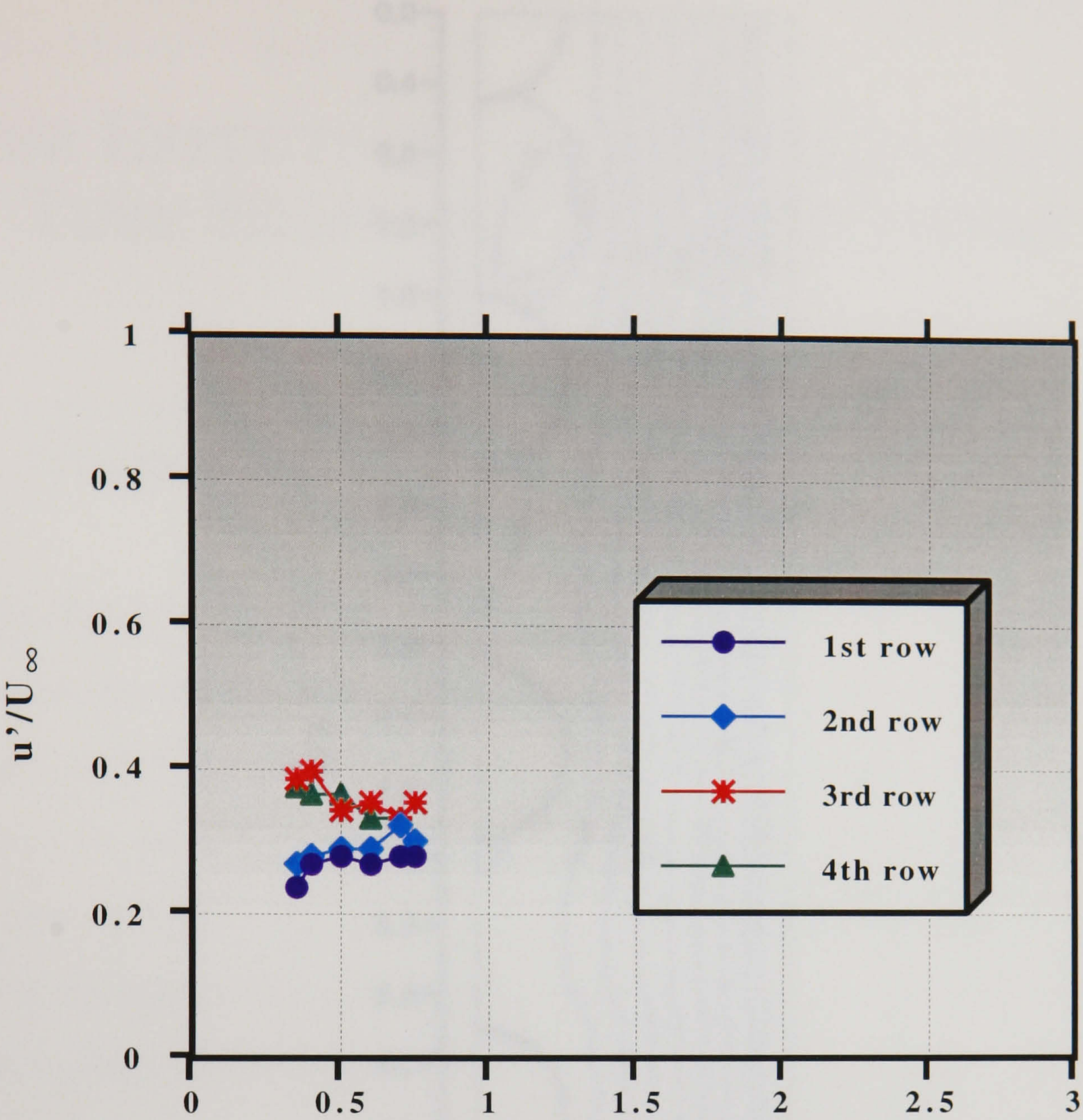

Figure 4.30. Development of the axial r.m.s. velocities, u'/U_∞, downstream of the first four rows in the 3.6 x 2.1 in-line array (Re_d = 12,858).

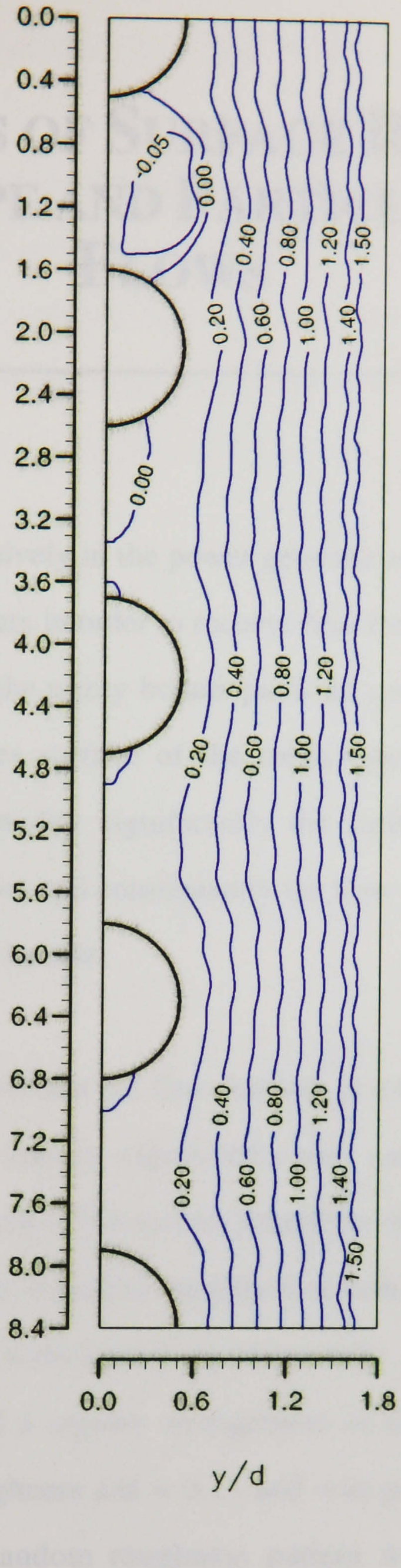

Figure 4.31. Streamline patterns in the 3.6 x 2.1 in-line array (Re_d = 12,858).

CHAPTER 5

THE EFFECTS OF SURFACE ROUGHNESS, TUBE SHAPE AND PARTICLE LADEN FLOWS

5.1 INTRODUCTION

Tube bundles are used extensively in the power generation industry as superheaters or economisers in utility boilers in order to recover heat from the combustion gases. During normal operation of the utility boilers particles contained in the flue gases may foul or erode the outer surface of the tubes (gas-side fouling). Particle deposition or erosion can modify significantly the surface roughness, nominal diameter and shape of the tubes and consequently the flow structure and subsequent particle deposition in the tube bundle.

In order to determine the extent that the flow features in a tube bundle are modified by the roughness of the tube surface, experiments were carried out in the 3.6 x 1.6 staggered array using rough tubes. The surface roughness of a tube bundle subjected to fouling is difficult to predict, therefore the effects of both uniformly and randomly distributed roughness were investigated experimentally. The evenly distributed roughness pattern comprised a regular arrangement of tightly spaced pyramidal elements with a relative roughness k/d = 0.14 and was produced by knurling the surface of the tubes. The random roughness pattern was produced by gluing spherical particles on the surface of the tubes. The latter caused an increase in the nominal diameter by approximately 12 % while the relative roughness k/d was approximately equal to 0.04. Evenly roughened tubes are more likely to occur in a real gas-side fouling environment when ash particles cause erosion of the tube

surface while the randomly roughened ones when particles deposit on a surface through a number of the mechanisms which have been described in Chapter 1.

Depending on the deposition mechanisms involved in a gas-side fouling situation, ash particles can be deposited only on the front or on the rear, on both the front and the rear or around the whole perimeter of the tubes (Skiepko and Lach, 1992). As a result, a number of different tube shapes may arise in different rows of a heat exchanger tube bundle, affecting the flow field around the tubes and subsequent particle deposition. In order to study the effect of altered tube shapes on the velocity characteristics of tube bundles, experiments were carried out in the 3.6 x 1.6 staggered array using tube shapes that are likely to occur in a real fouling environment based on predictions made by a fouling model developed by the National Technical University of Athens (Bouris-Burry and Bergeles, 1994, Bergeles et al, 1995; Bergeles et al, 1996). According to this model, under real operating conditions in a typical utility heat exchanger particle deposition occurs only on the front of the tubes and mainly in the first two rows of a 3.6 x 1.6 staggered array. The predictions showed that asymptotic fouling conditions are reached within 2 weeks (Bergeles et al, 1995), after which no deposit growth is observed, but the shape of the deposits remains essentially similar after 8 hours of fouling. Therefore, the predicted tube shapes in the first two row cylinders of the aforementioned array after 8 hours of fouling were approximated by two different tapered cylinders for the first and second rows. The exact geometry of both the surface patterns and the shapes of the tapered tubes used in the experiments has been described in detail in Chapter 2. The experimental techniques and conditions were identical to those employed in the study of the 3.6 x 1.6 staggered array with smooth circular tubes described in Chapter 3. The axial velocity component was measured in detail in all three configurations. The transverse component was measured in detail only in those configurations in which the axial velocities indicated significant changes. In order to determine the extent that the wake characteristics are modified

by the parameters investigated, detailed velocity measurements were taken along the wake axes and the results were compared with those obtained with smooth circular cylinders. The working fluid was water and the Re_d was 12,858. The effect of surface roughness on the pressure drop was also studied in the Re_d range of 4,000 to 12,858.

Furthermore, since most flows occurring in a fouling environment are particle laden ones, particles were introduced in the flow over the 3.6 x 2.1 in-line array and their mean and r.m.s. velocities in the axial direction were measured in selected transverse planes using the amplitude discrimination technique described in Chapter 2. The experimental conditions were otherwise identical to those used in the study of the single-phase flow over the 3.6 x 2.1 in-line array described in Chapter 4. The results are compared with the single-phase velocity measurements presented in Chapter 4.

5.2 THE EFFECT OF SURFACE ROUGHNESS

5.2.1 MEAN VELOCITY DISTRIBUTIONS

Profiles of the normalised axial mean velocities, U/U_∞, measured in the 3.6 x 1.6 rough staggered tube bundle with evenly distributed roughness are shown in Figure 5.1. The results are compared with those for the smooth tube bundle. It can be seen that the flow is hardly affected by this type of roughness across most of the flow. The same is true for the transverse mean velocities (V/U_∞) which are shown in Figure 5.2, compared with the corresponding ones for the smooth tube arrangement. Since the axial mean velocities - which were measured first - showed no significant effects, measurements of the transverse component were only made in 4 transverse planes halfway between successive rows of tubes.

In contrast, the randomly distributed pattern appeared to modify the flow features of the staggered array. The mean velocity vectors obtained for this configuration are shown in Figure 5.3. In comparison to the flow pattern obtained with smooth tubes (Figure 3.1), the flow across the randomly roughened tube bundle is more distorted, reaching higher velocities in the interstitial flow passages which can be attributed partly to the increased nominal diameter of the tubes and partly to higher flow constriction imposed by the modified wake regions. Regions of intense recirculation are evident downstream of the first three tubes. The corresponding axial mean velocity profiles (U/U_∞) are shown in Figure 5.4 (a) and they are compared with those for the smooth staggered array. U/U_∞ values are in general higher in the flow passages between columns of tubes, while smaller positive and/or larger negative U/U_∞ values are observed in the wake regions. The U/U_∞ contours (Figure 5.4 (b)) show that the interstitial velocities are higher by approximately 0.25 U_∞. It is also evident that the wake regions are elongated. This is most pronounced downstream of the second and third row where the magnitude of the negative velocities is generally higher than in the smooth staggered array. Transverse mean velocities, V/U_∞, (Figures 5.5 (a) and (b)) are in some locations higher in magnitude than those measured with the smooth tubes, especially in the first three rows. Differences up to 0.25 U_∞ can be observed in the second and third rows (Figure 5.5 (a)).

According to the literature surveyed in Chapter 1 surface roughness can promote boundary layer transition from laminar to turbulent in the flow over a single cylinder or a tube bundle, which enhances the heat transfer in tube bundles. Therefore surface roughness is used as a means of heat transfer augmentation in tube bundle heat exchangers. The effect of surface roughness is determined by the ratio of the height of the roughness elements to the thickness of the boundary layer. Schlichting (1968) distinguished between three regimes with respect to the effects of roughness on the resistance to flow by rough pipes: the *hydraulically smooth regime* in which all

protrusions are contained within the laminar sub-layer; the *transition regime* in which protrusions extend partly outside the laminar sub-layer and the *completely rough regime* in which protrusions reach outside the laminar sub-layer. Although the height of the surface elements in both surface patterns studied was greater than the thickness of the boundary layer predicted by NTUA no significant effects could be observed. Achenbach (1989) pointed out that the roughness elements affect the flow predominantly where it is most sensitive to disturbances, i.e. in the critical Re_d number regime. Therefore, very high Re_d numbers, of the order of 10^5, may be needed to quantify the effect of surface roughness clearly enough. The present results, however, confirm that surface roughness has not any significant effect in subcritical flow conditions for the Re_d investigated, unless the roughness elements cause a significant change in the nominal diameter, in which case they distort the flow field around the tubes.

5.2.2 TURBULENCE LEVEL DISTRIBUTIONS

The distributions of the normalised axial (u'/U_∞) and transverse (v'/U_∞) r.m.s. velocities obtained with rough tubes exhibit the same trends with the mean velocities: no significant effect of surface roughness is observed for the evenly distributed pattern (Figures 5.6 and 5.7) while the opposite is true for the randomly distributed roughness (Figures 5.8 and 5.9). The distribution of u'/U_∞ in the randomly rough tubes is nearly identical to that for smooth tubes up to the third row (Figure 5.8 (a)). u'/U_∞ levels further downstream are consistently higher than those for the smooth tube array. They also exhibit a different pattern (Figure 5.8 (b)), since maximum velocities with values around 0.80 U_∞ are reached in the flow passage between the fourth and fifth row cylinders, compared with 0.50 U_∞ in the smooth array.

Figures 5.9 (a) and (b) present the distribution of v'/U_∞ in profile and contour from respectively. Major differences with the smooth array results can be observed. Firstly, the turbulence levels downstream of the first and second row are lower than the corresponding levels in the smooth array by 0.2 and 0.1 U_∞ respectively. The maximum v'/U_∞ value observed downstream of the second row of the smooth array was not present in this array. On the contrary, maximum v'/U_∞ values equal to 0.9 - 1.0 U_∞ appear downstream of the third and fourth rows. As a result, the interstitial turbulence levels between rows 4 and 5 are higher by 0.1 U_∞ compared with the smooth tube levels.

Figures 5.10 and 5.11 show that turbulence might be considered isotropic up to the third row and anisotropic further downstream. The largest differences between the two components (up to 0.5 U_∞) are observed downstream of the third row. Anisotropy, however, is not only confined to the wake region as it happens in the smooth array but extends to the flow passages as well.

5.2.3 WAKE CHARACTERISTICS

The centreline axial mean velocity profiles (u'/U_∞) downstream of the first four rows of both rough tube bundles are compared with those obtained with smooth cylinders in Figures 5.12 (a) through (d). The profiles downstream of the first and third rows of the evenly rough cylinders are identical to those for smooth cylinders. However, some differences are observed downstream of the second and fourth rows: the stagnation point has been shifted closer to the tube downstream of the second row whereas the opposite trend is observed downstream of the fourth row. These contradictory trends are difficult to understand. Further investigation is needed to clarify this observation.

The centreline mean velocities are significantly affected by the randomly distributed roughness: the magnitude of the negative velocities is generally large in all rows and especially downstream of the second row (0.65 U_∞) and the rear stagnation point has moved further downstream in all rows but the first one. Thus, the length of the recirculation zone (l_r) formed downstream of the first row is smaller by 0.1 d than that for smooth cylinders. The recirculation bubbles downstream of subsequent rows are elongated with lengths equal to 1.6 d, 1 d and 0.8 d downstream of the second, third and fourth rows respectively. The width of the recirculation bubbles (w_r) exhibits the same trends as it can be seen from the streamline patterns plotted in Figure 5.13: it is slightly lower than that for smooth cylinders downstream of the first row but significantly larger in downstream rows. The estimated length and width of the recirculation bubbles are compared with those obtained with smooth cylinders in Table 5.1. The differences observed can be attributed to the fact that the separation point and consequently the wake features may be strongly affected by the local roughness characteristics.

Table 5.1. Length and width of the recirculation bubbles in 3.6 x 1.6 staggered array with randomly rough cylinders.

		w_r/d		l_r/d	
Row	**x/d (l/d)**	**randomly rough**	**smooth**	**randomly rough**	**smooth**
1	0.8 (0.3)	0.44	0.46	1.05	1.15
	1.2 (0.7)	0.21	0.37		
2	2.4 (0.3)	0.67	0.46	1.6	1.1
	2.8 (0.7)	0.52	0.34		
	3.2 (1.1)	0.35			
3	4.0 (0.3)	0.56	0.21	1	0.475
	4.4 (0.7)	0.45			
4	5.6 (0.3)	0.31			0.3
	6.0 (0.7)	0.13		0.8	

- l/d represents distance from the tube surface and x/d the corresponding axial location at which the width is estimated.
- l_r/d is measured from the tube surface and not from the centre of the tubes.

The centreline axial r.m.s. velocities are compared in Figures 5.14 (a) through (d). The distributions obtained with evenly rough tubes are similar to those for smooth tubes whereas those for the randomly rough tubes attain higher r.m.s. velocities downstream of the second, third and fourth rows. It was shown in both Chapters 3 and 4 that the centreline u'/U_∞ values in staggered arrays increase with distance from the tube surface up to the rear stagnation point, around which they reach a maximum, and decrease slowly thereafter. Therefore, the higher centreline u'/U_∞ values found downstream of the second, third and fourth rows of the randomly rough staggered array are due to the fact that the corresponding rear stagnation points occur further downstream than those in the smooth array.

5.2.4 PRESSURE DROP

Figure 5.15 compares the pressure drop coefficients measured in the two rough arrays with those in the smooth array. The pressure drop data confirm the negligible effect of the evenly distributed roughness as opposed to that of the randomly distributed one: the pressure drop coefficients for the evenly distributed roughness are identical to those obtained with smooth tubes within 3% whereas those for the randomly distributed ones are 43% higher. These higher pressure drop coefficients explain the differences observed and they confirm that an increase in the nominal diameter caused by the roughness elements is responsible for the significant changes found. The variation of pressure drop with Re_d exhibits the same trend, a slight reduction with increasing Re_d, in all three configurations which is in agreement with the published literature.

5.3 THE EFFECT OF TUBE SHAPE

5.3.1 MEAN VELOCITY CHARACTERISTICS

Figure 5.16 (a) presents the axial mean velocity profiles, U/U_∞, obtained in the 3.6 x 1.6 staggered array with tapered cylinders. The profiles are compared with those obtained with circular cylinders: velocities in the main flow through the gaps of successive rows are similar. The flow accelerates as it passes over the recirculation bubbles. The profiles downstream of the first cylinder show some significant differences since the recirculation characteristics have changed, as will be shown later. As a result the velocity gradients are steeper than those obtained with circular cylinders. Downstream of the second row the profiles do not show any significant differences. It must be noted that some of the small differences observed between the two sets of data might be attributed partly to the fact that the measurement grid used in the present study is denser than that used with circular tubes resulting in more

detailed information and comparisons between the two should be made with caution. Contour plots of U/U_∞ (Figure 5.16 (b)) exhibit a pattern that is different than that obtained with circular cylinders (Figure 3.2 (b)): velocities attain higher values in the flow passage between the tube columns whereas downstream of the first row the velocities are lower.

The mean velocity distributions downstream of the tapered cylinders can be compared with those of the circular tubes by examining the centreline development of U/U_∞, shown in Figures 5.17 (a) and (b). Downstream of the first row (Figure 5.17 (a)) the centreline profiles of the tapered and circular tubes are identical up to the point of maximum negative velocity. This is found at the same location in both tubes, that is at 0.6 d from the tube surface and its value is the same for both tubes, 0.47 U_∞. However, the recovery of the axial velocity is faster in the tapered cylinders with the flow accelerating more rapidly and reaching the rear stagnation point earlier, at 0.95 d downstream of the tube surface. The maximum positive velocity occurs at 1.6 d and its value is 0.73 U_∞, compared to 0.44 U_∞ found in the first row of the staggered bank with circular tubes. From that point onwards there is a velocity decay region as the downstream cylinder is approached and the velocity reaches finally a value comparable to that measured with the circular tubes at l/d = 1.8. Similarly, downstream of the second row (Figure 5.17(b)) the maximum negative velocity occurs earlier, at 0.4 d from the tube surface, but its value is the same as that attained with circular cylinders. Once again the velocity recovers quickly with the rear stagnation point occurring at 0.9 d whereas the maximum positive velocity is reached at around 1.4 - 1.6 d. Its value is equal to 0.63 U_∞ as compared to 0.47 U_∞ in the circular tube array. Velocity decays rapidly as the downstream cylinder is approached and its final value at 1.8 d is similar to that for circular tubes.

As observed above, the maximum negative centreline axial mean velocities in the wakes of the circular and tapered tubes are similar. This finding may appear to

contradict those of earlier investigations of flows over bluff bodies: for example, Taylor and Whitelaw (1984) reported that the magnitude of the maximum centreline velocity is smaller for a cone than for a disk of identical area blockage ratio. However, it should be noted that in the present investigation the difference in bluffness between the two different tube shapes is considerable smaller than that between the cone and the disk mentioned earlier. The bluffness of a body is defined as the amount that the body diverges the flow and it is greater the greater the angle at which the separation streamline leaves the point of separation. Bluffness can be described quantitatively by means of the face pressure coefficient as suggested by Humphries and Vincent (1976). The face pressure coefficient is calculated by integrating the surface pressure distribution ahead of the separation point and it is unique for a given shape of body. Since no surface pressure measurements were made in this investigation, the differences in bluffness between the circular and the tapered cylinders cannot be quantified. It should be emphasised, however, that most of the bluff bodies referred to in the published literature have fixed points of separation as opposed to cylinders. Therefore, comparisons between the present findings and those for bluff bodies such as cones and disks should be made with great care.

5.3.2 TURBULENCE CHARACTERISTICS

The distribution of the axial r.m.s. velocities, u'/U_∞, is presented in profile and contour form in Figures 5.18 (a) and (b) respectively. The profiles obtained look identical to those for the circular tubes, with some small differences observed only at the wake interfaces where steep velocity gradients usually occur. The same can be observed in the contour plot, especially downstream of the second row. These differences are consistent with the small differences in mean velocity gradients downstream of the tapered tubes.

Figures 5.19 (a) and (b) present the centreline development of u'/U_∞ downstream of the first and second rows respectively. The results for the circular cylinders are also shown on these figures. u'/U_∞ values downstream of the first row are slightly higher for the tapered cylinders up to the rear stagnation point and then decrease more rapidly than with the circular tubes. The same features are observed downstream of the second row with the difference that the r.m.s. levels become almost equal to those of the second-row circular cylinder as the downstream cylinder is approached. The maxima of centreline axial r.m.s. velocities are 0.45 U_∞ and 0.53 U_∞ for the first and second rows respectively and are not significantly higher than those in the circular tube configuration (0.43 U_∞ and 0.50 U_∞ respectively).

Published studies on flows over bluff bodies report on lower values of axial centreline turbulence intensity in less bluff bodies. For example, the maximum centreline turbulence intensity of a disk is higher than that for a cone with the turbulent kinetic energy of the latter being only 60 % of the former (Taylor and Whitelaw, 1984). The present results, however, do not show similar trends for the reasons explained in the previous section. Furthermore, the flow over the two tapered cylinders in a staggered arrangement differs significantly from that over a single bluff body, due to interference between the two cylinders which affects the location of the separation point and the local velocities and consequently the evolution of the wakes.

5.3.3 RECIRCULATING PARAMETERS

The recirculation bubbles formed downstream of the two tapered cylinders were examined in detail and parameters of interest such as the length, maximum width, recirculating mass-flow rate as well as the vorticity thickness were estimated. The estimated values are shown in Table 5.2 and are compared with the corresponding ones for circular cylinders.

The length of the recirculation bubbles formed downstream of the tapered cylinders is equal to 0.95 d and 0.9 d for the first and second rows respectively, as compared to 1.15 and 1.1 d for the circular tubes. The forebody shape thus affects the recirculation length: decreasing the bluffness shortens the recirculation regions by 0.2 d (17 % and 18 % in the first and second rows respectively). This is in agreement with published results (Taylor and Whitelaw, 1984).

The width of the recirculation bubbles was estimated from the separation streamlines. The streamlines for this configuration are shown in Figure 5.20. Comparing these patterns with the ones found for circular tubes (Figure 3.25) it can be observed that the streamlines undergo a larger curvature towards the x-axis as the flow passes over the second row cylinder; this is associated with higher transverse velocities due to the streamlined shape of the second row cylinder. The shear layer separating from the first row has a maximum width of 0.37 d as compared to 0.46 d estimated for the circular tube. This means that decreasing the bluffness of the first cylinder results in a 20 % narrower recirculation width. The width of the recirculation bubble formed downstream of the second row was found to be equal to 0.52 d, 13 % wider than the one for the smooth staggered bank (0.46 d). It must be noted that all the above mentioned widths refer to the width of the shear layer or the half-width of the bubble.

The normalised recirculating mass-flow rates ($\dot{m}_r / \dot{m}$) were found to be 0.1 and 0.13 for the first and second rows respectively, compared to 0.15 and 0.10 for the circular tubes. Therefore, the recirculation bubble downstream of the first tapered cylinder has 33 % less mass than in the circular tube case, whereas that located downstream of the second row has 30 % more mass than the corresponding circular tube recirculation.

According to previously reported findings, decreasing the bluffness gives rise to narrower and shorter recirculation bubbles with smaller recirculating mass-flow rates (Taylor and Whitelaw, 1984). However, although the present results for the first row tube are consistent with the data of Taylor and Whitelaw, the results for the second row tube are not. It is not clear why the recirculation length downstream of the second row is shorter and the width shows the opposite trend than the one expected according to the literature. Further investigation is needed to clarify these contradictory trends. However, as already mentioned earlier in this chapter, the flows over bluff bodies reported in the literature are characterised by fixed separation points and are determined primarily by the bluffness parameter. In the present study, however, both the location of the separation points and the bluffness of the tubes in the two first rows are expected to be different due to flow interference effects and the different forebody shapes. Therefore, direct comparisons between the present results and published ones - as for example those by Taylor and Whitelaw - or any generalisations of the effect of the tube shape cannot be made.

Table 5.2. Recirculating parameters for the 3.6 x 1.6 staggered bank with tapered cylinders.

		w_r/d		l_r/d		$\dot{m}_r / \dot{m}$		δ		δ'	
Row	**x/d**	tapered	circular	tapered	circular	tapered	circular	tapered	circular	tapered	circular
1	0.8	0.37	0.46	0.95	1.15	0.1	0.15	0.12	0.14	0.15	0.18
	1.2	0.17	0.37					0.20	0.23	0.17	0.19
2	2.4	0.52	0.46	0.9	1.1	0.13	0.10	0.10	0.18	0.13	0.23
	2.8	0.33	0.34					0.33	0.32	0.27	0.26

The vorticity thickness (δ) and its spreading rate (δ') were also estimated. The results for the first row are very close to those obtained with circular tubes and even closer to the results for a single cylinder in cross-flow (McKillop and Durst, 1984) shown

in Table 3.1. However, both the vorticity thickness and its spreading rate at a distance of 0.8 d from the surface of the second row cylinder (x/d = 2.4) are smaller than the corresponding values determined for the smooth tube bank and are closer to the values for the first row cylinder. At a distance of 1.2 d from the tube surface (x/d = 2.8), however, the values are similar to those with the smooth tubes.

5.4 PARTICLE VELOCITIES OF A SOLID/LIQUID FLOW OVER THE IN-LINE ARRAY

Diakon (Perspex/Plexiglass) particles were suspended in the flow over the in-line array and their mean and r.m.s. velocities were measured using the amplitude discrimination technique described in Chapter 2. The characteristic properties of the particles are listed in Table 5.3 (page 208). The size range of the particles was 250-355 μm and the mean diameter 282 μm. Attempts were made to find a particle size that would satisfy the criteria of dynamic and geometric similarity with CFD calculations for the deposition of Al_2O_3 particles under real operating conditions (Bergeles et al, 1996). Dynamic similarity could be achieved by matching the Stokes numbers between the computational and experimental two-phase systems. CFD calculations referred to a continuous phase of air with velocities of 12 m/s, significantly higher than those that could be reached in our water experimental facility, a cylinder diameter d = 38 mm, almost four times the one employed in our experiments and a mean particle diameter of 216 μm. Under these conditions, dynamic similarity could be achieved only if particles extremely large in comparison with the cylinder diameter of 10 mm were used, failing the condition of geometric similarity. Therefore, failing to determine the particle size by similarity rules, the size range mentioned above was chosen arbitrarily.

The particle size distribution information was obtained by image processing techniques. That involved capturing images of some particle samples with the

camera and processing the acquired images with appropriate software. The OPTILAB^{TM} image processing and analysis software was used which can perform particle detection, counting and sizing. The images of the particle samples should be calibrated first by entering the dimensions between any two points in the image in real units. Particle detection and counting involves measurements of objects in an image that fall within a specified intensity and size range. In the case of binary images they all have the same intensity (generally equal to 1 and the background is equal to 0). In grey level images this corresponds to an interval of grey level values. Apart from the number of particles, area statistics information can be obtained as well as individual reports on various morphological parameters like areas, lengths, shape equivalence, shape features. The mean particle diameter was estimated through a parameter called Waddel Disk Diameter which is equal to the diameter of the disk with the same area as the particle. In order to check how spherical the particles were a parameter called Heywood Circularity Factor was estimated. The latter is defined as the ratio of the particle perimeter to the perimeter of a circle with the same area as the particle. The closer this factor is to 1 the closer the shape of the object is to that of a disk. Distribution plots could also be obtained with respect to the parameter estimated. The mean diameter based on three different images of particle samples was found to be equal to 282 μm and the average circularity factor equal to 0.82 which is close to 1, i.e. the majority of the particles used can be considered to be spherical. 40 ml of particles were introduced to the flow corresponding to a volumetric concentration of approximately 0.024 %. It should be noted that the concentration of the particles could not be increased further due a limitation imposed by the depth of field over which light was required to pass.

The terminal velocity of the Diakon particles due to drag and gravity was calculated for the flow of a single particle in a carrier phase of water using the following formula (Nouri et al, 1987):

$$U_T = \sqrt{\frac{4d_p(\rho_p - \rho)g}{3\rho C_D}} \tag{5.1}$$

If laminar (Stokes) flow around the particle is implied and C_D is taken equal to 10 the terminal velocity of the particle is 8.2 mm/s (0.009 U_∞). A higher value of the terminal velocity, equal to 39 mm/s (0.042 U_∞), is obtained using the above formula for the case of turbulent flow around the particle with C_D = 0.44. It has been reported, however, that the drag of the particles is further reduced in a suspension and as a result the terminal velocities are larger in a suspension than for a single particle. The particle Reynolds number, Re_p, was estimated using both values of the terminal velocity and it was found equal to 2.3 and 11 respectively. The characteristic response time for the particles is given by (for Stokes flow):

$$\tau_p = \frac{d_p^2 \rho_p}{18\mu} \tag{5.2}$$

Alternatively the equation:

$$\tau_p = \frac{d_p^2(1+2\rho_p/\rho)}{36\nu} \tag{5.3}$$

may be used (Hardalupas et al, 1989). The particle response time was found equal to 5.21 ms if equation (5.2) was used and equal to 7.42 ms if equation (5.3) was used. A rough estimation of a characteristic fluid response time τ_f can be made using either the hydraulic diameter of the duct upstream of the test section or the cylinder diameter as characteristic dimensions. In the first case the fluid response time is 77 ms whereas in the second 11 ms. The cylinder diameter is a more representative characteristic dimension but again this is a rough estimation since all other time scales of the flow are not available. All the characteristic particle parameters estimated above are listed in Table 5.3.

The Stokes number, defined as the ratio of the fluid response time to the particle response time (Hardalupas et al, 1989), is a measure of the particle response to the fluid flow. For the present study, the Stokes number based on the above definition is greater than unity, meaning that the particles used are 'totally responsive' - they follow the corresponding fluid response times.

Table 5.3. Particle properties and characteristic parameters.

Mean diameter (d_p)	282 μm	
Size range	250-355 μm	
Material	Diakon	
Density (ρ_p)	1180 kg/m^3	
Terminal Velocity (U_T)	8.2 mm/s (C_D=10)	39 mm/s (C_D=0.44)
Particle Re_p ($U_T d_p/\nu$)	2.31	11
Particle response time (τ_p)	5.21 ms (eq. 5.2)	7.42 ms (eq.5.3)
Fluid response time (d/U_∞)	11 ms	

The axial particle mean velocities (U_p) measured at five axial stations (x/d = 0.0, 0.85, 2.95, 5.05 and 7.15) are shown in Figures 5.21 (a) - (e) respectively. In order to aid the interpretation of the results, the particle mean velocities are normalised with U_∞ and are shown together with the corresponding single-phase fluid velocities (U_f/U_∞) which were presented in Chapter 4. Figure 5.21 (a) shows that particles lead the fluid as the flow enters the tube bundle (x/d = 0.0). The relative velocities (U_p - U_f) are, on average, 74 mm/s, and are larger than the estimated particle terminal velocity (39 mm/s for turbulent flow around the particle). Downstream of the first row (x/d = 0.85), the particles lead the fluid in the main stream by 0.04 U_∞ (for 0.8 < y/d < 1.8) but they lag at the interface between the shear layer and the recirculation bubble where steep velocity gradients are present (Figure 5.21 (b)). The magnitude

of the relative velocities in these locations is on average 0.18 U_∞. Negative velocities in the recirculation bubble are, by 0.05 U_∞ on average, higher for the particles than for the fluid although the opposite might be expected due to the effect of gravity. At all downstream axial stations (x/d = 2.95, 5.05, 7.15) the particles lead the fluid in all transverse locations (Figures 5.21 (c) - (e)). The magnitude of the relative velocities is, on average, 89 mm/s, and is again larger than the estimated terminal velocity of the particles. The interpretation of the relative velocities and the comparisons with the terminal velocity, however, should be made with care: firstly because the fluid velocities in the two-phase situation - i.e. when fluid velocities are measured in the presence of the particles - may differ; secondly, the estimation of the terminal velocities is subject to uncertainty due to the assumptions involved in the drag coefficient of the particles. Relative velocities larger than the estimated terminal velocity of the particles were also measured by Nouri et al (1987) in a solid-liquid pipe flow. The differences were partly attributed to the presence of non-uniform velocity and concentration gradients in the flow. The relative velocities can be accurately determined only when the solid and liquid velocities are measured simultaneously by means of phase-Doppler anemometry as discussed below.

Figures 5.22 (a) - (e) present the normalised axial particle r.m.s. velocities, u'_p/U_∞, compared with the corresponding single-phase fluid r.m.s. velocities (u'_f/U_∞). Comparisons between the particle and fluid velocities should be made with care as the fluid turbulence levels measured in the presence of particles may be different. Particle r.m.s. velocities are identical to those of the single-phase flow upon entrance to the tube bundle (x/d = 0.0, Figure 5.22 (a)). Downstream of the first row (x/d = 0.85, Figure 5.22 (b)) u'_p values are identical to u'_f for $0.8 < y/d < 1.8$. u'_p are higher, by 0.05 U_∞ on average, than u'_f in the recirculation region and at the interface between the latter and the shear layer. Particle r.m.s. velocities are on average identical to the fluid ones in most transverse locations downstream of the second row (x/d = 2.95, Figure 5.22 (c)). In the wake region, however, u'_p are higher than u'_f, by

0.03 U_∞ on average. Further downstream (at x/d = 5.05 and 7.15, Figures 5.22 (d) - (e)), u'_p values are higher than u'_f in the mainstream flow (by of 0.02 U_∞ on average) and lower in the wake regions (by 0.05 U_∞ on average).

The above results indicate that the particles in general follow the flow as might be expected for neutrally buoyant particles. Small differences between the solid- and liquid velocities are observed primarily in the wake regions and regions of steep velocity gradients. Similar trends have been reported by other investigators. For example, Nouri et al (1984) found that neutrally buoyant particles suspended in a liquid flow around conical and disk-shaped baffles, in general, followed the fluid motion. The mean flow results showed small differences in the solid- and liquid-velocities only in regions where there was considerable acceleration or deceleration of the flow. Particle mean velocity profiles were flatter than the single-phase ones with particle velocities being lower in the recirculation and the recovery regions. In general, particle r.m.s. velocities were found to be lower than the single-phase ones. However, in regions of steep velocity gradients particle turbulence levels exceeded the single-phase ones which is in agreement with some of the present findings. Similar results were reported by Nouri et al (1987) for a solid-liquid baffled flow. The particle characteristics were similar to those in Nouri et al (1984). A study of a gas/solid flow around a circular cylinder (Lambert et al, 1988) showed that 100 μm particles did not follow the recirculating flow in the wake but they seemed to move towards the centreline with a reduced axial velocity caused by the opposing fluid motion. Particle r.m.s. velocities in the axial direction were found to be irregular. They were found to be lower than the single-phase fluid r.m.s. velocities in most locations outside the wake but up to three times higher in the wake. These findings are in agreement with some of the present findings. However, the differences between the particle and fluid r.m.s. velocities reported by Lambert et al are significantly larger than those observed in the present investigation.

The present data provide a useful assessment of the velocities of (neutrally buoyant) particles suspended in a liquid tube bundle flow. However, the differences found between the measured particle velocities and the fluid velocities may not be representative of the two-phase flow over the tube bundle since the fluid velocities were measured in the absence of the solid phase. The presence of the solid phase may modify the velocity characteristics of the liquid (continuous) phase: for example, the turbulence of the continuous phase may be suppressed or promoted depending on the particle size (Gore and Crowe, 1991). Therefore, simultaneous measurements of both phases are needed in order to determine quantitatively the changes caused in the mean flow and turbulence characteristics of the continuous phase by the suspension of the particles. Such measurements can be made using phase-Doppler anemometry which is based on the spatial frequency distribution of the scattered light modulation. The phase shift in the frequency of Doppler signals recorded at various angles of observation varies with particle size (Yianneskis, 1987). Phase-Doppler anemometry utilises this property to distinguish between the two-phases and has been implemented to measure particle-laden flows in many configurations. Hardalupas et al (1989, 1992), for example, developed a phase-Doppler anemometry technique to measure the velocity characteristics of particle-laden jets and sudden-expansion flows respectively.

5.5 CLOSURE

The effects of surface roughness and forebody shape of the tubes on the flow over the 3.6 x 1.6 staggered array were investigated experimentally. Applying an evenly distributed roughness pattern on the tubes has a negligible effect on the flow. On the contrary, a randomly distributed roughness causes significant changes in the mean and r.m.s. velocity distributions as well as the wake characteristics of the array, partly due to the increase of the nominal diameter of the tube caused by this type of roughness and partly due to the local characteristics of the surface elements. The

former is confirmed by pressure drop data. The forebody shape of the tubes also affects the flow, especially in the wake regions. The recirculation bubbles are shorter as expected, but their width does not show any consistent trends due to the complex nature of the flow in arrays as opposed to that of single bluff bodies. Particle velocity measurements taken in the 3.6 x 2.1 in-line arrangement indicated that in general the particles follow the flow. In the following chapter the development and application of a liquid thermographic technique for the measurement of wall temperature distributions in the in-line array is described.

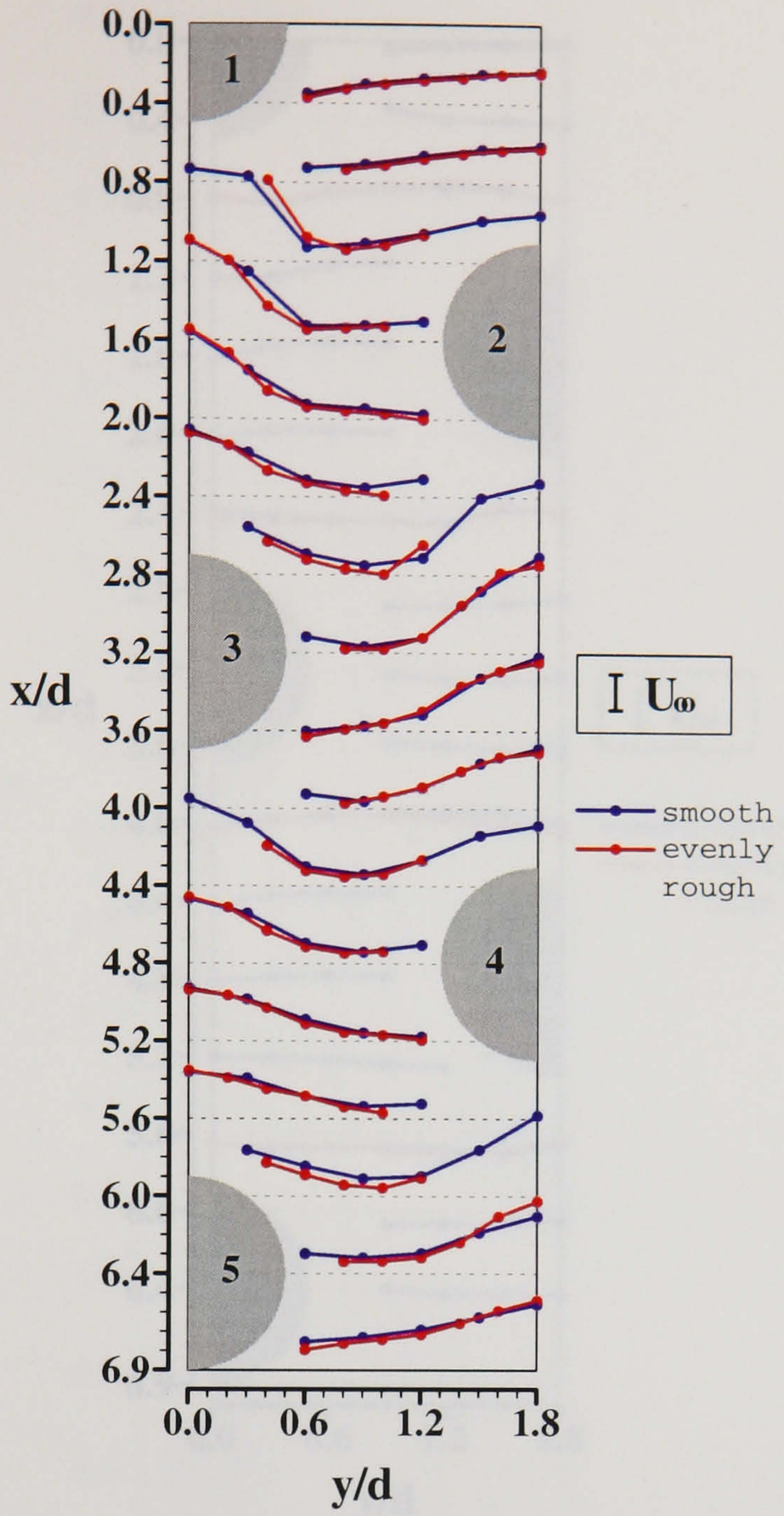

Figure 5.1. U/U_∞ profiles in the 3.6 x 1.6 rough staggered array with evenly distributed roughness and comparison with the smooth tube array (Re_d = 12,858).

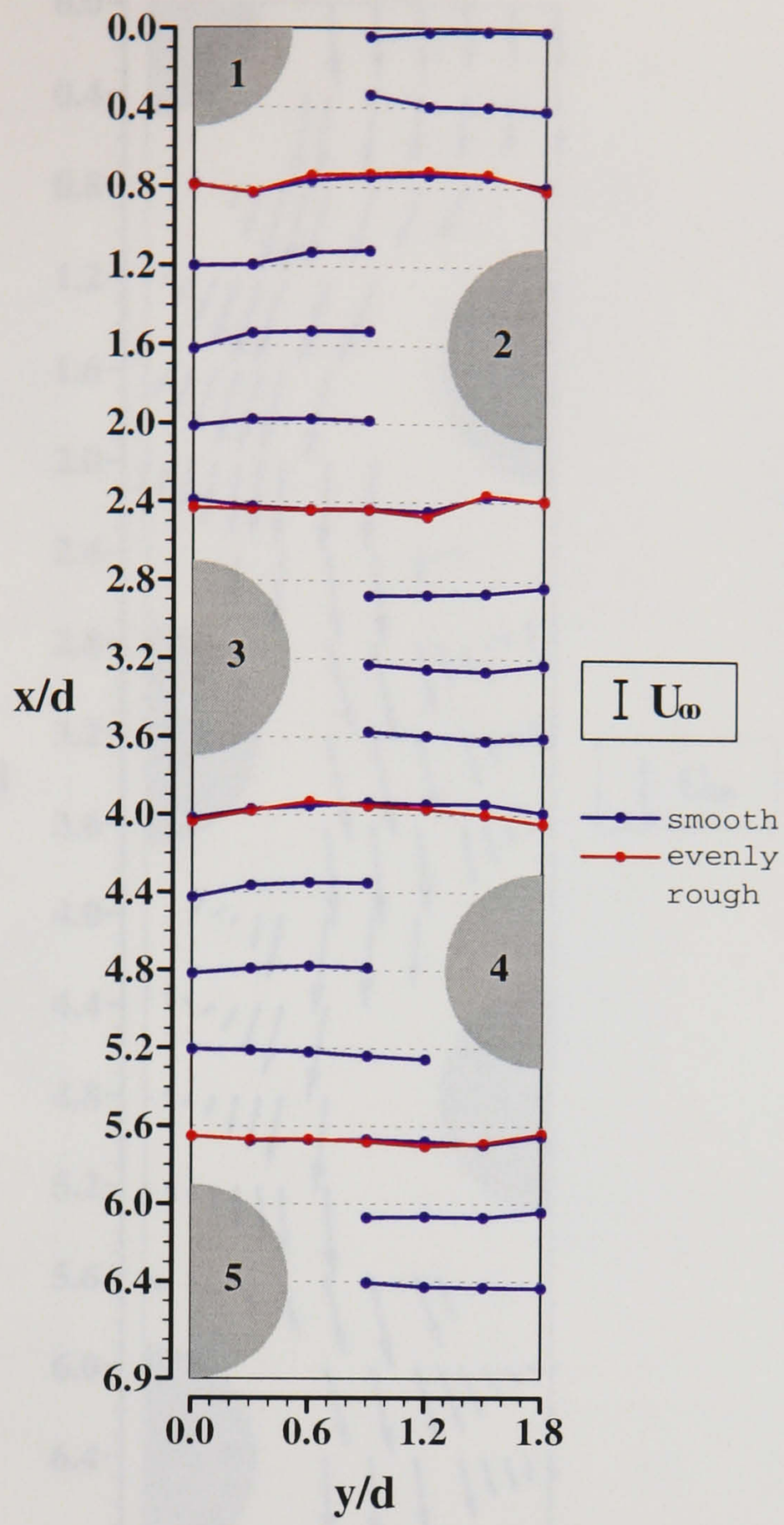

Figure 5.2. V/U_∞ profiles in the 3.6 x 1.6 rough staggered array with evenly distributed roughness and comparison with the smooth tube array (Re_d = 12,858).

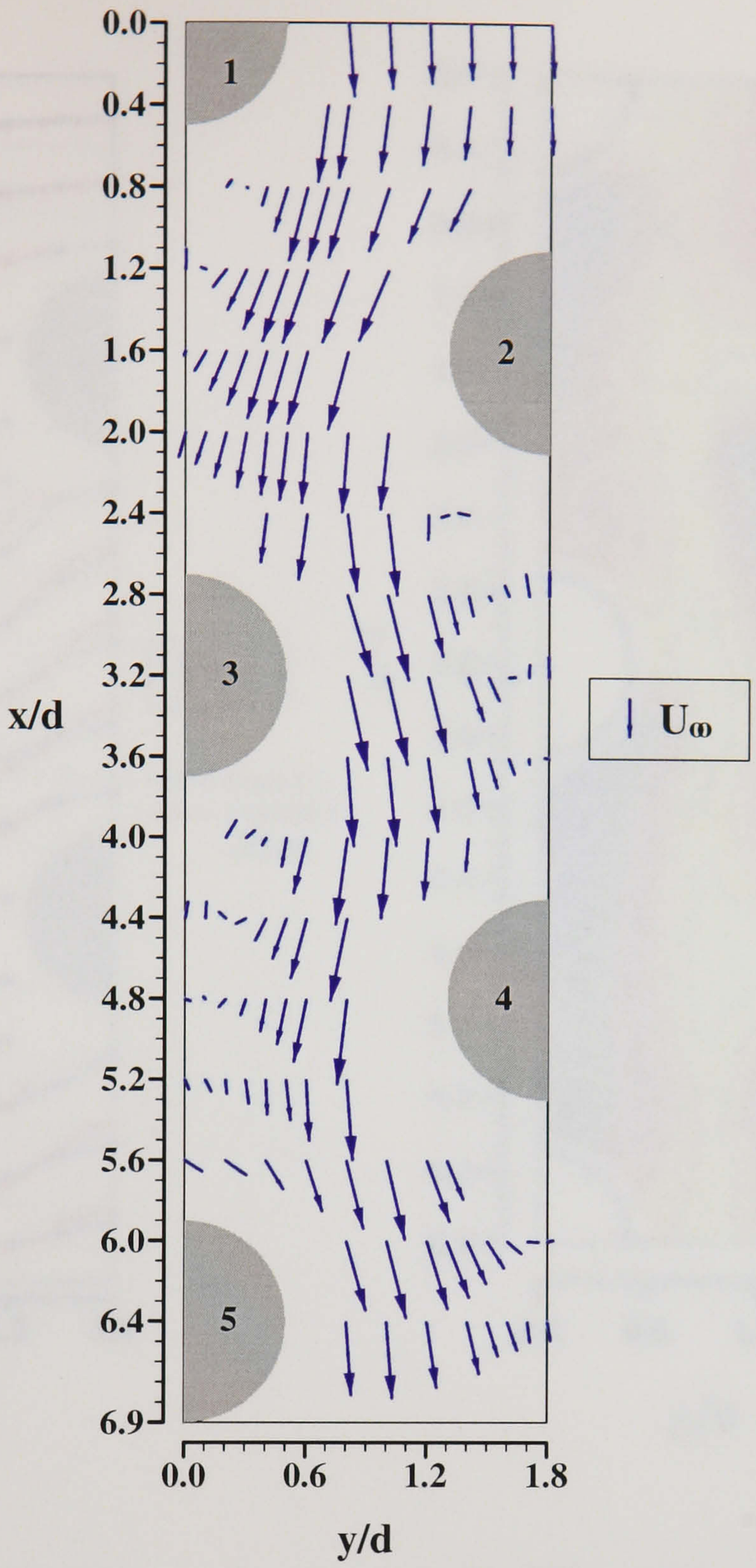

Figure 5.3. Velocity vectors in the 3.6 x 1.6 rough staggered array with randomly distributed roughness (Re_d = 12,858).

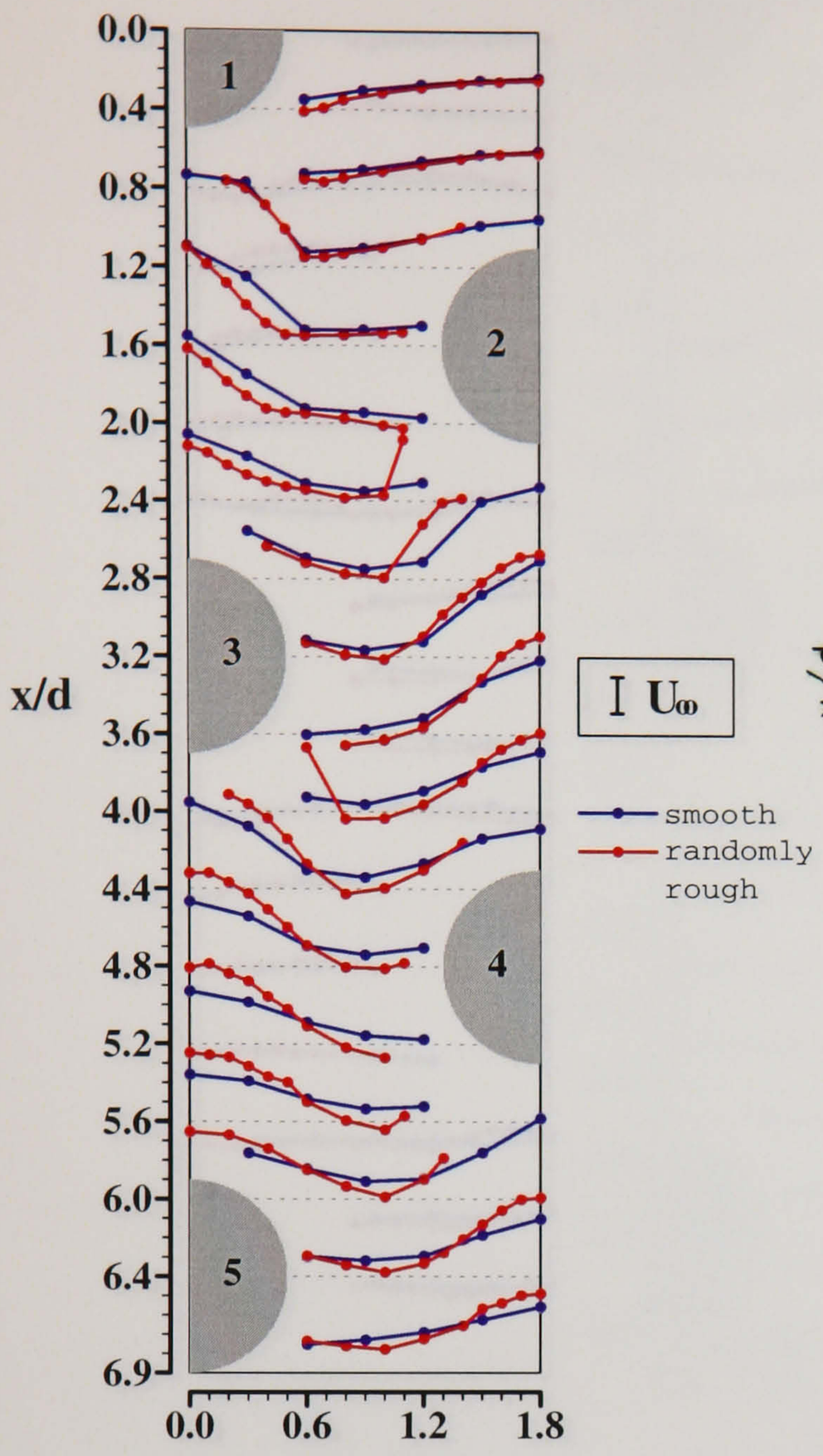

(a) U/U_∞ profiles

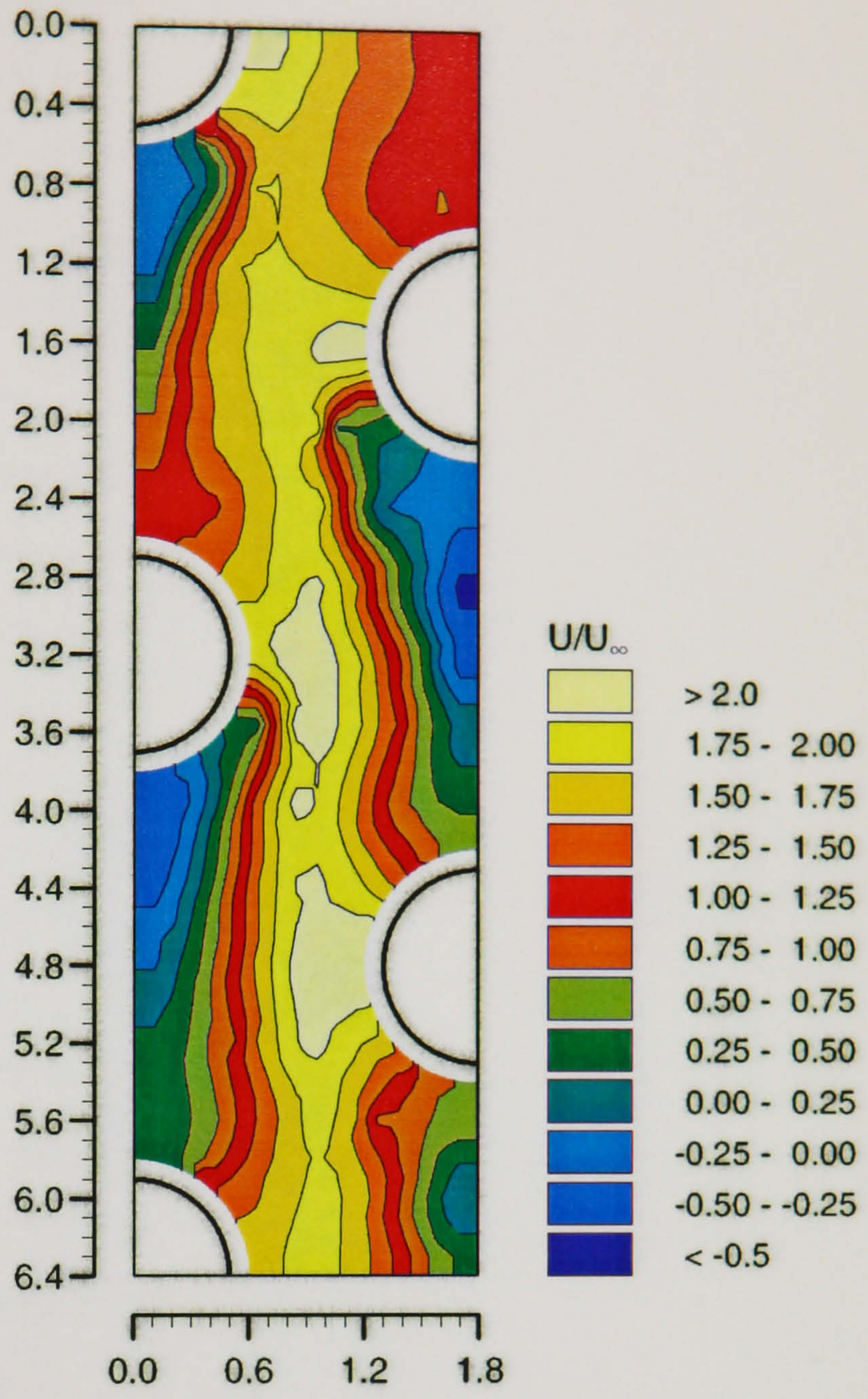

(b) U/U_∞ contours

Figure 5.4. Distribution of axial mean velocities, U/U_∞, in the 3.6 x 1.6 rough staggered array with randomly distributed roughness (Re_d = 12,858).

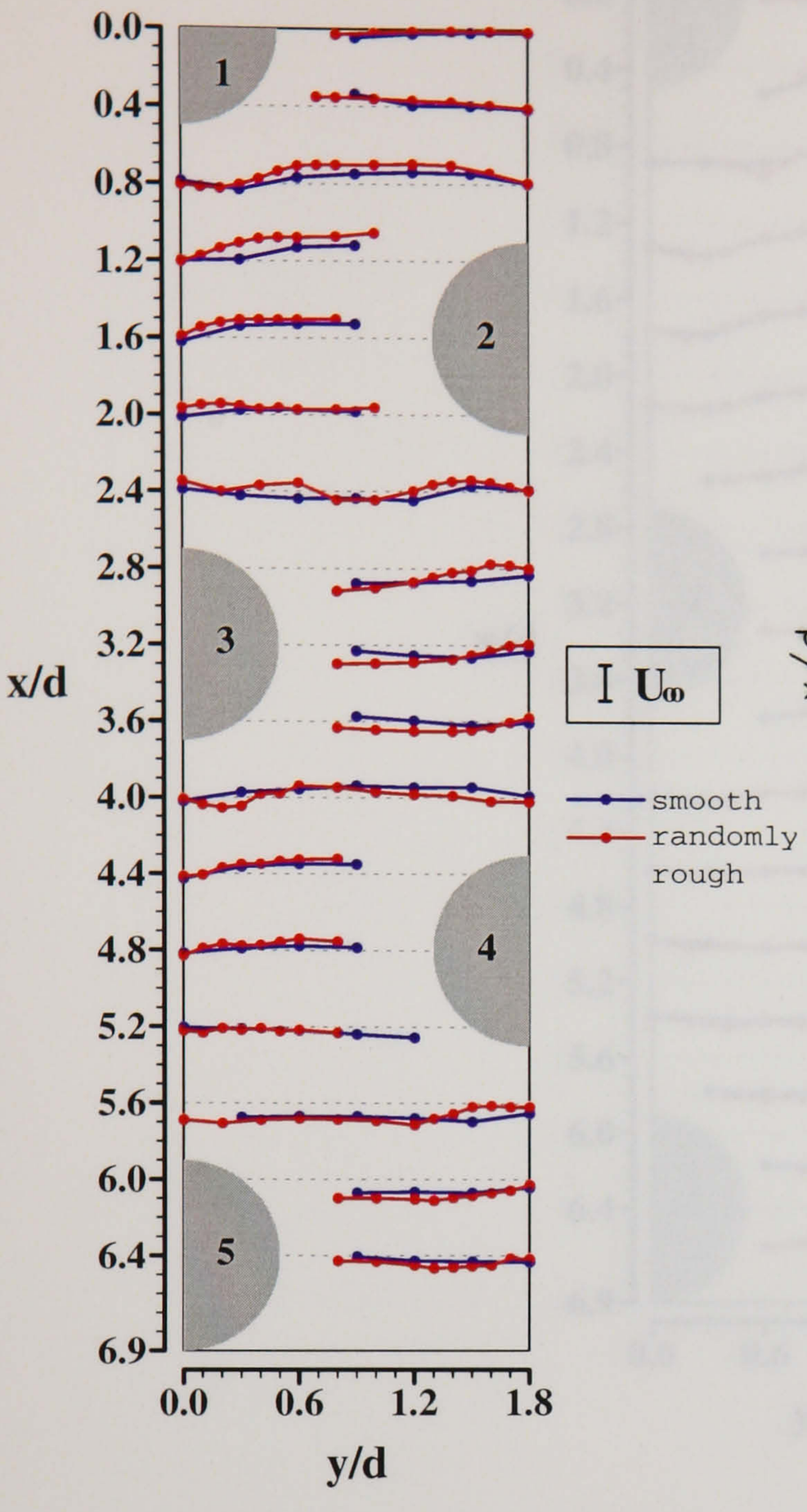

(a) V/U_∞ profiles

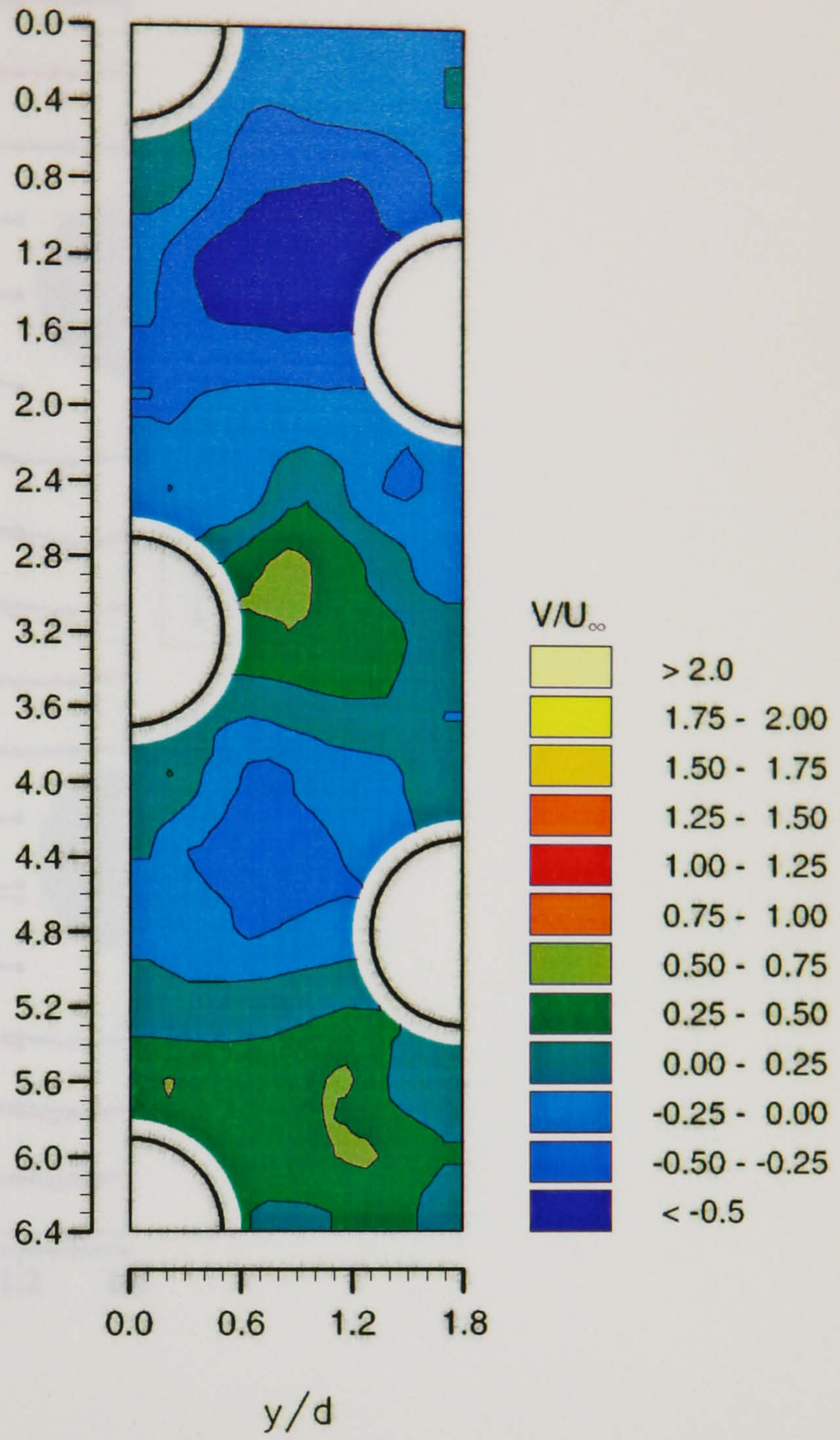

(b) V/U_∞ contours

Figure 5.5. Distribution of transverse mean velocities, V/U_∞, in the 3.6 x 1.6 rough staggered array with randomly distributed roughness (Re_d = 12,858).

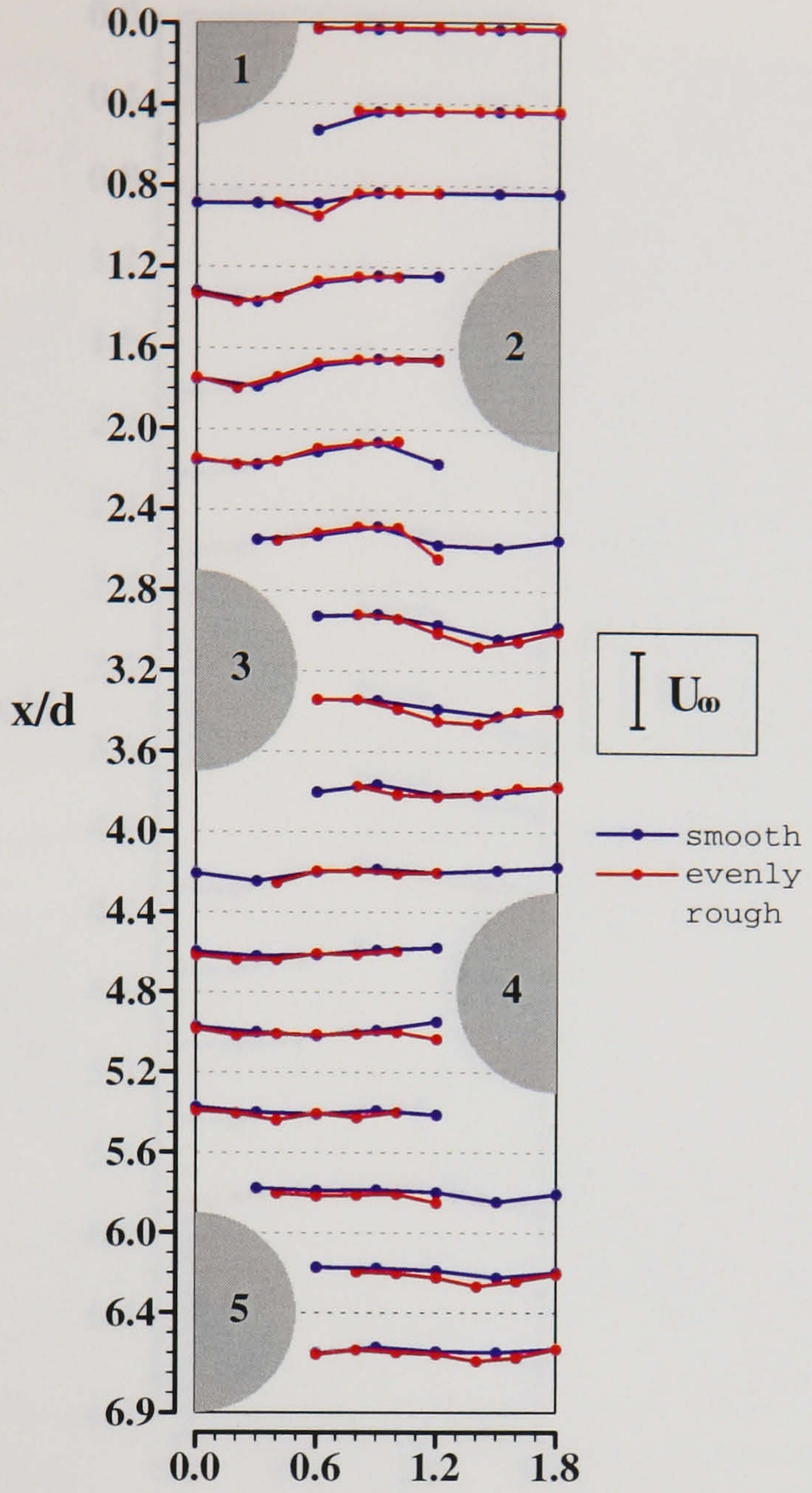

Figure 5.6. u'/U_∞ profiles in the 3.6 x 1.6 rough staggered array with evenly distributed roughness and comparison with the smooth tube array (Re_d = 12,858).

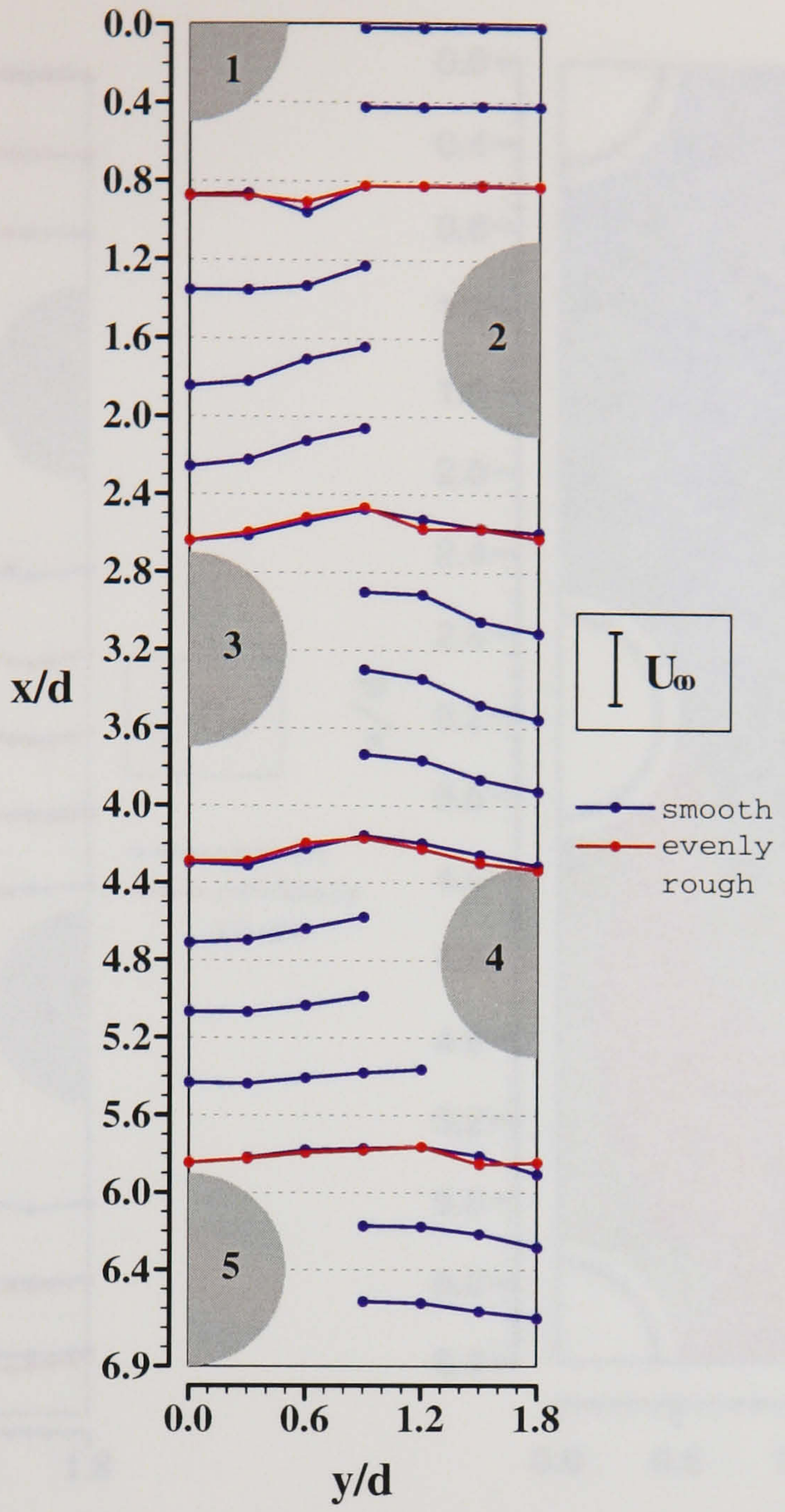

Figure 5.7. v'/U_∞ profiles in the 3.6 x 1.6 rough staggered array with evenly distributed roughness and comparison with the smooth tube array (Re_d = 12,858).

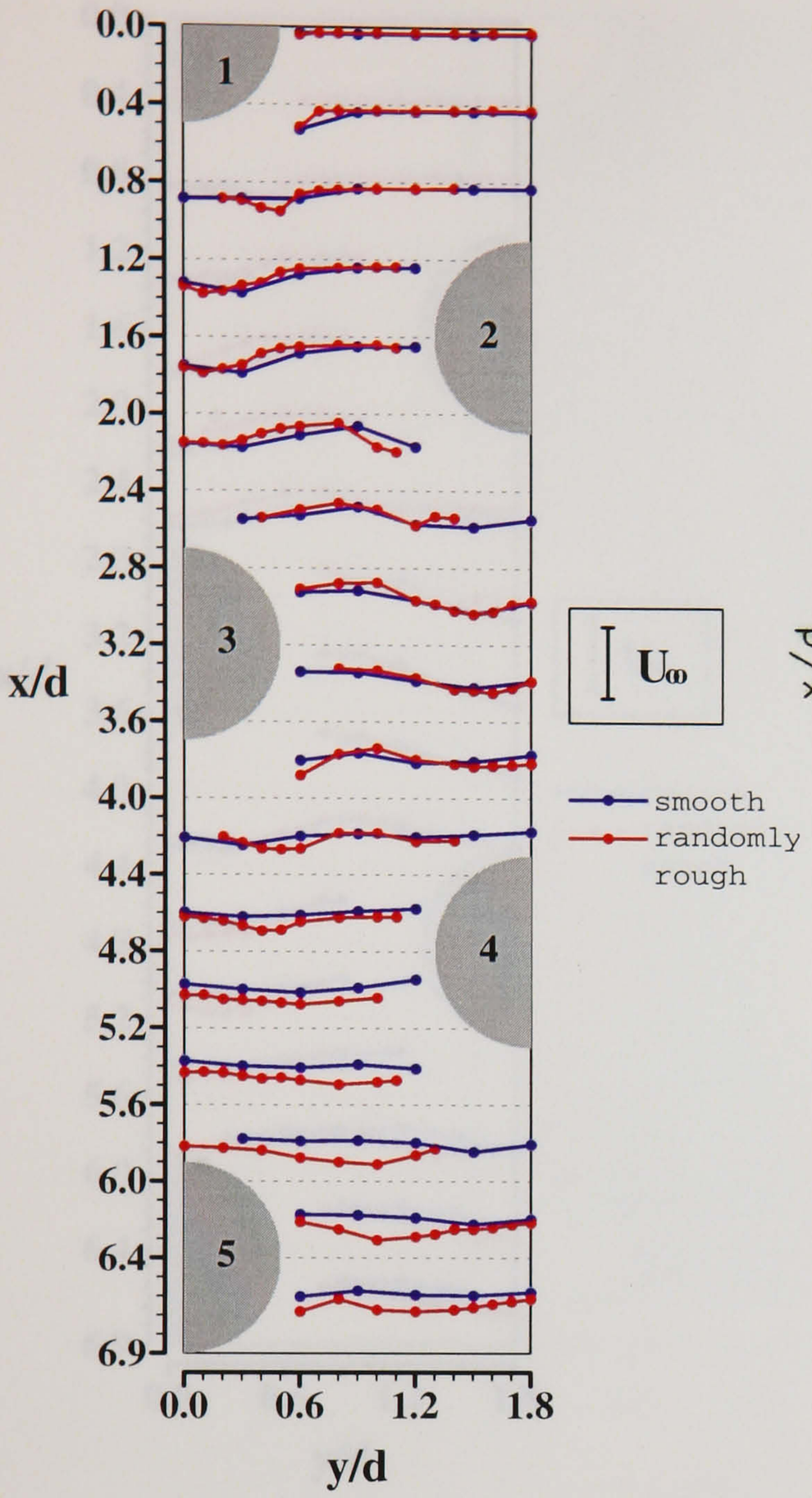

(a) u'/U_∞ profiles

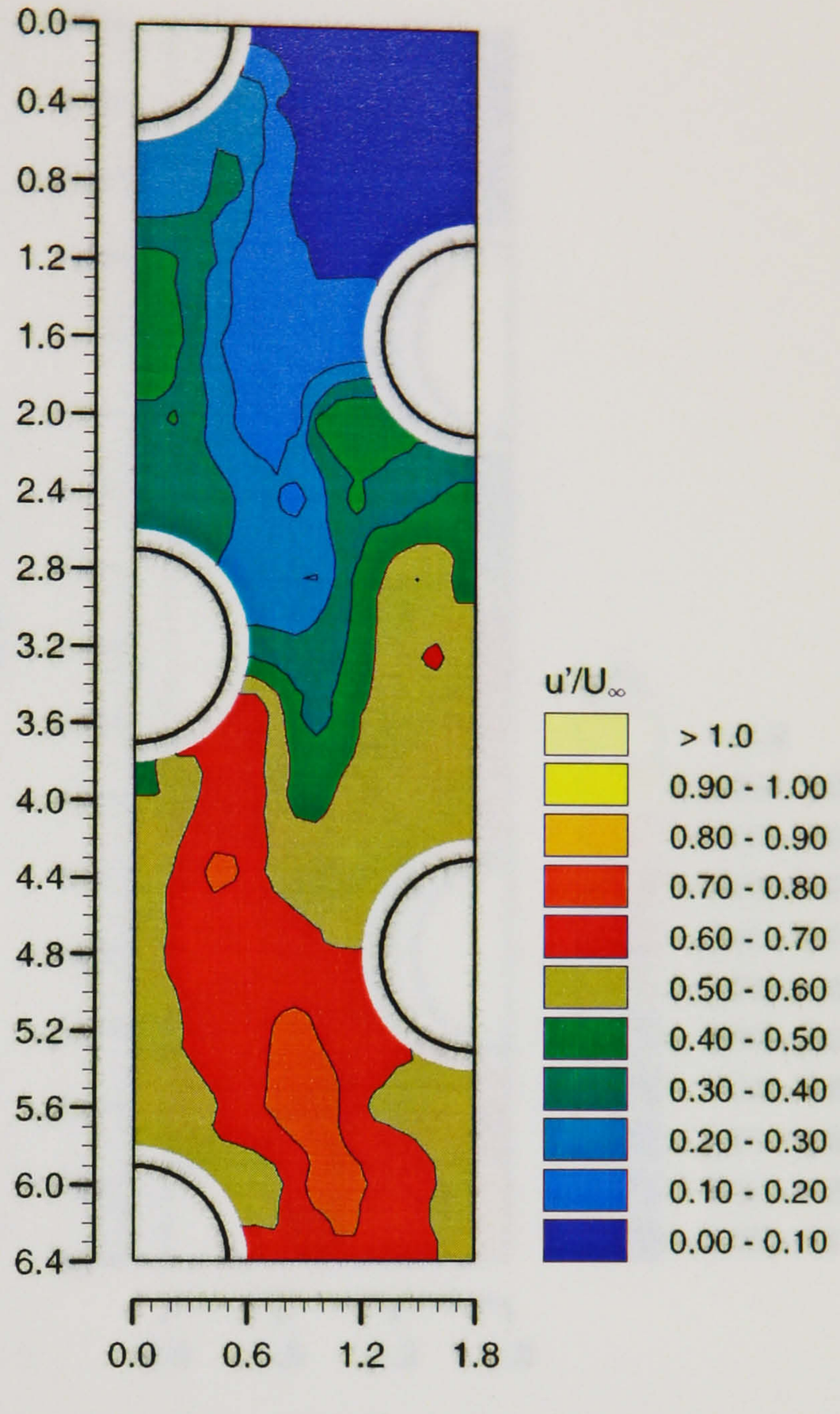

(b) u'/U_∞ contours

Figure 5.8. Distribution of axial r.m.s. velocities, u'/U_∞, in the 3.6 x 1.6 rough staggered array with randomly distributed roughness (Re_d = 12,858).

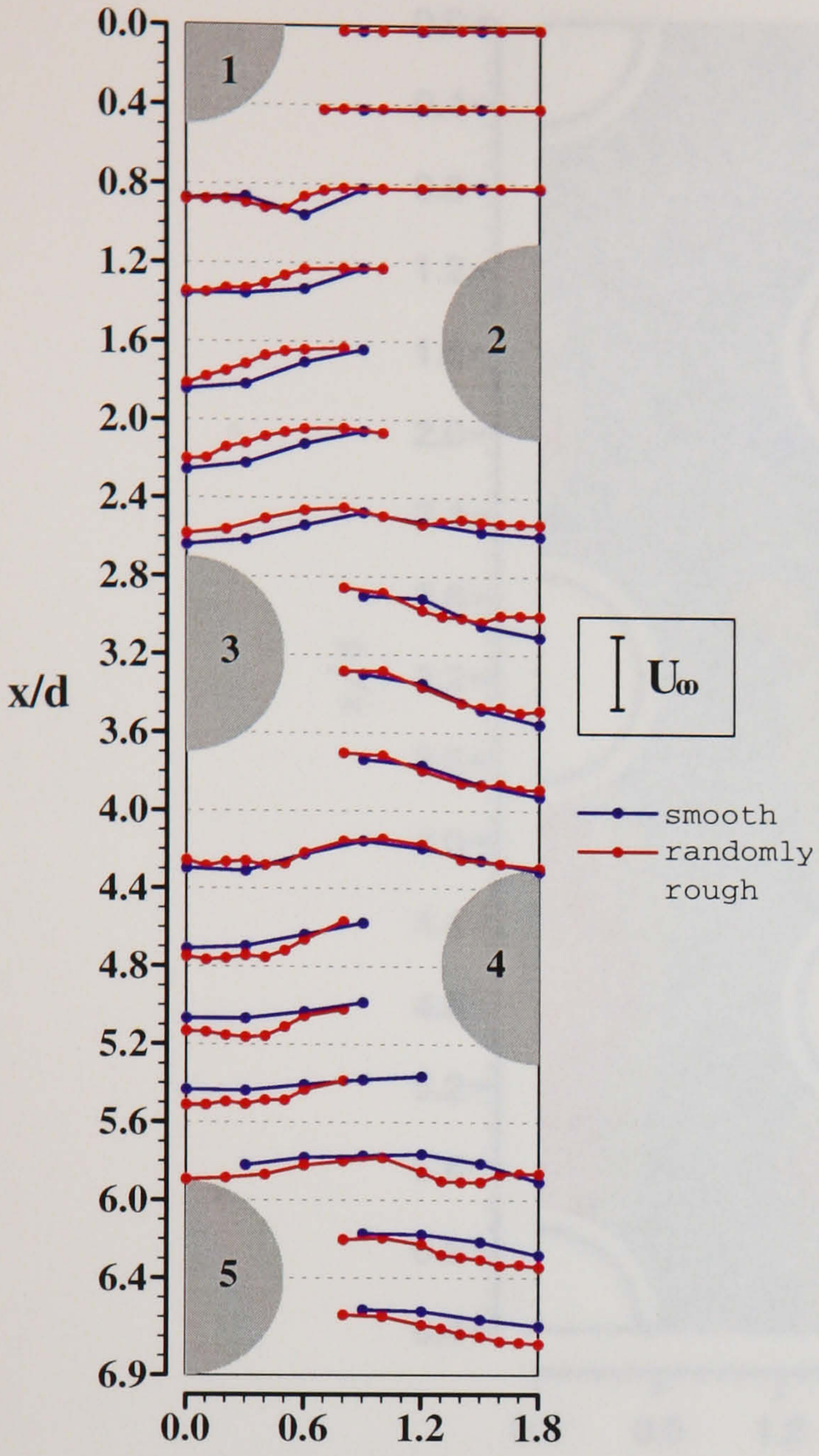

(a) v'/U_∞ profiles

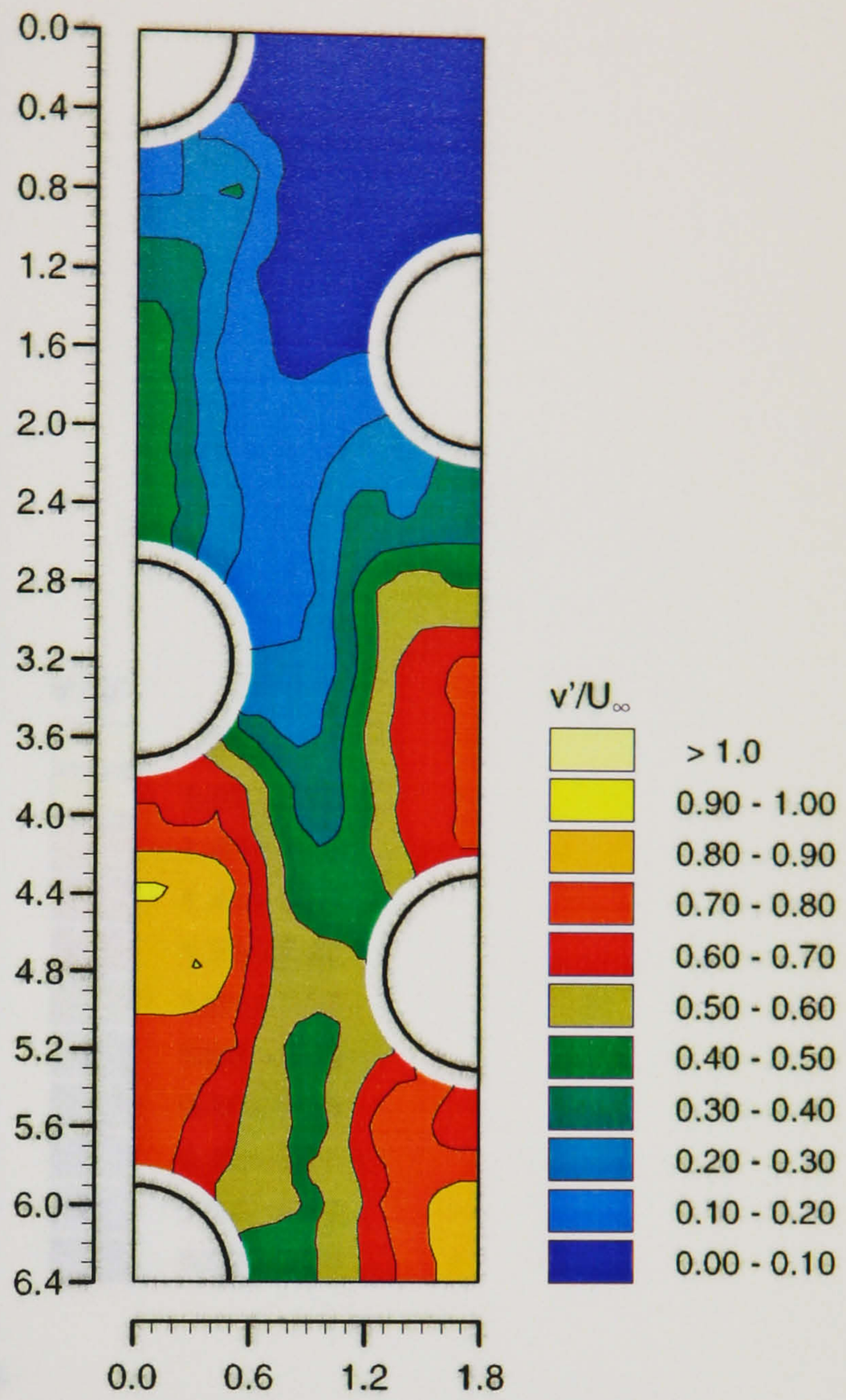

(b) v'/U_∞ contours

Figure 5.9. Distribution of transverse r.m.s. velocities, v'/U_∞, in the 3.6 x 1.6 rough staggered array with randomly distributed roughness (Re_d = 12,858).

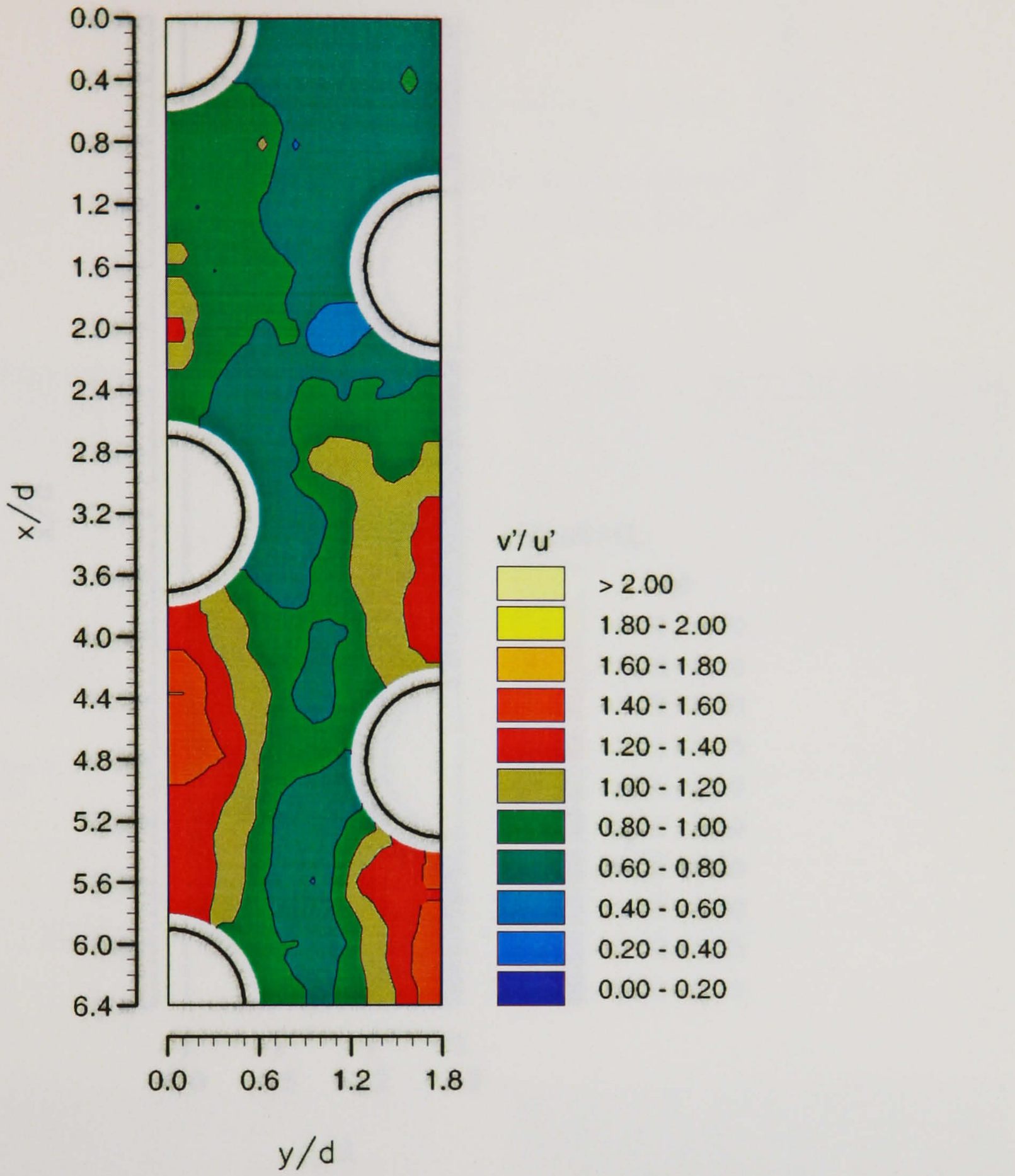

Figure 5.10. Distribution of v'/u' in the 3.6 x 1.6 rough staggered array with randomly distributed roughness (Re_d = 12,858).

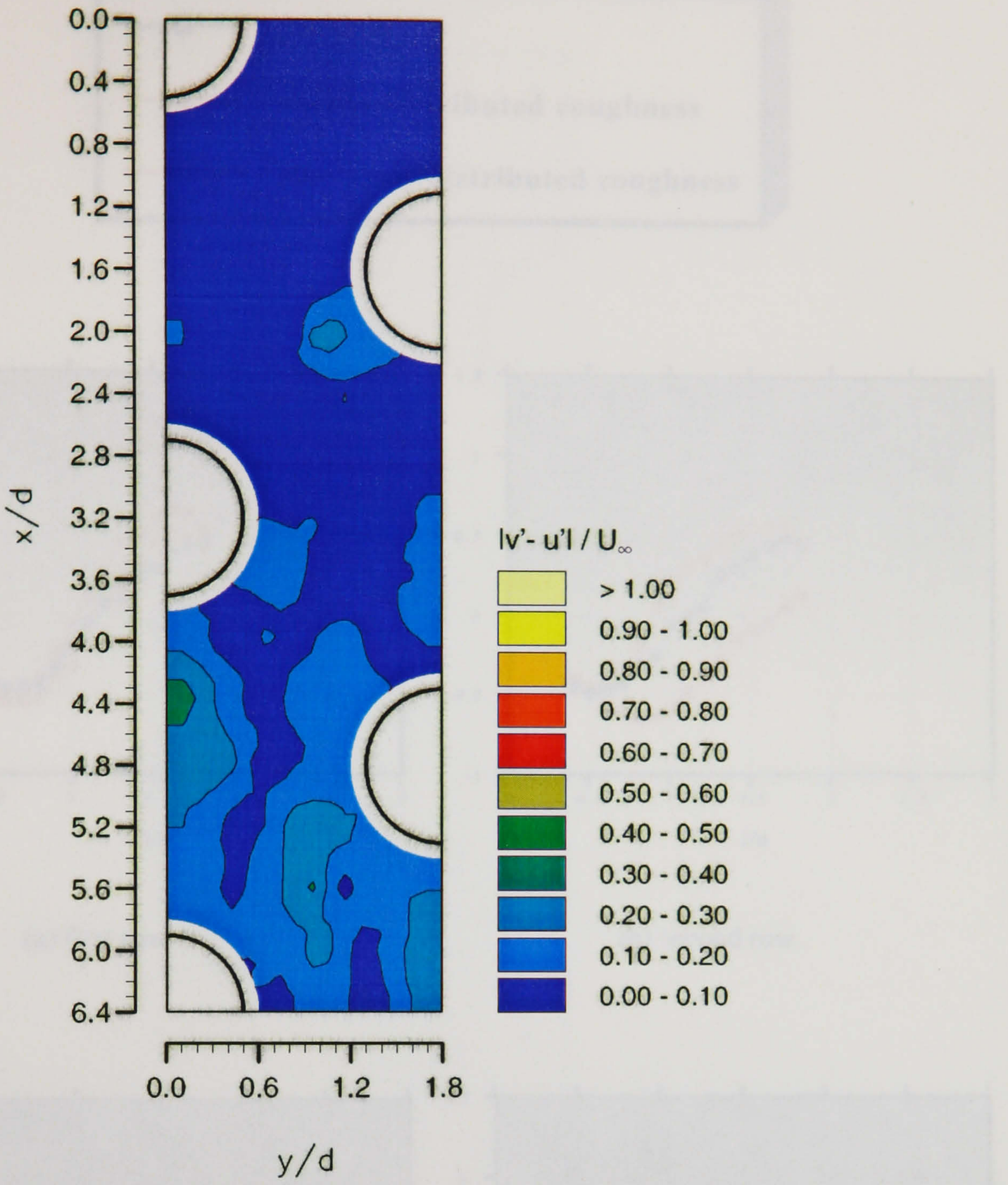

Figure 5.11. Distribution of $|v'-u'| / U_\infty$ in the 3.6 x 1.6 rough staggered array with randomly distributed roughness (Re_d = 12,858).

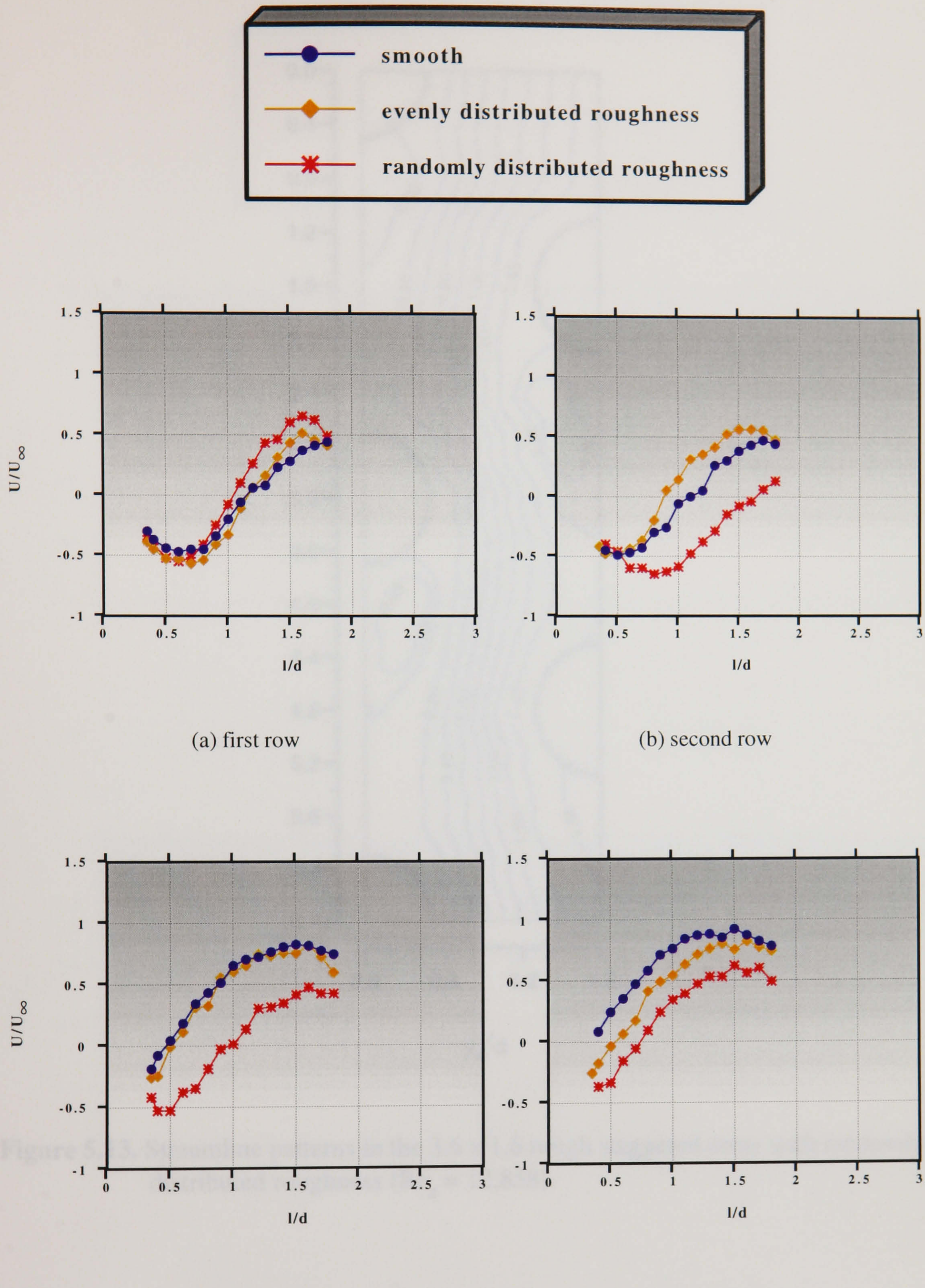

(a) first row

(b) second row

(c) third row

(d) fourth row

Figure 5.12. Comparison of the centreline U/U_∞ profiles between the smooth and rough staggered arrays (Re_d = 12,858).

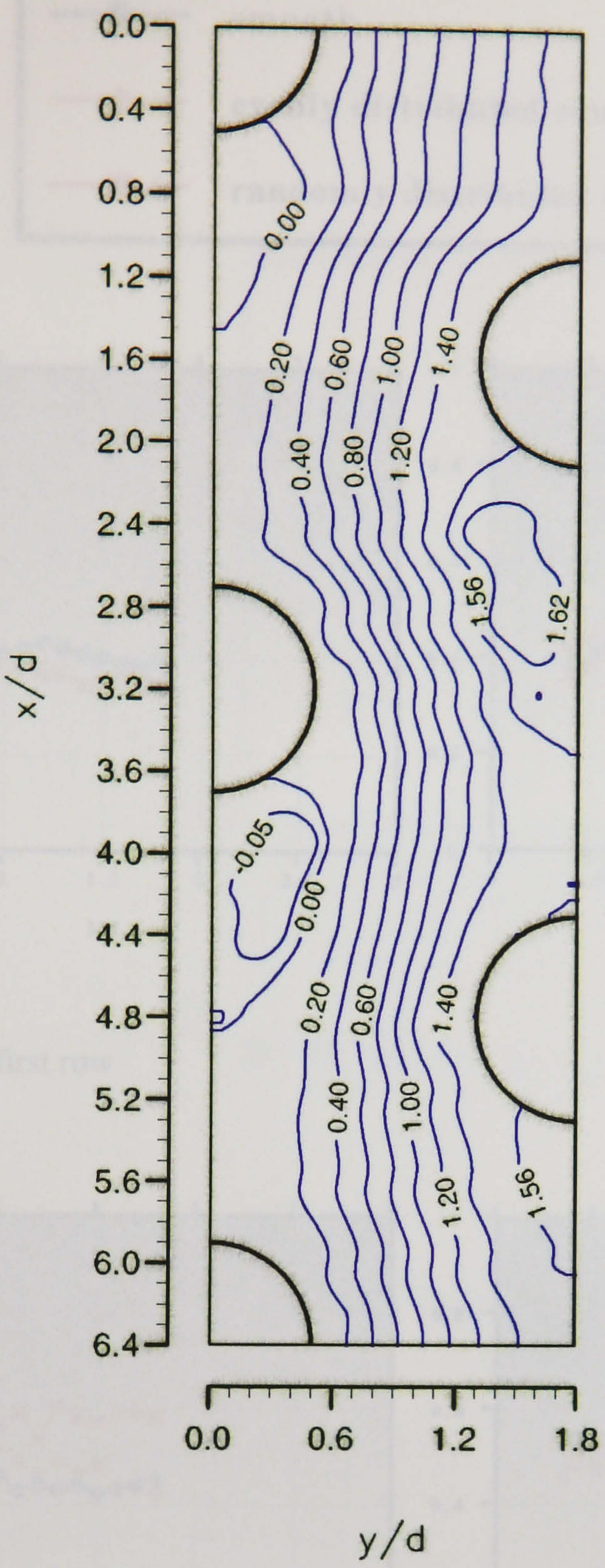

Figure 5.13. Streamline patterns in the 3.6 x 1.6 rough staggered array with randomly distributed roughness (Re_d = 12,858).

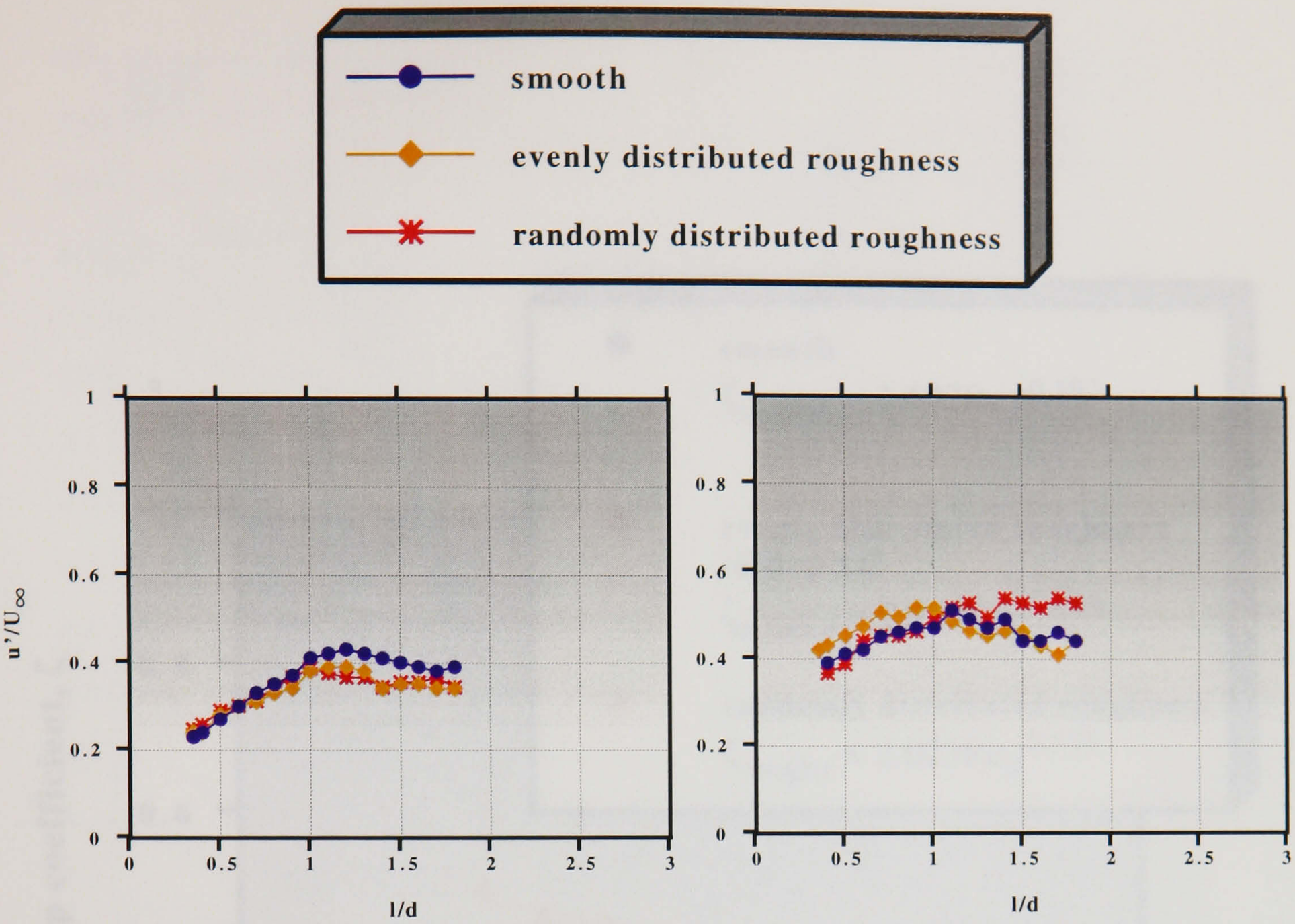

(a) first row

(b) second row

(c) third row

(d) fourth row

Figure 5.14. Comparison of the centreline u'/U_∞ profiles between the smooth and rough staggered arrays (Re_d = 12,858).

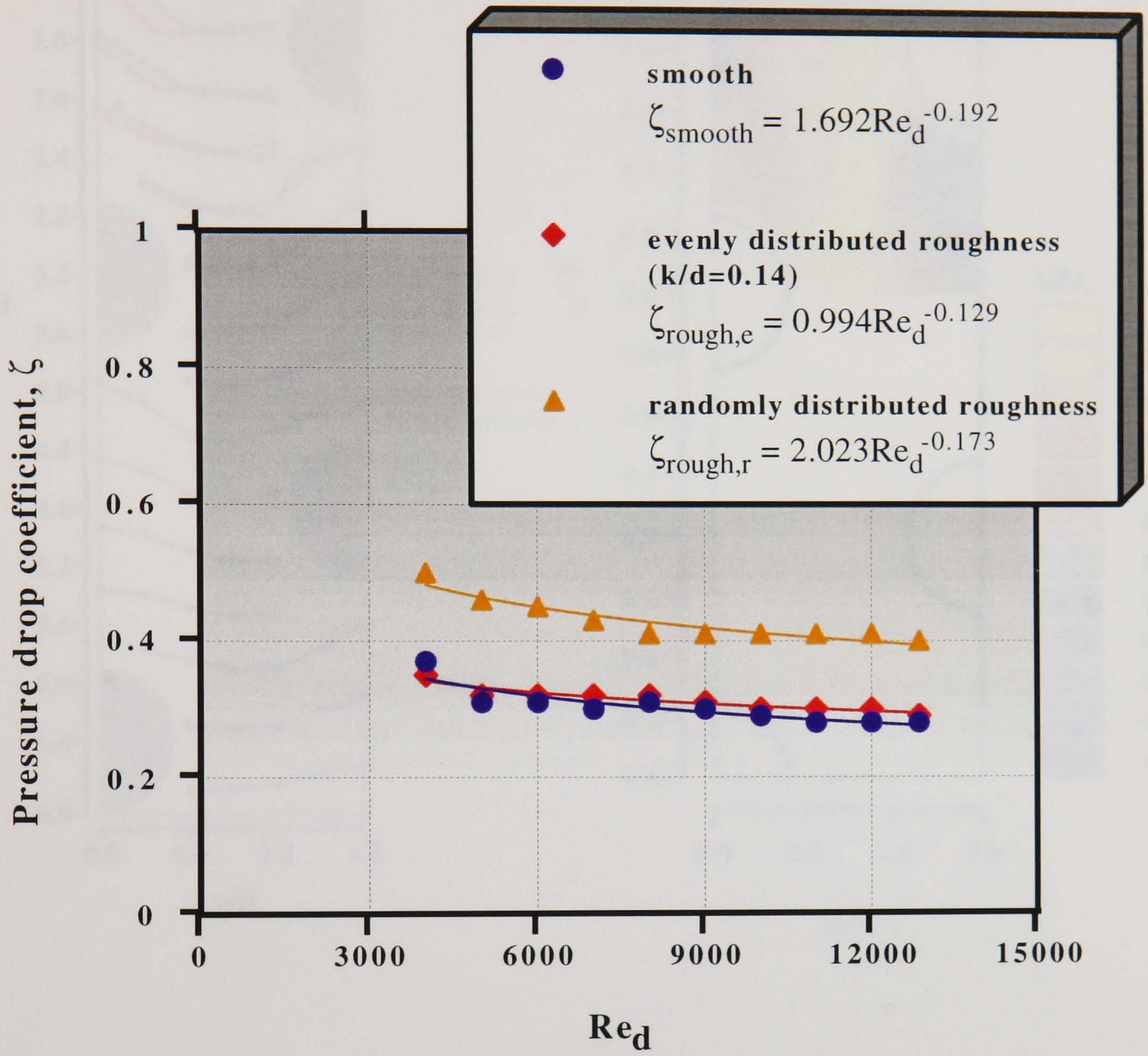

Figure 5.15. The effect of tube surface roughness on the pressure drop across the 3.6 x 1.6 staggered array.

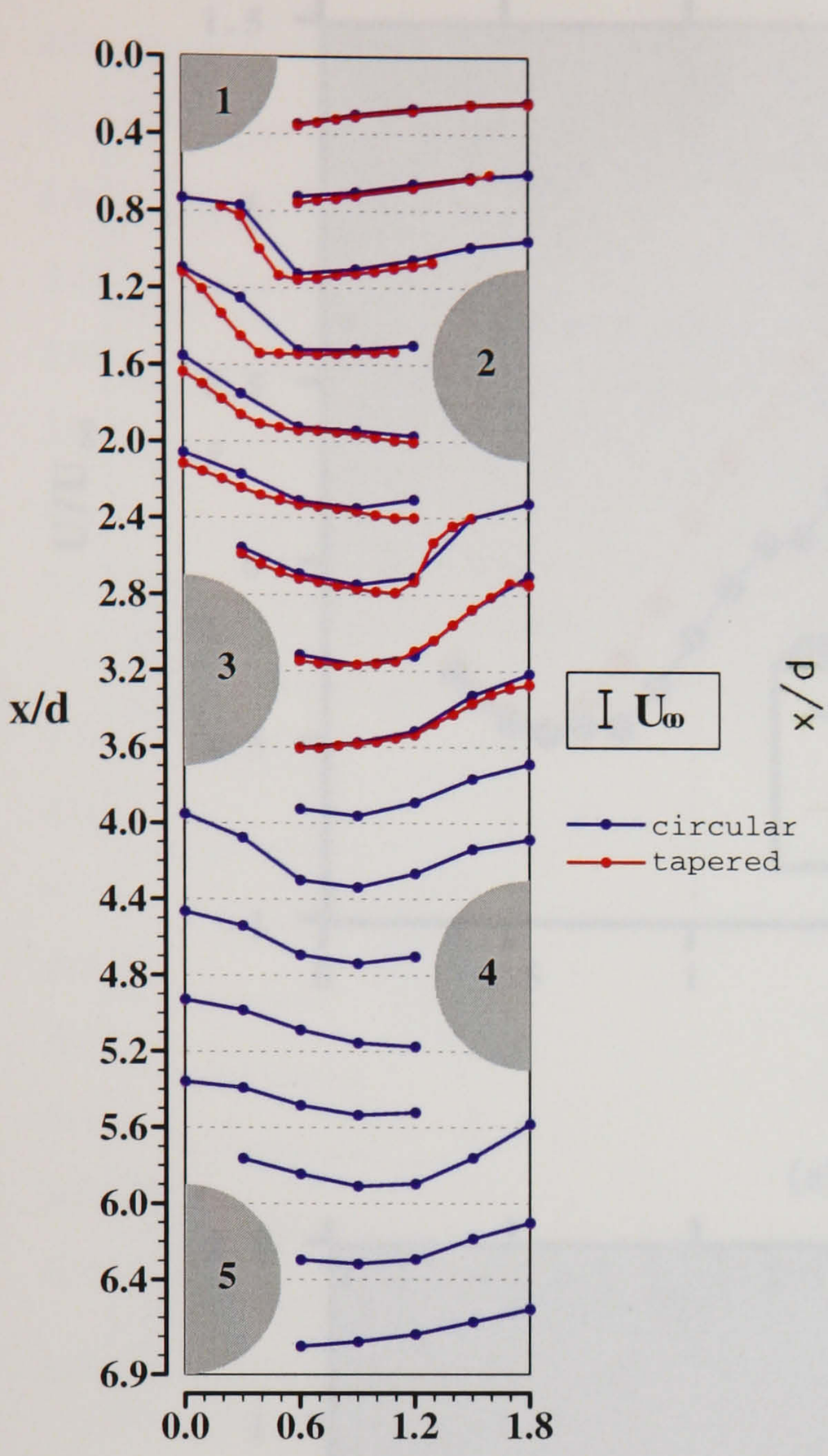

(a) U/U_∞ profiles

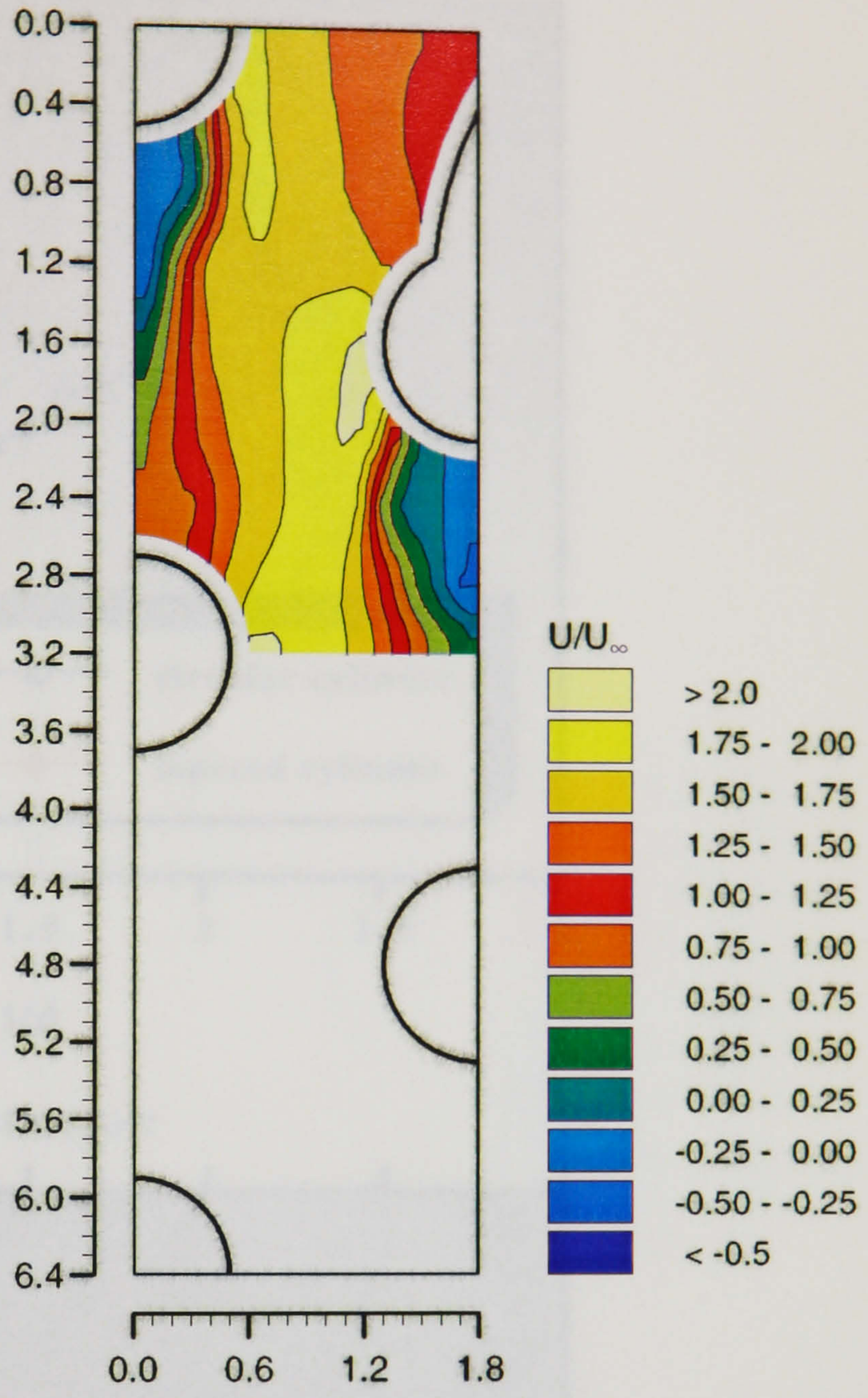

(b) U/U_∞ contours

Figure 5.16. Distribution of axial mean velocities, U/U_∞, in the 3.6 x 1.6 staggered array with tapered cylinders in the first two rows (Re_d = 12,858).

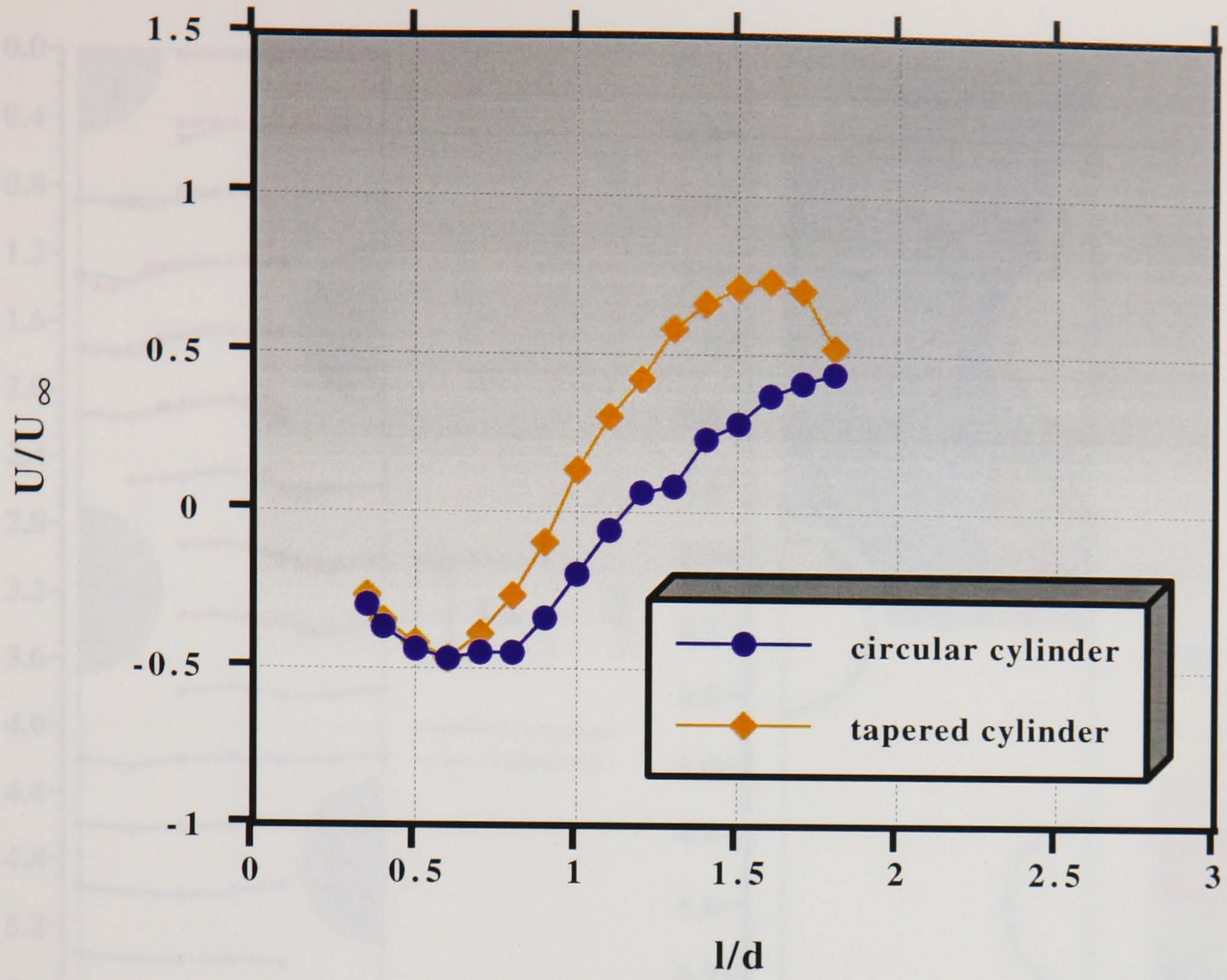

(a) first row

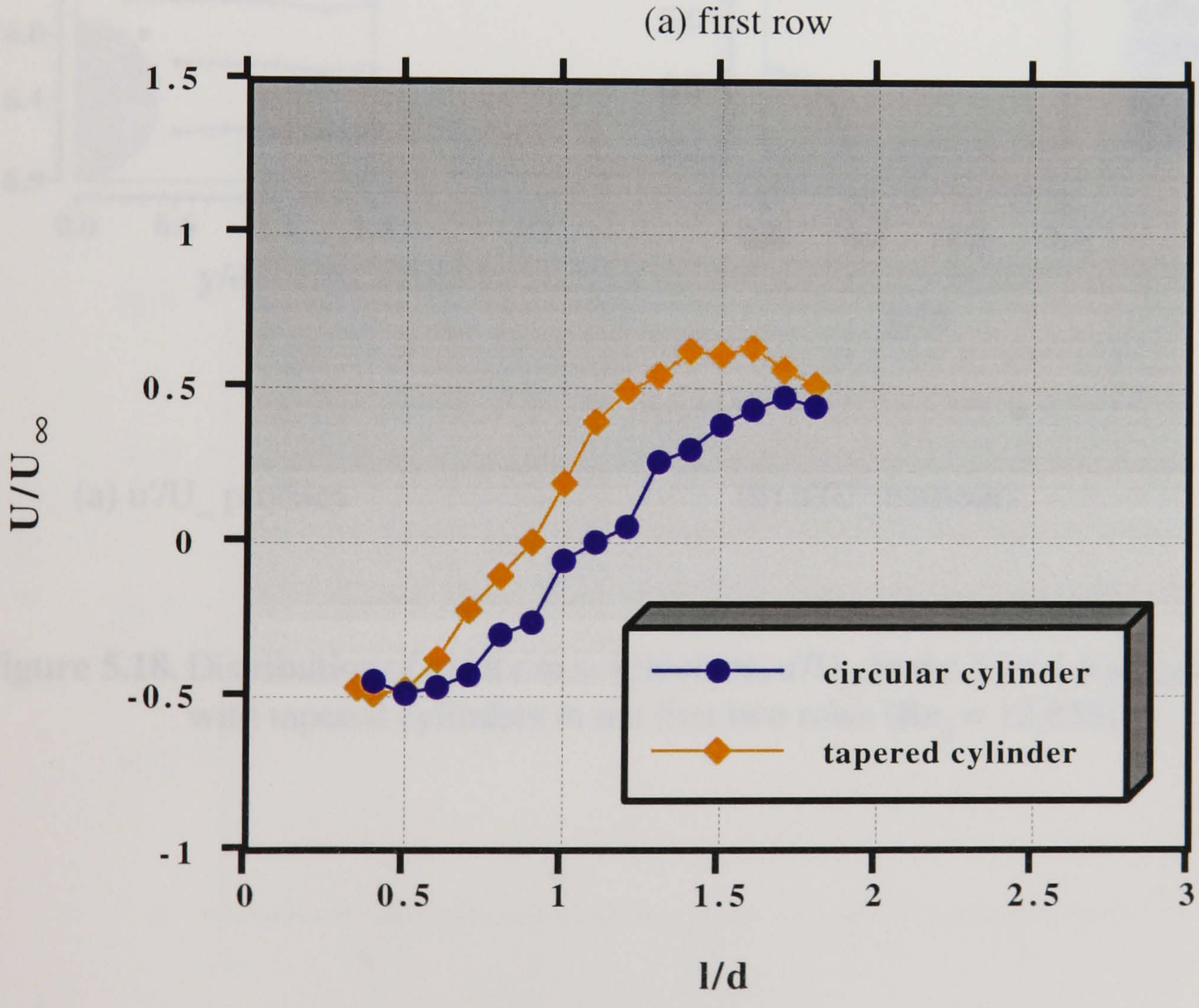

(b) second row

Figure 5.17. Centreline development of U/U_∞ in the 3.6 x 1.6 staggered array with tapered cylinders in the first two rows and comparison with circular cylinders (Re_d = 12,858).

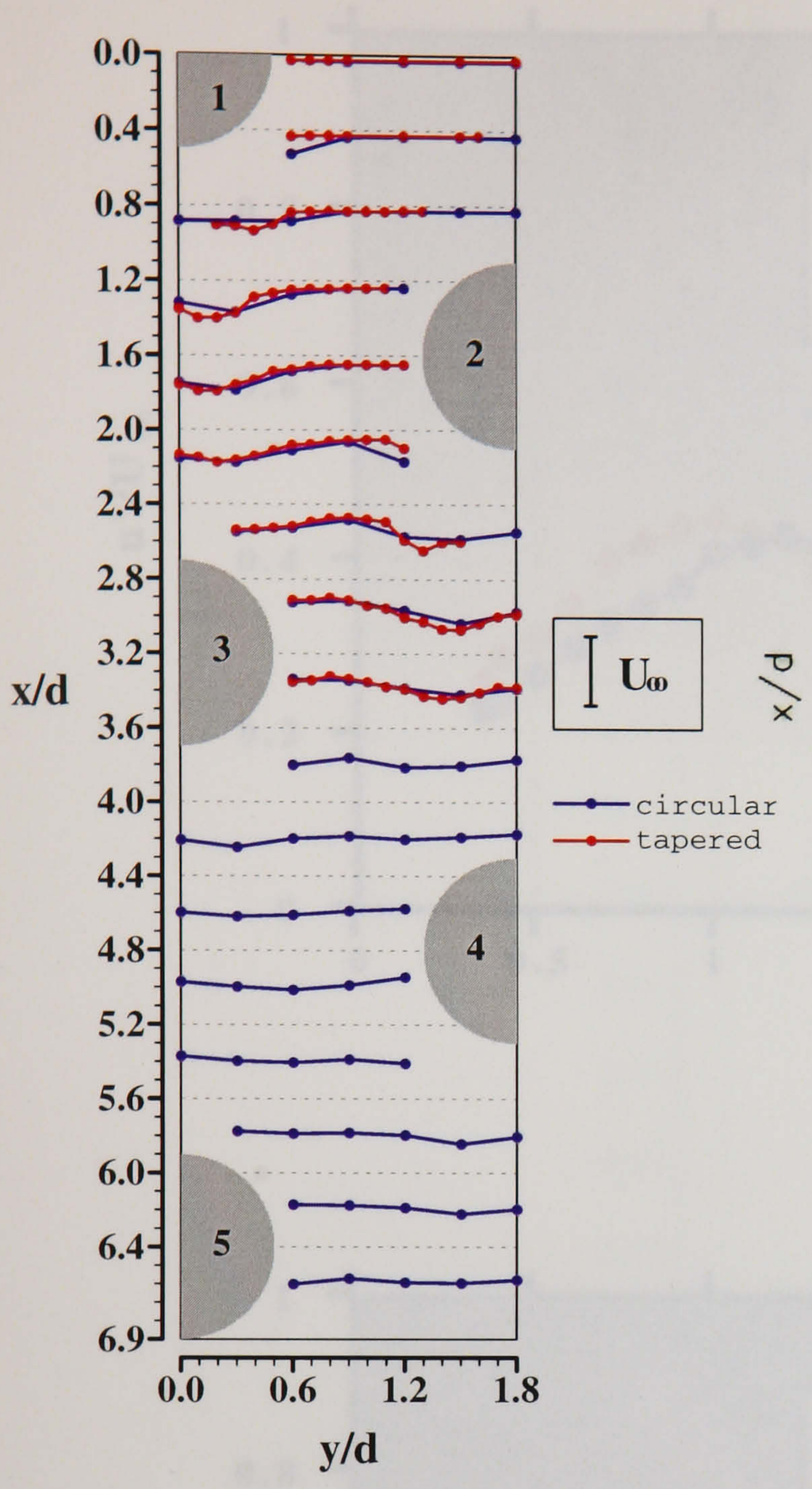

(a) u'/U_∞ profiles

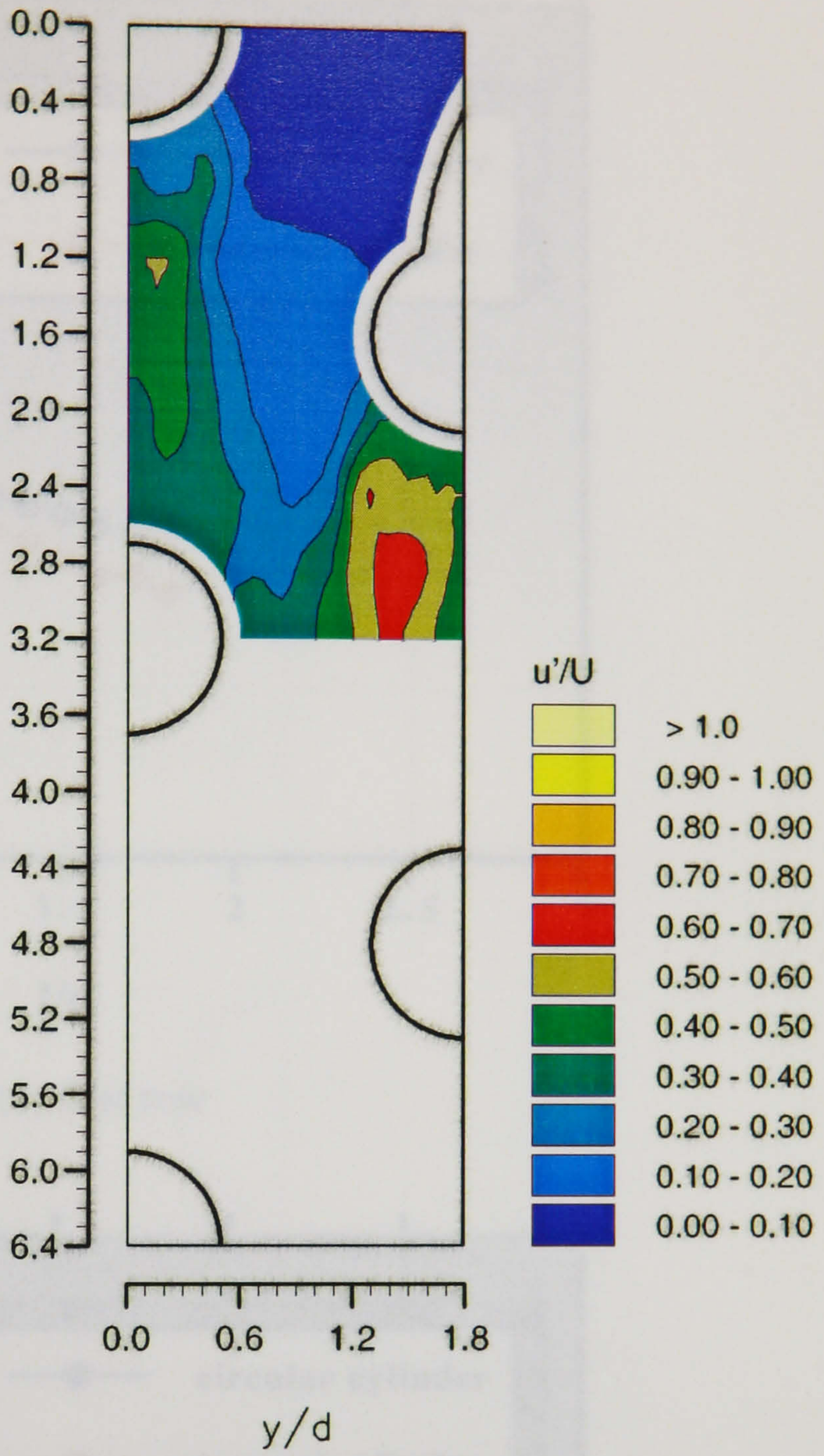

(b) u'/U_∞ contours

Figure 5.18. Distribution of axial r.m.s. velocities, u'/U_∞, in the 3.6 x 1.6 staggered array with tapered cylinders in the first two rows (Re_d = 12,858).

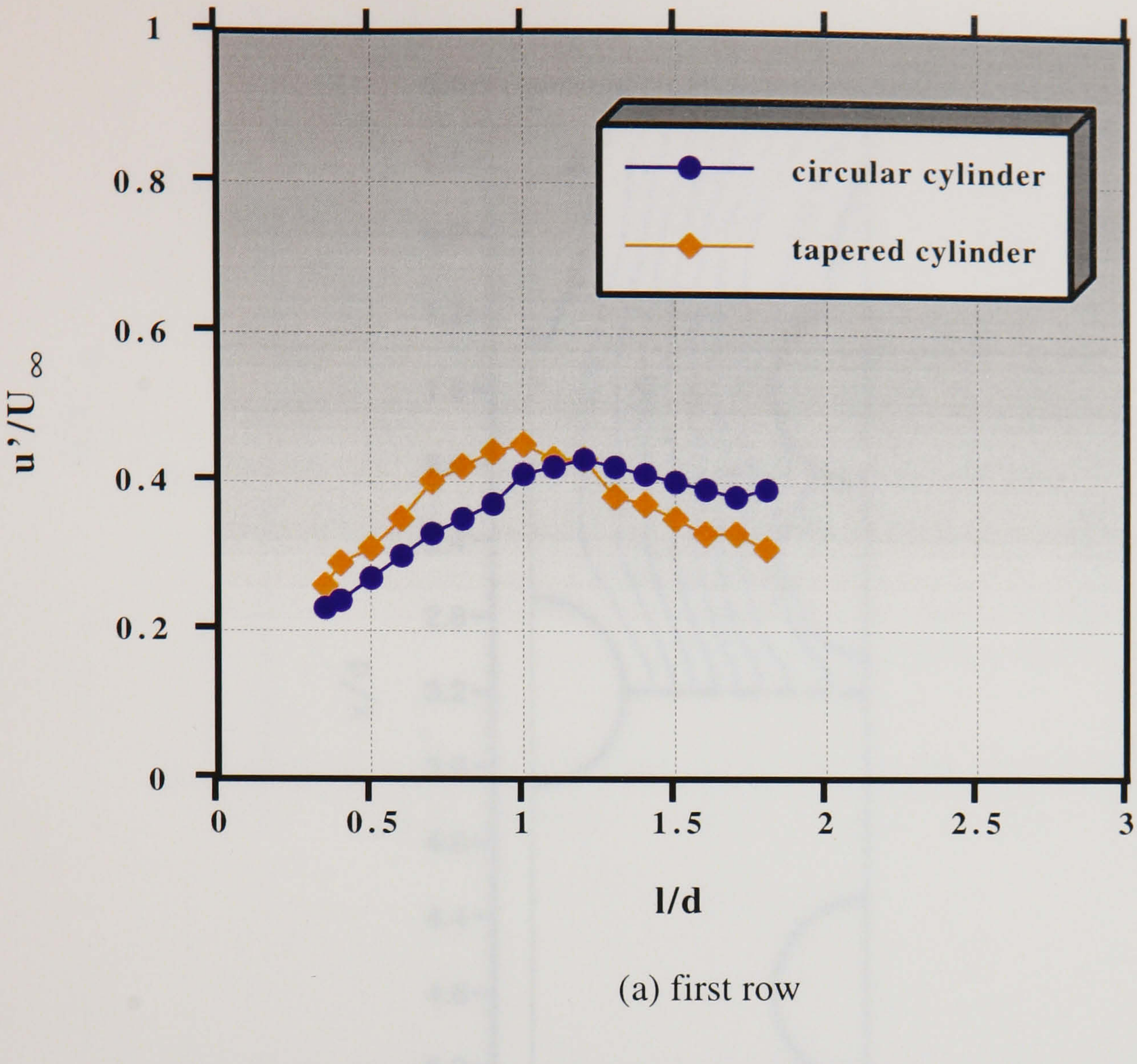

(a) first row

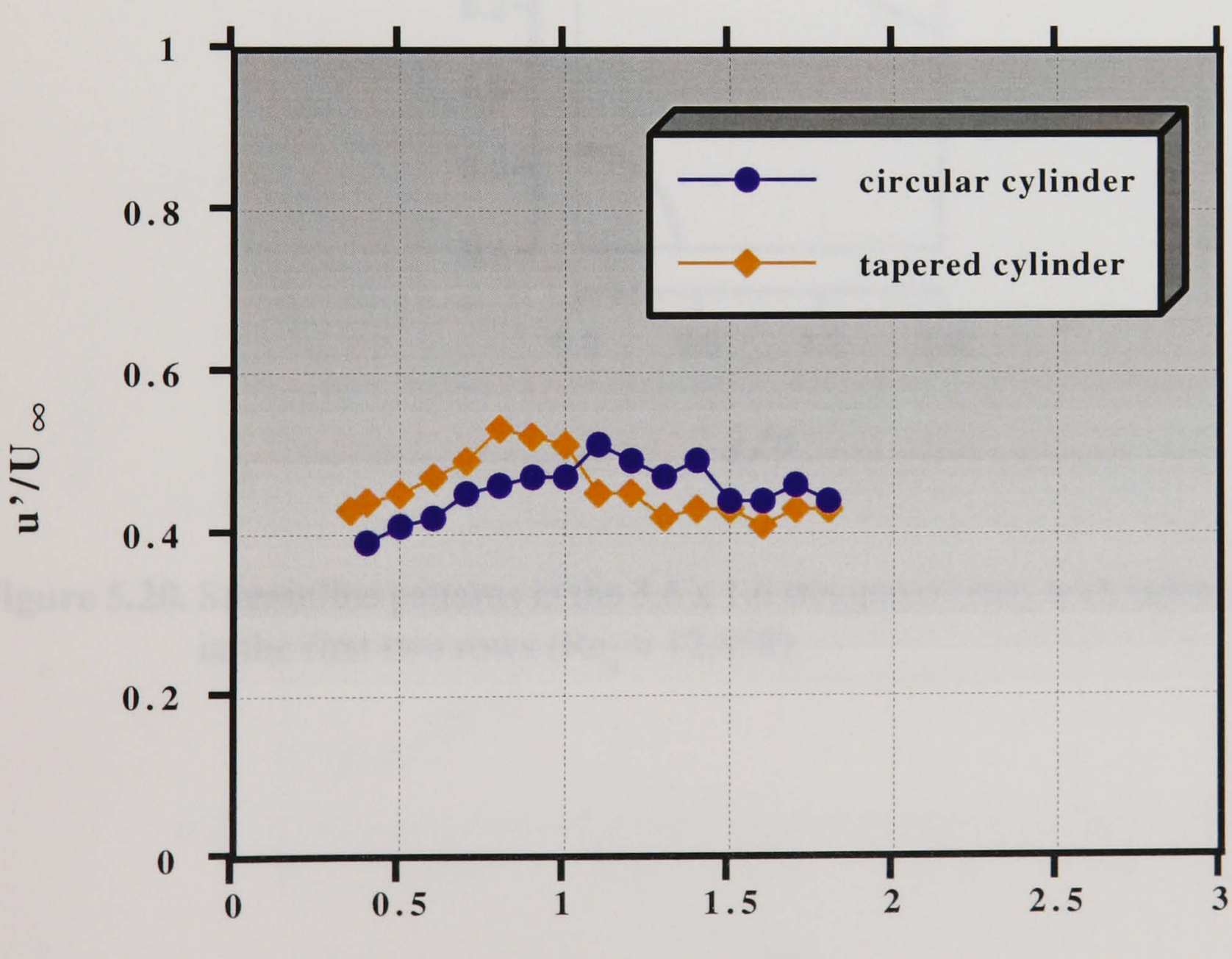

(b) second row

Figure 5.19. Centreline development of u'/U_∞ in the 3.6 x 1.6 staggered array with tapered cylinders in the first two rows and comparison with circular cylinders (Re_d = 12,858).

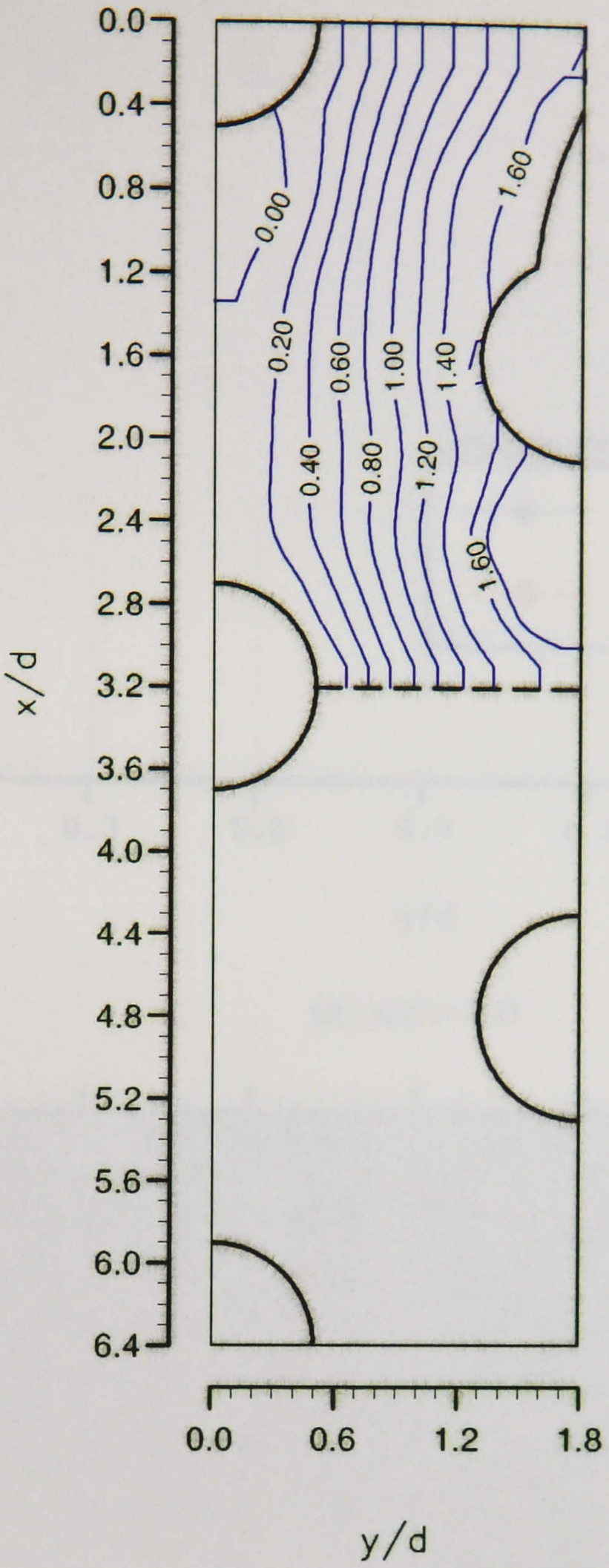

Figure 5.20. Streamline patterns in the 3.6 x 1.6 staggered array with tapered cylinders in the first two rows (Re_d = 12,858).

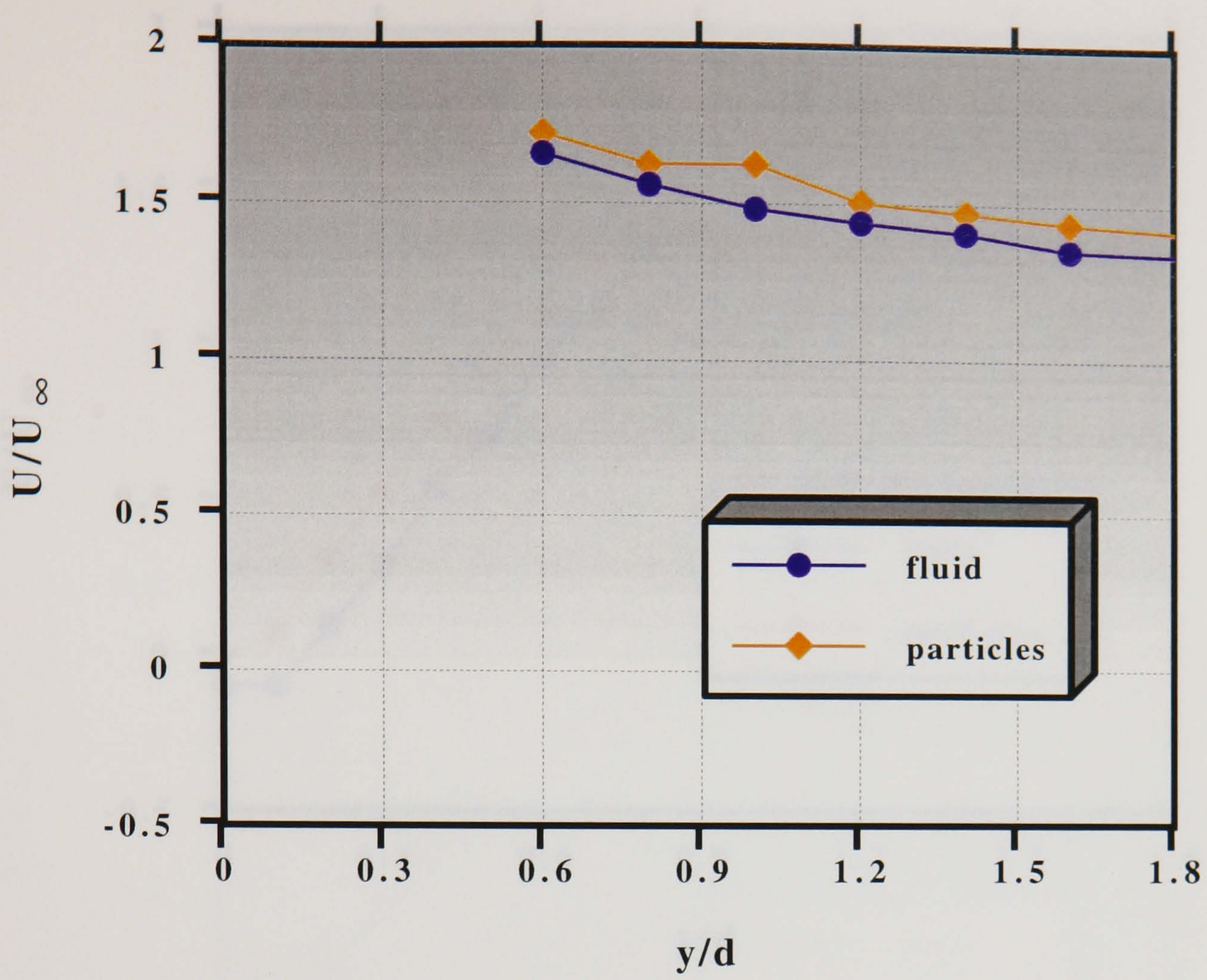

(a) x/d = 0.0

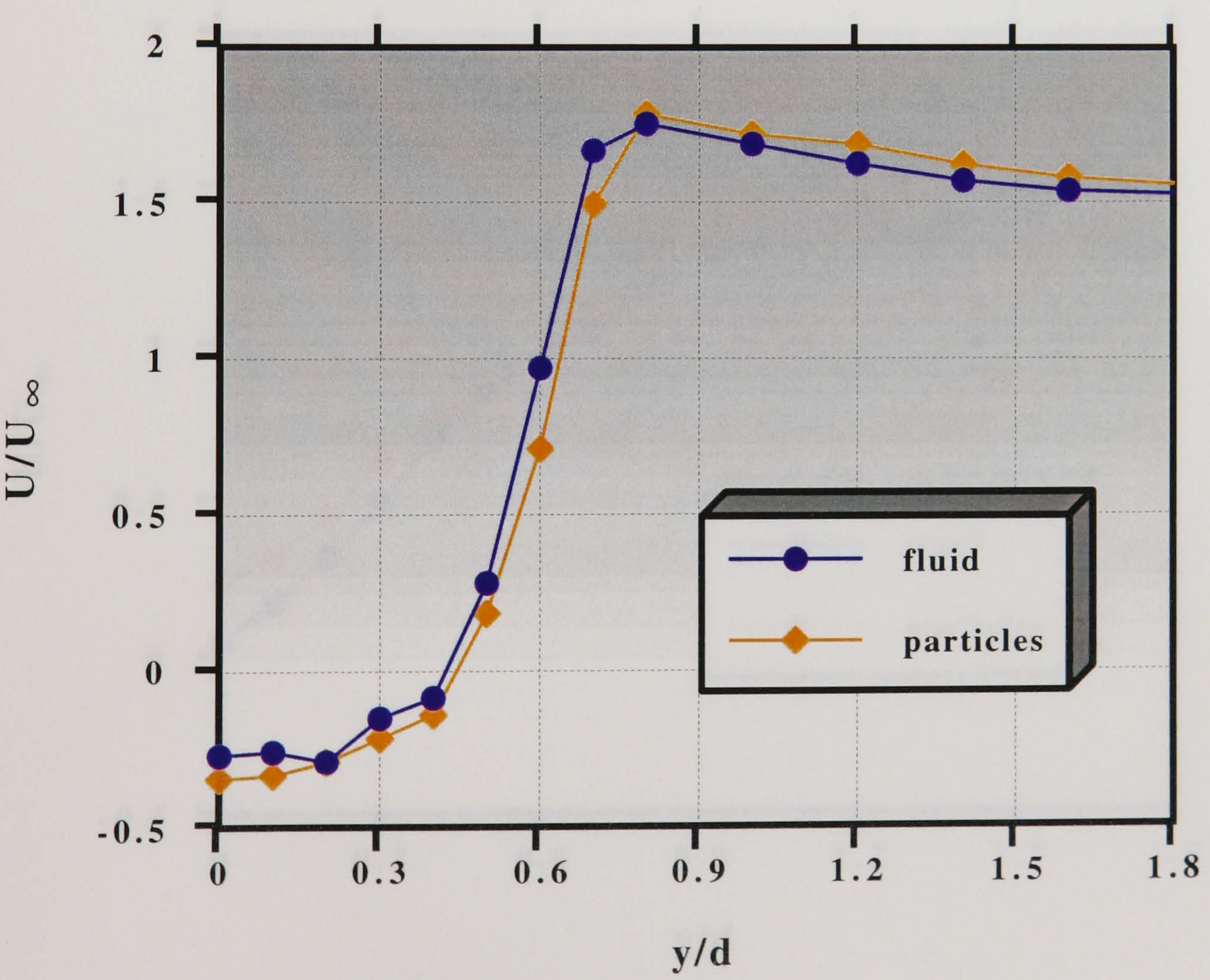

(b) x/d = 0.85

Figure 5.21. Single-phase and particle axial mean velocity profiles, U/U_∞, in the 3.6 x 2.1 in-line array (Re_d = 12,858).

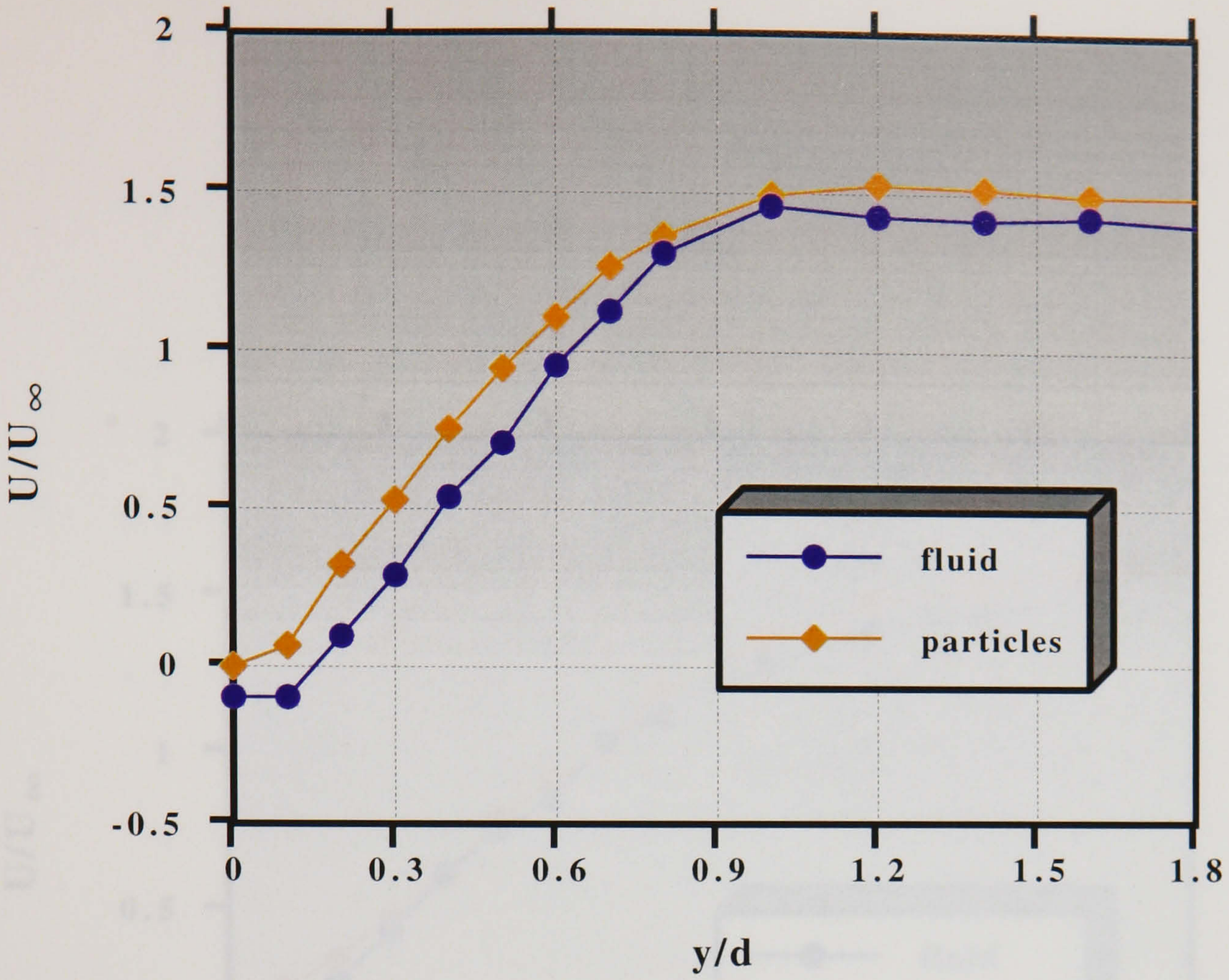

(c) x/d = 2.95

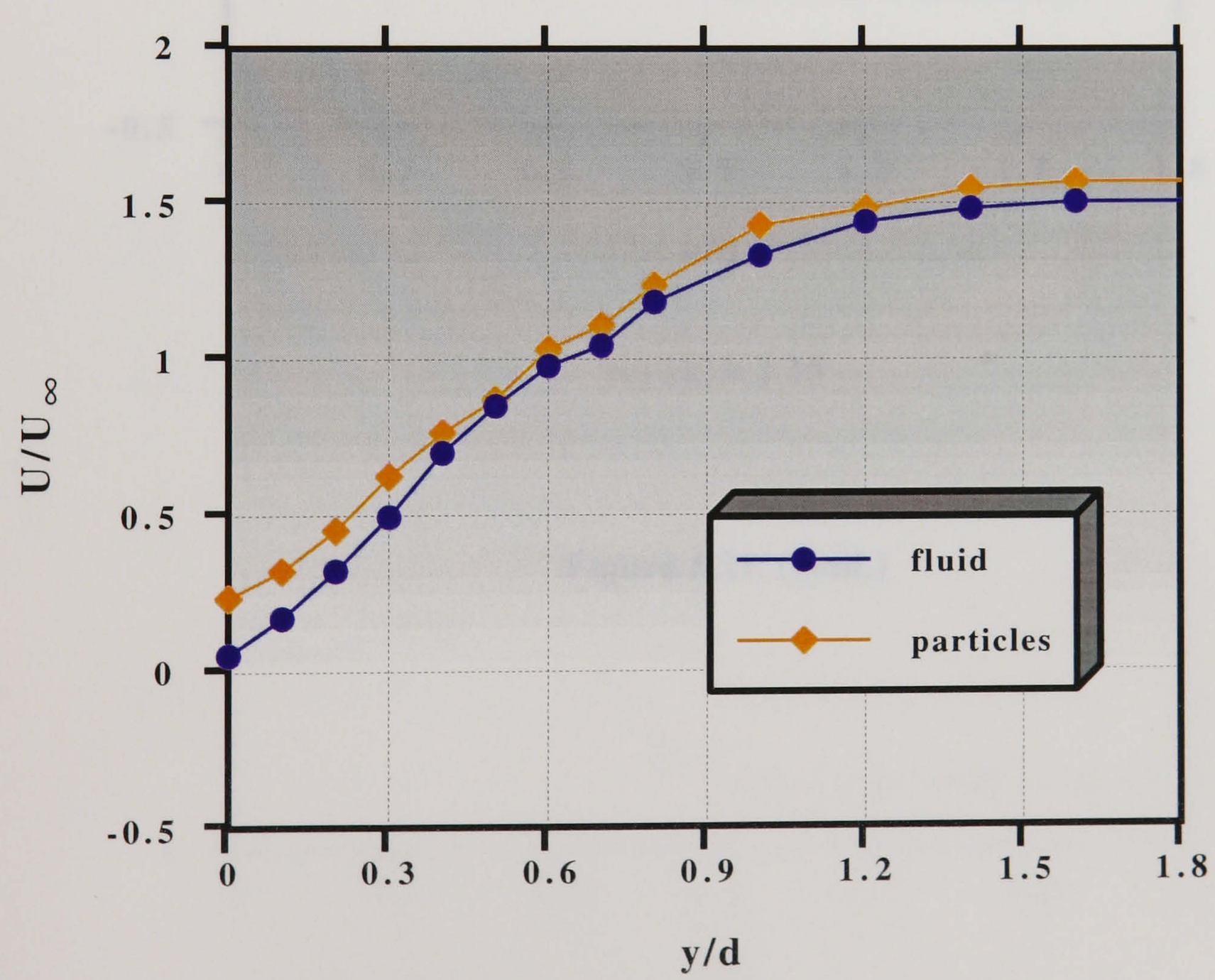

(d) x/d = 5.05

Figure 5.21. (cont.)

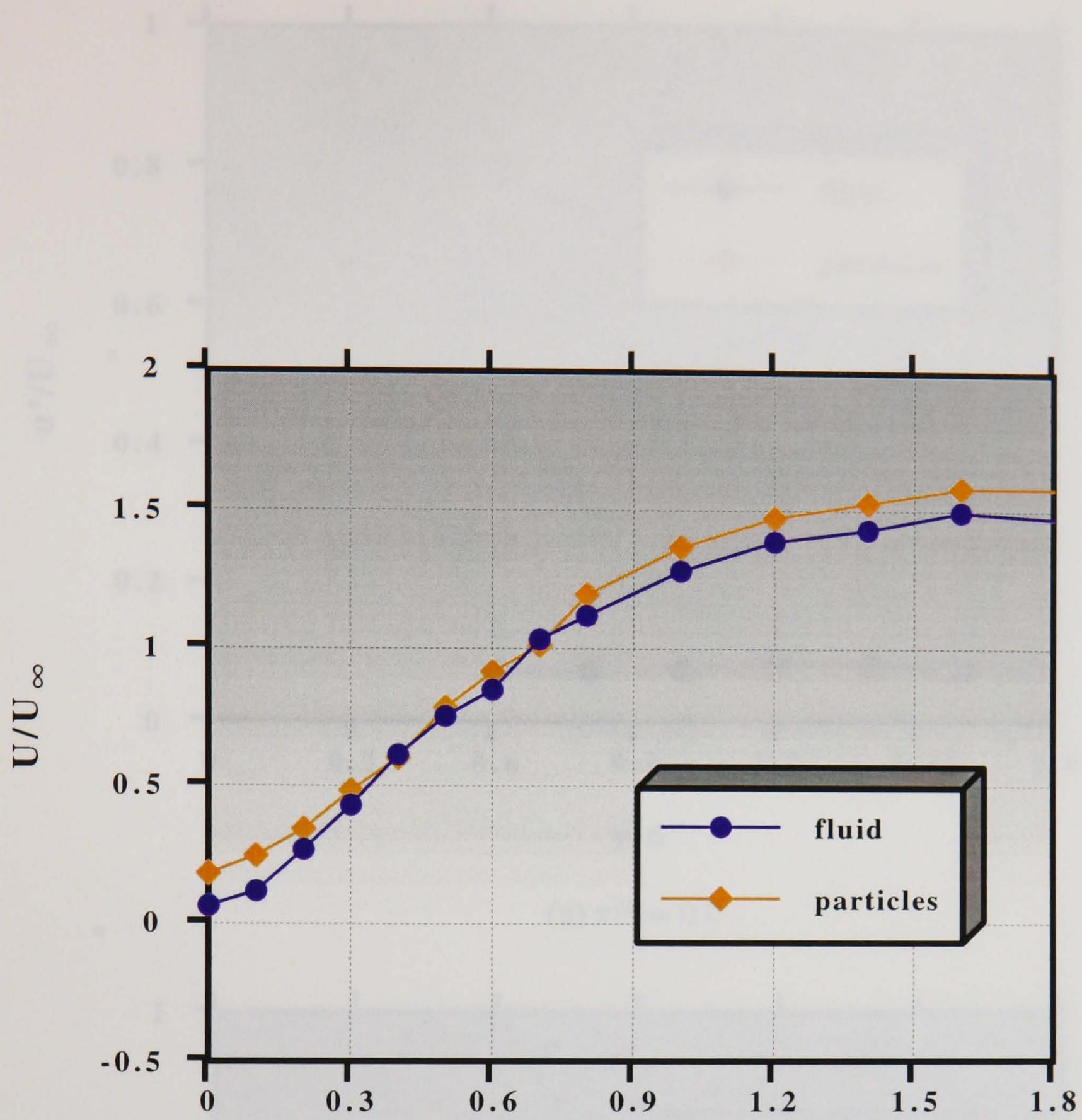

(e) x/d = 7.15

Figure 5.21. (cont.)

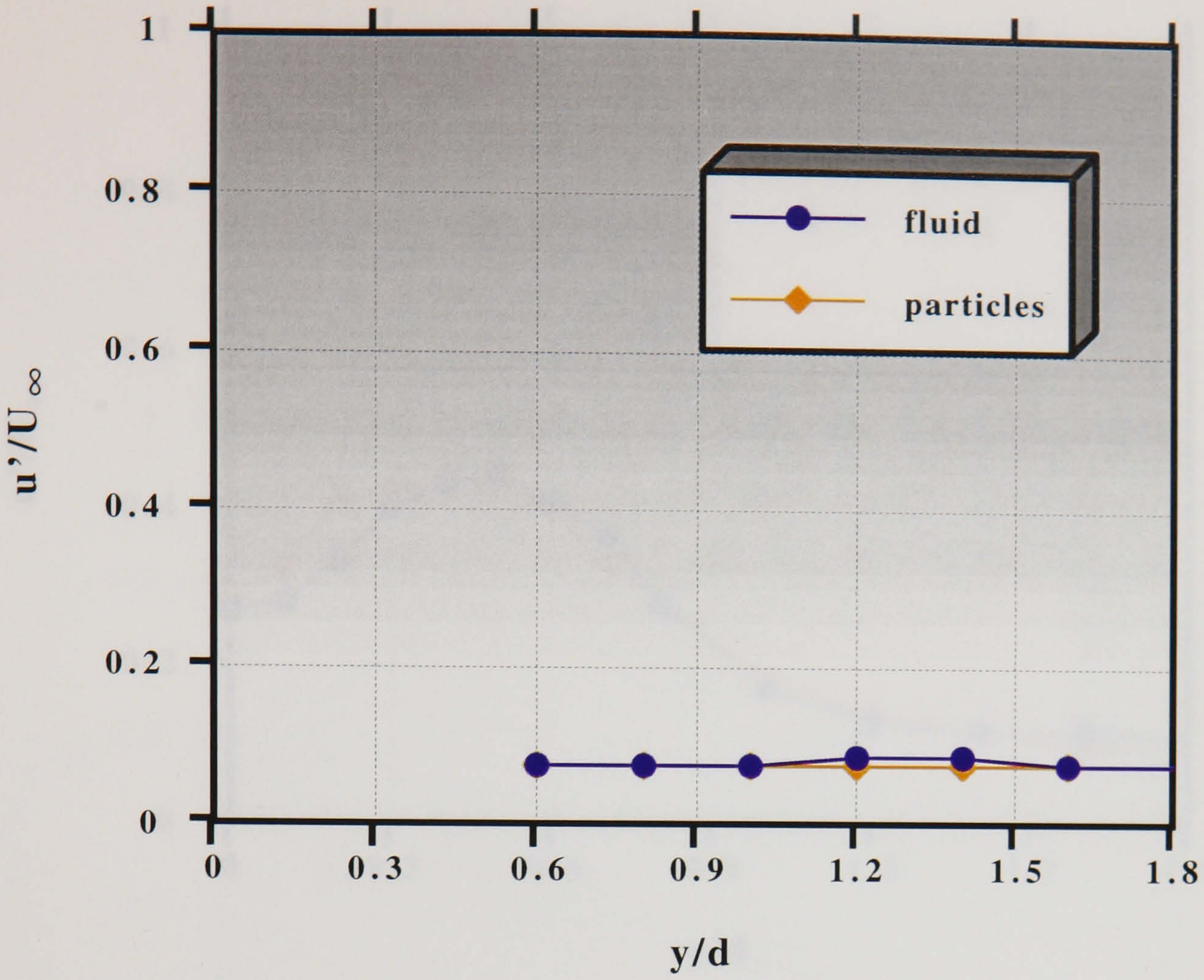

(a) x/d = 0.0

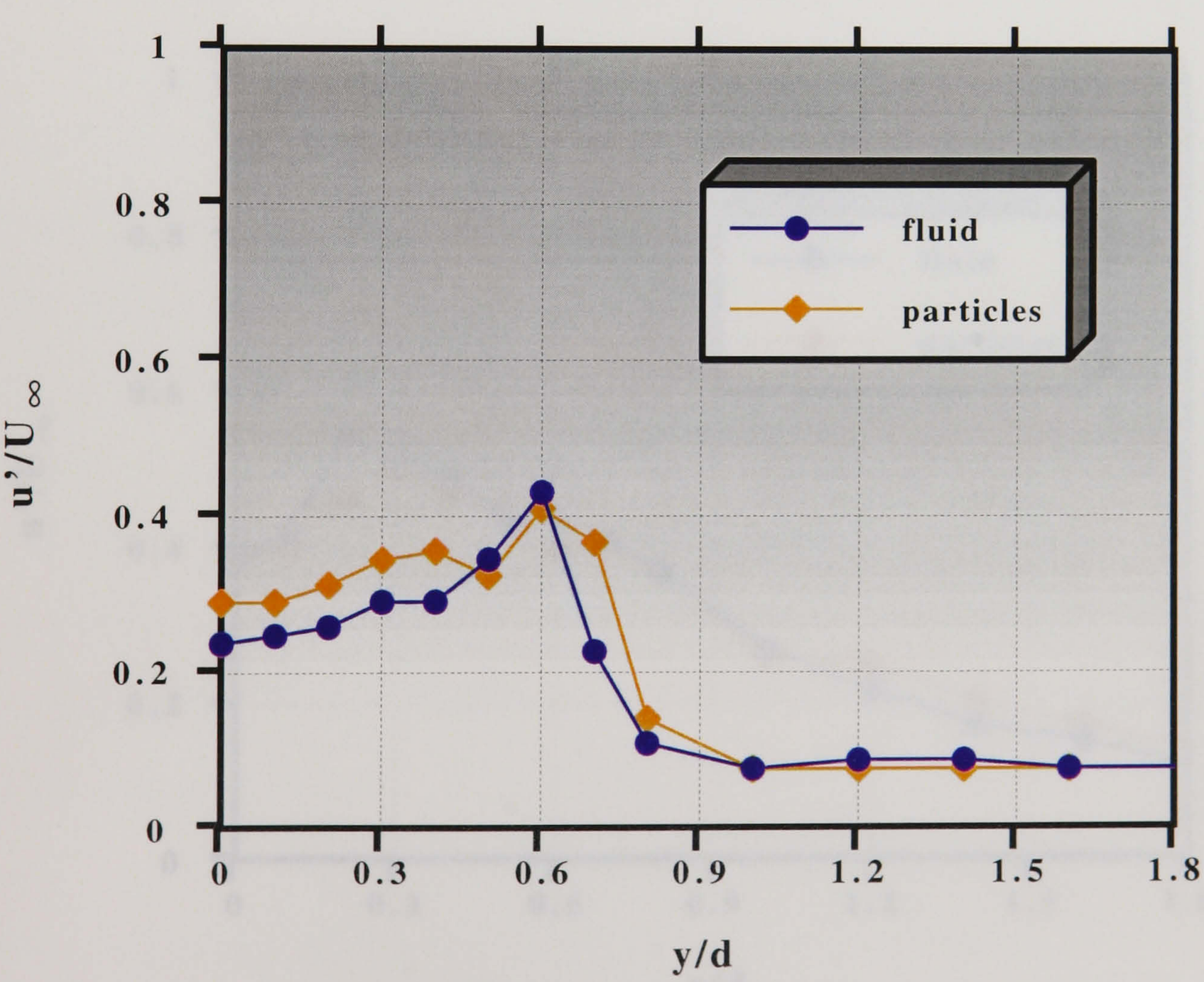

(b) x/d = 0.85

Figure 5.22. Single-phase and particle axial r.m.s. velocity profiles, u'/U∞, in the 3.6 x 2.1 in-line array (Re_d = 12,858).

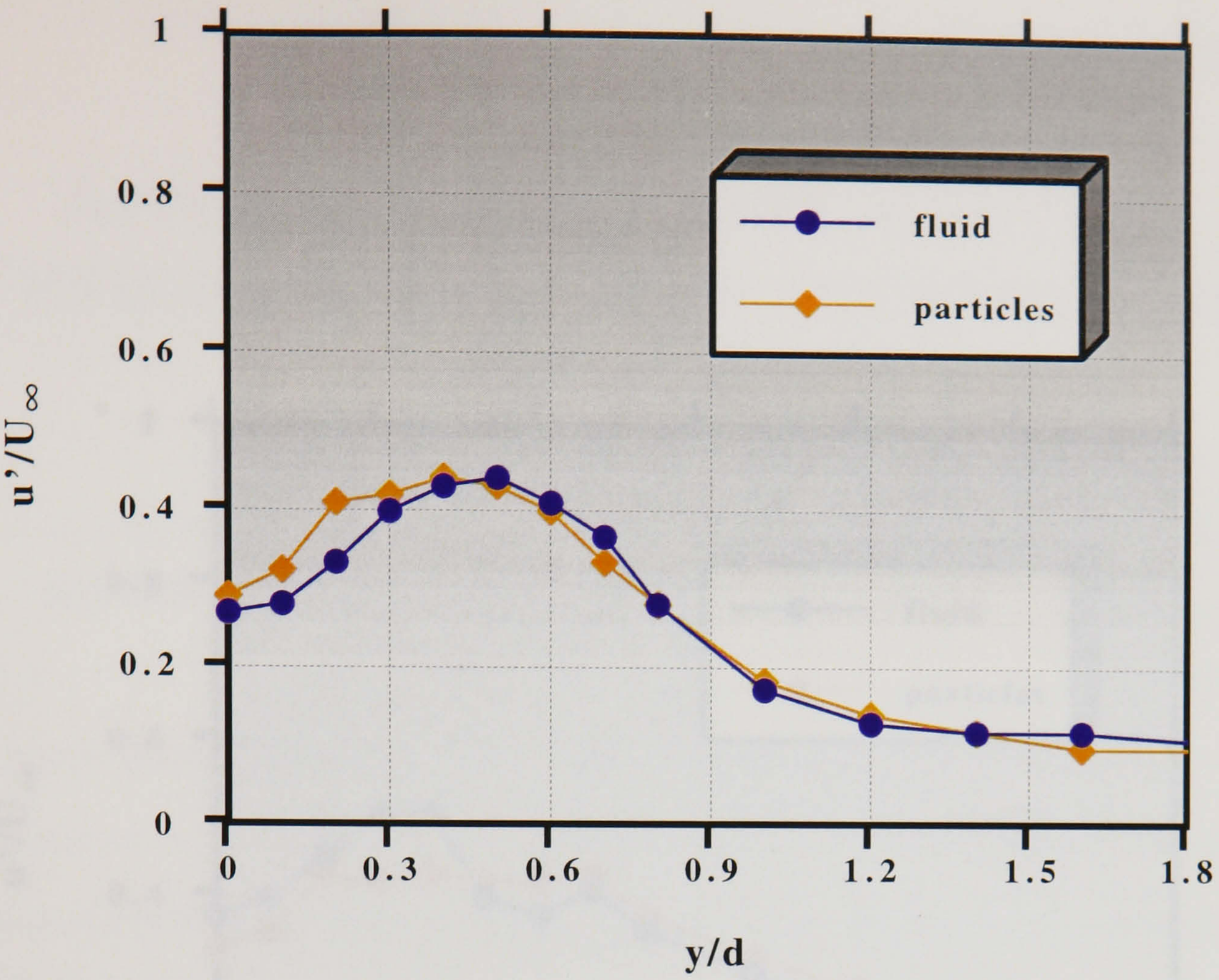

(c) x/d = 2.95

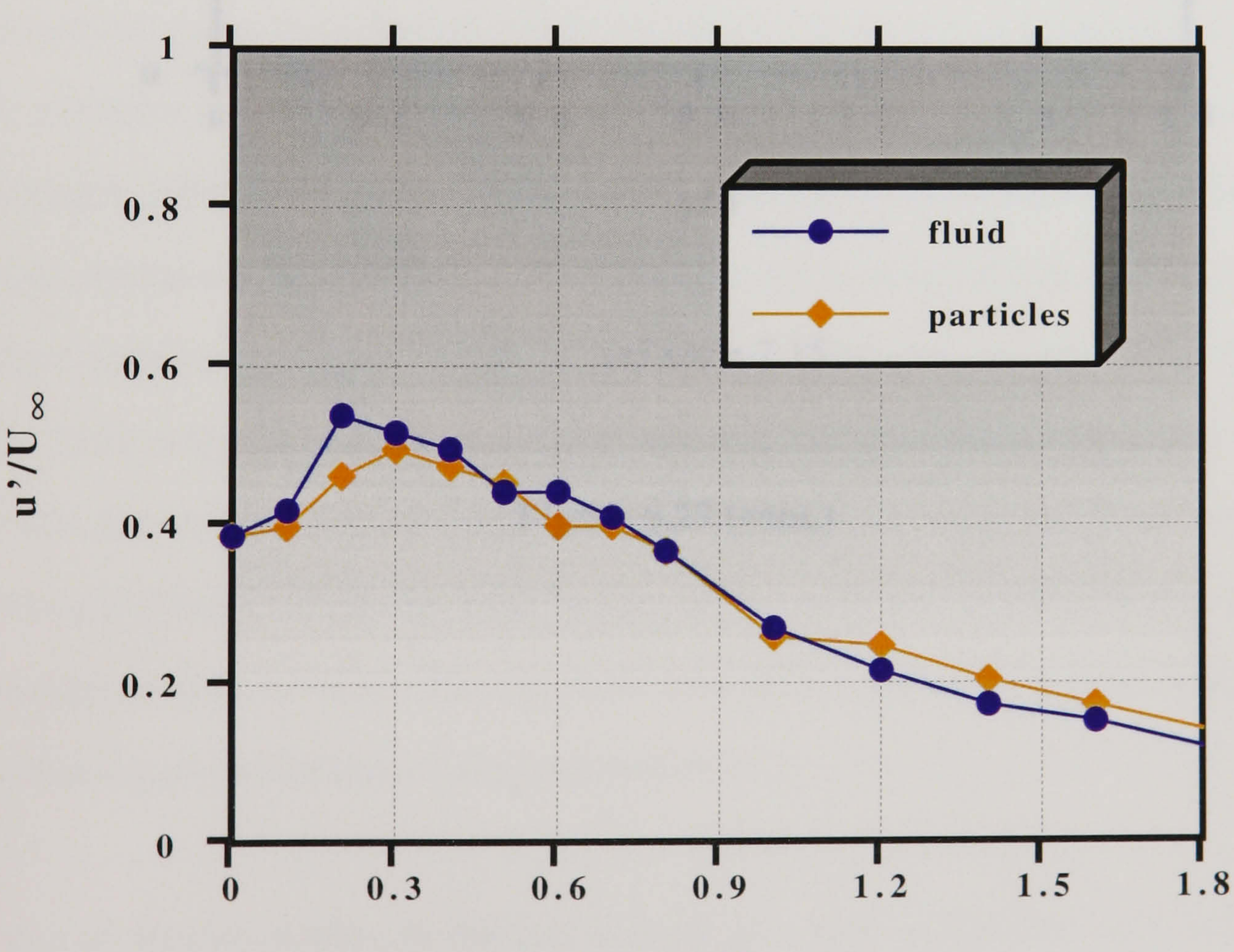

(d) x/d = 5.05

Figure 5.22. (cont.)

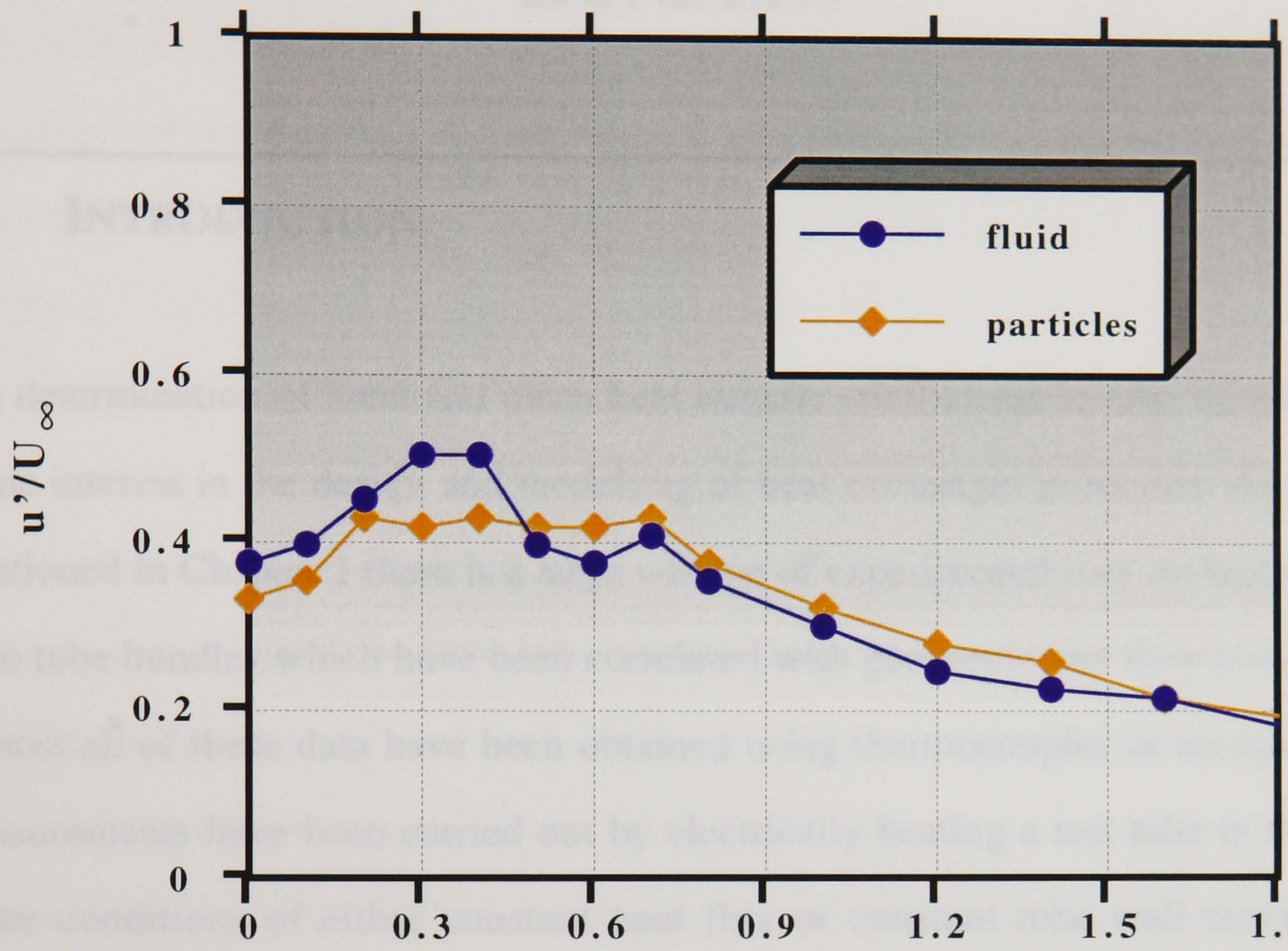

(e) x/d = 7.15

Figure 5.22.(cont.)

CHAPTER 6

APPLICATION OF LIQUID CRYSTAL THERMOGRAPHIC TECHNIQUES IN TUBE BUNDLES

6.1 INTRODUCTION

The determination of local and mean heat transfer coefficients in tube bundles is of prime interest in the design and modelling of heat exchanger processes. As already mentioned in Chapter 1 there is a large volume of experimental data on heat transfer from tube bundles which have been correlated with geometric and flow parameters. Almost all of these data have been obtained using thermocouples as sensors. Most measurements have been carried out by electrically heating a test tube in the bank under conditions of either constant heat flux or constant tube wall temperature (Achenbach, 1989, 1991; Aiba, 1982a, b, etc). Some investigators measured the rate of steam condensation inside the tubes of the bundle in order to determine the heat transfer coefficients (Huge, 1937; Michaelides et al, 1986; Stephan and Traub, 1986; Traub, 1990) whereas others determined heat transfer coefficients indirectly from mass transfer measurements using the analogy between mass and heat transfer (Merker and Hanke, 1986a, b). Both heating tests - with tube bundles heated either electrically or with hot water flowing inside the tubes - and cooling tests with cold water flowing inside the tubes have been reported.

The use of thermocouples as thermal sensors is a well established and accurate method of determining convective heat transfer coefficients. However, since thermocouples are point sensors, measurements of temperature distributions over a surface require a large number of sensors and can be time-consuming. This problem

can be ameliorated by using thermochromic liquid crystals as local surface temperature indicators. Liquid crystal thermography is a relatively new technique. It utilises the different colours displayed by liquid crystals which are a function of the temperature of the surface on which the crystals have been applied. The colour information can be viewed and recorded by means of photographic and video cameras and analysed using appropriate image processing techniques. The advantages of the technique are that the experimental set up can be less complex and less expensive compared to other techniques and that the temperature of an entire surface can be obtained, i.e. local heat transfer coefficients can be determined for every point on the surface.

As it will be shown later in this chapter liquid crystal thermography has been applied successfully in flow configurations involving flat surfaces. The extension of the technique to curved surfaces, however, is restricted by some inherent difficulties stemming from the curvature effects on the observation angle and consequently the colour interpretation of the liquid crystal displays. As a result very few investigations have dealt with configurations involving curved surfaces and only one recent investigation has been concerned with tube bundle flows. In the present study, a liquid crystal thermographic technique was developed and applied to a forced convection flow over a tube bundle in order to determine surface temperature distributions. Liquid crystal sheets were attached to the tube surfaces of the in-line tube bundle described in Chapter 2 and the colour images displayed by the crystals were captured and processed by digital image processing techniques. The principles and previous applications of the technique, the image processing equipment used and the experimental procedures are described in the following sections.

6.2 LIQUID CRYSTALS

The term *liquid crystals* was introduced by Lehmann in 1890 (as cited by Gennes, 1974 and Meier et al, 1975) to describe a state of matter that is intermediate between the solid crystalline and the ordinary (isotropic) liquid phase. Liquid crystals flow like ordinary liquids but they also exhibit anisotropic properties like solid crystals. Because of the intermediate nature of their state, liquid crystals are also called *mesophases* or *mesomorphic phases*.

Liquid crystals can be formed from a number of organic compounds either by varying the temperature, e.g. by heating a solid crystal above its melting point, or by varying the concentration, e.g. by adding a solvent. Mesomorphic phases of the first kind are called *thermotropic* whereas those of the second *lyotropic*. Thermotropic liquid crystals have found applications in industrial and lyotropic in biological systems mainly.

Three types of thermotropic liquid crystals were distinguished by G. Friedel (as cited by Gennes, 1974 and Meier et al, 1975) with respect to the orientation of the long molecular axes: *smectic*, *nematic* and *cholesteric*. Many compounds may form more than one of the above mesophases depending on the temperature: for example smectic types at temperatures above the melting point and either nematic or cholesteric types at higher temperatures.

Smectic (from the Greek word σμηγμα = soap) is the name given by G. Friedel to certain mesophases with mechanical properties reminiscent of soaps. Smectic liquid crystals are characterised by a layered structure as shown in Figure 6.1. There are various types which are classified as smectic A, B, C, etc. The centres of gravity of the elongated molecules are arranged in equidistant planes and their long axes are parallel to a preferred direction, $\vec{n}$. This direction may be normal to the planes

(smectic A) or tilted by a certain angle (smectic C). Inside each layer the centres of gravity may be arranged randomly or regularly.

The term *nematic*, coined also by G. Friedel, comes from the Greek word νημα = thread and refers to certain thread like defects which are commonly observed in such materials. Nematic mesophases are positionally disordered and orientationally ordered, i.e. the centres of gravity of the molecules are distributed randomly as in ordinary liquids while the long molecular axes are aligned preferentially along one direction $\vec{n}$. The molecules are also allowed to rotate freely about their long axes. A schematic of the molecular arrangement of the nematic liquid crystals is shown in Figure 6.2.

Cholesteric liquid crystals were named after cholesterol since many cholesterol esters form this type of liquid crystals. The cholesteric mesophase is formed by compounds or mixtures the molecules of which are chiralic (i.e. different from their mirror image). Their structure, shown in Figure 6.3, can be described as a twisted nematic structure: considering a certain plane, the molecules are aligned parallel to a preferred direction as in a nematic phase. When proceeding in a direction normal to that plane the preferred direction $\vec{n}$ of the molecules rotates continuously resulting in a helical structure. The pitch p of the structure is defined by the distance along the helical axis over which the preferred direction $\vec{n}$ of the molecules is rotated by 2π. p varies widely and can be adjusted to any desired value by adding appropriate amounts of a chiralic compound to a nematic liquid crystal. An infinite pitch corresponds to the nematic structure.

Because of their helical structure cholesteric liquid crystals exhibit unique optical properties. The most striking feature is the selective light reflection (Bragg reflection) which is the origin of the brilliant colours that are displayed under certain conditions. For a given angle of incidence of light (θ_I) and angle of observation (θ_S)

the wavelength of the light reflected by the liquid crystal is given by (Adams et al, 1969):

$$\lambda = 2\bar{n}p\cos\frac{1}{2}\{\sin^{-1}(\frac{\sin\theta_I}{\bar{n}}) + \sin^{-1}(\frac{\sin\theta_S}{\bar{n}})\} \qquad (6.1)$$

where $\bar{n}$ is the mean refractive index.

The pitch of a cholesteric liquid crystal and hence the wavelength of the Bragg reflected light depends strongly on temperature. Usually the pitch decreases when the temperature is increased, shifting the reflected light to shorter wavelengths. As a result, certain cholesteric liquid crystals exhibit colour changes over the entire colour scale from red to violet when the temperature is varied over a particular range. This process is normally reversible and the colours are displayed in a reverse sequence with falling temperature to that with rising temperature. This property of the cholesteric liquid crystals makes them very attractive as thermal sensors and gives rise to a number of applications such as the qualitative and quantitative determination of surface temperatures (e.g. detection of hot points in microcircuits, localisation of tumours and fractures in humans) and the visualisation of flows with temperature gradients.

The response, resolution and the temperature range over which the colours are displayed depend on the chemical composition of the specific cholesteric compound. It should be noted, however, that since the pitch of the cholesteric helix is sensitive to other agents apart from the temperature colour shifts may occur for example by changing electric or magnetic fields (utilised in liquid crystal display systems), or by changing the pressure or the concentration of gases or vapours. As indicated by equation (6.1) shorter wavelengths (i.e. colours shifted to blue) are also observed for increasing angles of illumination or observation.

Liquid crystals for thermographic applications are commercially available in three forms, as sheets, emulsions and solutions. In sheet form a thin layer of crystals is placed between a mylar plastic sheet and a black absorptive background. The sheets are attached on a surface by means of an adhesive. In emulsion form the liquid crystals are encapsulated in gelatin capsules suspended in a water based slurry. They are applied as a thin film on a black substrate by spaying or with a brush. The water evaporates leaving a thin liquid crystal coating on the surface. In solution form the crystals are dissolved in a solvent which evaporates after application.

6.3 THERMOGRAPHIC APPLICATIONS OF LIQUID CRYSTALS

Liquid crystal thermography has been developed as a simple and inexpensive tool in several areas of heat transfer research, particularly in convective flows. Since the 1970s a number of convection studies using liquid crystal techniques have been reported. An overview of the application of liquid crystals for the qualitative and quantitative determination of surface temperature and convective heat transfer coefficients in various flow configurations can be found in Yianneskis (1988).

Experimental studies of convective heat transfer using liquid crystals are based either on steady-state or transient temperature measurements. In the steady-state experiments a heating element - usually an electrically conductive coating or foil - is used to provide a uniform wall flux boundary condition. The surface temperature is measured and the heat transfer coefficients are calculated using Newton's Law of cooling. Conversely, transient experiments involve a sudden temperature step change of either the test section or the fluid and the response of the liquid crystal coating is monitored. The surface temperature is measured as a function of time and the heat transfer coefficients can be obtained for example from a transient heat conduction equation.

The main methods used to quantify the colour content of the crystal display can be broadly divided into true colour and intensity-based techniques. True colour image processing techniques are usually associated with wide-band liquid crystals and correlate the surface temperature with the hue displayed by the crystals through extensive calibration procedures. Intensity-based techniques are used mainly with narrow-band liquid crystals. Surface temperature measurements are obtained by observing an increase in the light intensity reflected by the surface under consideration when the liquid crystal response temperature is reached.

A wide range of flow configurations have been studied using liquid crystal thermography based on the above techniques. For example, Cooper et al (1975) obtained qualitative and quantitative surface temperature distributions in a uniformly heated cylinder in subcritical and critical cross-flow. An electrical resistive carbon impregnated paper (Temsheet) was used as a source of heating and encapsulated liquid crystals were applied on the surface. Crystal strips with different sensitivities were used in order to obtain the circumferencial temperature distributions. Calibration was performed by visual observation in a water bath. Simonich and Moffat (1982) presented detailed heat transfer measurements on a concave surface for turbulent flow in a water channel. They used crystal sheets attached to a vapour deposited gold sheet to determine the transient effects on the wall heat transfer.

Davies et al (1984) assessed various types of electrical heating elements and demonstrated the suitability of the liquid crystal thermographic techniques in a number of flow configurations. Rojas and Yianneskis (1984) designed and tested a liquid crystal sheet/heating element assembly to measure wall heat transfer coefficients in ducted flows. The heating element was a stainless steel foil and a uniform heat flux condition was obtained by passing electrical current through it. Distributions of wall temperatures and heat transfer coefficients were obtained in the flows downstream of a straight long square duct and of a 90° bend of strong

curvature. The accuracy of the measured heat transfer coefficients was 11 %. Ogden and Hendrics (1984) demonstrated the use of a liquid crystal coating for temperature measurements in a heated ellipsoid placed in a water tunnel: only qualitative information was obtained.

Platzer et al (1992) determined local heat transfer coefficients in rotor/stator configurations typical of gas turbines. The transient technique was used in which the rotor/stator system was exposed to a sudden step change in convective fluid temperature and an image processing system based on true colour recognition was employed. Ashford-Frost et al (1992) used a transient wall heating technique to determine the distributions of the local heat transfer coefficients on the tube plate ligaments of a shell boiler. A monochromatic filter was used during the recording of the images by the video camera. Fiebig et al (1994) used a transient technique to measure heat transfer coefficients on the plates of fin-and-tube heat exchangers with both round and elliptic tubes in the presence of vortex generators. The temporal development of the isotherms was recorded. Illumination by a monochromatic Argon-Ion laser was used and the isotherms were detected by the reflected wavelength. The experimental uncertainty was estimated to be up to 5 % depending on the heating times used. Convective heat transfer coefficients in a plate fin of a fin-and-tube heat exchanger were also determined by Critoph and Holland (1996). A steady state liquid crystal technique was developed in which the surface was heated directly by means of a powerful uniform light source. The position of an isotherm was recorded for a given heat flux to the fin surface. A series of flux densities were used to obtained isotherms for the whole surface. The isotherms were identified by the initial transition of the crystal colour display from black to red. The heat transfer coefficients for each isotherm were calculated and interpolated so that their distribution over the whole surface could be obtained.

Watwe and Hollingsworth (1994) applied liquid crystal thermography to observe time-dependent temperature patterns on an electrically heated surface during the onset of nucleate pool boiling. Yan et al (1995) developed a transient liquid crystal technique for local in-tube condensation heat transfer measurements. The local condensing heat transfer coefficients inside a horizontal smooth circular tube were determined with a true colour image processing technique. Tanda et al (1995) used a true colour/steady state liquid crystal technique to study forced convection heat transfer from a flat plate in the presence of vortex generators. A similar flow configuration was studied by Schulz et al (1996) using a transient liquid crystal technique. Measurements were carried out on a test plate and the surface was monochromatically illuminated using an Argon-Ion laser. An automated detection technique for the time of appearance of an isotherm on the test surface was developed. The intensity history of every single pixel on the test surface was recorded during the measuring time. These data were analysed to detect the maximum of the intensity peak of the light reflected by the liquid crystals which characterised the appearance of the isotherm. Ashford-Frost et al (1996a) applied a steady state technique to determine convective heat transfer coefficients on a flat surface due to the impingement of an axisymmetric jet. The method was based on the detection of the isotherm by varying the heat flux.

A number of visualisation studies have also been reported based on true colour image processing. For example, Dabiri and Gharib (1991) developed a technique to determine the temperature field in a two-dimensional cross section of a flow field. The application of the technique to the study of a heated vortex ring was demonstrated. Gomiciaga (1995) studied natural convection in a cavity. Lee (1995) visualised the flow in a mixing vessel and estimated mixing times. Asford-Frost et al (1996b) visualised the natural convection flow from a heated horizontal cylinder.

Most of the convective heat transfer applications outlined above involve flat surfaces due to the inherent difficulties associated with the application of the technique to curved surfaces. These stem from the fact that the reflection of light from a curved liquid crystal substrate occurs at different angles relative to the angles of illumination and observation. As indicated by equation (6.1) changes in viewing and illumination angles affect the interpretation of the colour information displayed. Hence, the results reported by Cooper et al (1975) and Yan et al (1995) for cylindrical surfaces are not expected to be accurate since the colour display of the liquid crystals was calibrated independently in a bath and a flat surface respectively. Furthermore, Cooper et al' s calibration data were obtained by visual observation and therefore they were subject to observation errors. Chan et al (1995) assessed the effect of viewing/illumination angle on the temperature-versus-hue relationship. Calibration data were obtained from an oblique flat surface coated with a thin layer of liquid crystals for a range of viewing/illumination angles from 0° to 66°. A fifth polynomial equation was fitted to the data and the temperature was correlated with both viewing/illumination angle and hue. The technique was applied to a semi-cylindrical surface exposed to a heated slot jet under transient conditions. Farina et al (1994) also studied the effects of lighting/viewing angle and lighting conditions on the calibration data. A colour correction technique was introduced to account for effects such as lighting, optical path etc. The lighting conditions were found to introduce a significant error in the hue-temperature curve. On-axis lighting and viewing arrangements introduced a temperature shift of only ± 0.25° C for angles up to 25°. The error was significantly larger for off-axis lighting/viewing arrangements. It was concluded that an illuminant-invariant hue-temperature calibration can be acquired for up to ± 25° of surface rotation when on-axis lighting/viewing is used together with colour correction techniques.

In view of the foregoing discussion, it is not surprising that liquid crystal techniques have not been applied to date for the determination of convective heat transfer

coefficients in tube bundles. To the knowledge of the author, no such studies were available in the literature at the time of this investigation. Only recently, McMahon and Murray (1996) developed a transient liquid crystal technique to determine heat transfer coefficients in a staggered tube bundle in cross-flow. The tube bundle consisted of three rows with $S_T/d = 2.0$ and $S_L/d = 1.25$. The tubes were 50 mm in diameter to facilitate adequate spatial resolution. The tube bundle was suddenly exposed to a heated air flow and the variation of the surface temperature with time was monitored. An intensity-based image processing technique was employed using single colour identification for the detection of isotherms. The transition from red to green was used for isotherm identification in the captured images. The difficulty in obtaining an exact colour match under variable lighting conditions and orientation was overcome by specifying a hue tolerance. The heat transfer coefficients were found to be in good agreement with published data and correlations.

A steady-state/true colour liquid crystal technique was employed in this investigation and it is described later in this chapter. The principles of colour measurement are first described in the following section.

6.4 COLOUR SPECIFICATION

Unlike other physical quantities, colour is difficult to define and measure. Colour is part of the human vision and involves psycho physical phenomena. Jean Judd, one of the pioneers of the colour science, defined colour as (as cited by Nassau, 1983):

> *that aspect of the appearance of objects and lights which depends upon the spectral composition of the radiant energy reaching the retina of the eye and upon its temporal and spatial distribution thereon.*

Although colour and light were considered by many natural philosophers throughout history (e.g. Aristotle, Democritus etc.), it was not until Newton's experiments that the foundations for the physical understanding of colour phenomena were laid. Newton showed that white light might be conceived as consisting of an agglomeration of light rays distinguishable from one another both by eye and by various physical properties. These components are called monochromatic radiations and they display a series of spectral colours observed in the rainbow and all the intermediate hues. The fundamental property that distinguishes one monochromatic radiation from another is the wavelength usually measured in nanometers (nm). The wavelengths of the visible spectrum range from 380 nm to 780 nm. Monochromatic radiations with wavelengths lying outside of this range are in general invisible to the eye.

A number of colour specification schemes have been formulated and adopted in an effort to quantify colour. In general, colour specification systems and recommendations on related topics have been provided by the *Commision Internationale de l' Eclairage* (CIE).

Trichromatic matching experiments formed the basis for a system of colour measurement. Based on the fact that there are three spectrally different sets of receptors in the retina, in trichromatic matching a test colour perceived by an observer is matched by an appropriate mixture of three matching stimuli: red (R), green (G) and blue light (B). The original colour matching experiments carried out by Guild (National Physical Laboratory) and Wright (Imperial College) (as cited by Wyzecki and Stiles, 1982 and Hunt, 1987) were combined and the data obtained under different experimental conditions were transformed to a common system in which the primary stimuli were monochromatic and with wavelengths of 700 nm (R), 546.1 nm (G) and 435.8 nm (B). The transformed data were used to define the CIE 1931 standard colorimetric observer. However, the amounts of the three primary

stimuli - known as tristimulus values - needed to match a given colour could take negative values. This is a result of summing and subtraction involved in the computation of the tristimulus values. Furthermore, colour-matching functions, obtained by plotting the R, G, B tristimulus values for a constant amount of power for each constant width wavelength interval throughout the spectrum, exhibited negative parts.

In order to eliminate the presence of negative numbers in colour specifications, the CIE adopted a transformation from the R, G, B system to one based on a new set of primary stimuli, X, Y, Z. The relationship between the two systems can be expressed as follows:

$$X = 0.49\,R + 0.31\,G + 0.20\,B \tag{6.2a}$$

$$Y = 0.1769\,R + 0.81240\,G + 0.01063\,B \tag{6.2b}$$

$$Z = 0.00\,R + 0.01\,G + 0.99\,B \tag{6.2c}$$

This CIE 1931 X, Y, Z colour specification system has been adopted internationally. The coefficients in the above equations have been carefully chosen so that tristimulus values would always be positive for all colours.

It is often desirable to express colour specifications in terms of the perceived colour attributes. Brightness, hue and colourfulness are the basic perceptual attributes of colour while lightness, and chroma are relative perceptual attributes, i.e. they describe an attribute relative to that of a similarly illuminated white. Hue is that attribute of a visual sensation according to which an area appears to be similar to one or to proportions of two of the perceived colours red, yellow, green and blue. Saturation is another attribute defined as the colourfulness of an area judged in proportion to its brightness (Hunt, 1987). In order to correlate the X, Y, or Z

tristimulus values with colour attributes their relative magnitudes are used. These are called *chromaticity co-ordinates* and they are defined as follows:

$$x = \frac{X}{X+Y+Z} \tag{6.3a}$$

$$y = \frac{Y}{X+Y+Z} \tag{6.3b}$$

$$z = \frac{Z}{X+Y+Z} \tag{6.3c}$$

It is clear that the sum of the three chromaticity co-ordinates is equal to unity. In this way if x and y are known z can be easily determined. Based on this property, two-dimensional diagrams, called *chromaticity diagrams* or *colour triangles*, can be constructed. Figure 6.4 shows a x, y chromaticity diagram obtained by plotting y as ordinate against x as abscissa. All colours can be mapped in the finite domain bounded by the *spectrum locus*, i.e. the curved line indicating where the colours of the spectrum lie, and the *purple boundary* which is the straight line that joins the two ends of the spectrum together. The position of the three matching stimuli R, G, B are also shown on this diagram. The area within the triangle formed by these points represents all the colours that can be matched by additive mixtures of these three stimuli. A characteristic property of the chromaticity diagrams is that any additive mixture between two colours is represented by a point that lies on the line passing through the chromaticity points corresponding to the constituents.

One serious disadvantage of the x, y chromaticity diagrams is that the distribution of colours is non-uniform since identical colour differences are not represented by lines of equal length, i.e. pairs of points representing colours with perceptual colour difference of the same magnitude are not equally distant. In order to minimise this effect, another chromaticity diagram was proposed by CIE in 1976. It is known as the CIE 1976 uniform chromaticity scale diagram and it is commonly referred to as the u', v' diagram. The u' and v' co-ordinates are related to x and y ones as follows:

$$u' = \frac{4x}{-2x + 12y + 3} \tag{6.4a}$$

$$v' = \frac{9y}{-2x + 12y + 3} \tag{6.4b}$$

Two approximate correlations of hue and saturation can be defined using the CIE 1976 u' and v' diagram: the u', v' *hue angle*, h, and the u', v' *saturation*, s defined by:

$$h = \arctan\left[\frac{(v' - v'_n)}{(u' - u'_n)}\right] \tag{6.5a}$$

$$s = 13\left[(u' - u'_n)^2 + (v' - v'_n)^2\right]^{1/2} \tag{6.5b}$$

where u'_n and v'_n are the u' and v' values for a reference white object - the colour stimuli usually taken as the spectral power of one of the CIE standard illuminants. The hue angle interval is determined by the sign of (v' - v'_n) and (u' - u'_n). The geometrical representation of h and s can be seen in the u', v' diagram shown in Figure 6.5. If C is the point representing the colour considered and N the reference white then h is the angle defined in an anticlockwise direction by the line NC and the horizontal line drawn from N to the right. s is equal to 13 times the distance NC.

In television and VDU displays the colours are also produced by additive mixtures of beams of red, green and blue. However, three phosphors (*E.B.U. phosphors*) are used as standard matching stimuli in European colour television (Hunt, 1987) which are different from those mentioned earlier. The chromaticities of these three primary stimuli are shown in Table 6.1 below:

Table 6.1. Chromaticities of the three primaries used in television.

Primary	***x***	***y***	***u'***	***v'***
Red	0.64	0.33	0.451	0.523
Green	0.29	0.60	0.121	0.561
Blue	0.15	0.06	0.175	0.158

The whole range of chromaticities that can be matched with the E.B.U phosphors is defined by the triangles shown in Figures 6.6 (a) and (b) plotted in x, y and u', v' chromaticity co-ordinates respectively. It is evident that these triangles cover a much smaller domain than the one defined by the spectrum locus and the purple boundary line.

The image processing system employed in the present investigation transforms RGB images to the hue, saturation and value (intensity) domain (HSV or HSI) by estimating the hue and saturation using equations (6.5a) and (6.5b) and the chromaticity values x, y, u', v' given in Table 6.1 above.

6.5 DATA ACQUISITION AND IMAGE PROCESSING SYSTEM

The data acquisition and image processing system used in this work to record and interpret the colour information of the liquid crystal displays is shown schematically in Figure 6.7. A CCD colour video camera (Sony EV1-1011P) is used to capture the colours displayed by the liquid crystals. The output signal from the camera is input to a S-VHS PAL video cassette recorder (Panasonic NV-FS200 HQ) and is recorded on videotapes at a rate of 25 frames per second. The quality of the images is monitored with a multi-system RGB monitor (JVC TM-150 PSN-K).

The recorded video images are input to a computer (Macintosh II fx) and captured as true colour RGB images using a frame grabber/digitiser card (Screen Machine) and associated software (SM Camera). In order to achieve the highest possible resolution the video images are captured into 1:1 scale (100 % digitisation) resulting in a an image of approximately 756 x 512 pixels. The grabbed images are digitised into 24-bit digital images composed of three planes of pixels where each pixel has a red, green and blue intensity, each coded on a 8-bit format (i.e. 256 levels) and they are stored on disk in TIFF format for subsequent analysis. This is carried out using a commercial image processing and analysis software(OPTILAB^{TM} /24 version 2.0). The RGB colour images are decomposed into three 8-bit grey level images of hue, saturation and value (HSV). A pixel-by-pixel analysis of the hue images is carried out in order to obtain the colour distribution displayed by the liquid crystals. The hue values corresponding to each pixel are saved in an ASCII format and they are translated into temperature using the hue-temperature relationships obtained through extensive calibration of the liquid crystals.

6.6 EXPERIMENTAL PROCEDURES

6.6.1 FLOW CONFIGURATION

The in-line tube bundle model (S_T/d = 3.6 and S_L/d =2.1) described in Chapter 2 was modified in order to measure temperature distributions on the tube surfaces by means of liquid thermographic techniques. This arrangement was chosen because it allowed more extensive optical access for the video camera recordings of the liquid crystal colour distributions than the other two configurations. The Perspex rods in the first 4 rows were replaced by copper tubes of a nominal diameter equal to 9.6 mm. This diameter was reduced down to 9 mm by machining so that the outside diameter of the tubes when covered with liquid crystal films is equal to 10 mm as in the case of Perspex rods. The thickness of the copper tube wall was 0.5 mm.

The liquid crystal sheets used were supplied by Hallcrest Ltd. Their attachment to the tube bundle geometry however is far more complicated than in the case of flat surfaces: the curved surface of the tubes, their small diameter and the use of water as working fluid imposed many difficulties. Many preliminary tests were made to determine the most appropriate way of attaching the liquid crystal sheets to the copper tubes as well as the temperature range suitable for the measurement of the wall temperature distributions around the tubes. Since the tube diameter was very small the liquid crystal sheets could not be attached to the tube surface only by means of an adhesive tape since the edges tended to peel off. An epoxy resin glue had to be used at the base of the tubes to eliminate this problem. The seam was positioned at the bottom of the tubes so that any effects on the boundary layer and consequently the flow over the tubes were avoided. However, it was observed that water could penetrate into the liquid crystal film causing the mylar plastic layer to peel off gradually while the rest of the film remained attached. A clear heat shrink tube was applied over the liquid crystal film to keep it in place and protect it from the water. Extreme care was taken during the heat shrinking process to avoid air bubbles being trapped between the liquid crystal film and the heat shrink tube. However, it was observed that the wall temperature distributions displayed were affected by the imperfect contact between the liquid crystal film and the heat shrink tube and the brightness of the colours displayed deteriorated. The use of encapsulated liquid crystals in a sprayable form was considered as an alternative. However, the latter are not water-resistant for the time needed to perform the experiments.

Finally, the problem was resolved by sealing the edges of the liquid crystal film using a sealant (Araldite). Since the temperature variations over the tube surface were expected to be small, liquid crystal sheets of the highest resolution were tried first, namely displaying colours in the range 35°-36° C. These were found inappropriate since no clear distributions could be observed. The next available

range, 29°-33° C, was tried and was finally selected for the experiments. The liquid crystal film was approximately 0.2 mm thick and comprised a transparent mylar plastic sheet, a layer of crystals and a black paint layer; it was attached on the tube surface by means of a double sided adhesive tape, 0.3 mm thick. A schematic diagram of the liquid crystal/ tube assembly is shown in Figure 6.8. Perspex rings with markings at 45° angle intervals were placed at the end of the tubes to indicate angular distance from the front stagnation point.

The modified test section, shown in Figure 6.9, was installed in the flow rig. A constant temperature water bath was used to pass water through the copper tubes and control its temperature. The temperature of the water in the flow rig was also controlled by means of the temperature controller described earlier in Chapter 2. The cross-flow Re_d was identical to that used for the fluid flow measurements, i.e. Re_d = 12,858. The flowrate of the water passing through the tubes was determined by the built-in pump in the water bath and was sufficiently low so that the internal flow was laminar. However, due to the small length of the tubes (72 mm) and the small tube surface area over which the temperature distribution is measured a uniform wall temperature condition could be achieved. The condition of constant heat flux was difficult to implement in a water flow rig since it requires the use of electrically heated tubes. Only one tube was heated and measured at a time.

Due to the restricted optical access in the tube bundle the tube surface under consideration could not be observed and recorded with the camera aligned to the horizontal direction. Therefore, two different viewing angles (above or below the horizontal) had to be employed in order to capture the colour distributions displayed by the liquid crystals over 180° from the front stagnation point of the tubes. The colours displayed in the first 90° from the front stagnation point were viewed and recorded from above and the remaining 90° from below. Viewing angles ranging from 13° to 22° were used. Extra care was taken in illuminating the tubes to be

measured. Low-intensity fluorescent tubes were used for illumination of the liquid crystal display and were placed in such a distance from the test section so that the heat generated by the tubes did not affect the colour displayed by the crystals. Efforts were made with care to illuminate the surface under consideration at an angle similar to that of observation.

6.6.2 CALIBRATION

Since the colours displayed by the liquid crystals depend highly on both the viewing and illumination angles, on-tube calibration of the variation of hue with temperature was necessary for each tube under each viewing angle. In order to do this, the temperatures of the water both inside and outside the copper tubes were kept equal and the colour displayed was recorded. Temperatures in the range of 29° to 35° were applied. The images obtained were processed using the image acquisition and processing software described earlier in this chapter. For each calibration temperature a single mean hue value was obtained by averaging the hue values of the captured images over a central area of 400 pixels x 200 pixels approximately.

Figures 6.10 (a) - (d) show typical calibration results obtained with the first and second row tubes. In order to obtain an expression for the variation of hue with temperature a third-order polynomial curve fit was applied to the calibration data over the temperature range of 29°C and 35°C. Due to scatter in the data, curve fitting was achieved when the data for the highest and lowest temperatures were omitted. The remaining data were well correlated by both a fifth-order and a third-order polynomial calibration curve. However, it was found that both polynomial curves produced identical temperature estimates for the same values of hue. Therefore, third-order calibration curves - as shown in Figures 6.10 (a) through (d) - were chosen for the determination of temperatures from hue values. Although the coefficient of the cubic term is very small - of the order of 10^{-6} - its neglect was

found to result in significant errors. Therefore, high precision is required in the calibration curves in order to obtain accurate temperature measurements.

The scatter in the calibration curve data can be primarily attributed to the viewing/illumination conditions: the inherent difficulties involved in illuminating uniformly the curved surfaces of the tubes, the changes of viewing and illumination angles along the periphery of the tubes and the difficulty in establishing on-axis viewing and illumination conditions with the present experimental arrangement. The standard deviation of the hue values used to calibrate the liquid crystals ranged from $\pm$ 2 to $\pm$ 16. The higher hue values - corresponding to the blue - produced the higher standard deviations. Smoothing of the captured images using various spatial filters built-in in the image processing software did not reduce the hue standard deviation significantly. Therefore, the data presented here were obtained from unfiltered images. The percentage temperature error resulting from the hue standard deviations was found to be less than 2.5 % on average. The maximum error associated with the curve fitting is 2% as indicated by the correlation coefficients, R, given in Figures 6.10 (a) - (d). Since these two errors, due to the standard deviation of the hue values and the curve fitting respectively, are independent, the square root of the sum of their squares was calculated to give a total temperature error for the calibration runs. The maximum total temperature error was found to be 3.2%. Another source of error is the temperature reading from the thermocouple installed in the flow rig. This error, however, is negligible and was not considered in the uncertainty analysis discussed above.

6.7 TEMPERATURE DISTRIBUTION MEASUREMENTS

Once the calibration at a particular viewing angle was completed, a temperature gradient was applied to the two streams until a colour distribution - and therefore a surface temperature distribution - could be observed along the tube circumference

which was subsequently recorded. In this way identical angles of observation and illumination could be established both during the calibration and the actual experiment. The temperature of the water inside the tubes was set to 50° C and that in the flow rig to 20° C when the temperature distribution on the first row was recorded. The cross-flow temperatures were set to 22° or 23° C for the measurements of surface temperatures in subsequent rows so that colour distributions could be observed.

Figures 6.11 (a) and (b) show characteristic distributions obtained in the first and second rows respectively. The temperature of the water flowing inside the tubes was 50 °C in both rows whereas that of the cross-flow was 20°C in the first row and increased to 22° C in the second row in order to obtain a colour distribution as with a fluid temperature of 20° C no colours could be observed on the surface of the second row tube. The upper and lower part of the cylinder were measured by recording under two different angles as already mentioned. The hue distribution obtained from the images was converted to a temperature distribution using the calibration curves shown in Figures 6.10 (a) - (d). Since the captured images are planar projections of the cylindrical tube surfaces considered, a transformation is needed from the pixel co-ordinates of the image to angular co-ordinates representing distance from the front stagnation point. Both the viewing angle and the surface curvature were taken into account. The very top and very bottom regions of the images were omitted from the calculation due to the relatively large optical distortion in these locations. Temperature values were averaged over angle intervals of 5°. The maximum uncertainty of the measured temperature distributions is expected to be the same as that of the calibration, 3.2 %, since the experimental conditions for both were identical.

The distribution obtained in the first row tube (Figure 6.11 (a)) exhibits the expected pattern for a heated cylinder that loses heat to a fluid stream: temperatures increase

up to the separation point and fall thereafter. Thus, the maximum temperature variation ΔT occurs at the separation point where there is maximum thermal resistance or minimum heat transfer. The separation point is located at around 90°-100° from the front stagnation point in the first row tube. Temperature variations are small. For example, the maximum ΔT measured does not exceed 1° C. This may be attributed to the low spatial resolution achieved with the 10 mm tubes and conduction losses through the copper wall, the adhesive tape and the mylar plastic. Higher temperature differences could not be applied to the two streams (inside and outside of the tubes) due to experimental restrictions imposed by the use of water as the working fluid as well as by the manner with which the liquid crystals are attached on the surface. Since the colour displayed by the liquid crystals depends both on the illumination and viewing angles, the calibration curves obtained were different for the two parts of the cylinder. Consequently, the temperatures measured at the same region of the cylinder (for example at around 90° from the front stagnation point) under different angles show some scatter. Therefore, the experimental uncertainty at these locations is expected to be larger than the one mentioned earlier. Temperatures could not be measured in the lower part of the second row tube (Figure 6.11 (b)). In both tubes the trends indicated by the results are qualitatively similar to those predicted by Bouris (1995).

The liquid crystal technique was successfully applied to determine tube surface temperature distributions. However, the above results indicate that although the technique has been shown to perform excellently in flat surfaces, its application to heat exchanger models can be very problematic. The main problems stem from the effects of curvature on the viewing/illumination angles and consequently on the colour interpretation and also the restricted optical access imposed by the complex tube bundle geometries. The data obtained in the present work displayed the expected trends but the temperature information that could be practically obtained was restricted. The ability to obtain detailed temperature distributions around the

tubes was demonstrated and in future similar experiments should be designed in test sections with larger tubes and/or with air as working fluid. In this way the spatial resolution can be improved and application of the liquid crystal sensors will be less cumbersome. The use of alternative colour detection techniques, such as intensity-based ones, in conjunction with transient experiments should be further explored as these may ameliorate some of the problems encountered, as demonstrated by McMahon and Murray (1996).

6.8 CLOSURE

In this chapter the principles of liquid crystal thermography and colour measurement were described. Previous applications of liquid crystal thermographic techniques for the determination of convective heat transfer coefficients were reviewed. The development and application of a steady state/true colour recognition technique to tube bundle flows was described. The results obtained demonstrated that detailed qualitative and quantitative information on surface temperature distributions can be obtained in tube bundles. A number of difficulties associated with the application of the technique to a geometry as complex as that of a tube bundle were identified. Means through which the accuracy of the technique could be improved were also identified.

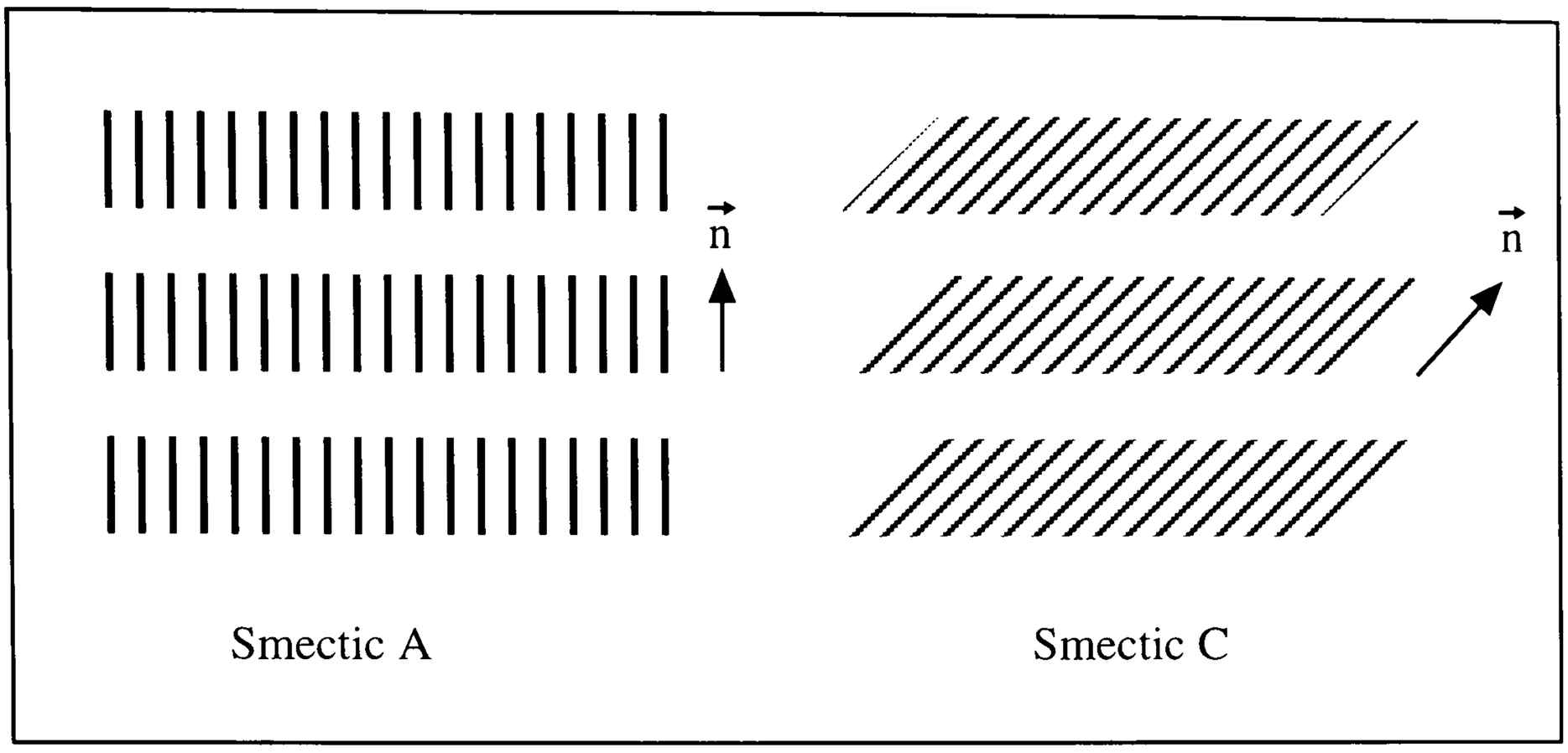

Figure 6.1. Molecular arrangement in smectic liquid crystals.

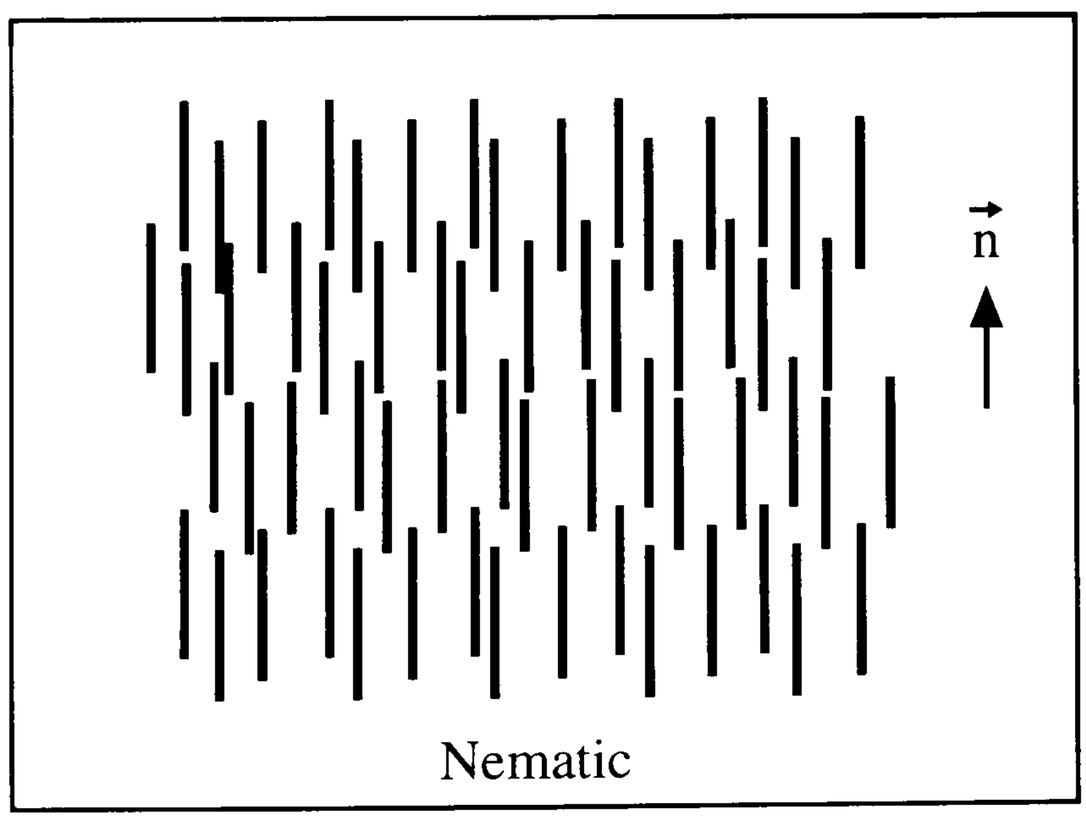

Figure 6.2. Molecular arrangement in nematic liquid crystals.

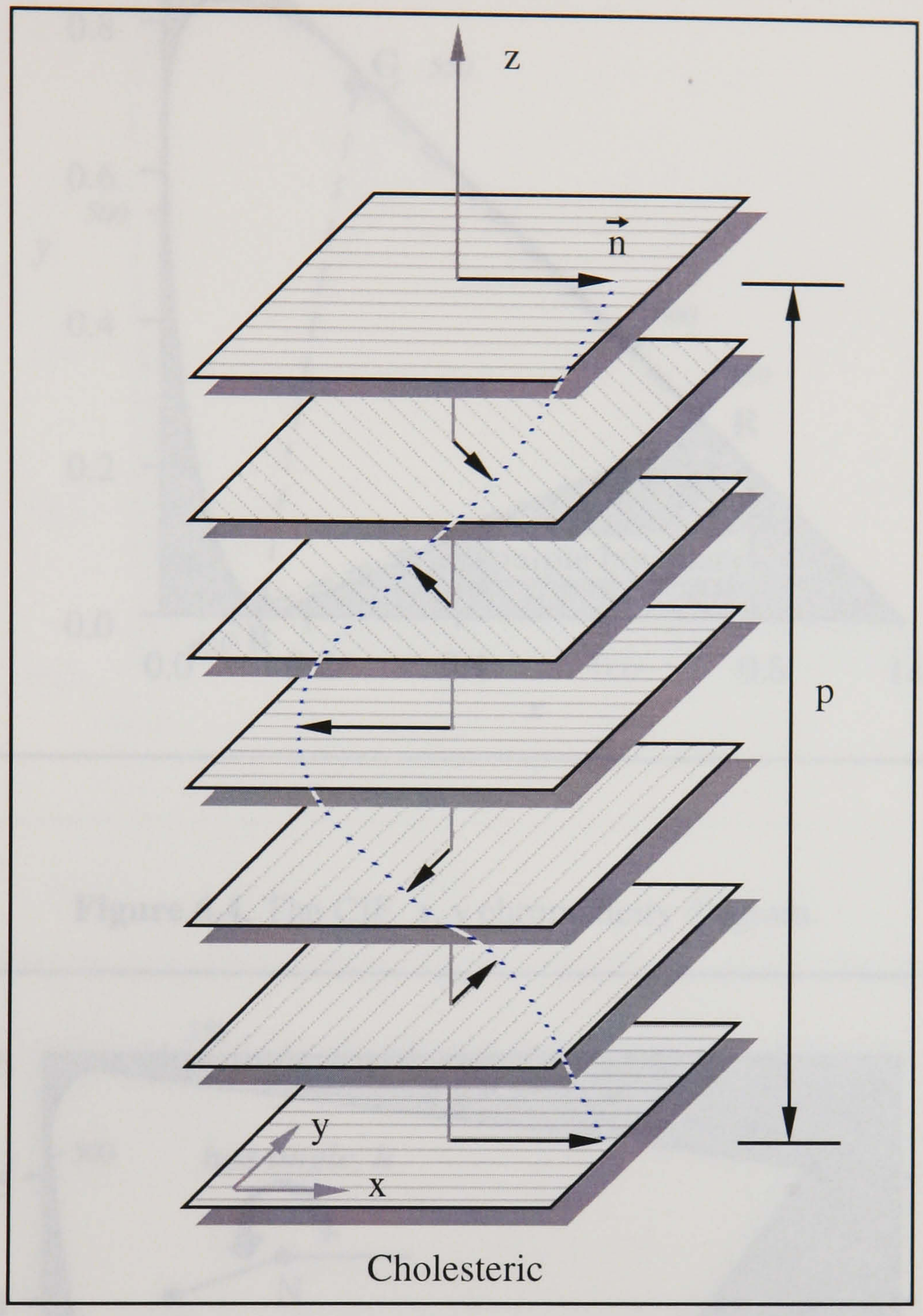

Figure 6.3. Molecular arrangement in cholesteric liquid crystals.

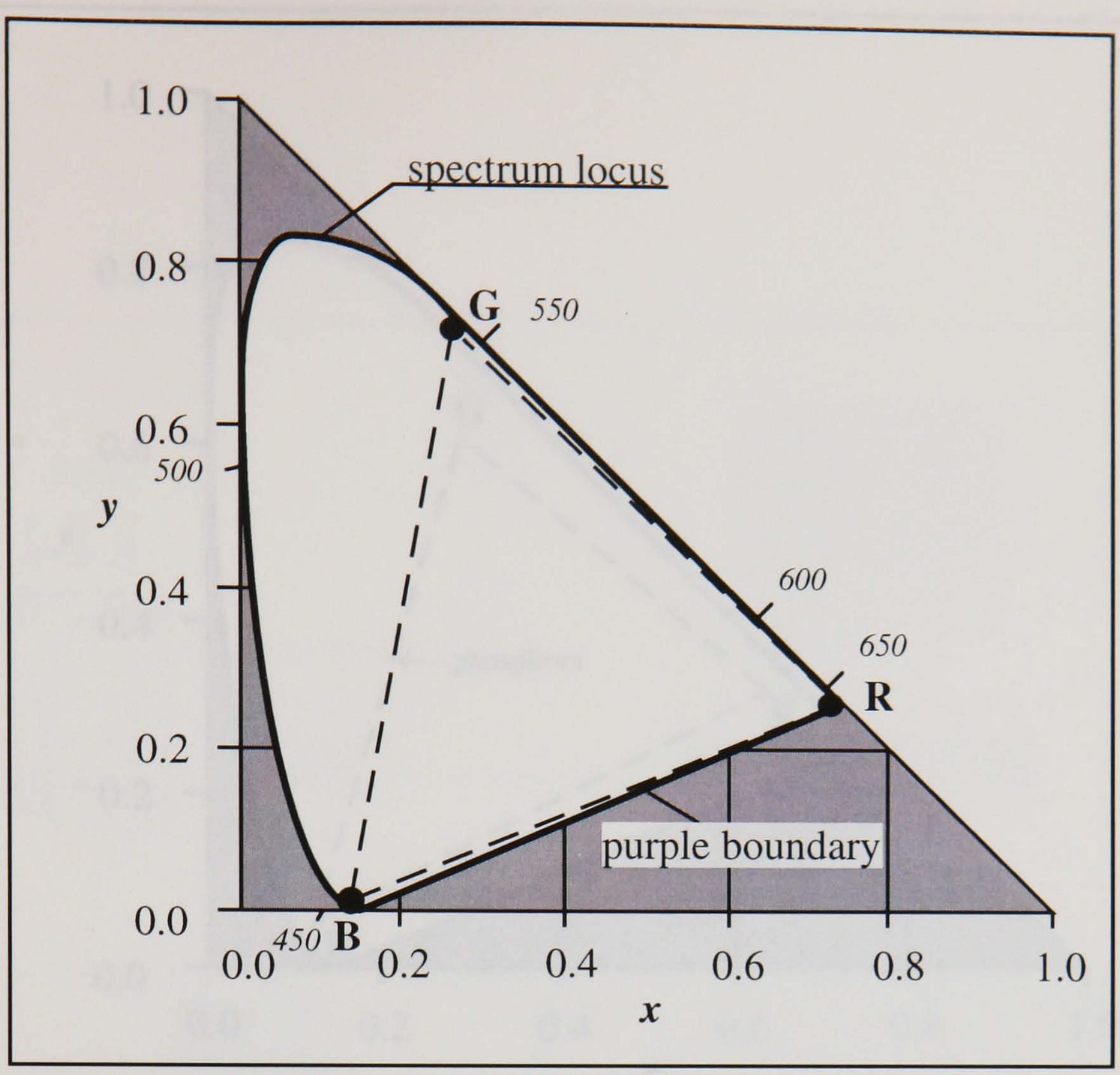

Figure 6.4. The CIE x, y chromaticity diagram.

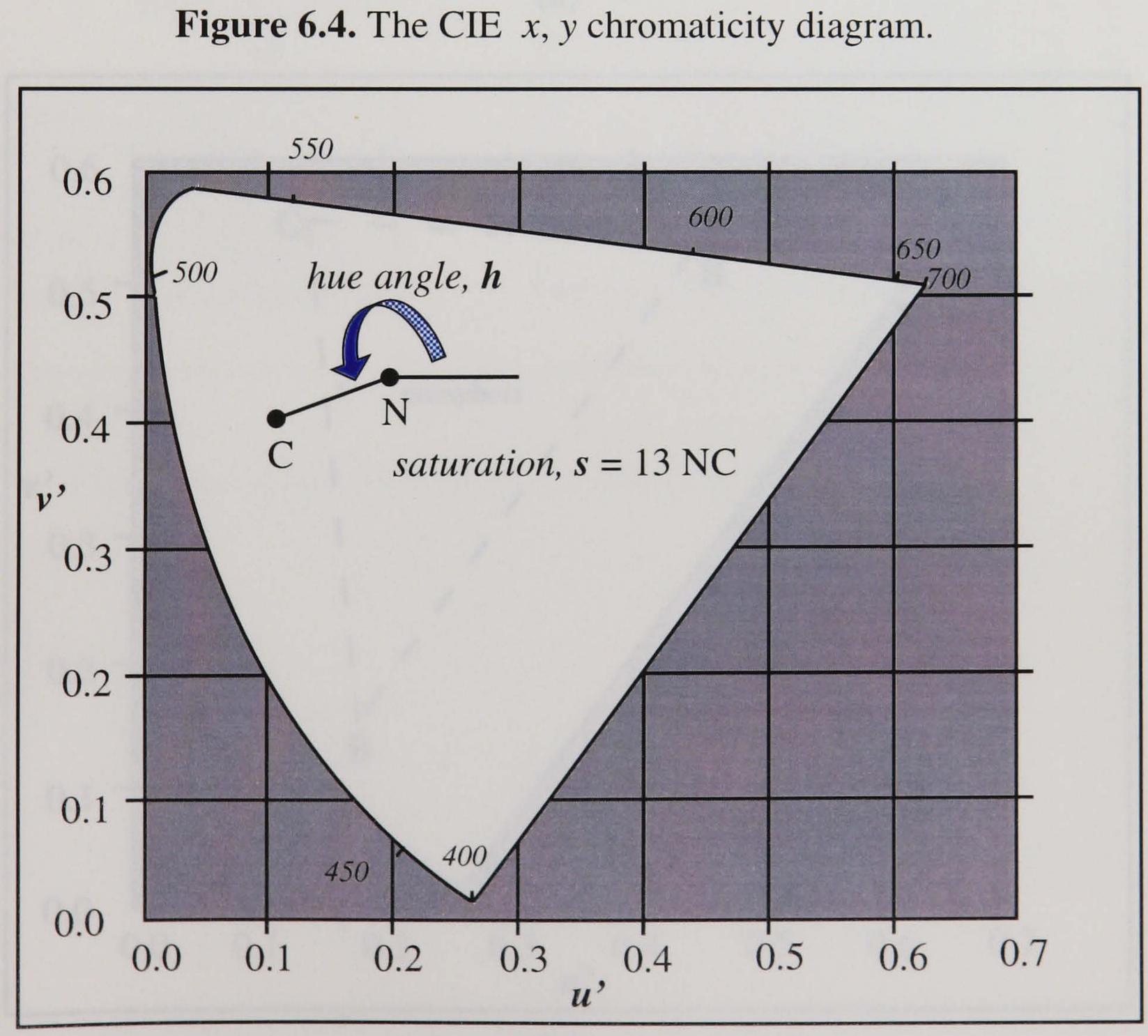

Figure 6.5. The CIE u', v' chromaticity diagram showing the definitions of hue and saturation.

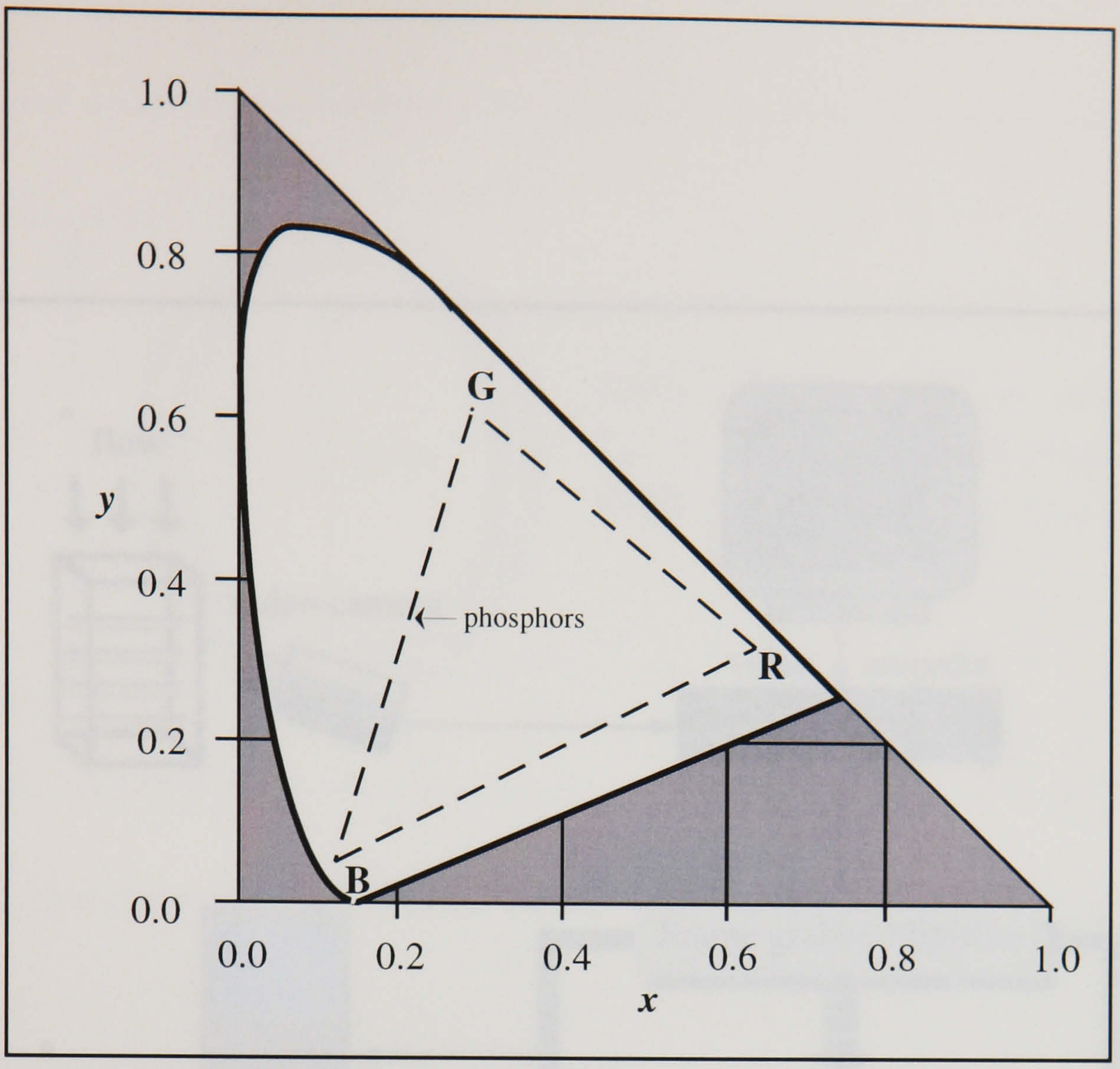

(a)

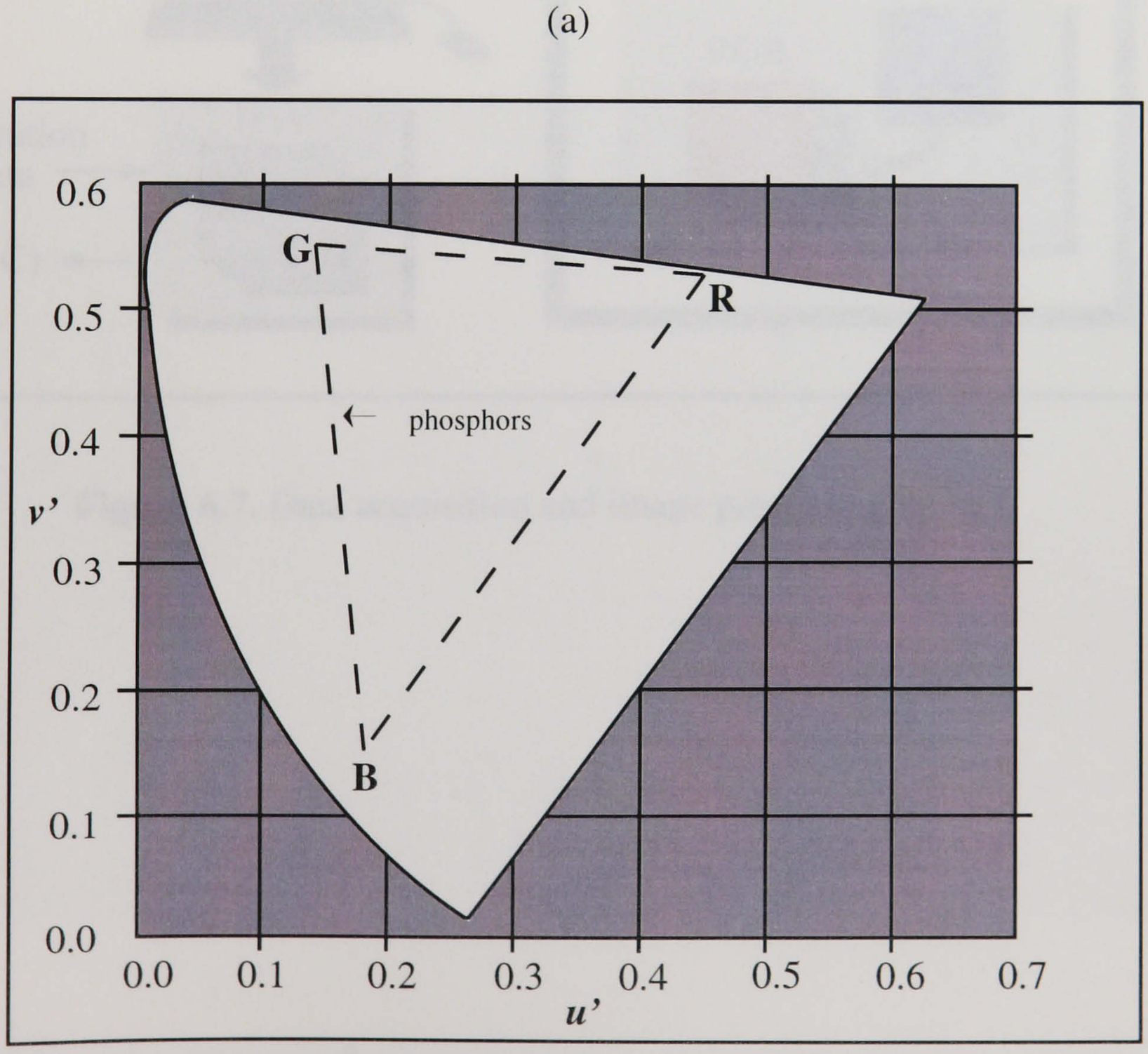

(b)

Figure 6.6. European colour television primaries shown in (a) the x, y chromaticity diagram and (b) the u', v' chromaticity diagram.

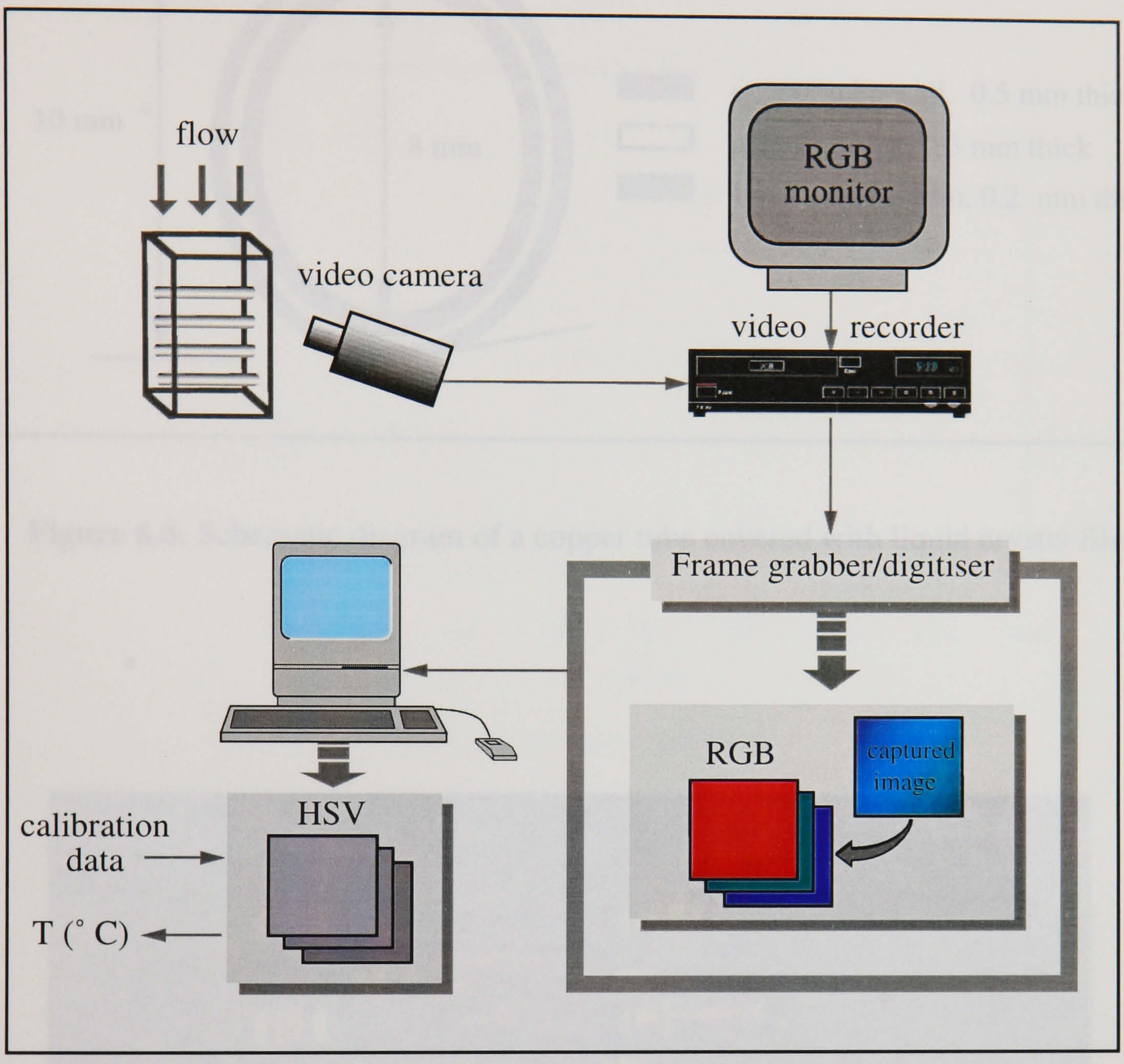

Figure 6.7. Data acquisition and image processing system.

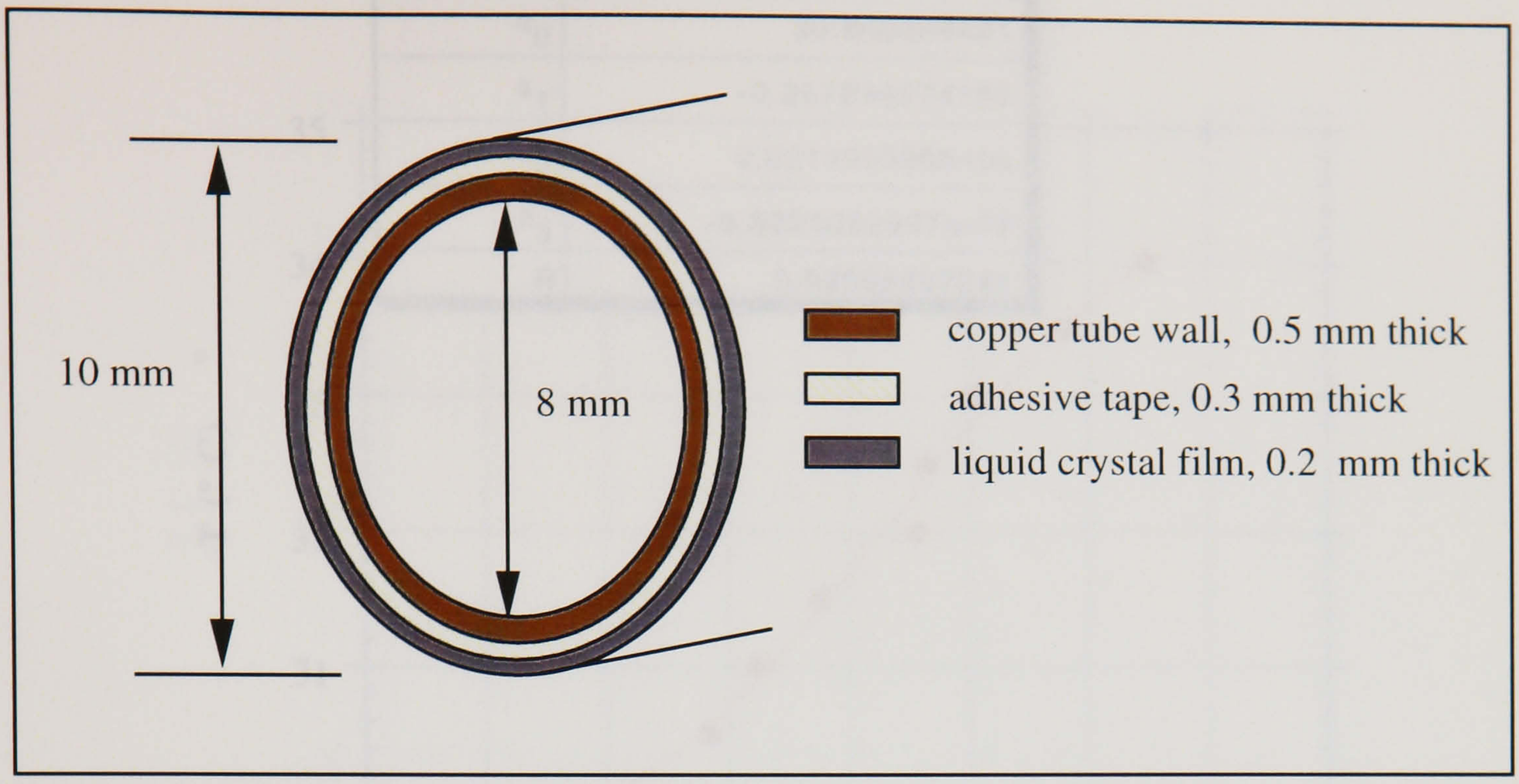

Figure 6.8. Schematic diagram of a copper tube covered with liquid crystal film.

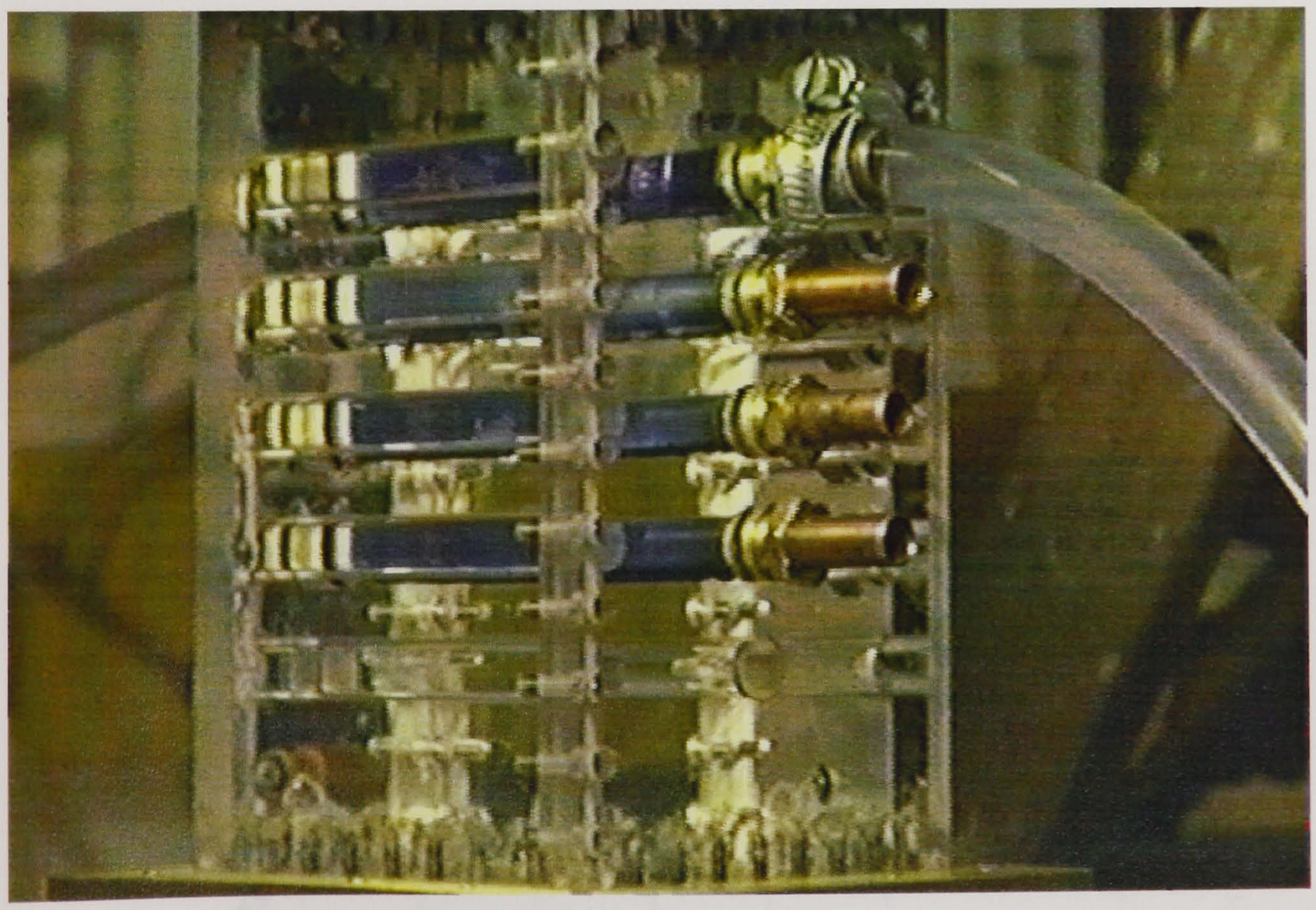

Figure 6.9. Video image of the modified in-line tube bundle model for temperature measurements using liquid crystals.

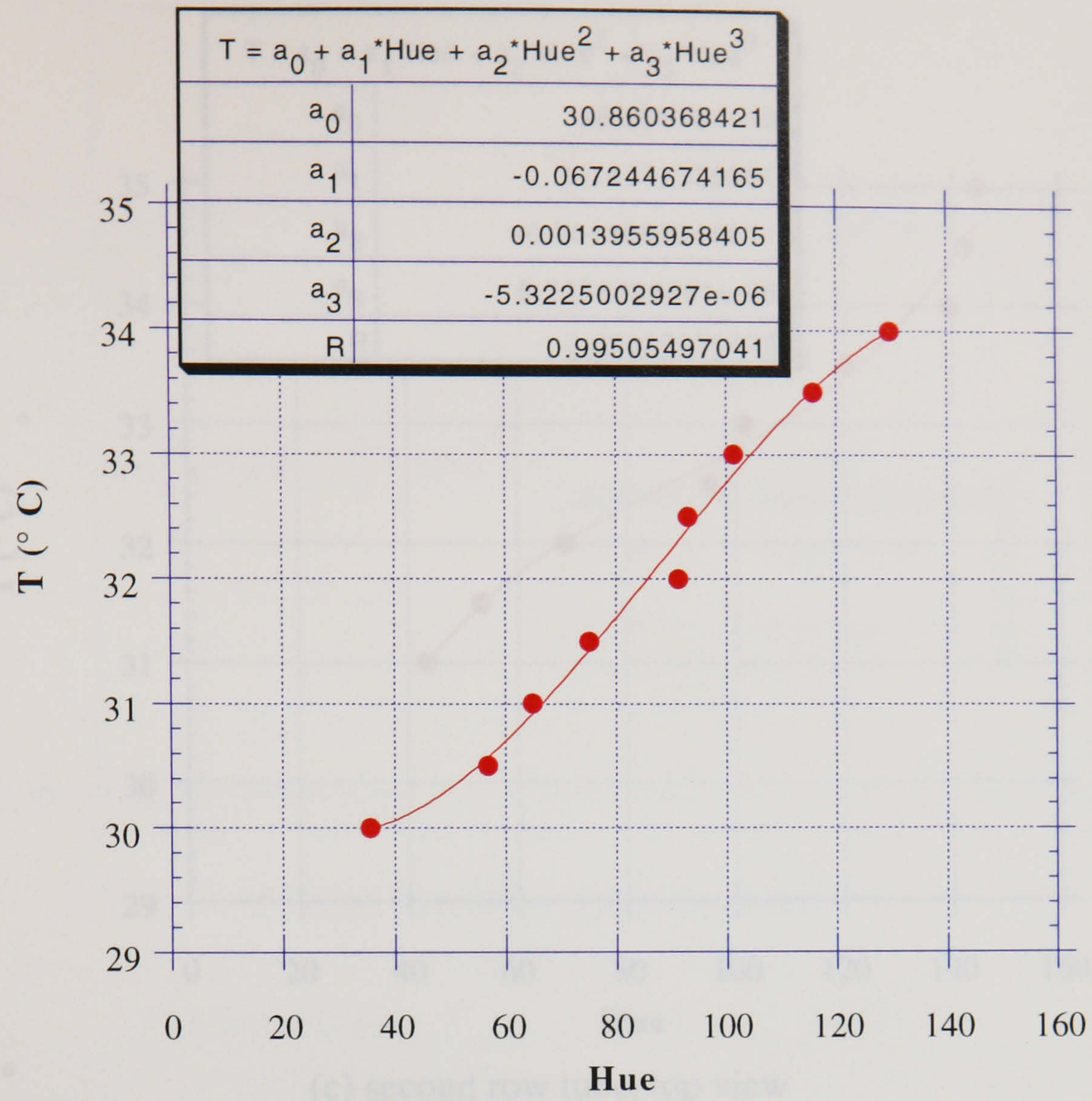

(a) first row tube, top view

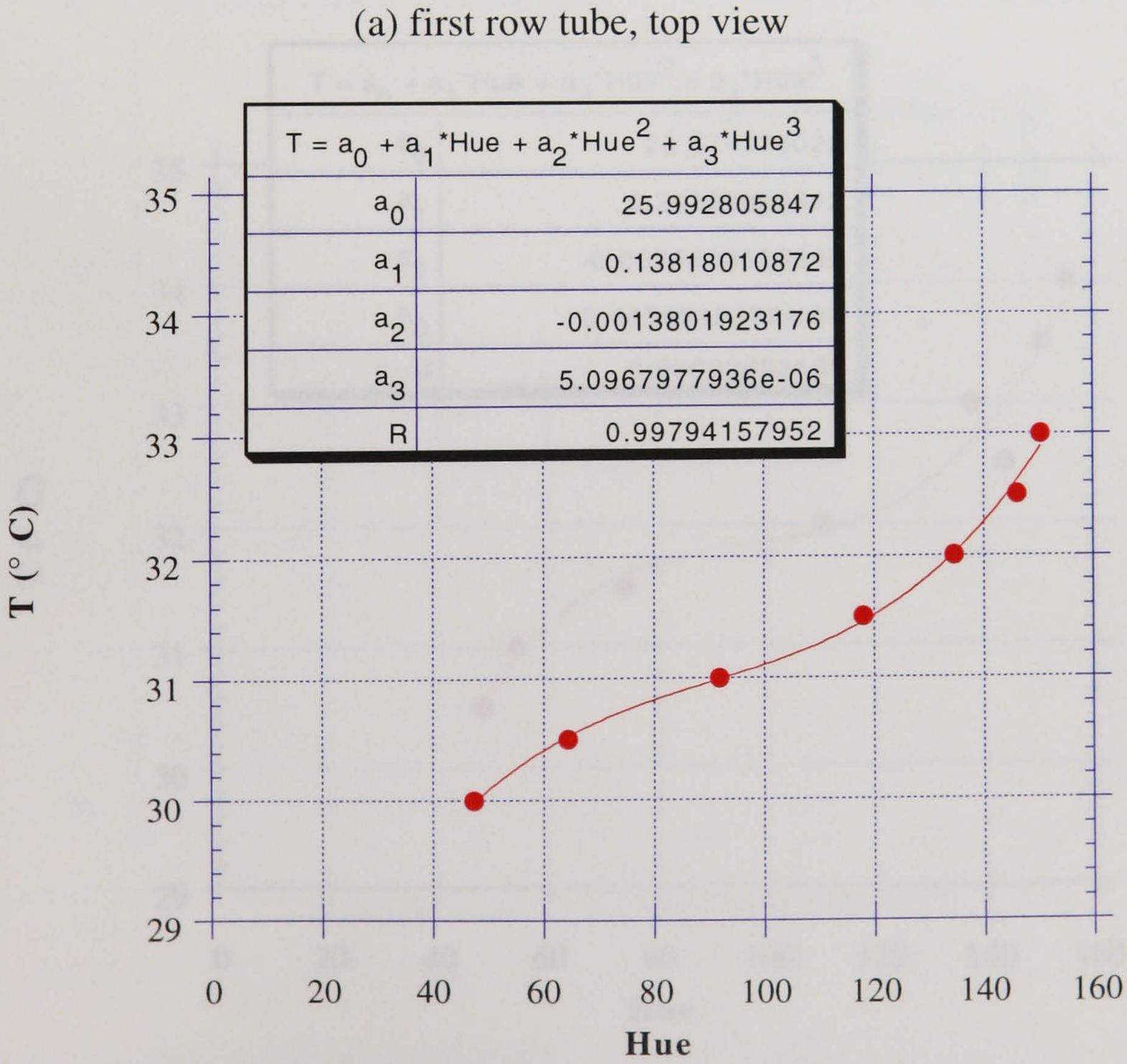

(b) first row tube, bottom view

Figure 6.10. Calibration curves for the first and second row tubes.

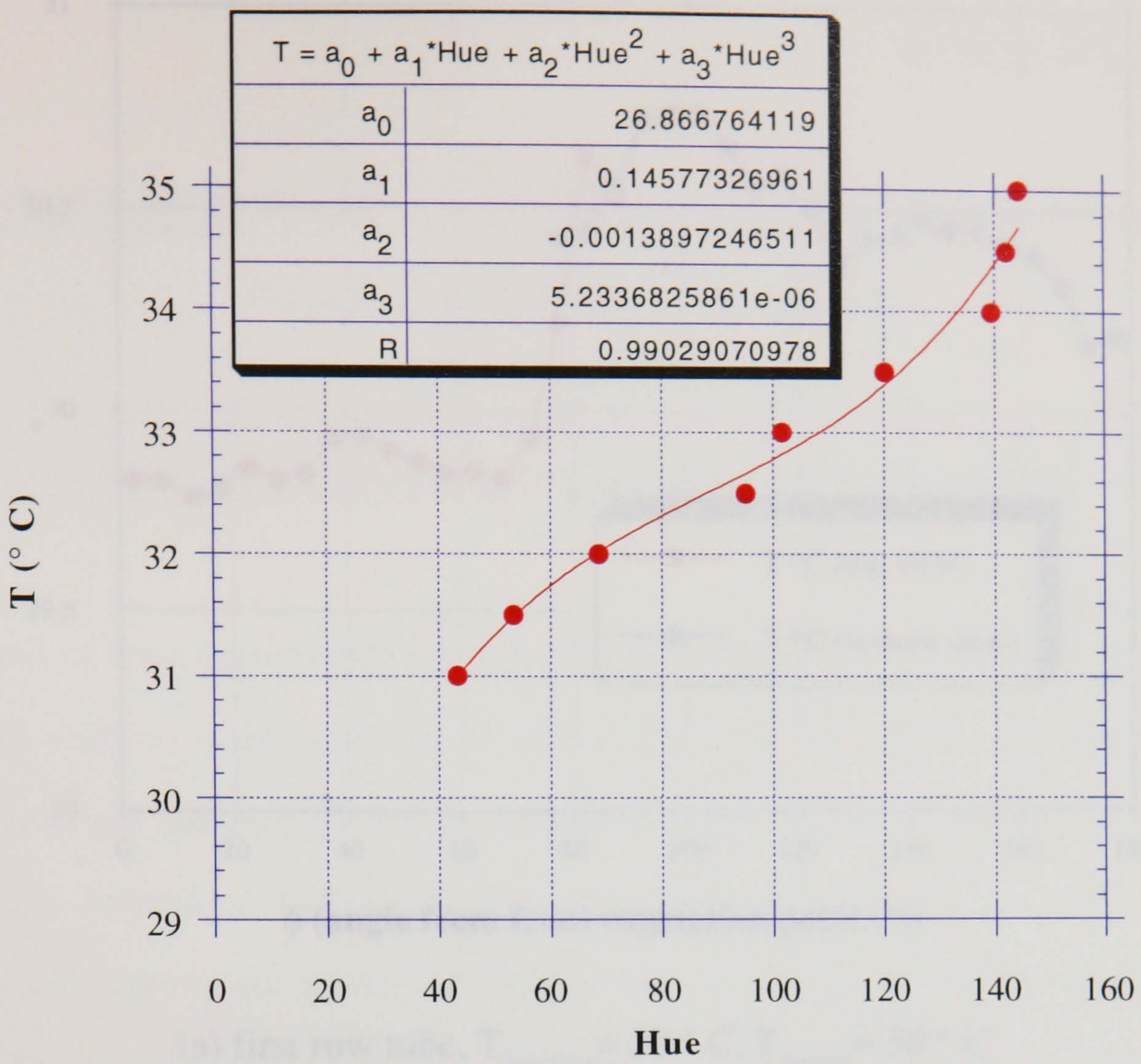

(c) second row tube, top view

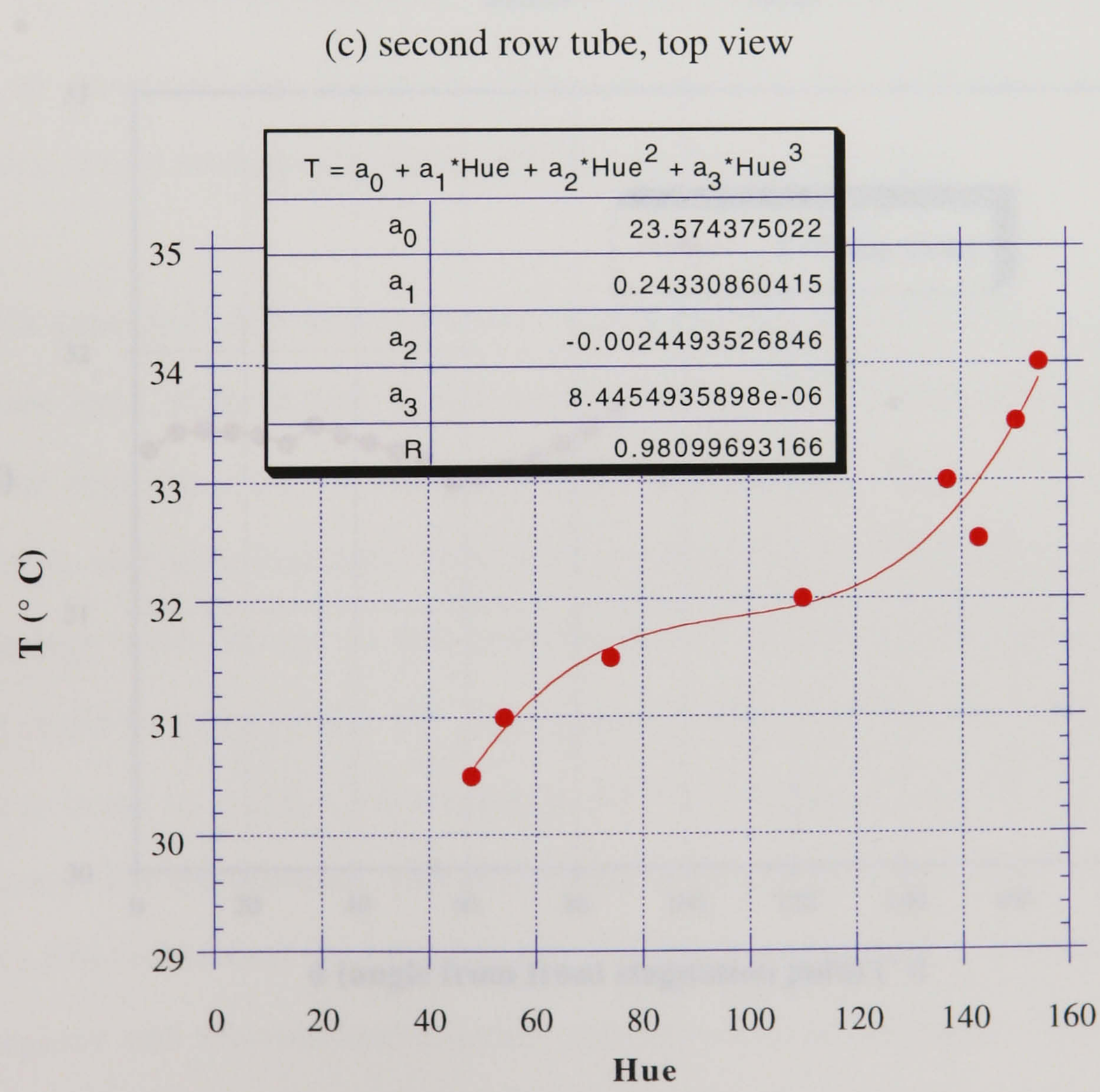

(d) second row tube, bottom view

Figure 6.10 (cont.).

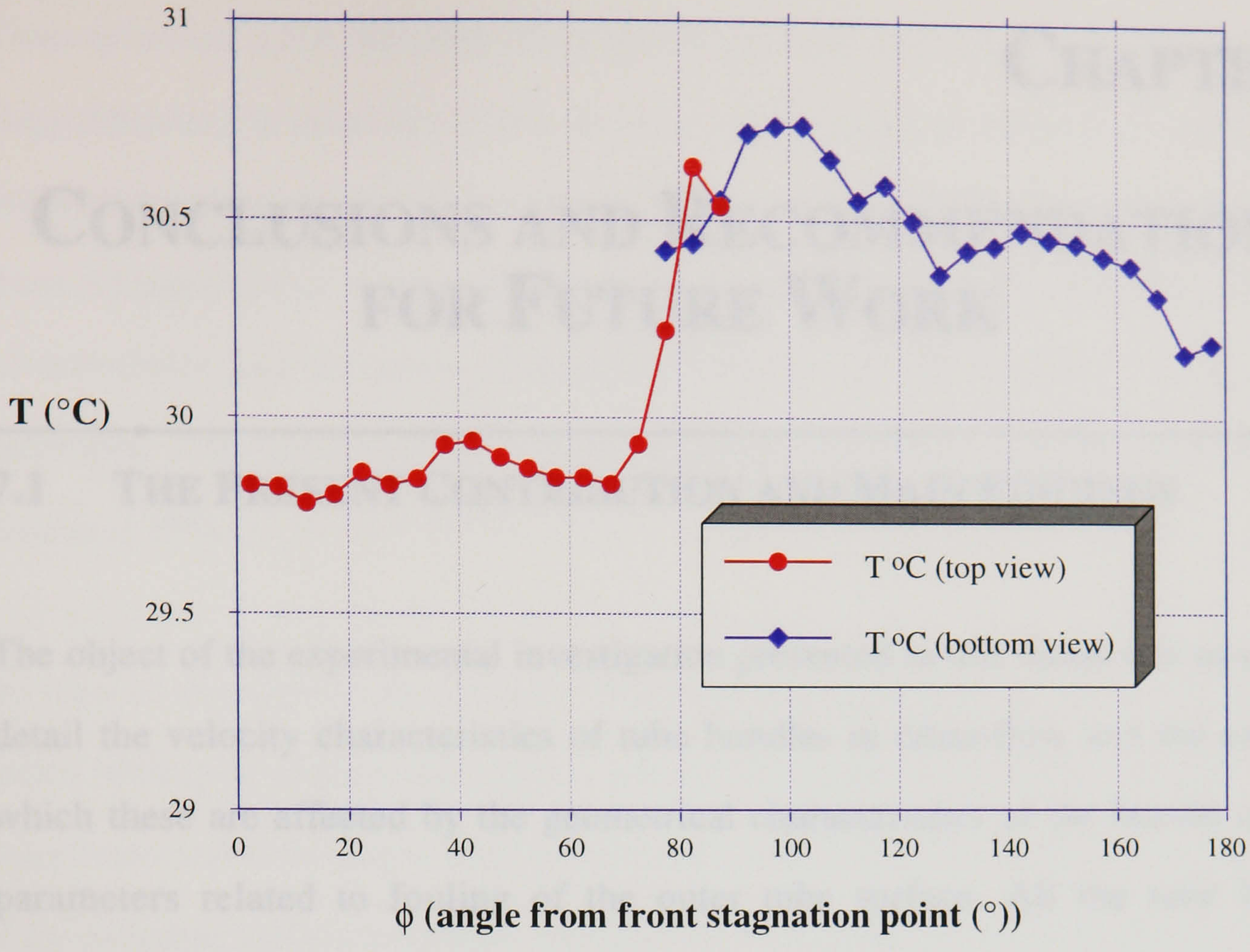

(a) first row tube, $T_{crossflow}$ = 20 ° C, $T_{internal}$ = 50 ° C

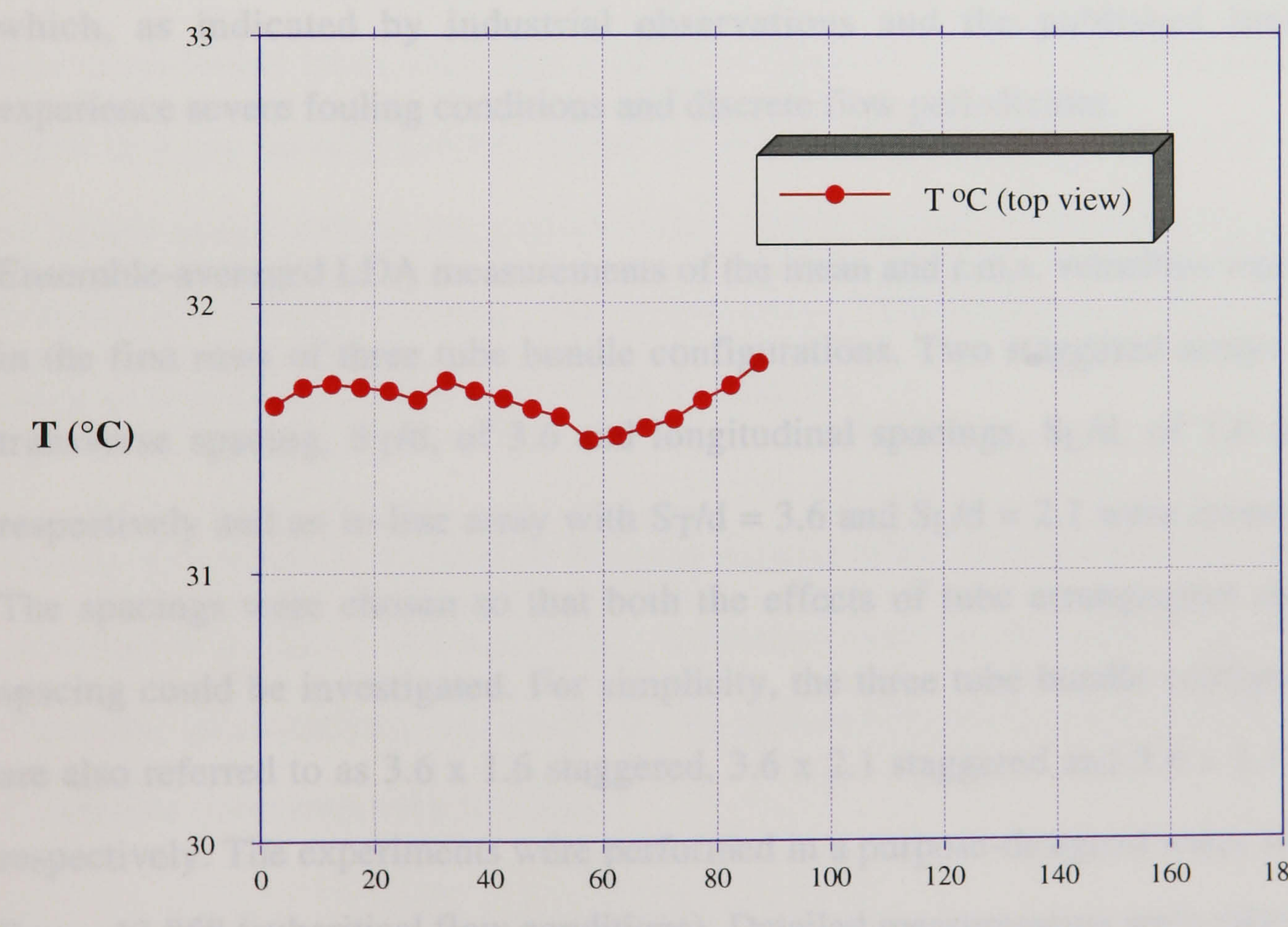

(b) second row tube, $T_{crossflow}$ = 22 ° C, $T_{internal}$ = 50 ° C

Figure 6.11. Wall temperatures measured in first (a) and second (b) row tubes (in-line tube bundle with S_T/d = 3.6, S_L/d = 2.1; Re_d=12,858).

CHAPTER 7

CONCLUSIONS AND RECOMMENDATIONS FOR FUTURE WORK

7.1 THE PRESENT CONTRIBUTION AND MAIN FINDINGS

The object of the experimental investigation presented in this thesis was to study in detail the velocity characteristics of tube bundles in cross-flow and the extent to which these are affected by the geometrical characteristics of the bundle or other parameters related to fouling of the outer tube surface. All the tube bundles investigated were scale models of typical heat exchangers used in lignite utility boilers. The project concentrated on the flow over the first rows of the tube bundles which, as indicated by industrial observations and the published literature, experience severe fouling conditions and discrete flow periodicities.

Ensemble-averaged LDA measurements of the mean and r.m.s. velocities were taken in the first rows of three tube bundle configurations. Two staggered arrays with a transverse spacing, S_T/d, of 3.6 and longitudinal spacings, S_L/d, of 1.6 and 2.1 respectively and an in-line array with $S_T/d = 3.6$ and $S_L/d = 2.1$ were investigated. The spacings were chosen so that both the effects of tube arrangement and tube spacing could be investigated. For simplicity, the three tube bundle configurations are also referred to as 3.6 x 1.6 staggered, 3.6 x 2.1 staggered and 3.6 x 2.1 in-line respectively. The experiments were performed in a purpose-designed water tunnel at $Re_d = 12{,}858$ (subcritical flow conditions). Detailed measurements were taken in the wake regions and relevant recirculating parameters were estimated. The pressure drop across the tube bundles was also measured. The effect of Re_d on both the wake characteristics and the pressure drop was investigated in the range of $Re_d = 3{,}104$ to 12,858 and $Re_d = 4{,}000$ to 12,858 respectively.

Time-resolved LDA velocity measurements were carried out in the 3.6 x 1.6 staggered array in order to identify dominant frequencies, quantify their effect on the measured turbulence levels and characterise fully the turbulence structure. From these measurements, autocorrelation functions, power spectra, time and length scales of turbulence and the rates of dissipation of the turbulence kinetic energy were estimated. The estimates were compared against numerical predictions provided by Bouris (1995).

In view of the significant changes occurring on the surface and shape of the tubes when fouling or erosion takes place, parametric studies of the effect of tube surface roughness and tube shape were performed in the 3.6 x 1.6 staggered arrangement. Two different surface roughness patterns, an evenly and a randomly distributed one, representative of those that may arise from fouling or erosion, were applied on the tubes and their effects on the mean flow and turbulence characteristics were studied. Simulated fouled tubes were also used in the first two rows of the array mentioned above to study the effect of tube shape. As most of the flows associated with fouling in lignite utility boilers are particle-laden flows, neutrally boyant particles were introduced to the cross-flow over the in-line array and their velocities were measured using an amplitude discrimination LDA technique.

Finally, due to the importance of the heat transfer in the design of tube bundle heat exchangers a liquid thermographic technique was developed and applied to determine quantitatively and qualitatively surface temperature distributions in the convective flows over tube bundles.

The main findings of this experimental study can be summarised as follows :

- The staggered tube bundles produce a complex flow pattern due to interference from neighbouring tubes. Pronounced flow reversal and steep velocity

gradients occur in the first two rows. High turbulence levels are generated with such arrangements which is beneficial in terms of heat transfer but the pressure drop is high as well. The turbulence in the wake regions is anisotropic. In general, the transverse r.m.s velocities reach higher values than the axial ones in these regions. The anisotropy is stronger downstream of the second row where the transverse r.m.s. velocities are twice as high as the axial ones. As a result, the turbulence kinetic energy is maximum downstream of the second row. This effect is more pronounced in the 3.6 x 2.1 staggered array than in the 3.6 x 1.6 one.

- The centreline velocity profiles downstream of the first and second rows are similar and exhibit characteristics typical of the flows over a single cylinder or bluff bodies in general. As a result the recirculating characteristics of the first two rows are similar. The measured recirculation length for the first two rows of the 3.6 x 1.6 staggered array is very close to that of a circular cylinder. The maximum wake width, however, is smaller than that of a single cylinder under subcritical flow conditions, probably due to the flow interference from neighbouring tubes. These parameters attain significantly smaller values in subsequent rows. Centreline r.m.s. velocities attain a maximum value around the rear stagnation point. The maximum values increase from row to row.

- Increasing the longitudinal spacing from 1.6 to 2.1 d in a staggered tube array results in lower turbulence levels. The recirculation bubbles are in general longer and wider and the recirculating mass-flow rate is increased. The vorticity thickness and its spreading rate decrease. There is a small effect of longitudinal spacing on the pressure drop: the pressure drop coefficient is reduced by 7 % on average when the relative longitudinal spacing is increased from 1.6 to 2.1 d confirming that pressure drop is primarily determined by the transverse spacing.

- When Re_d is decreased the pressure drop coefficient increases slightly in agreement with published data. The length of the recirculation regions in staggered arrays also increases logarithmically. This effect is evident in the 3.6 x 1.6 staggered array but far less pronounced in the 3.6 x 2.1 array. The maximum r.m.s. velocities in the wakes scale with Re_d.

- In-line tube bundles exhibit a less distorted flow pattern characterised mainly by high velocity flow lanes between tube columns and little mixing between adjacent flow lanes. Turbulence levels are generally lower than those found in the staggered arrangement but the pressure drop is also lower. The turbulence is again anisotropic in the wake regions with the transverse r.m.s. velocities reaching higher values than the axial ones. The anisotropy is more pronounced downstream of the third and fourth rows. The shear layer separating from the first row does not roll up to form a recirculation bubble, as indicated by the centreline mean velocities measured downstream of the first row cylinder. The width of the separated layer from the first row is greater than that in the staggered array. In contrast, in subsequent rows the rear stagnation point occurs close to the tube surface and the recirculation regions are smaller. The magnitude of the negative mean velocities downstream of the first row in the in-line array is comparable to the corresponding one in the staggered arrays but it is much lower downstream of the second row. Maxima centreline r.m.s. velocities in the in-line tube bank are much lower than the ones in the staggered arrangement confirming the low levels of turbulence generated by the in-line bank as opposed to the staggered ones.

- Time-resolved measurements in the 3.6 x 1.6 staggered array showed evidence of a discrete periodicity with a St of 0.26 attributed to vortex shedding from the cylinders. Evidence of flow instabilities was also found in the 3.6 x 2.1 staggered array as the distributions of skewness and kurtosis of the ensemble-averaged velocity measurements showed significant deviations from Gaussian

behaviour in some regions of the flow. The amplitude of the dominant frequency detected in the 3.6 x 1.6 staggered array increases from row to row, reaches a maximum between the third and fourth rows and decreases further downstream.

- The low frequency fluctuations associated with vortex shedding action were effectively separated from the high frequency fluctuations that represent the real turbulence by means of a notch filtering technique. Filtered axial r.m.s. velocities in the 3.6 x 1.6 staggered array are by up to 50 % lower than the unfiltered ones in locations of intense vorticity. The filtered r.m.s. velocities are in better agreement with numerical predictions. This might be partly expected since CFD calculations of the flow do not take the vortex shedding into account.

- The micro time scales estimated from filtered data vary from 0.4 to 2.2 ms with an average value of 0.7 ms. The integral time scales range from 1.5 ms to 8 ms with an average value of 4 ms. Length scales estimated from time scale estimates using the mean velocity as a convective velocity show some unexpected trends due to the fact that the Taylor's hypothesis is not satisfied everywhere in the flow field. A more appropriate convective velocity which takes turbulence levels into account shows some promise in improving the accuracy of the estimates in the wake regions where the Taylor's hypothesis fails. The estimation of the rate of dissipation is subject to the same uncertainties concerning the length scale estimates. Therefore, sharply increasing values in the wake regions are observed and only the ε formulation based on a dimensional argument seems to provide reasonable results. Qualitative and/or quantitative agreement with numerical estimates is achieved in some locations in the flow which is very encouraging given the approximations involved in the estimation of ε.

- Applying an evenly distributed roughness pattern on the tubes of the 3.6 x 1.6 staggered array did not affect the flow since the velocity, pressure drop and wake

characteristics were found similar to those in the smooth tube array. However, when particles were glued on the tube surface in order to produce a randomly distributed roughness pattern - akin to that found in a real fouling environment as soon as particles start depositing on the surface - significant changes on the flow characteristics were observed: the mean velocities in the flow stream between successive rows were higher, the distributions of the r.m.s. velocities differed significantly and the turbulence levels were generally higher than those of the smooth tube arrangement. The observed differences can be partly attributed to the blockage (smaller transverse pitch) caused by an increase in the tube diameter as suggested by the higher pressure drop coefficients obtained with that arrangement.

- Changes in the forebody shape of the tubes as a result of some initial particle deposition affect the flow in the 3.6 x 1.6 staggered array. It is therefore reasonable to expect that subsequent particle deposition will be affected as during heat exchanger operation the deposit is expected to grow gradually on the front of the tubes. The effects of the forebody shape are more evident in the recirculation characteristics. However, the maximum centreline r.m.s. velocities as well as the maximum centreline negative velocities are not significantly affected by the forebody shape of the tubes.

- Particle velocity measurements in the in-line tube bank indicate that in general the particles follow the flow, as might be expected by their characteristic response time. Small differences between the particle and the fluid velocities were observed in the recirculation bubbles and regions of steep velocity gradients.

- A steady state/true colour recognition liquid crystal thermographic technique was developed and applied for the measurement of wall temperature distributions in tube bundle flows. The results obtained demonstrated that detailed qualitative and quantitative information on surface temperature distributions can be obtained in tube

bundles. A number of difficulties associated with the application of the technique to curved surfaces and complex geometries such as those of a tube bundle were identified and areas where further investigation is needed in order to improve the accuracy of the technique were suggested.

The measurements described in this thesis have been used extensively for the evaluation of CFD predictions of tube bundle flows based on the k-ε model. Comparisons between the measured velocities reported in this thesis and CFD predictions of the flow were made. The CFD predictions have shown good qualitative agreement with the present results (see also Balabani and Yianneskis, 1996b). Quantitative agreement, however, has been found to be relatively poor. The predicted turbulence levels are underestimated as might be expected due to the inherent assumptions of the k-ε model and the existence of periodic phenomena which are not accounted for in the modelling.

7.2 RECOMMENDATIONS FOR FUTURE WORK

Although the experiments described in this thesis provide an extensive and accurate quantification of the flow fields generated by tube bundles and fill a substantial gap of knowledge in the published literature, there are some areas where further investigation is recommended in order to improve the understanding of tube bundle flows and the accuracy of the measurement techniques employed.

In view of the significant effects of the tube spacing and tube arrangement it seems evident that detailed information similar to that presented in this thesis should be obtained for a wider range of configurations. Although the general features of the flow are expected to be the same, different flow patterns might be expected to occur at various ranges of pitch ratios. Such studies will be very useful in assessing and classifying the interference effects between adjacent cylinders. More effort should

be directed towards small spacings due to the increasing interest in the design of compact heat exchangers. Further development of fundamental studies of the flow over simpler assemblies, as for example two cylinders in various configurations, will improve the understanding of the more complicated tube bundle flows. Experiments at higher Re_d, in the critical range or above, will provide a much needed advancement of the understanding of the flows, as most work reported to-date has been concerned with subcritical flows.

The information obtained from the time-resolved measurements was particularly useful for the characterisation of the flows. Similar data are scarce in the literature. Extension of these studies to a wider range of configurations will enable the effect of the tube geometry on the Strouhal numbers and the time scales of the flow to be quantified. In view of the controversy concerning the nature of the vorticity excitation mechanism, flow visualisation studies should accompany the research studies suggested above. Larger scale models would be preferable for flow visualisation studies since the resolution would be improved. Measurements should be carried out in tube bundle models with more rows so that the existence of turbulence buffeting in deep tube bundles reported in the literature can be investigated.

Larger scale models in conjunction with refractive index matching techniques will facilitate near wall measurements to be taken in tube bundles. Such measurements will provide detailed information about the development of the boundary layer and will aid the refinement of CFD calculations of the flow.

Due to the approximations involved in the estimation of the length scales and therefore the rate of dissipation of the turbulence kinetic energy a more appropriate technique is necessary. More accurate estimates of the length scales can be obtained from spatial correlation data which necessitate velocity measurements obtained

simultaneously at two locations in the flow. A two-measurement volume laser anemometer could be promising and should be investigated in future work.

Particle-laden flows in tube bundles should be studied in more detail using phase-Doppler anemometry. This technique allows the determination of both the dispersed and the carrier phase velocities simultaneously. In that way the effect of the dispersed phase on the turbulence characteristics of the carrier phase can be determined for various particle sizes. Well-designed particle deposition experiments in tube bundles would be particularly useful in modelling gas-side (particulate) fouling in heat exchangers.

The determination of the heat transfer coefficients in tube bundle convective flows is of prime importance in the performance of heat exchangers. Therefore, considerable effort should be directed towards improving the accuracy of the liquid crystal thermographic techniques for tube bundle applications. Future similar experiments should be designed in test sections with larger tubes so that the spatial resolution can be improved. The use of air as working fluid will make the attachment of liquid crystal films on the tube surface less problematic. In addition, the illumination of the tube surfaces should be improved and the use of alternative colour detection techniques, such as intensity-based ones, in conjunction with transient experiments should be further explored as these may ameliorate some of the problems encountered.

REFERENCES

Abd-Rabbo, A. and Weaver, D.S. (1986). A flow visualisation study of flow development in a staggered tube array. *J. Sound and Vibration*, Vol. 106, No. 2, pp. 241 - 256.

Absil, L.H.J. (1988). Laser Doppler measurements of mean turbulence quantities, time-and spatial correlation coefficients in the wake of a circular cylinder. Proc. 4th Int. Symposium on Applications of Laser Anemometry to Fluid Mechanics, Lisbon.

Achenbach, E. (1971). Influence of surface roughness on the cross-flow around a circular cylinder. *J. Fluid Mech.*, Vol. 46, No. 2, pp. 321 - 335.

Achenbach, E. (1983). Heat transfer and pressure drop of staggered and in-line heat exchangers at high Reynolds numbers. In Heat Exchangers: Theory and Practice (Ed. J. Taborek, G. F. Hewitt and N. Afgan), Hemisphere Publishing, pp. 287 - 298.

Achenbach, E. (1989). Heat transfer from a staggered tube bundle in cross-flow at high Reynolds numbers. *Int. J. Heat Mass Transfer*, Vol. 32, No. 2, pp. 271-280.

Achenbach, E. (1991). Heat transfer from smooth and rough in-line tube banks at high Reynolds number. *Int. J. Heat Mass Transfer*, Vol. 34, No. 1, pp. 199 - 207.

Adams, J., Haas, W. and **Wysocki, J. (1969).** Light scattering properties of cholesteric liquid crystal films. In Liquid Crystals 2 (Ed. G.H.Brown), Gordon and Breach Science Publishers, London, pp. 601 - 610.

Adrian, R.J. and **Yao, C.S. (1987).** Power spectra of fluid velocities measured by laser Doppler velocimetry. *Experiments in Fluids*, Vol. 5, pp. 17-28.

Aiba, S., Tsuchida, H. and **Ota, T. (1982a).** Heat transfer around tubes in in-line tube banks. *Bulletin of the JSME*, Vol. 25, No. 204, pp. 919 - 926.

Aiba, S., Tsuchida, H. and **Ota, T. (1982b).** Heat transfer around tubes in staggered tube banks. *Bulletin of the JSME*, Vol. 25, No. 204, pp. 927 - 933.

Antonia, R.A., Zhou, Y. and **Matsumura (1993).** Spectral characteristics of momentum and heat transfer in the turbulent wake of a circular cylinder. *Experimental Thermal and Fluid Science*, Vol. 6, pp. 371 - 375.

Ashford-Frost, S., Edwards, R.J., Graham, D.P., Lowesmith, B.J., Jambunathan, K. and **J.M. Rhine (1992).** Measurement of convective heat transfer coefficients, on the ligaments of a model shell boiler tube plate using liquid crystal thermography. Proc. 3rd U.K. National Heat Transfer Conference incoprorating 1st European Conference on Thermal Sciences, 16 - 18 September 1992, Birmingham, U.K., Vol. 1, pp. 351 - 359.

Ashford-Frost, S., Jambunathan, K., Whitney, C.F. and **Ball, S. J. (1996a).** Heat transfer from a flat plate to a turbulent axisymmetric impinging jet. Proc. Int. Seminar on Optical Methods and Data Processing in Heat and Fluid Flow, 18-19 April 1996, IMechE Conference Transactions, paper C516/031/96, pp. 71 - 79.

Ashford-Frost, S., Ju, X. Y., Jambunathan, K. and **Wu X. (1996b).** Application of liquid crystals to particle image velocimetry. Proc. Int. Seminar on Optical Methods and Data Processing in Heat and Fluid Flow, 18-19 April 1996, IMechE Conference Transactions, paper C516/031/96, pp. 71 - 79.

Balabani, S. and **Yianneskis, M. (1993a)**. Flow and heat transfer characteristics of tube bundles in crossflow. King's College London, Department of Mechanical Engineering Report EM/93/05.

Balabani, S. and **Yianneskis, M. (1993b)**. Gas-side fouling: Particulate deposition mechanisms, modelling and operational studies. King' s College London, Department of Mechanical Engineering Report EM/93/13.

Balabani, S. and **Yianneskis, M. (1994).** Wake characteristics of tube bundles in crossflow. Proc. Eurotherm Seminar No. 40: Combined Energy and Water Management in Industry, Thessaloniki, Greece, October 1994.

Balabani, S. and **Yianneskis, M. (1996a).** Turbulence scales and spectra in staggered tube bundles. Paper presented at the 8th Int. Symposium on Applications of Laser Techniques to Fluid Mechanics, July 8-11, 1996, Lisbon.

Balabani, S. and **Yianneskis, M. (1996b).** An experimental study of the mean flow and turbulence structure of cross-flow over tube bundles. *Proc. of IMechE, Part C, Journal of Mech. Eng. Science* (in print).

Balabani, S., Bergeles, S., Burry, D. and **Yianneskis, M. (1994)** Velocity characteristics of the crossflow over tube bundles. Proc. 7th Int. Symposium on Applications of Laser Techniques to Fluid Mechanics, Lisbon, Vol II, pp. 39.3.1-39.3.8.

Ball, W.F., Pettifer, H.F. and **Waterhouse, C.N.F. (1983).** Laser Doppler velocimeter measurements of turbulence in a direct-injection diesel combustion chamber. I.Mech.E, Conference on Combustion in Engineering, 1983, Paper no. C52/83.

Bates, C. J. (1982). Experimental investigation of the flow through various cylindrical tube bundles. Proc. Int. Symp. Applications of LDA to Fluid Mechanics, Lisbon, Paper 15.3.

Batham, J. P. (1973). Pressure distributions on circular cylinders at critical Reynolds numbers. *J. Fluid Mech.*, Vol. 57, No. 2, pp. 209 - 228.

Bemrose, C.R. and **Bott, T.R. (1984).** Correlations for gas-side fouling of finned tubes. Proc. First U.K. National Conference on Heat Transfer, Leeds, Institution of Chemical Engineers Symposium Series No. 86, Vol. 1, pp. 357 - 367.

Bendat, J. S. and **Piersol, A.G. (1971).** Random data: analysis and measurement procedures, Wiley-Interscience.

Bergeles, G., Bouris-Burry, D., Yianneskis, M., Balabani, S., Kravaritis, A., and **Itskos, S. (1995).** Effects of fouling on the efficiency of heat exchangers in lignite utility boilers. Proc. European Seminar on Energy Efficiency in Industry, Brussels, 1995, 10 pp.

Bergeles, G., Yianneskis, M., Kravaritis, A., Balabani, S., Bouris-Burry, D. and **Itskos, S. (1996).** Effects of fouling on the effieciency of heat exchangers in lignite utility boilers. Final Report, Joule II Research Programme, Contract No. JOU2-CT92-0014.

Bergelin, O.P., Davis, E.S. and **Hull, H.L. (1949).** A study of three tube arrangements in unbaffled tubular heat exchangers. *Trans. ASME*, Vol. 71, pp. 369 - 374.

Bisset, D. K., Antonia, R.A. and **Britz, D. (1990b).** Structure of large-scale vorticity in a turbulent far wake. *J. Fluid Mech.*, Vol. 218, pp. 463 - 482.

Bisset, D. K., Antonia, R.A. and **Browne, L.W.B. (1990a).** Spatial organisation of large structuers in the turbulent far wake of a cylinder. *J. Fluid Mech.*, Vol. 218, pp. 439 - 461.

Bloor, M.S. (1964). The transition to turbulence in the wake of a circular cylinder. *J. Fluid Mech.*, Vol.19, pp. 290 - 304.

Bloor, M.S. and **Gerrard, J. H. (1966).** Measurements on turbulent vortices in a cylinder wake. *Proc. Roy. Society London: Series A*, Vol. 294, pp. 319 - 342.

Bott, T.R. (1988). Gas-side fouling. In Fouling Science and Technology, (Eds. L.F. Melo, T.R. Bott and C.A. Bernardo), Kluwer Academic Publishers, pp. 191 - 203.

Bouris, D. (1995). Personal communication.

Bouris-Burry, D. and **Bergeles, G. (1994).** A model for deposition of ash particles onto a solid surface. Proc. Eurotherm Seminar No. 40: Combined Energy and Water Management in Industry, Thessaloniki, Greece, October 1994.

Brown, G.L. and **Roshko,A. (1974).** On density effects and large structure in turbulent mixing layers. *J. Fluid Mech.*, Vol. 64, No. 4, 775-816.

Buchhave, P., George, W.K. and **Lumley, J.L. (1979).** The measurement of turbulence with the laser-Doppler anemometer. *Ann. Rev. Fluid Mech.*, Vol. 11, pp. 443-503.

Cantwell, B. and **Coles, D. (1983).** An experimental study of entrainment and transport in the turbulent near wake of a circular cylinder. *J. Fluid Mech.*, Vol. 136, pp. 321 - 374.

Cenedese, A., Costantini, A. and **Romano, G.P. (1992).** LDA spectral measurements in a turbulent boundary layer. *Experimental Thermal and Fluid Science*, Vol. 5, pp. 281-289.

Chan, T.L., Leung, T.P., Jambunathan, K. and **Ashford-Frost, S. (1995).** Calibration of thermochromic liquid crystals applied to an oblique surface. Proc. 4th U.K. National Conference on Heat Transfer, 26-27 September 1995, IMechE Conference Transactions, paper C510/059/95. pp. 61 - 66.

Chen, Y.N. (1977). The sensitive tube spacing region of tube bank heat exchangers for fluid elasting coupling in crossflow. ASME Symposium Fluid Structure Interaction Phenomena in Pressure Vessel and Piping Systems (Eds. M.K. Au-Yang and S.J. Brown), 1977, pp. 1-18.

Cheung, R.S.W (1989). An investigation of flow patterns inside inlet ports. PhD Thesis, King's College London, University of London.

Collinson, A.E And Robinson, R.G.J. (1991). Cross-flow Strouhal numbers in square and triangular pitch tube arrays at Re from 0.8-3.5 x 10^5. In Flow Induced Vibrations , I.Mech.E, Paper C416/083, pp. 217-229.

Cooper, T. E., Field, R. J. and **Meyer, J. F. (1975).** Liquid crystal thermography and its application to the study of convective heat transfer. *Trans. ASME, J. Heat Transfer*, August 1975, pp. 442 - 450.

Critoph, R.E. and **Holland, M.K. (1996).** A study of local heat transfer coefficients in a plate fin-tube heat exchanger using a steady state liquid crystal technique. Proc. Int. Seminar on Optical Methods and Data Processing in Heat and Fluid Flow, 18-19 April 1996, IMechE Conference Transactions, paper C516/002/96, pp. 39 - 46.

Dabiri, D. and **Gharib, M. (1991).** Digital particle image thermometry: The method and implementation. *Experiments in Fluids*, Vol. 11, pp. 77 - 86.

Davies, R. M., Rhines, J. M. and **Sidhu, B. S. (1984).** The application of the liquid crystal technique to the experimental modelling of forced convective heat transfer in industrial heating processes. Proc. 1st U.K. National Heat Transfer Conference, Leeds, U.K., 3-5 July, 1984.

Djenidi, L. and **Antonia, R.A. (1995).** LDA measurements: Power spectra estimation. Dantec Information, Vol. 14, January 1995, pp.12-15.

Drain, L. E. (1980). The laser Doppler technique. John Wiley and Sons, UK.

Durâo, D. F. G. and **Whitelaw, J. H. (1976).** The influence of sampling procedure on the velocity bias in turbulent flows. The Accuracy of Flow Measurements by Laser Doppler Methods, Proc. LDA-Symposium, Copenhagen 1975, pp. 138 -149.

Durâo, D. F. G. and **Whitelaw, J. H. (1978).** Velocity characteristics of the flow in the near wake of a disk. *J. Fluid Mech.*, Vol. 85, No. 2, pp. 369 - 385.

Durâo, D. F. G., Laker, J. and **Whitelaw, J. H. (1980).** Bias effects in laser Doppler anemometry, *J. Phys. E.:Sci. Instrum.*, Vol 13, p. 442 - 445.

Durst, F., Melling, A. and **Whitelaw, J. H. (1976).** Principles and practice of Laser-Doppler anemometry. Academic Press, London.

Elphick, I.G., Martin, W.W. and **Currie, I. G. (1982).** Application of LDA to high Reynolds number cross flow. Proc. Int. Symposium on Applications of LDA to Fluid Mechanics, Lisbon, Paper 15.1.

Epstein, N. (1988). Particulate fouling of heat transfer surfaces: mechanisms and models. In Fouling Science and Technology (Eds. L.F. Melo, T.R. Bott and C.A. Bernardo), Kluwer Academic Publishers, pp. 143 - 164.

Farell, C. and **Blessmann, J. (1983).** On critical flow around smooth cylinders. *J. Fluid Mech.*, Vol. 136, pp. 375 - 391.

Farina, D.J., Hacker, J.M., Moffat, R.J. and **Eaton, J.K. (1994).** Illuminant invariant calibration of thermochromic liquid crystals. *Experimental Thermal and Fluid Science*, Vol. 9, pp. 1 - 12.

Ferre, J.A., Mumford, J.C., Savill, A.M. and **Giralt, F. (1990).** Three-dimensional large-eddy motions and fine-scale activity in a plane turbulent wake. *J. Fluid Mech.*, Vol. 210, pp. 371 - 414.

Fiebig, M., Valencia, A. and **Mitra, N.K (1994).** Local heat transfer and flow losses in fin-and-tube heat exchangers with vortex generators: a comparison of round and flat tubes. *Experimental Thermal and Fluid Science*, Vol. 8, pp. 35 - 45.

Fitzpatrick, J.A. and **Donaldson, I.S. (1980).** Row depth effects on turbulence spectra and acoustic vibrations in tube banks. *J. Sound and Vibration*, Vol. 73, No. 2, pp. 225-237.

Fitzpatrick, J.A., Lambert, B. and **Murray, D.B. (1992).** Measurements in the separation region of a gas - particle cross flow. *Experiments in Fluids*, Vol.12, pp. 329 - 341.

Fox, T.A. and **West, G.S. (1990).** On the use of end plates with circular cylinders. *Experiments in Fluids*, Vol. 9, No. 4, pp. 237-339.

Gaster, M. and **Roberts, J.B. (1975).** Spectral analysis of randomly sampled signals. *J. Inst. Maths. Applics.*, Vol. 15, pp. 195-216.

Gaster, M. and **Roberts, J.B. (1977).** The spectral analysis of randomly sampled records by a direct transfrom. *Proc. R. Soc. Lond. A*, Vol. 354, pp.27-58.

Gennes, P.G. (1974). The physics of liquid crystals. Clarendon Press, Oxford.

George, W.K. (1975). Limitations to measuring accuracy inherent in the Laser Doppler signal. The Accuracy of Flow Measurements by Laser Doppler Methods, Proc. LDA-Symposium, Copenhagen 1975, pp. 20 - 64.

George, W.K. and **Lumley, J.L. (1973).** The laser-Doppler velocimeter and its application to the measurement of turbulence. *J. Fluid Mech.*, Vol. 60, No. 2, pp. 321-362.

Gerrard, J. H. (1966). The mechanics of the formation region of vortices behind bluff bodies. *J. Fluid Mech.*, Vol. 25, No. 2, pp. 401 - 413.

Gerrard, J. H. (1967). Experimental investigation of separated boundary layer undergoing transition to turbulence. *Phys. Fluids Supplement*, Vol. 10, No. 9, Part II, pp. S98 - S100.

Glen, N.F. and **Howarth, J.H. (1988).** Modelling refuse incineration fouling. Proc. 2nd UK National Conference on Heat Transfer, Glasgow, 1988, IMechE. Vol. 1, paper C119/88, pp. 401 - 420.

Glen, N.F. and **Howarth, J.H. (1989).** A deposition model for pulverised coal firing. Institute of Physics, Short Meeting Series, No. 23, pp. 33 - 48, The Institute of Physics.

Glen, N.F., Flynn, S., Grillot, J.M. and **Mercier, P. (1992).** Measurement and modelling of fouling on finned tubes. In Fouling Mechanisms: Theoretical and Practical Aspects, Proc. Eurotherm Seminar No. 23, Grenoble, France (Eds. M. Bohnet, T.R. Bott, A.J. Karabelas, P.A. Pilavachi, R. Semeria and R. Vidil), Editions Europeennes Thermique et Industrie, pp. 181 - 188.

Gomiciaga, R.P (1995). An experimental and numerical study of natural convection in cavities heated from below. PhD Thesis, King's College London, University of London.

Gore, R.A. and **Crowe, R.A. (1991).** Modulation of turbulence by a dispersed phase. *Trans. ASME, J. Fluids Engineering*, Vol. 113, pp. 304 - 307.

Gosman, A.D. And Ahmed, A.M.Y. (1987). Measurement and multidimensional prediction of flow in an axisymmetric port/valve assembly. SAE Paper 870592.

Gould, R.D. and **Benedict, L.H. (1994).** Comparison of length scale estimates for a sudden expansion flow estimated from spatial and auto correlation LDV measurements. *Experiments in Fluids*, Vol. 17, No. 4, pp.285-287.

Grimison, E. D. (1937). Correlation and utilisation of new data on flow resistance and heat transfer for cross flow of gases over tube bundles. *Trans. ASME*, Vol. 59, pp. 583 - 594.

Güven, O., Farell, C. and **Patel, V.C. (1980).** Surface-roughness effects on the mean flow past circular cylinders. *J. Fluid Mech.*, Vol. 98, No. 4, pp. 673 - 701.

Habib, M.A. and **Whitelaw, J.H. (1979).** Velocity characteristics of a confined coaxial jet. *Trans. ASME, J. Fluids Engineering,* Vol. 101, pp. 521-529.

Halim, M.S. (1988). Detailed velocity measurements of flow through staggered and in-line tube banks in cross-flow using laser Doppler anemometry. PhD Thesis, University of Manchester.

Halim, M.S. and **Turner, J.T. (1986)**. Measurements of cross flow development in a staggered tube bundle. Proc. 3rd Int. Symposium on Applications of Laser Anemometry to Fluid Mechanics, Lisbon, 1986, paper 21.7.

Hardalupas, Y., Taylor, A.M.K.P. and **Whitelaw, J.H. (1989).** Velocity and particle-flux characteristics of turbulent particle-laden jets. *Proc. R. Soc. Lond. A*, Vol. 426, pp. 31 - 78.

Hardalupas, Y., Taylor, A.M.K.P. and **Whitelaw, J.H. (1992).** Particle dispersion in a vertical round sudden-expansion flow. *Phil. Trans. R. Soc. Lond. A*, Vol 341, pp. 411-442.

Heskestad, G. (1965). A generalised Taylor's hypothesis with application for high Reynolds number turbulent shear flows. *Trans. ASME, J. Applied Mech.*, Vol. 32, pp. 735-739.

Hill, R.S., K.C. Shim and **R.I. Lewis (1986).** Sources of excitation in tube banks due to vortex shedding. *Proc. Instn Mech. Engrs.*, Vol. 200, No. C4, pp. 293-301.

Hinze, J.O. (1975). Turbulence, 2nd Edition, McGraw-Hill.

Huge, E.C. (1937). Experimental investigation of effects of equipment size on convection heat transfer and flow resistance in cross flow of gases over tube banks. *Trans. ASME*, Vol. 59, pp. 573 -581.

Humphries, W. and **Vincent, J.H. (1976).** Near wake properties of axisymmetric bluff body flows. *Appl. Sci. Res.*, Vol. 32, pp. 649 - 669.

Hunt, R.W.G. (1987). Measuring Colour. Ellis Horwood, London.

Jacob, M. (1938). Heat transfer and flow resistance in cross flow of gases over tube banks. *Trans. ASME*, Vol. 60, pp. 384-386.

Katinas, V. and **Tumosa, A. (1992).** Heat transfer and fluid dynamics in asymmetric transverse flows over bundles of tube in heat exchangers. In Recent Advances in Heat Transfer (Eds. B. Sundén and A. Zukauskas), Elsevier, pp. 532 - 540.

Kresta, S.M. (1991). Characterization, Measurement and Prediction of the Turbulent Flow in Stirred Tanks. PhD Thesis, McMaster University, USA.

Lambert, B., Fitzpatrick, J. A. and **Murray, D.B. (1988).** LDA measurements for large particle flows over a circular cylinder. Proc. 4th Int. Symposium on Applications of Laser Anemometry to Fluid Mechanics, Lisbon, 1988.

Le Coz, J.F., Henriot, S. and **Pinchon, P. (1990).** An experimental and computational analysis of the flow field in a four-valve spark ignition engine-focus on cycle-resolved turbulence. SAE Paper 900056.

Lee, K.C. (1995). An experimental investigation of the trailing vortex structure and mixing characteristics of stirred vessels. PhD Thesis, King's College London, University of London.

Ljungkrona, L. and Sundén, B. (1993). Flow visualisation and surface pressure measurements on two tubes in an in-line arrangement. *Experimental Thermal and Fluid Science*, Vol. 6, pp. 15 - 27.

Ljungkrona, L., Norberg, C. and **Sundén, B. (1991a)**. Flow around two tubes in an in-line arrangement; flow visualisation and pressure measurements. In Experimental Heat Transfer, Fluid Mechanics and Thermodynamics (Eds. J.F. Keffer, R.K. Shah and E.N. Ganic), Elsevier Science Publishing, pp. 333 - 340.

Ljungkrona, L.R., Sundén, B.A., Goyder, H.G.D and **Teh, C.E. (1991b).** Wall pressure distribution on an in-line tube bundle in cross-flow. Proc. IMechE International Conference on Flow Induced Vibrations, Brighton, 1991, Paper C416/062, Mechanical Engineering Publications, London, pp.517-522.

Maekawa, T. and **Mizuno, S. (1967).** Flow around the separation point and in the near-wake of a circular cylinder. *Phys. Fluids Supplement*, Vol. 10, No. 9, Part II, pp. S184 - S186.

Mahmoudi, S. S. M. (1993). Velocity and mixing characteristics of stirred vessels with two impellers. PhD Thesis, King's College London, University of London.

Massey, B.S. (1983). Mechanics of Fluids, 5th edition, Van Nostrand Reinhold, UK.

Massons, J., Ruiz, X. and **Diaz, F. (1989).** Image processing of the near wakes of stationary and rotating cylinders. *J. Fluid Mech.*, Vol. 204, pp. 167 - 184.

McDonnell, C. and **Fitzpatrick, J.A. (1992).** Spectral analysis of turbulent flows from LDA measurements. Proc. 6th Int. Symposium on Applications of Laser Anemometry to Fluid Mechanics, Lisbon, pp. 8.3.1 - 8.3.5.

McKillop, A.A. and **Durst, F. (1984)**. LDA experiments of separated flow behind a circular cylinder. Proc. 2nd Int. Symposium on Applications of Laser Anemometry to Fluid Mechanics, Lisbon, 1984, paper 14.4.

McLaughlin, D.K. and **Tiederman, W. G. (1973).** Biasing correction for individual realisation laser anemometer measurements in turbulent flows, *Phys. of Fluids*, Vol. 6, No. 12, pp. 2082 - 2088.

McMahon, B. and **Murray, D.B. (1996).** Local heat transfer measurements in a tube array using the transient method and liquid crystal thermography. Proc. Int. Seminar on Optical Methods and Data Processing in Heat and Fluid Flow, 18-19 April 1996, IMechE Conference Transactions, paper C516/003/96, pp. 47 - 56.

Meier, G., Sackmann, E. and **Grabmaier, J.G. (1975).** Applications of liquid crystals. Springer Verlag, Berlin-Heidelberg.

Melling, A. (1975). Investigation of flows in non-circular ducts and other configurations by laser Doppler anemometry. PhD Thesis, Imperial College, University of London.

Melling, A. (1977). Axisymmetric, turbulent flow in a motored reciprocating engine. Imperial College Mech. Eng. Dept. Report CHT/77/4, 1977.

Merker, G.P. and **Hanke, H.** (1986a). Heat transfer and pressure drop on the shell - side of tube- banks having oval - shaped tubes. *Int. J. Heat Mass Transfer*, Vol. 29, No. 12, pp. 1903 - 1909.

Merker, G.P. and **Hanke, H.** (1986b). Measurements of local mass transfer coefficients and pressure distribution along the shell - side of oval - shaped tubes in cross flow heat exchangers. In Heat Transfer 1986, Proc. 8th Int. Heat Transfer

Conference, San Francisco (Eds. C.L. Tien, V.P. Carey and J. K. Ferrell). Hemisphere Publishing, Vol. 6, pp. 2721 - 2726.

Meyer, K.E. (1994). Experimental and numerical investigation of turbulent flow and heat transfer in staggered tube bundles. PhD Thesis. Technical University of Denmark.

Michaelides, E.E. , Chang, Y. and **Bosworth, R.T.** (1986). Heat transfer coefficients and friction factors for banks of flexible vibrating tube in cross - flow. In Heat Transfer 1986, Proc. 8th Int. Heat Transfer Conference, San Francisco (Eds. C.L. Tien, V.P. Carey and J. K. Ferrell), Hemisphere Publishing, Vol. 6, pp. 2757 - 2762.

Mueller, A.C. (1983). Experimental data and correlations for tube banks. In Low Reynolds Number Flow Heat Exchangers, Advanced Study Institute Book (Eds. S. Kakac, R. K. Shah and A. E. Bergles), Hemisphere Publishing, pp. 415 - 429.

Murray, D.B. and **Fitzpatrick, J.A. (1991).** Heat transfer in a staggered tube array for a gas- solid suspension flow. *Trans. ASME, J. Heat Transfer*, Vol. 113, pp. 865 - 873.

Nadarajah, S. (1992). An experimental investigation of flows through inlet ports and valves, PhD Thesis, King's College London, University of London.

Nakamura, Y. and **Tomonari, Y. (1982).** The effects of surface roughness on the flow past circular cylinders at high Reynolds numbers. *J. Fluid Mech.*, Vol. 123, pp. 363 - 378.

Nassau, K. (1983). The physics and chemistry of colour. John Wiley & Sons.

Nebres, J. and **Batill, S. (1993).** Flow about a circular cylinder with a large-scale surface perturbation. *Experiments in Fluids*, Vol. 15, 369-379.

Nishimura, T. (1986). Flow across tube bundles. In Encyclopedia of Fluid Mechanics (Ed. N.P. Cheremisinoff), Gulf, Houston, Ch.23, Vol. 1, pp. 763 - 785.

Nishimura, T., Itoh, H. and **Miyashita, H. (1993).** The influence of tube layout on flow and mass transfer characteristics in tube banks in the transitional flow regime. *Int. J. Heat Mass Transfer*, Vol. 36, No. 3, pp. 553 - 563.

Norsworthy, K.H. (1979). Fourier transformation and spectrum analysis of sparsely sampled signals. In Laser Velocimetry and Particle Sizing (Eds. H.D.Thomson and W.H. Stevenson), Hemisphere, pp. 314 - 327.

Nouri, J.M., Whitelaw, J.H. and **Yianneskis, M. (1984).** The flow of dilute suspensions of particles around axisymmetric baffles, Imperial College, Mech. Eng. Dept. Internal Report FS/84/18.

Nouri, J.M., Whitelaw, J.H. and **Yianneskis, M. (1987).** Particle motion and turbulence in dense two-phase flows. *Int. J. Multiphase Flow*, Vol. 13, No. 6, pp. 729 - 739.

Nowshiravani, S., Dybbs, A., Edwards, R.V. and Farrokhalaee, T. (1982). Velocity measurements in rod bundles. Proc. Int. Symposium on Applications of LDA to Fluid Mechanics, Lisbon, 1982, Paper 15.5.

Oengöeren, A. and **Ziada, S. (1995).** Vortex shedding, accoustic resonance and turbulent buffeting in normal triangle tube arrays. In Flow-Induced Vibration (Ed. Bearman), Balkema, Rotterdam, pp. 295 - 313.

Ogden, T.R. and **Hendrics, E.W. (1984).** Liquid crystal thermography in water tunnels. *Experiments in Fluids*, Vol. 2, pp. 65 - 66.

Owen, P.R. (1965). Buffeting excitation of boiler tube vibration. *J. Mech. Engng. Science*, Vol. 7, pp. 431-439. *Cited by* Fitzpatrick and Donaldson (1980).

Owen, P.R. (1969). Pneumatic transport. *J. Fluid Mech.*, Vol. 39, No. 2, pp. 407 - 432.

Papavergos, P.G. and **Hedley, A.B. (1984).** Particle deposition velocity from turbulent flows. *Chem. Eng. Res. Des.*, Vol. 62, pp. 275 - 295.

Pettigrew, M.J. and **Taylor, C.E. (1991).** Fluidelastic instability of heat exchanger tube bundles: Review and design recommendations. *Trans. ASME, J. Pressure Vessel Technology*, Vol. 113, pp. 242-256.

Pierson, O.L. (1937). Experimental investigation of the influence of tube arrangement on convection heat transfer and flow resistance in cross flow of gases over tube banks. *Trans. ASME*, Vol. 59, pp. 563 -572.

Pilavachi, P.A. and **Isdale, J.D. (1992).** European Community R & D strategy in the field of heat exchanger fouling. Projects. In Fouling Mechanisms: Theoretical and Practical Aspects, Proc. Eurotherm Seminar No. 23, Grenoble, France (Eds. M. Bohnet, T.R. Bott, A.J. Karabelas, P.A. Pilavachi, R. Semeria and R. Vidil), Editions Europeennes Thermique et Industrie, pp. 13 - 20.

Platzer, K. H. , Hirsch, C., Metzger, D. E. and **Wittig, S. (1992).** Computer-based areal surface temperature and local heat transfer measurements with thermochromic liquid crystals (TLC). *Experiments in Fluids*, Vol. 13, pp. 26 - 32.

Polak, D.R. and **Weaver, D.S. (1995).** Vortex shedding in normal triangular tube arrays. *J. Fluids and Structures*, Vol. 9, pp. 1-17.

Press, W.H., Flannery, B.P., Teukolsky, S.A. and **Vetterling, W.T. (1986).** Numerical recipes, the art of scientific computing, Cambridge University Press.

Price, S. J., Paidoussis, M.P. and **Mark, B. (1995).** Flow visualisation of the interstitial cross-flow through parallel triangular and rotated square arrays of cylinders. J. *Sound and Vibration*, Vol. 181, No. 1, pp. 85 - 98.

Rae, G.J. and **Wharmby, J.S.** (1987). Strouhal numbers for in-line tube arrays. Proc. Int. Conference on Flow Induced Vibrations, Bowness-on Windermere, England, 1987, Paper E4, pp.233-242.

Rajan, P.K. and **Munukutla, S.S. (1992).** A comparative study of three techniques for estimation of turbulence energy spectrum. *Experiments in Fluids*, Vol. 12, pp. 422-424.

Rask, R.B. (1981). Comparison of window, smoothed-ensemble, and cycle-by-cycle data reduction techniques for laser Doppler anemometer measurements of in-cylinder velcocity. In Fluid Mechanics of Combustion Systems (Eds T.Morel, R.P. Lohmann and J.M. Rackley), ASME, New York.

Ribeiro, J. L. D. (1991a). Effects of surface roughness on the two-dimensional flow past circular cylinders I: mean forces and pressures. *Journal of Wind Engineering and Industrial Aerodynamics*, Vol. 37, pp. 299 - 309.

Ribeiro, J. L. D. (1991b). Effects of surface roughness on the two-dimensional flow past circular cylinders II: fluctuating forces and pressures. *Journal of Wind Engineering and Industrial Aerodynamics*, Vol. 37, pp. 311 - 326.

Roberts, J.B. and **Gaster, M. (1980).** On the estimation of spectra from randomly sampled signals: a method of reducing variability. *Proc.R.Soc.Lond. A*, Vol. 371, pp.235-258.

Roberts, J.B., Downie, J. and **Gaster, M. (1980).** Spectral analysis of signals from laser Doppler anemometer operating in the burst mode. *J. Phys. E: Sci. Instrum.*, Vol. 13, pp. 977-981.

Rodi, W. and **Scheurer, G. (1986).** Scrutinising the k-ε turbulence model under adverse pressure gradient conditions. *Trans. ASME, J. Fluids Engineering*, Vol. 108, pp. 174-179.

Rojas, J. and **Yianneskis, M. (1984).** The development of liquid crystal technique for the measurement of wall heat transfer coefficients in ducts. Imperial College, Mech. Eng. Dept. Report FS/84/27.

Roshko, A. (1961). Experiments on the flow past a circular cylinder at very high Re number. *J.Fluid Mech.*, Vol. 10, No. 3, 345-356.

Schlichting, H. (1968). Boundary Layer Theory. 6th edition, McGraw Hill.

Schulz, K., Behle, M. and **Leiner, W. (1996).** High local resolution measurements of heat transfer coefficients by liquid crystal thermography. Proc. Int. Seminar on Optical Methods and Data Processing in Heat and Fluid Flow, 18-19 April 1996, IMechE Conference Transactions, paper C516/016/96, pp. 57 - 69.

Shih, W.C.L., Wang, C., Coles, D. and **Roshko, A. (1993).** Expriments on flow past rough cylinders at large Reynolds numbers. *Journal of Wind Engineering and Industrial Aerodynamics*, Vol. 49, pp. 351 - 368.

Simonich, J. C. and **Moffatt, R. J. (1982).** Local measurements of turbulent boundary layer heat transfer on a concave surface using liquid crystals. Report No. HMT - 35, Stanford University, U.S.A, August 1982.

Simonin, O. and **Barcouda, M. (1986).** Measurements of fully developed turbulent flow across tube bundle. Proc. 3rd Int. Symposium on Applications of Laser Anemometry to Fluid Mechanics, Lisbon, paper 21.5.

Simonin, O. and **Barcouda, M. (1988).** Measurements and prediction of turbulent flow entering a staggered tube bundle. Proc. 4th Int. Symposium on Applications of Laser Anemometry to Fluid Mechanics, Lisbon, paper 5.23.

Simpson, H.C., Beggs, G.C. and **Raouf, M.I.N. (1984).** Air-water mist flow over extended surface tube banks. Proc. 1st U.K. National Conference on Heat Transfer, Leeds, 1984, Institution of Chemical Engineers Symposium Series No.86, Vol.2, pp. 745-760.

Skiepko, T. and **Lach, J. (1992).** Effect of fouling shape on overall heat transfer coefficient for a boiler tube with outer fouling layer. In Recent Advances in Heat Transfer (Eds. B.Sundén and A. Zukauskas), Elsevier, pp. 591-605.

Srikantaiah, D.V. and **Coleman, H.W. (1985).** Turbulence spectra from individual realization laser velocimetry data. *Experiments in Fluids*, Vol. 3, pp. 35-44.

Stephan, K. and **Traub, D. (1986).** Influence of turbulence intensity on heat transfer and pressure drop in compact heat exchangers. In Heat Transfer 1986, Proceedings of the 8th International Heat Transfer Conference, San Francisco (Eds. C.L. Tien, V.P. Carey and J. K. Ferrell), Hemisphere Publishing, Vol. 6, pp. 2739 - 2744.

Sterritt, D.C. and **Murray, D.B. (1992).** Heat-transfer mechanisms in an in-line tube bundle subject to a particulate cross flow. *Proc. Instn. Mech. Engrs.-Part C: J. Mechanical Engineering Science*, Vol. 206, pp. 317-326.

Sterritt, D.C., Murray, D.B. and **Fitzpatrick, J.A. (1992).** Heat transfer in an in - line tube bundle with a gas-particle cross flow. Heat Transfer - Proc. 3rd U.K. National Conference incorporating 1st European Conference on Thermal Sciences, Birmingham, 1992, Vol. 2, pp. 1172 - 1179.

Suen, K. O. (1992). Investigation of gas flow in a motored high speed diesel engine by laser-Doppler anemometry. PhD Thesis, King's College London, University of London.

Taborek, J., Aoki, T., Ritter, R.B., Palen, J.W. and **Knudsen, J.G. (1972).** Fouling: the major unresolved problem in heat transfer. *Chemical Engineering Progress*, Vol. 68, No. 2, pp. 59 - 67.

Tanda, G., Stasiek, J. and **Collins, M. W. (1995).** An experimental study by liquid crystals of forced convection heat transfer from a plate with vortex generators. Proc. 4th U.K. National Conference on Heat Transfer, 26-27 September 1995, IMechE Conference Transactions, paper C510/106/95. pp. 141 - 145.

Taylor, A.M.K.P. and **Whitelaw, J.H. (1984).** Velocity characteristics in the turbulent near wakes of confined axisymmetric bluff bodies. *J. Fluid Mech.*, Vol. 139, pp. 391 - 416.

Telionis, D.P., Gundappa, M. and **Diller, T.E. (1992).** On the organisation of flow and heat transfer in the near wake of a circular cylinder in steady and pulsed flow. *Trans. ASME, Journal of Fluids Engineering*, Vol. 114, pp. 348 - 355.

TEMA (1988). Standards of Tubular Exchanger Manufacturers Association, 7th edition, Tarrytown, NY 10591.

Tennekes, H. and **Lumley, J.L. (1972).** A first course in turbulence, MIT Press.

Traub, D. (1990). Turbulent heat transfer and pressure drop in plain tube bundles. *Chem. Eng. Process.*, Vol. 28, pp. 173 - 181.

Tropea, C. (1987). Turbulence-induced spectral bias in laser anemometry. *AIAA Journal*, Vol. 25, No. 2, pp. 306-309.

Tufte, P.H. and **Beckering, W. (1975).** A proposed mechanism for ash fouling burning Northern Great Plains Lignite. *Trans. ASME, Journal of Engineering for Power*, July 1975, pp. 407 - 412.

Varty, R.L. and **Currie, I.G. (1984a).** Measurements near a laminar separation point. *J. Fluid Mech.*, Vol. 138, pp. 1 - 19.

Varty, R.L. and **Currie, I.G. (1984b).** Index-matched laser-anemometer measurements of cross-flow in tube bundles. Proc. 2nd Int. Symposium on Applications of Laser Anemometry to Fluid Mechanics, Lisbon, Portugal, Paper 5.4.

Wallis, R. Pendennis (1939). A photographic study of fluid flow between banks of tubes. *Proc. IMechE*, Vol. 142, pp. 379 - 387.

Watwe, A.A. and **Hollingsworth, D.K. (1994).** Liquid crystal images of surface temperature during incipient pool boiling. *Experimental Thermal and Fluid Science*, Vol. 9, pp. 22 - 33.

Weaver, D.S. and **Abd-Rabbo, A. (1985).** A flow visualisation study of a square array of tubes in water crossflow. *Trans. ASME, J. Fluids Engineering*, Vol. 107, pp. 354 - 363.

Weaver, D.S. and **Fitzpatrick, J.A. (1988).** A review of cross-flow induced vibrations in heat exchnager tube arrays. *J. Fluids and Structures*, Vol. 2, pp. 73 - 93.

Weaver, D.S., Fitzpatrick, J.A. and **ElKashan, M. (1987).** Strouhal numbers for heat exchanger tube arrays in crossflow. *Trans. ASME, J. Pressure Vessel Technology*, Vol. 109, pp. 219 - 223.

Weaver, D.S., Lian, H.Y. and **Huang, X.Y. (1991).** A study of vortex shedding in a normal triangular tube array. In Flow Induced Vibrations, I.Mech.E, Paper C416/091, pp. 511 - 515.

Weaver, D.S., Lian, H.Y. and **Huang, X.Y. (1993).** Vortex shedding in rotated square arrays. *J. Fluids and Structures*, Vol. 7, pp. 107 - 121.

Wu, H., Patterson, G.K. and **Van Doorn, M. (1989).** Distribution of turbulence energy dissipation rates in a Rushton turbine stirred mixer. *Experiments in Fluids*, Vol. 8, pp. 153-160.

Wu, J., Welch, L.W., Welch, M.C., Sheridan, J. and Walker, G.J. (1994). Spanwise wake structures of a circular cylinder and two circular cylinders in tandem. *Experimental Thermal and Fluid Science*, Vol. 9, pp. 299 - 308.

Wyszecki, G. and **Stiles, W.S. (1982).** Color Science: concepts and methods, quantitative data and formulae, 2nd edition, John Wiley & Sons, USA.

Yan, X., Baughn, J. W., Rabas, T. J. and **Arman, B. (1995).** Liquid-crystal transient technique for measurement of in-tube local condensing heat transfer coefficients. *Experimental Heat Transfer*, Vol. 8, pp. 17 - 32.

Yanta, W. J. (1973). Turbulence measurements with a laser - Doppler velocimeter. Naval Ordnance Labs, White Oak, Silver Spring, Report NOLTR 73 - 94.

Yianneskis, M. (1982). Flow in reciprocating engine cylinders and curved ducts. PhD Thesis, Imperial College of Science and Technology, University of London.

Yianneskis, M. (1987). Velocity, particle sizing and concentration measurement techniques for multiphase flow. *Powder Technology*, Vol. 49, pp. 261 - 269.

Yianneskis, M. (1988). Thermal monitoring by liquid crystals. *Journal of Condition Monitoring*, vol. 2, pp. 139-151.

Yianneskis, M., Tindal, M.J. and **Nadarajah (1991).** Measurement of turbulence scales, moments, and spectra in engine flows. Proc. I.Mech.E., Experimental Methods in Engine Research and Development, pp. 127-133.

Zdravkovich, M.M. (1977). Review of flow interference between two circular cylinders in various arrangements. *Trans. ASME. J. Fluids Engineering*, Vol. 99, No. 4, pp. 618 - 633.

Zdravkovich, M.M. (1987). The effects of interference between circular cylinders in cross flow. *Journal of Fluids and Structures*, Vol. 1, pp. 239 - 261.

Ziada, S. and **Oengöeren, A. (1991).** Vorticity shedding and acoustic re sonance in an in-line tube bundle. Part one: vorticity shedding. In Flow Induced Vibrations, I.Mech.E., Paper C416/047, pp. 497-509.

Ziada, S., Oengöeren, A. and **Bühlmann, E. T. (1989).** On acoustical resonance in tube arrays Part I: Experiments. *J. Fluids and Structures*, Vol. 3, pp. 293 - 314.

Zukauskas, A. (1972). Heat transfer from tubes in crossflow. In Advances in Heat Transfer (Eds. J.P. Hartnett and T.F. Irvine), Academic Press, Vol. 8, pp. 93 - 160.

Zukauskas, A. (1983). Problems of heat transfer augmentation for tube banks in cross flow. In Heat Exchangers: Theory and Practice (Eds. J. Taborek, G. F. Hewitt and N. Afgan), Hemisphere Publishing, pp. 311 - 321.

Zukauskas, A. (1989). High-performance single-phase heat exchangers (Ed. J. Karni), Hemisphere Publishing, USA.

Zukauskas, A. A. and **Ulinskas, R.V. (1978).** Heat transfer efficiency of tube bundles in crossflow at critical Reynolds numbers. *Heat Transfer-Soviet Research*, Vol. 10, No. 5, pp. 9 - 15.

Zukauskas, A. A. and **Ulinskas, R.V. (1983).** Surface roughness as means of heat transfer augmentation for banks of tubes in crossflow. In Heat Exchangers: Theory and Practice (Eds. J. Taborek, G. F. Hewitt and N. Afgan), Hemisphere Publishing, pp. 311 - 321

APPENDIX I

FOURIER TRANSFORM

By applying Fast Fourier Tansform (FFT) the velocity data are transformed from the time domain to the frequency domain where they are described by a series of amplitudes as functions of the corresponding frequencies. The Fourier transform of a velocity field is a decomposition into waves of different wavelength, each of which is associated with a single Fourier coefficient.

For N consecutive values of a function sampled at a time interval h:

$$h_k \equiv h(t_k), \qquad t_k = k\,h, \qquad k = 0,1,2,....N-1$$

the discrete Fourier transform H_n is given by:

$$H_n \equiv \sum_{k=0}^{N-1} h_k e^{2\pi i k n / N} \tag{I.1}$$

The relation between the discrete Fourier transform of a set of numbers and their continuous Fourier transform when they are viewed as samples of a continuous function sampled at an interval h is $H(f_n) \approx h\,H_n$.

The discrete frequencies for the computation of the Fourier trasform for a block of N data points recorded at a time interval h are given by :

$$f_n = \frac{k}{Nh} \qquad \text{with } n = 0,1,....., N-1 \tag{I.2}$$

The formula for the discrete inverse Fourier transform that recovers the set of h_k's exactly from the H_n's is:

$$h_k \equiv \frac{1}{N}\sum_{n=0}^{N-1} H_n e^{-2\pi ikn/N} \tag{I.3}$$

The above definitions are those given by Press et al (1986). Various definitions of the Fourier Transform can be found in signal processing textbooks. The main difference is that the exponential term of the Fourier coefficients is usually negative in electrical engineering applications. Other differences stem from the normalisation of the Fourier coefficients by the length of the record.

Using *Mathematica* lengthy algorithms for the estimation of the Fourier coefficients do not have to be written since built-in commands for Fourier and inverse Fourier transforms are available. Furthermore, there is no restriction about the number of data points, e.g. that the number of data points should be a power of 2 which is usually the case when Fast Fourier Transform algorithms are used. The definitions used by *Mathematica* for the Fourier Transforms differ slightly from the ones in equations (I.1) and (I.3) in that the coefficients are normalised by the square root of the number of points. However, no correction is needed since both the Fourier and inverse Fourier transforms are carried out by *Mathematica*. A correction is necessary for the estimation of the power spectral density (PSD) only when the amplitude of the PSD estimates is of interest (e.g. in order to check that the sum of the PSD elements is equal to the r.m.s. squared or if correlation coefficients are estimated via FFT procedures).

APPENDIX II

POWER SPECTRA ESTIMATION

Although raw Fourier transformed data convey a lot of information about the frequencies present in a signal it is common practice to display and interpret spectral information by means of power spectra, where the amplitude of the spectrum is defined in terms of the power spectral density (PSD), that is the power per frequency interval. There are two techniques normally employed for the estimation of power spectral density: using FFT procedures (a periodogram) or via correlation estimates (a correlogram). More recent techniques are also available: a comparative study of techniques for the estimation of turbulence energy spectrum is given by Rajan and Munukutla (1992).

The periodogram technique was used in the present study. Again the definitions of PSD estimates found in the literature vary a lot due partly to different definitions of the discrete Fourier transform used but mostly to the normalisation of the power spectrum. Since the purpose in estimating the power spectra is mainly qualitative, i.e. to determine what frequencies are present in the flow, any definition could be used. However, in order to be consistent with the definition of the one-dimensional energy spectrum given by Hinze (1975):

$$\int_0^\infty E(f)df = \overline{u^2} \qquad \text{(II.1)}$$

where the r.h.s. term is the r.m.s. of the velocity fluctuations squared and E(f)df is the contribution to the latter of frequencies between f and f+df, various PSD estimators were tried at first, using a simple sinusoidal signal. It was found that both the definition by Press et al (1986) :

$$P(0) = P(f_o) = \frac{1}{N^2}\left|H_o\right|^2$$

$$P(f_k) = \frac{1}{N^2}\left[\left|H_k\right|^2 + \left|H_{N-k}\right|^2\right] \qquad k = 1,\ 2,\ldots..,\ (\frac{N}{2} - 1) \qquad \text{(II.2)}$$

$$P(f_c) = P(f_{N/2}) = \frac{1}{N^2}\left|H_{N/2}\right|^2$$

with f_k defined only for the zero and positive frequencies (as given in equation (I.2)) and the definition by Bendat and Piersol (1971) for one-sided power spectra (the positive frequency range of the PSD):

$$\tilde{G}_k = \frac{2h}{N}\left|H_k\right|^2 \qquad \text{(II.3)}$$

are appropriate because they are normalised in such a way that the sum of the PSD amplitudes up to the Nyquist frequency is equal to the r.m.s. of the data squared. On the contrary, the definition used by Kresta (1991) was found not appropriate in terms of the method of normalisation used.

However, the spectrum computed in this way is an estimate of the true spectrum since it is computed from a single time record of a random signal. The reliability of the PSD estimates can be improved and the variance can be reduced if a smoothing or averaging process is performed. This can be performed with one of the following techniques:

- block averaging: the original record is divided into data blocks of equal length, the PSD is estimated for each block and the PSD estimates at each frequency are averaged (this will result in reduced frequency resolution) or
- frequency smoothing: the periodogram estimates at K consecutive discrete frequencies are summed up or averaged to obtain a 'smoother' estimate at the mid

frequency of those K values. Summing is used instead of averaging solely to retain the normalisation property (Press et al, 1986).

A suitable window function can also be applied to the time series to reduce the effects of leakage. Many window functions can be found in the signal processing literature but for the purposes of this study the choice of window function is not that important. The Hanning window is one of the most commonly-employed window functions and was used in this study.

Cenedese et al (1992) applied most of the above techniques to LDA velocity data measured in a boundary layer. They concluded that the combination of block averaging and windowing operations gives the best results. A typical power spectrum estimated using 5 blocks of 1024 data and by applying a Hanning window is shown in Figure 3.14 in Chapter 3. Although the resolution is lower in this case the power spectrum is smoother than that obtained straight from the application of (II.3) to the data.

APPENDIX III

FILTERING TECHNIQUES FOR THE REMOVAL OF PERIODIC COMPONENTS

In order to isolate the high frequency fluctuations that represent the real turbulence and subsequently estimate the autocorrelation function and the turbulent scales, the frequency spectrum must be filtered first to remove any frequencies associated with the variation of the mean flow. Three techniques were examined:

a) the notch filtering technique;

b) low-pass filtering in the frequency domain;

c) moving window averaging in the time domain;

Notch filtering

The vortex shedding observed in the flow under investigation does not occur at a clearly defined frequency but rather at a narrow frequency band (notch). Furthermore, it is this flow periodicity that introduces a 'pseudo-turbulence' in the flow and it must be removed in order to estimate the real turbulence characteristics. The *notch filter* is a type of digital (recursive) filter specially designed to remove only a narrow frequency band around a specific frequency $\omega = \omega_0$ and it seems appropriate. Filtering takes place in the frequency domain and the following steps are followed: a FFT is applied to the velocity data, the resulting spectrum is multiplied with the notch filter function and finally an inverse FFT is applied to obtain the filtered velocity time series.

The filter frequency response function is generally defined as (Press et al, 1986):

$$H(f) = \frac{\sum_{k=0}^{M} c_k e^{-2\pi i(fh)}}{1 - \sum_{j=1}^{N} d_k e^{-2\pi i(fh)}} \qquad \text{(III.1)}$$

where h is the sampling time interval and the c's and d's are the filter coefficients given by the following equations for the case of notch filtering (Press et al, 1986):

$$\begin{aligned} c_o &= \frac{1+\omega_o^2}{(1+\alpha\omega_o)^2+\omega_o^2} \\ c_1 &= -2\frac{1-\omega_o^2}{(1+\alpha\omega_o)^2+\omega_o^2} \\ c_2 &= c_o \\ d_1 &= 2\frac{1-\alpha^2\omega_o^2-\omega_o^2}{(1+\alpha\omega_o)^2+\omega_o^2} \\ d_2 &= -\frac{(1-\alpha\omega_o)^2+\omega_o^2}{(1+\alpha\omega_o)^2+\omega_o^2} \end{aligned} \qquad \text{(III.2)}$$

where:

$\omega = \tan(\pi fh)$

ω_o = centre frequency of the notch and

α = width of the frequency notch as a fraction of ω_o.

The parameter α depends on the characteristics of the notch, that is the amplitude and the width of the frequency band. Since the vortex shedding notch varies in amplitude from point to point in the flow, different values of α ranging from 0.2 to 0.7 were needed in order to effectively remove the vortex shedding frequencies.

The application of the notch filtering technique to the velocity data is demonstrated in Figures III.1 and III.2. Figure III.1 shows a typical amplitude spectrum before (a) and after (b) filtering out the vortex shedding frequency. Figure III.2 shows the unfiltered velocity data, the filtered data (high frequency fluctuations) and the low

frequency velocity variation obtained after subtracting the filtered from the unfiltered data. Both Figures III.1 and III.2 refer to the same set of data

Moving window averaging and low-pass filtering

Moving window averaging and low pass filtering are equivalent techniques, the difference being that the first is applied in the time domain whereas the second in the frequency domain. Both techniques have been used widely in reciprocating engine flow studies where discrimination has to be made between the cycle-to-cycle variations of the flow and the in-cycle turbulence. The window averaging employed in engine research is slightly different to that employed here because averaging takes place over a crankangle range. In the technique used here mean velocity values are calculated for subsequent subsets of the instantaneous velocity data. More specifically, in order to estimate the bulk velocity and its variation with time, each 'bulk velocity' point U_i is derived by averaging (r+1) instantaneous velocity data points lying in the data window [$u_{i-r/2}$ to $u_{i+r/2}$] with r being the size of the window and i = r/2+1, ..., (N+1)-r/2. The procedure is repeated until (N-r) bulk velocity data are obtained. Data from the original velocity trace are used in the beginning and the end of the bulk velocity time series in order to have a record of length N. The bulk velocity estimates are subtracted from the instantaneous signal to obtain the fluctuating component.

The technique is straightforward but the choice of the window size is arbitrary. Various window sizes must be tried in order to select the most suitable one. This was done by inspecting how good the curve-fitting between the expected bulk velocity variation and the original trace was but also by checking the amplitude spectra of the bulk velocity estimates and the fluctuating component. If a very small window was used then high frequency fluctuations were removed together with the low frequency variations. On the other hand, if a large window was used the vortex shedding notch

was not removed. The window size depends also on the sampling rate. Since the sampling rate used in this study varied from one point in the flow to the other, the window size had to be adjusted accordingly. The instantaneous, bulk and fluctuating velocity variations obtained by applying moving window averaging to the trace used in Figures III.1 and III.2 are shown in Figure III.3. A window of 41 data points was found to be the most suitable since it removed the vortex shedding notch as it can be seen from Figures III.4 (a) and (b) where the amplitude spectra of the fluctuating and bulk velocity variation are shown respectively.

Low pass filtering is carried out in the frequency domain: the Fourier coefficients above a pre-selected cut-off frequency are set to zero and an inverse FFT is carried out to yield the low frequency signal. The latter is then subtracted from the instantaneous velocity record to yield the high frequency part of the signal. The selection of the cut-off frequency is the most critical part and it is arbritrary like the window size mentioned above. Le Coz et al (1990) suggested that the cut-off frequency can be taken either as the highest frequency in the ensemble mean velocity or the inverse of the decay time of the random component in the autocorrelation function. They also observed that, as might be expected, the high frequency contribution decreases when the cut-off frequency is increased. In the flow under study, however, it was considered reasonable to select the vortex shedding frequency as a cut-off frequency. Since the former is a frequency band the cut-off frequency expected to be more suitable is the one that results in the removal of the whole vortex shedding notch.

The bulk and fluctuating velocity component variations obtained by low-pass filtering are shown in Figure III.5. Notch filtering was found to be the most appropriate of the three techniques and was used for the analysis of the velocity data.

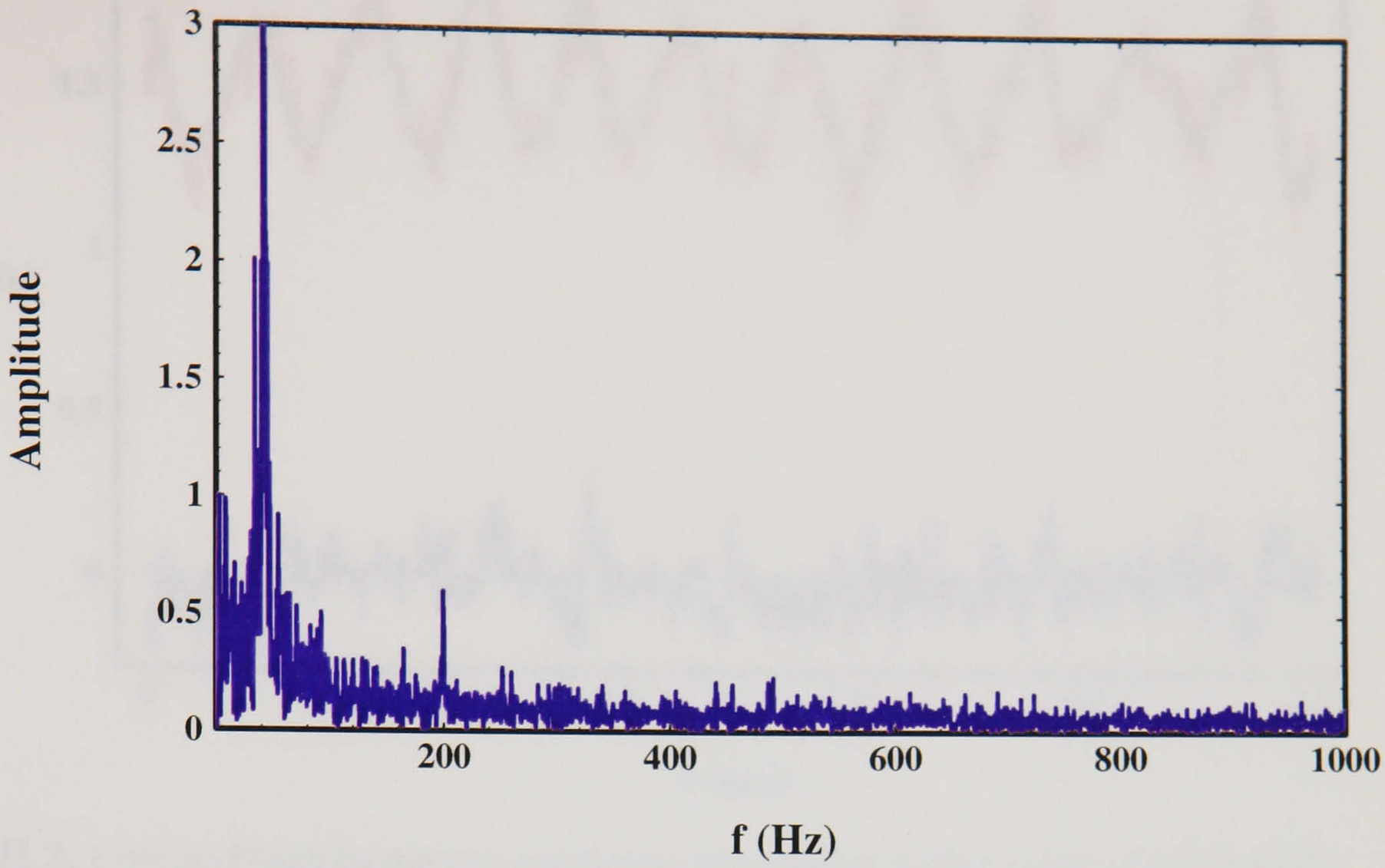

(a)

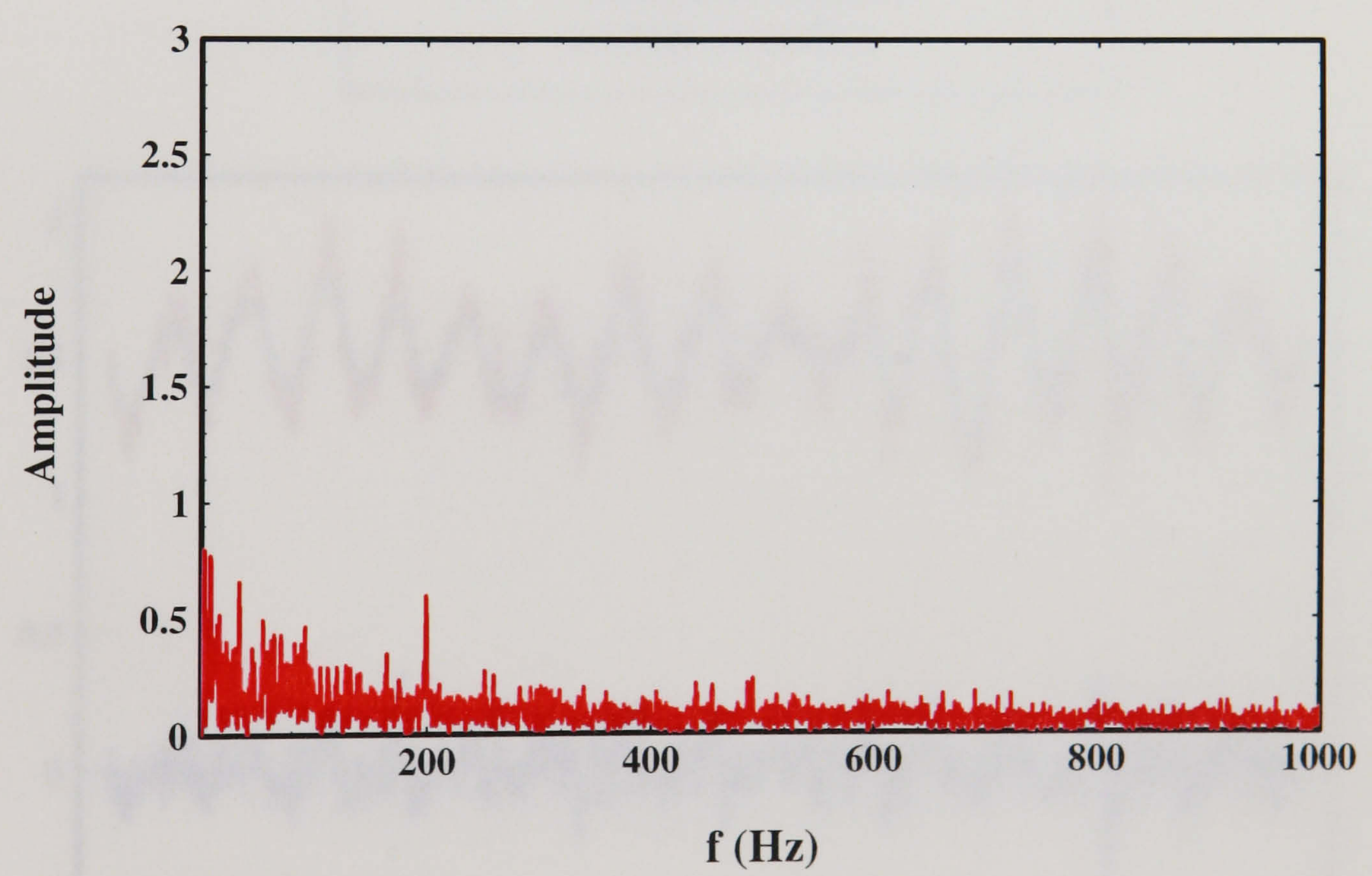

(b)

Figure III.1. Amplitude spectrum of velocity recording at x/d=1.6 and y/d=0.6 before (a) and after (a) applying notch filtering to the vortex shedding frequency; dc component is also removed.

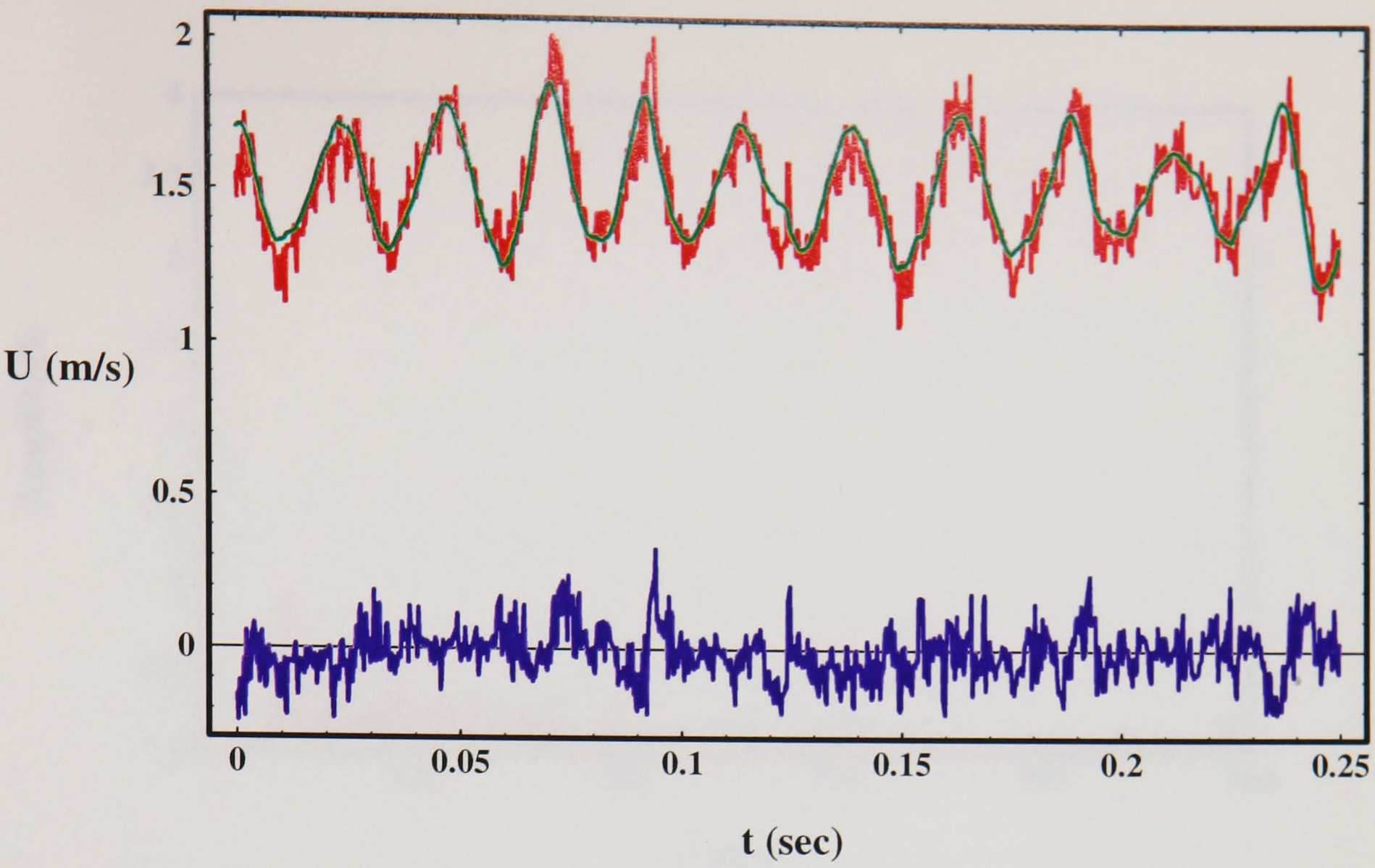

Figure III.2. Low and high frequency variations obtained at x/d=1.6 and y/d=0.6 when notch filtering is applied; only part of the record is shown.

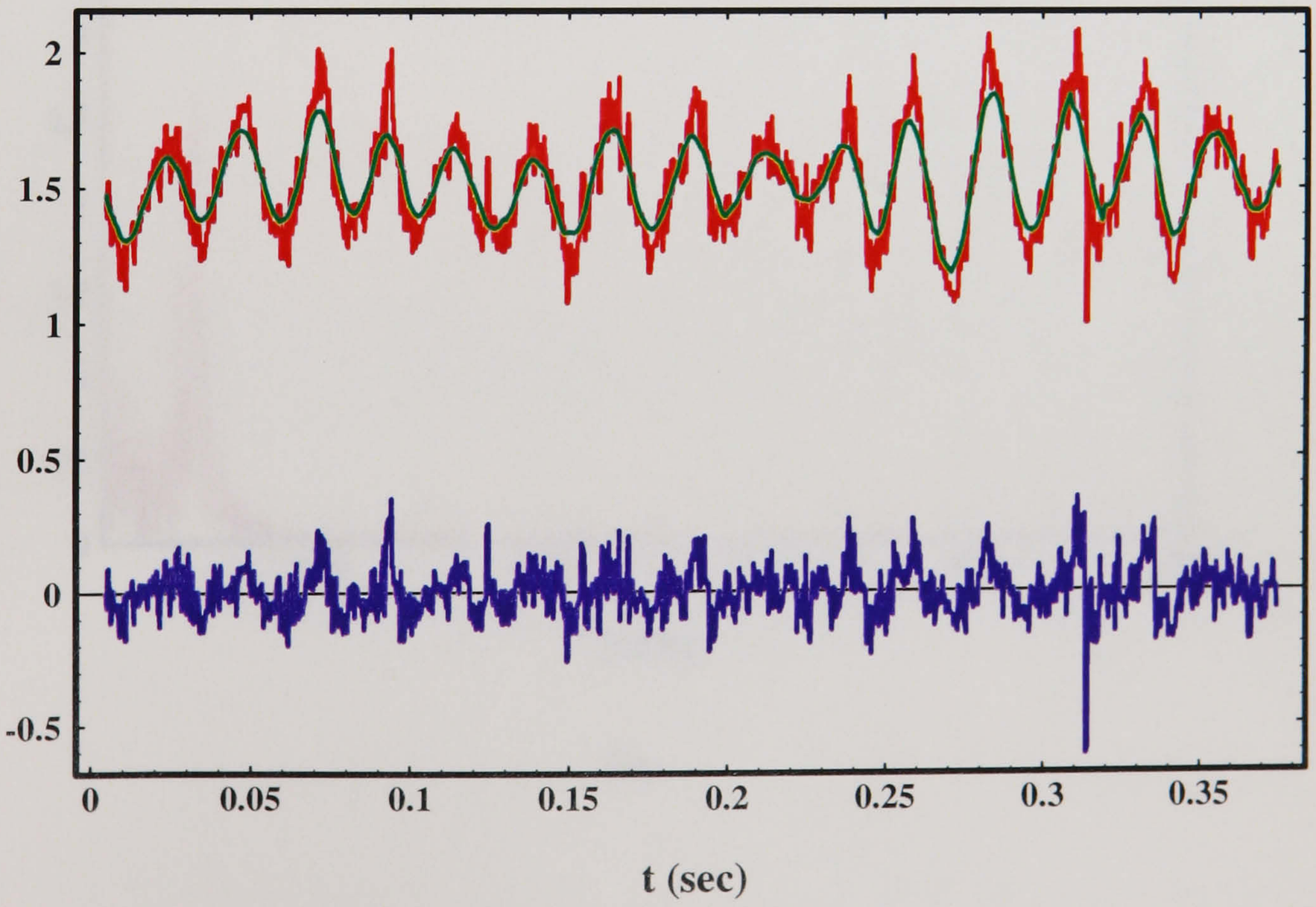

Figure III.3. Low and high frequency variations obtained at x/d=1.6 and y/d=0.6 when moving window averaging is applied (window size = 41); only part of the record is shown.

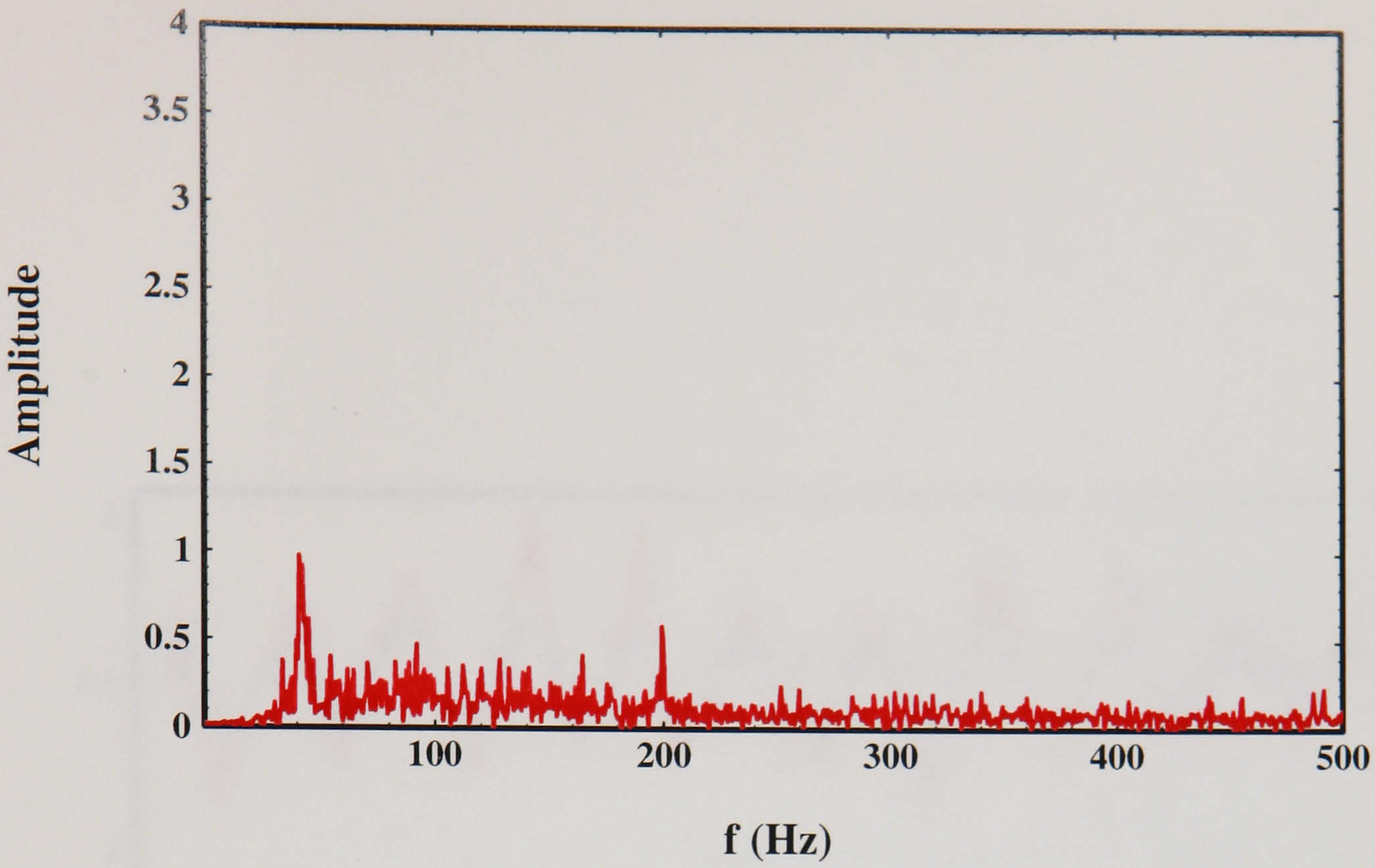

(a)

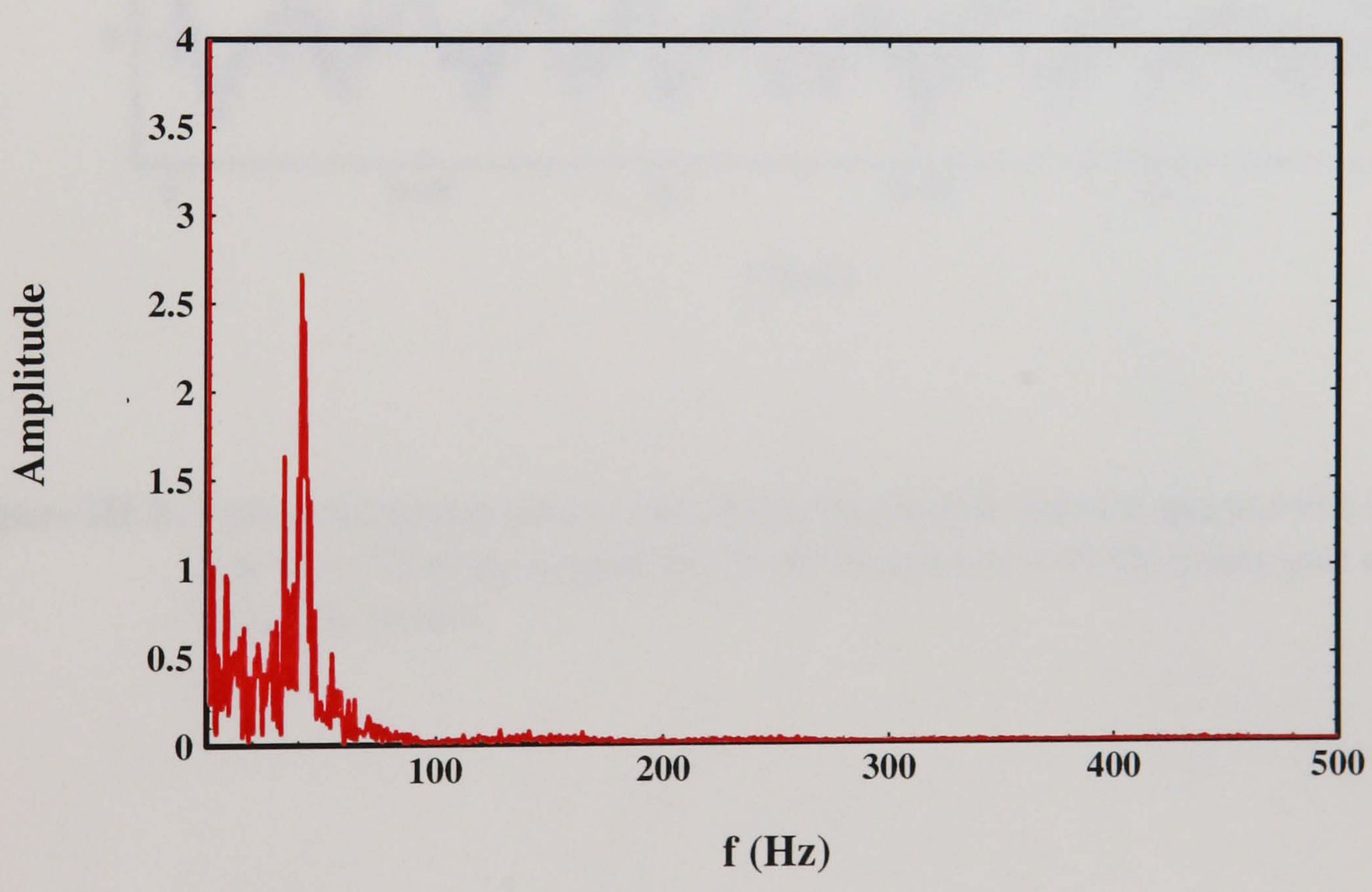

(b)

Figure III.4. Amplitude spectra of the high (a) and low (b) frequency oscillations at x/d=1.6 and y/d=0.6 obtained with moving window averaging (window size=41).

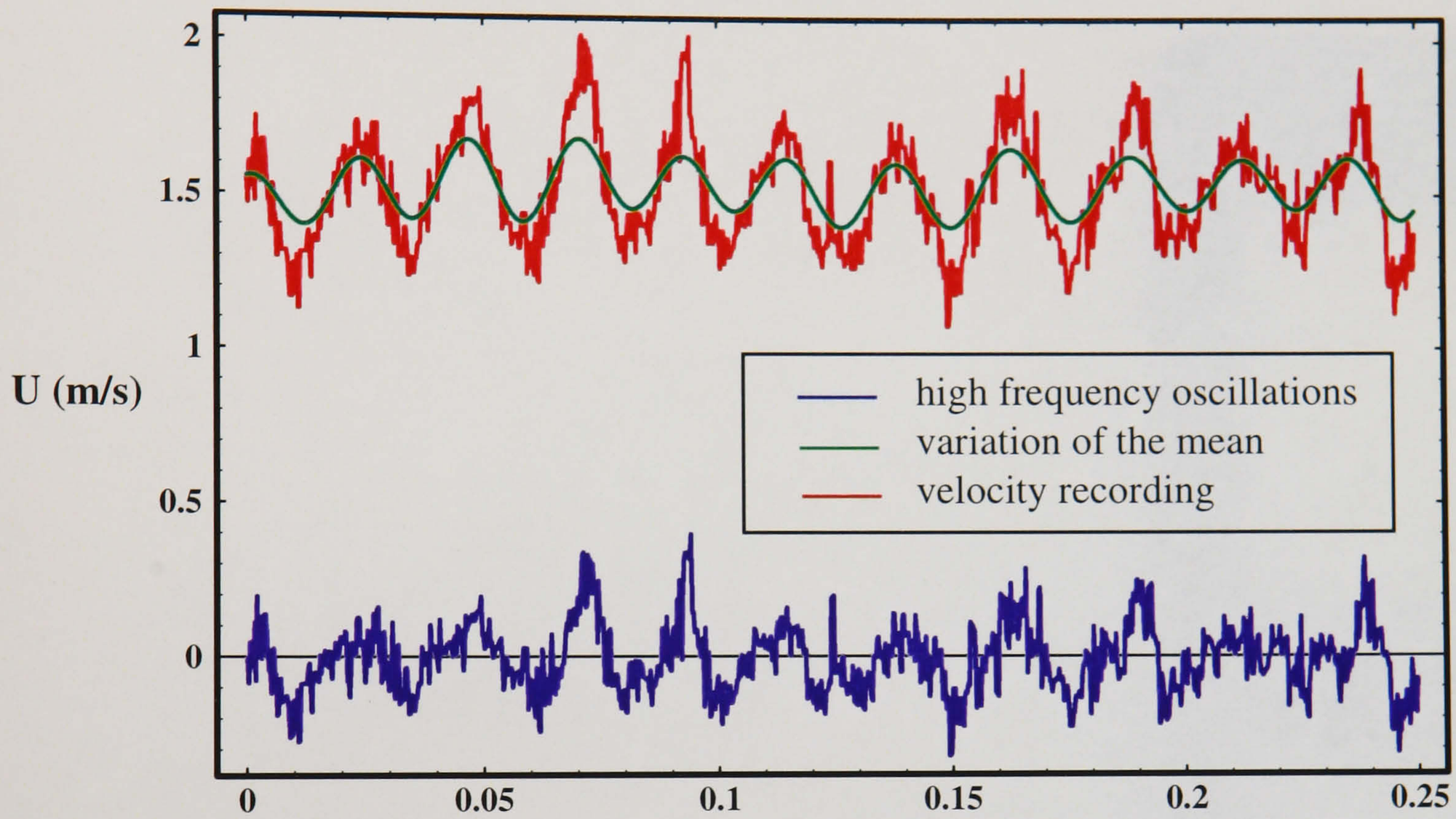

Figure III.5. Low and high frequency variations obtained at x/d=1.6 and y/d=0.6 when low pass filtering is applied (cut-off frequency = 49 Hz); only part of the record is shown.